STATE OF CALIFORNIA • DEPARTMENT OF TRANSPORTATION

TECHNICAL REPORT DOCUMENTATION PAGE

TR0003 (REV 10/98)

ADA Notice

For individuals with sensory disabilities, this document is available in alternate formats. For information call (916) 654-6410 or TDD (916) 654-3880 or write Records and Forms Management, 1120 N Street, MS-89, Sacramento, CA 95814.

1. REPORT NUMBER	2. GOVERNMENT ASSOCIATION NUMBER	3. RECIPIENT'S CATALOG NUMBER
CA17-2539		

4. TITLE AND SUBTITLE

Interaction of MSE Abutments with Bridge Superstructures under Seismic Loading – Shaking Table Tests

5. REPORT DATE

01/2018

6. PERFORMING ORGANIZATION CODE

7. AUTHOR

John S. McCartney, P. Benson Shing, Yewei Zheng, Wenyong Rong, and Patrick J. Fox

8. PERFORMING ORGANIZATION REPORT NO.

UCSD/SSRP 18-01

9. PERFORMING ORGANIZATION NAME AND ADDRESS

Department of Structural Engineering
School of Engineering
University of California, San Diego
La Jolla, California, 92093-0085

10. WORK UNIT NUMBER

11. CONTRACT OR GRANT NUMBER

65A0556

12. SPONSORING AGENCY AND ADDRESS

California Department of Transportation
Division of Engineering Services
1801 30th Street, MS #9-2/5I
Sacramento, California 95816

13. TYPE OF REPORT AND PERIOD COVERED

Final Report

14. SPONSORING AGENCY CODE

15. SUPPLEMENTARY NOTES

This project will also include a second final report for FHWA Pooled Fund project 1892AEA entitled "Interaction of MSE Abutments with Bridge Superstructures under Seismic Loading – Numerical Simulations".

16. ABSTRACT

This report presents results from shaking table tests on half-scale mechanically-stabilized earth (MSE) bridge abutments. The testing program consists of five tests where the direction of shaking is in the longitudinal direction of the bridge beam, and one test where the direction of shaking is perpendicular to the bridge beam. The longitudinal shaking tests include a baseline configuration and a parametric study of different configurations to investigate the effects of bridge surcharge stress, reinforcement spacing, reinforcement stiffness, and steel reinforcement on the seismic response of MSE bridge abutments. Experimental design of the scale model followed established similitude relationships for shaking table testing in a 1g gravitational field, including scaling for of geometry, reinforcement stiffness, backfill soil modulus, bridge surcharge stress, and characteristics of the earthquake motions. Facing displacements, bridge seat settlements, accelerations, vertical and lateral stresses, reinforcement strains, and contact forces between the bridge beam and bridge seat were measured for different instrumented sections to evaluate the three-dimensional dynamic response during a series of applied shaking motions. Results indicate that reinforcement spacing and reinforcement stiffness have the most significant effects on the facing displacements and bridge seat settlements for dynamic loading conditions.

17. KEY WORDS	18. DISTRIBUTION STATEMENT	
Mechanically stabilized earth, bridge abutments, seismic response, shaking table testing, geogrids	No restrictions. This document is available to the public through the National Technical Information Service, Springfield, Virginia 22161	
19. SECURITY CLASSIFICATION *(of this report)*	**20. NUMBER OF PAGES**	**21. COST OF REPORT CHARGED**
None	367	

DISCLAIMER

This document is disseminated in the interest of information exchange. The contents of this report reflect the views of the authors who are responsible for the facts and accuracy of the data presented herein. The contents do not necessarily reflect the official views or policies of the State of California or the Federal Highway Administration. This publication does not constitute a standard, specification or regulation. This report does not constitute an endorsement by the California Department of Transportation of any product described herein.

For individuals with sensory disabilities, this document is available in Braille, large print, audiocassette, or compact disk. To obtain a copy of this document in one of these alternate formats, please contact: the Division of Research and Innovation, MS-83, California Department of Transportation, P.O. Box 942873, Sacramento, CA 94273-0001.

University of California, San Diego
Department of Structural Engineering
Structural Systems Research Project

Report No. SSRP 18-01

Interaction of MSE Abutments with Bridge Superstructures under Seismic Loading – Shaking Table Tests

by

John S. McCartney, Ph.D., P.E.
Associate Professor

P. Benson Shing, Ph.D.
Professor and Chair

Yewei Zheng, Ph.D.
Postdoctoral Research Scholar

Wenyong Rong
Graduate Research Assistant

Patrick J. Fox, Ph.D., P.E.
Shaw Professor and Department Head

Final Report submitted to the California Department of Transportation
under Contact No. 65A0556

Department of Structural Engineering
University of California, San Diego
La Jolla, California 92093-0085

January 2018

STRUCTURAL SYSTEMS
RESEARCH PROJECT

Report No.
SSRP 18-01

Interaction of MSE Abutments with Bridge Superstructures under Seismic Loading – Shaking Table Tests

by

John S. McCartney

P. Benson Shing

Yewei Zheng

Wenyong Rong

Patrick J. Fox

Final Report.

January 2018

Department of Structural Engineering
University of California, San Diego
La Jolla, California 92093-0085

ACKNOWLEDGEMENTS

Financial support for this study provided by the California Department of Transportation (Caltrans) Project 65A0556 with Federal Highway Administration (FHWA) Pooled Fund Project 1892AEA is gratefully acknowledged. The authors thank Charles Sikorsky of Caltrans and Lu Saechao of Washington DOT for their supervision of these projects, respectively. The authors thank Kathryn Griswell of Caltrans, Tony Allen of Washington DOT, and Jim Higbee of Utah DOT for their constructive comments on this report as well as on progress reports throughout the project. The authors also thank the staff and undergraduate research assistants at the UCSD Powell Structural Laboratories for their help with the experimental work. The geogrids used in this study were provided by Tensar International Corporation.

ABSTRACT

This report presents results from shaking table tests on half-scale mechanically-stabilized earth (MSE) bridge abutments. The testing program consists of five tests where the direction of shaking is in the longitudinal direction of the bridge beam, and one test where the direction of shaking is perpendicular to the bridge beam. The longitudinal shaking tests include a baseline configuration and a parametric study of different configurations to investigate the effects of bridge surcharge stress, reinforcement spacing, reinforcement stiffness, and steel reinforcement on the seismic response of MSE bridge abutments. Experimental design of the scale model followed established similitude relationships for shaking table testing in a 1*g* gravitational field, including scaling of geometry, reinforcement stiffness, backfill soil modulus, bridge surcharge stress, and characteristics of the earthquake motions. Facing displacements, bridge seat settlements, accelerations, vertical and lateral stresses, reinforcement strains, and contact forces between the bridge beam and bridge seat were measured for different instrumented sections to evaluate the three-dimensional dynamic response during a series of applied shaking motions. Results indicate that reinforcement spacing and reinforcement stiffness have the most significant effects on the facing displacements and bridge seat settlements for dynamic loading conditions.

Table of Contents

Chapter 1 Introduction

Although the concept of reinforced soil has been used for millennia, the design approach for reinforced soil was formalized by Henri Vidal in the early 1960s. Since that time, reinforced soil technology has been used in many fill-type construction applications, including reinforced slopes, embankments, and retaining walls. Reinforced soil in retaining walls has seen extensive use in transportation infrastructure because it provides many advantages over traditional gravity- or cantilever-type retaining walls, including lower cost, faster and easier construction, and acceptable deformation performance under static and seismic loading conditions (Berg et al. 2009). Two design philosophies for using reinforced soil retaining walls have been adopted by the US Federal Highway Administration (FHWA), mechanically-stabilized earth (MSE) walls and geosynthetic reinforced soil (GRS) walls. The design philosophy for MSE walls is described in detail in FHWA-NHI-10-024 (Berg et al. 2009). MSE walls involve either inextensible metallic reinforcements or extensible geosynthetic reinforcements embedded in compacted granular soil, and the reinforcement spacing and length is determined in design by assuming that they are tie-back anchors. The design philosophy for GRS walls is described in detail in FHWA-HRT-11-026 (Adams et al. 2011a). GRS walls involve closely-spaced geosynthetic reinforcements (spacing $\leq$ 12 inches) embedded in compacted granular soil to form a GRS composite material. Despite the difference in design philosophies for MSE and GRS walls, many technical papers use these acronyms interchangeably when describing retaining walls and bridge abutments reinforced with geosynthetics. In the literature review for this report, the term "GRS" is used when discussing geosynthetic reinforced soil structures in general, even when they may not have been designed following the reinforcement spacing requirement in the GRS design philosophy described by Adams et al. (2011a).

In recent years, MSE walls have been used as bridge abutments where the bridge beam load is applied as a surcharge to the top of a reinforced soil mass via a shallow footing. This concept offers significant cost and construction time savings in comparison to traditional pile-supported bridge abutment designs and can reduce differential settlements between the bridge and approach roadways (Abu-Hejleh et al. 2002). The Earth Retaining Systems, Substructures, Loads, and General Earthquake Committees of Caltrans released a joint position paper on MSE bridge abutments (Caltrans 2017). In the joint position paper, MSE walls were approved for use in Type 1 and Type 2 MSE bridge abutments, which are shown in Figure 1.1 and Figure 1.2, respectively. The bridge beam load is supported by a footing resting on the MSE wall for the Type 1 MSE bridge abutment, whereas the bridge beam load is supported on a footing resting on piles for the Type 2 MSE bridge abutment. Even though the Type 1 and Type 2 MSE bridge abutments have been approved for use by Caltrans, their response under seismic loading is uncertain and further refinements may be needed for their design. In addition, the FHWA has developed a newer bridge abutment design called the geosynthetic reinforced soil-integrated bridge system (GRS-IBS) shown in Figure 1.3 in which the bridge superstructure and the approach fill are more integrated,

with the bridge beam resting directly on the reinforced soil mass (Adams et al. 2011a). However, this GRS-IBS abutment has not been approved for use by Caltrans (Caltrans 2017). Therefore, this study only focuses on understanding the seismic response of Type 1 MSE bridge abutments.

Many studies have shown that the MSE and GRS bridge abutments have acceptable deformations under service load conditions. For example, Lee and Wu (2004) reviewed several case studies of in-service GRS bridge abutments (Won et al. 1996; Abu-Hejleh et al. 2002), and reported generally satisfactory performance in terms of lateral facing displacements and bridge seat settlements under service load conditions. Several case histories for in-service geosynthetic reinforced soil-integrated bridge system (GRS-IBS) abutments also have been reported, and each show good field performance regarding bridge settlement, abutment compression, and differential settlement (Adams et al. 2007, 2008, 2011b; Warren et al. 2010; Budge et al. 2014; Saghebfar et al. 2017).

A concern regarding the use of MSE bridge abutments is that the magnitude of vertical settlements of the backfill during a major earthquake is uncertain, and research is needed to clarify if the magnitude of these vertical settlements may be large enough to impose unacceptable stresses in a multi-span bridge beam with internal (column) supports. Associated lateral displacements of the MSE bridge abutment due to seismic loading are also a potential concern. Thus, while MSE bridge abutment technology offers substantial cost- and time-savings for construction, there are concerns regarding the use of this technology in high seismic areas like California and little information is available to validate numerical simulations that can be used to guide designers on how to improve the seismic response of these structures. Yen et al. (2011) conducted post-earthquake reconnaissance for the 2010 Maule Earthquake, and found that a MSE bridge abutment exhibited no signs of lateral or vertical displacements after shaking. However, the bridge suffered minor damage that may have resulted from the severe bridge skew angle. Shaking table tests conducted by Helwany et al. (2012) on a 3.6 m-high GRS bridge abutment indicated no significant distress during shaking with horizontal accelerations up to 1*g*. Due to the limited information on the seismic performance of MSE bridge abutments in the field and in previous shaking table tests, more experimental testing and evaluation are needed to understand the potential issues and for impacts of different design variables on the performance characteristics of MSE bridge abutments.

The overall purpose of this project was to investigate the seismic response of MSE bridge abutments through physical testing and numerical modeling. The specific objectives are to understand the effects of different variables on the seismic response of MSE bridge abutments, including the bridge surcharge stress, geosynthetic reinforcement spacing, geosynthetic reinforcement stiffness, type of reinforcement (steel vs. geosynthetic), and direction of shaking (transverse and longitudinal). Understanding the seismic response of MSE bridge abutments includes understanding the facing displacements, bridge seat settlements, and interactions between the bridge seat and the bridge beam. This report focuses on the experimental results obtained from physical testing of reduced-scale models configured to follow the Type 1 MSE bridge abutment

design in Figure 1.1 as closely as possible given the constraints of the shaking table facility used in this project. This report presents results and analysis from a total of six shaking table tests on half-scale MSE bridge abutments with various configurations and loading conditions. The variables noted above are investigated via comparison of instrumentation results from the six tests performed. A separate report will be published on the results of the numerical simulations along with associated design guidance for the seismic response of MSE bridge abutments.

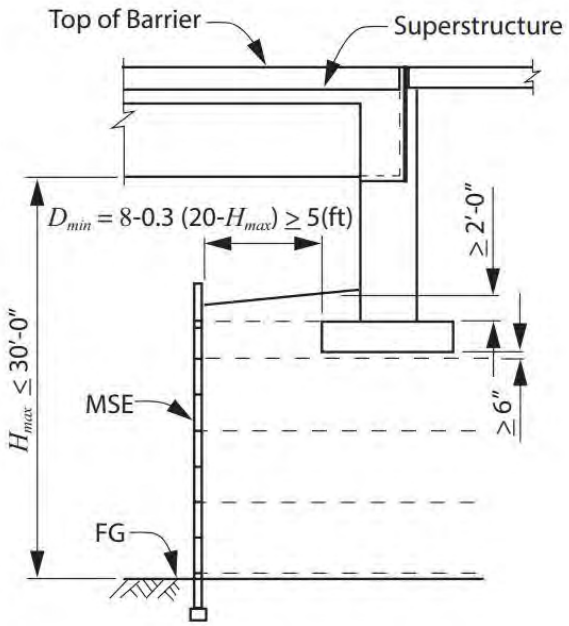

Figure 1.1 Typical geometry for Type 1 MSE bridge abutment (Caltrans 2017).

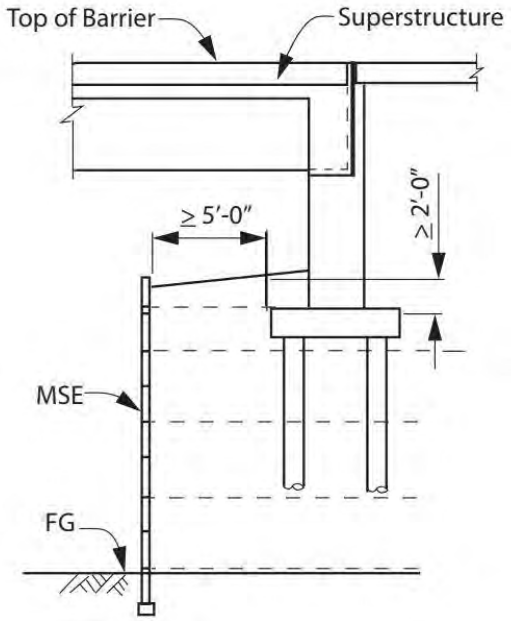

Figure 1.2 Typical geometry for Type 2 MSE bridge abutment (Caltrans 2017).

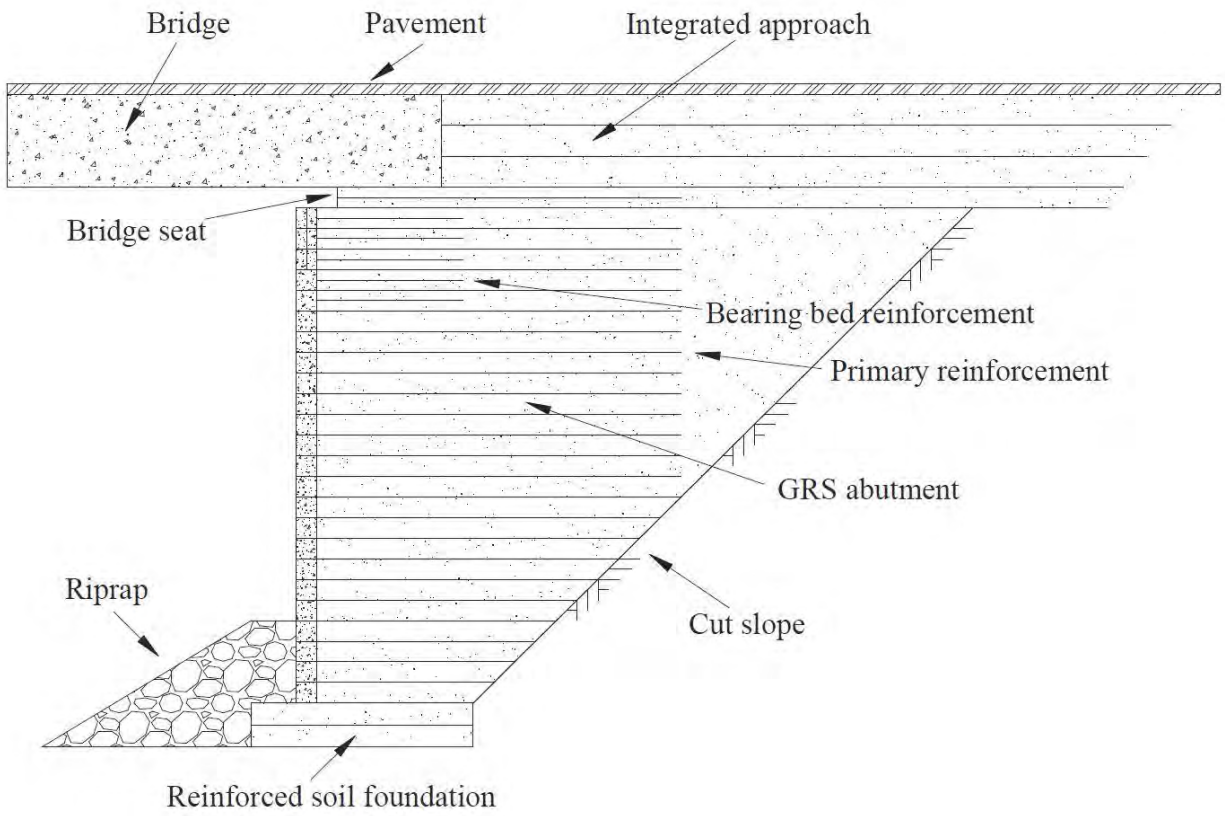

Figure 1.3 Typical geometry for GRS-IBS bridge abutment (after Adams et al. 2011a).

Chapter 2 Literature Review

2.1 Static Response in Laboratory Model Tests

The geotechnical research group at the Royal Military College (RMC) of Canada conducted a testing program to investigate the behavior of full-scale GRS retaining wall model tests that started in 1987. The behavior of GRS retaining walls were measured during construction, under working stresses, and under surcharge stresses approaching failure. The GRS wall models were 3.6 m-high and 3.4 m-wide and were tested in plane strain conditions. The backfill soil extended approximately 6 m from the facing, which was sufficient so that there was both a reinforced soil zone behind the wall facing and a retained soil zone without geosynthetic reinforcement. The backfill soil was a uniformly graded sand with rounded particles with a peak plane strain friction angle of 44°. The reinforcements included biaxial polypropylene (PP) and polyester (PET) geogrids. Bathurst et al. (2000) investigated the effects of reinforcement stiffness, reinforcement spacing, and wall facing type on the performance of GRS walls. Four GRS wall models were constructed and loaded up to the surcharge stress of 115 kPa. Results indicate that lateral facing displacements can be reduced by increasing reinforcement stiffness or decreasing vertical reinforcement spacing. The toe of the GRS walls was found to carry a significant portion of the total horizontal earth forces. Bathurst (2006) and Bathurst et al. (2006, 2009) reported results for another series of 11 full-scale GRS wall models to investigate the effects of reinforcement type, reinforcement stiffness, reinforcement spacing, backfill compaction effort, wall facing stiffness and batter. Results indicated that peak loads in the reinforcement for a wrapped-face wall were about 3.5 times larger than those for modular block face wall at the end of construction, and increased about 2 times under the surcharge stress of 80 kPa. The modular block facing acted as a structural element that reduced lateral facing displacements and reinforcement strains. For the GRS walls with modular block facing and incremental panel facing, connection loads were the largest in the reinforcement at the end of construction. Results also indicated that the effect of compaction effort was as important as reinforcement stiffness at the end of construction. However, the effect became attenuated as the surcharge stress increased, and the effect was almost erased at the surcharge stress of 30 kPa.

Ehrlich et al. (2012), Ehrlich and Mirmoradi (2013), Mirmoradi et al. (2016), and Mirmoradi and Ehrlich (2016) conducted a series of physical model tests to investigate the effects of compaction effort, facing stiffness, and toe resistance on the behavior of GRS walls. The 1.5 m-high model wall was subjected to a surcharge stress of 100 kPa to simulate the bottom potion of a 7 m-high prototype GRS wall. The backfill soil was a well-graded sand, and the reinforcement was a PET geogrid. The summation of mobilized tensile forces along the reinforcement layers for the GRS wall with heavy compaction at the end of construction were much larger than for the wall with light compaction. However, the difference decreased with increasing surcharge stress, and the summation of tensile forces were approximately the same at the surcharge stress of 100 kPa. For the restrained toe condition, the facing stiffness had an important effect on the reinforcement

tensile forces. The mobilized tensile forces were also affected by the properties of the interface between the facing column and foundations soil. A higher toe restraint resulted in greater toe load and lower reinforcement tensile forces, and smaller lateral facing displacements.

2.2 Static Response in Field Loading Tests

Experimental studies, including field and laboratory loading tests, have been conducted for large-scale GRS piers and abutments and generally indicated satisfactory performance under service load conditions and relatively large load capacity (Adams 1997; Gotteland et al. 1997; Ketchart and Wu 1997; Wu et al. 2001, 2006a; Nicks et al. 2013, 2016; Adams et al. 2014; Iwamoto et al. 2015). Lee and Wu (2004) reviewed the results of several large-scale loading tests and suggested that the bearing capacity can be high for closely spaced reinforcement and well graded and well compacted backfill soil.

Gotteland et al. (1997) conducted full-scale loading tests to investigate the failure behavior of GRS walls as bridge support structures. The tested model consisted of two GRS wall sections with one reinforced using woven geotextiles and the other using nonwoven geotextiles. The backfill material was a fine sand with a friction angle of 30° and an apparent cohesion of 2 kPa, and was compacted to the maximum dry density corresponding to the standard Proctor compaction effort. An intermediate reinforcement in the woven geotextile reinforced soil wall was shorter than in that in the nonwoven geotextile reinforced soil wall. Loading was applied on top of each GRS wall through a foundation slab. For the nonwoven geotextile-reinforced soil wall, the applied load at failure was 140 kN/m with a settlement of 36 mm, while for the woven geotextile-reinforced soil wall the applied load at failure was 123 kN/m with a settlement of 33 mm.

Adams (1997) reported full-scale loading tests on a 5.4 m-high bridge pier at the Turner-Fairbank Highway Research Center in McLean, Virginia. The GRS bridge pier was reinforced using woven geotextile at a vertical spacing of 0.2 m. The backfill material was a well-graded gravel and was compacted to 95% of the maximum dry density corresponding to the standard Proctor compaction effort. The GRS bridge pier had a settlement of 13 mm and maximum lateral facing displacement of 6 mm at the intermediate height of 3.0 m under a surcharge stress of 200 kPa, which indicated the satisfactory performance of GRS bridge pier under service load conditions. At the full height of 5.4 m, the GRS bridge pier settlements were 25 mm and 70 mm under vertical stresses of 415 kPa and 900 kPa, respectively.

Ketchart and Wu (1997) conducted full-scale loading tests on two GRS bridge piers and one GRS bridge abutment. The outer GRS bridge pier and GRS bridge abutment were 7.6 m high and the center pier was 7.3 m high. Each structure was reinforced using woven geotextile at a vertical spacing of 0.2 m. The backfill was a “road base” material with 13% of fines. The applied vertical stresses are 232 kPa and 130 kPa on the outer pier and abutment, respectively. Measured

settlements were 36.6 mm for the GRS bridge pier and 27.1 mm for the GRS bridge abutment, corresponding to vertical strains of 0.35% and 0.48%, respectively.

Wu et al. (2001) conducted loading tests on two GRS bridge abutments that supported a 36 m-span steel arch bridge in Black Hawk, Colorado. In each GRS bridge abutment, two square footings were placed on top of the lower wall and one strip footing was constructed on the upper wall. The GRS bridge abutments were reinforced using woven geotextile at a vertical spacing of 0.3 m. The backfill material was an on-site soil with 12% of fines and had a friction angle of 31.3° and cohesion of 34.3 kPa. Four square footings were preloaded to a vertical stress of 245 kPa, and then reloaded to the design stress of 150 kPa. Results indicated that settlements of four square footings under the design stress could be reduced by a factor of 1.5 to 6 by preloading to a vertical stress of 245 kPa.

Wu et al. (2006a) reported results for the NCHRP full-scale loading tests on back-to back GRS bridge abutments conducted at the Turner-Fairbank Highway Research Center in McLean, Virginia. The GRS bridge abutment models were 4.65 m high and were constructed in a back-to-back configuration. A non-plastic silty sand with a friction angle of 37.3° and an apparent cohesion of 20 kPa was used as the backfill material. The GRS bridge abutments had both primary and secondary reinforcements (three layers at the top). Two woven geotextile reinforcements, one with an ultimate strength of 70 kN/m and the other one with an ultimate strength of 21 kN/m, were used. At a maximum allowable vertical stress of 200 kPa, the compressions of GRS bridge abutments were 40 mm and 72 mm, respectively. During continued loading, the two GRS bridge abutments failed at applied vertical stresses of 814 kPa and 414 kPa, respectively, corresponding to abutment compressions of 163 mm and 175 mm, respectively.

A series of performance tests on 2 m-high GRS mini-piers were conducted by the FHWA to investigate the effects of various factors on the behavior of GRS composite structures (Nicks et al. 2013a, 2016; Adams et al. 2014; Iwamoto et al. 2015). Results indicated that reinforcement spacing and strength have the most important effects on the ultimate capacity. Bearing bed reinforcements are effective on increasing the ultimate bearing capacity, but cannot reduce deformations for service load conditions. Also, increasing levels of backfill compaction and use of well graded backfill materials can increase the stiffness of a GRS composite pier.

2.3 Dynamic Response in Centrifuge Tests

Sakaguchi (1996) conducted dynamic centrifuge tests to simulate a 4.5 m high GRS wall. Three geotextile reinforcements with different maximum tensile strength and reinforcement length were used. Results indicated that lateral facing displacements generally decreased with increasing reinforcement length, and the optimal reinforcement length was between 2/3H and H, where H is the total height of the GRS wall. The maximum reinforcement tensile strength had little effect on

the seismic response of GRS walls, as the tensile forces developed during seismic events were well below the tensile strengths.

Takemura and Takahashi (2003) conducted centrifuge tests to investigate the effects of reinforcement length, vertical reinforcement spacing, and backfill dry density on the dynamic response of GRS walls. The prototype GRS walls were 7.5 m high and were subjected to sinusoidal excitation. Results showed that a GRS wall specimen with lower backfill dry density experienced larger horizontal displacements and larger reinforcement tensile strains.

Siddharthan et al. (2004) carried out dynamic centrifuge tests on bar mat-reinforced soil retaining walls subjected to step waves and earthquake ground motions. Test results showed that the maximum lateral facing displacement typically occurred at the mid-height of the walls, and the walls with longer reinforcement had less deformations.

Nova-Roessig and Sitar (2006) conducted a series of dynamic centrifuge tests on GRS slopes and GRS walls using geosynthetic and metal grids reinforcements. Results showed that amplification occurred when the maximum acceleration of input motion is smaller than 0.4*g*-0.5*g*, whereas attenuation occurred for stronger input motions. Nova-Roessig and Sitar (2006) suggested that the amplification and attenuation effects be considered in the seismic design of reinforced soil structures.

Liu et al. (2010) conducted dynamic centrifuge tests on three GRS walls with modular block facing. Two walls were subjected to the Kobe earthquake ground motion with the peak ground acceleration (PGA) scaled to 0.24*g*, and the other was excited using a sinusoidal wave with a PGA of 0.114*g*. Accelerations were amplified considerably in both the reinforced and retained zones under modest seismic shaking. Liu et al. (2010) suggested that the acceleration amplification be considered in the seismic design.

2.4 Dynamic Response in *1g* Shaking Table Tests

1*g* shaking table testing technique has been used to investigate the dynamic response of reinforced soil structures since the 1970s. However, due to the limitation of size and capacity of typical shaking tables, most of the tests were conducted for reduced-scale model, in which soil and reinforcement properties need to be properly scaled. The similitude relationships between the reduced-scale model and prototype structure have been proposed by Iai (1989), Sugimoto et al. (1994), and Telekes et al. (1994). Early studies focused on metallic reinforced soil walls till the late 1980s, and a number of tests started to investigate the seismic performance of GRS walls since the 1990s, mainly focusing on GRS walls with rigid facing and wrapped-face, and then GRS walls with modular block facing gained more popularity. Several full-scale shake table tests have also been conducted for this type of walls, which provided valuable results (Ling et al. 2005, 2012; Fox et al. 2015).

Richardson and Lee (1975) pioneered the use of shaking table tests on a series of 300 mm-high reduced-scale soil walls reinforced with aluminum strips subjected to sinusoidal motions to investigate the failure modes. Results indicated that strip pullout with ductile behavior is more desirable than strip breakage that causes sudden collapse. This study was followed by a 6 m-high full-scale steel reinforced soil wall subjected to both forced vibrations and blast excitations, and results showed reinforced soil walls could withstand severe shaking even designed for static criteria (Richardson et al. 1977). Wolfe et al. (1978) carried out a series of shaking table tests on 610 mm-high reinforced soil walls subjected to horizontal, vertical, and combined horizontal and vertical excitations. Similar responses were observed for excitations in horizontal direction only and both directions, thus the effect of vertical component could be ignored in the design. Chida et al. (1982) carried out a series of shaking table tests on 4.4 m-high steel reinforced soil walls and found that the average peak horizontal acceleration in the soil behind the walls was equal to the PGA for ground motion frequencies less than 3 Hz. Nagel and Elms (1985) tested seven 320 mm-high walls reinforced using wide satin ribbons at the University of Canterbury, and observed that all walls remained vertical during failure except for the bottom panel. Results indicated that reinforcement density and length affected the failure surface geometry. This study was followed by shake table tests for six 1 m-high reinforced soil walls by Fairless (1989), which showed that the seismic shaking cause dramatic increases in tensile forces for the reinforcing strips and permanent outward displacements when the ground acceleration exceeds a yield acceleration.

A number of shaking table tests have been conducted for GRS walls with various facing conditions since the late 1980s (Koga et al. 1988; Koga and Washida 1992; Sakaguchi et al. 1992; Murata et al. 1994; Budhu and Halloum 1994; Sakaguchi 1996; Koseki et al. 1998; Matsuo et al. 1998). Murata et al. (1994) tested 2.5 m-high GRS walls with gabion and rigid concrete panel facings subjected to both sinusoidal and scaled earthquake motions. Results indicated that acceleration amplification was negligible up to the mid-height of the walls, and then increased to about 1.5 at the top, and the sinusoidal motion resulted in greater deformations than scaled earthquake motions. Sakaguchi (1996) performed shaking table tests to compare the dynamic responses of a 1.5 m-high wrapped-face GRS wall and three unreinforced conventional type retaining walls. The GRS wall failed at a much higher acceleration than the other unreinforced walls, but experienced larger deformations under smaller accelerations. Koseki et al. (1998) conducted shaking table tests on 500 mm-high GRS walls with rigid facing and conventional type retaining walls. The model walls were subjected to a sinusoidal excitation at a frequency of 5 Hz and showed a primary failure mode of overturning with tilting of wall facing after shaking. Results also indicated that increasing reinforcement length for top layers could increase the resistance against the overturning failure. Matsuo et al. (1998) conducted shaking table tests on six 1.0 m- to 1.4 m-high GRS walls to investigate the effects of various factors on the dynamic response, and found that increasing reinforcement length is the most effective means to reduce lateral facing displacements, and the wall with continuous rigid facing experienced larger lateral displacements than the wall with segmental facing panels. Ramakrishnan et al. (1998) tested two GRS walls with wrapped-face and

modular block facing, respectively, and observed that the modular block facing wall can sustain two times the critical acceleration than the wrapped-face wall. An analytical method was also developed to calculate the critical acceleration.

El-Emam and Bathurst (2004; 2005; 2007) performed a series of shaking table tests on reduced-scale reinforced soil walls with a full-height rigid facing panel to investigate the effects of toe boundary conditions, facing conditions, reinforcement layout, and input motion on dynamic response. Fourteen 1/6 scale walls with a full-height rigid facing panel were subjected to stepped-amplitude sinusoidal loading. The model walls were 1 m-high and the backfill soil zone was 2.4 m long. Excitations were applied in 0.05*g* increments with a duration of 5 seconds and continued until excessive wall deformations occurred. The backfill soil had a peak friction angle of 51° and a dilation angle of 15°. Experimental results showed that facing lateral displacements could be reduced by using smaller facing panel mass, inclined facing panels, longer reinforcement, stiffer reinforcement, and smaller reinforcement vertical spacing. Reinforcement load was the largest near the facing connections both at the end of construction and during shaking. The summation of reinforcement connection loads generally decreased with increasing facing mass, greater horizontal toe restraint and greater facing inclination angle. A restrained toe with a stiff facing panel was found to carry a significant portion of total horizontal earth force for both static and dynamic conditions.

Ling et al. (2005) conducted full-scale shaking table tests on three GRS walls with modular block facing for the Kobe earthquake ground motion. The walls were 2.8 m-high and had a 0.2 m-thick foundation soil. Walls 1 and 2 were subjected to horizontal shaking only, whereas Wall 3 was subjected to both horizontal and vertical shaking. For the first excitation, the ground motion record was scaled to a PGA of 0.4*g*, and to PGA of 0.8*g* for the second excitation. The backfill and foundation soil was a fine sand with medium relative density and a friction angle of 38°. Experimental results showed that the GRS walls experienced negligible deformation under moderate earthquake loading (PGA = 0.4*g*) and performed well under strong earthquake loading with a PGA of 0.8*g*. Ling et al. (2005) found that using longer reinforcement for the top layer and smaller reinforcement vertical spacing could improve the seismic performance. Vertical acceleration did not have a major effect on wall deformations, but increased vertical stresses at foundation level and reinforcement loads. Ling et al. (2012) performed another set of shaking table tests on GRS walls constructed using a silty sand backfill soil with 43.3% fines content. The backfill and foundation soil had a friction angle of 39° and apparent cohesion of 40 kPa. These walls were subjected to both horizontal and vertical components of the Kobe earthquake motion. Comparing experimental results with previous tests results (Ling et al. 2005), Ling et al. (2012) found that GRS walls constructed using low-quality backfill soil had better seismic performance than otherwise identical walls with sandy backfill with respect to wall deformations, dynamic earth pressures and reinforcement forces. Ling et al. (2012) suggested that the good seismic performance was due to the apparent cohesion of the fine-grained soils. However, the use of apparent cohesion

in the design is cautioned, as this cohesion value could vary significantly due to environmental changes during the service life of GRS walls.

Latha and Krishna (2008) studied the influence of backfill soil relative density on the seismic response of GRS walls with wrapped-face and full-height rigid facing panel. A total of 24 walls were subjected to sinusoidal excitations. Lateral facing displacements for walls with wrapped facing were generally much larger than walls with a full-height rigid facing panel. The effects of backfill soil relative density were pronounced only at low relative densities and higher base excitations. Krishna and Latha (2009) also investigated the effects of reinforcement properties on seismic performance of GRS walls with a full-height rigid facing. Reinforcement layers, even with low tensile strength, were very effective on reducing lateral facing displacements compared with measured displacements of unreinforced walls. However, acceleration amplification within the backfill was not much influenced by reinforcement properties. Latha and Santhanakumar (2015) also conducted shake table tests for a series of 600 mm-high GRS walls with rigid facing and modular block facing, and concluded that increasing backfill soil relatively density has important effects on reducing lateral facing displacements and settlements for walls with both rigid facing and modular block facing.

Guler and Enunlu (2009) performed shaking table tests for two half-scale 2 m-high GRS walls with modular block facing and different reinforcement lengths. For the model wall with shorter reinforcement, lateral facing displacements and dynamic tensile forces in reinforcement were larger, and a shallower internal failure surface was observed than the other wall with longer reinforcement. Guler and Selek (2014) reported a series of eight reduced-scale shaking table tests to investigate the effects of various factors, including PGA, reinforcement length and spacing, model scale, and treatment of top two facing blocks, on the seismic performance of GRS walls. The similitude relationships proposed by Iai (1989) were followed in this series of tests. Results indicated that accelerations were not affected by model size, but displacements for prototype structure increased with decreasing model size. Lateral facing displacements were not significantly affected by reinforcement length and spacing, which might be attributed to the relatively high reinforcement stiffness and apparent cohesion for the backfill soil.

Fox et al. (2015) conducted a full-scale shaking table test on a 6.1 m-high GRS wall with modular block facing using a large soil confinement box. The confinement box had a fundamental frequency of 22 Hz, which is above the normal operating frequency band of the shaking table. Accordingly, the box moved in phase with the table and provided a rigid boundary condition. The GRS wall experienced a permanent displacement of 56 mm at the top after a series of sinusoidal and earthquake motions. The ultimate state of the GRS wall indicated moderate damage, including two significant cracks in the backfill soil with a width of more than 30 mm - one at the back of the reinforced soil zone and one near the rear boundary - but no collapse.

Helwany et al. (2012) conducted large-scale shaking table tests on a GRS bridge abutment at the U.S. Army Engineering Research and Development Center – Construction Engineering Research Laboratory (ERDC-CERL) using the Triaxial Earthquake and Shock Simulator (TESS). The GRS bridge abutment model had a total height of 3.6 m, including a 3.2 m-high lower wall and 0.4 m-high upper wall. The abutment was reinforced using a woven geotextile with a vertical spacing of 0.2 m. The backfill soil was poorly-graded gravel with sand and clay, and had a friction angle of 44°. The bridge superstructure had a total weight of 445 kN and yielded an average vertical stress of 111 kPa on the abutment. In the shaking table tests, the GRS bridge abutment model was subjected a series of horizontal sinusoidal motions with increasing amplitude in the longitudinal direction. The first test was performed using a sinusoidal motion at a frequency of 1.5 Hz with an amplitude of 0.15*g* for 20 seconds. Four additional tests were conducted at a frequency of 3 Hz with amplitudes of 0.3*g*, 0.45*g*, 0.67*g*, and 1.0*g*. No damage was observed until the acceleration reached 0.67*g*, and no significant distress occurred for accelerations up to 1*g*. The incremental bridge seat settlement was approximately 50 mm when the acceleration increased from 0.67*g* to 1.0*g*. In general, the GRS bridge abutment remained functional under sinusoidal motion with horizontal accelerations up to 1.0*g*.

2.5 Summary

Overall, the field investigations of Yen et al. (2011) indicated good performance of GRS bridge abutments in terms of facing displacements and bridge seat settlements under service load conditions. The shaking table tests by Helwany et al. (2012) indicated that GRS bridge abutments have satisfactory performance when subjected to longitudinal shaking. However, more experiments and evaluations are needed to understand the potential issues and performance characteristics for various configurations under dynamic loading conditions. Further, GRS bridge abutments are different from long GRS walls as they may be affected by three-dimensional motion during earthquakes, with different responses in the directions longitudinal and transverse to the bridge beam. Because the constraints for movement are different in the longitudinal and transverse directions, shaking in the transverse direction may lead to a different deformation response than shaking in the longitudinal direction. To address these needs, this report presents results from shaking table tests on MSE bridge abutments having different configurations subjected to a series of earthquake motions in the directions longitudinal and transverse to the bridge beam to evaluate the general seismic performance of MSE bridge abutments.

Chapter 3 Shaking Table Testing Program

3.1 Introduction

A total of six shaking table tests on MSE bridge abutments were performed using the indoor shaking table at the University of California, San Diego (UCSD) Powell Structural Laboratory. The shaking table has areal footprint dimensions of 16 ft × 10 ft and a maximum payload capacity of 80 kips. The table slides horizontally in one direction on two stationary shafts and is driven by a servo-hydraulic actuator with a static capacity of 110 kips, dynamic capacity of 91.5 kips, and maximum stroke of ± 6.0 inches. The shaking table was refurbished prior to this study to increase the fidelity of dynamic motion (Trautner et al. 2017).

Details of the shaking table testing program performed as part of this study are summarized in Table 3.1. The testing program consists of five tests where the direction of shaking is in the longitudinal direction of the bridge beam, referred to as longitudinal shaking tests (Tests 1-5), and one test where the direction of shaking is perpendicular to the bridge beam, referred to as a transverse shaking test (Test 6). The longitudinal shaking tests include a baseline configuration (Test 1) and a parametric study to investigate the effects of bridge surcharge stress (Test 2), reinforcement spacing (Test 3), reinforcement stiffness (Test 4), and steel reinforcement (Test 5) on the seismic response of MSE bridge abutments. The transverse shaking test (Test 6) has a similar configuration to Test 1 except that the input motions are applied in the transverse direction and the length of the abutment was reduced to fit on the table.

Table 3.1 Shaking table test plan (values in model scale)

Test	Variable	Bridge surcharge stress (psf)	Reinforcement spacing (in.)	Reinforcement stiffness (kips/ft)	Global stiffness (kips/ft)[1]	Shaking direction
1	Baseline case	1380	6	26	45	Longitudinal
2	Bridge surcharge stress	900	6	26	45	Longitudinal
3	Reinforcement spacing	1380	12	26	24	Longitudinal
4	Reinforcement stiffness	1380	6	13	23	Longitudinal
5	Steel reinforcement	1380	6	330	572	Longitudinal
6	Shaking direction	1380	6	26	45	Transverse

[1] defined as $\sum_{i=1}^{n} J_i / h$, where J_i = index stiffness of each reinforcement layer, n = number of reinforcement layers, and h = lower wall height (Bathurst et al. 2009).

3.2 Similitude Relationships

Considering the size and payload capacity of the indoor shaking table at UCSD, reduced-scale model tests were conducted with a length scaling factor of $\lambda = 2$. The length scaling factor is defined as the ratio of prototype length to model length, so a value of $\lambda = 2$ denotes a half-scale model test. A MSE bridge abutment with a total height of 18 ft and a bridge beam clearance height of 15 ft, which satisfies the requirement for non-freeway roads (Stein and Neuman 2007), was selected as the prototype structure. Therefore, half-scale MSE bridge abutment models with a total height of 9 ft and a bridge beam clearance height of 7.5 ft were constructed and tested on the shaking table.

The similitude relationships proposed by Iai (1989) have been widely used for 1*g* shaking table tests on geotechnical engineering structures, including tests on reinforced soil walls (El-Emam and Bathurst 2004, 2005, 2007; Guler and Enunlu 2009; Sabermahani et al. 2009; Guler and Selek 2014; Latha and Santhanakumar 2015; Panah et al. 2015). The theoretical scaling factors for the similitude relationships from Iai (1989) are summarized in Table 3.2. Model geometry, geosynthetic reinforcement stiffness, backfill soil modulus, bridge surcharge stress, and frequencies of the earthquake motions were scaled accordingly for $\lambda = 2$ using the factors given in Table 3.2.

Table 3.2 Similitude relationships for 1*g* shaking table testing (Iai 1989).

Variable	Theoretical scaling factor	Scaling factor for $\lambda = 2$
Length	λ	2
Material density	1	1
Strain	1	1
Mass	λ^3	8
Acceleration	1	1
Velocity	$\lambda^{1/2}$	1.414
Stress	λ	2
Modulus	λ	2
Stiffness	λ^2	4
Force	λ^3	8
Time	$\lambda^{1/2}$	1.414
Frequency	$\lambda^{-1/2}$	0.707

3.3 Material Properties

3.3.1 Backfill Soil

3.3.1.1 Geotechnical Characterization

The backfill soil used in this study was obtained from a local quarry, where it was manufactured by mixing rock dust and washed concrete sand. A sieve analysis was performed to characterize the particle size distribution of the backfill soil, as shown in Figure 3.1. The backfill soil has a coefficient of uniformity C_u = 6.1, coefficient of curvature C_z = 1.0, and is classified as a well-graded sand (SW) according to the USCS (Unified Soil Classification System). The sand has a fines content of 2.5% (i.e., percent passing No. 200 sieve). This well-graded sand exceeds the backfill material requirements for MSE walls and abutments (Berg et al. 2009) and GRS-IBS abutments (Adams et al. 2011a).

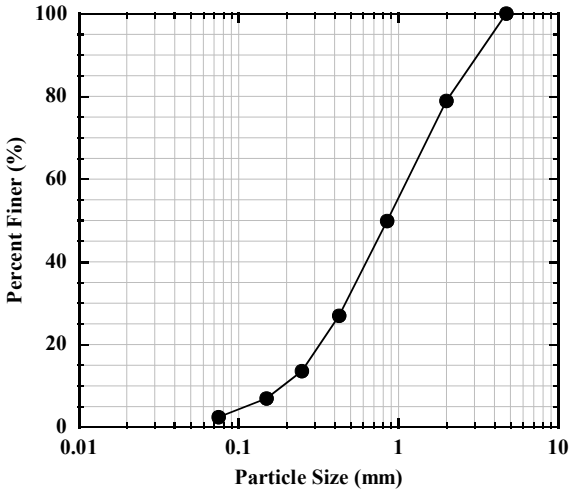

Figure 3.1 Gradation curve for the SW sand.

The measured maximum and minimum dry unit weights are $\gamma_{d,max}$ = 118.9 pcf and $\gamma_{d,min}$ = 87.8 pcf according to ASTM D4253 and D4254, respectively, and the corresponding minimum and maximum void ratios are e_{min} = 0.371 and e_{max} = 0.853 with a measured specific gravity of G_s = 2.61 according to ASTM D854.

3.3.1.2 Compaction Behavior

A standard Proctor compaction test was performed according to ASTM D698 to define the compaction curve for the backfill soil. The maximum dry unit weight of the sand according to the standard Proctor compaction effort was 117.1 pcf, at a gravimetric water content of 11.4%. However, inspection of the standard Proctor compaction curve shown in Figure 3.2 indicates that compaction water content does not have a significant effect on dry unit weight for this sand (i.e., the curve is essentially flat without an obvious optimal compaction condition).

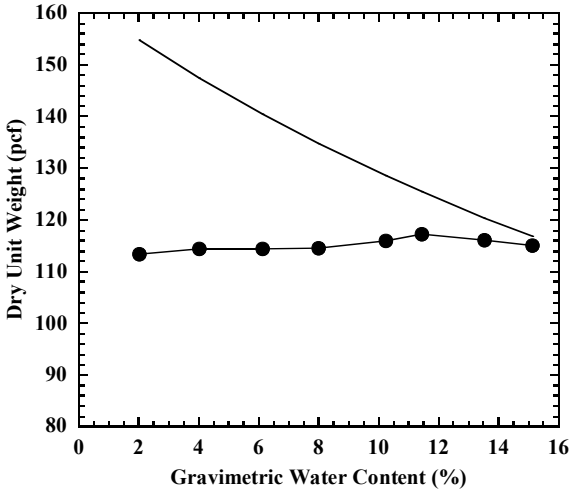

Figure 3.2 Compaction curve for the SW sand.

3.3.1.3 Selection of Target Compaction Conditions

For this sand, a relative density of 85% corresponds to a relative compaction of 96% with respect to the maximum dry unit weight of 117.1 pcf corresponding to the standard Proctor compaction effort, which is within the typical range of backfill soil compaction requirements for MSE bridge abutments in the field (Berg et al. 2009). A triaxial test was conducted for a dry sand specimen compacted at a relative density D_r = 85% under an effective confining stress of σ'_3 = 10 psi to represent the average stress-strain response of the backfill in the prototype structure. To meet the similitude relationships for backfill soil modulus, a series of drained triaxial compression tests were performed for specimens compacted at various relative densities under an effective confining stress of σ'_3 = 5 psi to find the target relative density for the backfill soil in the half-scale model shaking table tests.

Test results for the deviator stress versus axial strain for these different triaxial tests are shown in Figure 3.3. As expected, the secant modulus and peak shear strength increase with increasing relative density. The principal stress ratios are shown in Figure 3.4, which represent the mobilization of friction during shear. Although the shapes of the principal stress ratio curves are the same as the deviator stress curves, evaluation of the principal stress ratio curves are normalized to account for the effects of the different confining stresses representative of the model and prototype MSE bridge abutments considered in this analysis. The principal stress ratio curve for the specimen with D_r = 85% and σ'_3 = 10 psi is similar to the curve for the specimen with D_r = 70% and σ'_3 = 5 psi. This indicates that a reduced-scale model (under lower effective confining stresses) with backfill soil compacted at D_r = 70% will have the same response as a prototype structure with backfill soil compacted at D_r = 85%. The secant moduli at different levels of axial strain are plotted in Figure 3.5. Theoretical soil secant moduli for σ'_3 = 5 psi are calculated based on the measured moduli for D_r = 85% and σ'_3 = 10 psi divided by the scaling factor of 2. Results confirm that a relative density of 70% yields similar secant moduli to the theoretical values for different levels of axial strain. The analyses shown in Figure 3.4 and Figure 3.5 confirm that the

backfill soil in the MSE bridge abutment models should be compacted at a relative density of 70% in order to have the behavior similar to that for a backfill compacted at D_r = 85% in the prototype MSE bridge abutments.

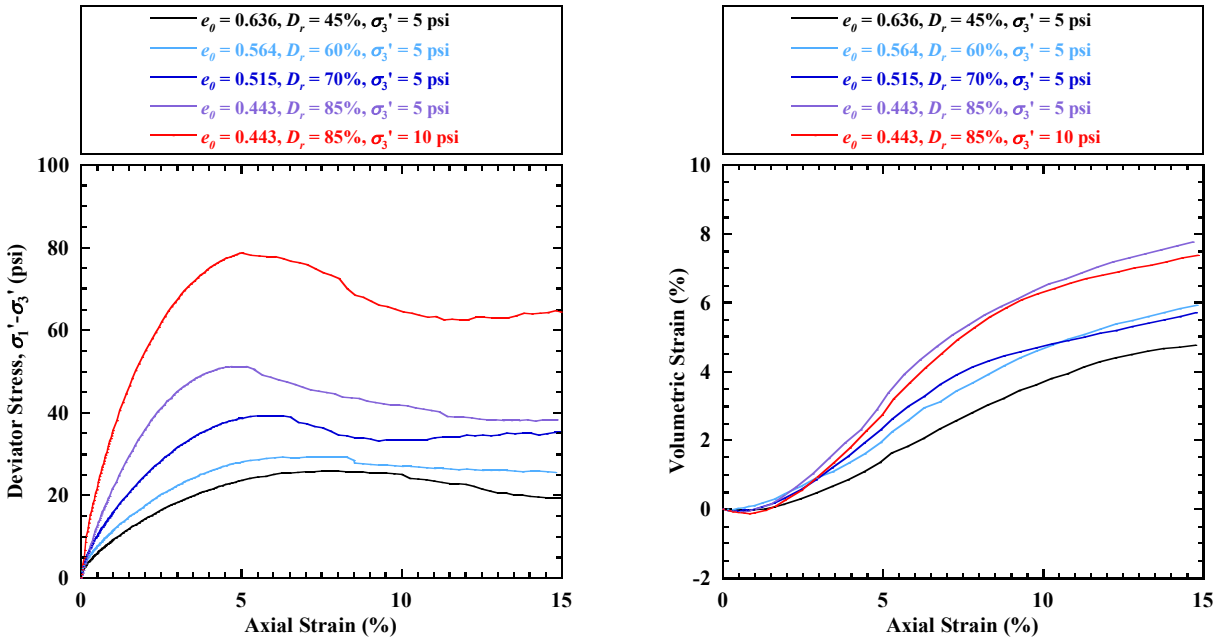

(a) (b)

Figure 3.3 Drained triaxial compression test results: (a) deviator stress vs. axial strain; (b) volumetric strain vs. axial strain.

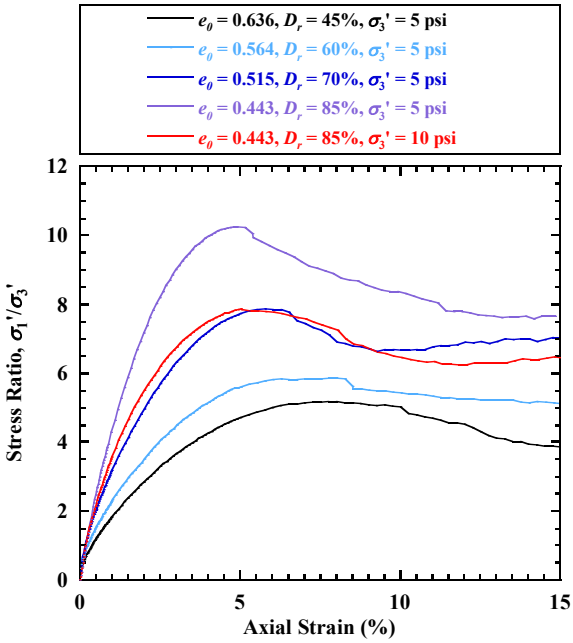

Figure 3.4 Principal stress ratio vs. axial strain.

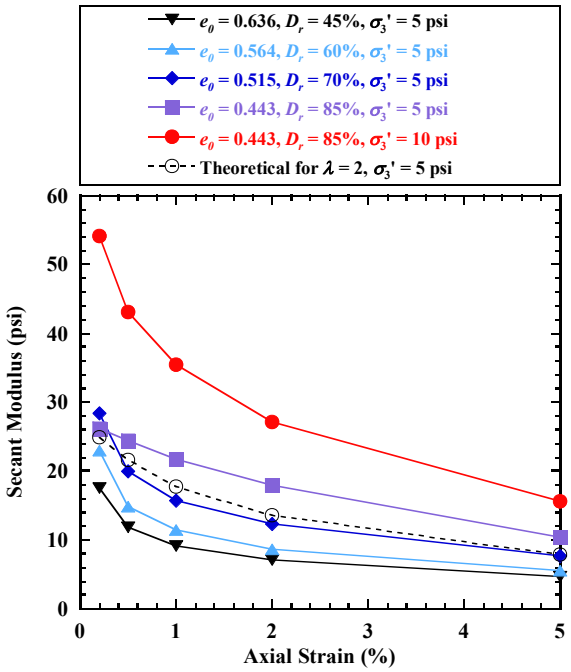

Figure 3.5 Secant moduli at different levels of axial strain.

Several trial experiments were performed on the backfill soil compacted with a vibrating plate compactor. It was found that a relative density of 70% could be attained repeatedly. The sand was compacted at gravimetric water content w_c = 5%, which was selected for the convenience of construction as it was difficult to maintain dry sand conditions in the laboratory. The impact of the non-zero gravimetric water content on the shear strength of the sand will be discussed later. The selected target compaction conditions for construction of the half-scale MSE bridge abutment models are shown in Figure 3.6.

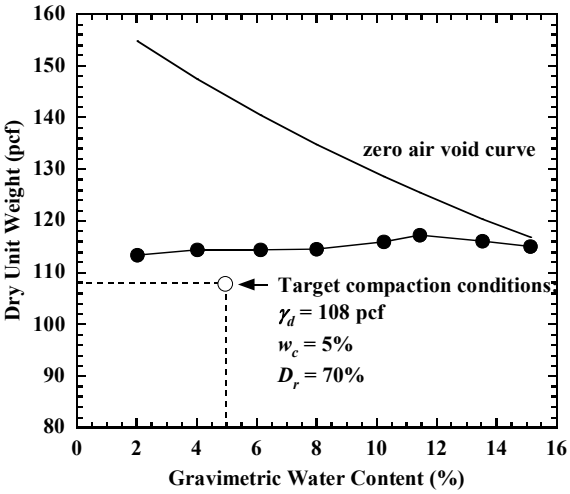

Figure 3.6 Target compaction conditions for the SW sand.

3.3.1.4 Shear Strength

Since the specimen is relatively narrow in the transverse direction due to the constraint of the UCSD shaking table dimensions, the stress state in the backfill soil is expected to be closer to triaxial compression conditions than plane strain compression conditions. A series of consolidated-drained (CD) triaxial compression tests were performed on dry sand specimens compacted at the target relative density of D_r = 70% to measure the shear strength and volume change behavior. The specimens were compacted within a latex membrane held in place by a split-wall compaction mold. After compaction, a vacuum was applied to the soil specimen, and the split mold was removed. The sand specimens had a diameter of 1.4 inches and height of 2.8 inches. Different levels of confining stress were applied to the different specimens prior to shearing at a constant axial strain rate of 1.0%/min. The volume change was recorded during drained shearing through monitoring of the volume of cell fluid. The triaxial test setup with a typical sand specimen during testing is shown in Figure 3.7.

Figure 3.7 Consolidated drained triaxial compression test setup.

The results from three triaxial compression tests performed at effective confining stresses of 2 psi, 5 psi, and 10 psi are shown in Figure 3.8. These mean effective stresses encompass the stress range expected in the half-scale MSE bridge abutment models. The sand was observed to show a clear peak value representative of dense conditions, and showed dilation after an initial contraction. A dilation angle of ψ = 13.0° was determined for the volumetric strains ranging from the axial strain at the point of maximum contraction to an axial strain of 5%. A linear Mohr-Coulomb failure envelope was fitted to the data as shown in Figure 3.9, and a peak friction angle of ϕ'_p = 51.3° and zero cohesion were calculated for the dry backfill sand with D_r = 70% (e_0 = 0.515).

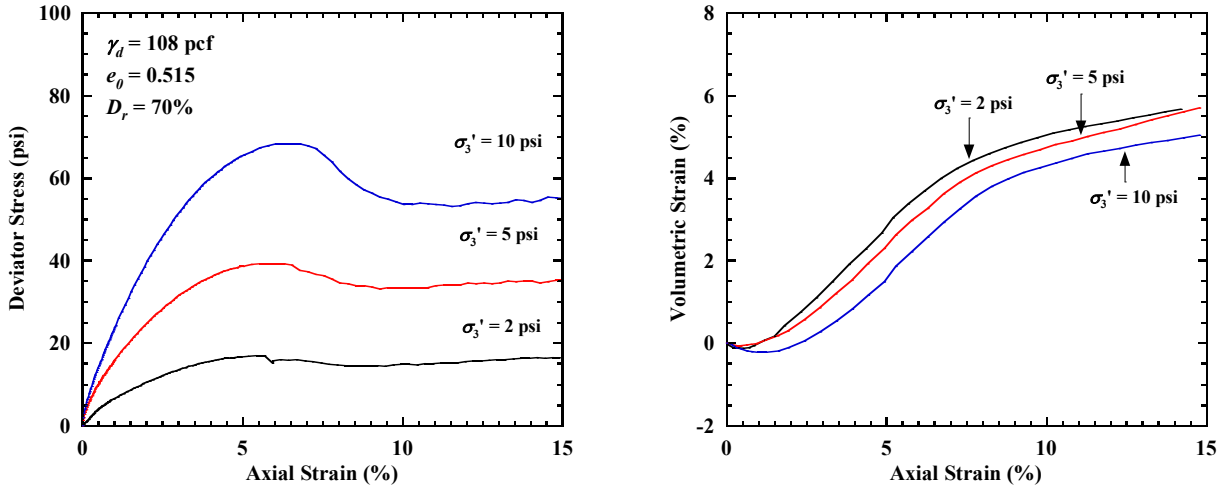

(a) (b)

Figure 3.8 Triaxial test results: (a) deviator stress vs. axial strain; (b) volumetric strain vs. axial strain.

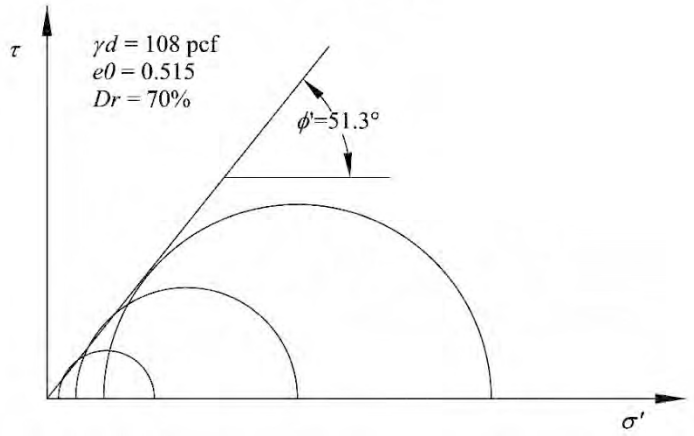

Figure 3.9 Mohr-Coulomb failure envelope.

3.3.1.5 Soil Water Retention Curve (SWRC)

A hanging column test was performed on a sand specimen with $D_r = 70\%$ to measure the soil water retention curve (SWRC) for both drying and wetting paths. Results are shown in Figure 3.10. The SWRC data was fitted using the model of van Genuchten (1980):

$$\theta = \theta_r + (\theta_{\max} - \theta_r)[1 + (\alpha_{vG}\psi_s)^{N_{vG}}]^{-(1-\frac{1}{N_{vG}})} \quad (3.1)$$

where θ is the volumetric water content (volume of water/total volume of soil in percent), ψ_s is the matric suction, θ_{max} is the volumetric water content at zero matric suction for either path, θ_r is the residual saturation, and α_{vG} and N_{vG} are the van Genuchten (1980) SWRC model parameters.

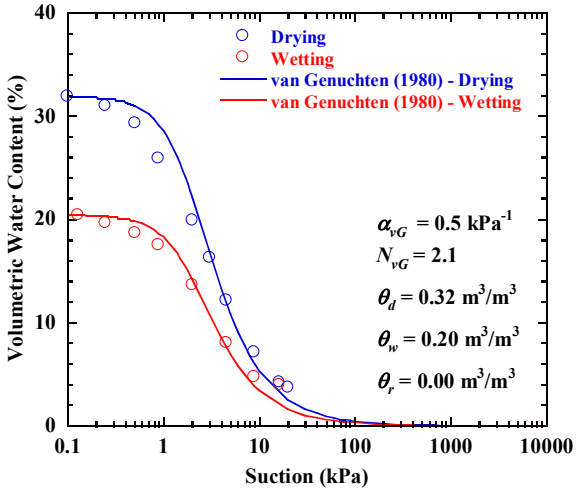

Figure 3.10 Wetting- and drying-path soil-water retention curve data with fitted relationship.

A summary of the backfill soil properties are presented in Table 3.3. These values can be used for both geotechnical characterization of the soil, and are also important input parameters for the numerical simulations that will be presented in the other report prepared as part of this study. Note that the peak friction angle of 51.3° and fines content of 2.5% for this well-graded sand are well beyond the minimum requirements for the backfill materials in the FHWA/AASHTO/Caltrans design guidelines (Adams et al. 2011a, Berg et al. 2009, Caltrans 2004), such as minimum $\phi' = 38°$ and maximum fines content of 12% for FHWA, and minimum $\phi' = 34°$ and maximum fines content of 15% for AASHTO and Caltrans. This may imply that the performance of the reduced-scale MSE bridge abutments evaluated in this study may have better seismic performance than MSE bridge abutments constructed using lower quality backfill soil near the minimum requirements for backfill materials in the design guidelines noted above.

Table 3.3 Backfill soil properties.

Property	Value
Specific gravity, G_s	2.61
Coefficient of uniformity, C_u	6.1
Coefficient of curvature, C_z	1.0
Maximum void ratio, e_{max}	0.853
Minimum void ratio, e_{min}	0.371
Peak friction angle, ϕ'_p (°)	51.3
Dilation angle, ψ (°)	13.0

3.3.2 Geogrid Reinforcement

The geosynthetic reinforcement is a uniaxial high-density polyethylene (HDPE) geogrid (Tensar LH800). The aperture size is 4.7 inches by 1.0 inch. A series of single rib tensile tests were conducted according to ASTM D6637 to evaluate the stiffness and strength of the geogrid. The single-rib geogrid specimen in the machine direction has four junctions (three apertures) with a length of 13.4 inches, and was loaded at a strain rate of 10%/min, as shown in Figure 3.11.

Figure 3.11 Single-rib tensile test setup.

Tensile tests were performed on single-rib geogrid apertures in the machine direction (MD) and cross-machine direction (CMD) at a strain rate of 10%/min. The results in Figure 3.12 show that the geogrid has secant stiffness at 5% strain $J_{5\%}$ = 26.0 kips/ft and ultimate strength T_{ult} = 2.8 kips/ft in the machine direction. Using the similitude relationships in Table 3.2, the tensile stiffness of this geogrid yields a value of 104 kips/ft for the prototype geogrid, which is in the typical range for field structures. The geogrid has $J_{5\%}$ = 5.5 kips/ft and T_{ult} = 0.3 kips/ft in the cross-machine direction, which are much lower than for the machine direction.

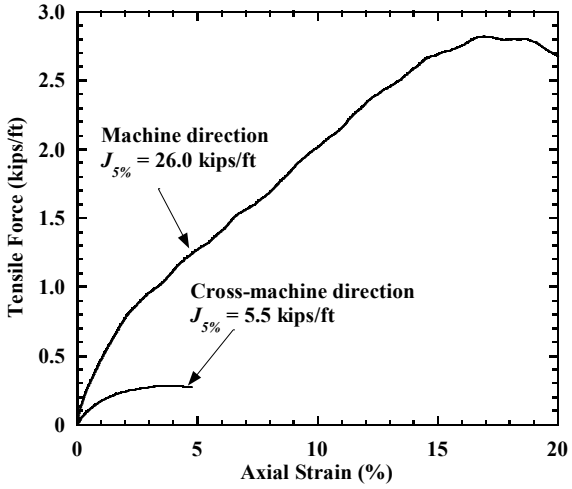

Figure 3.12 Load-strain curves for the geogrid in the MD and CMD.

Tensile tests were also conducted at strain rates of 1, 5, 10, 50, and 100%/min to investigate the effect of strain rate. Results, as shown in Figure 3.13, indicate that tensile stiffness and strength increase with increasing strain rate. Secant stiffness at 1% and 5% axial strains for different strain rates are plotted in Figure 3.14. When strain rate increases from 1 to 100%/min, the secant stiffness increases from 27.4 kips/ft to 68.5 kips/ft for 1% axial strain and increases from 15.1 kips/ft to 39.8 kips/ft for 5% axial strain.

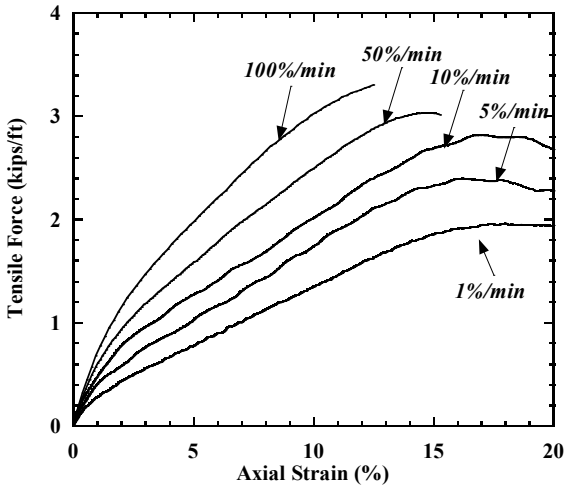

Figure 3.13 Effect of loading rate on load-strain curves for geogrid in the MD.

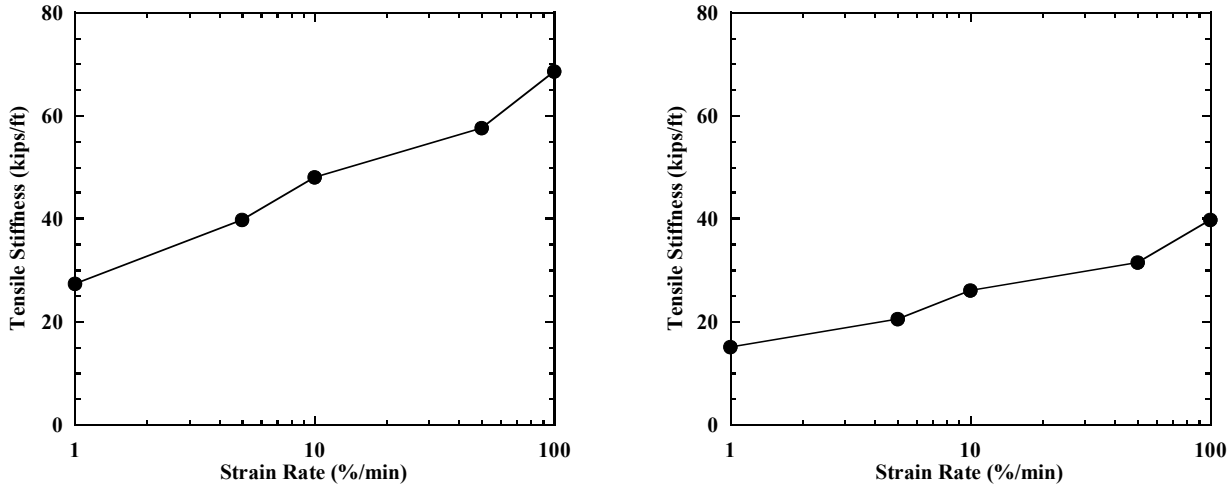

Figure 3.14 Effect of strain rate on secant stiffness in the MD for strain levels of: (a) 1% strain; (b) 5% strain.

3.3.3 Welded Wire Mesh

Steel welded wire mesh was used as reinforcement for Test 5. The test setup for the welded wire is shown in Figure 3.15, and the load-strain curve is shown in Figure 3.16. The wire has a linear response for strains smaller than 0.3%, and the corresponding initial stiffness is 330 kips/ft.

Figure 3.15 Tensile test on steel welded wire mesh.

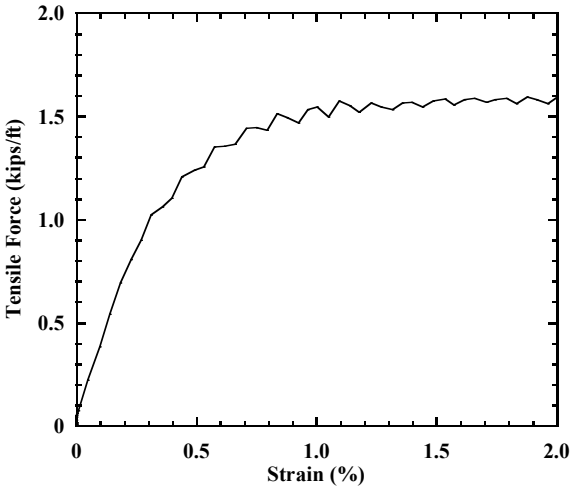

Figure 3.16 Load-strain curve for the steel welded wire mesh.

3.3.4 Facing Elements

Facing elements for MSE bridge abutments vary depending on the desired aesthetics and contractor approach. This project used a modulus block facing in the MSE bridge abutment models to give more flexibility in scaling and in the mode of reinforcement-wall connections. To meet the similitude relationships in Table 3.2, concrete modular facing blocks from Keystone, Inc., with dimensions of 12 inches × 10 inches × 6 inches (length × width × height) were selected. A layer of geogrid reinforcement was placed between each course of blocks with a contact area exceeding 80% of the block-to-block contact surface. Fiberglass pins were inserted through the geogrid apertures to assist with block alignment and did not significantly enhance the block-geogrid connections. Accordingly, the block-geogrid connections are assumed to be essentially frictional.

3.4 Test Configuration

3.4.1 Longitudinal Test

The shaking table test configuration of the bridge system for longitudinal test is shown in Figure 3.17. The bridge beam has dimensions of 21 ft × 3 ft × 1.5 ft (length × width × height), and is placed on a bridge seat that rests on the MSE bridge abutment at one end and on a concrete support wall that rests on a sliding platform at the other end. The bottom of the concrete support wall is rigidly connected to the shaking table using steel beams and experiences the same motion as the table. The bridge beam represents a longitudinal slice of a prototype bridge superstructure whose length was selected to accommodate the available laboratory space. Elastomeric bearing pads (model NEOSORB, Voss Engineering, Inc.) with plan dimensions of 1.5 ft × 3 ft, thickness of 1 inch, and elastic modulus of 522 psi were placed under both ends of the bridge beam. The expansion joint (i.e., gap) between the bridge beam and vertical back wall of the bridge seat is 1 in wide. During shaking, the bridge beam interacts with the MSE bridge abutment and support wall through friction developed on the bearing pads and potentially contacts (i.e., impacts) with the back wall of the bridge seat. The clear distance between the top of the wall facing and bottom of the bridge beam is 6 inches.

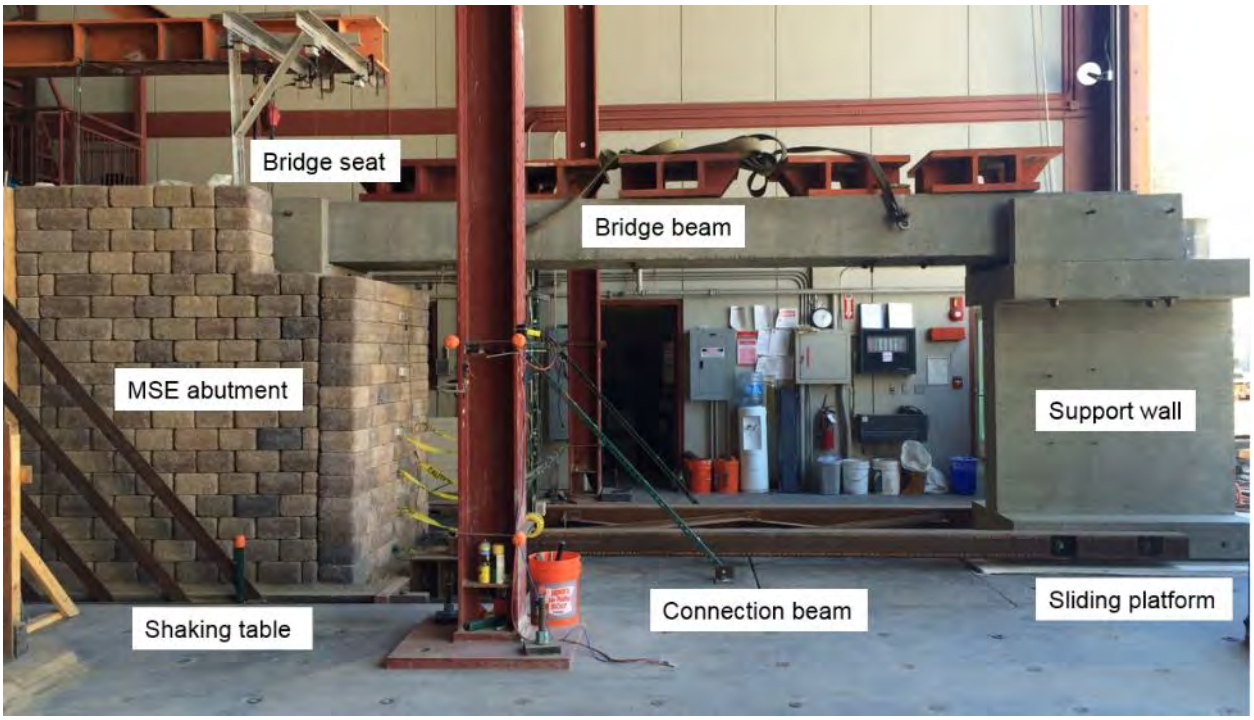

Figure 3.17 Shaking table test configuration of bridge system for the longitudinal tests.

The self-weight of the concrete bridge beam is 14.5 kips, and additional dead weights (steel plates) of 7.5 kips are evenly distributed and rigidly attached to the beam to produce the desired total bridge weight (22.0 kips) while keeping the mass center of the beam relatively low to minimize rocking. The total weight of the beam and dead weights produces an average vertical stress of 2530 psf on top of the bridge seat. The bridge seat has a self-weight of 1.6 kips and a bottom surface

with plan dimensions of 2.2 ft × 4.3 ft. The average vertical stress on the backfill soil from the bridge seat is 1380 psf, which corresponds to a prototype vertical stress of 2760 psf and is in the typical range for MSE bridge abutments in the field (Berg et al. 2009). For Test 2, only the bridge beam was placed (i.e., no additional dead weight), so the average vertical stress on the abutment is 900 psf, corresponding to a vertical stress of 1800 psf for prototype structure.

The MSE bridge abutment has modular block facing on three sides, including a front wall facing perpendicular to the longitudinal direction and two side wall facings perpendicular to the transverse direction. The back of the MSE bridge abutment is supported by a rigid reaction wall consisting of a steel frame with plywood face. The reaction wall was designed to be sufficiently stiff to provide at-rest conditions during construction and experience minimal deflections during shaking. Although the reaction wall moves in phase with the shaking table and thus does not reproduce the deformation boundary condition of a retained soil mass in the field, this simple configuration can be readily incorporated into numerical simulations for calibration purposes. To reduce effects of the reaction wall on the abutment response, the length of the retained soil zone was maximized within the geometry and payload constraints of the table. The total weight of the entire bridge system is 100 kips.

The MSE bridge abutment model has a total height of 9 ft, consisting of a 7 ft-high lower MSE wall and a 2 ft-high upper wall, resting on a 6 in-thick foundation soil layer placed directly on the shaking table. A top view diagram is shown in Figure 3.18(a) and cross-sectional view diagrams in the longitudinal and transverse directions are shown in Figure 3.18(b) and Figure 3.18(c), respectively. The abutment has plan dimensions of 7.8 ft × 7.0 ft, including wall facing blocks. The bridge seat rests on top of the backfill soil for the lower MSE wall and has a setback distance of 6 inches from each of the three wall facings. The lower MSE wall was constructed in fourteen 6 inch-thick soil lifts. Each lift includes reinforcement layers in the longitudinal direction (i.e., direction of shaking), and the transverse direction. The longitudinal reinforcement layers are frictionally connected to the front wall facing and extend 4.9 ft into the backfill soil. The transverse reinforcement layers are frictionally connected to each side wall facing and extend 2.6 ft into the backfill soil, and meet (but are not connected) at the center. The transverse reinforcement layers and side wall facing blocks are offset by 1 inch vertically from the longitudinal reinforcement layers and front wall facing blocks. Although longitudinal and transverse reinforcement layers are in close proximity vertically, the maximum particle size of the backfill soil is sufficiently small to permit typical soil-reinforcement interaction. The length of the retained soil zone between the reinforced soil zone and reaction wall is 2.1 ft. Transverse reinforcement layers support the side walls in the retained soil zone and are not connected to transverse reinforcements in the reinforced soil zone. The setback distance between the bridge seat and the back edge of the facing blocks of 6 inches in the model is smaller than the required distance of 5.0 ft as specified by Caltrans (See Figure 1.1) because of the geometric restraints on the table.

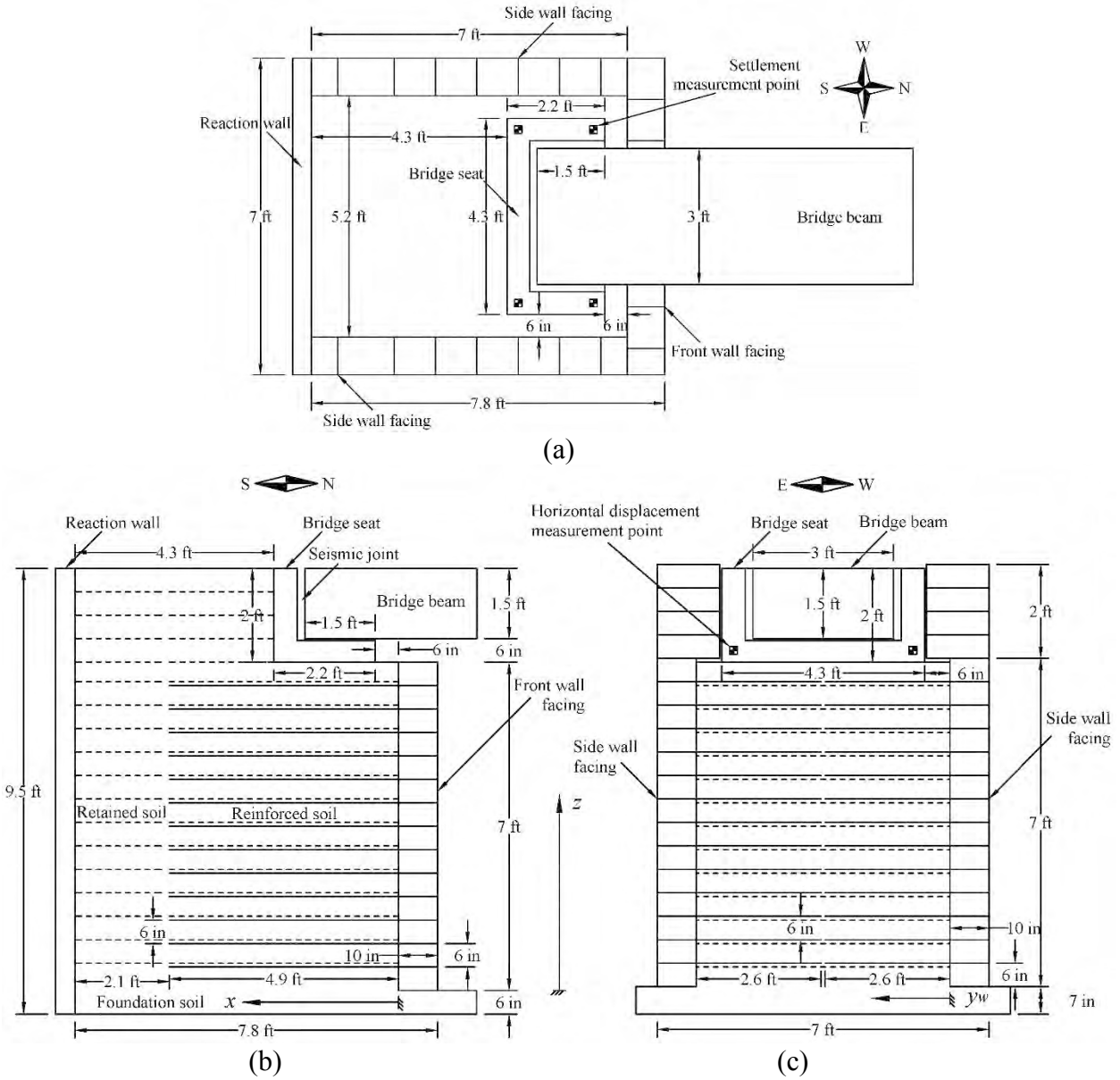

Figure 3.18 MSE bridge abutment model for the baseline longitudinal test: (a) top view; (b) longitudinal cross-sectional view; (c) transverse cross-sectional view. Note: dashed lines indicate reinforcement layers perpendicular to diagram.

The support wall for the other end of the bridge beam is a reinforced concrete block that rests on a sliding platform, as shown in Figure 3.19. Based on the low friction boundary concept developed by Fox et al. (1997, 2006), this platform consists of 273 rolling stainless steel balls (diameter = ¾ inches) sandwiched between two stainless steel plates (thickness = ¼ inches). The steel balls are placed inside a plastic guide plate (thickness = ½ inches) with 273 oversized holes (diameter = 1 inches) to keep the balls orderly during shaking tests. A ½ inch-thick rubber sheet is placed between the sliding platform and the support wall to reduce stress concentrations on the sliding platform. The base of the support wall is connected to the shaking table using steel beams to

transmit table motions and ensure that the entire system is shaken uniformly. The rigid sliding platform is acknowledged to not simulate the flexibility of a MSE bridge abutment at the other end of the bridge, but was selected to be a simple boundary condition that could be accurately quantified in numerical simulations.

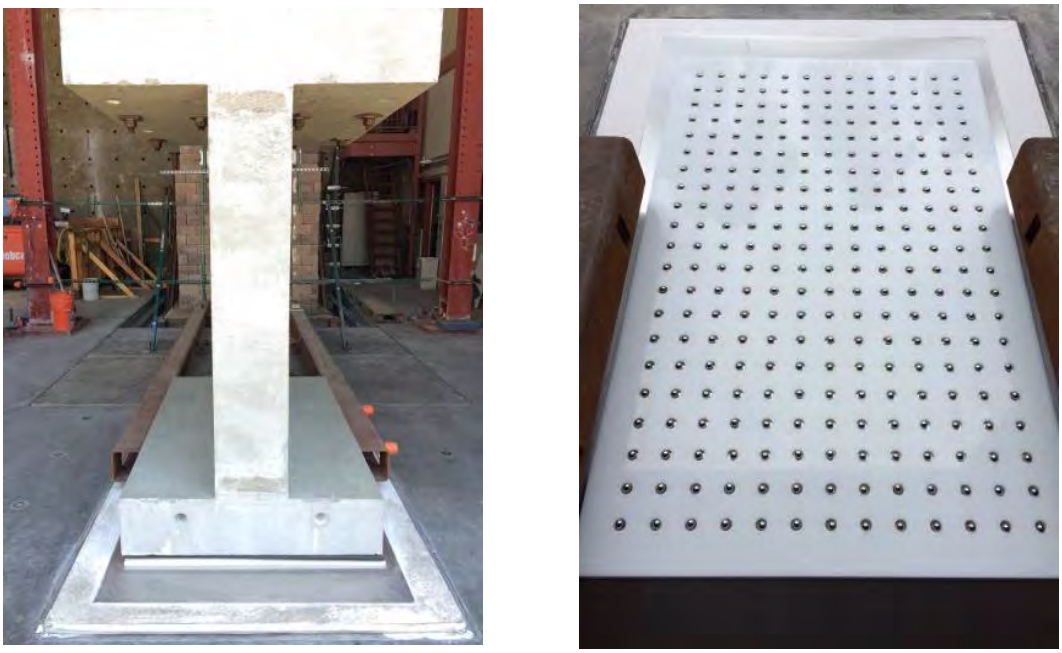

(a) (b)

Figure 3.19 Bridge support wall: (a) end view; (b) low friction sliding platform.

3.4.2 Transverse Test

The shaking table test configuration of the bridge system for transverse test is similar to longitudinal test except that the specimen was rotated 90 degrees so that the shaking motions can be applied in the transverse direction, as shown in Figure 3.20. Braces were welded to the connection beams to increase the stiffness in the transverse direction. The retained soil zone of the MSE bridge abutment was removed to accommodate the available table space. The dimensions for the MSE bridge abutment model for transverse test is shown in Figure 3.21. The dimensions are essentially the same as longitudinal test except that the abutment specimen for transverse test has plan dimensions of 5.8 ft × 7.0 ft with no retained soil zone.

Figure 3.20 Shaking table test configuration of bridge system for the transverse test.

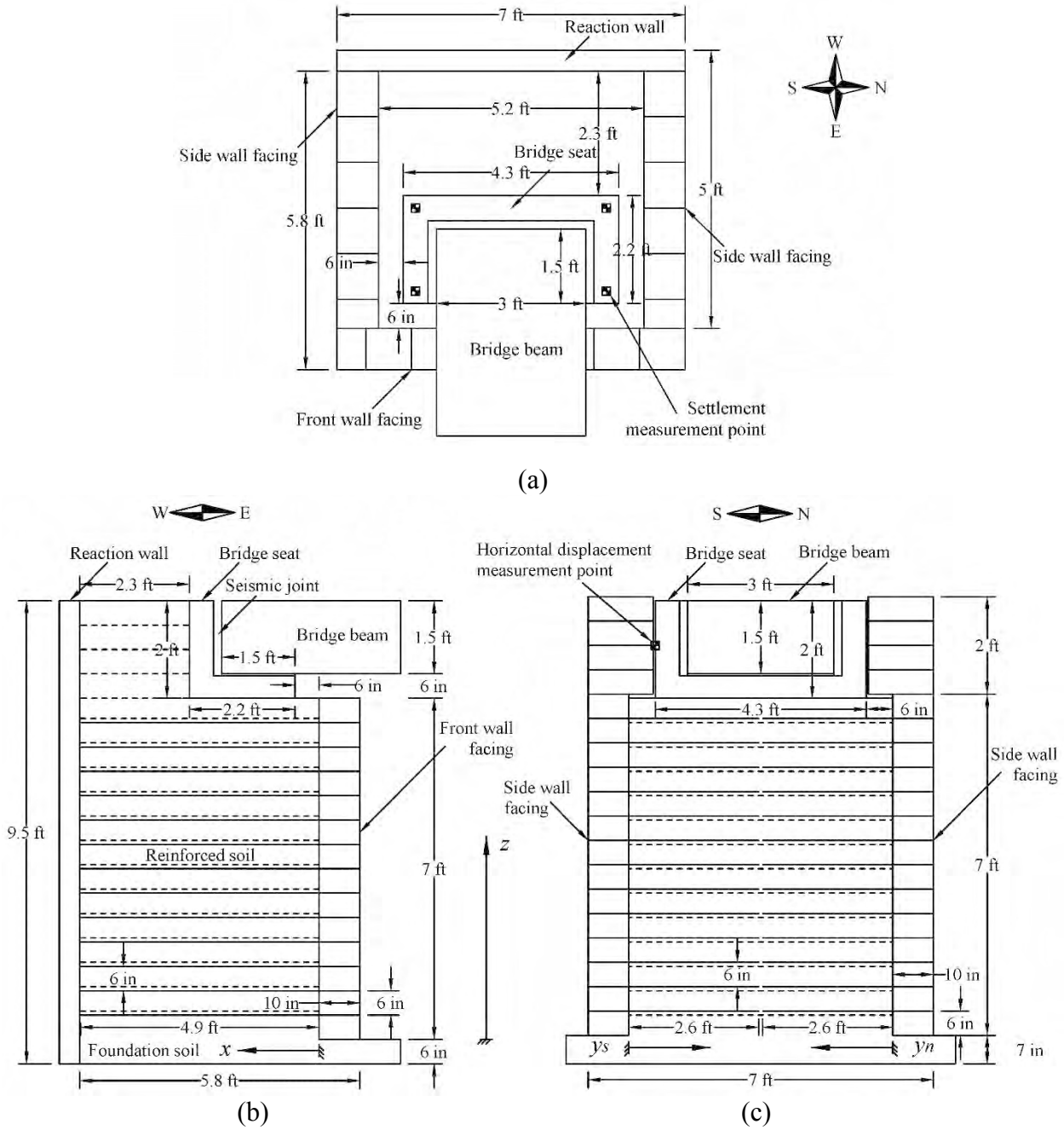

Figure 3.21 MSE bridge abutment model for the transverse test: (a) top view; (b) longitudinal cross-sectional view; (c) transverse cross-sectional view. Note: dashed lines indicate reinforcement layers perpendicular to diagram.

3.5 Instrumentation

3.5.1 Sensors

Specimen data was collected using an automatic data acquisition system with 160 channels and a simultaneous sampling rate of 256 Hz during shaking. Figure 3.22 shows sensors for the shaking table tests, including string potentiometers (Model P-5A/15A/25A/30A/40A Rayelco, PATRIOT Sensors and Controls Corp.), linear potentiometers (Model 606, BEI sensors), total pressure cells (Model SPT-3K/6K, AFB Engineered Test System), load cells (Model 1220BF-50K, Interface Inc.), accelerometers (Model CXL02LF1, Crossbow), and geogrid strain gauges (KFG-2-120-C1-11, Kyowa Americas, Inc.).

Horizontal displacements for the wall facing blocks at different elevations, bridge seat, reaction wall, bridge beam, and support wall in the shaking direction were measured using string potentiometers, and horizontal displacements of the wall facing blocks perpendicular to the shaking direction were measured using linear potentiometers. String potentiometers were used to measure settlements at the four corners of the bridge seat. String potentiometers were mounted on rigid reference frames apart from the shaking table and had sufficient tension to measure dynamic motions for the frequency band of the test. The string potentiometer measurements were corrected using measured horizontal displacements of the shaking table in the longitudinal direction to yield relative displacements with respect to the table. Earth pressure cells were seated into 1.5 inch-thick PVC plates with plan dimensions of 5 inches × 8 inches for horizontal orientation and 8 inches × 8 inches for vertical orientation. The PVC plates provide a flush surface to improve measurements of vertical and horizontal total stresses. Two load cells were embedded in the south end of the bridge beam to measure potential contact forces between the bridge beam and bridge seat during shaking. Accelerometers were attached on the wall facing and placed within the reinforced and retained soil zones, and attached on the structures to measure horizontal accelerations in the longitudinal direction. Geogrid tensile strains were measured using strain gauges mounted in pairs at the mid-point of longitudinal ribs, with one gauge on top and the other on bottom to correct for rib bending (Bathurst et al. 2002). Considering that strain gauge measurements may be affected by attachment technique and non-uniform stiffness along a rib (Bathurst et al. 2002), tensile tests were conducted to obtain a correction factor (CF), defined as the ratio of global strain to gauge strain. The calibration results for loading rates of 1%/min, 10%/min, and 100%/min are shown in Figure 3.23. The average CF value calculated from the data is 1.1, and is not affected significantly by the loading rate. All measured geogrid strains were corrected using this CF value. Within the MSE bridge abutment specimen, strains were measured at 4 points along each of 5 geogrid layers for the baseline case.

(a) (b)

(c) (d)

(e) (f)

Figure 3.22 Sensors: (a) string potentiometer; (b) linear potentiometer; (c) pressure cell, (d) load cell; (e) accelerometer; (f) geogrid strain gauge.

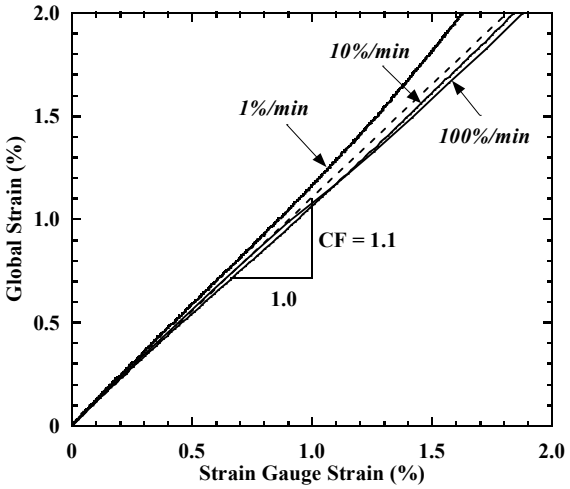

Figure 3.23 Calibration relationship for strain gauge measurements based on geogrid tensile tests with different loading rates.

3.5.2 Longitudinal Test

Instrumented sections for longitudinal tests are shown in Figure 3.24, including a longitudinal centerline section L1, longitudinal off-centerline section L2, and transverse section T1. The detailed instrumentation for each section are shown in Figure 3.25. The longitudinal centerline section L1 has extensive instrumentation to investigate the seismic response of MSE bridge abutment in the longitudinal direction. The longitudinal off-centerline section L2 has an offset of 18 in west from L1, and measurements are used to evaluate the plane strain assumptions in current design guidelines. Transverse section T1 has distance of 19 inches from the front wall facing, and measurements are used to evaluate the 3D effects on the response of MSE bridge abutment subjected to longitudinal shaking.

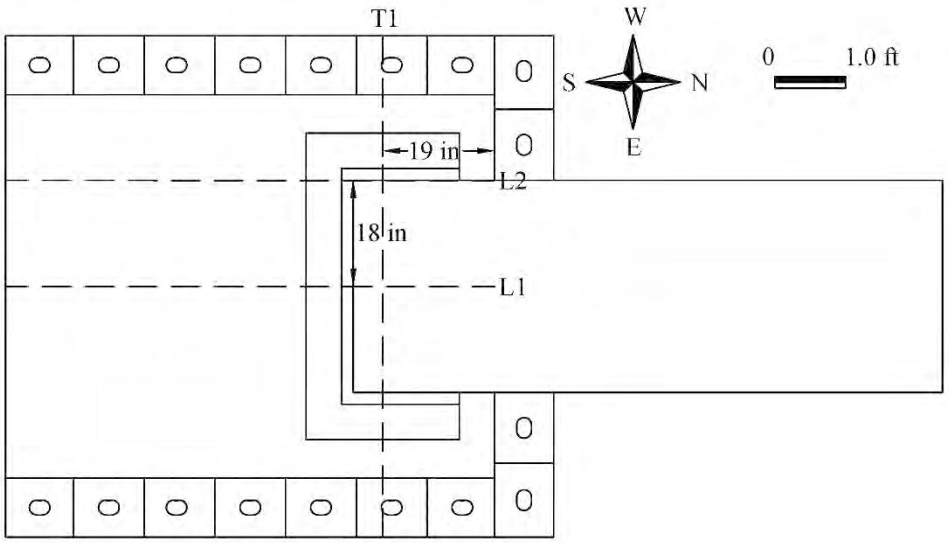

Figure 3.24 Instrumented sections for longitudinal test (shaking direction from North to South).

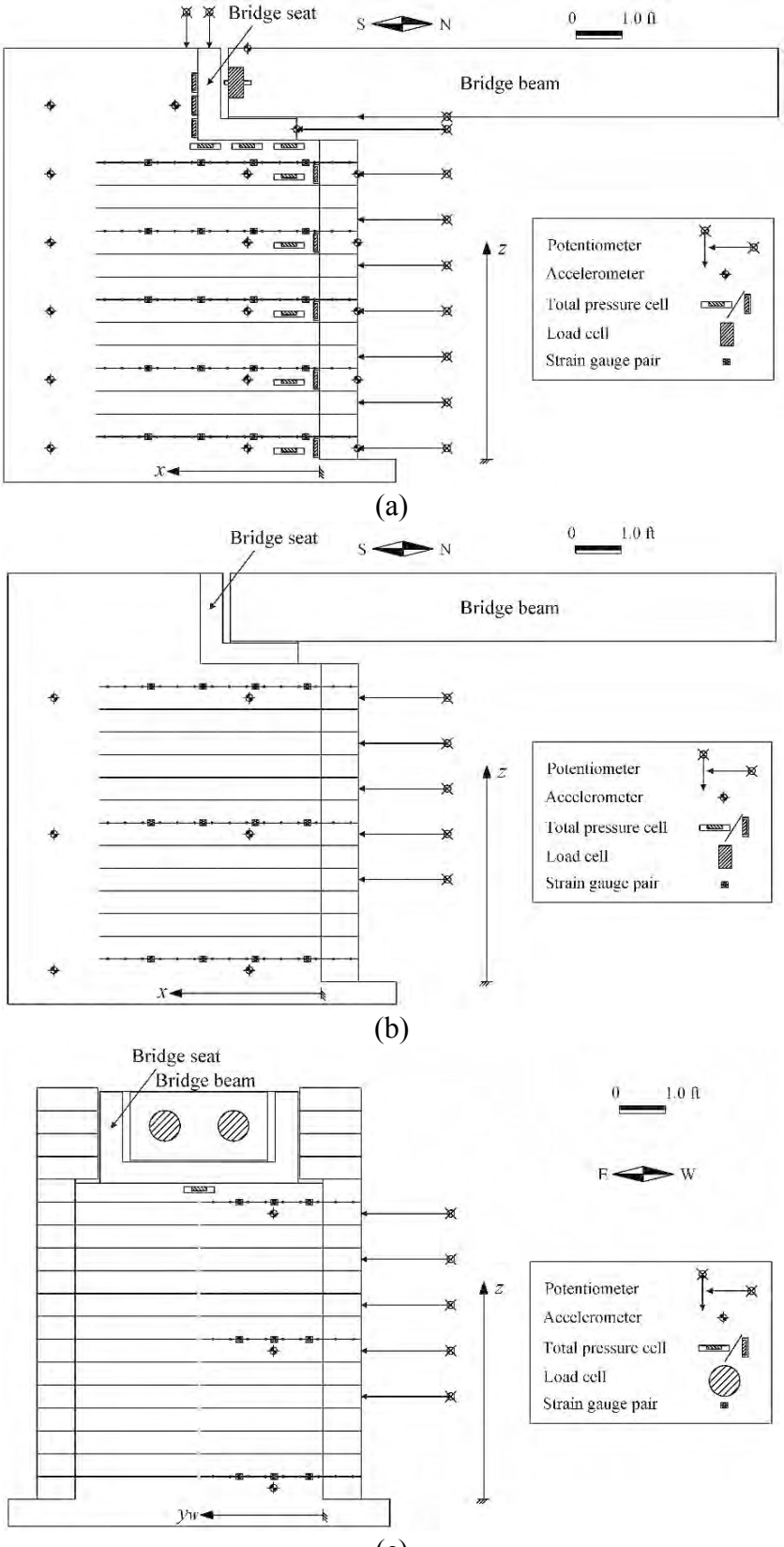

Figure 3.25 Instrumentation for longitudinal test: (a) L1; (b) L2; (c) T1.

3.5.3 Transverse Test

Instrumented sections for longitudinal tests are shown in Figure 3.26, including a transverse section T1 under the bridge seat, transverse section T2 behind bridge seat, and longitudinal centerline section L1. The detailed instrumentation for each section are shown in Figure 3.27. The transverse section T1 has extensive instrumentation to investigate the seismic response of MSE bridge abutment in the transverse direction. Measurements for longitudinal centerline section L1 are used to evaluate the 3D effects on the response of MSE bridge abutment subjected to transverse shaking.

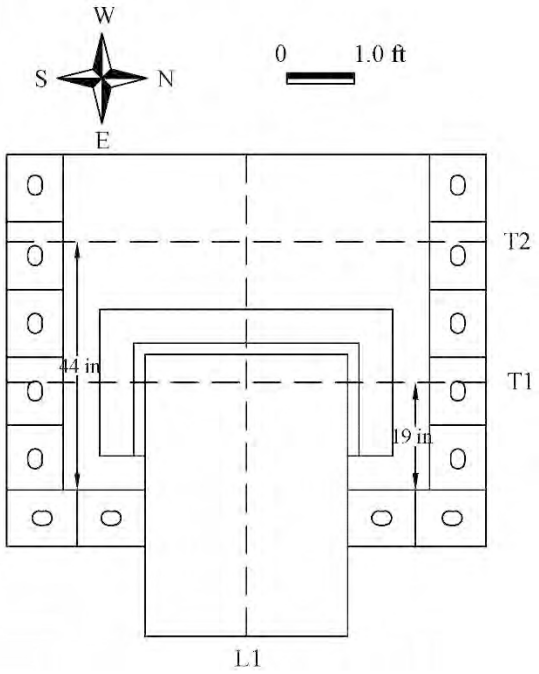

Figure 3.26 Instrumented sections for transverse test (shaking direction from North to South).

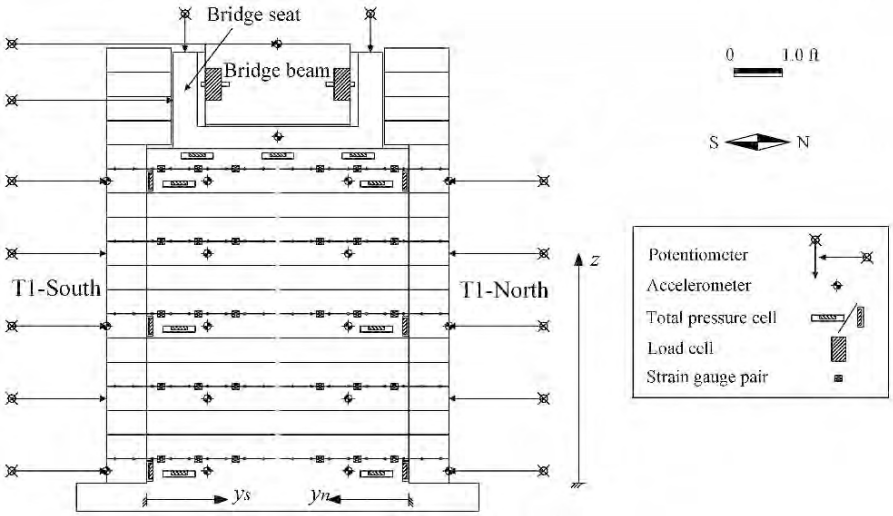

(a)

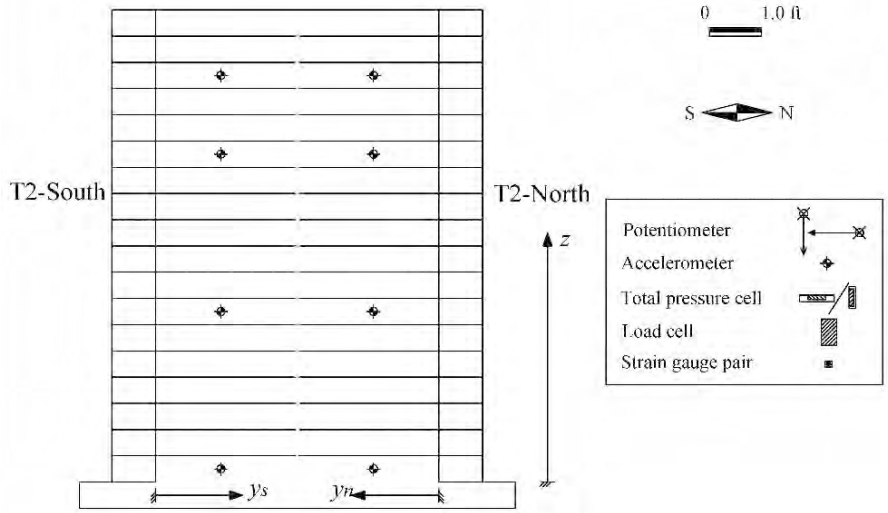

(b)

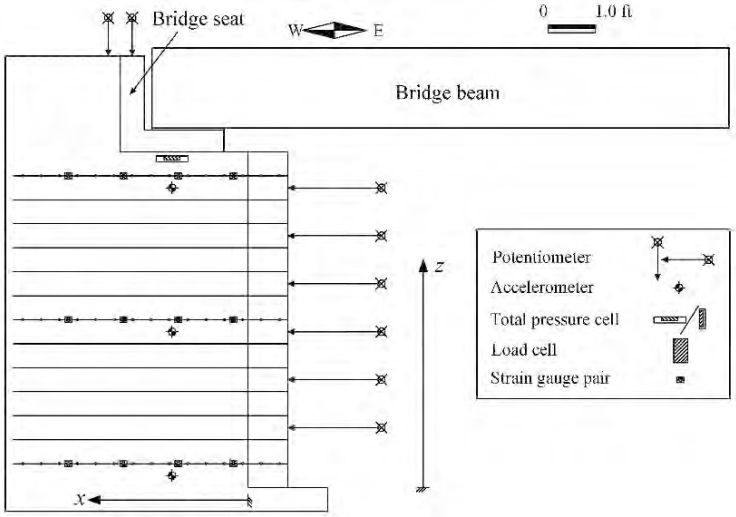

(c)

Figure 3.27 Instrumentation for transverse test: (a) T1; (b) T2; (c) L1.

3.6 Construction

A 6 inch-thick foundation sand layer was first placed within the edge containment of the shaking table and at a higher relative density (D_r = 85%) than the backfill sand to provide a firm base for the MSE bridge abutment. The table surface has transverse shear fins to transfer motion to the foundation layer with minimal slippage. The first course of facing blocks was placed and leveled on the foundation layer, with the side wall blocks offset vertically by 1 inch from the front wall blocks. This offset was needed to avoid direct contact between longitudinal and transverse geogrid layers and maintain interaction with the backfill soil. Although not used in actual MSE bridge abutments, this technique was necessary for the current study due to width constraints of the shaking table. As a result of the 1 inch offset, the side wall and front wall facing blocks could not be interlocked in a typical masonry pattern at the corners.

Longitudinal and transverse reinforcement layers were placed horizontally within the backfill soil from the block contact interfaces and are shown in Figure 3.28(a) and (b), respectively. The transverse reinforcement would not be expected to significantly affect abutment behavior in the longitudinal direction because geogrid stiffness in the cross-machine direction is much lower than in the machine direction. During construction, geogrid layers were placed between the blocks for over 80% of the block-to-block contact surface. Fiberglass pins were inserted through the geogrid apertures to assist with block alignment and did not significantly enhance the block-geogrid connections, which were essentially frictional. Although the upper 2 to 3 courses of block are typically grouted together in the field, particularly for higher seismic areas (Helwany et al. 2012), the upper course of blocks remained ungrouted for this test. After construction of the lower MSE wall, the bridge seat was placed on top of the backfill soil for the lower wall and the 2 ft-high upper wall was constructed in four lifts with only transverse reinforcement layers. Finally, the concrete bridge beam with additional dead weights was placed on the bridge seat and support wall. A bridge beam is typically placed prior to construction of upper wall in the field; however, the beam was added last in the current study for convenience.

(a)

(b)

Figure 3.28 Construction of MSE bridge abutment: (a) longitudinal reinforcement layer; (b) transverse reinforcement layer.

During construction of each soil lift, backfill sand was compacted with a target gravimetric water content of $w_c = 5\%$ and target relative density $D_r = 70\%$ using a vibratory plate compactor. Random soil samples were collected for each lift during construction to measure the actual gravimetric water content. The measured gravimetric water content profiles are shown in Figure 3.29 and indicates values ranging from 2.9 to 9.6%. Considering that the compaction curve is relatively flat for this sand, the variation in water content is unlikely to significantly affect compacted dry unit weight.

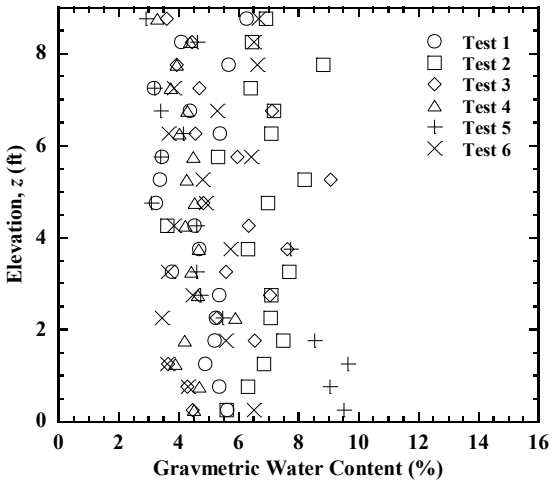

Figure 3.29 As-constructed gravimetric water content profiles.

The gravimetric water content profiles can be combined with the SWRC to estimate the apparent cohesion c_a using the suction stress concept of Lu et al. (2010):

$$c_a = \sigma^s \tan\phi' = S_e \psi_s \tan\phi' \tag{3.2}$$

where σ^s = suction stress, ψ_s = matric suction, and S_e = effective saturation, defined as:

$$S_e = \frac{\theta - \theta_r}{\theta_{\max} - \theta_r} \tag{3.3}$$

The calculated profiles of apparent cohesion for drying and wetting conditions in Figure 3.30. Apparent cohesion is essentially uniform at approximately 40 psf for both conditions. Apparent cohesion can have an important effect on the ultimate state of reinforced soil walls (Vahedifard et al. 2014, 2015), and unsaturated conditions can have a significant effect on the stiffness of sand (Khosravi et al. 2010).

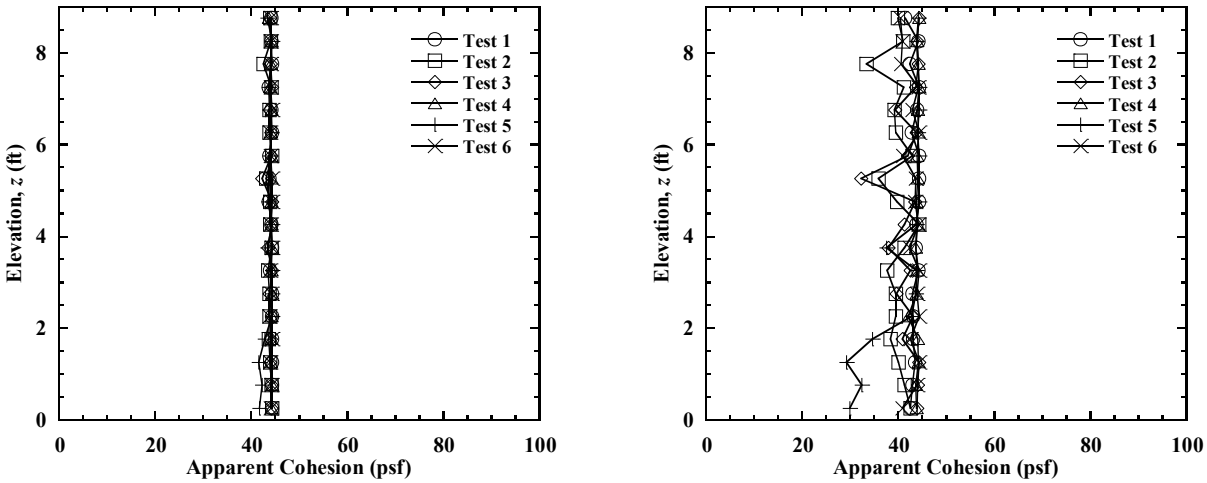

(a) (b)

Figure 3.30 Calculated apparent cohesion profiles: (a) drying condition; (b) wetting condition.

Sand cone tests were performed at selected elevations after compaction of the lift to measure actual dry unit weight, and results for all specimens are shown in Figure 3.31. The actual dry unit weight ranges from 101.8 to 113.2 pcf, and the corresponding relative density ranges from 54 to 86%. Due to the variability in the unit weight values interpreted from the sand cone tests, it is assumed that the achieved dry unit weight values in the shaking table experiments are consistent enough for direct comparison with each other. A summary of average gravimetric water content, dry unit weight, and relative density for each specimen is presented in Table 3.4.

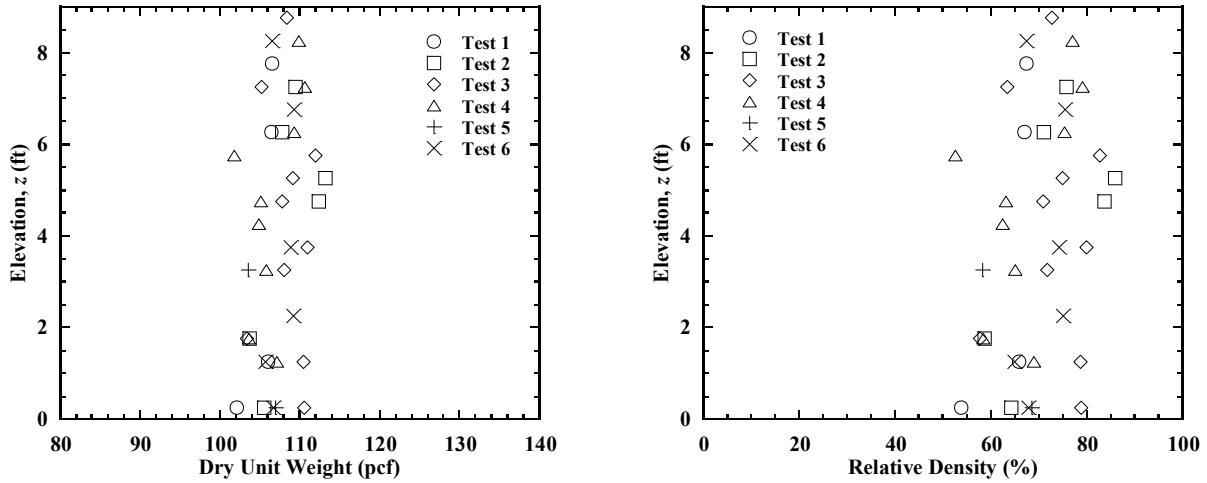

(a) (b)

Figure 3.31 Sand cone results: (a) dry unit weight; (b) relative density.

Table 3.4 Average gravimetric water content, dry unit weight, and relative density for each test.

Test	Average gravimetric water content (%)	Average dry unit weight (pcf)	Average relative density (%)
1	4.7	105.4	64
2	6.7	108.7	73
3	5.5	108.6	73
4	4.3	106.5	67
5	5.5	105.3	64
6	5.0	107.8	65

3.7 Input Motions

A series of motions, including white noise, earthquake, and sinusoidal motions, were applied to the MSE bridge abutment system in sequence, with a short pause (approximately 5 minutes) between each motion. The shaking table was operated in acceleration-control mode for white noise motions and displacement-control mode for earthquake and sinusoidal motions. A summary of the input motions for shaking table testing is presented in Table 3.5.

Table 3.5 Input motions for shaking table.

Shaking event	Motion	Model-scale duration (s)	Peak ground acceleration (*g*)	Peak ground displacement (in.)
1	White Noise	120.0	0.10	0.11
2	1940 Imperial Valley	28.3	0.31	2.57
3	White Noise	120.0	0.10	0.11
4	2010 Maule	100.4	0.40	4.25
5	White Noise	120.0	0.10	0.11
6	1994 Northridge[1]	28.3	0.58	3.49
7	White Noise	120.0	0.10	0.11
8	Sin @ 0.5 Hz	40.0	0.05	1.97
9	Sin @ 1 Hz	40.0	0.10	0.98
10	Sin @ 2 Hz	40.0	0.20	0.49
11	Sin @ 5 Hz	40.0	0.25	0.10
12	White Noise	120.0	0.10	0.11

[1] The Northridge earthquak motion was applied after the sinusoidal motions in Test 1

White noise motions were used to characterize natural frequencies of the bridge system, and identify any changes in system response (i.e., changes in global system modulus and damping) due to plastic strains incurred during previous shaking events. The nominal white noise motion has a peak acceleration of 0.1*g*, a root-mean-square (RMS) acceleration of 0.025*g*, and frequency content ranging from 0.1 to 50 Hz, as shown in Figure 3.32.

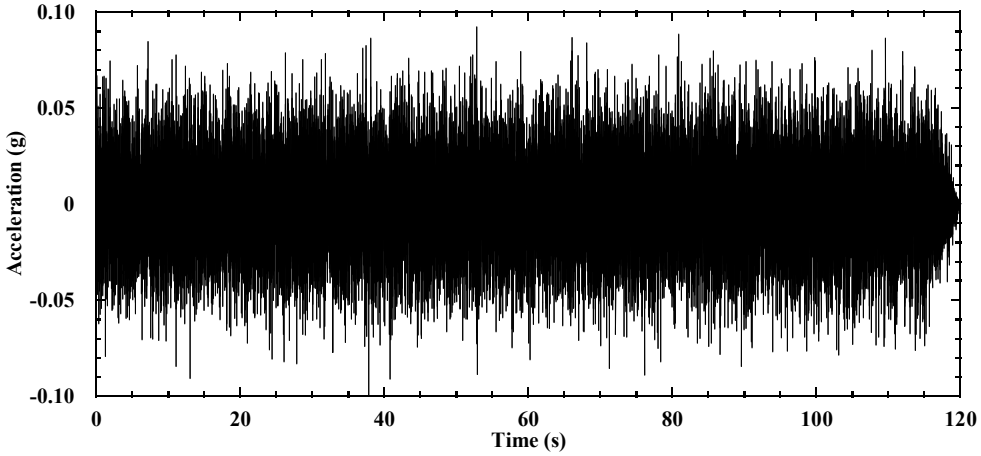

Figure 3.32 White noise motion.

Shaking tests were conducted using earthquake motions scaled from the strike-slip 1940 Imperial Valley earthquake (El Centro station), the subduction zone 2010 Maule earthquake (Concepcion station), and the strike-slip 1994 Northridge earthquake (Newhall station) records. Acceleration and displacement time histories for the original Imperial Valley record are shown in Figure 3.33, and indicate a peak ground acceleration (PGA) of 0.31*g* and peak ground displacement (PGD) of 5.14 inches. To obtain the input acceleration time history for the shaking test, also shown in Figure 3.33(a), acceleration amplitudes of the original record were not scaled and frequencies were scaled (increased) by a factor of $\sqrt{2}$. The scaled displacement time history is shown in Figure 3.33(b) and was obtained by double integration of the scaled acceleration. The displacement motion indicates PGD = 2.57 inches, which is one-half of the PGD for the original record. Scaled input motions for the Maule and Northridge earthquake records were obtained similarly, and yield PGA = 0.40*g* and PGD = 4.25 inches for the Maule motion and PGA = 0.58*g* and PGD = 3.49 inches for the Northridge motion, as shown in Figure 3.34 and Figure 3.35, respectively. The time increment is 0.00707 s for the scaled Imperial Valley and Northridge motions, and is 0.00354 s for the Maule motion.

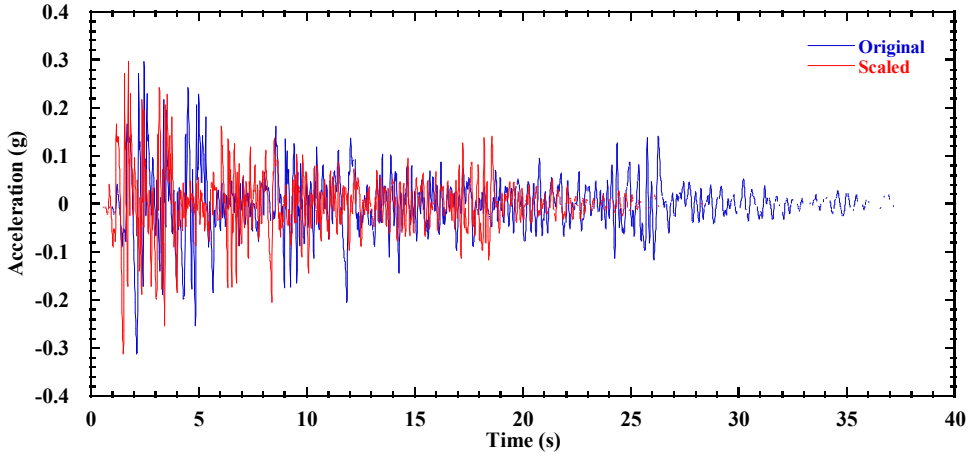

(a)

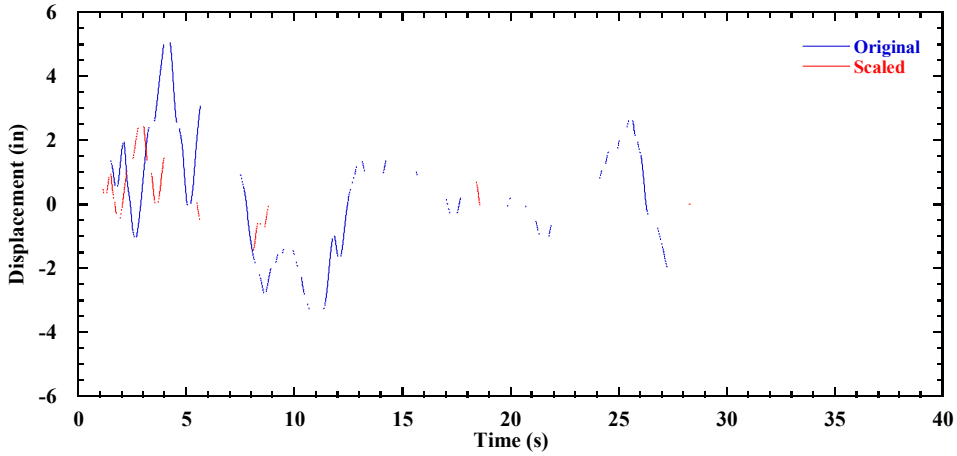

(b)

Figure 3.33 Original records and scaled motions for the 1940 Imperial Valley earthquake (El Centro station): (a) acceleration time history; (b) displacement time history.

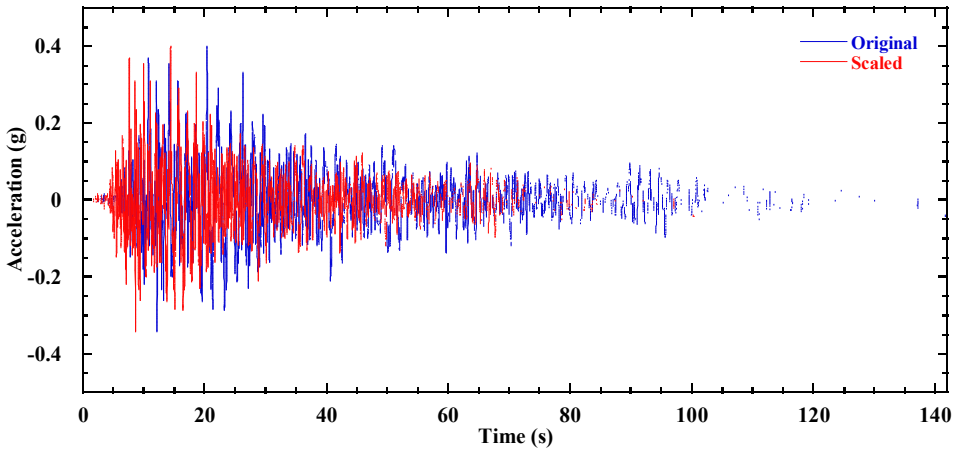

(a)

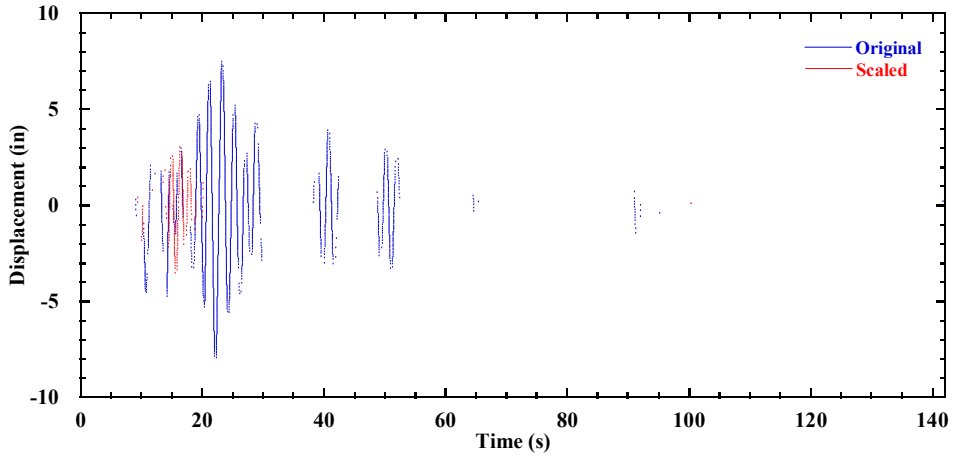

(b)

Figure 3.34 Original records and scaled motions for the 2010 Maule earthquake (Concepcion station): (a) acceleration time history; (b) displacement time history.

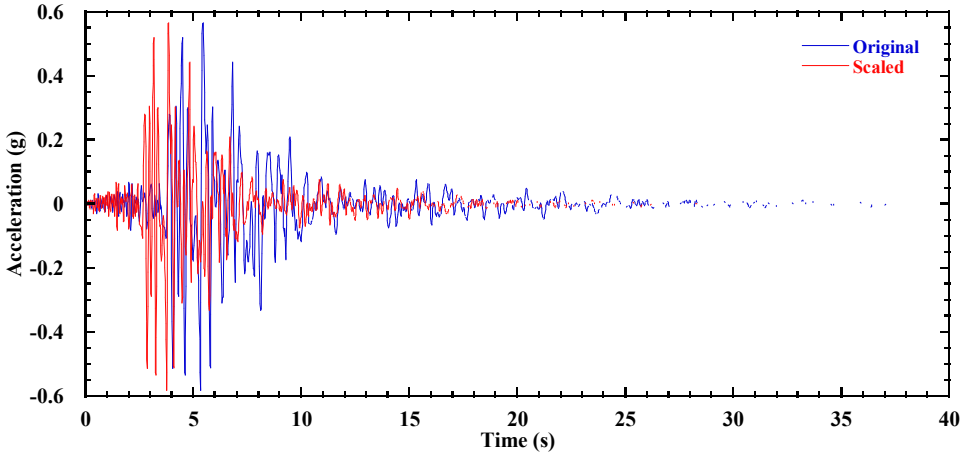

(a)

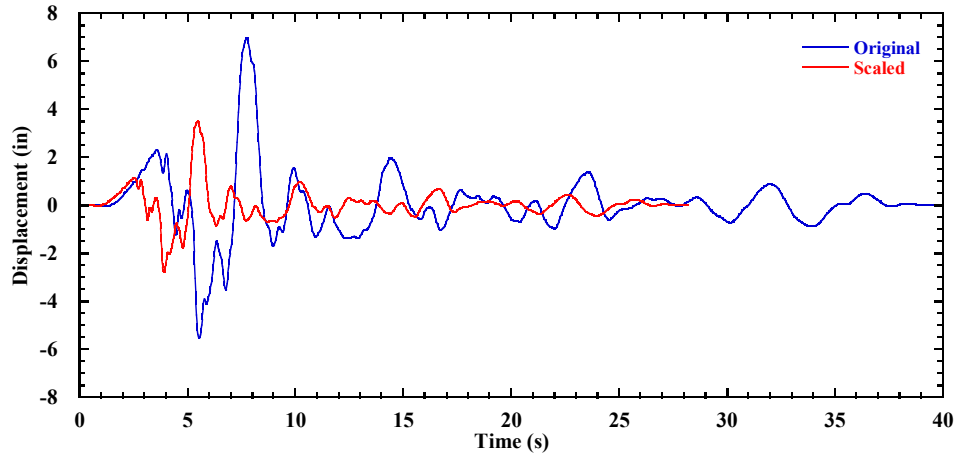

(b)

Figure 3.35 Original records and scaled motions for the 1994 Northridge earthquake (Newhall station): (a) acceleration time history; (b) displacement time history.

Chapter 4 Longitudinal Test Results and Analysis

This chapter presents results and analysis for the longitudinal tests on the MSE bridge abutments (Tests 1-5). In addition to the characterization tests for the system identification and testing system performance, results are presented in this chapter including facing displacements, bridge seat and bridge beam displacements, accelerations, vertical and lateral stresses, reinforcement strains, and contact forces between the bridge seat and bridge beam during a series of shaking events in the longitudinal direction. Detailed results including time histories for Test 1 (baseline case) are presented and discussed to describe the general behavior of MSE bridge abutments, and synthesis results from different tests are compared and discussed to investigate the effects of different design parameters.

When processing the data, the string potentiometer measurements for horizontal displacements of the front wall facing, bridge seat, and bridge beam were corrected using the measured horizontal displacements of the shaking table in the direction of shaking to yield relative displacements with respect to the table. In the direction of shaking, horizontal displacements and accelerations toward the north direction (Figure 3.18) are defined as positive. In the direction perpendicular to shaking, outward displacements of the side wall facings are defined as positive. Consistent with geotechnical sign conventions, downward vertical settlements are defined as positive. For static loading (construction stages), Stage 1 involved construction of the lower MSE wall, Stage 2 involved construction of the bridge seat and upper wall, and Stage 3 involved placement of the bridge beam atop the MSE bridge abutment. All presented results are in model-scale, and results should be adjusted using the similitude relationships in Table 3.2 to obtain corresponding values for prototype structures.

4.1 System Identification

System identification tests were conducted using the white noise motions at different stages of the shaking program. The first such test was conducted on the reaction wall itself prior to construction of the MSE bridge abutment. Amplitudes of the horizontal acceleration transfer functions (i.e., output divided by input in frequency domain) of the reaction wall with respect to the shaking table are shown in Figure 4.1(a). The reaction wall has a fundamental frequency of 37.5 Hz, which is well above the operating frequency band of the shaking table and fundamental frequency of the MSE bridge abutment. Therefore, the reaction wall is not expected to resonate during shaking and should move essentially in phase with the shaking table.

White noise tests also were conducted on the MSE bridge abutment system before and after each earthquake motion to detect changes in fundamental frequency due to softening of the backfill soil. Amplitudes of the horizontal acceleration transfer functions for the bridge beam and bridge seat with respect to the shaking table in the longitudinal direction for the initial white noise test (Shaking event 1) are shown in Figure 4.1(b). The results indicate fundamental frequencies of 5.5 Hz and 11.9 Hz for the bridge beam and bridge seat, respectively. Amplitudes of the horizontal acceleration transfer functions for the MSE bridge abutment (measured at x = 1.6 ft, z = 6.25 ft) with respect to the shaking table for white noise tests before and after the earthquake motions are shown in Figure 4.1(c). The MSE bridge abutment has the same fundamental frequency as the bridge seat (11.9 Hz) before the Imperial Valley motion. The corresponding fundamental frequency for the prototype MSE bridge abutment is 8.4 Hz according to the scaling factors in Table 3.2. After the Imperial Valley motion, the fundamental frequency of the abutment decreased from 11.9 to 11.3 Hz, and then decreased further to 10.9 Hz after the Maule motion. These decreases are attributed to shear modulus reduction of the backfill soil associated with shear strain development during successive shaking events.

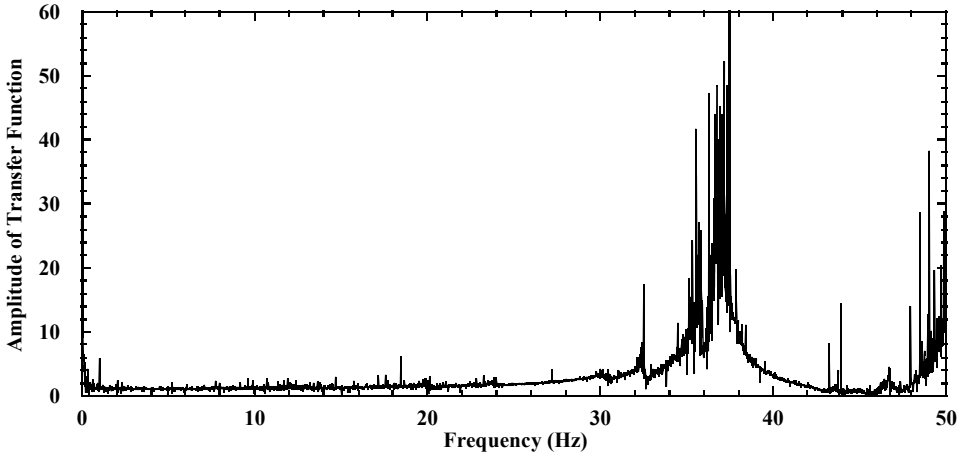

(a)

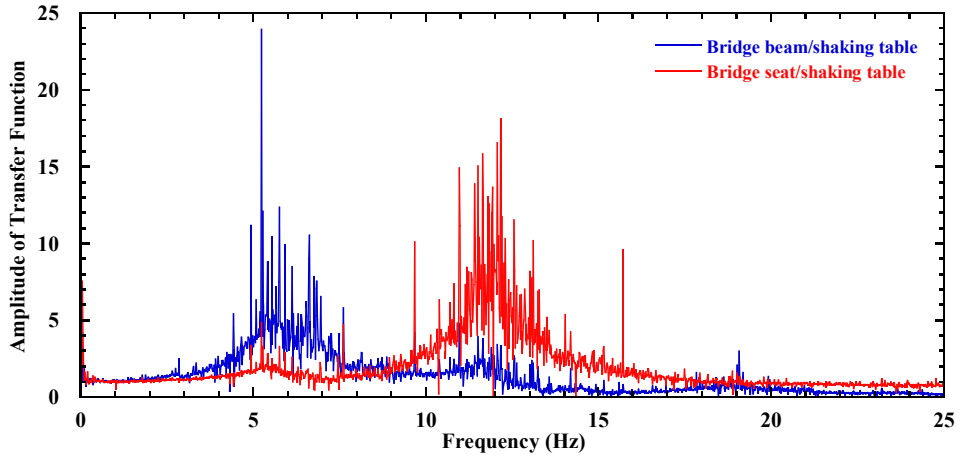

(b)

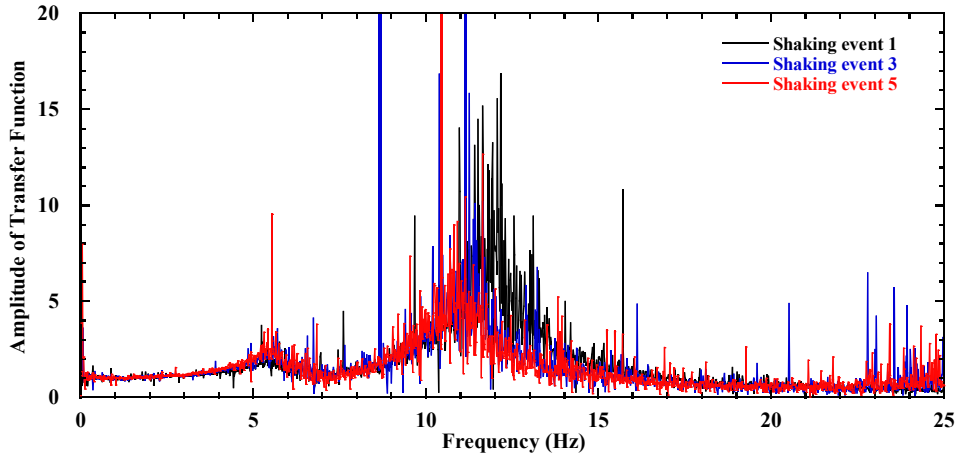

(c)

Figure 4.1 Horizontal acceleration transfer function amplitudes for white noise tests in Test 1: (a) reaction wall only; (b) bridge seat and bridge beam for the initial white noise motion; (c) MSE bridge abutment before and after the first two earthquake motions.

4.2 Testing System Performance

The characterization of the testing system performance is critical for the longitudinal test because the configuration of the bridge system with one end (i.e., support wall) moving on a sliding platform off the shaking table is unique and has not been evaluated in a previous shaking table experiment. The approach used in this study permits a unique evaluation of the MSE bridge abutment response in a longitudinal configuration.

The performance of the testing system (i.e., the shaking table and the connected support wall resting on the sliding platform) was evaluated by comparing the target input (referred to as target) and the measured actual (referred to as actual) displacement and acceleration responses in the direction of shaking. The testing system responses for the Imperial Valley, Maule, and Northridge motions in Test 1 are shown in Figure 4.2, Figure 4.3, and Figure 4.4, respectively, and a summary of the target and measured peak responses of the shaking table for the three earthquake motions is presented in Table 4.1.

Table 4.1 Shaking table response for earthquake motions in Test 1.

Shaking event	Earthquake motion	Model-scale duration (s)	Target PGA (*g*)	Actual PGA (*g*)	Target PGD (in.)	Actual PGD (in.)
2	Imperial Valley	28.3	0.31	0.42	2.57	2.57
4	Maule	100.4	0.40	0.58	4.25	4.25
11	Northridge	28.3	0.58	1.09	3.49	3.49

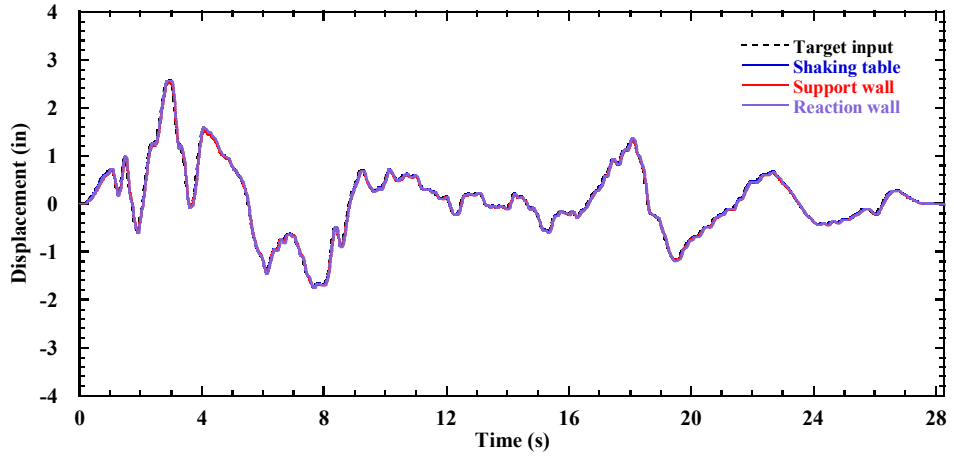

(a)

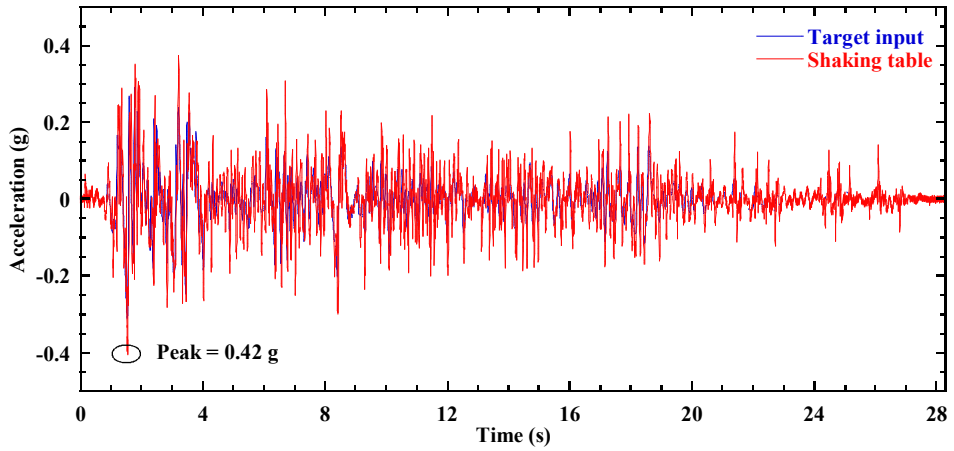

(b)

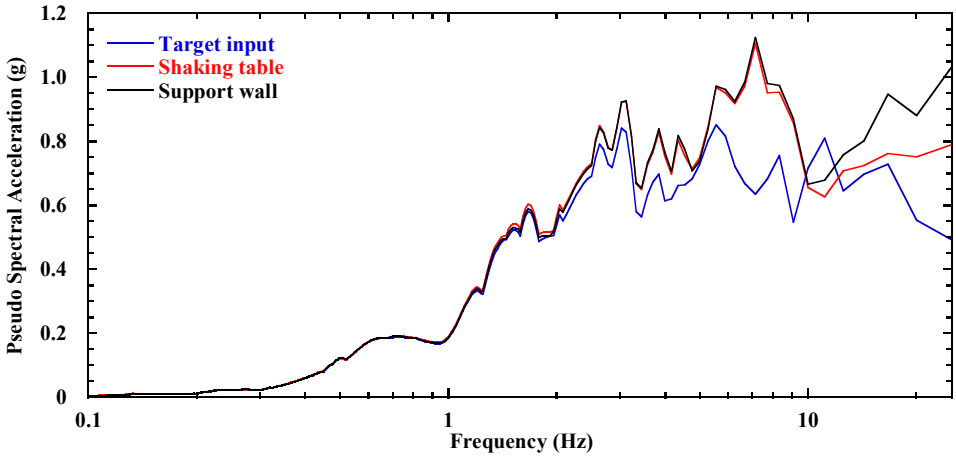

(c)

Figure 4.2 Testing system response for the Imperial Valley motion in Test 1: (a) displacement time history; (b) acceleration time history; (c) response spectra (5% damping).

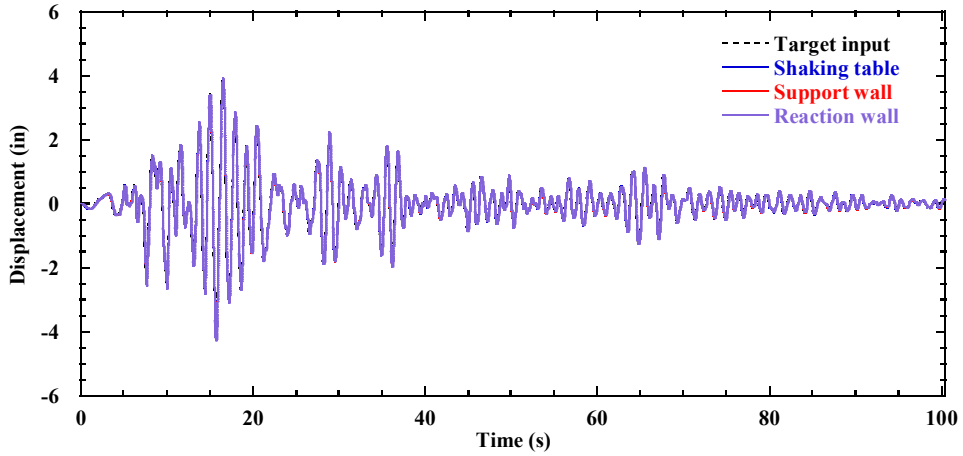

(a)

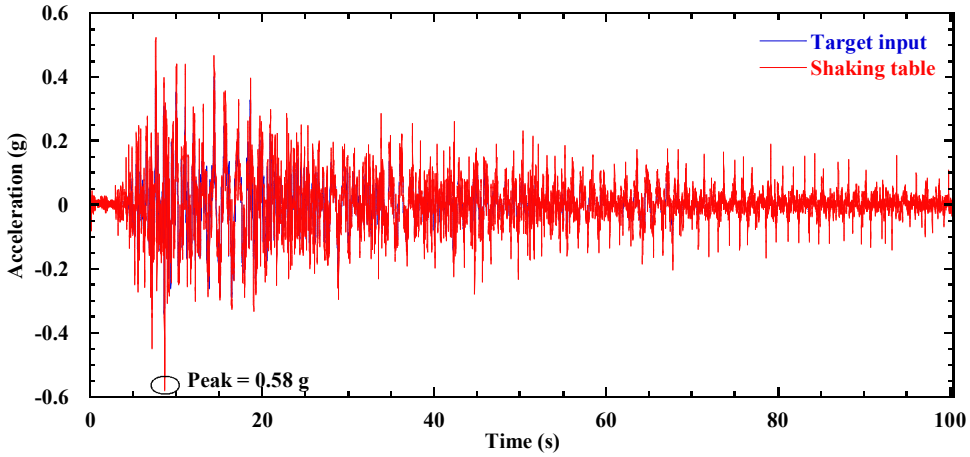

(b)

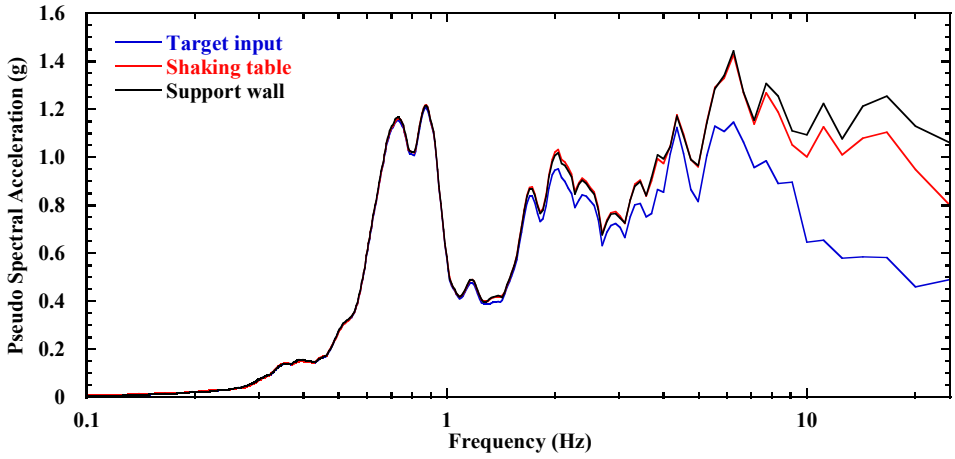

(c)

Figure 4.3 Testing system response for the Maule motion in Test 1: (a) displacement time history; (b) acceleration time history; (c) response spectra (5% damping).

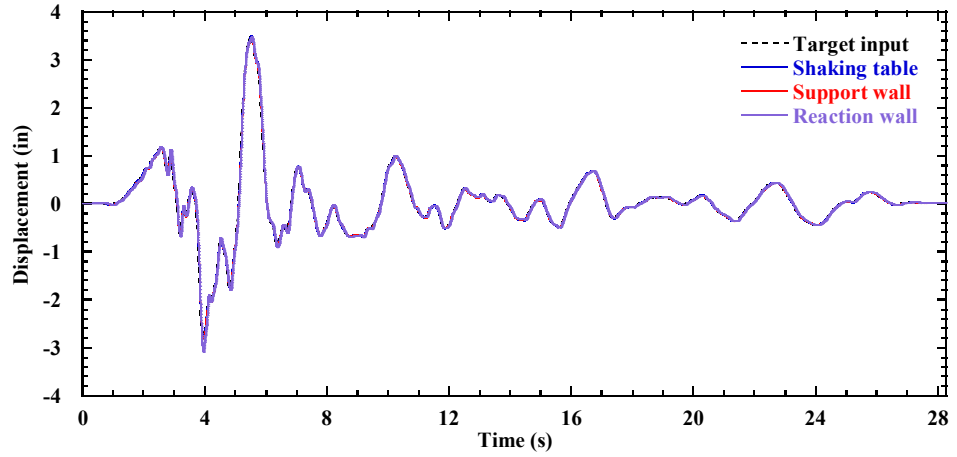

(a)

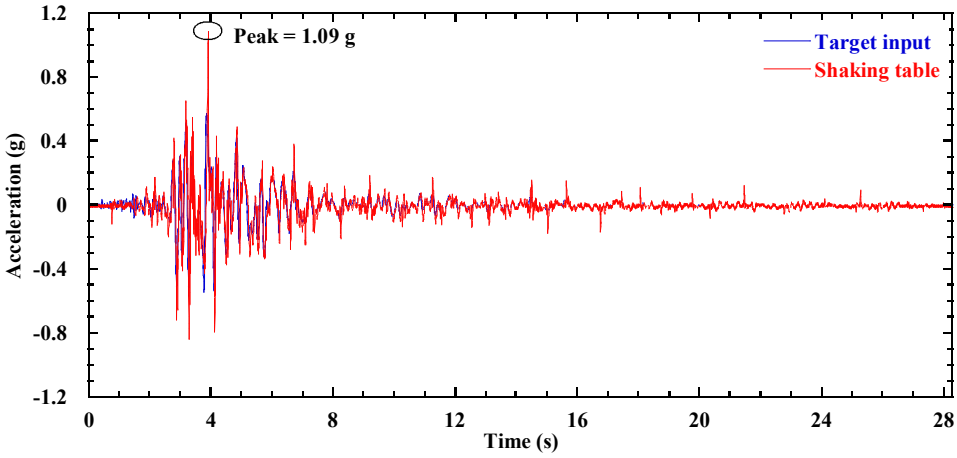

(b)

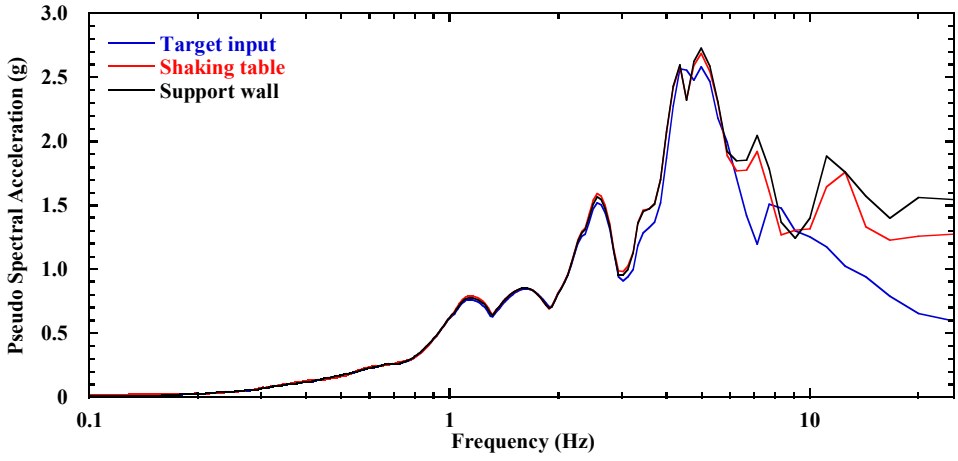

(c)

Figure 4.4 Testing system response for the Northridge motion in Test 1: (a) displacement time history; (b) acceleration time history; (c) response spectra (5% damping).

The measured displacement time histories of the shaking table, reaction wall, and support wall are in agreement and are essentially identical to the target input for all three earthquake motions. This indicates that (1) the shaking table performed well in displacement-control mode for the earthquake motions despite the high payload used in the experiments; (2) the reaction wall is sufficiently stiff and moved essentially in-phase with the shaking table; and (3) the steel connection beams and sliding platform successfully transmitted table motions to the base of the support wall.

The measured acceleration time history for the shaking table, generally matches well with the target input accelerations, but shows larger peak accelerations. For instance, the measured peak acceleration of the shaking table for the Imperial Valley motion is 0.42*g* at 1.6 s, which is larger than the target value of 0.31*g*. The shaking table was refurbished prior to this study to increase the fidelity of dynamic motion. After repair of the shaking table, overshooting of peak accelerations was still observed, but the overshooting was much smaller than before repair, which indicates that the performance of the shaking table has been improved (Trautner et al. 2017). The overshooting is likely due to the inertia of the shaking table itself, and may have been affected by the response of the structures on the shaking table.

The pseudo-spectral accelerations of the shaking table and target motion are in good agreement for frequencies less than 10 Hz for all three motions, which indicates that the shaking table adequately reproduced the salient characteristics of the target input motions. The actual pseudo-spectral acceleration at the fundamental frequency of 11.9 Hz for the MSE bridge abutment is slightly larger than the target value for all three motions. In general, results show that the shaking table followed the target input motion, and the support wall moved in phase with the shaking table.

4.3 Facing Displacements

4.3.1 Static Loading

Facing displacements were measured for the longitudinal centerline and off-centerline sections (referred to as L1 and L2 as labeled in Figure 3.24) and the transverse section T1 (referred to as T1). Facing displacement profiles for the three instrumented sections after the three stages of construction are shown in Figure 4.5, and the maximum values of facing displacement profiles are presented in Table 4.2.

For Stage 1, facing displacement profiles for the longitudinal sections L1 and L2 are similar, and have maximum displacements of 0.09 inches and 0.08 inches, respectively, both at an elevation z = 2.25 ft above the foundation soil level. Transverse section T1 has smaller facing displacements with a maximum value of 0.05 inches at the mid-height of the wall. Although the shapes of facing displacement profile for the longitudinal and transverse sections are different, the magnitudes of the facing displacements are small, and it is difficult to identify a consistent shape to reflect construction effects. For Stage 2, facing displacements increased slightly due to construction of the bridge seat and upper wall. For Stage 3, the upper half section of the wall increased approximately 0.04 inches for all three sections. The maximum displacement for L1 is 0.13 inches at z = 5.25 ft, and the maximum value for T1 is 0.09 inches at z = 4.25 ft. In general, the longitudinal sections L1 and L2 had similar facing displacement profiles for construction stages, and the transverse section T1 showed smaller displacements.

Table 4.2 Maximum facing displacements (in.) for construction stages in Test 1 (model-scale).

Construction stage	L1	L2	T1
Stage 1	0.09	0.08	0.05
Stage 2	0.10	0.10	0.05
Stage 3	0.13	0.14	0.09

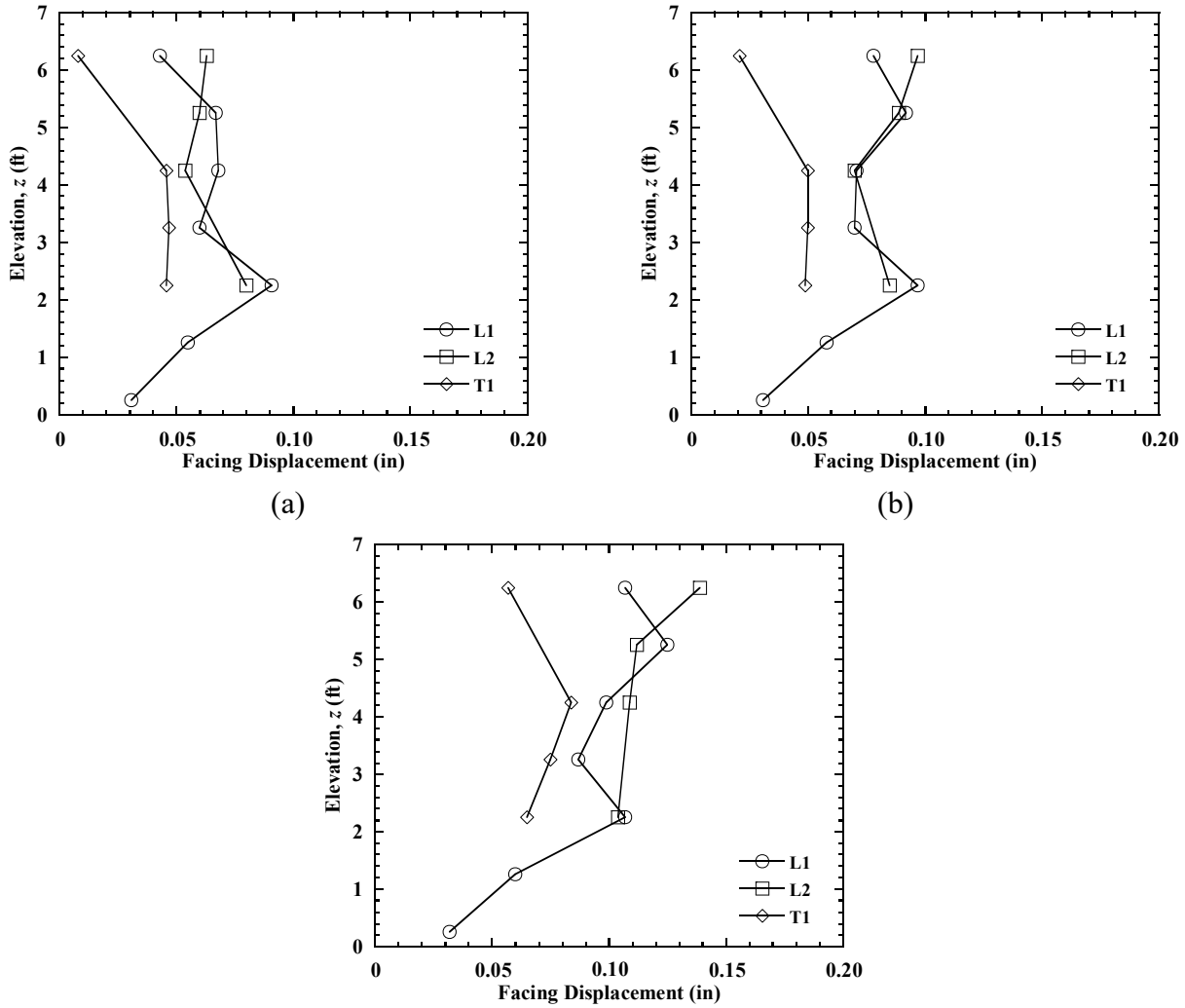

Figure 4.5 Facing displacement profiles for construction stages in Test 1: (a) Stage 1; (b) Stage 2; (c) Stage 3.

Facing displacement profiles for different tests (Tests 1-5) after Stages 1 and 3 are shown in Figure 4.6 and Figure 4.7, respectively, and the maximum values of the facing displacement profiles are presented in Table 4.3. For Stage 1, facing displacements of the longitudinal section L1 are the largest for Test 4 with a maximum value of 0.19 inches at z = 3.25 ft, and the facing displacement profiles for Test 3 also show slightly larger facing displacements than Tests 1, 2, and 5 with a maximum displacement of 0.11 inches at the same elevation. For the transverse section T1, facing displacements for Tests 2, 3, and 4 are similar and are larger than for Tests 1 and 5. For Stage 1, Test 1 had similar facing displacements with Test 2 for L1, but smaller displacements for T1, which may be attributed to greater compaction near the side wall facings for Test 2 during construction, as the specimens for Tests 1 and 2 have the same configuration at this stage.

For Stage 3, the facing displacements measured for L1 in Tests 3 and 4 are larger than those measured in Tests 1, 2, and 5, with maximum values of 0.20 and 0.24 inches, respectively, which indicate that the reinforcement stiffness and spacing have important effects on the facing displacements. Test 1 has larger facing displacements than Test 2 for the upper section of the wall due to the greater surcharge stress in Test 1. For instance, the maximum facing displacement of 0.13 inches for L1 in Test 1 at z = 5.25 ft is greater than 0.09 inches at the same elevation for Test 2. Test 5 has the smallest facing displacements due to the much larger reinforcement stiffness than other tests. Larger facing displacements for T1 are observed in Tests 3 and 4, as shown in Figure 4.7(b), similar to the observations for L1 in these tests. Facing displacements for T1 in Test 2 are larger than Test 1, which is consistent with the observations from Stage 1.

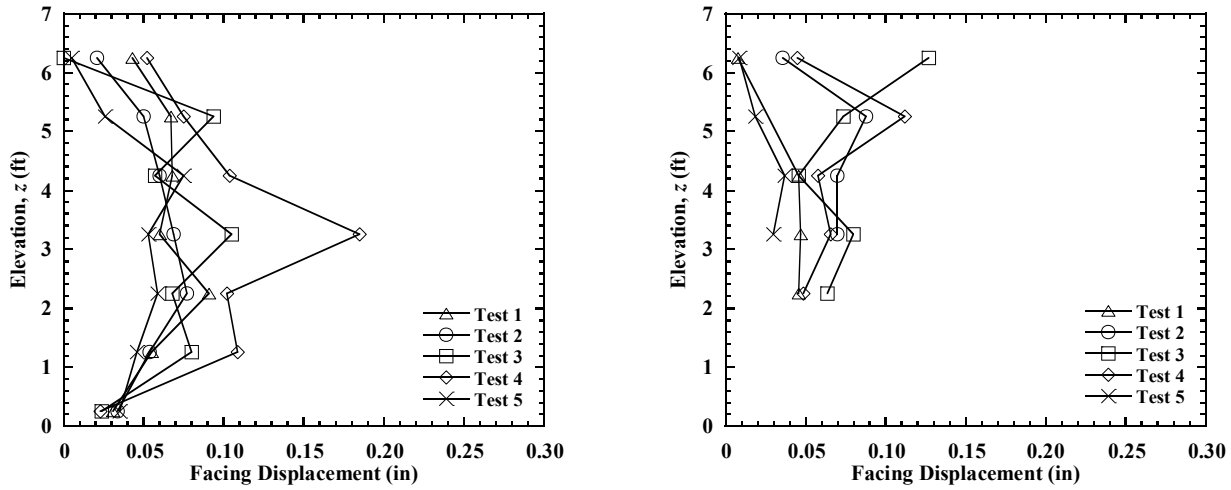

Figure 4.6 Facing displacement profiles for Stage 1 in Tests 1 to 5: (a) L1; (b) T1.

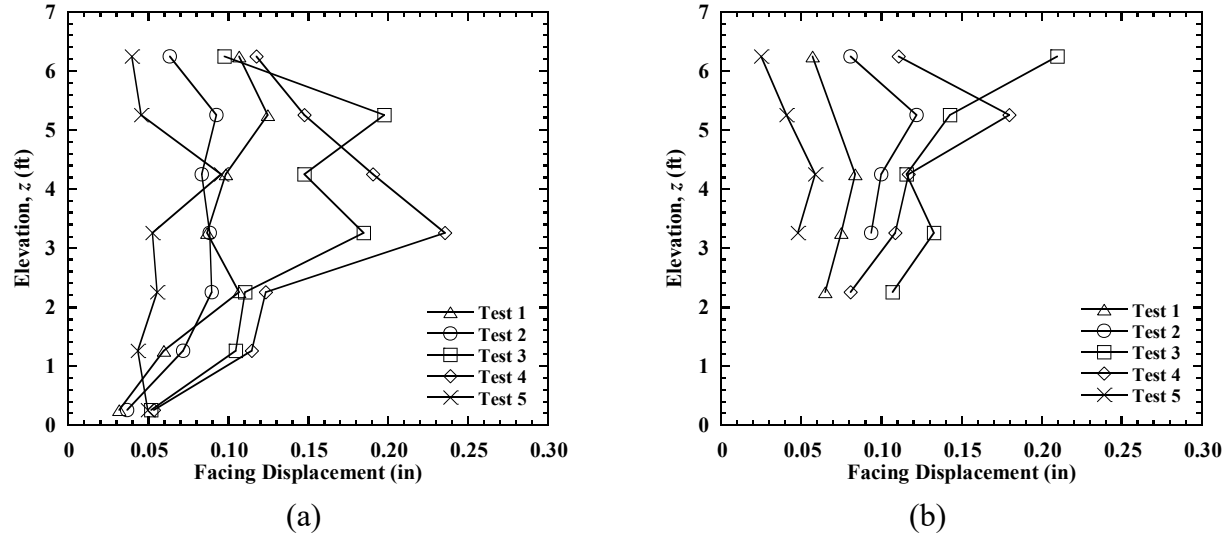

Figure 4.7 Facing displacement profiles for Stage 3 in Tests 1 to 5: (a) L1; (b) T1.

Table 4.3 Maximum facing displacements (in.) for construction stages in Tests 1 to 5 (model-scale).

Construction stage	Test 1		Test 2		Test 3		Test 4		Test 5	
	L1	T1	L1	T1	L1	T1	L1	T1	L1	T1
Stage 1	0.09	0.05	0.08	0.09	0.11	0.13	0.19	0.11	0.08	0.04
Stage 2	0.10	0.05	0.09	0.11	0.13	0.17	0.20	0.14	0.09	0.06
Stage 3	0.13	0.09	0.09	0.12	0.20	0.21	0.24	0.18	0.10	0.06

Facing displacements for Stages 1 and 2 might be subjected to the influences of construction technique (e.g., backfill soil compaction and facing block alignment) to some extent. In order to better understand the effects of different design parameters for static loading conditions, the incremental facing displacements due to placement of bridge beam (from Stages 2 to 3) for L1 and T1 are plotted in Figure 4.8. For the longitudinal section L1, Test 3 has the largest incremental facing displacements with a maximum value of 0.08 inches at z = 5.25 ft, and the incremental facing displacement is 0.06 inches for Test 4 at the same elevation. Tests 1 and 2 have similar incremental facing displacements for the lower section of the wall, but the incremental facing displacements of the upper section in Test 1 are slightly larger than Test 2, as expected. Test 5 has the smallest incremental facing displacements with a maximum value of 0.01 inches at the top of the wall. Similar to the incremental facing displacement profiles for L1, Test 3 has the largest incremental facing displacements for T1, while Test 5 has the smallest displacements. The facing displacement profiles for Tests 1 and 4 are similar. The incremental facing displacements of T1 for Test 1 are larger than Test 2, though the cumulative facing displacements are smaller at the end of construction (Figure 4.7).

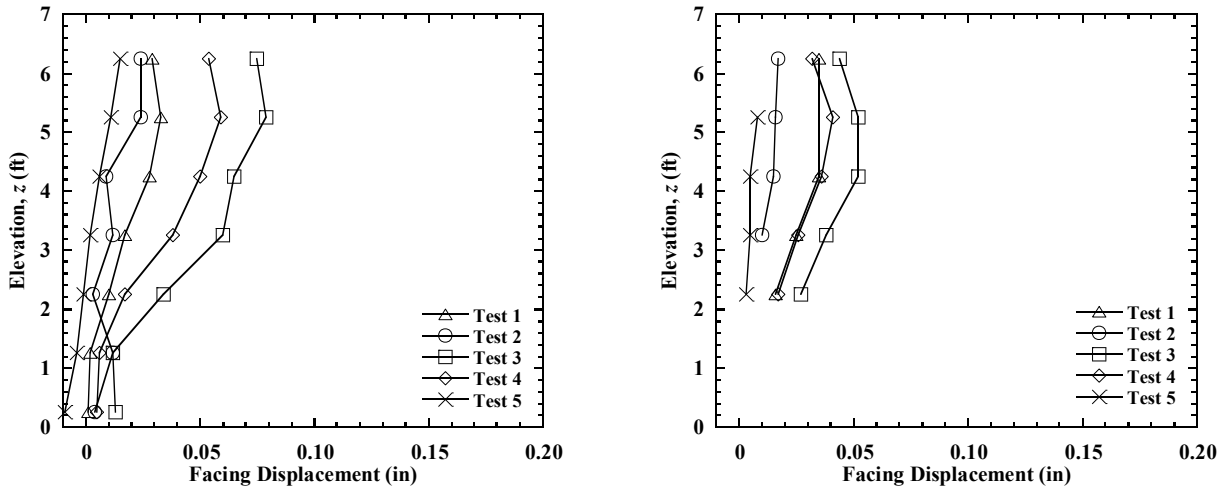

Figure 4.8 Incremental facing displacement profiles due to bridge beam placement (from Stages 2 to 3) in Tests 1 to 5: (a) L1; (b) T1.

Results in this section indicate that the reinforcement spacing and stiffness have important effects on the facing displacements of MSE bridge abutments for static loading conditions. Facing displacements increase with increasing reinforcement spacing and decreased reinforcement stiffness. The MSE bridge abutment using steel reinforcement with much larger tensile stiffness than geosynthetic reinforcement has the smallest facing displacements. Greater bridge surcharge stress also induces larger facing displacements for the upper section of the wall in both the longitudinal and transverse directions.

4.3.2 Dynamic Loading

Profiles of incremental maximum and residual facing displacements of the three instrumented sections for each earthquake motion are shown in Figure 4.9, and maximum values of the incremental facing displacement profiles are presented in Table 4.4. The maximum facing displacement profiles correspond to the specific times associated with maximum incremental outward facing displacement measurements.

For the Imperial Valley motion, the maximum outward displacements of the front wall for L1 are slightly larger than for L2, with maximum values of 0.15 and 0.14 inches, respectively. These maximum values occur at the top of the wall for both sections. The facing displacement profiles for L1 and L2 correspond to the specific times associated with maximum facing displacement measurements of L1 (i.e., t = 1.59 s for the Imperial Valley motion). The maximum outward displacement profile of the west side wall facing (t = 1.98 s) for the transverse direction T1 has a similar trend to the longitudinal sections L1 and L2, with an approximately linear increase with increasing elevation with a maximum value of 0.15 inches at the top of the wall. Residual facing displacements for three sections are also similar, and range from 0.02 to 0.06 inches and generally increase toward the top of the wall. Visual comparison of the maximum and residual facing displacement profiles clearly indicates that dynamic facing displacements are largely recovered after shaking, especially for the upper section of the wall. Figure 4.9 also indicates that shaking in the longitudinal direction induced facing displacements in the transverse direction for the side walls.

Figure 4.9(b) shows that the magnitudes of both the maximum and residual facing displacements for the Maule motion are similar to the Imperial Valley motion. However, the maximum facing displacements for the Northridge motion are much larger than for the other two motions. Maximum facing displacements increase almost nearly with increasing elevation for all sections. The longitudinal sections L1 and L2 have similar maximum displacement profiles with maximum values of 0.40 and 0.35 inches at the top of the wall, whereas the transverse section T1 has much larger facing displacements with a maximum value of 0.69 inches at the same elevation. The residual facing displacements are similar for the three sections, and also increase with elevation up to 0.13 inches.

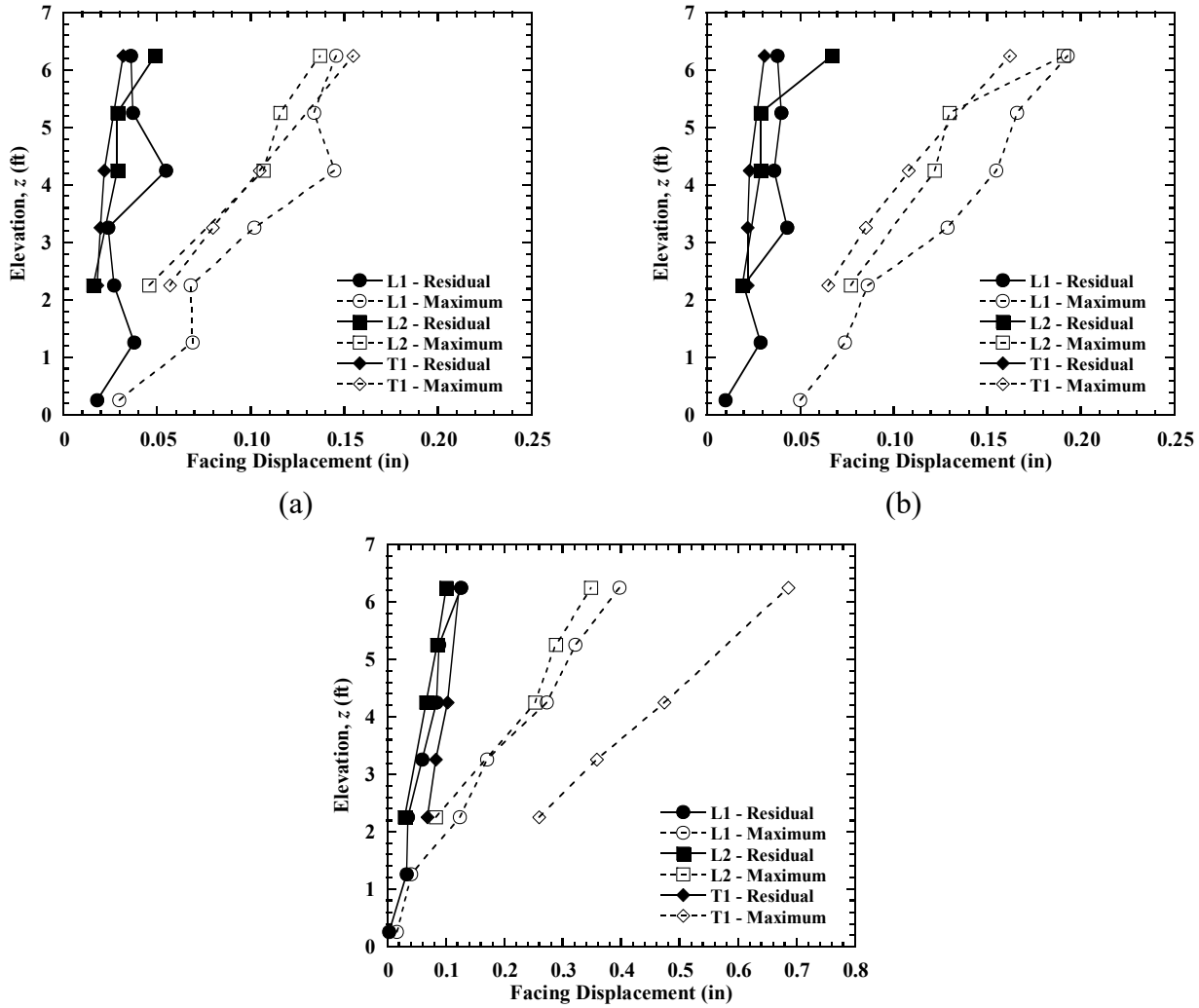

Figure 4.9 Incremental facing displacement profiles in Test 1: (a) Imperial Valley motion; (b) Maule motion; (c) Northridge motion.

Table 4.4 Maximum incremental facing displacements (in.) for earthquake motions in Test 1 (model-scale).

Earthquake motion	L1		L2		T1	
	Maximum	Residual	Maximum	Residual	Maximum	Residual
Imperial Valley	0.15	0.06	0.14	0.05	0.15	0.03
Maule	0.19	0.04	0.19	0.07	0.16	0.03
Northridge	0.40	0.13	0.35	0.10	0.69	0.12

Incremental residual facing displacement profiles for the Imperial Valley, Maule, and Northridge motions in Tests 1 to 5 are shown in Figure 4.10, Figure 4.11, and Figure 4.12, respectively. For instance, for the Imperial Valley motion, facing displacements for L1 are the largest in Test 3 (increased reinforcement spacing) with a maximum value of 0.17 inches at the top of the wall. Test 4 (reduced reinforcement stiffness) has similar facing displacements to Test 4 for the lower section of the wall, but smaller facing displacements for the upper section with a maximum value of 0.12 inches at the top of the wall. Tests 1, 2, and 5 have smaller reinforcement vertical spacing and larger reinforcement stiffness than Tests 3 and 4, also have smaller facing displacements under dynamic loading. In contrast to the facing displacements under static loading, Test 1 (baseline case) has smaller facing displacements than Test 2 (reduced bridge surcharge stress) under dynamic loading, which is attributed to the larger backfill soil stiffness under greater bridge surcharge stress for Test 1. Similar trends for facing displacements of L2 are also observed in Figure 4.10(b), but the magnitudes of facing displacements are slightly smaller than L1. For instance, the maximum facing displacement of 0.13 inches for L2 at the top of the wall in Test 3 is smaller than the maximum value of 0.17 inches at the same elevation for L1. For the facing displacements of T1, Test 3 also has the largest facing displacements with a maximum value of 0.09 inches at the top of the wall, and Test 4 shows a similar trend with Test 3, but with smaller facing displacements.

Facing displacements for Tests 1 and 2 are similar and range from 0.02 to 0.03 inches, and Test 5 has the smallest facing displacements. Facing displacements for the Maule motion are similar to the Imperial Valley motion with similar trends, while the Northridge motion has larger facing displacements. For the Northridge motion, Test 1 experienced larger facing displacements than Test 2, which is different from the other two motions. This is attributed to the softer behavior of the MSE bridge abutment in Test 1 before shaking because the Northridge motion was applied after the sinusoidal motions for Test 1.

In general, the reinforcement spacing and stiffness show the most significant effects on facing displacements under dynamic loading. Facing displacements increase significantly with increased reinforcement spacing and reduced reinforcement stiffness. In contrast to static loading, facing displacements are smaller for greater bridge surcharge stress under dynamic loading, which is attributed to the greater backfill soil stiffness under the confining stress associated with the greater bridge surcharge stress.

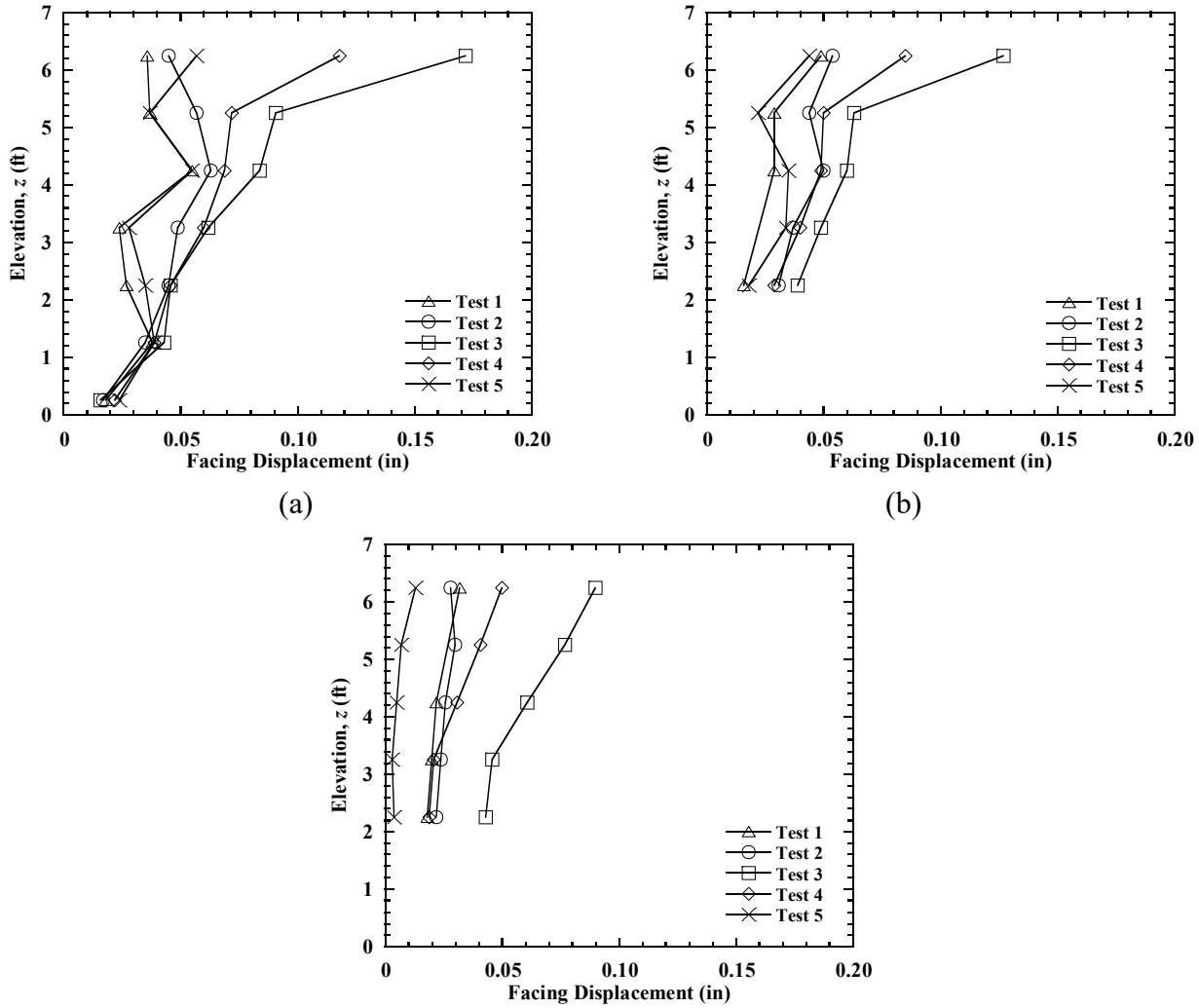

Figure 4.10 Incremental residual facing displacement profiles for the Imperial Valley motion in Tests 1 to 5: (a) L1; (b) L2; (c) T1.

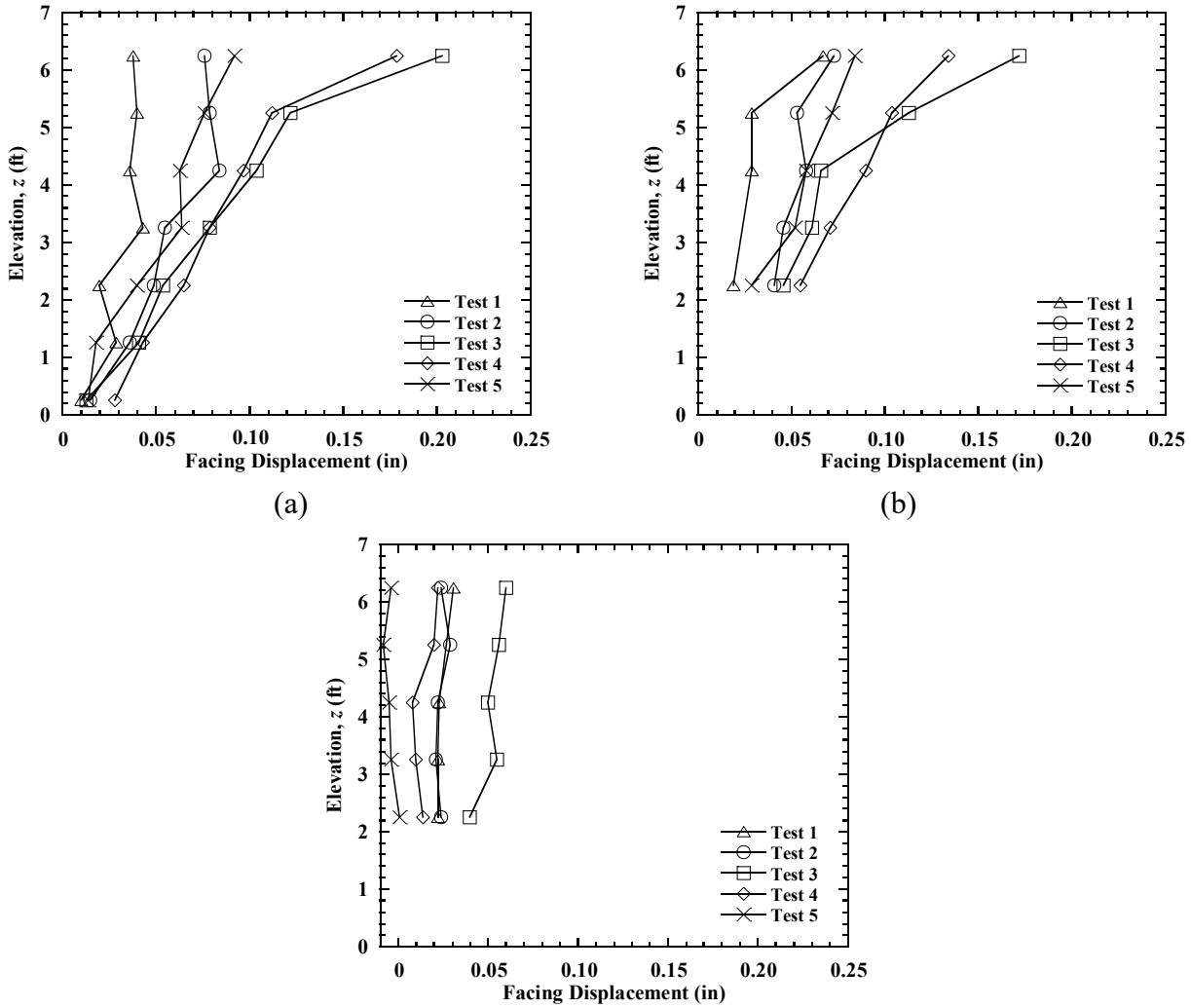

Figure 4.11 Incremental residual facing displacement profiles for the Maule motion in Tests 1 to 5: (a) L1; (b) L2; (c) T1.

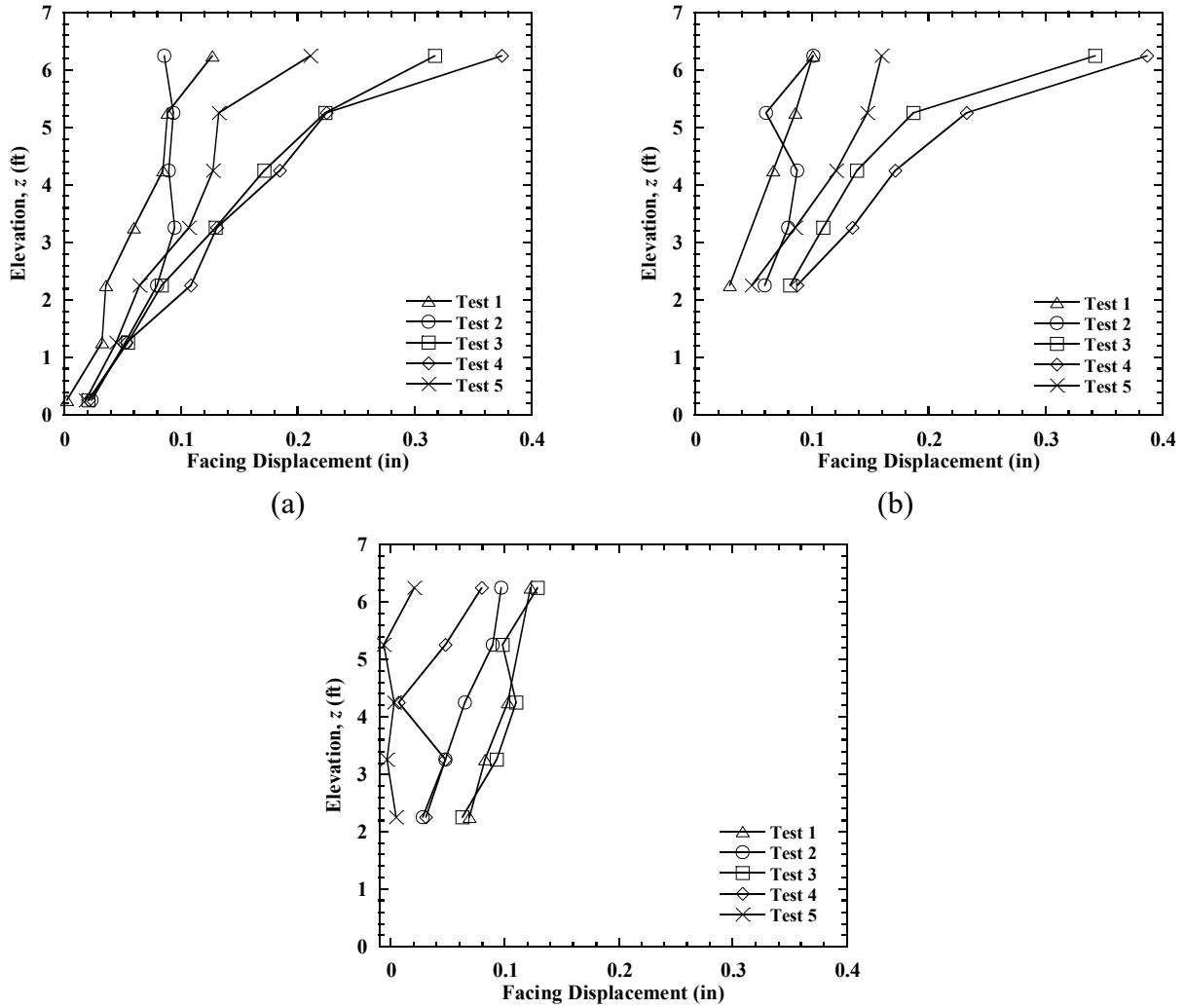

Figure 4.12 Incremental residual facing displacement profiles for the Northridge motion in Tests 1 to 5: (a) L1; (b) L2; (c) T1.

Table 4.5 Maximum incremental residual facing displacements (in.) for earthquake motions in Tests 1 to 5 (model-scale).

Earthquake motion	Test 1		Test 2		Test 3		Test 4		Test 5	
	L1	T1	L1	T1	L1	T1	L1	T1	L1	T1
Imperial Valley	0.06	0.03	0.06	0.03	0.12	0.09	0.12	0.05	0.06	0.01
Maule	0.04	0.03	0.08	0.03	0.18	0.06	0.18	0.02	0.09	0
Northridge	0.13	0.12	0.09	0.10	0.21	0.13	0.21	0.08	0.21	0.01

4.4 Bridge Seat and Bridge Beam Displacements

4.4.1 Bridge Seat Settlements

4.4.1.1 Static Loading

Settlements of the bridge seat were measured under static and dynamic loading at the four locations shown in Figure 3.18. One of the string potentiometers on the southeast (SE) side of the bridge seat was not working for Stage 3 (placement of the bridge beam) but was replaced before application of the earthquake motions. Settlement time histories of bridge seat corner measurements and average values for Stage 3 are shown in Figure 4.13. The settlements due to application of the bridge beam were relatively instantaneous and did not vary significantly over time, indicating negligible creep. The settlement on the west side of the bridge seat (NW and SW) is 0.12 inches, while the settlement on the east (NE) is 0.03 inches. This indicates tilting of the bridge seat toward the west side after placement of the bridge beam. The average bridge seat settlement is 0.09 inches after construction for 92 hours. The small fluctuations in the measured settlements over time observed in Figure 4.13 may have occurred due to temperature changes in the laboratory.

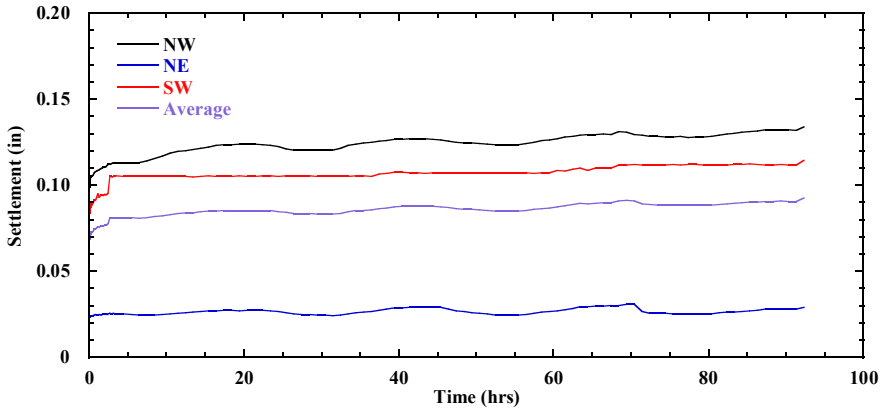

Figure 4.13 Time histories of bridge seat settlements for Stage 3 in Test 1.

The average bridge seat settlements due to placement of bridge beam for different tests are presented in Table 4.6. Test 3 (increased reinforcement spacing) has the largest bridge seat settlement of 0.14 inches, whereas Test 5 (steel reinforcement) has the smallest settlement of 0.05 inches. Settlements for Tests 1 (baseline) and 4 (reduced reinforcement stiffness) are 0.09 inches, and are both larger than the settlement of 0.06 inches for Test 2(reduced bridge surcharge stress). Results indicate that reinforcement spacing has the most significant effect on bridge seat settlement under static loading. As expected, greater bridge surcharge stress results in larger settlement under static loading.

Table 4.6 Average bridge seat settlement (in.) for Stage 3 in Tests 1 to 5 (model-scale).

Construction stage	Test 1	Test 2	Test 3	Test 4	Test 5
Stage 3	0.09	0.06	0.14	0.09	0.05

4.4.1.2 Dynamic Loading

Time histories of incremental bridge seat corner settlement for the four string potentiometers during application of the earthquake motions in Test 1 are shown in Figure 4.14, and the average incremental bridge seat settlements are shown in Figure 4.15. During the Imperial Valley motion, the maximum value is 0.12 inches. The average residual settlement is 0.06 inches, which corresponds to a vertical strain of 0.07% for the 7 ft-high lower wall. Average incremental bridge seat settlements for each earthquake motion in Test 1 are summarized in Table 4.7. For the Maule motion, the bridge seat had maximum dynamic settlement of 0.28 inches and residual settlement of 0.06 inches. Maximum dynamic settlement for the Northridge motion is 0.28 inches, and the residual value is 0.09 inches (0.1% vertical strain), which corresponds to 0.18 inches at prototype scale. At t = 3.98 s during the Northridge motion, the north side of the bridge seat (NW and NE) had a positive settlement of 0.07 inches, whereas the south side (SW and SE) had a negative settlement (i.e., uplift) of 0.07 inches, which indicated rocking of the bridge seat in the N-S direction (i.e., the direction of shaking). The residual settlement on the west side (NW and SW) is larger than the east side (NE and SE), which indicated that the bridge seat tilted further toward the west after shaking.

Table 4.7 Average incremental bridge seat settlements (in.) in Test 1 (model-scale).

Earthquake motion	Maximum dynamic settlement	Minimum dynamic settlement	Residual settlement
Imperial Valley	0.12	0.00	0.06
Maule	0.28	-0.01	0.06
Northridge	0.28	-0.03	0.09

Time histories of average incremental bridge seat settlement during the Imperial Valley, Maule, Northridge motions for different tests are shown in Figure 4.16. For instance, during the Maule motion, Test 3 has the largest dynamic settlements of 0.41 inches, and the maximum dynamic settlements for Tests 1, 2, 4, and 5 are similar and range from 0.28 to 0.31 inches. The minimum dynamic settlements are small for all tests. Test 3 has the largest residual settlement of 0.22 in, which corresponds to a vertical strain of 0.27%, whereas Test 1 has the smallest residual settlement of 0.06 inches. The residual settlements are 0.12, 0.15, and 0.07 inches for Tests 2, 4, and 5, respectively.

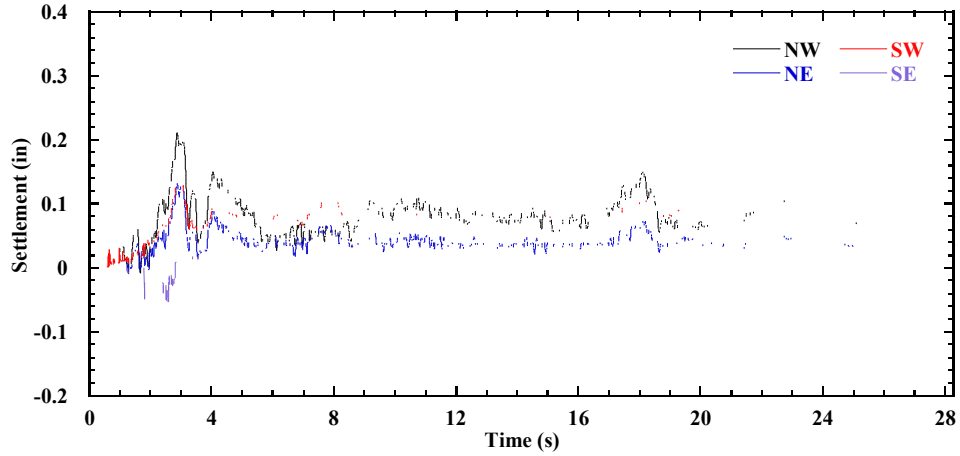

(a)

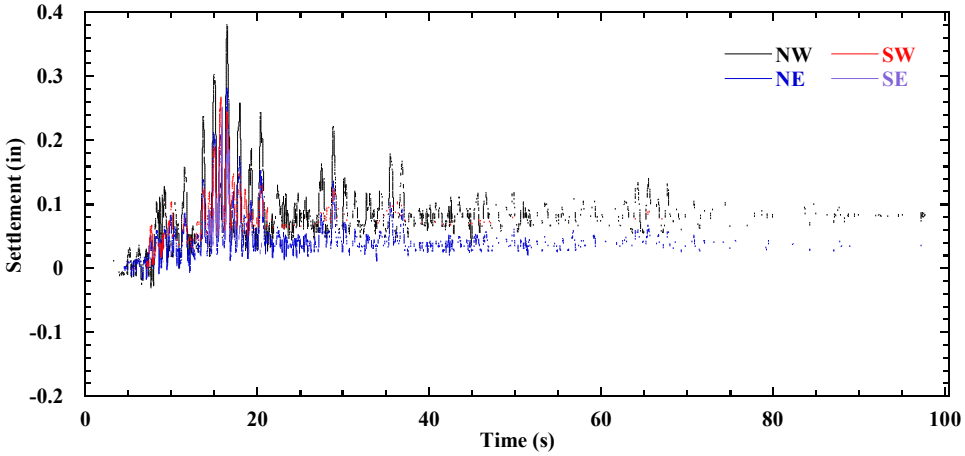

(b)

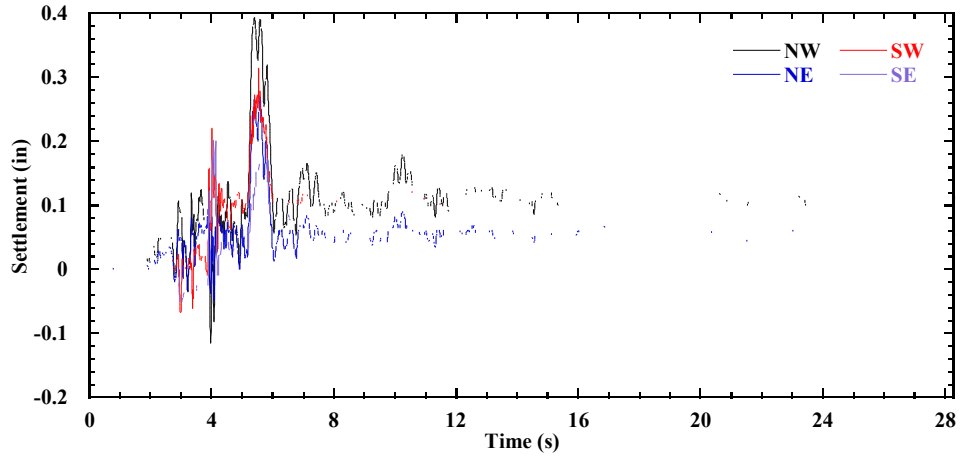

(c)

Figure 4.14 Time histories of incremental bridge seat corner settlements in Test 1: (a) Imperial Valley motion; (b) Maule motion; (c) Northridge motion.

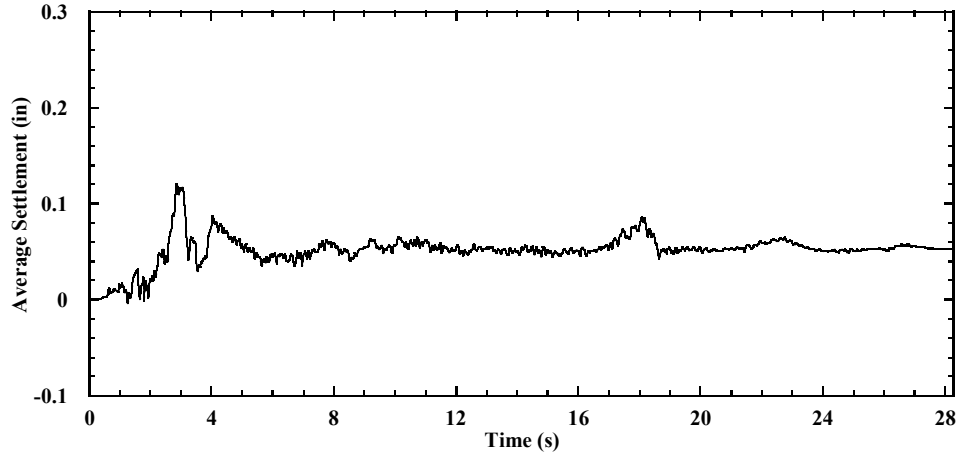

(a)

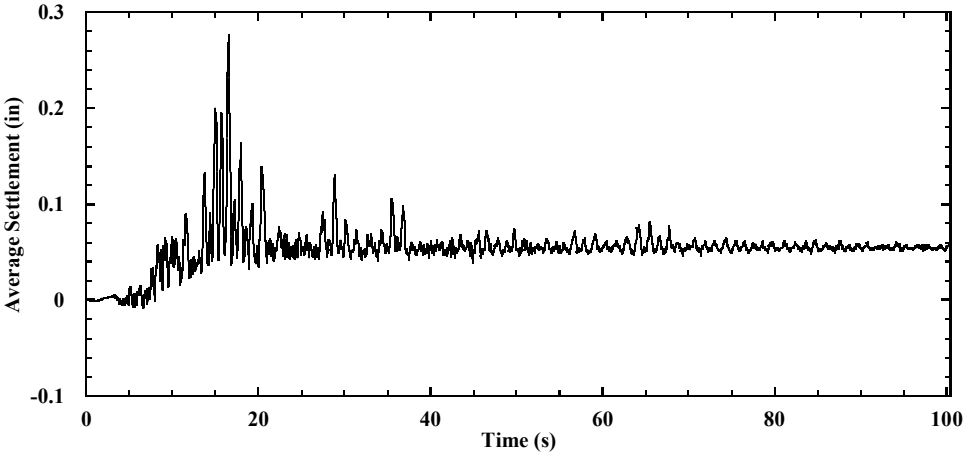

(b)

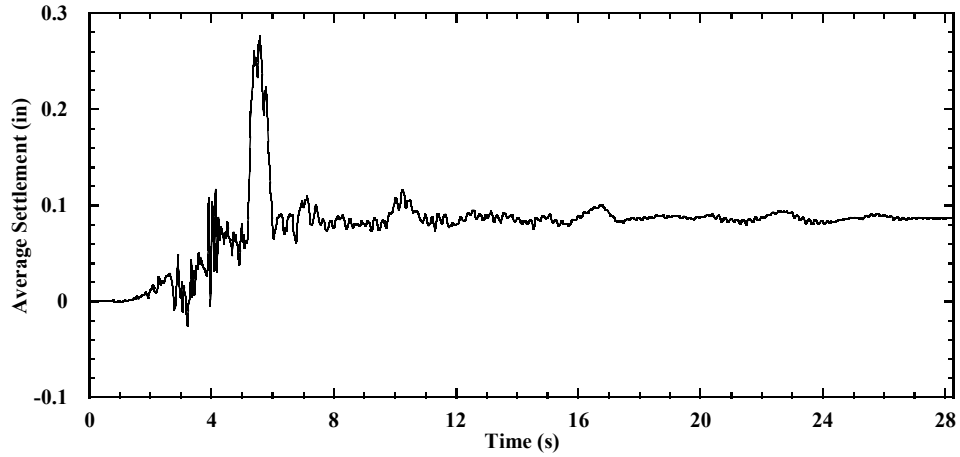

(c)

Figure 4.15 Time histories of average incremental bridge seat settlements in Test 1: (a) Imperial Valley motion; (b) Maule motion; (c) Northridge motion.

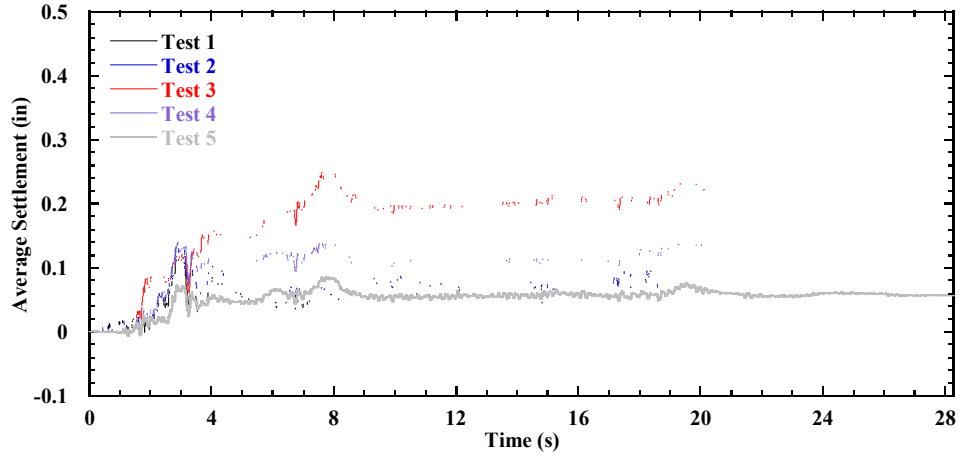

(a)

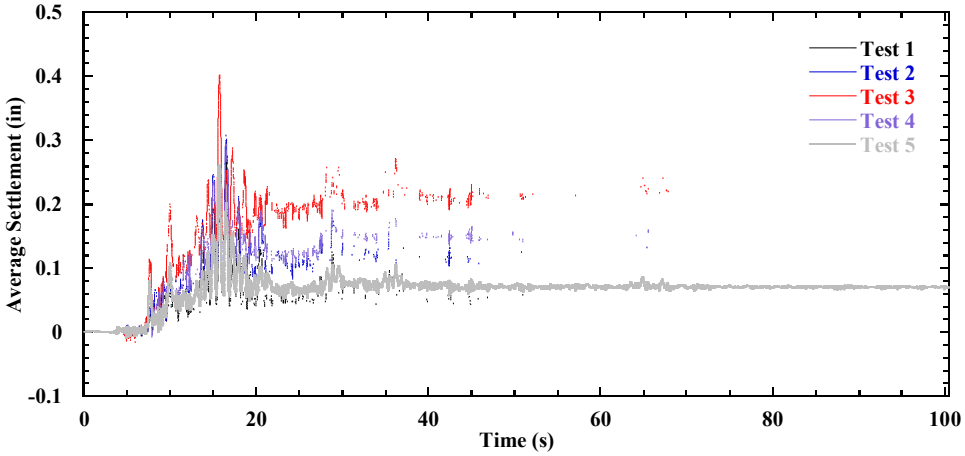

(b)

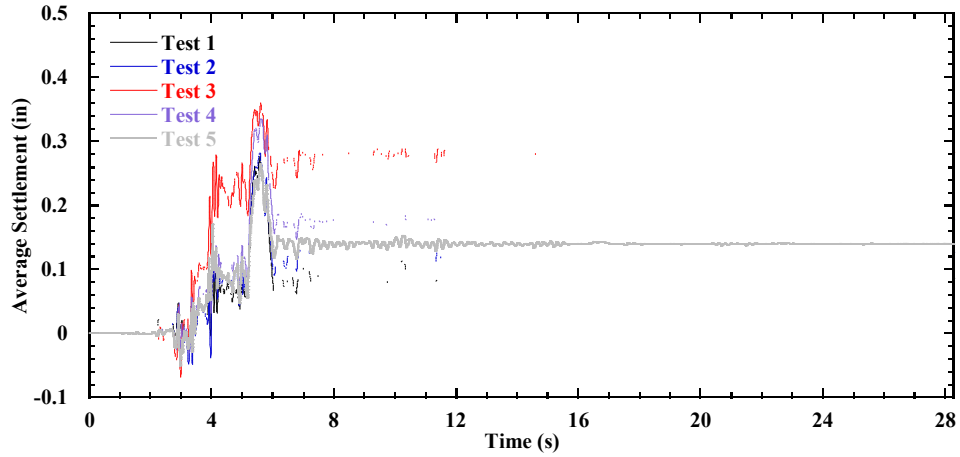

(c)

Figure 4.16 Time histories of average incremental bridge seat settlements in Tests 1 to 5: (a) Imperial Valley motion; (b) Maule motion; (c) Northridge motion.

Average incremental residual bridge seat settlements for different testing stages in Tests 1 to 5 are shown in Figure 4.17 and the incremental values are presented in Table 4.8. Test 3 (increased reinforcement spacing) has the largest bridge seat settlements for all testing stages, which indicate that reinforcement spacing has the most significant effect for both static and dynamic loading conditions. The incremental residual settlement is 0.28 inches for the Northridge motion, which corresponds to a vertical strain of 0.34%. Test 4 (reduced reinforcement stiffness) also shows larger bridge seat settlements than Test 1 (baseline case) for all testing stages, and this indicates that reinforcement stiffness also has an important effect, especially for dynamic loading condition. Therefore, reducing reinforcement vertical spacing and increasing reinforcement stiffness can effectively reduce bridge seat settlements for both static and dynamic loading conditions. Test 2 (reduced bridge surcharge stress) has smaller bridge seat settlements than Test 1 under static loading, but larger settlements under dynamic loading. The greater bridge surcharge stress for Test 1 yielded larger a backfill soil stiffness, and thus resulted in smaller bridge seat settlements under dynamic loading, which are also consistent with the facing displacements. Test 5 has smaller bridge seat settlement than Test 1 under static loading, but similar settlements for the Imperial Valley and Maule motions. This may be attributed to the relatively large opening of the thin wire mesh that resulted in relatively weak interaction between the sand particles and steel reinforcement under dynamic loading.

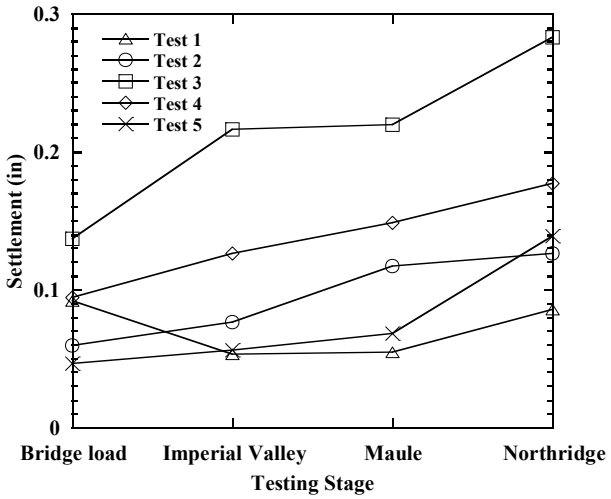

Figure 4.17 Average incremental bridge seat settlement for different testing stages.

Table 4.8 Average incremental residual bridge seat settlements (in.) (model-scale).

Earthquake motion	Test 1	Test 2	Test 3	Test 4	Test 5
Imperial Valley	0.06	0.07	0.22	0.13	0.06
Maule	0.06	0.12	0.22	0.15	0.07
Northridge	0.09[1]	0.13	0.28	0.18	0.14

[1] The Northridge earthquake motion was applied after the sinusoidal motions for Test 1.

4.4.2 Bridge Seat and Bridge Beam Horizontal Displacements

Horizontal displacements in the longitudinal direction for the bridge seat and bridge beam were measured at the locations shown in Figure 3.18, time histories of incremental horizontal displacement for the earthquake motions in Test 1 are shown in Figure 4.18. Displacements at the east and west sides of the bridge seat are similar with respect to both trend and magnitude for all three motions. This indicates essentially uniform translational movement of the bridge seat in the longitudinal direction during shaking. The bridge beam experienced larger horizontal displacements than the bridge seat during shaking, which indicated sliding of the bridge beam with respect to the bridge seat. The horizontal displacements for the bridge seat and bridge beam are highly dependent on the characteristics of the earthquake motions.

Time histories of incremental horizontal displacement for the bridge seat relative to the top of MSE bridge abutment (measurements taken at the facing block z = 6.25 ft for L1) and bridge beam relative to the bridge seat are shown in Figure 4.19. For the Imperial Valley and Maule motions, the bridge seat had relatively small magnitudes of horizontal displacement on the MSE bridge abutment, which indicates that the bridge seat essentially moved together with the MSE bridge abutment during shaking. The bridge beam had residual relative horizontal displacements with respect to the bridge seat for the two motions of 0.09 and -0.01 inches, respectively. For the Northridge motion, the bridge beam experienced significant sliding with respect to the bridge seat during shaking. The maximum and minimum dynamic relative horizontal displacements are 0.81 and -1.18 inches, respectively, and the residual horizontal displacement is -0.17 inches. Final inspection revealed significant slide marks on both sides of the elastomeric bearing pad, which suggests that relative displacements between the bridge beam and bridge seat occurred primarily as a result of sliding on the pad and not shear deformation of the pad itself. The width of the expansion joint is also associated with the relative horizontal displacement of the bridge beam with respect to the bridge seat and will be discussed later.

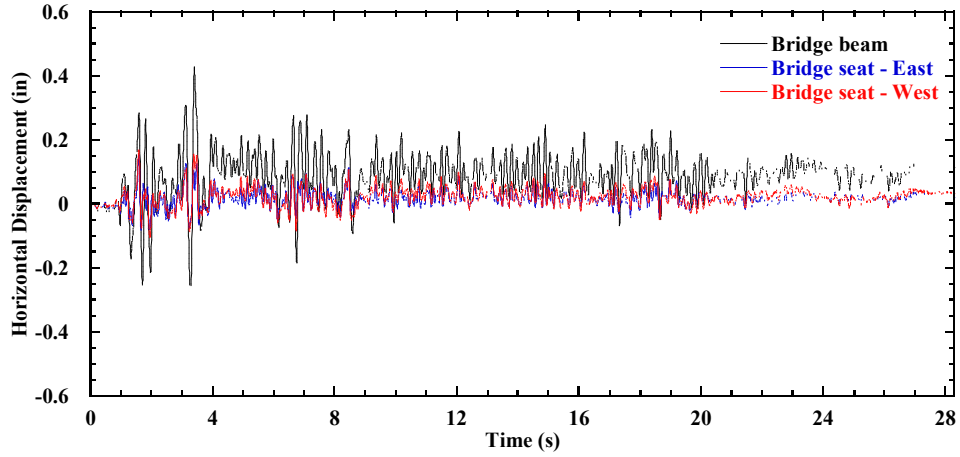

(a)

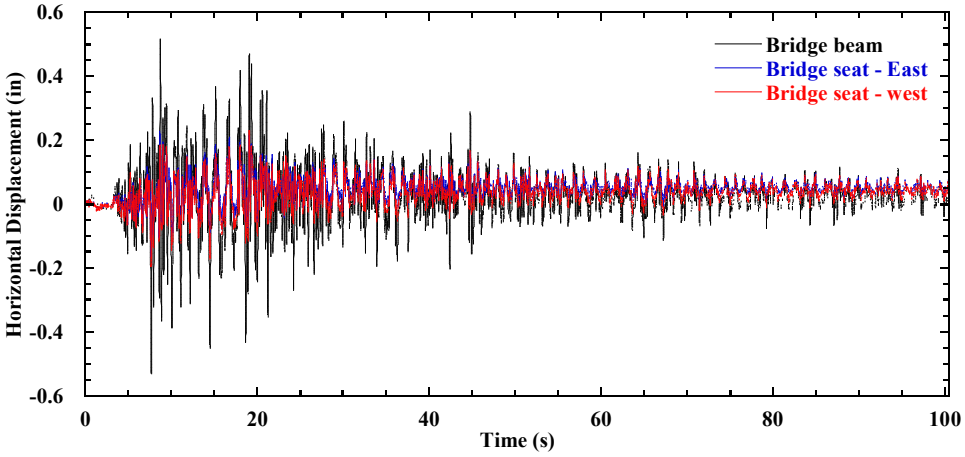

(b)

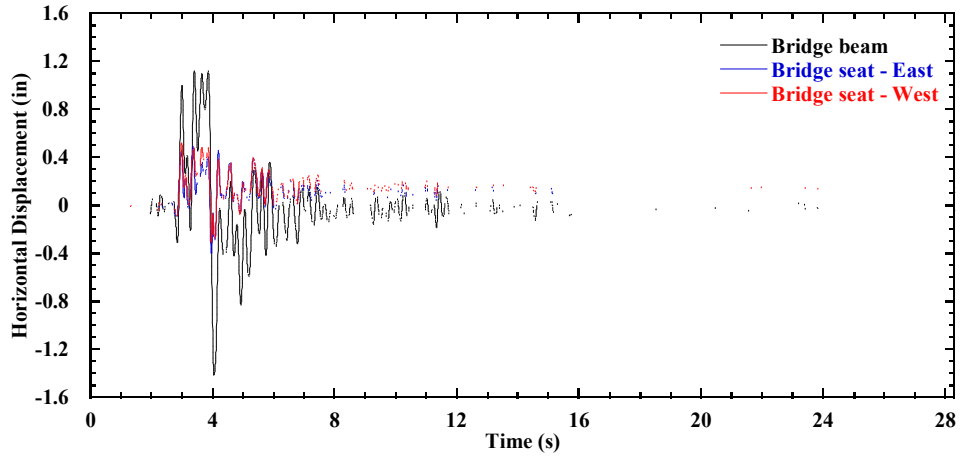

(c)

Figure 4.18 Time histories of incremental horizontal displacement for bridge seat and bridge beam in Test 1: (a) Imperial Valley motion; (b) Maule motion; (c) Northridge motion.

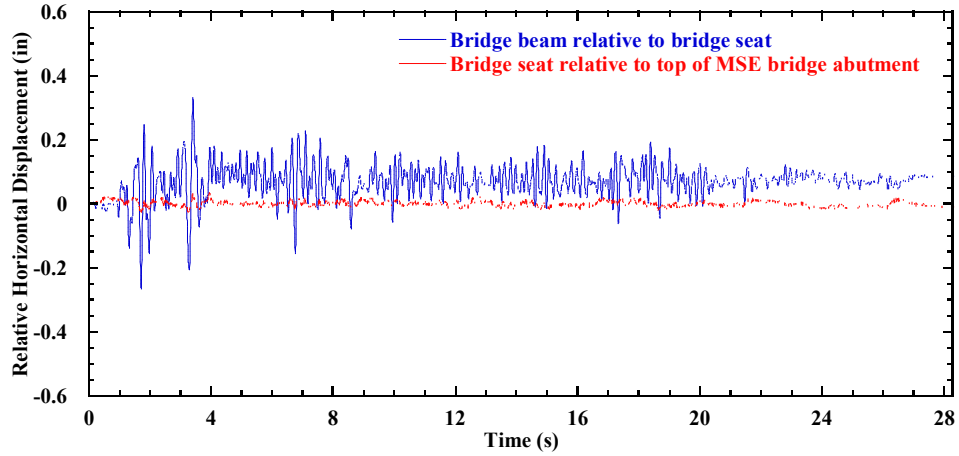

(a)

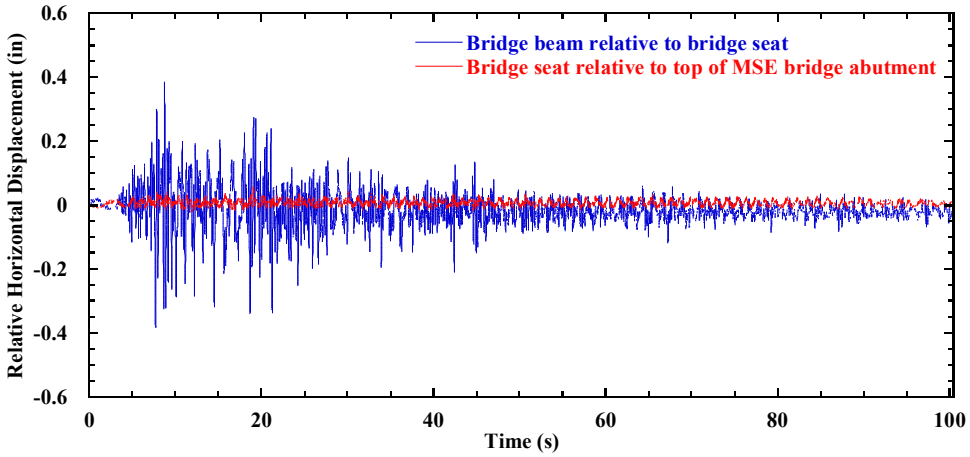

(b)

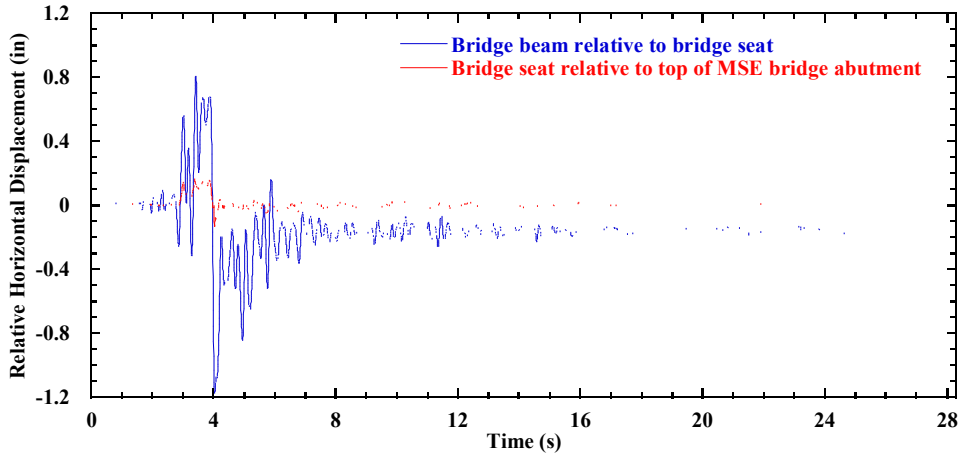

(c)

Figure 4.19 Time histories of incremental relative horizontal displacement for bridge seat and bridge beam in Test 1: (a) Imperial Valley motion; (b) Maule motion; (c) Northridge motion.

4.5 Accelerations

4.5.1 Bridge Seat and Bridge Beam

In the seismic design of MSE bridge abutments, the bridge seat is typically treated as a gravity retaining wall for external stability evaluation. However, there is no guidance on the selection of acceleration for the bridge seat in the current design guidelines. The acceleration of bridge beam also is important in the design, as the inertial forces are transferred to the bridge seat through frictions on the bearings and potential contact forces on the backwall of the bridge seat.

Time histories of horizontal acceleration in the longitudinal direction for the bridge seat and bridge beam for earthquake motions in Test 1 are shown in Figure 4.20. For the Imperial Valley motion, the bridge seat had a peak acceleration of 0.63*g*, while the bridge beam had a smaller peak acceleration of 0.53*g*, and the peak accelerations are 0.66*g* and 0.63*g*, respectively, for the Maule motion. For the Northridge motion, the peak accelerations are much larger than the other two motions, and the peak accelerations are 1.81*g* and 1.52*g* for the bridge seat and bridge beam, respectively.

The root-mean-square (RMS) method can be used to mitigate the effects of high frequency noise and also characterize the amplitude and frequency content of a measured response (Kramer 1996; El-Emam and Bathurst 2005). The calculated ratios for the bridge seat and bridge beam RMS accelerations in Tests 1 to 5 normalized by the shaking table RMS acceleration are presented in Table 4.9. In Test 1, for the Imperial Valley motion, the bridge beam has an acceleration amplification ratio of 1.80, and is greater than the ratio of 1.60 for the bridge seat. For the Maule motion, the ratios decrease to 1.73 and 1.38 for the bridge beam and bridge seat, respectively. In general, the RMS acceleration ratios for the bridge beam are larger than the bridge seat.

For the Imperial Valley motion, the bridge seat in Tests 1 and 2 has larger acceleration ratios than in Tests 3, 4, and 5. The acceleration ratio for the bridge beam is the largest for Test 2, which is likely due to the smaller bridge surcharge stress. The acceleration ratio for the bridge beam in Test 1 is smaller than in Tests 3, 4, and 5. The trend of acceleration ratios for the bridge beam is the same for the Maule motion. However, the bridge seat has the smallest acceleration ratio in Test 1, while the acceleration ratios are similar in Tests 2, 3, 4, and 5.

Table 4.9 RMS acceleration ratios for bridge seat and bridge beam in Tests 1 to 5 (model-scale).

Earthquake motion	Test 1		Test 2		Test 3		Test 4		Test 5	
	Seat	Beam	Seat	Beam	Seat	Beam	Seat	Beam	Seat	Beam
Imperial Valley	1.60	1.80	1.58	2.29	1.52	2.01	1.52	2.00	1.46	1.99
Maule	1.38	1.73	1.46	2.02	1.48	1.81	1.48	1.82	1.42	1.88
Northridge	1.45	1.58	1.55	1.64	1.48	1.51	1.48	1.50	1.53	1.57

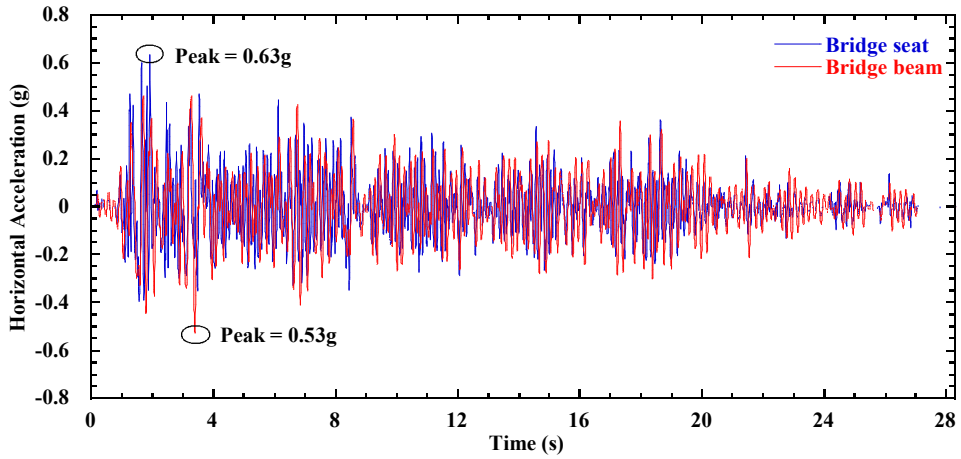

(a)

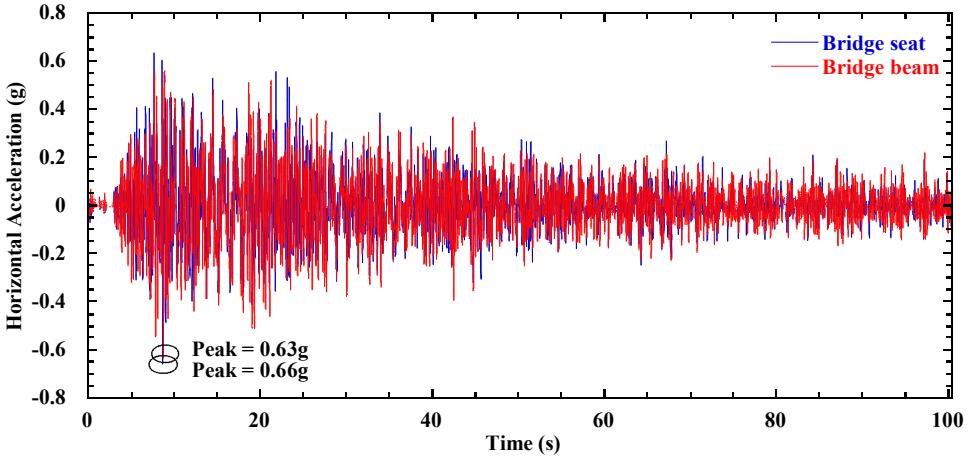

(b)

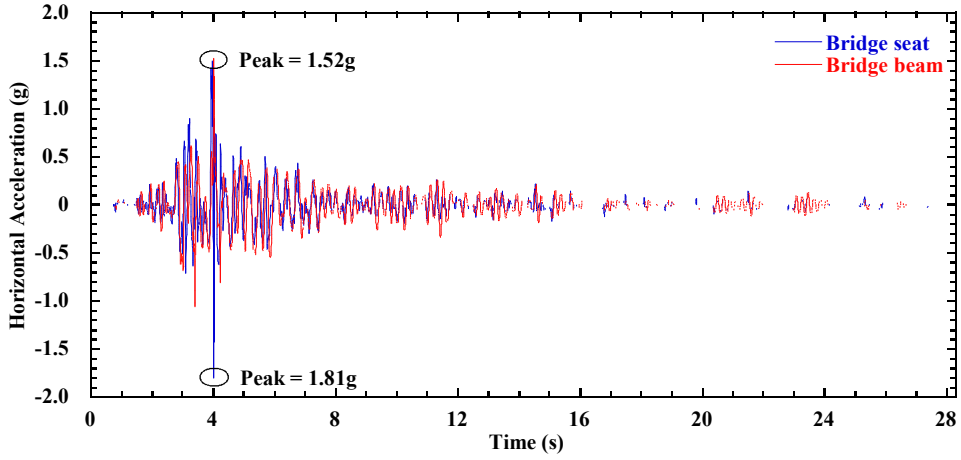

(c)

Figure 4.20 Time histories of horizontal acceleration for bridge seat and bridge beam in Test 1: (a) Imperial Valley motion; (b) Maule motion; (c) Northridge motion.

4.5.2 MSE Wall

Figure 4.21 shows the RMS acceleration ratio profiles of L1 for earthquake motions in Test 1, where the RMS acceleration at each location is normalized by the actual shaking table RMS acceleration. For the Imperial Valley motion, acceleration ratio increases essentially linearly with elevation for all three sections and again indicates increasing amplification toward the top of the wall. Maximum acceleration ratios were measured at the top of the wall (z = 6.25 ft), and are equal to 1.56, 1.57, and 1.59 for the retained soil zone, reinforced soil zone, and front wall facing, respectively. Similar trends are also observed for the Maule and the Northridge motions, but the acceleration ratios are smaller. For instance, the acceleration ratios at the top in the reinforced soil zone are 1.34 and 1.39 for the Maule and the Northridge motions, respectively, which are smaller than the value of 1.57 for the Imperial Valley motion. In general, for all three earthquake motions, the acceleration amplification ratios increase slightly from the retained soil zone to reinforced soil zone to wall facing. The decreasing amplification behavior as shaking proceeded may be due to the softening of the soil (i.e., shear modulus reduction) under successive earthquake motions. However, further investigations are needed to confirm this using numerical simulations.

RMS acceleration ratio profiles for L1 and L2 in Test 1 are shown in Figure 4.22. For the reinforced soil zone, the acceleration ratios for L1 and L2 are similar for the lower section, whereas the acceleration ratios for L1 are larger than L2 for the upper section. The acceleration ratio at the top of L1 has an acceleration ratio of 1.57 for the Imperial Valley motion, which is larger than the value of 1.47 at the same elevation for L2. For the retained soil zone, the acceleration profiles for L1 and L2 are similar.

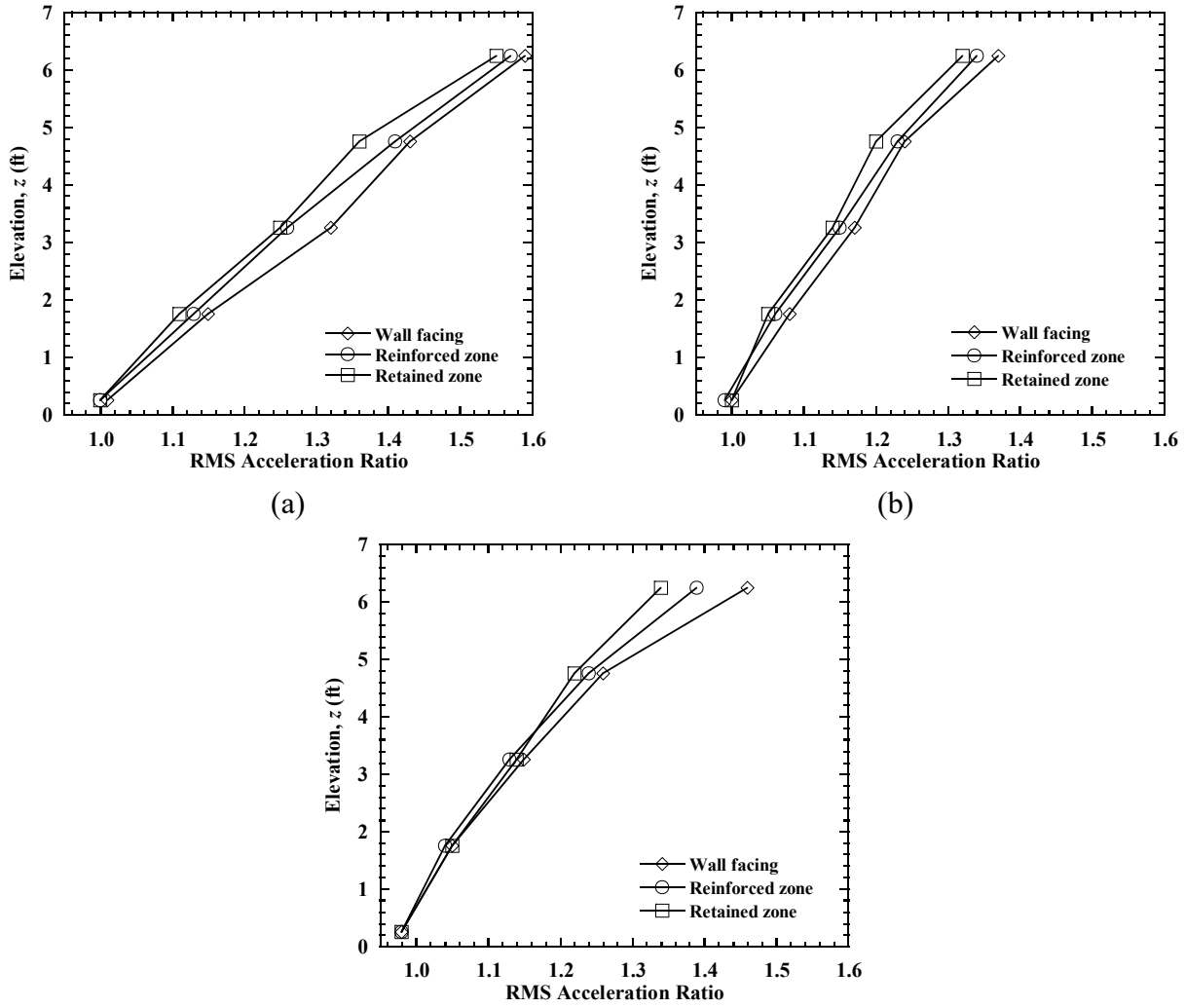

Figure 4.21 RMS acceleration ratio profiles for L1 in Test 1: (a) Imperial Valley motion; (b) Maule motion; (c) Northridge motion.

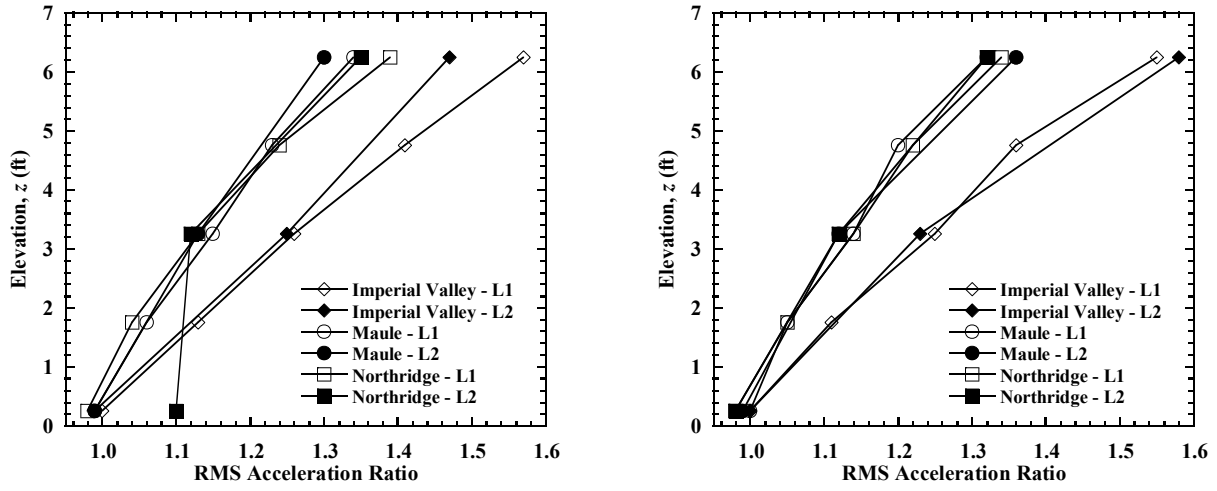

Figure 4.22 RMS acceleration ratio profiles for L1 and L2 in Test 1: (a) reinforced soil zone; (b) retained soil zone.

Acceleration ratio profiles for L1 in the reinforced soil zone and retained soil zone in Tests 1 to 5 for the Imperial Valley, Maule, and Northridge motions, are shown in Figure 4.23, Figure 4.24, and Figure 4.25, respectively. For the Imperial Valley motion, Test 1 has the largest acceleration ratios for both the reinforced and retained soil zones. Accelerations ratios for Test 2 are smaller than Test 1, which indicate that the acceleration amplification increases with increasing bridge surcharge stress for the MSE bridge abutments. Acceleration ratios for Tests 3, 4, and 5 are similar in both the reinforced and retained soil zones, and are much smaller than Test 1. This indicates that acceleration ratios increase with decreasing reinforcement spacing and increasing reinforcement stiffness.

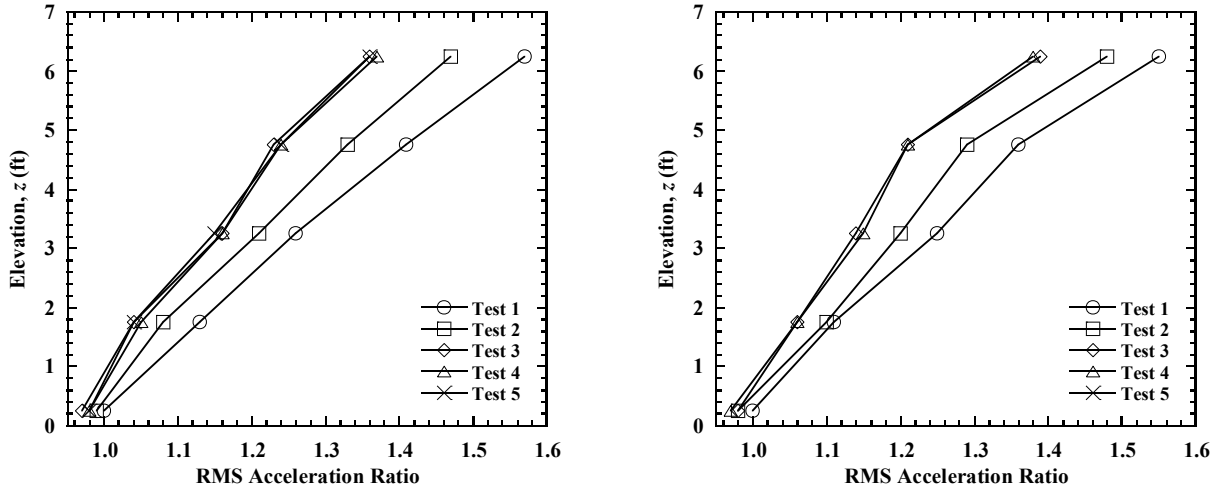

Figure 4.23 RMS acceleration ratio profiles of L1 for the Imperial Valley motion: (a) reinforced soil zone; (b) retained soil zone.

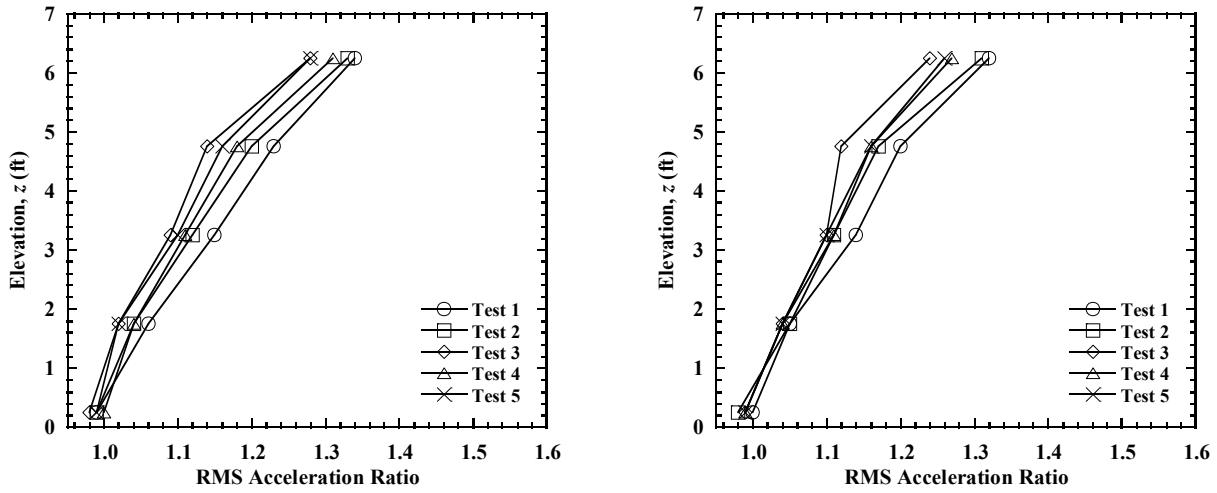

(a) (b)

Figure 4.24 RMS acceleration ratio profiles of L1 for the Maule motion: (a) reinforced soil zone; (b) retained soil zone.

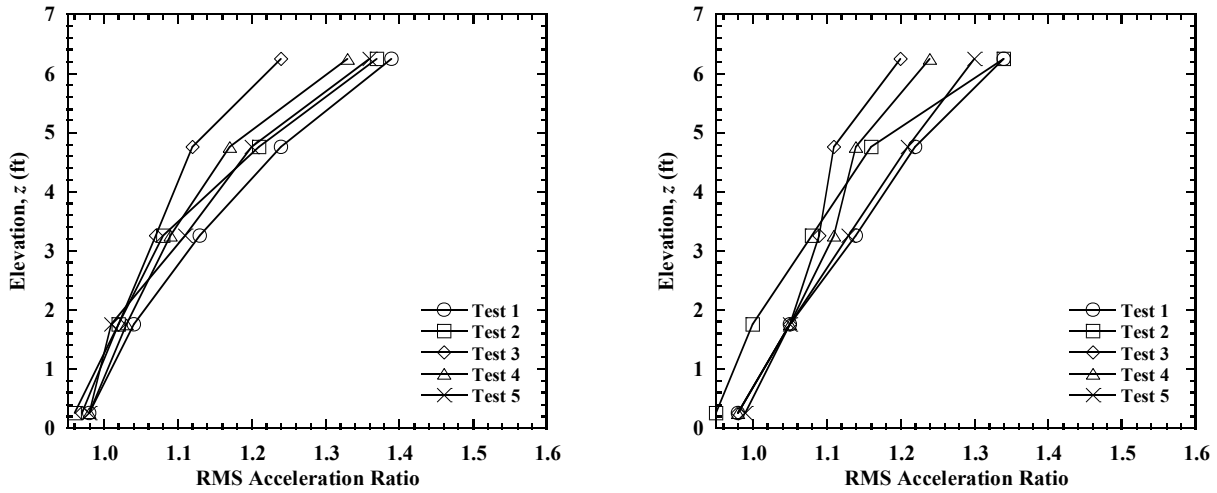

(a) (b)

Figure 4.25 RMS acceleration ratio profiles of L1 for the Northridge motion: (a) reinforced soil zone; (b) retained soil zone.

4.6 Vertical and Lateral Stresses in the Backfill Soil

4.6.1 Vertical Stresses in the Backfill Soil

Profiles of the initial (before shaking), maximum (during shaking), and residual (after shaking) vertical stresses in Test 1, along with the estimated vertical stresses using the AASHTO (2012) method for static loading conditions, are shown in Figure 4.26. For the Imperial Valley motion, the maximum vertical stress is 15.1 psi at the top of the wall, but recovered to 10.7 psi after shaking. The change of vertical stress during shaking is mainly due to rocking of the bridge seat. The residual vertical stresses increased slightly as compared to initial values after shaking. Similar observations are also observed for the Maule motion. For the Northridge motion, the maximum vertical stresses during shaking are much larger than the initial values due to strong shaking. The residual vertical stress profile is similar to the estimated vertical stress profile under static loading, which might be attributed to the change of arching chains within the backfill soil during shaking.

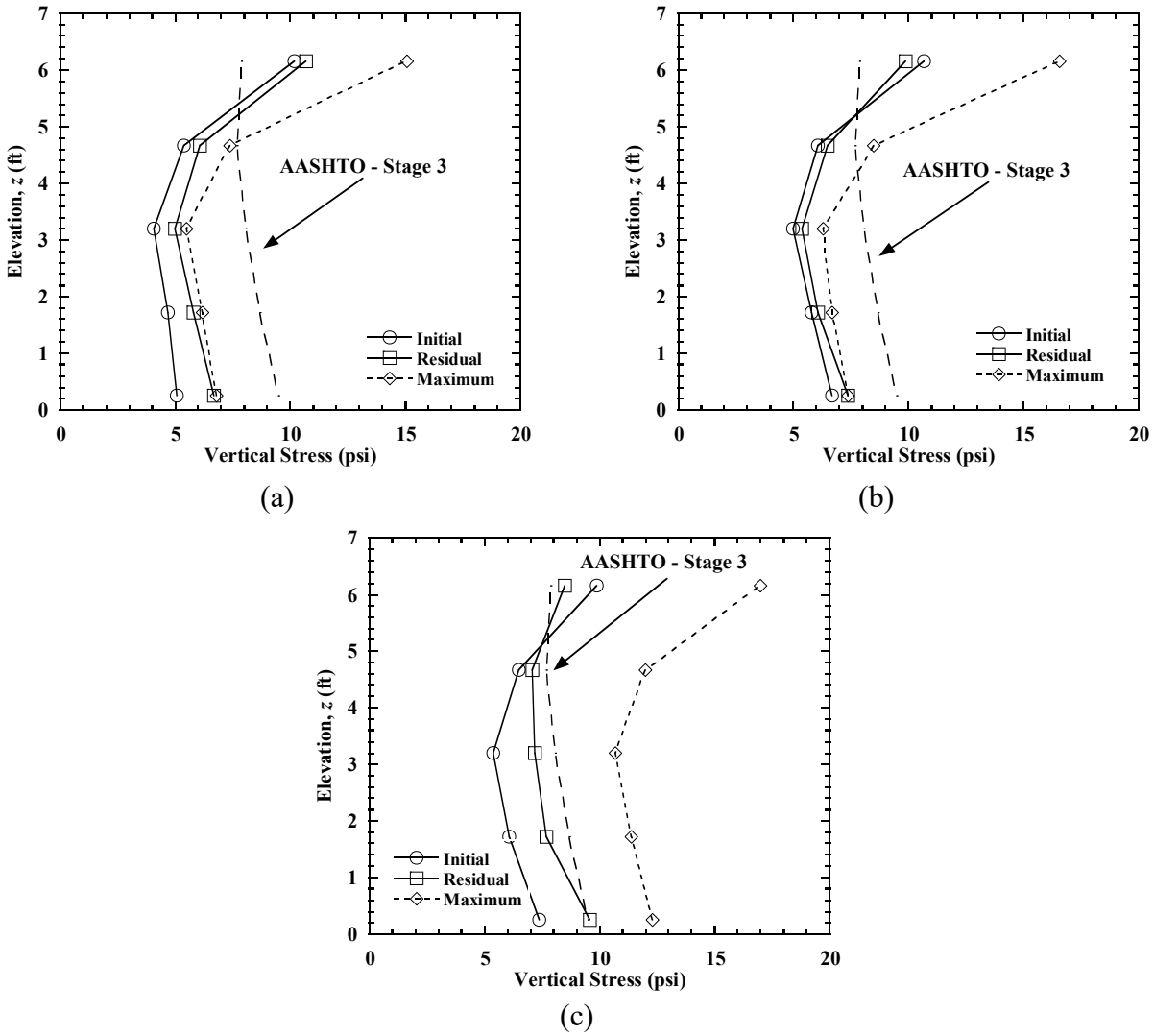

Figure 4.26 Vertical stress profiles behind wall facing in Test 1: (a) Imperial Valley motion; (b) Maule motion; (c) Northridge motion.

The vertical stress profiles for the Imperial Valley, Maule, and Northridge motions in Tests 1 to 5 are shown in Figure 4.27, Figure 4.28, and Figure 4.29, respectively. For the Imperial Valley motion, maximum dynamic vertical stress profiles show the maximum value at the top of the wall for Test 1, while at the bottom of the wall with a triangular distribution for Tests 2, 3, 4, and 5. The residual vertical stress profiles also show consistent shapes with the maximum vertical stress profiles, and the measured vertical stresses are generally smaller than estimated values under static loading. For the Maule motion, the residual vertical stresses are closer to the calculated values. For the Northridge motion, the maximum vertical stresses are larger than for the other two motions due to the strong shaking. The residual vertical stress profile for Test 1 is similar to the calculated vertical stress profile, while the residual vertical stresses in Tests 2, 3, 4, and 5 increase approximately linearly with decreasing elevation (increasing depth) with smaller values than the calculated values at the top of the wall and larger values at the bottom of the wall.

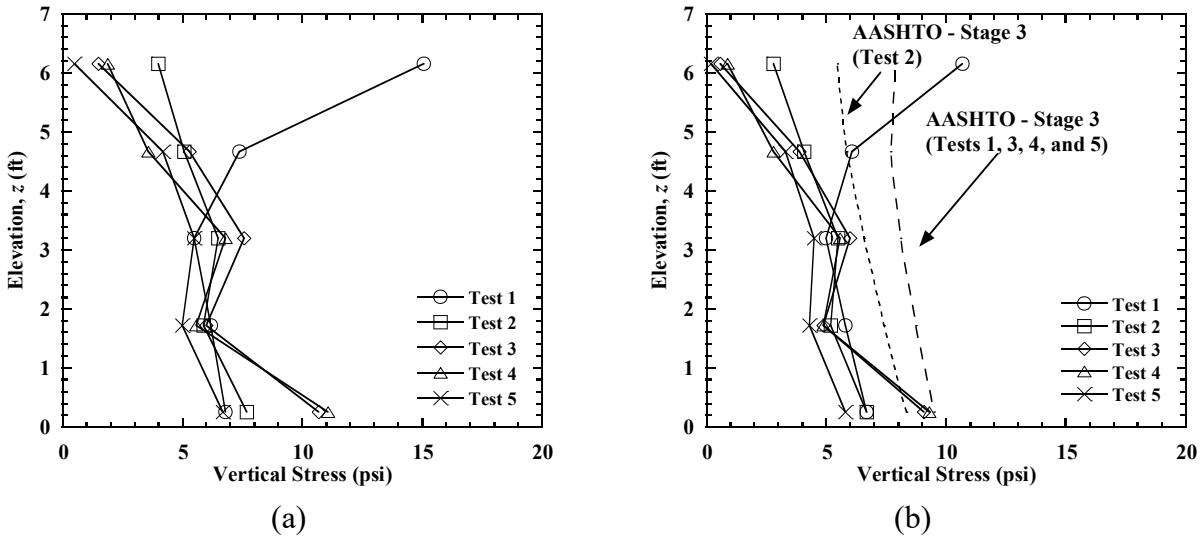

Figure 4.27 Vertical stress profiles behind wall facing for the Imperial Valley motion: (a) maximum vertical stress; (b) residual vertical stress.

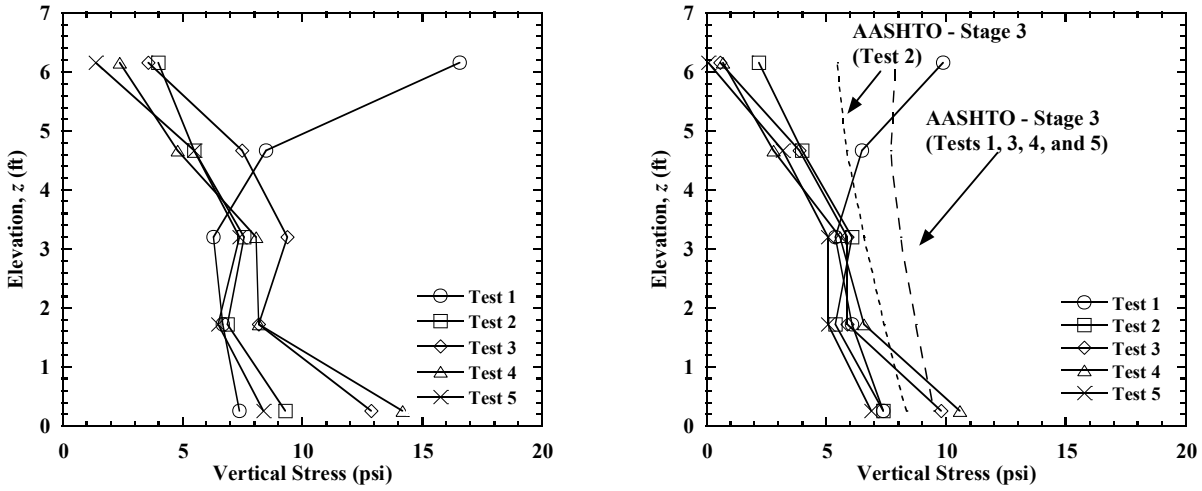

(a) (b)

Figure 4.28 Vertical stress profiles behind wall facing for the Maule motion: (a) maximum vertical stress; (b) residual vertical stress.

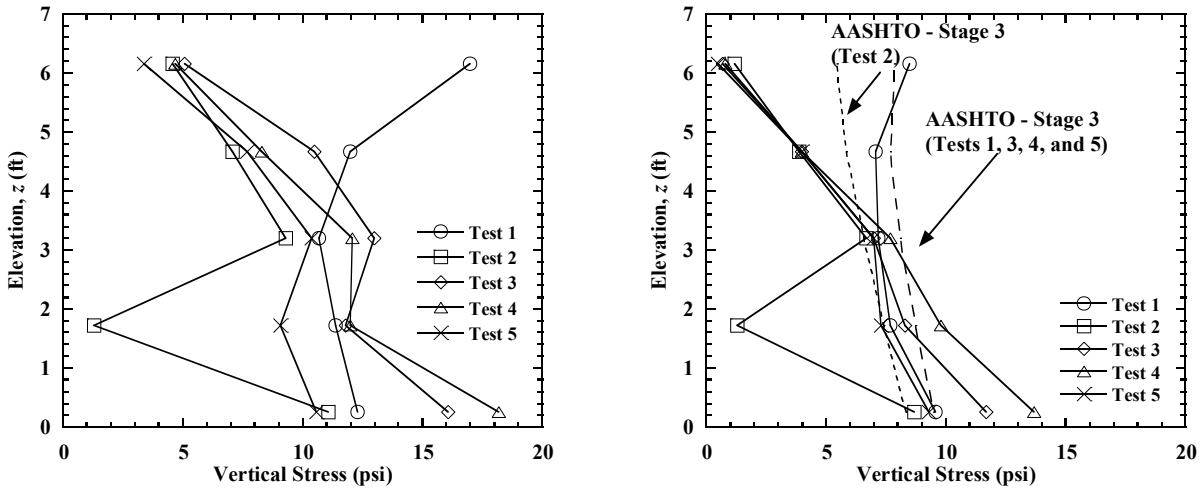

(a) (b)

Figure 4.29 Vertical stress profiles behind wall facing for the Northridge motion: (a) maximum vertical stress; (b) residual vertical stress.

4.6.2 Lateral Stresses in the Backfill Soil

Profiles of the initial (before shaking), maximum (during shaking), and residual (after shaking) lateral stresses in Test 1, along with the estimated lateral stresses using the AASHTO (2012) method for static loading conditions, are shown in Figure 4.30. The maximum dynamic lateral stress occurred at the top of the wall for the Imperial Valley and Maule motions, and reached 1.5 psi and 1.6 psi, respectively. After shaking, the dynamic lateral stresses were almost all recovered. For the Northridge motion, the maximum dynamic lateral stresses increased significantly as compared to the initial lateral stresses due to the strong shaking, and the maximum lateral stress is 2.4 psi at z = 4.75 ft. The residual lateral stress profile is similar the calculated lateral stress profile under static loading. The dynamic lateral stresses are a result of both the inertial forces of the backfill soil due to shaking and the dynamic vertical stresses associated with rocking of the bridge seat.

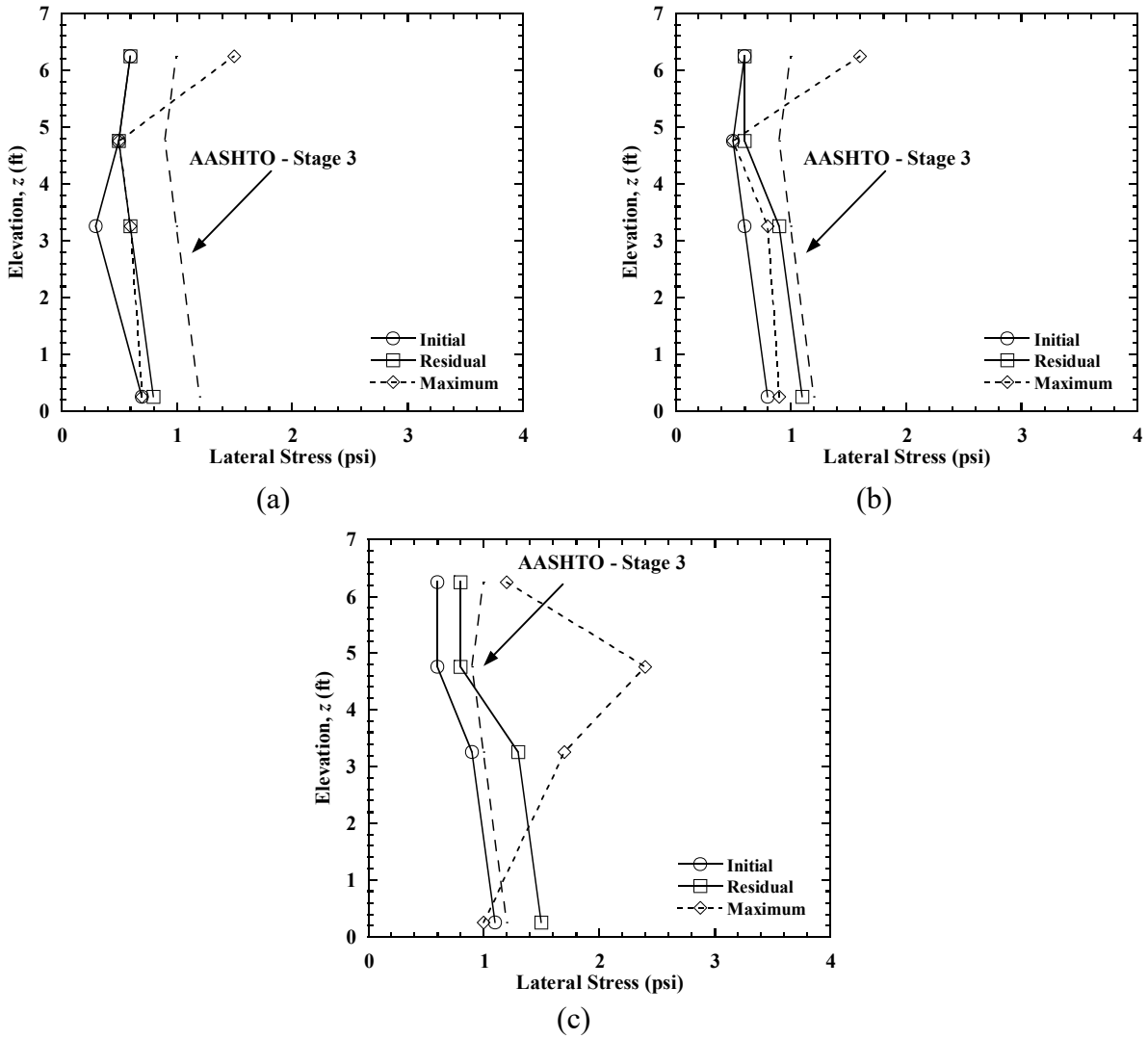

Figure 4.30 Lateral stress profiles behind wall facing in Test 1: (a) Imperial Valley motion; (b) Maule motion; (c) Northridge motion.

The lateral stress profiles for the Imperial Valley, Maule, and Northridge motions are shown in Figure 4.31, Figure 4.32, and Figure 4.33, respectively. For the Imperial Valley motion, maximum dynamic lateral stress profiles show maximum values at the top for Tests 1 and 2, while at the bottom of the wall for Tests 3, 4, and 5. The residual lateral stresses at the top of the wall for Tests 1 and 2 after shaking are 0.6 psi and 0.8 psi, respectively. The measured lateral stresses are generally smaller than calculated values under static loading. For the Maule motion, the residual lateral stresses become closer to the calculated values under static loading. For the Northridge motion, the maximum lateral stresses are larger than the other two motions due to the strong shaking.

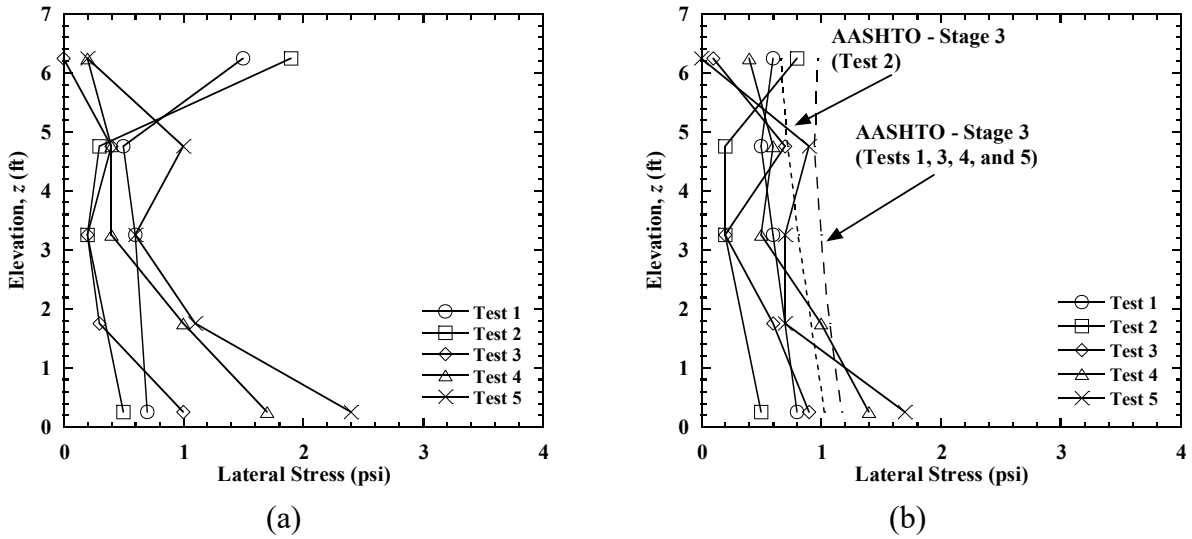

Figure 4.31 Lateral stress profiles behind wall facing for the Imperial Valley motion: (a) maximum lateral stress; (b) residual lateral stress.

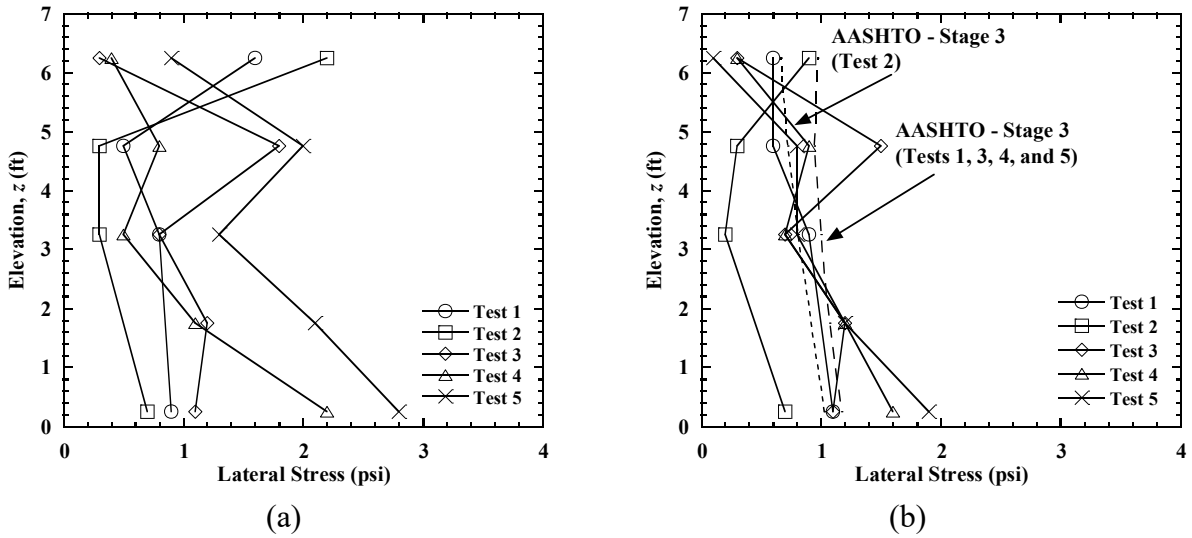

Figure 4.32 Lateral stress profiles behind wall facing for the Maule motion: (a) maximum lateral stress; (b) residual lateral stress.

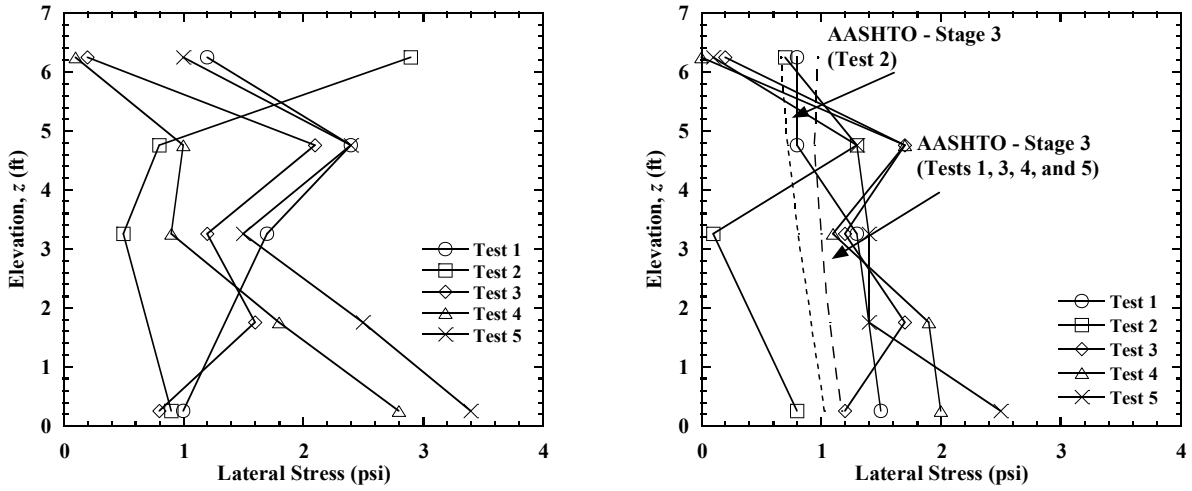

(a) (b)

Figure 4.33 Lateral stress profiles behind wall facing for the Northridge motion: (a) maximum lateral stress; (b) residual lateral stress.

4.7 Reinforcement Strains

4.7.1 Static Loading

Reinforcement strain distributions in the longitudinal sections L1 and L2 for construction stages in Test 1 are shown in Figure 4.34. Each measurement represents the average value from a pair of top and bottom gauges, and zero strain at the free end of each reinforcement layer is also plotted. For Stage 1, the reinforcement strain distributions in L1 show maximum strains near the connections (at distance x = 0.3 ft from the front wall facing) for layers 1, 4, and 7, and under the bridge seat (x = 2.6 ft) for layer 10. The reinforcement strains in layer 13 are relatively small and do not show a clear maximum value. For Stage 2, reinforcement strains near the connections and under the bridge seat increased slightly due to construction of the bridge seat and upper wall. The reinforcement strains in L2 generally show similar distributions to L1 with respect to both magnitude and trend for Stages 1 and 2. For Stage 3, reinforcement strains in L1 had greater increases near the connections for layers 1, 4, and 7, and under the bridge seat for layers 10 and 13 due to placement of the bridge beam. The reinforcement strains in layers 1 and 7 for L1 show similar magnitudes of strain to L2. However, the reinforcement strains in layer 13 under the bridge seat for L2 had much larger increase than L1. The reinforcement strain at x = 1.5 ft in layer 13 is 0.15% for L2, which is much larger than the value of 0.05% for L1. This is attributed to tilting of the bridge seat toward the west side for Stage 3 as shown in Figure 4.13.

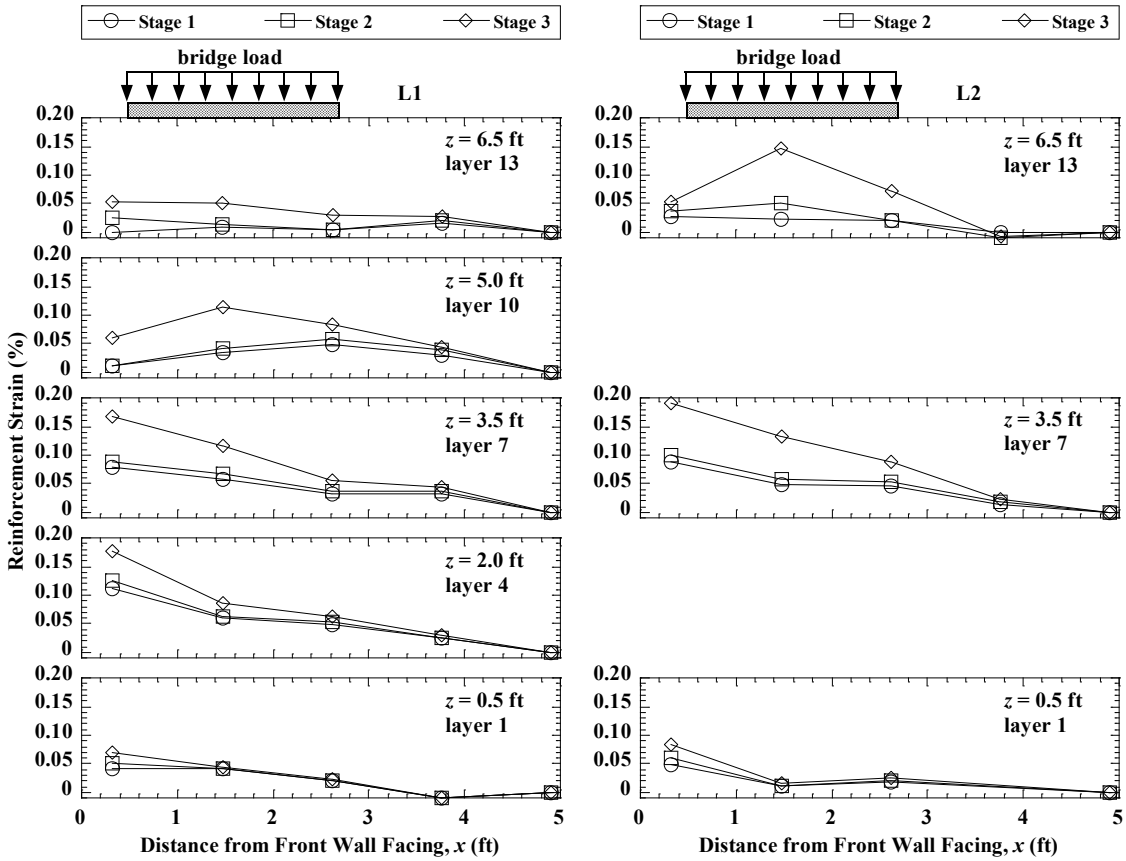

Figure 4.34 Reinforcement strain distributions in L1 and L2 for construction stages in Test 1.

Reinforcement strain distributions in the transverse section T1 for construction stages in Test 1 are shown in Figure 4.35. For Stage 1, layers 1 and 7 show maximum strains near the connections, and layer 13 shows relatively small strains. For Stage 2, construction of the bridge seat resulted in greater increases in layer 13 both near the connection and under the bridge seat. For Stage 3, the placement of bridge beam caused significant increases of reinforcement strain in layers 7 and 13. The reinforcement strain at y_w = 1.1 ft from the west side wall facing reached 0.14%, which is similar to the strain value of 0.15% at the same elevation for the longitudinal section L2 (also on the west side).

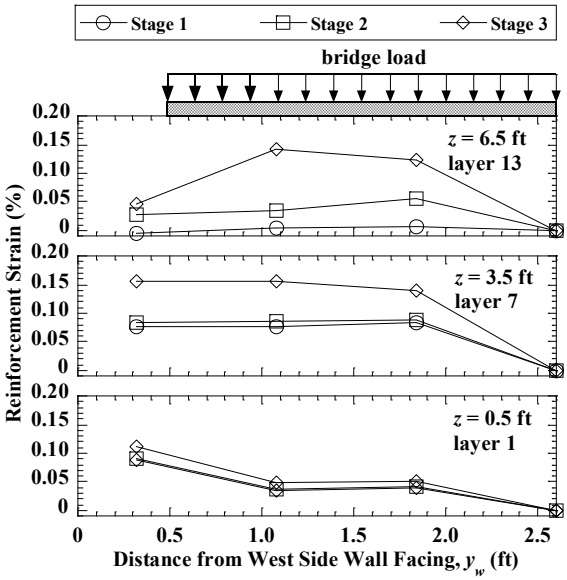

Figure 4.35 Reinforcement strain distributions in T1 for construction stages in Test 1.

Reinforcement strain distributions in the longitudinal sections L1 and L2 for Stages 1 and 3 in Tests 1 to 4 are shown in Figure 4.36 and Figure 4.37, respectively. For the longitudinal off-centerline section L2, reinforcement strains were measured only for layer 7 in Test 3. For Stage 1, the magnitudes of reinforcement strain in L1 are relatively small and show generally similar values. The reinforcement strains at x = 1.5 ft in layer 1 for L2 in Test 4 shows much larger value than the other tests, which may be due to over compaction for this layer in Test 4. For Stage 3, the reinforcement strains in L1 and L2 in Tests 3 and 4 are the larger than in Tests 1 and 2.

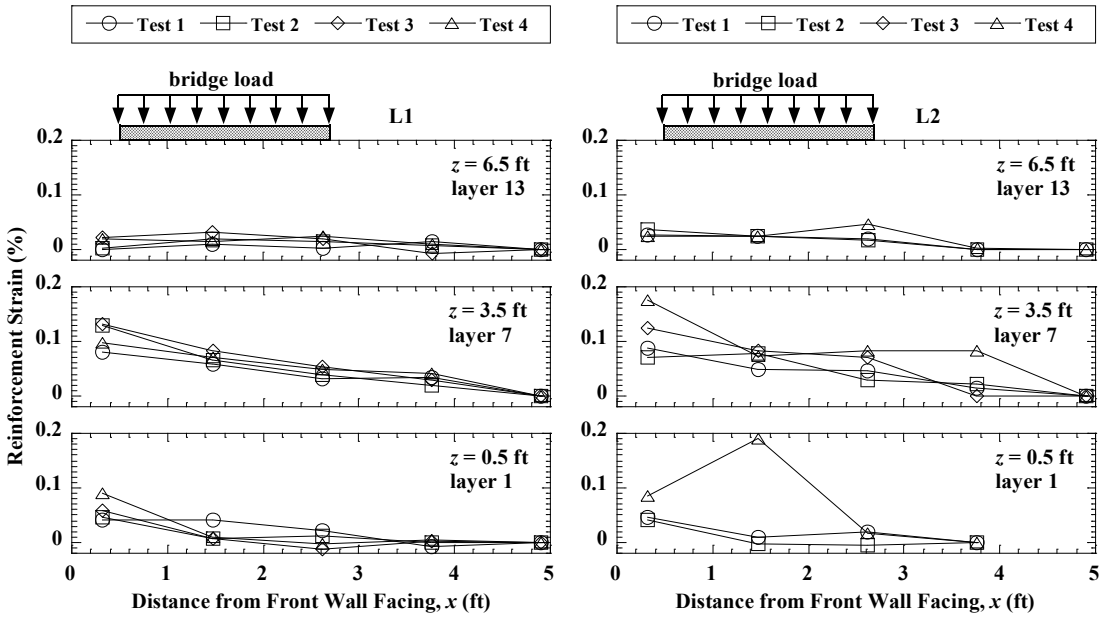

Figure 4.36 Reinforcement strain distributions in L1 and L2 for Stage 1 in Tests 1 to 4.

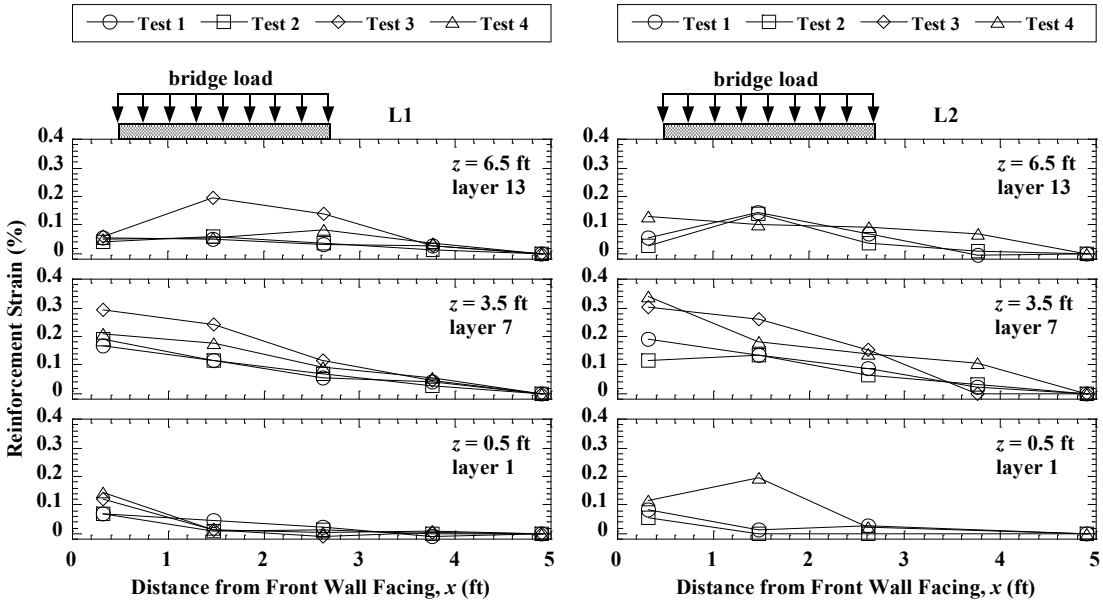

Figure 4.37 Reinforcement strain distributions in L1 and L2 for Stage 3 in Tests 1 to 4.

The incremental reinforcement strain distributions due to placement of the bridge beam (from Stages 2 to 3) in L1 and L2 are shown in Figure 4.38. Results for L1 and L2 show that the incremental strains in Test 3 are larger than the other tests for all layers shown, especially for layers 7 and 13, which indicates that reinforcement spacing has the most significant effect. The incremental strains in Test 4 also have larger strain values than Tests 1 and 2 for both L1 and L2. This indicates that reinforcement stiffness also has important effects on the reinforcement strains. As expected, for both L1 and L2, the incremental strains in Test 1 with greater bridge surcharge stress are larger than the incremental strains in Test 2.

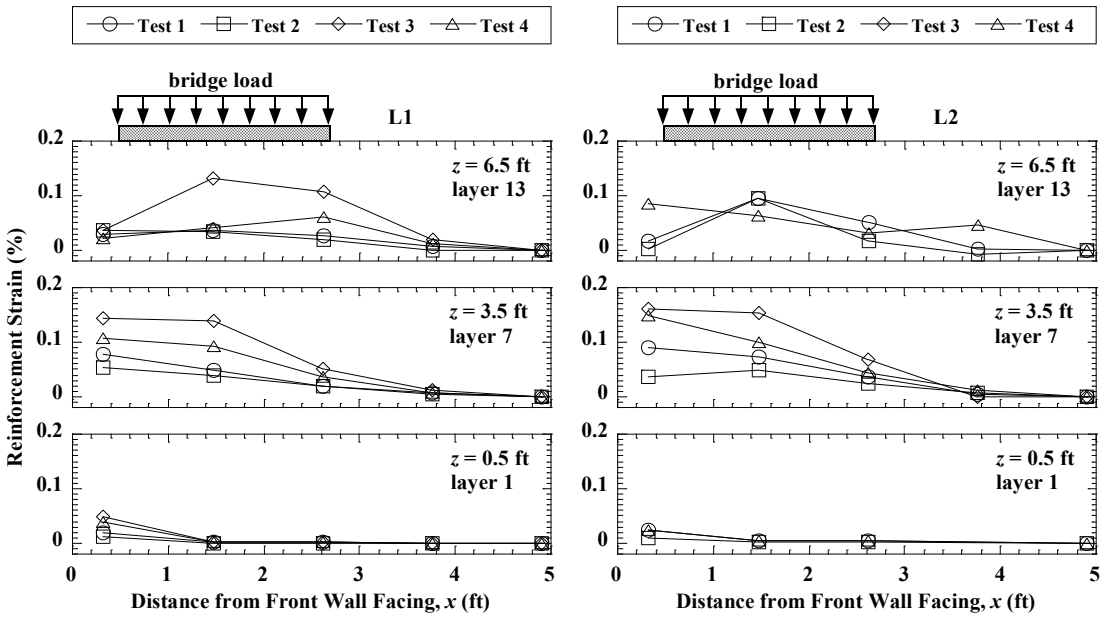

Figure 4.38 Incremental reinforcement strain distributions in L1 and L2 due to bridge beam placement (from Stages 2 to 3) in Tests 1 to 4.

Reinforcement strain distributions in the transverse section T1 for Stages 1 and 3 in Tests 1 to 4 are shown in Figure 4.39 and Figure 4.40, respectively, and the incremental reinforcement strain distributions due to placement of the bridge beam (from Stages 2 to 3) are shown in Figure 4.41. In general, results are consistent with the longitudinal sections, and confirm that reinforcement spacing and stiffness have important effects on reinforcement strains under static loading.

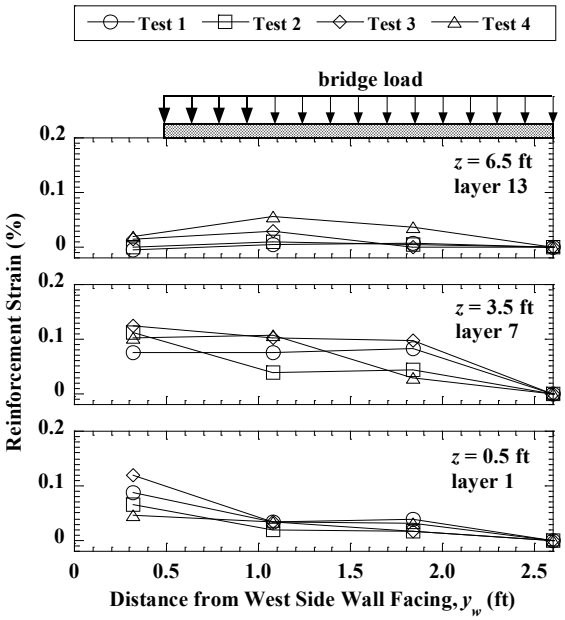

Figure 4.39 Reinforcement strain distributions in T1 for Stage 1 in Tests 1 to 4.

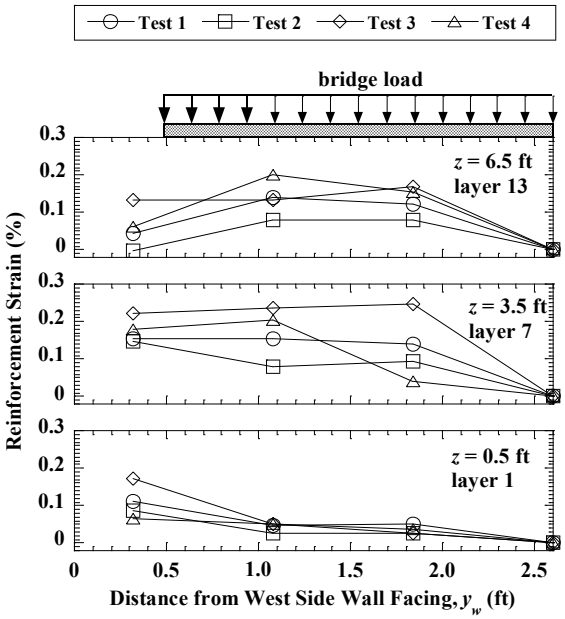

Figure 4.40 Reinforcement strain distributions in T1 for Stage 3 in Tests 1 to 4.

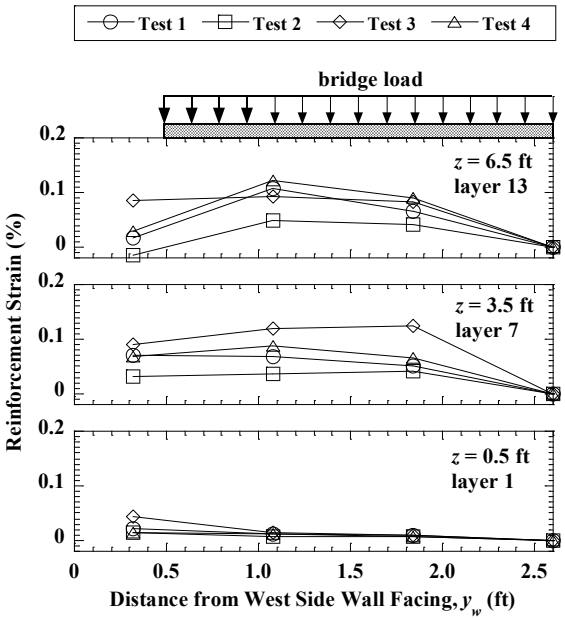

Figure 4.41 Incremental reinforcement strain distributions in T1 due to bridge beam placement (from Stages 2 to 3) in Tests 1 to 4.

4.7.2 Dynamic Loading

Reinforcement strain distributions in L1 and L2 with the initial (before shaking), maximum (during shaking), minimum (during shaking), and residual (after shaking) values during the Imperial Valley, Maule, and Northridge motions are shown in Figure 4.42, Figure 4.43, and Figure 4.44, respectively. During the Imperial Valley motion, maximum strains in L1 are highest near the connections (x = 0.3 ft) for layers 1, 4, and 7, and under the bridge seat (x = 1.5 ft) for layers 10 and 13, whereas minimum strains generally are close to the initial values. The maximum dynamic strain values indicate increased strains near the connections, which is attributed to the inertial forces of the facing blocks. Except for the bottom reinforcement layer, residual strains near the connections increased only slightly as compared to the initial values and indicate that the majority of dynamic reinforcement strains were recovered. Residual strains under the bridge seat increased significantly, especially for the upper layers. The maximum and residual reinforcements strains in L2 are similar to L1 for layers 1 and 7, while are much larger than L1 for layer 13 due to tilting of the bridge seat toward the west side. The maximum dynamic strain under the bridge seat (x = 1.5 ft) in layer 13 is 0.29% in L2, but is only 0.14% at the same location for L1. Similar observations are also found for the Maule and Northridge motions with larger magnitudes of maximum and residual reinforcement strains.

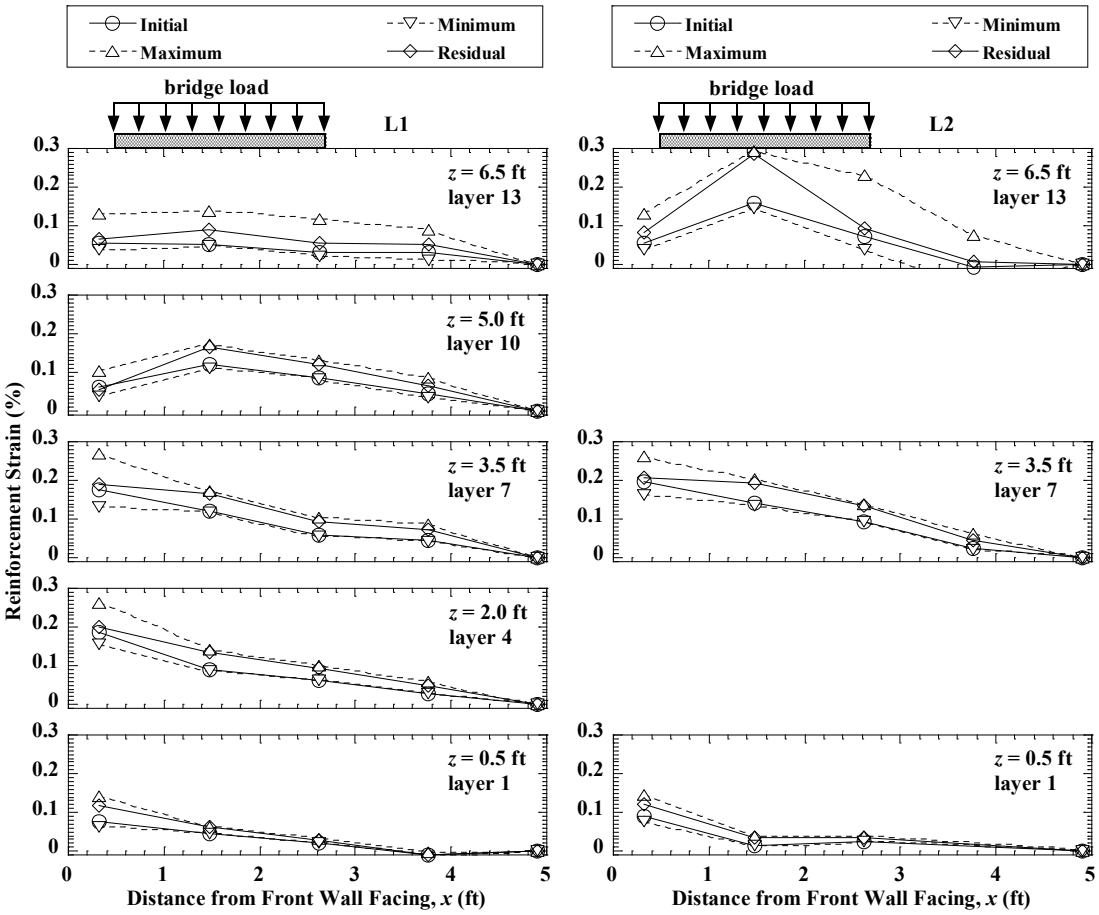

Figure 4.42 Reinforcement strain distributions in L1 and L2 during the Imperial Valley motion in Test 1.

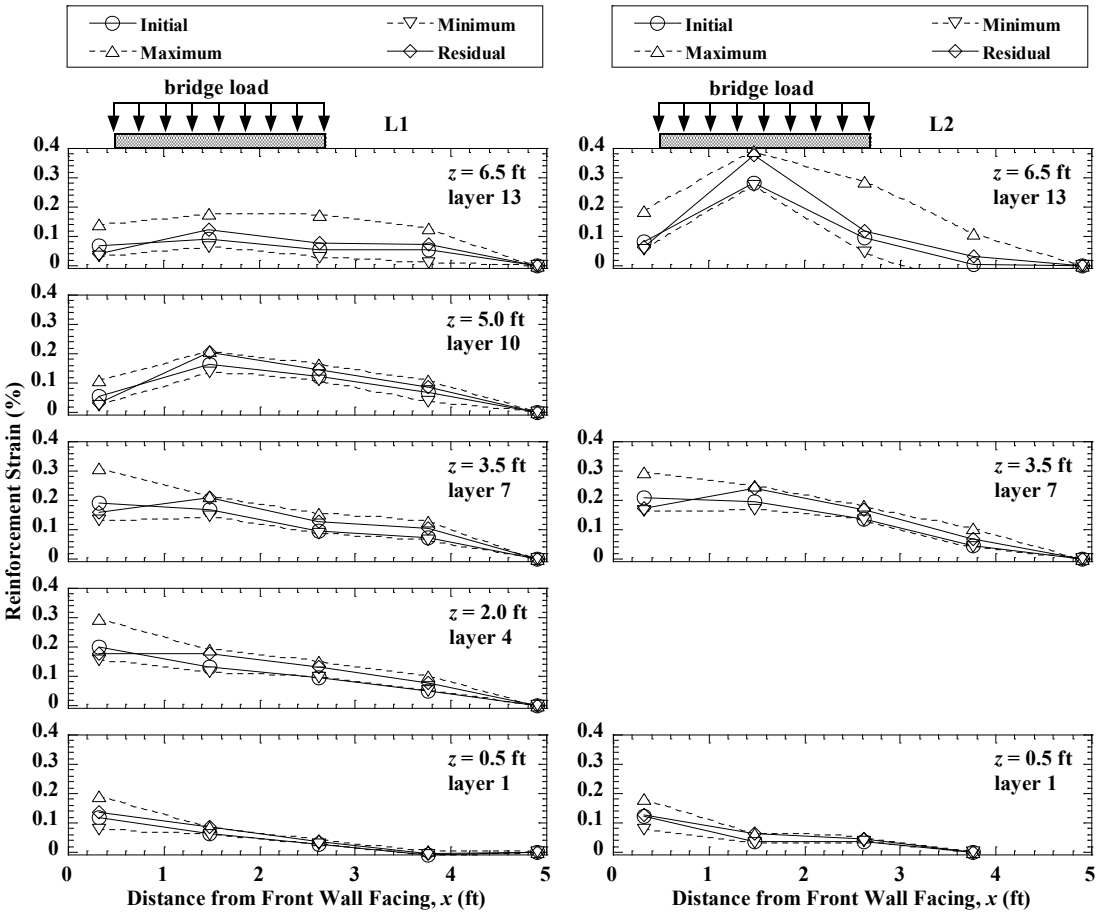

Figure 4.43 Reinforcement strain distributions in L1 and L2 during the Maule motion in Test 1.

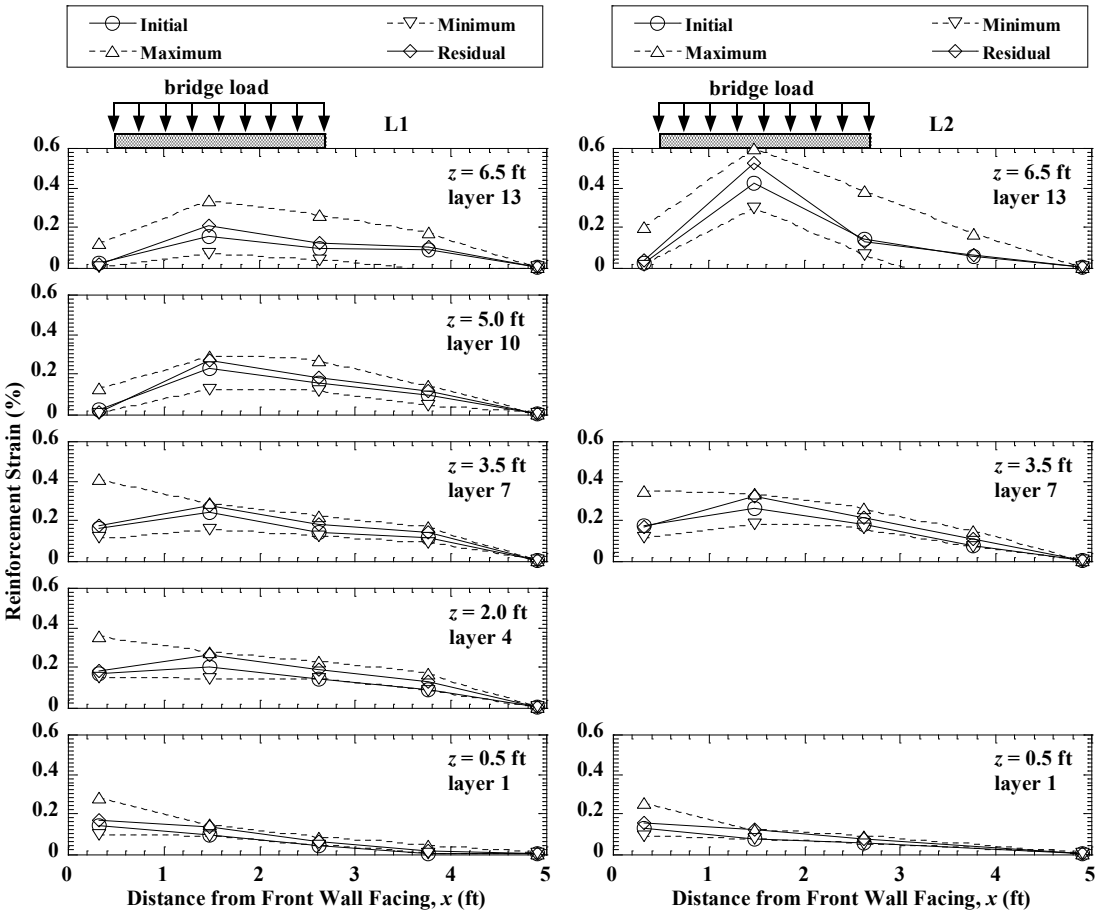

Figure 4.44 Reinforcement strain distributions in L1 and L2 during the Northridge motion in Test 1.

Reinforcement strain distributions in the transverse section T1 during the Imperial Valley, Maule, and Northridge motions are shown in Figure 4.45, Figure 4.46, and Figure 4.47, respectively. Similar to the longitudinal sections, the highest initial and residual strains occurred near the connections for layers 1 and 7, and under the bridge seat for layer 13. During shaking, minimum strains are close to the initial values and maximum strains are close to the residual values. Therefore, dynamic strains generally were not recovered after shaking for the reinforcement layers in the transverse direction. Data indicate that shaking caused significant increases in strain for the transverse reinforcement, which suggests that, in addition to longitudinal reinforcement analysis, analysis of transverse reinforcement is important for seismic design.

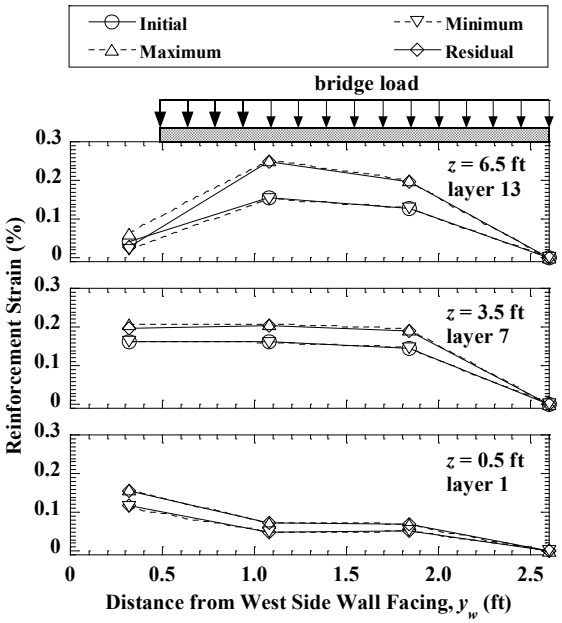

Figure 4.45 Reinforcement strain distributions in T1 during the Imperial Valley motion in Test 1.

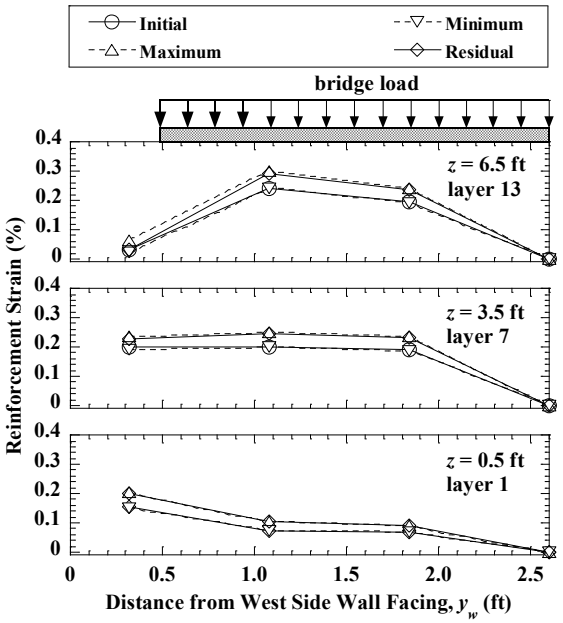

Figure 4.46 Reinforcement strain distributions in T1 during the Maule motion in Test 1.

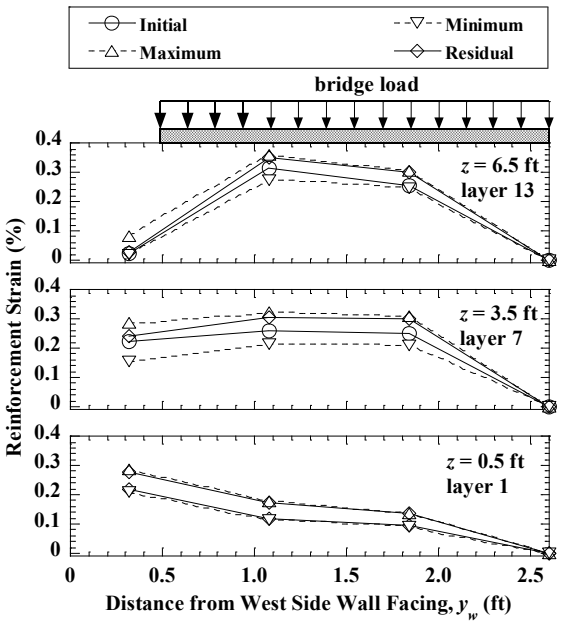

Figure 4.47 Reinforcement strain distributions in T1 during the Northridge motion in Test 1.

Residual reinforcement strain distributions in the longitudinal sections L1 and L2 are shown in Figure 4.48. The Northridge motion was applied after the sinusoidal motions in Test 1. For the longitudinal sections, the residual reinforcement strains increased significantly under the bridge seat due to successive shaking events. For instance, the reinforcement strain of 0.11% at x = 1.5 ft in layer 10 for L1 at the end of construction (EOC) increased to 0.16% after the Imperial Valley motion, to 0.20% after the Maule motion, and to 0.27% after the Northridge motion. Reinforcement strain near the connections increased only for the bottom layer 1, and experienced even slight decreases for the other upper layers. This may be attributed to the loosening of backfill soil near the connections due to the inertial forces of facing blocks. Residual reinforcement strain distributions in the transverse section T1 are shown in Figure 4.49. Results are consistent with the longitudinal sections that residual strain increased significantly under the bridge seat for upper layers (i.e., layers 7 and 13) and near the connections for lower layer (i.e., layer 1).

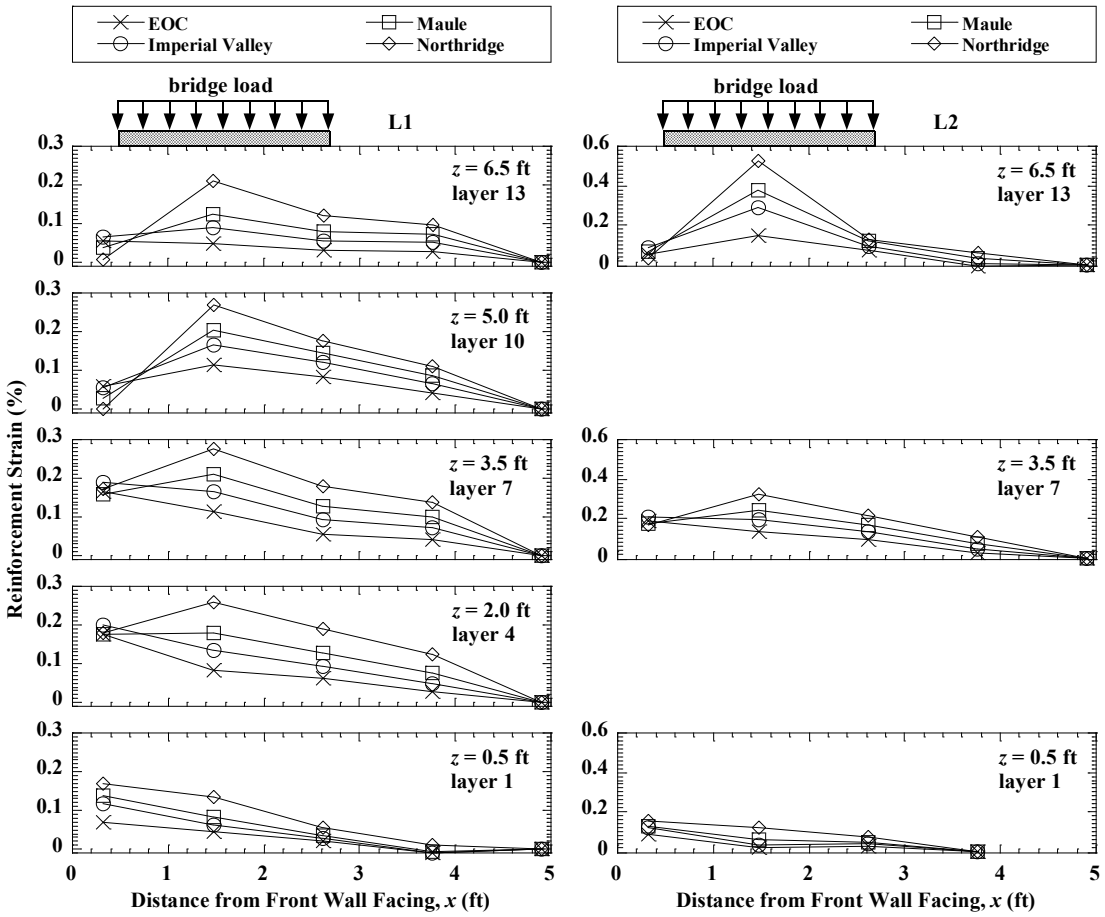

Figure 4.48 Residual reinforcement strain distributions in L1 and L2 in Test 1.

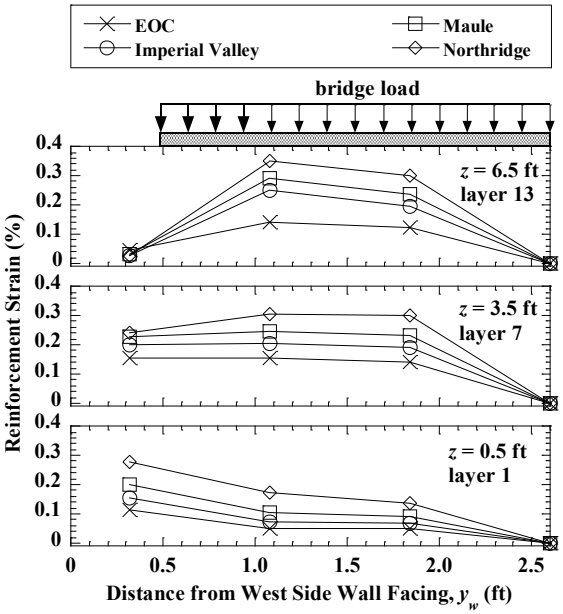

Figure 4.49 Residual reinforcement strain distributions in T1 in Test 1.

Incremental residual reinforcement strain distributions in L1 and T1 in Tests 1 to 4 for the Imperial Valley, Maule, and Northridge motions are shown in Figure 4.50, Figure 4.51, and Figure 4.52, respectively. For the Imperial Valley motion, the incremental reinforcement strains in L1 and T1 in Tests 3 and 4 are generally larger than in Tests 1 and 2. For instance, the incremental strains under the bridge seat (x = 1.5 ft) in layer 13 for L1 are 0.04%, 0.07%, 0.21%, and 0.14% in Tests 1 to 4, respectively. Similar trends are also observed for the Maule and Northridge motions. Results indicate that reinforcement spacing and stiffness have important effects on the reinforcement strains under dynamic loading.

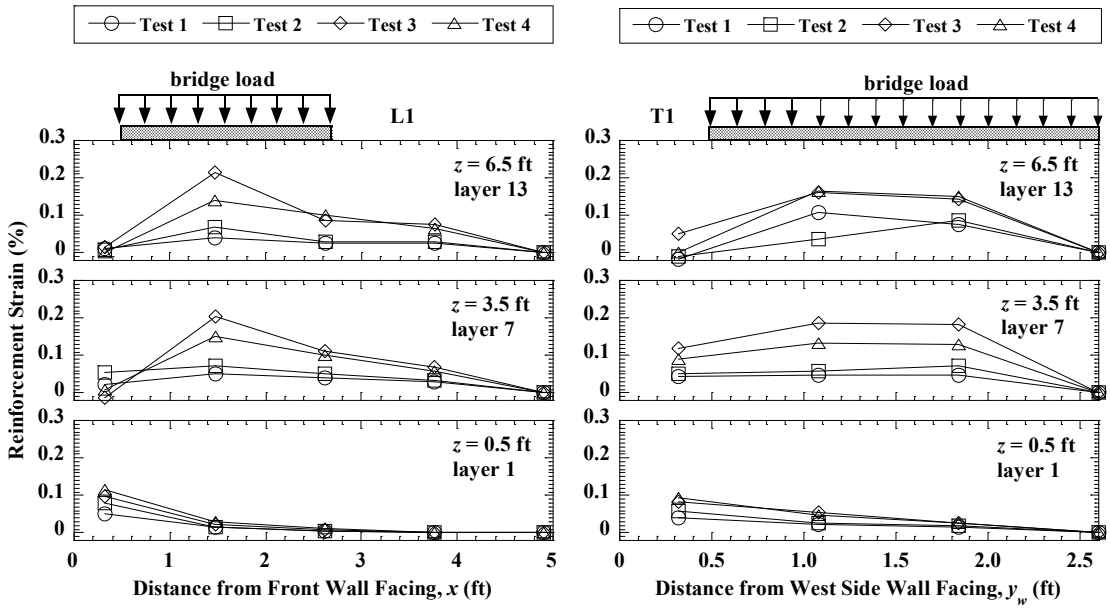

Figure 4.50 Incremental residual reinforcement strain distributions in L1 and T1 for the Imperial Valley motion in Tests 1 to 4.

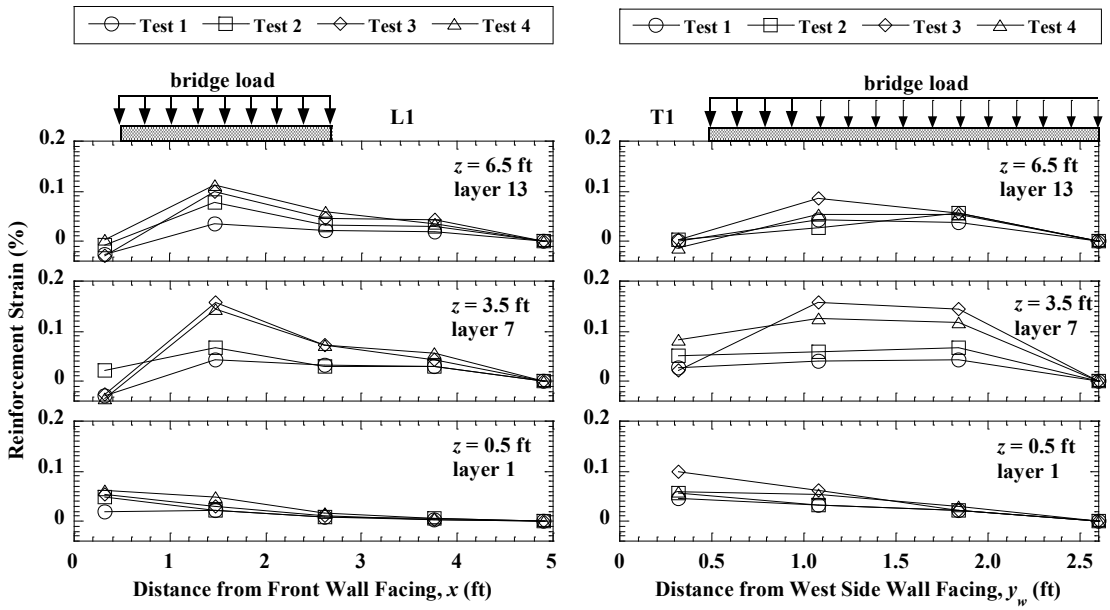

Figure 4.51 Incremental residual reinforcement strain distributions in L1 and T1 for the Maule motion in Tests 1 to 4.

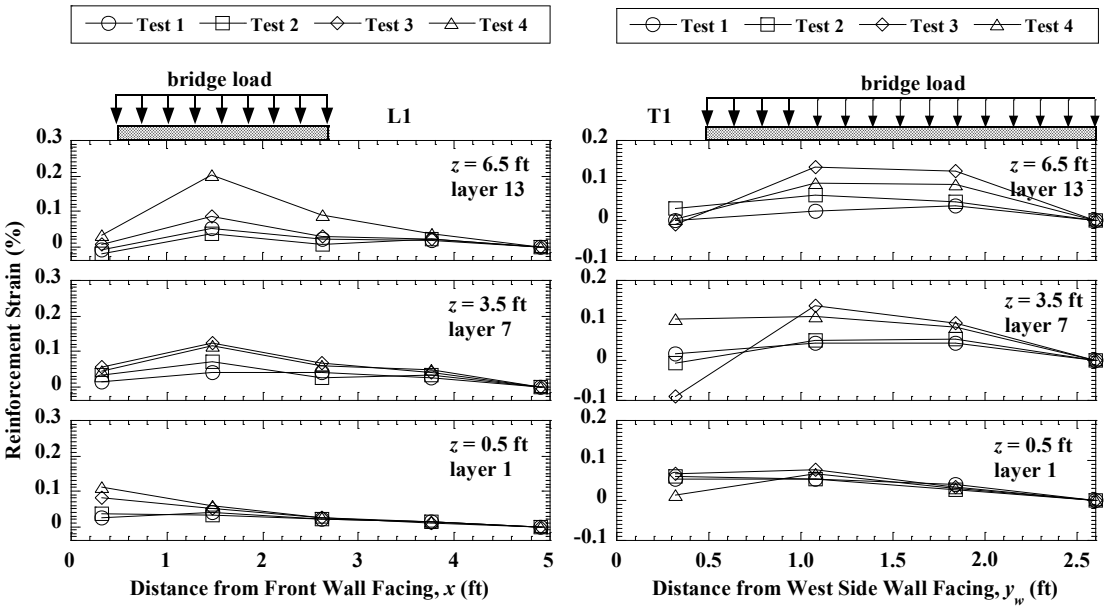

Figure 4.52 Incremental residual reinforcement strain distributions in L1 and T1 for the Northridge motion in Tests 1 to 4.

Steel reinforcement (welded wire mesh) was used in Test 5, and the reinforcement strain distributions for the longitudinal and transverse sections are shown in Figure 4.53 and Figure 4.54, respectively. Several strain gauges were broken during construction of the MSE bridge abutment.

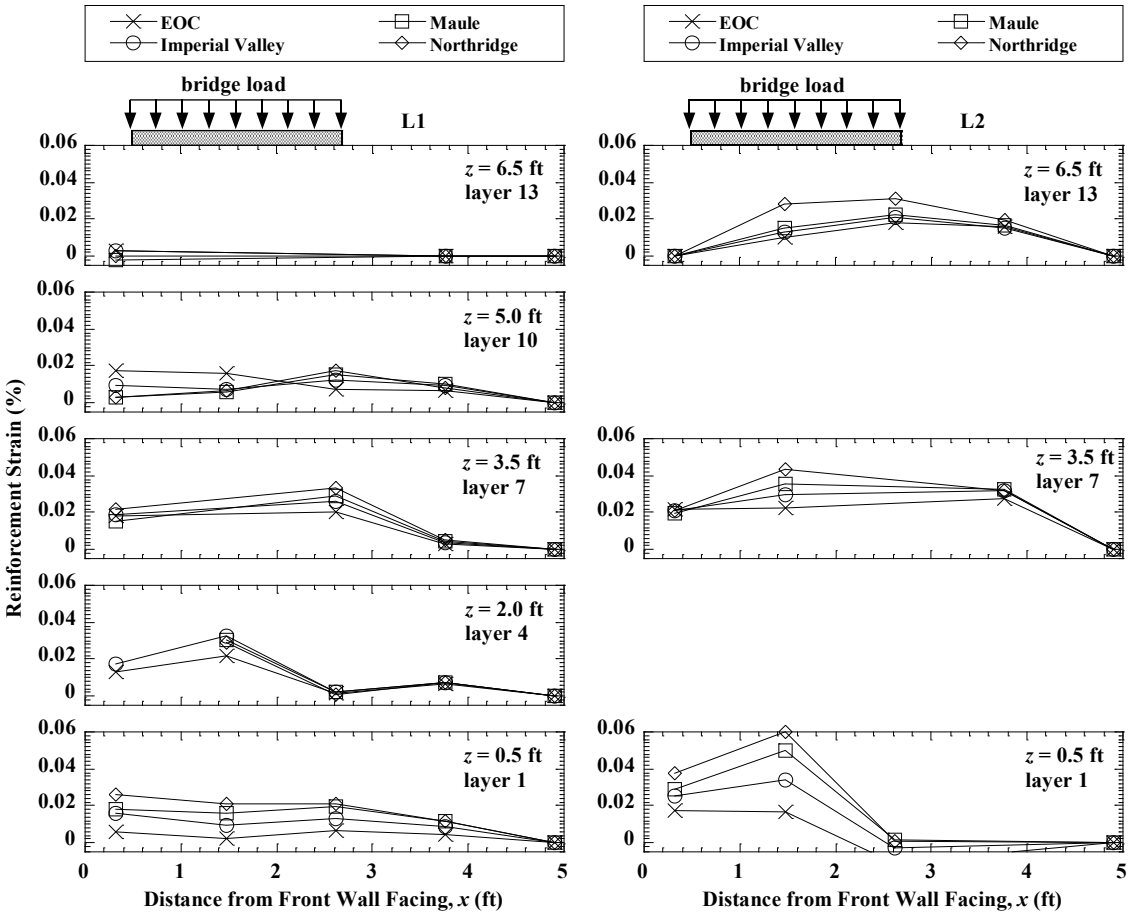

Figure 4.53 Residual reinforcement strain distributions in L1 and L2 in Test 5.

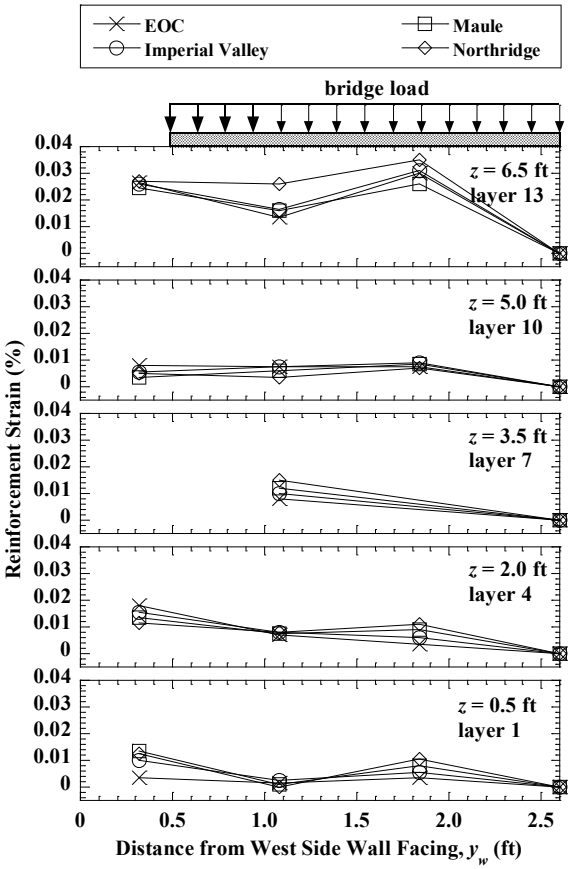

Figure 4.54 Residual reinforcement strain distributions in T1 in Test 5.

4.8 Contact Forces

The bridge beam had relative horizontal displacements with respect to the bridge seat, and thus the width of expansion joint changed during shaking. Horizontal contact forces between the bridge seat and bridge beam generate when the width of expansion joint reduces to zero. For all the longitudinal tests for the Imperial Valley and Maule motions, the maximum and minimum dynamic relative displacements are smaller than the initial width of the expansion joint before the shaking event. This indicates that joint closure and bridge seat-beam contact did not occur for the shaking of these two motions. However, joint closure occurred for the Northridge motion, although this may have partially occurred due to the different initial joint width between the bridge beam and bridge seat for this motion due to permanent changes in joint width during the preceding earthquake motions. This is a topic that deserves further study using numerical simulations.

Time histories of joint width for earthquake motions are shown in Figure 4.55. For the Imperial Valley motion, the initial joint width was 1.15 inches, and varied in the range of ± 0.31 inches during shaking, and had a residual width of 1.22 inches. The joint width did not vary significantly during the Maule motion, and had a residual width of 1.24 inches. For the Northridge motion (after a series of sinusoidal motions), the initial width of the joint was 1.22 inches before shaking. During shaking, the width reached a maximum value of 1.87 inches at t = 3.88 s, and reduced to zero at t = 4.02 s as shown in Figure 4.55(c), which resulted in horizontal contact forces of 22.1 kips between the bridge seat and bridge beam, as shown in Figure 4.56. This corresponds to a contact force of 176.8 kips for the prototype structure. This contact force is relatively large and should be considered in the seismic design of MSE bridge abutments.

The maximum horizontal contact forces for all the longitudinal tests during the Northridge motion are presented in Table 4.10. The maximum horizontal contact force is the smallest with a value of 15.4 kips for Test 3. There is not a consistent trend to identify the effect of different parameters on contact forces.

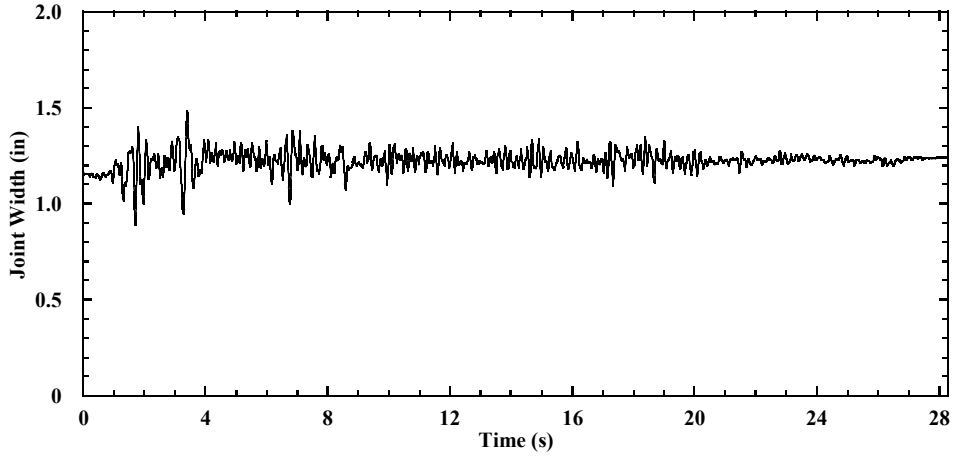

(a)

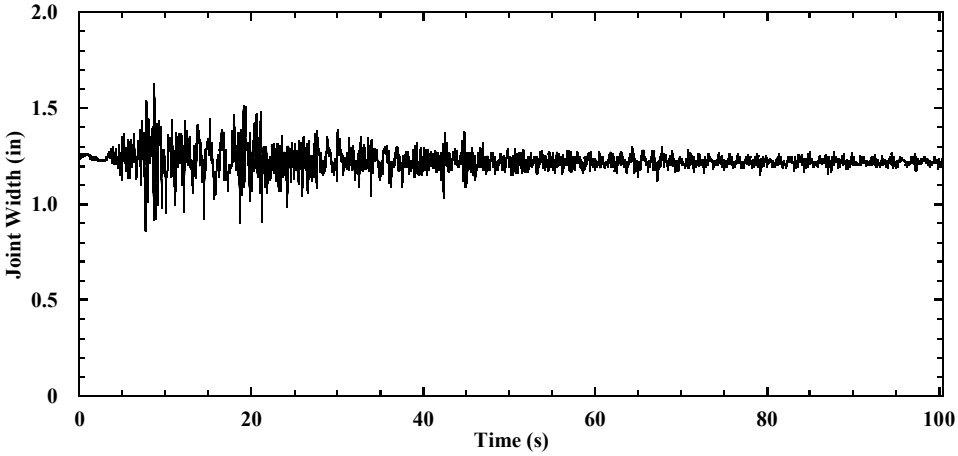

(b)

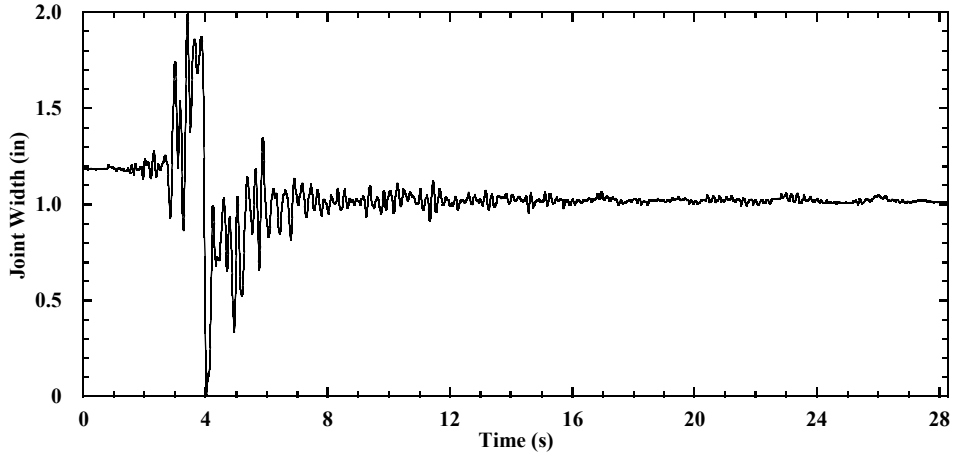

(c)

Figure 4.55 Time histories of joint width on the north side in Test 1: (a) Imperial Valley motion; (b) Maule motion; (c) Northridge motion.

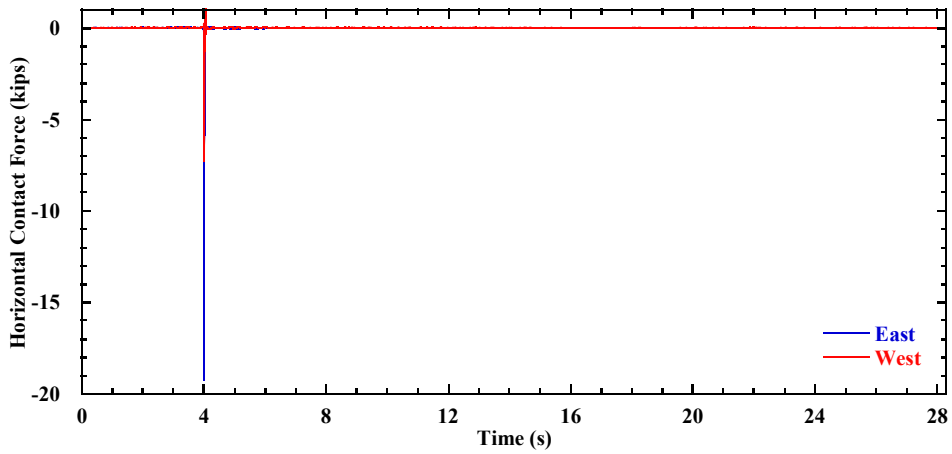

Figure 4.56 Horizontal contact forces between bridge beam and bridge seat for the Northridge motion in Test 1.

Table 4.10 Maximum contact forces (kips) for the Northridge motion.

Earthquake motion	Test 1	Test 2	Test 3	Test 4	Test 5
Northridge	22.1	24.8	15.4	23.6	26.5

Chapter 5 Transverse Test Results and Analysis

This chapter presents results and analysis for the transverse test on the MSE bridge abutment in the baseline configuration (Test 6). In addition to the characterization tests on system identification and testing system performance, results are presented in this chapter including, facing displacements, bridge seat and bridge beam displacements, accelerations, lateral and vertical stresses, reinforcement strains, and contact forces between the bridge seat and bridge beam during a series of earthquake motions in the transverse direction.

When processing the data, the string potentiometer measurements for horizontal displacements of the side wall facings were corrected using measured horizontal displacements of the shaking table in the direction of shaking to yield relative displacements with respect to the table. Horizontal displacements and accelerations toward the north direction (Figure 3.21) are defined as positive. In the direction of shaking, outward displacements of the side wall facings are defined as positive. In the direction perpendicular to shaking, outward displacements of the front wall facing are defined as positive. Consistent with geotechnical sign conventions, downward vertical settlements are defined as positive. For static loading (construction stages), Stage 1 involved construction of the lower MSE wall, Stage 2 involved construction of the bridge seat and upper MSE wall, and Stage 3 involved placement of the bridge beam atop the MSE bridge abutment. All presented results are in model-scale, and results should be adjusted using the similitude relationships in Table 3.2 to obtain corresponding values for prototype structures.

5.1 System Identification

System identification tests were conducted using the white noise motions before and after each of the earthquake motions to detect changes in fundamental frequencies of the bridge system in the transverse direction. Amplitudes of the horizontal acceleration transfer functions for the bridge beam, bridge seat, MSE bridge abutment (measured at y_s = 1.25 ft, z = 6.25 ft), and support wall with respect to the shaking table for the initial white noise motion (Shaking event 1) are shown in Figure 5.1(a). The fundamental frequency is 7.7 Hz for the bridge beam, and is 11.7 Hz for the bridge seat and MSE bridge abutment, and is 3.6 Hz for the support wall in the transverse direction. Horizontal acceleration transfer functions of the MSE bridge abutment with respect to the shaking table for the white noise motions before and after each earthquake motion are shown in Figure 5.1(b), and indicates that the fundamental frequency decreased to 10.5 Hz from the initial frequency of 11.7 Hz after successive shaking events due to shear modulus reduction of the backfill soil associated with shear strain development.

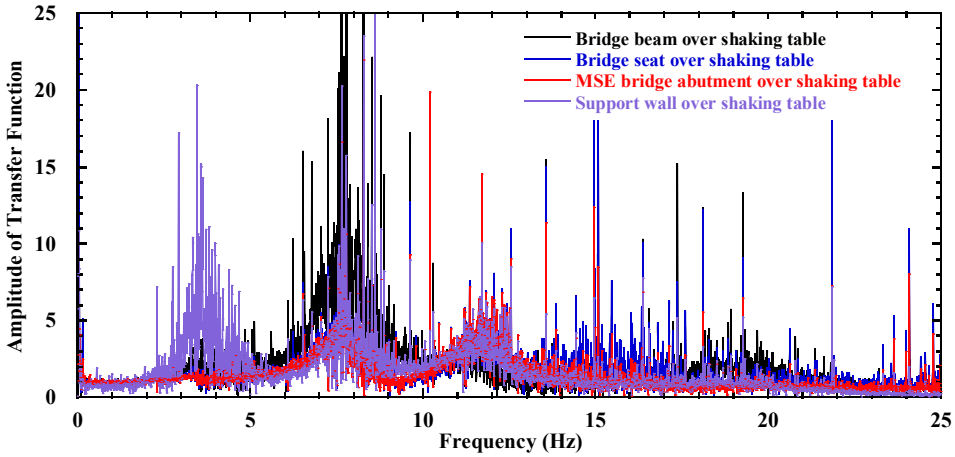

(a)

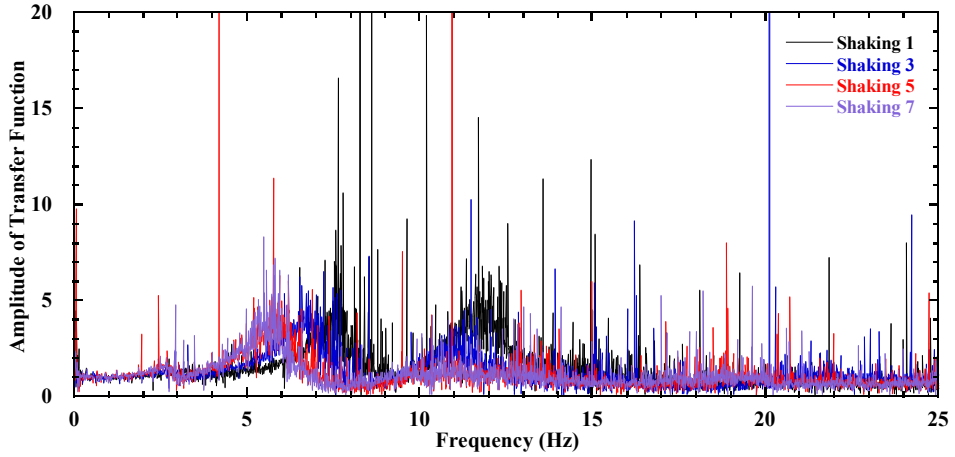

(b)

Figure 5.1 Horizontal acceleration transfer functions amplitudes for white noise tests in Test 6: (a) bridge seat, bridge beam, MSE bridge abutment, and support wall for the initial white noise test; (b) MSE bridge abutment before and after each earthquake motion.

5.2 Testing System Performance

The characterization of the testing system performance is critical for the transverse test because the configuration of the support wall connected to one side of the shaking table is unique and has not been evaluated in a previous shaking table experiment. Since the shaking table is used to drive the motion of the support wall in an unbalanced manner, rocking and cantilever type motions of the support wall are expected in the transverse test. The approach used in this study permits a unique evaluation of the MSE bridge abutment response in a transverse configuration.

The performance of the testing system (i.e., the shaking table and the connected support wall resting on the sliding platform) was evaluated based on the measured displacement and acceleration responses in the direction of shaking. The testing system responses for the Imperial Valley, Maule, and Northridge motions in Test 6 are shown in Figure 5.2, Figure 5.3, and Figure 5.4, respectively, and a summary of the target and measured peak responses of the shaking table for the three earthquake motions is presented in Table 5.1.

Table 5.1 Shaking table response for earthquake motions in Test 6.

Shaking event	Earthquake motion	Model-scale duration (s)	Target PGA (*g*)	Actual PGA (*g*)	Target PGD (in.)	Actual PGD (in.)
2	Imperial Valley	28.3	0.31	0.42	2.57	2.57
4	Maule	100.4	0.40	0.56	4.25	4.25
6	Northridge	28.3	0.58	0.86	3.49	3.49

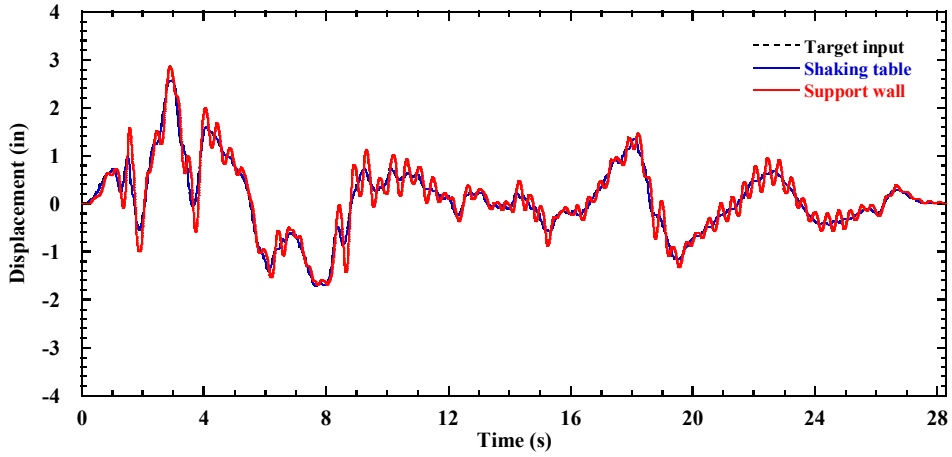

(a)

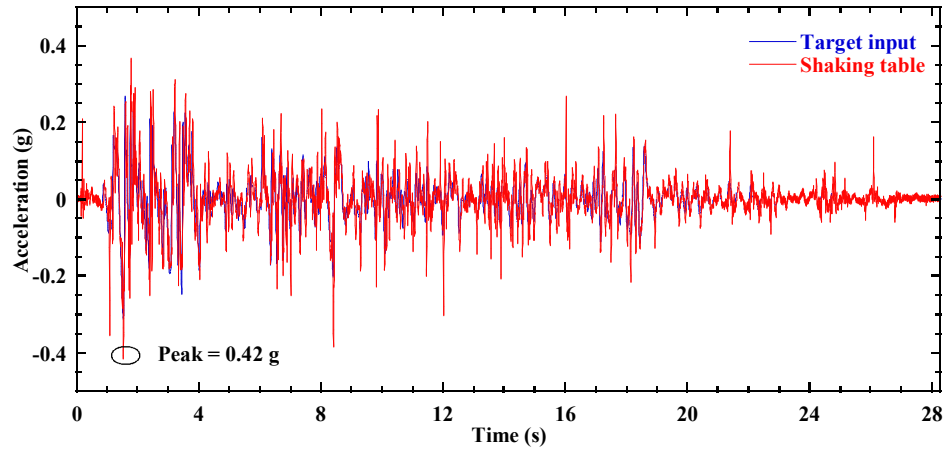

(b)

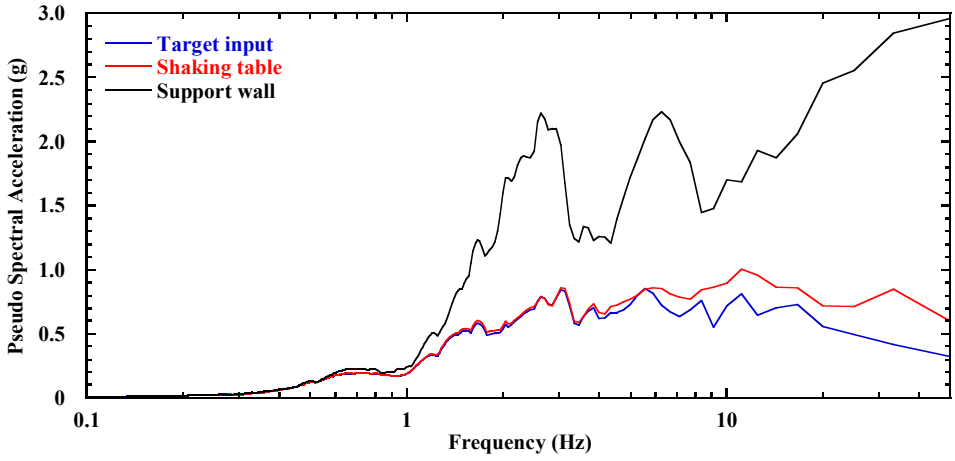

(c)

Figure 5.2 Testing system response for the Imperial Valley motion in Test 6: (a) displacement time history; (b) acceleration time history; (c) response spectra (5% damping).

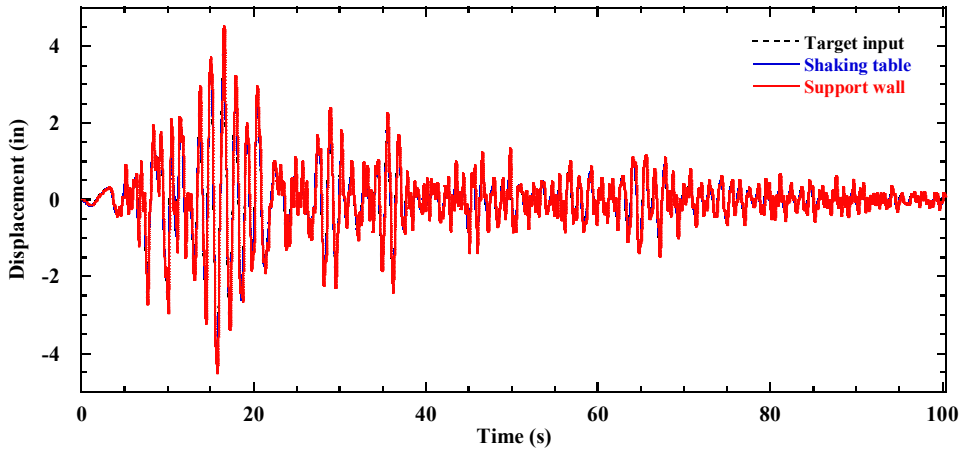

(a)

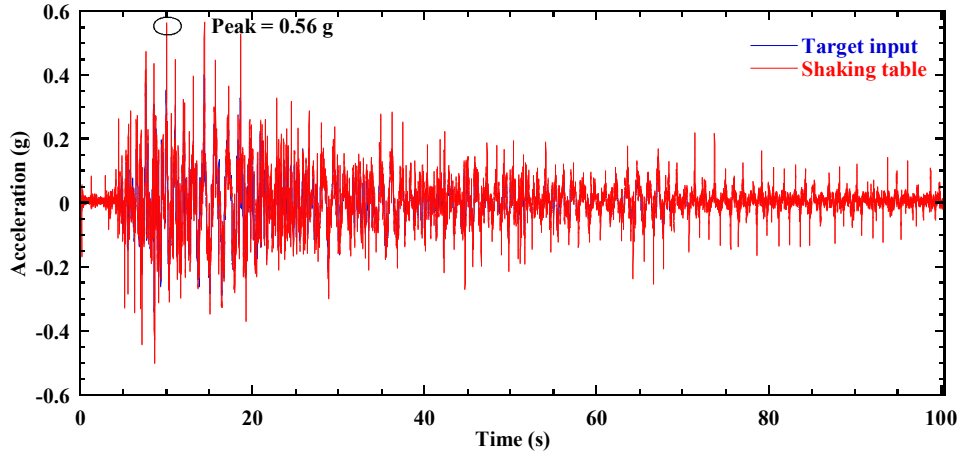

(b)

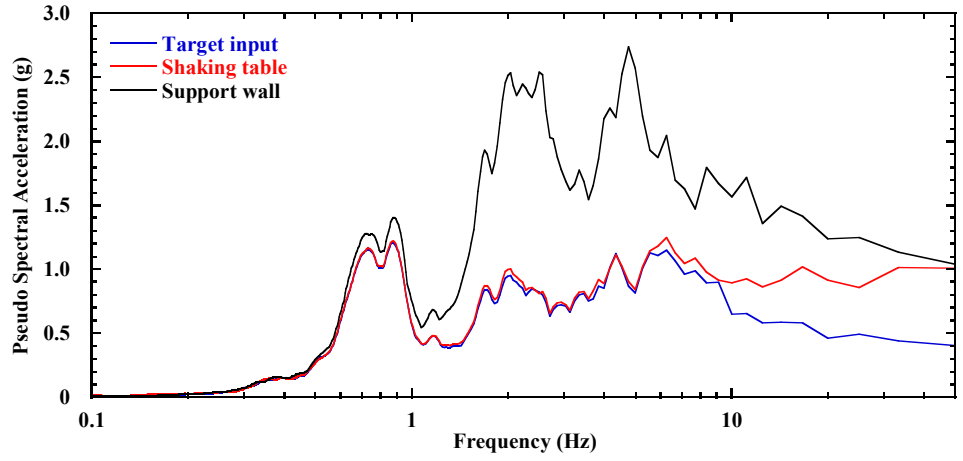

(c)

Figure 5.3 Testing system response for the Maule motion in Test 6: (a) displacement time history; (b) acceleration time history; (c) response spectra (5% damping).

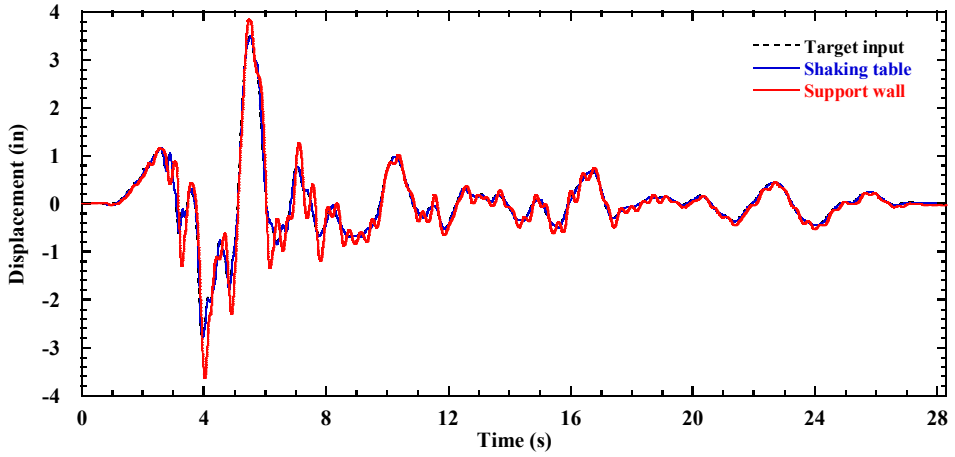

(a)

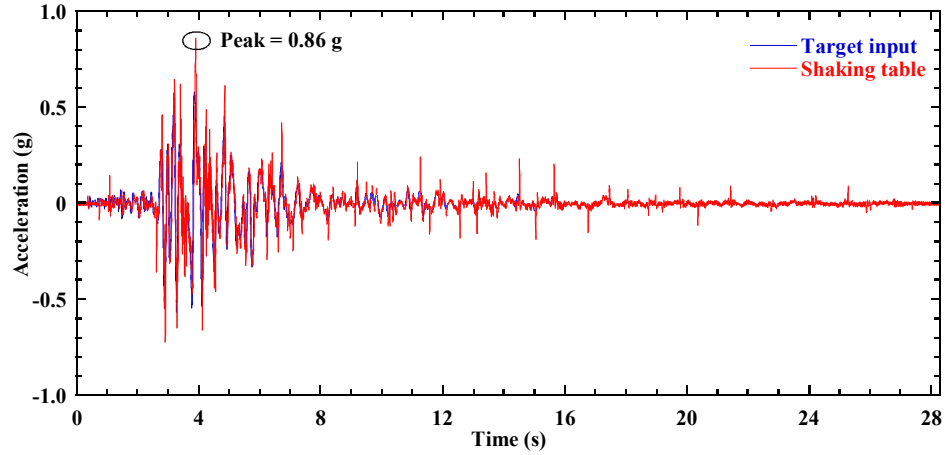

(b)

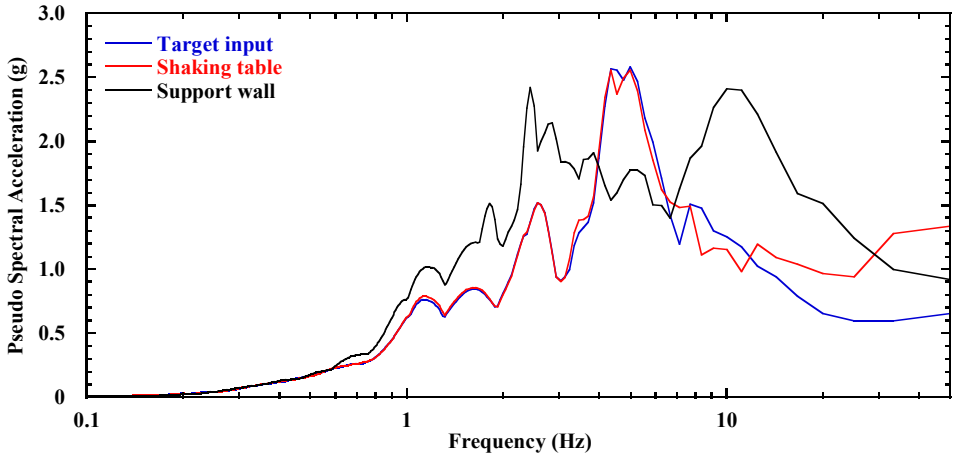

(c)

Figure 5.4 Testing system response for the Northridge motion in Test 6: (a) displacement time history; (b) acceleration time history; (c) response spectra (5% damping).

The measured displacement time histories of the shaking table are in good agreement with the target input for all three motions, whereas the displacement time histories of the support wall show larger peak values due to the inertial forces of the support wall. For the Imperial Valley motion, the displacement time history of support wall follows the general trend of the target input motion, but contains some low frequency content. This is due to the resonance of support wall during shaking, as the fundamental frequency of 3.6 Hz for the support wall is close to the predominant frequencies of the scaled Imperial Valley motion.

The measured acceleration time history of the shaking table in general matches well with the target input accelerations, but had larger peak accelerations. For instance, the measured PGA of 0.86*g* for the shaking table is larger than the target input value of 0.58*g*. The shaking table was refurbished prior to this study to increase the fidelity of dynamic motion. After repair of the shaking table, overshooting of peak accelerations was still observed, but the overshooting was much smaller than before repair, which indicates that the performance of the table has been improved (Trautner et al. 2017). The overshooting is likely due to the inertia of the table itself and is also affected by the size of the payload on the table.

The pseudo-spectral accelerations of the shaking table and target motion are in good agreement for frequencies less than 10 Hz for all three motions, which indicates that the shaking table adequately reproduced the salient characteristics of the target input motions. The actual pseudo-spectral acceleration at the fundamental frequency of 11.7 Hz for the MSE bridge abutment is slightly larger than the target value for all three motions. The pseudo-spectral accelerations for the support wall are much larger than the target values because the fundamental frequencies of 3.6 Hz for the support wall is in the frequency range for typical earthquake motions. Although the support wall is out of phase with larger peak values, this effect was unavoidable due to the shaking in an unbalanced manner. However, the focus of this experiment is on the MSE bridge abutment, and this out of phase behavior is only expected to affect the interaction between the support wall and bridge beam on the east side of the testing system.

5.3 Facing Displacements

5.3.1 Static Loading

Facing displacements were measured on the south and north sides of the transverse section T1 (referred to as T1-South and T1-North as labeled in Figure 3.26) and the longitudinal centerline section L1 (referred to as L1). Facing displacement profiles for the three instrumented sections after the three stages of construction are shown in Figure 5.5, and the maximum values of facing displacement profiles are presented in Table 5.2.

For Stage 1, facing displacements for T1-South and T1-North are similar with maximum facing displacements of 0.03 and 0.04 inches, respectively, both at an elevation z = 3.25 ft above the foundation soil level. The maximum facing displacement for L1 is 0.06 inches also at z = 3.25 ft. Although the shapes of the longitudinal and transverse facing displacement profiles are different, the magnitudes of the facing displacements are small, and it is difficult to identify a consistent shape to reflect construction effects. For Stage 2, facing displacements increased slightly due to construction of the bridge seat and upper wall. For Stage 3, the application of the bridge beam caused an increase in facing displacements for all three sections, with greater increases in displacements near the top of the wall. For Stage 3, T1-South and T1-North have similar facing displacement profiles with maximum values of 0.06 inches, while the maximum facing displacement for L1 is 0.09 inches.

Table 5.2 Maximum facing displacements (in.) for construction stages in Test 6 (model-scale).

Construction stage	T1-South	T1-North	L1
Stage 1	0.03	0.04	0.06
Stage 2	0.04	0.04	0.07
Stage 3	0.06	0.06	0.09

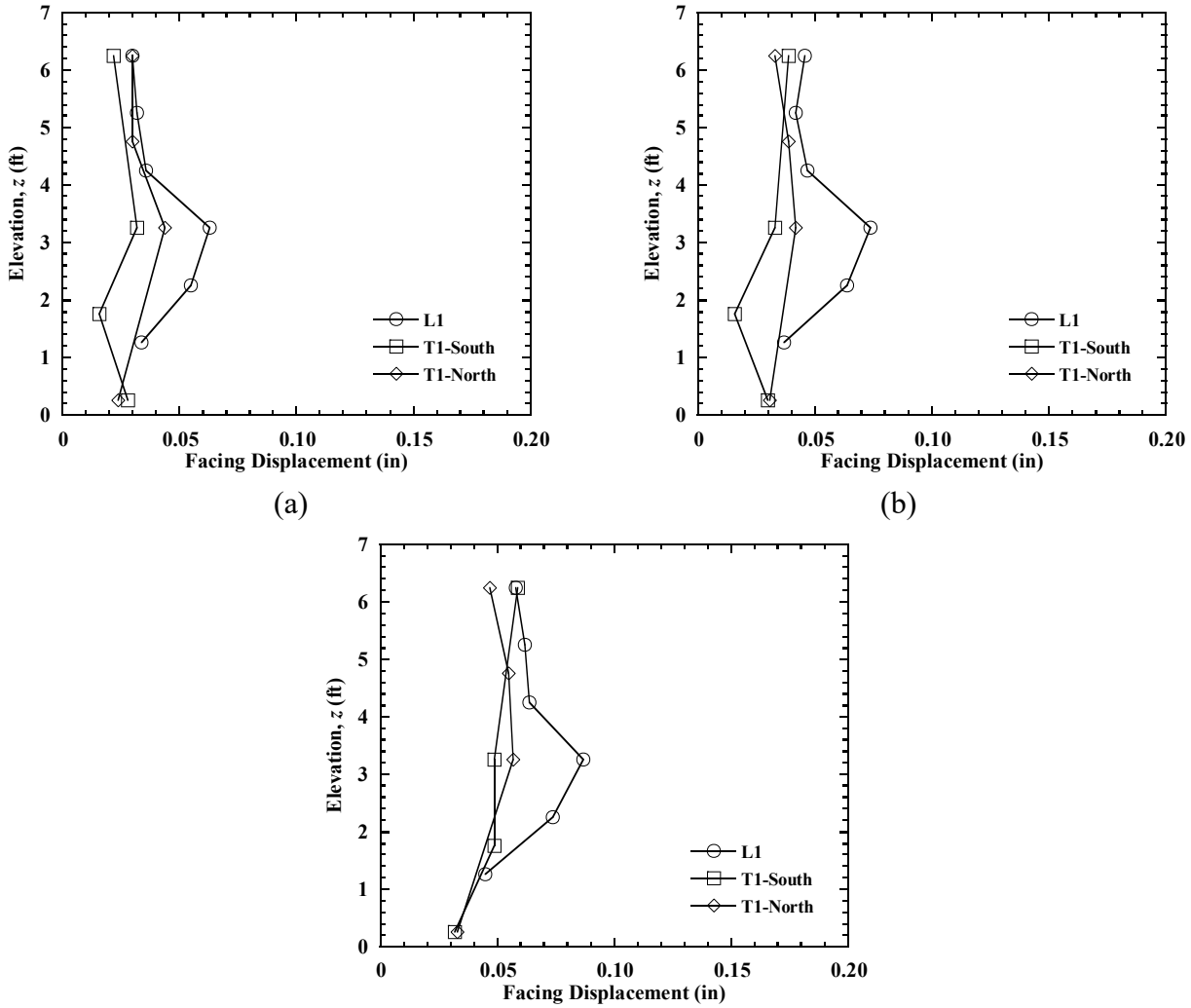

Figure 5.5 Facing displacement profiles for construction stages in Test 6: (a) Stage 1; (b) Stage 2; (c) Stage 3.

5.3.2 Dynamic Loading

Incremental maximum and residual facing displacement profiles for different earthquake motions are shown in Figure 5.6, and maximum values of the incremental facing displacements from the profiles are presented in Table 5.3. The maximum facing displacement profiles correspond to the specific times associated with maximum incremental outward facing displacement measurements for each section.

For the Imperial Valley motion, the maximum facing displacement profiles for T1-South and T1-North are similar, with maximum values of approximately 0.2 inches at z = 6.25 ft. After shaking, most of the dynamic facing displacements were recovered. The maximum residual facing displacements are approximately 0.04 inches for both sections at the top. The longitudinal section L1 has a maximum facing displacement of 0.06 inches and residual facing displacement of 0.05

inches at z = 6.25 ft. For the Maule motion, T1-South had larger maximum facing displacements than T1-North, with maximum values of 0.67 and 0.37 inches, respectively, that occured at different times. After shaking, T1-South had an outward residual facing displacement of 0.09 inches at z = 6.25 ft, whereas T1-North had an inward facing displacement of 0.07 inches at the same elevation. For the Northridge motion, facing displacements are much larger than those observed in the Imperial Valley and Maule motions. Maximum displacements at z = 6.5 ft are 1.37 and 0.52 inches for T1-South and T1-North, respectively. The outward residual facing displacement at z = 6.25 ft is 0.37 inches for T1-South, whereas T1-South has inward residual facing displacements with a maximum value of 0.18 in at the same elevation. The maximum dynamic facing displacement for L1 is 0.16 inches at z = 6.25 ft, with a residual value of 0.13 inches after shaking.

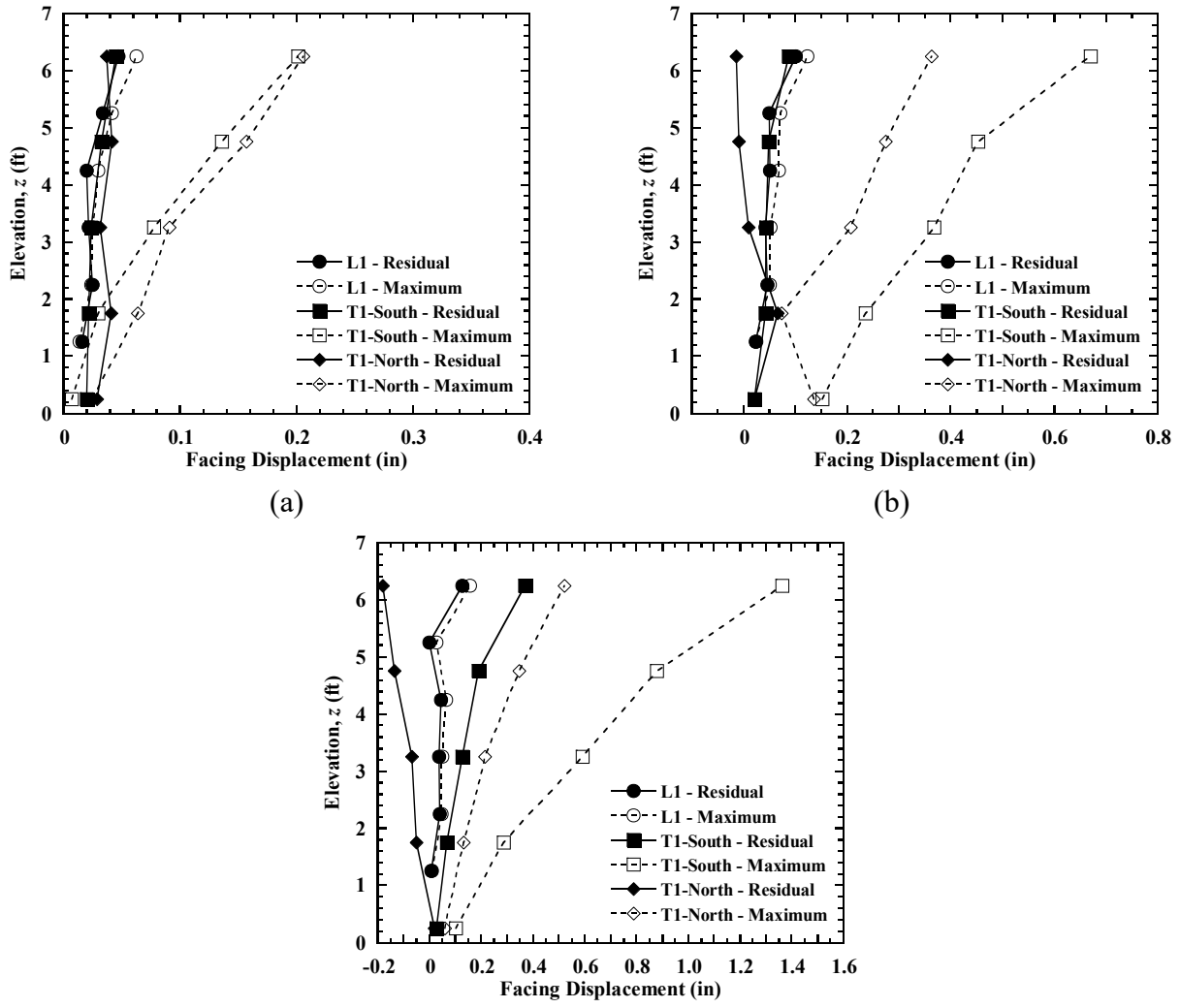

Figure 5.6 Incremental facing displacement profiles in Test 6: (a) Imperial Valley motion; (b) Maule motion; (c) Northridge motion.

Table 5.3 Maximum incremental facing displacements (in.) for earthquake motions in Test 6 (model-scale).

Earthquake motion	T1-South		T1-North		L1	
	Maximum	Residual	Maximum	Residual	Maximum	Residual
Imperial Valley	0.20	0.04	0.20	0.04	0.06	0.05
Maule	0.67	0.09	0.37	0.07	0.13	0.10
Northridge	1.37	0.37	0.52	0.02	0.16	0.13

The maximum incremental residual facing displacements for Tests 1 and 6 are presented in Table 5.4. In Test 1, facing displacements for the side wall were measured only for T1-North, but facing displacements for T1-South are supposed to be the same as T1-North, as shaking was applied in the direction perpendicular to the two symmetric transverse sections (i.e., T1-South and T1-North). Results indicate that shaking in both the longitudinal and transverse directions yielded similar maximum facing displacements for the longitudinal section L1 during all three earthquake motions, and resulted in similar maximum facing displacements for the transverse sections during the Imperial Valley and Maule motions. However, shaking in the transverse direction caused much larger maximum facing displacements for T1-South during the Northridge motion than shaking in the longitudinal direction. Facing displacements in the direction perpendicular to the direction of shaking indicate the 3D effects of 1D shaking.

Table 5.4 Maximum incremental residual facing displacements (in) for earthquake motions in Tests 1 and 6 (model-scale).

Earthquake motion	Test 1 (Longitudinal shaking)		Test 6 (Transverse shaking)		
	L1	T1-North	L1	T1-South	T1-North
Imperial Valley	0.06	0.03	0.05	0.04	0.04
Maule	0.04	0.03	0.10	0.09	0.07
Northridge	0.13	0.12	0.13	0.37	0.02

5.4 Bridge Seat and Bridge Beam Displacements

5.4.1 Bridge Seat Settlements

5.4.1.1 Static Loading

Settlements of the four corners of the bridge seat were measured under static and dynamic loading, as shown in Figure 3.21. One of the string potentiometers on the northwest (NW) side of the bridge seat was not working during the placement of the bridge beam but was replaced before application of the earthquake motions. Settlement time histories of bridge seat corner measurements and average values for Stage 3 are shown in Figure 5.7. The settlements due to application of the bridge beam did not occur uniformly and a sudden but small shift was observed 3 hours after the bridge beam placement. This may have been due to the arching effects that readjusted. Nonetheless, the displacements stabilized after 5 hours and did not vary significantly, indicating negligible creep. The small fluctuations in the measured settlements over time observed in Figure 5.7 may have occurred due to temperature changes in the laboratory. A slight tilting of the bridge seat toward the south side after placement of the bridge seat was observed: the settlement on the south side of the bridge seat (SW and SE) is 0.08 inches, while the settlement on the north side (NE) is 0.04 inches. The average bridge seat settlement is 0.06 inches after 94 hours from the time of the bridge beam placement.

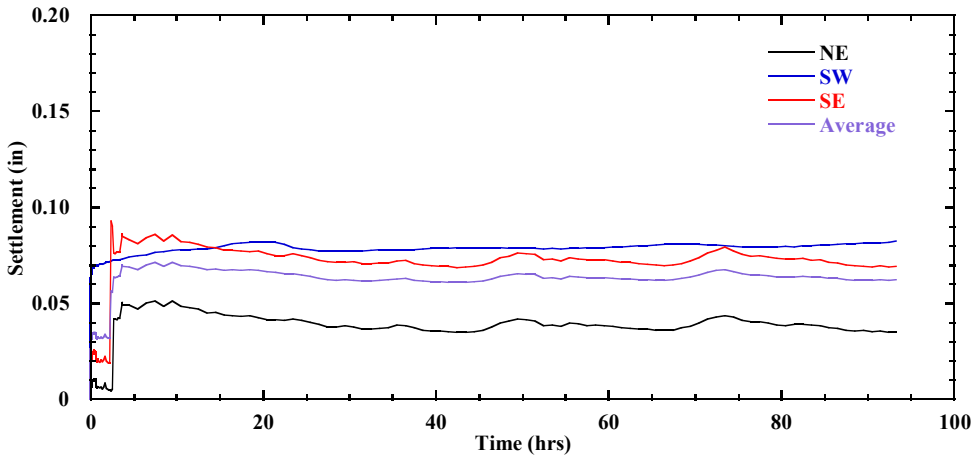

Figure 5.7 Time histories of bridge seat settlements for Stage 3 in Test 6.

5.4.1.2 Dynamic Loading

Time histories of incremental bridge seat corner settlement for the four string potentiometers during application of the earthquake motions are shown in Figure 5.8, and the average incremental bridge seat settlements are shown in Figure 5.9 and Table 5.5. For the Northridge motion, at t = 4.13 s, the south side of the bridge seat (SW and SE) had a dynamic settlement of 0.26 inches, whereas the north side (NW and NE) had a negative settlement (i.e., uplift) of 0.16 inches, which indicated rocking of the bridge seat in the N-S direction (i.e., the direction of shaking). The residual settlement on the south side (SW and SE) is larger than the north side (NW and NE), which indicated that the bridge seat tilted further toward the south after shaking. As shown in Figure 5.9(c) for the Northridge motion, the average maximum dynamic settlement is 0.24 inches and the average minimum dynamic value is -0.08 inches. The uplift is likely due to the differences in the inertial movements of the bridge beam and the MSE bridge abutment. The average residual settlement of the bridge seat is 0.19 inches, which corresponds to a vertical strain of 0.22% for the 7ft-high lower MSE wall.

Table 5.5 Average incremental bridge seat settlements (in.) for earthquake motions in Test 6 (model-scale).

Earthquake motion	Maximum dynamic settlement	Minimum dynamic settlement	Residual settlement
Imperial Valley	0.13	0	0.10
Maule	0.37	0	0.19
Northridge	0.24	-0.08	0.19

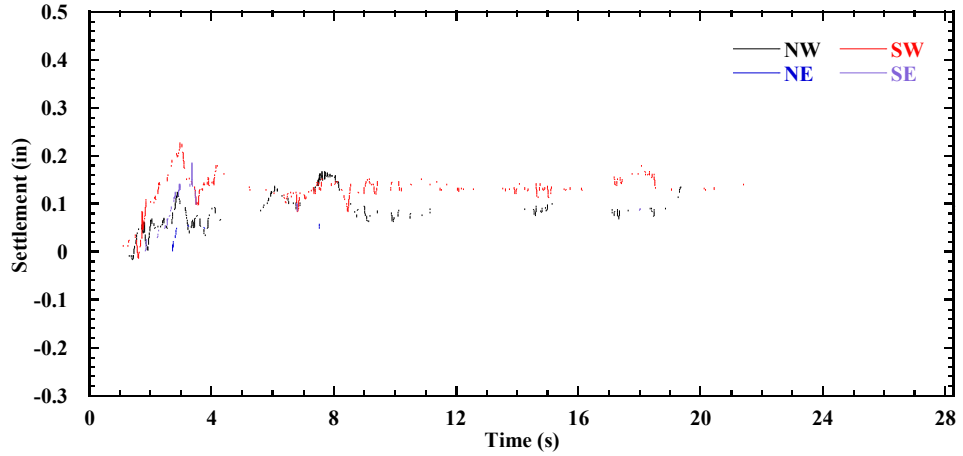

(a)

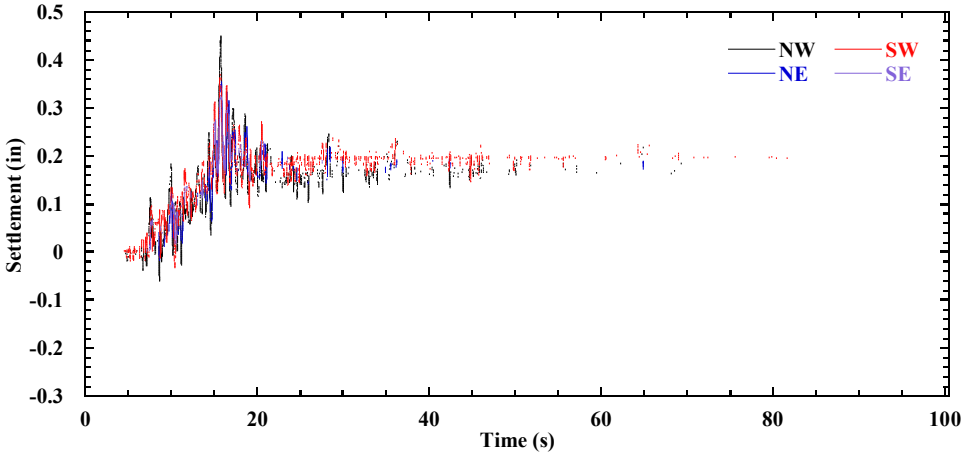

(b)

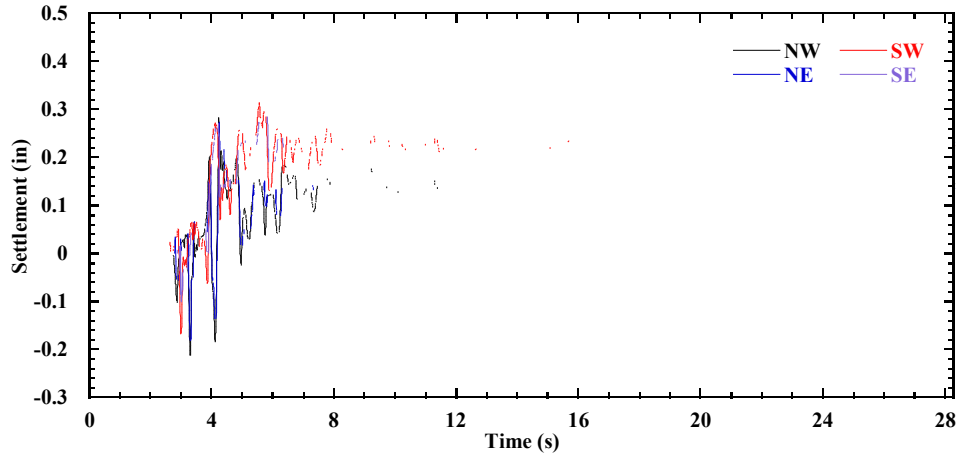

(c)

Figure 5.8 Time histories of incremental bridge seat corner settlement in Test 6: (a) Imperial Valley motion; (b) Maule motion; (c) Northridge motion.

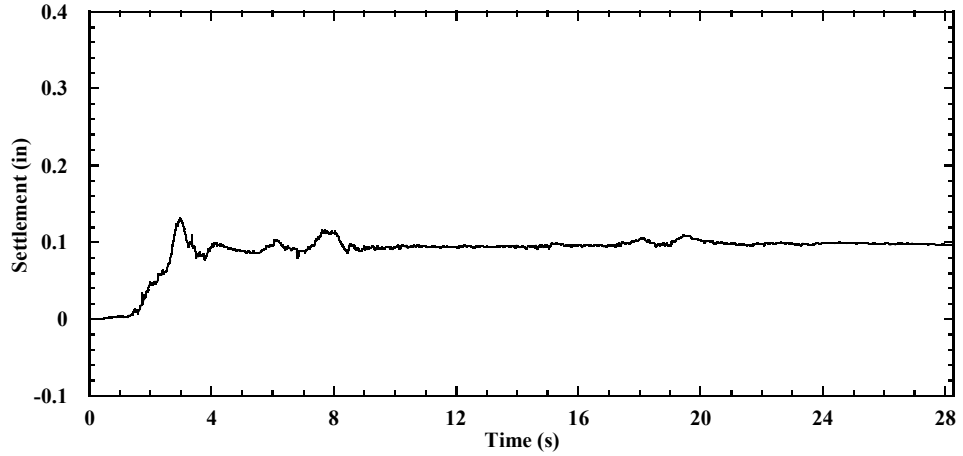

(a)

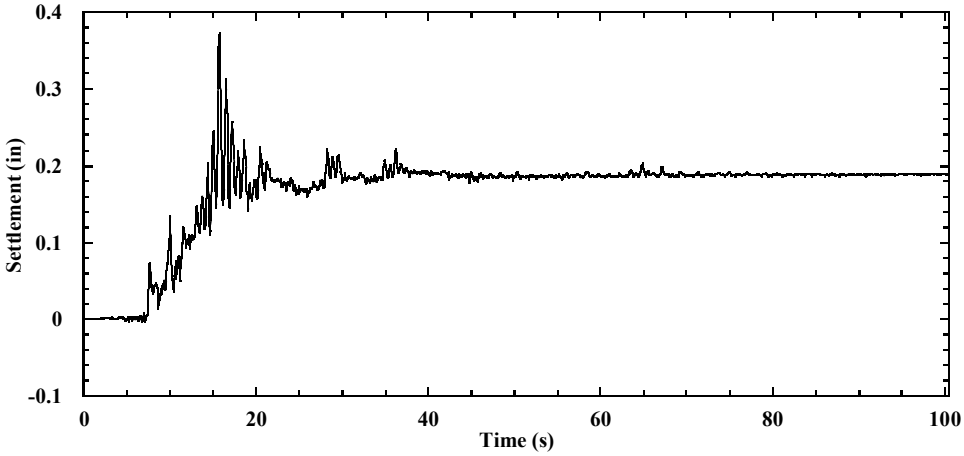

(b)

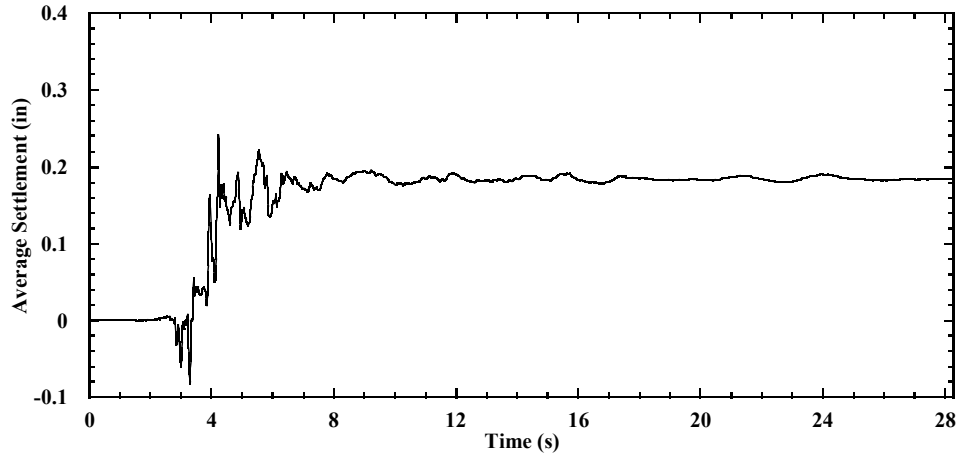

(c)

Figure 5.9 Time histories of average incremental bridge seat settlement in Test 6: (a) Imperial Valley motion; (b) Maule motion; (c) Northridge motion.

A comparison of time histories of the average incremental bridge seat settlement for earthquake motions in Tests 1 and 6 is shown in Figure 5.10, and the average incremental residual bridge seat settlements are presented in Table 5.6. The actual displacement time histories of shaking table in both tests were similar despite the difference in payloads.

For the Imperial Valley motion, the maximum dynamic settlements are similar for both tests, but the residual bridge seat settlement of 0.10 inches for Test 6 is larger than the value of 0.06 inches for Test 1. For the Maule motion, the maximum dynamic settlement and residual settlement for Test 6 are 0.37 and 0.19 inches, respectively, which are larger than the corresponding values of 0.28 and 0.06 inches for Test 1. For the Northridge motion, the maximum dynamic settlement for Test 6 is 0.24 inches, which is smaller than the value of 0.28 inches observed in Test 1. However, the residual bridge seat settlement of 0.19 inches for Test 6 is greater than the value of 0.09 inches for Test 1. In general, the average residual bridge seat settlement for Test 6 are much larger than Test 1. The larger settlement for shaking in the transverse direction is likely due to the lack of soil confinement on the two sides of the bridge seat in the transverse direction, while the backwall of the bridge seat was confined by the backfill soil for the upper wall in the longitudinal direction.

Table 5.6 Average incremental residual bridge seat settlements (in.) for earthquake motions in Tests 1 and 6 (model-scale).

Earthquake motion	Test 1 (Longitudinal shaking)	Test 6 (Transverse shaking)
Imperial Valley	0.06	0.10
Maule	0.06	0.19
Northridge	0.09	0.19

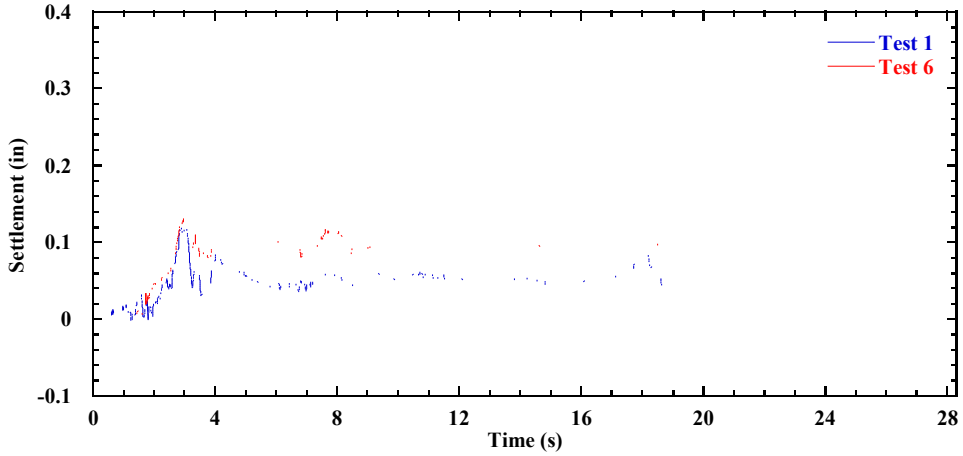

(a)

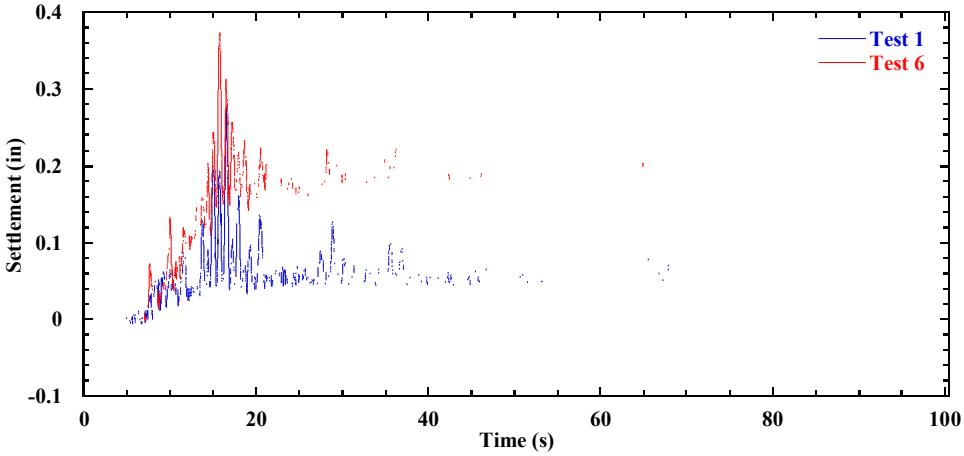

(b)

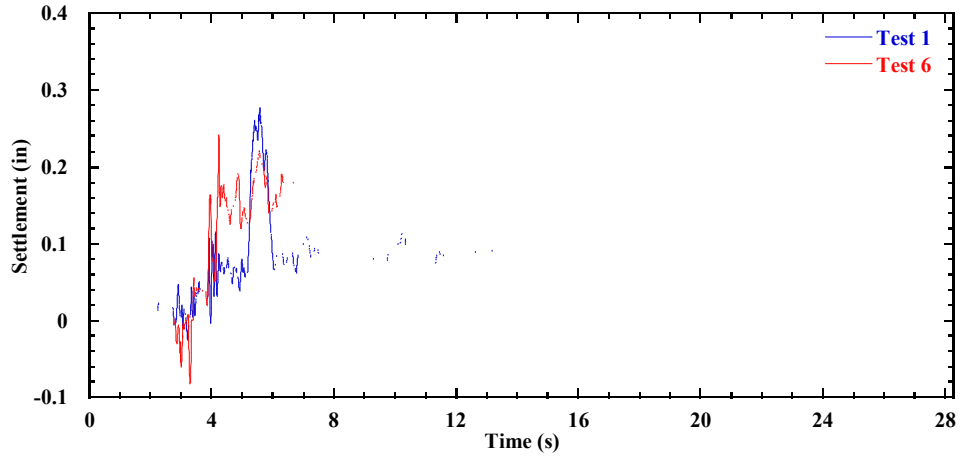

(c)

Figure 5.10 Time histories of average incremental bridge seat settlement in Tests 1 and 6: (a) Imperial Valley motion; (b) Maule motion; (c) Northridge motion.

5.4.2 Bridge Seat and Bridge Beam Horizontal Displacements

Horizontal displacements in the transverse direction for the bridge seat and bridge beam were measured at the locations shown in Figure 3.21, and time histories of incremental horizontal displacement for the earthquake motions are shown in Figure 5.11. The residual horizontal displacement for bridge seat is essentially zero for the Imperial Valley and Maule motion, but shows a permanent displacement of 0.67 inches toward the south side after the Northridge motion. The bridge beam experienced larger horizontal displacements than the bridge seat during shaking, which indicated sliding of the bridge beam with respect to the bridge seat. The horizontal displacements for the bridge seat and bridge beam are highly dependent on the characteristics of the earthquake motions.

Time histories of incremental horizontal displacement for bridge seat relative to the top of MSE bridge abutment (i.e., measurements taken at the facing block z = 6.25 ft for T1-North) and bridge beam relative to the bridge seat are shown in Figure 5.12. For the Imperial Valley motion, the bridge seat had relatively small magnitudes of horizontal displacement on the MSE bridge abutment, and the bridge beam had a residual relative horizontal displacement of 0.13 inches with respect to the bridge seat toward the north side. For the Maule motion, the bridge beam experienced a sudden sliding on the bridge seat with a horizontal displacement of approximately 0.8 inches at t = 10 s and had a permanent sliding distance of 0.63 inches toward the north side after shaking. For the Northridge motion, both the bridge seat and bridge beam experienced significant sliding toward the south side at t = 4 s and had residual relative horizontal displacements of 0.51 and 0.42 inches, respectively. The width of expansion joint is also associated with the relative horizontal displacement of the bridge beam with respect to the bridge seat and will be discussed later.

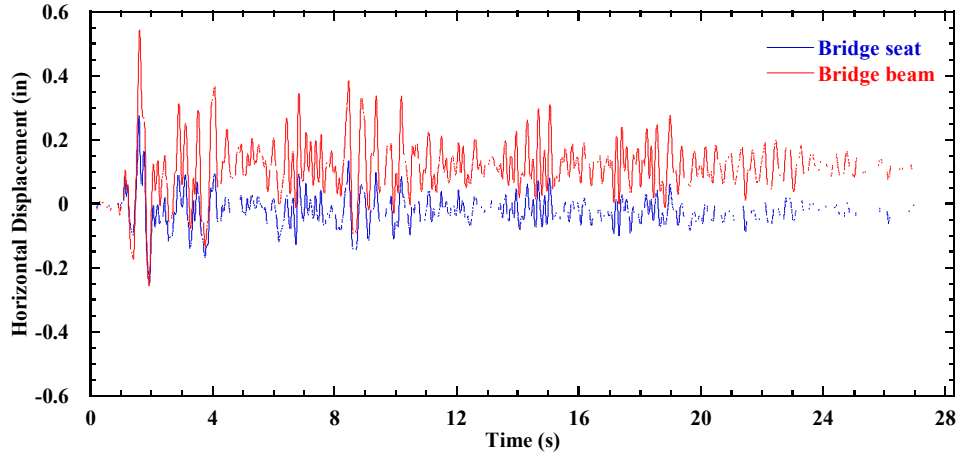

(a)

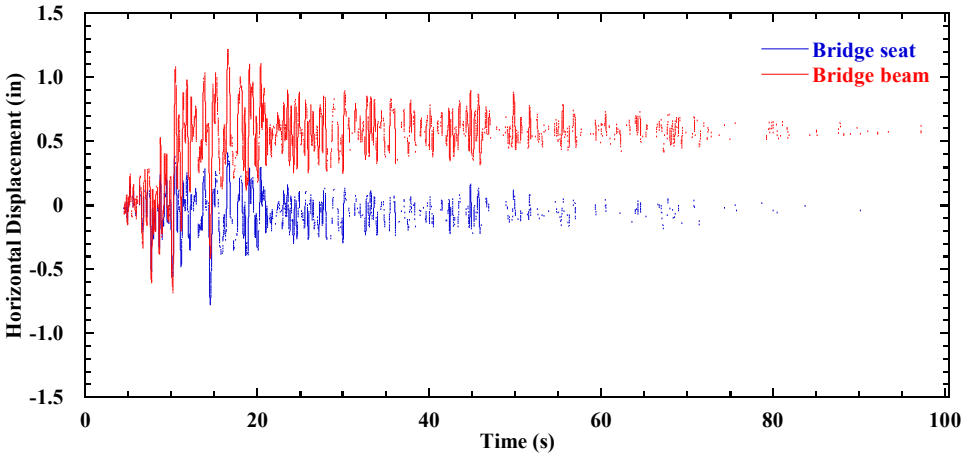

(b)

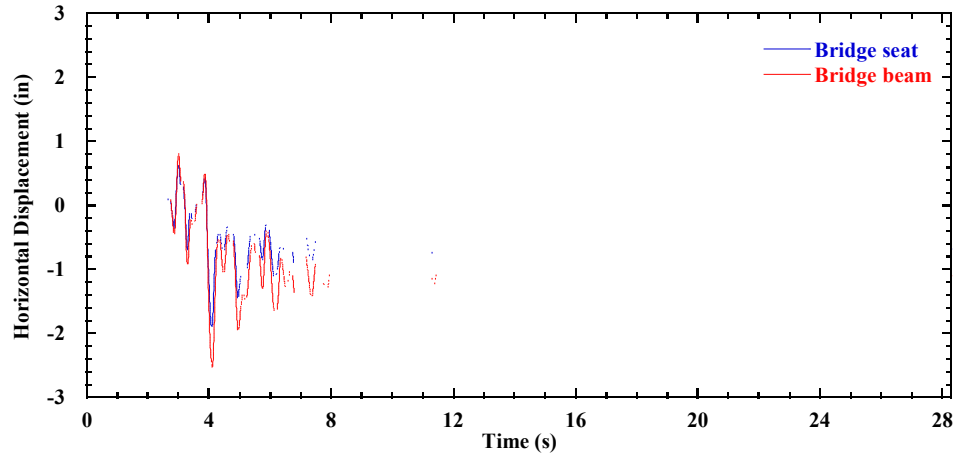

(c)

Figure 5.11 Time histories of incremental horizontal displacement for bridge seat and bridge beam in Test 6: (a) Imperial Valley motion; (b) Maule motion; (c) Northridge motion.

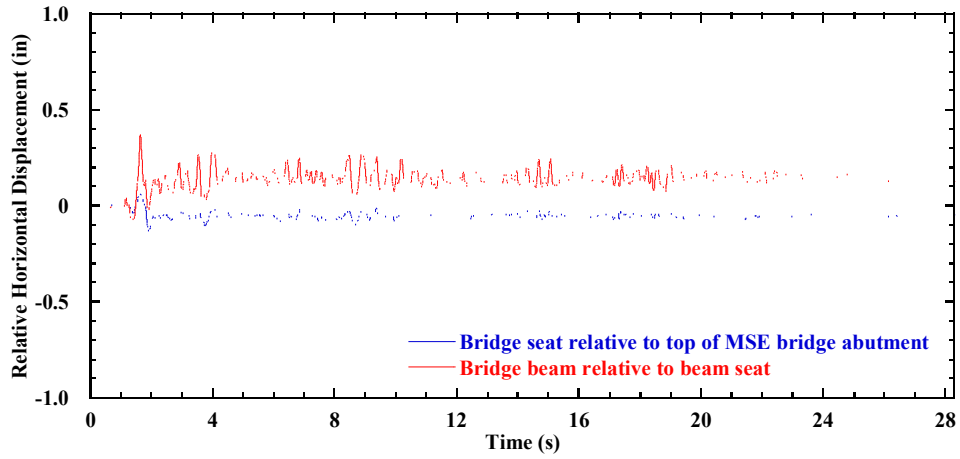

(a)

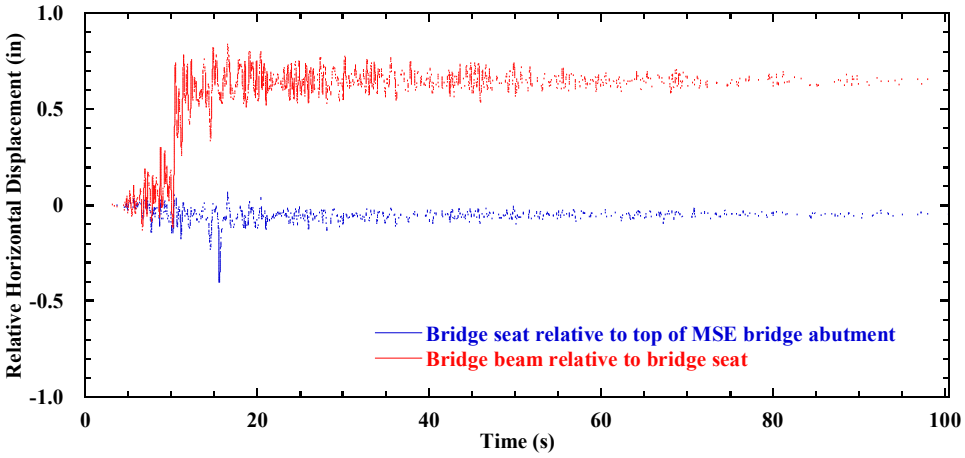

(b)

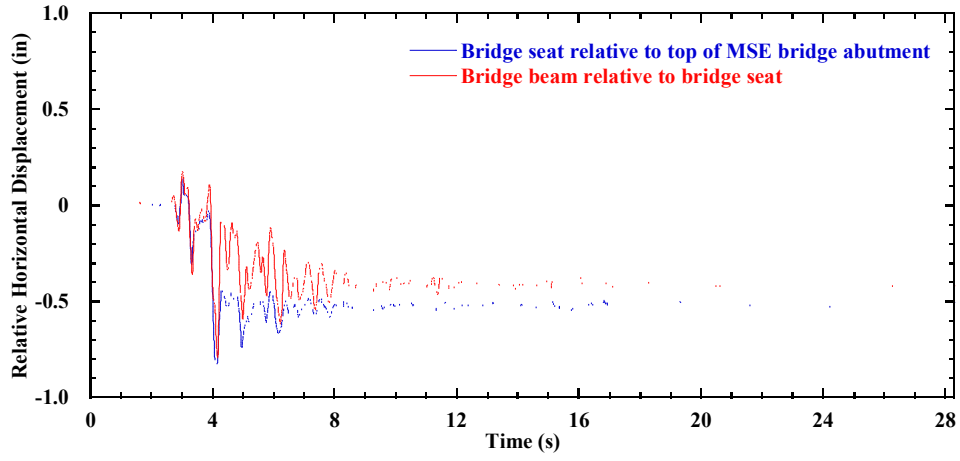

(c)

Figure 5.12 Time histories of incremental relative horizontal displacement for bridge seat and bridge beam in Test 6: (a) Imperial Valley motion; (b) Maule motion; (c) Northridge motion.

5.5 Accelerations

5.5.1 Bridge Seat and Bridge Beam

Time histories of horizontal accelerations for bridge seat and bridge beam are shown in Figure 5.13. For instance, the bridge seat had a peak acceleration of 1.02*g* for the Northridge motion, and the bridge beam had a peak acceleration of 1.82*g*, which is much larger than the peak value of the shaking table (0.86*g*).

The root-mean-square (RMS) method can be used to mitigate effects of high frequency noise and also characterize amplitude and frequency content in a measured response (Kramer 1996; El-Emam and Bathurst 2005). The calculated ratios for the bridge seat and bridge beam RMS accelerations normalized by the shaking table RMS acceleration are presented in Table 5.7. For the Imperial Valley motion, the bridge beam has an acceleration amplification ratio of 1.79, and is greater than the ratio of 1.39 for the bridge seat. For the Maule motion, the ratios decrease to 1.55 and 1.27 for the bridge beam and bridge seat, respectively, and further decrease to 1.34 and 1.11 for the Northridge motion. In general, the RMS acceleration ratios for the bridge beam are larger than the bridge seat. RMS acceleration ratios for the bridge seat and bridge beam in Test 1 are also shown in Table 5.7, and indicate that the acceleration amplification ratios are larger for shaking in the longitudinal direction than in the transverse direction for the same earthquake motions.

Table 5.7 RMS acceleration ratios of bridge beam and bridge seat for earthquake motions in Tests 1 and 6 (model-scale).

Earthquake motion	Test 1		Test 6	
	Bridge seat	Bridge beam	Bridge seat	Bridge beam
Imperial Valley	1.60	1.80	1.39	1.79
Maule	1.38	1.73	1.27	1.55
Northridge	1.45	1.58	1.11	1.34

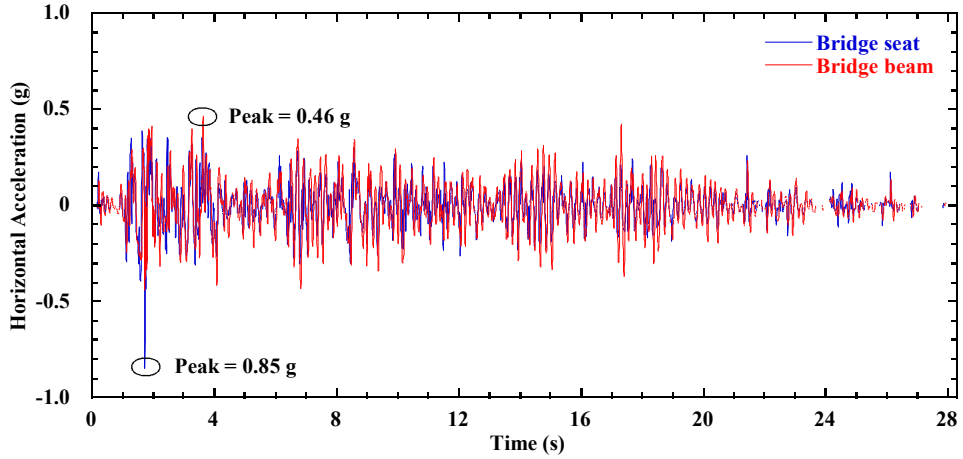

(a)

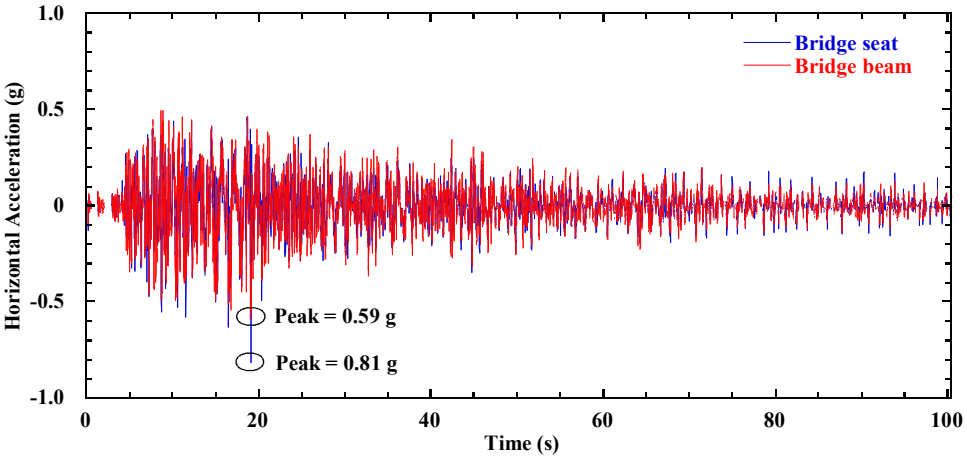

(b)

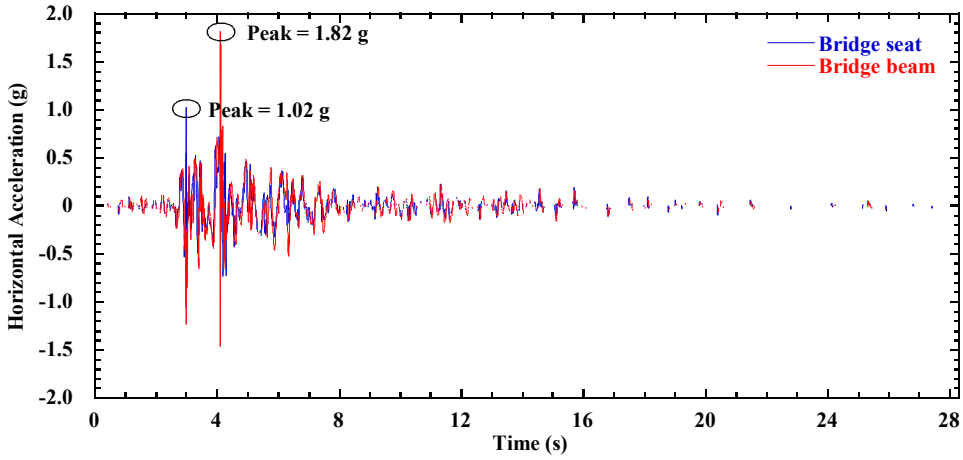

(c)

Figure 5.13 Time histories of horizontal acceleration for bridge seat and bridge beam in Test 6: (a) Imperial Valley motion; (b) Maule motion; (c) Northridge motion.

5.5.2 MSE Wall

The RMS acceleration ratio profiles of wall facing and reinforced soil zone for T1-South and T1-North are shown in Figure 5.14. For the Imperial Valley motion, profiles for T1-South and T1-North in the reinforced soil zone show nonlinear increase of acceleration ratio with elevation. For instance, the acceleration ratio for T1-North increases from 0.97 at z = 0.25 ft to 1.16 at z = 4.75 ft, and then increases significantly to 1.32 at z = 6.25 ft. Similar profiles also are observed for the Maule motion, and this indicates that accelerations amplify more toward the top. The acceleration ratios are the largest for the Imperial Valley motion, with a maximum ratio of 1.32 at the top for T1-North in the reinforced soil zone, and the maximum ratio at the same location is 1.19 for the Maule motion. However, the acceleration ratios are generally close to 1.0 for the Northridge motion, which indicates essentially no amplification with elevation. The deceasing amplification behavior as shaking proceeded may be due to the softening of the soil (i.e., shear modulus reduction) under successive earthquake motions. However, further investigations are needed to confirm this using numerical simulations. In general, acceleration ratio profiles of wall facing and reinforced soil zone are similar for T1-South and T1-North. The ratios for the wall facing are slightly larger than for the reinforced soil zone probably due to lower confinement.

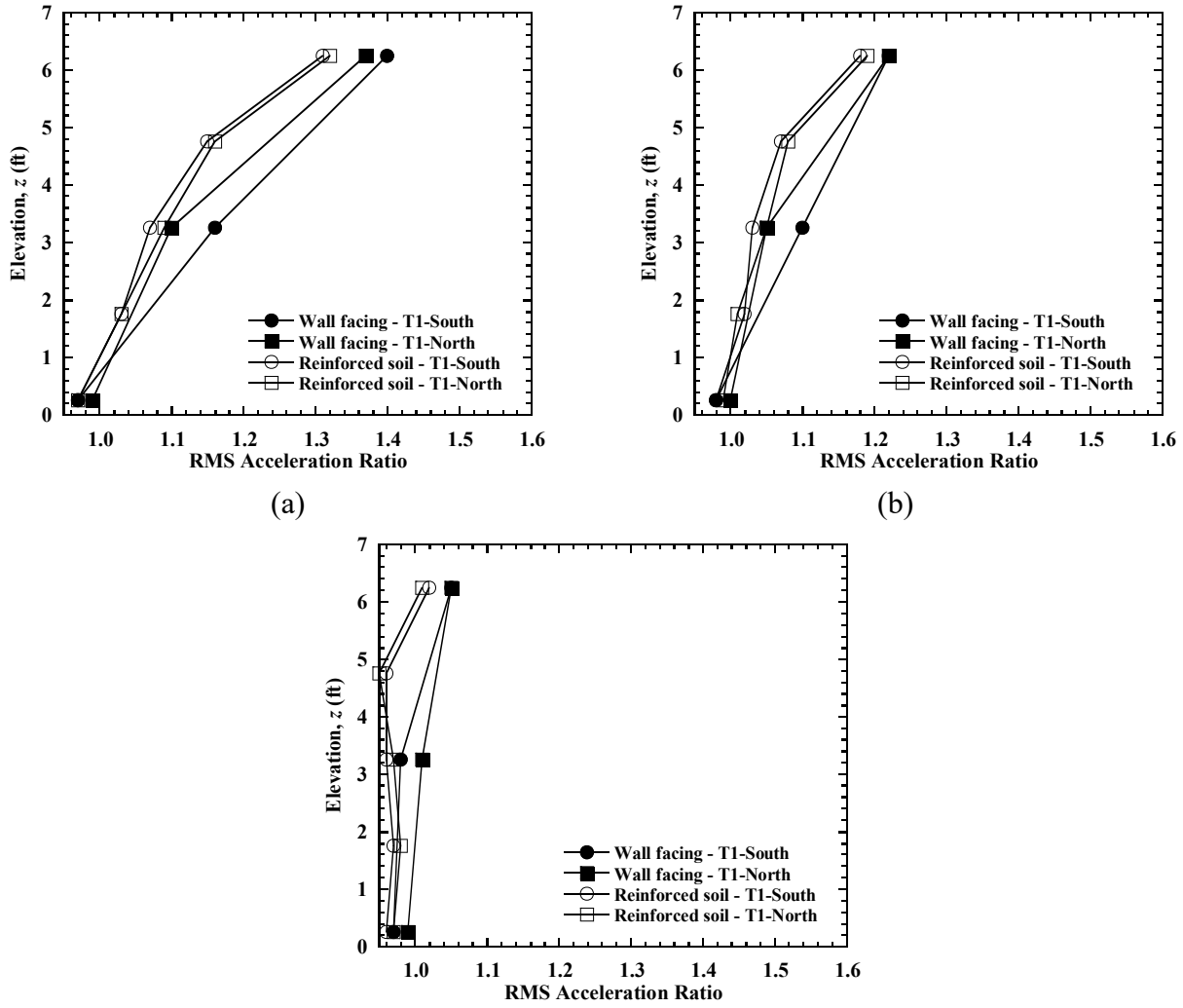

Figure 5.14 RMS acceleration ratio profiles for T1-South and T1-North in Test 6: (a) Imperial Valley motion; (b) Maule motion; (c) Northridge motion.

The RMS acceleration ratio profiles for the transverse sections T1 and T2 are shown in Figure 5.15. Transverse section T1 is under the bridge seat, while transverse section T2 is behind the bridge seat (and thus has lower vertical stresses in the backfill soil). The RMS acceleration ratio profiles for T2 also show nonlinear increase with elevation, and the acceleration ratios for the upper wall (z = 7.75 ft) confirm that soil accelerations amplify more toward the top. In general, transverse section T2 has slightly larger acceleration ratios than transverse section T1 at z = 6.25 ft for all three earthquake motions.

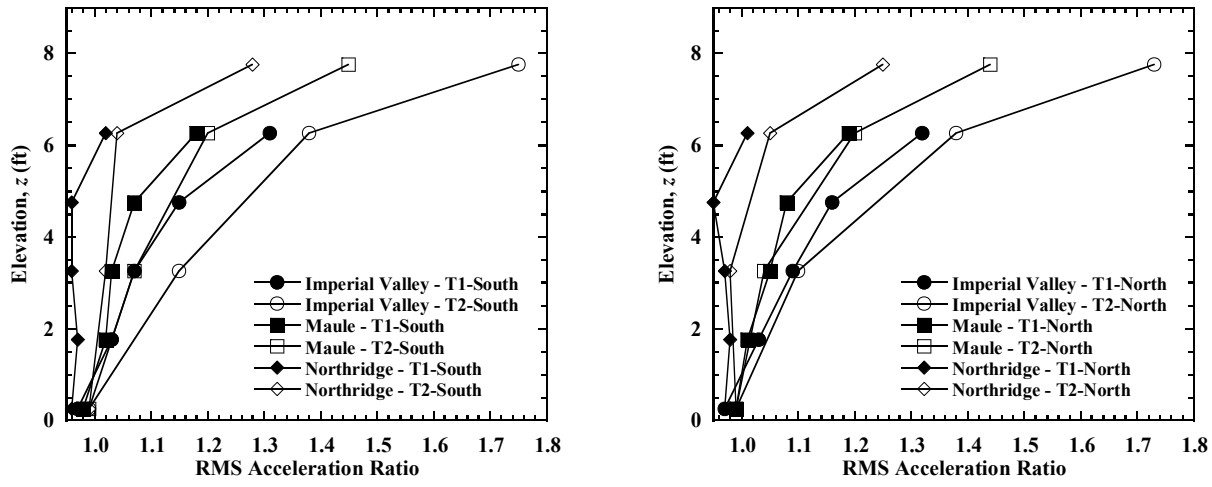

(a) (b)

Figure 5.15 RMS acceleration ratio profiles for T1 and T2 in Test 6: (a) T1-South; (b) T1-North.

5.6 Vertical and Lateral Stresses in the Backfill Soil

5.6.1 Vertical Stresses in the Backfill Soil

Profiles for the initial (before shaking), maximum dynamic (during shaking), and residual (after shaking) vertical stresses for earthquake motions are shown in Figure 5.16. For the Imperial Valley motion, the maximum vertical stress is 11.0 psi at the mid-height of the wall for T1-South and is 10.8 psi at the top of the wall for T1-North. After shaking, the residual vertical stresses are larger than the initial values, which might be attributed to the change of arching chains in the backfill soil due to shaking. The maximum dynamic vertical stress at the mid-height of the wall for T1-South is 14.7 psi during the Maule motion and is 19.0 psi during the Northridge motion. For the Northridge motion, the residual vertical stress profiles are similar to the initial profiles, which indicates that the arching chains may have be eliminated due to shaking.

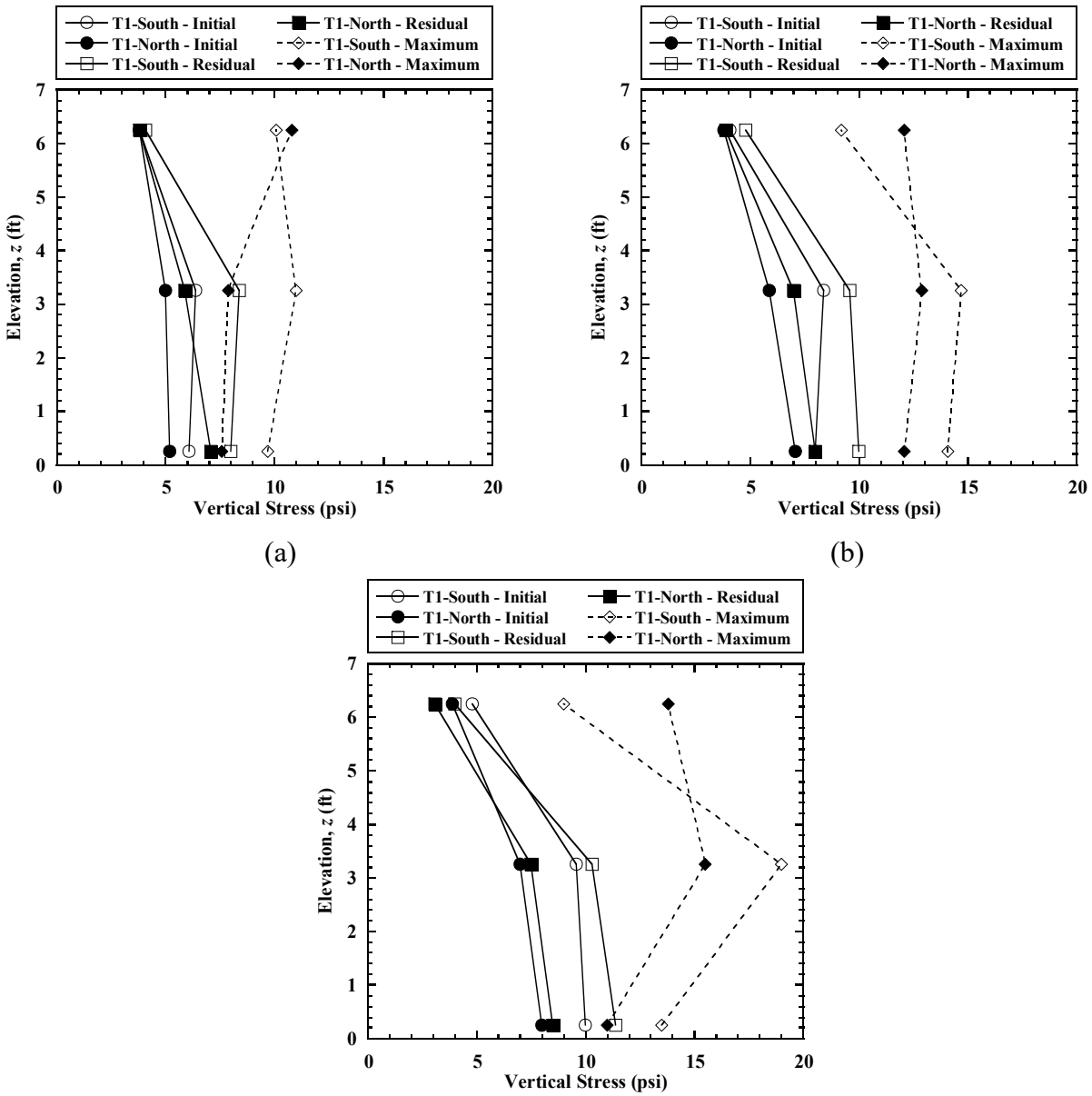

Figure 5.16 Vertical stress profiles in Test 6: (a) Imperial Valley motion; (b) Maule motion; (c) Northridge motion.

5.6.2 Lateral Stresses in the Backfill Soil

Lateral stress profiles behind the wall facing for earthquake motions are shown in Figure 5.17. For the Imperial Valley motion, the maximum lateral stresses are 1.1 psi and 1.3 psi for T1-South and T1-North, respectively, and both occurred at the top of the wall. Similar to the vertical stress profiles, residual lateral stresses are generally larger than initial stresses. The maximum lateral stress for T1-South is 1.5 psi at the bottom of the wall for the Maule motion and is 2.6 psi for the Northridge motion at the same location. On the other hand, the maximum values for T1-North were observed at the top of the wall and are 1.5 psi and 2.0 psi for the two motions, respectively. As shaking proceeded from the Imperial Valley to the Maule to the Northridge motion, the differences between the initial and residual lateral stress profiles became smaller, and are consistent with the observations for vertical stress profiles shown in Figure 5.16.

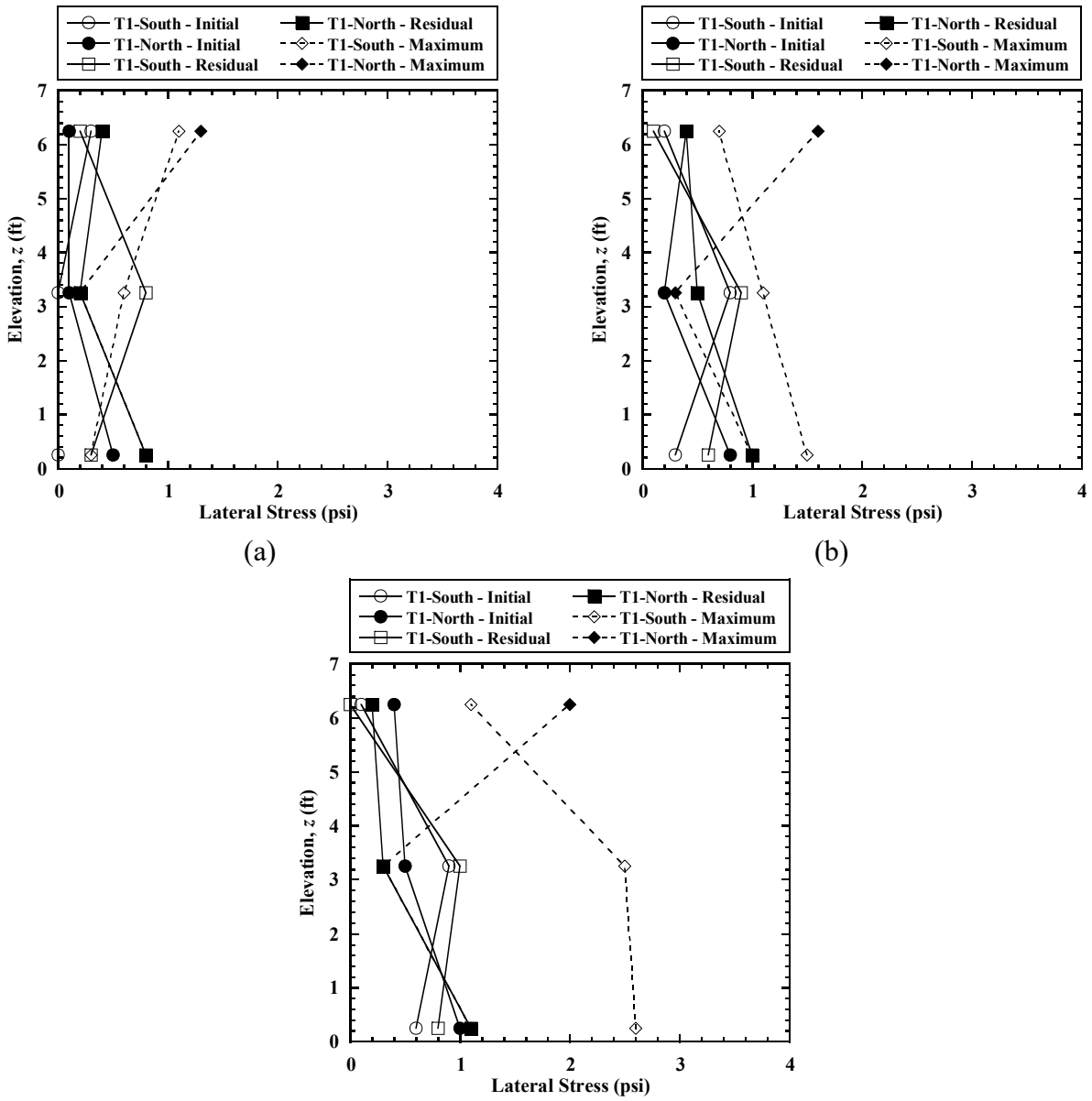

Figure 5.17 Lateral stress profiles in Test 6: (a) Imperial Valley motion; (b) Maule motion; (c) Northridge motion.

5.7 Reinforcement Strains

5.7.1 Static Loading

Reinforcement strain distributions for the geogrid layers on the south and north sides of transverse section T1 (T1-South and T1-North) for construction stages are shown in Figure 5.18. Each measurement represents the average value from a pair of top and bottom gauges, and zero strain at the free end of each reinforcement layer is also plotted.

For Stage 1, reinforcement strain distributions for T1-South and T1-North are similar, and show maximum strains at 0.3 ft from each facing (near the connection) for layers 1 and 4, and at 1.1 ft from each facing for layers 7 and 10. For Stage 2, reinforcement strains for layer 13 increased due to placement of bridge seat, but had little increases for the lower layers. For Stage 3, reinforcement strains increased significantly due to placement of the bridge beam, especially for the upper layers. Reinforcement strain distributions for T1-South and T1-North show similar magnitudes of strain for layers 1, 4, and 7, but significantly different magnitudes of strain for layers 10 and 13. The reinforcement strains of layers 10 and 13 under the bridge seat for T1-South are much larger than for T1-North. This is attributed to the tilting of the bridge seat toward the south side for Stage 3 as shown in Figure 5.7. The reinforcement strain at y_s = 1.1 ft of layer 13 for T1-South reached 0.13%, which is more than twice greater than the strain value (0.06%) at y_n = 1.1 ft for T1-North. In general, at the end of construction, the maximum strain occurred near the connections for layers 1 and 4, and at 1.1 ft from each side wall facing for layers 7, 10, and 13.

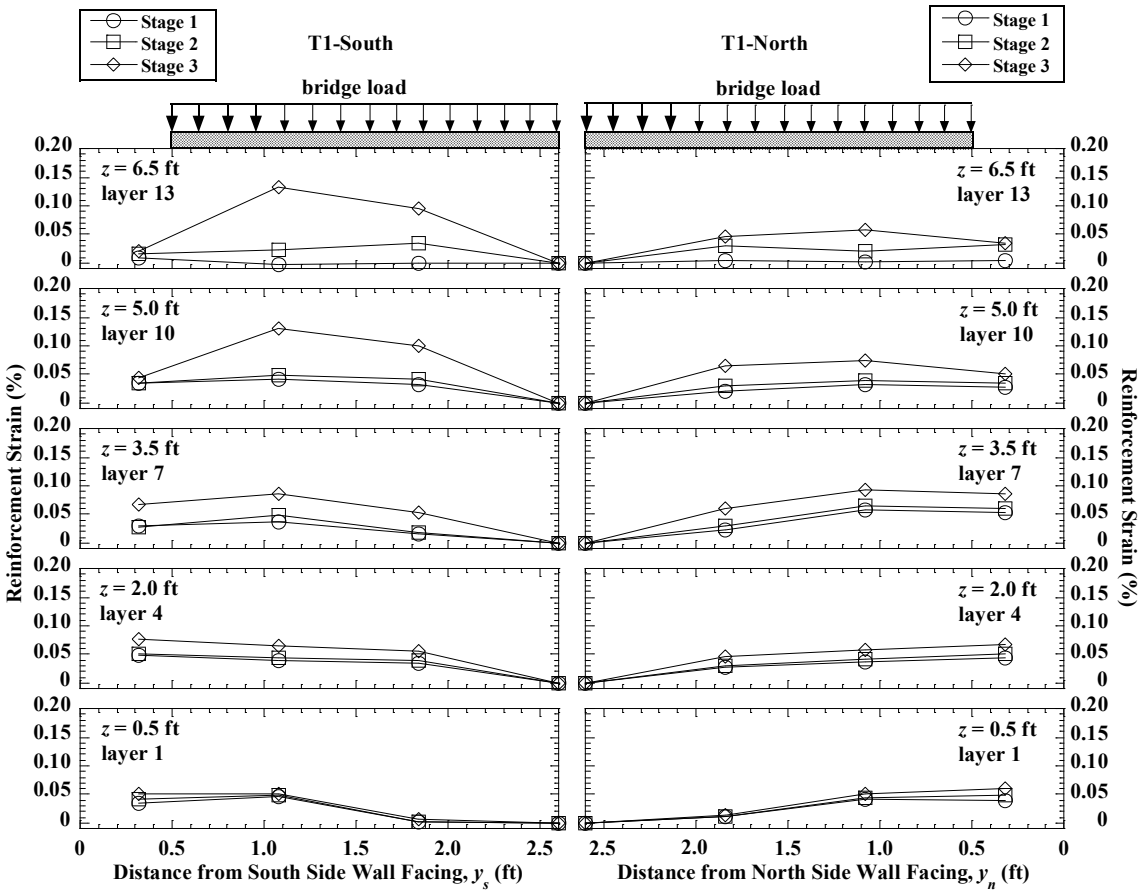

Figure 5.18 Reinforcement strain distributions of T1-South and T1-North for construction stages in Test 6.

5.7.2 Dynamic Loading

Reinforcement strain distributions of T1-South and T1-North with the initial (before shaking), maximum (during shaking), minimum (during shaking), and residual (after shaking) values during the Imperial Valley, Maule, and Northridge motions are shown in Figure 5.19, Figure 5.20, and Figure 5.21, respectively. The reinforcement strains near the connections experienced significant increases during shaking. For instance, during the Northridge motion, the maximum strain near the connection of layer 7 for T1-South reached 0.51%, which corresponds to a dynamic strain increment of 0.47% as compared to the initial value (0.04%). However, the residual reinforcement strains near the connections for all layers are almost the same as initial values, which indicates that the dynamic reinforcement strains were recovered after shaking. Results in Figure 5.21 indicate that reinforcement strains near the connections for the transverse sections could have significant dynamic increment during shaking. Therefore, analysis of reinforcement connection strengths for transverse section is important for seismic design.

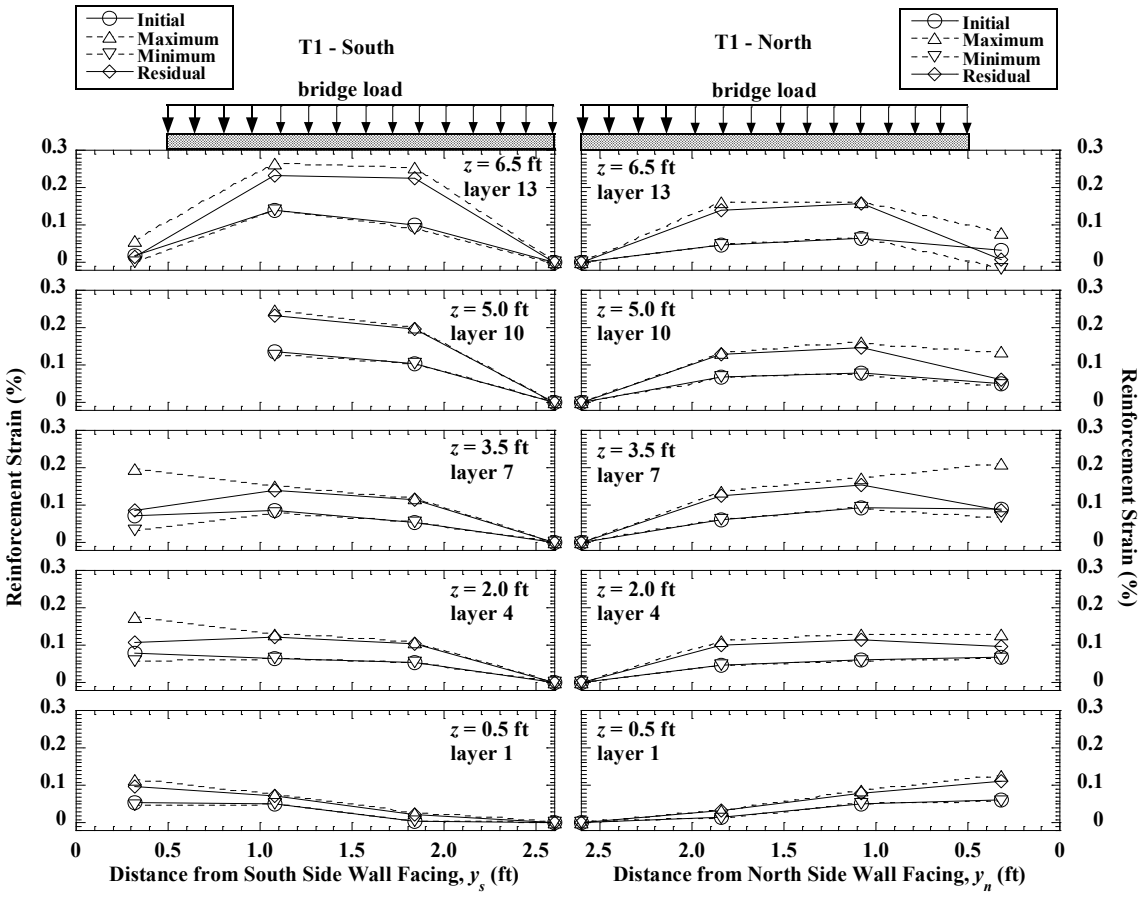

Figure 5.19 Reinforcement strain distributions for T1-South and T1-North during the Imperial Valley motion in Test 6.

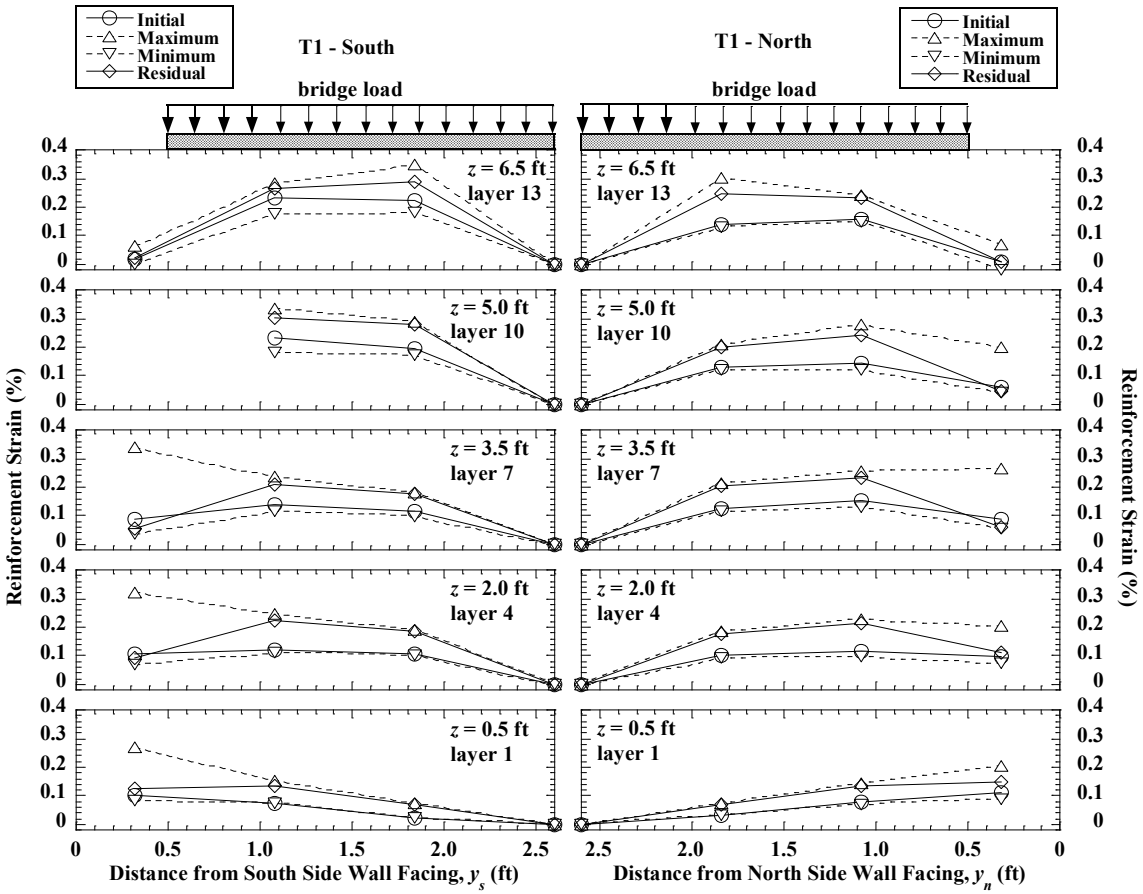

Figure 5.20 Reinforcement strain distributions for T1-South and T1-North during the Maule motion in Test 6.

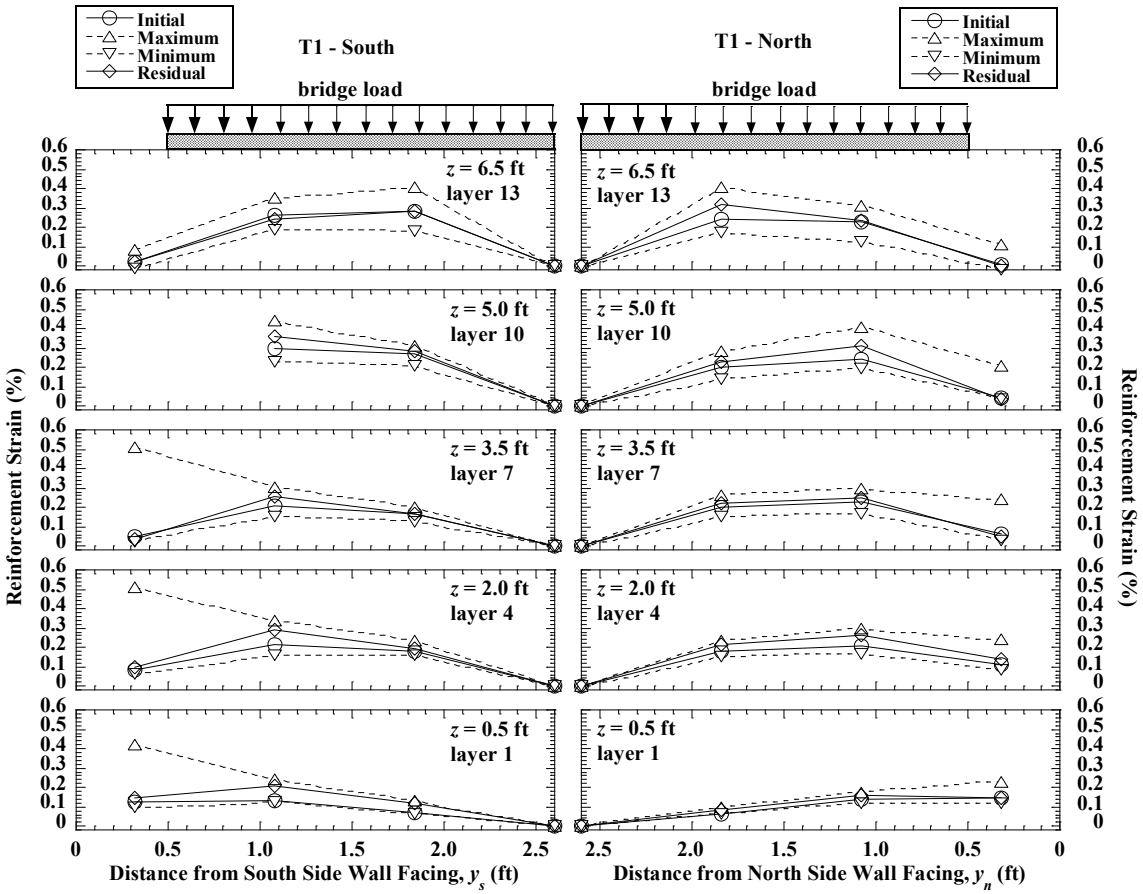

Figure 5.21 Reinforcement strain distributions for T1-South and T1-North during the Northridge motion in Test 6.

The reinforcement strain distributions for the longitudinal section L1 during the Imperial Valley, Maule, and Northridge motions are shown in Figure 5.22, Figure 5.23, and Figure 5.24, respectively. In general, reinforcement strains for the bottom layer experienced little change during shaking, while the mid-height and upper layers had larger dynamic strains. Most of the dynamic strains were not recovered after shaking. Results indicate that shaking in the transverse direction caused increases of strain for the reinforcement layers in the longitudinal direction, which is consistent with the facing displacements for L1 under shaking in the transverse direction.

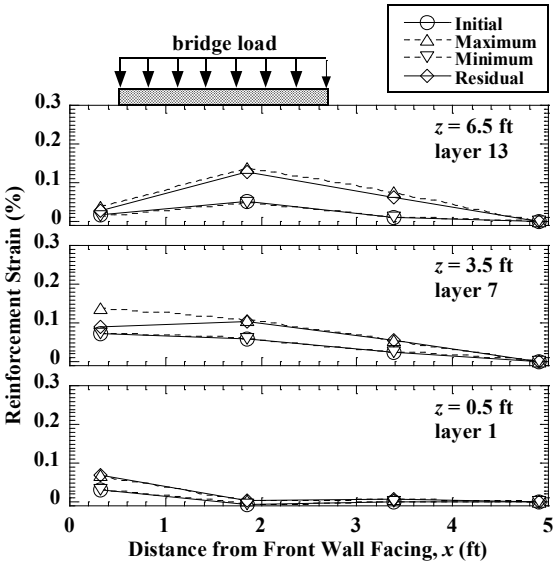

Figure 5.22 Reinforcement strain distributions for L1 during the Imperial Valley motion in Test 6.

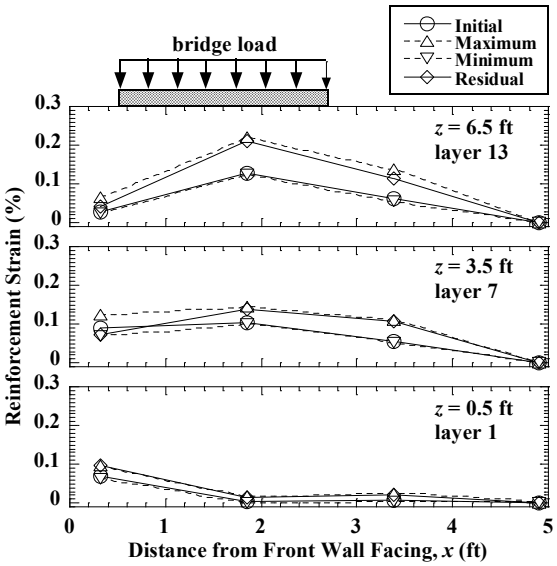

Figure 5.23 Reinforcement strain distributions for L1 during the Maule motion in Test 6.

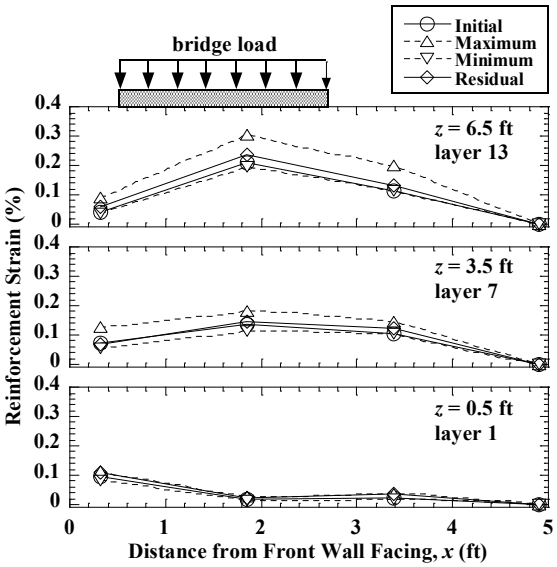

Figure 5.24 Reinforcement strain distributions for L1 during the Northridge motion in Test 6.

Residual reinforcement strain distributions for T1-South and T1-North are shown in Figure 5.25. Reinforcement strains under the bridge seat increased significantly due to successive shaking events. For instance, the reinforcement strain of 0.13% at y_s = 1.1 ft of layer 10 for T1-South at the end of construction (EOC) increased to 0.23% after the Imperial Valley motion, to 0.30% after the Maule motion, and to 0.36% after the Northridge motion. Reinforcement strains near the connections increased only for bottom layers (e.g., layer 1 for T1-South and T1-North), but not for upper layers. In general, the maximum residual strains occurred near the connection for layer 1, and under the bridge seat for other layers after earthquake motions.

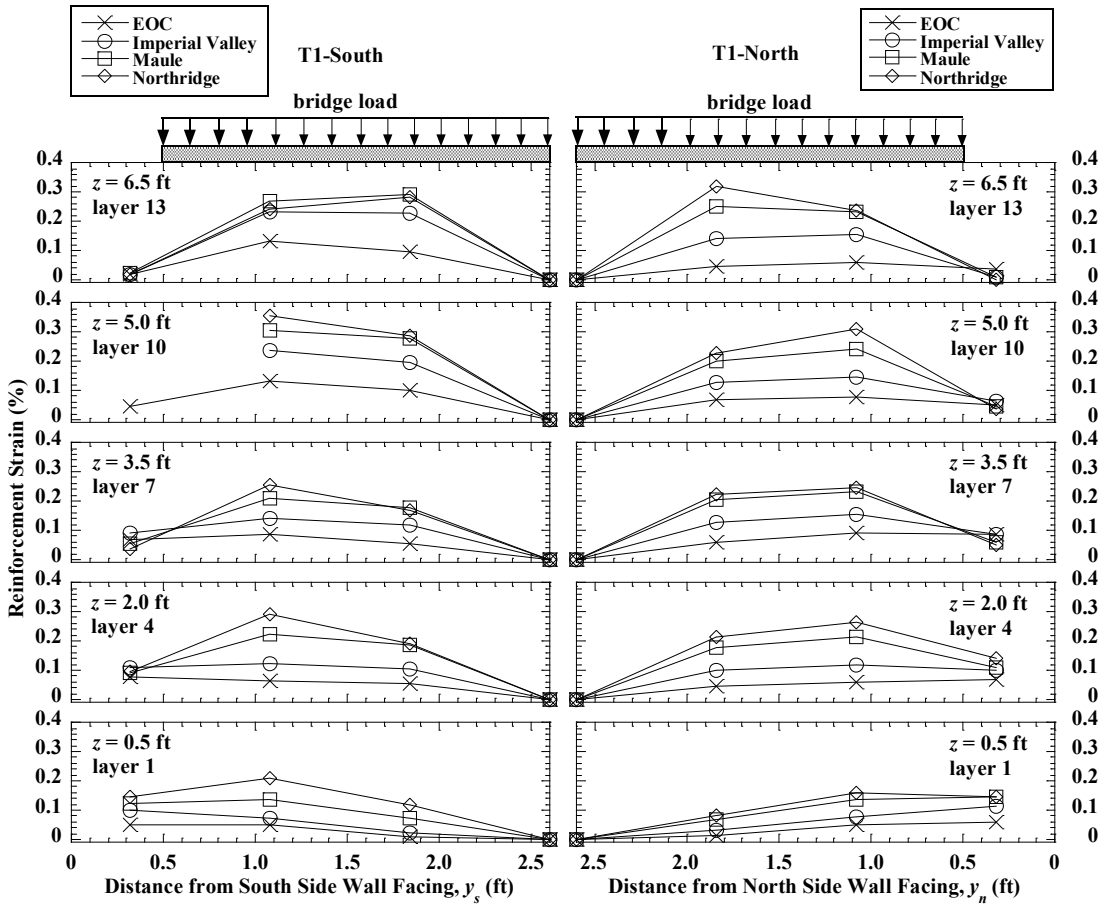

Figure 5.25 Residual reinforcement strain distributions for T1-South and T1-North in Test 6.

Residual reinforcement strain distributions for L1 are shown in Figure 5.26. Maximum strains occurred near the connection for layer 1 and under the bridge seat for layers 7 and 13 at the end of construction. Similar to T1-South and T1-North, reinforcement strains increased significantly near the connections for the bottom layer and under the bridge seat for the mid-height and upper layers after successive shaking events, but the magnitudes are generally smaller than for reinforcement layers at the same elevations for the transverse sections T1-South and T1-North.

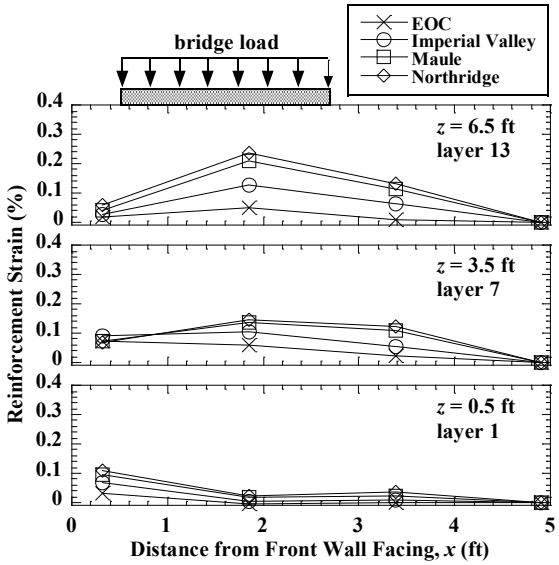

Figure 5.26 Residual reinforcement strain distributions for L1 in Test 6.

5.8 Contact Forces

The bridge beam had relative horizontal displacements with respect to the bridge seat, and thus the width of expansion joint changed during shaking. Horizontal contact forces between the bridge seat and bridge beam generate when the width of expansion joint reduces to zero. Time histories of joint width on the north side for earthquake motions are shown in Figure 5.27. The initial joint width on the north side was 0.95 inches. The total width of the two joints on the south and north sides was 2.0 inches, so the initial joint width on the south side was 1.05 inches. For the Imperial Valley motion, the joint width on the north side reduced to a minimum value of 0.57 inches at t = 1.64 s, and had a residual width of 0.82 inches after shaking. Joint closure was not observed for the Imperial Valley motion. For the Maule motion, the joint closure on the north side reduced to zero first time at t = 14.91 s and generated a horizontal contact force of 1.2 kips, as shown in Figure 5.28, and then the joint closure occurred many times on the same (north) side till t = 50 s. The maximum horizontal contact force was 3.9 kips at t = 16.62 s. The residual joint width was 0.19 inches after the Maule motion. For the Northridge motion, joint closure on the north side occurred only one time at t = 3.02 s and resulted in a horizontal contact force of 3.9 kips, as shown in Figure 5.28. The joint reached the maximum width of 0.98 in at t = 4.17 s. After the Northridge motion, the joint (north side) remained open with a width of 0.59 inches, and the width of the other joint (south side) was 1.37 inches. Although the joint closure during the different earthquake motions is affected by the initial joint width at the start of each motion, and thus may overestimate the effects of joint closure, the initial joint widths can be used in numerical simulations to properly account for these effects.

A comparison of horizontal contact forces for earthquake motions in Tests 1 and 6 is presented in Table 5.8. Joint closure was observed during the Maule motion only for Test 6, but were observed during the Northridge motion for both Tests 1 and 6. During the Northridge motion, the maximum horizontal contact force of 22.1 kips for Test 1 is much larger than the maximum value of 4.0 kips for Test 6, which indicates understandably that shaking in the longitudinal direction resulted in greater horizontal contact forces than shaking in the transverse direction.

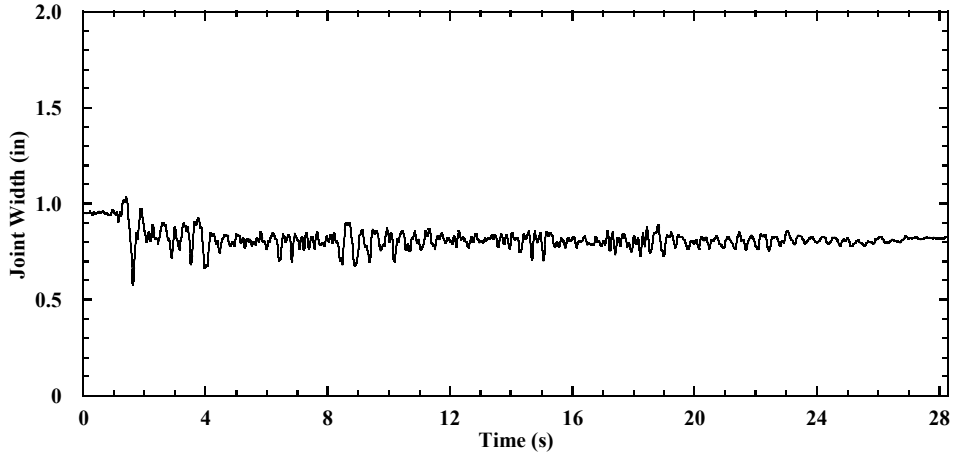

(a)

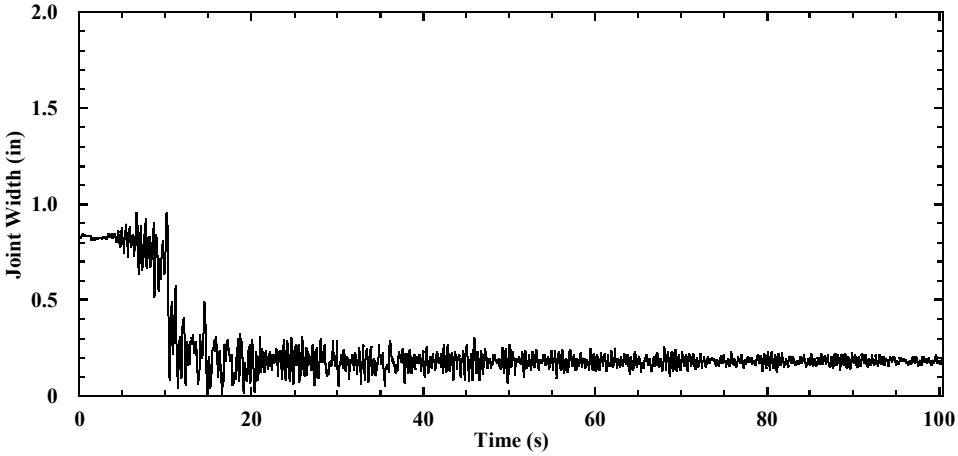

(b)

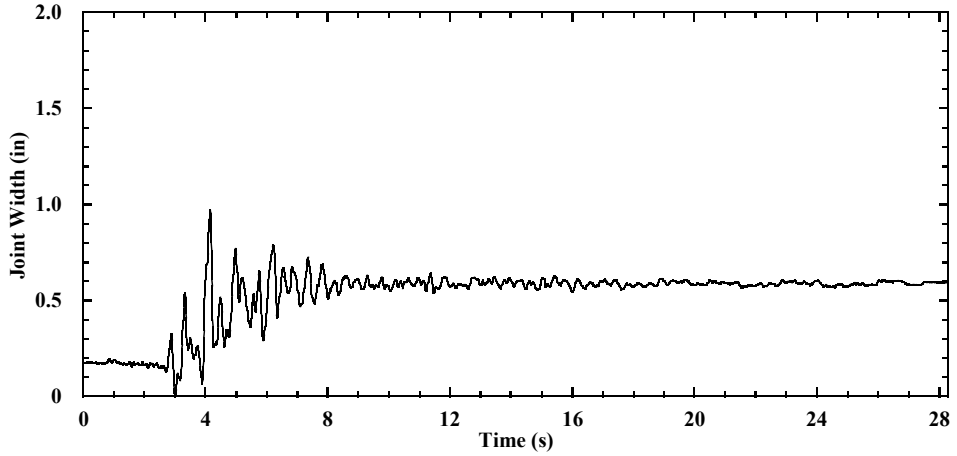

(c)

Figure 5.27 Time histories of joint width on the north side in Test 6: (a) Imperial Valley motion; (b) Maule motion; (c) Northridge motion.

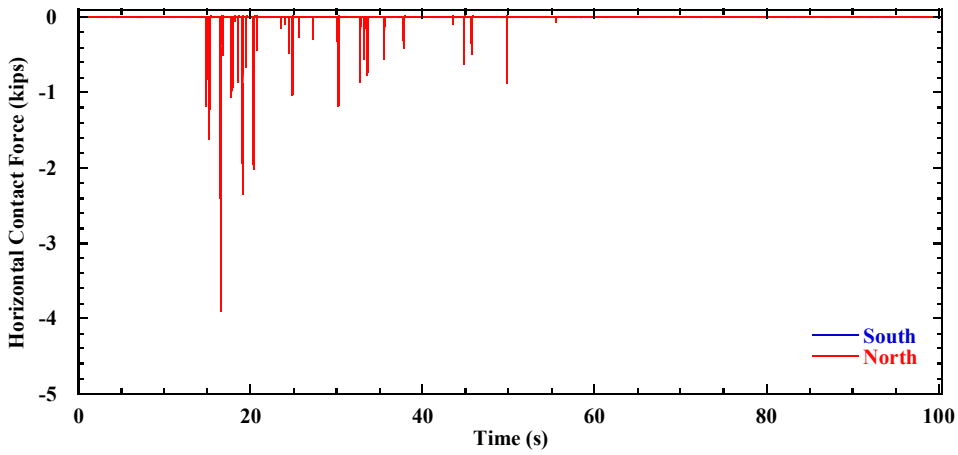

(a)

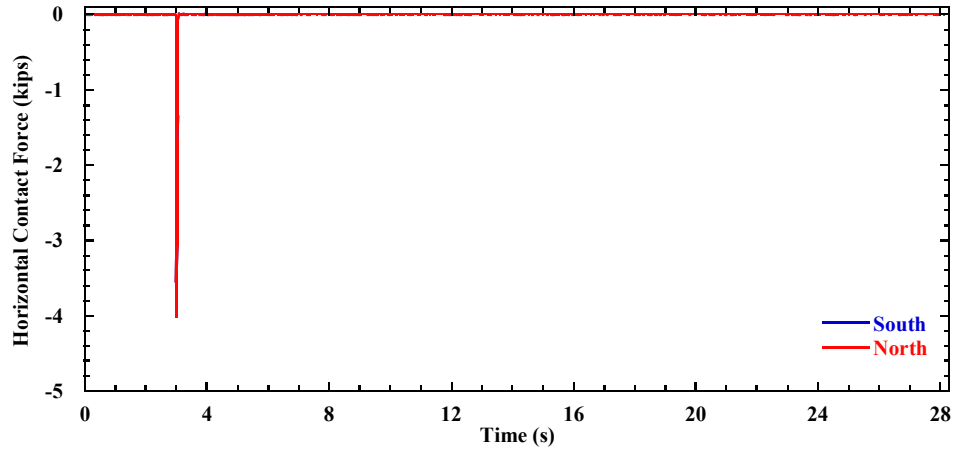

(b)

Figure 5.28 Time histories of horizontal contact forces between the bridge seat and bridge beam in Test 6: (a) Maule motion; (b) Northridge motion.

Table 5.8 Maximum horizontal contact forces (kips) in Tests 1 and 6 (model-scale).

Earthquake motion	Test 1 (Longitudinal shaking)	Test 6 (Transverse shaking)
Imperial Valley	-	-
Maule	-	3.9
Northridge	22.1[1]	4.0

[1] The Northridge earthquake motion was applied after the sinusoidal motion for Test 1.

Chapter 6 Conclusions and Recommendations

6.1 Conclusions

A series of six shaking table tests was conducted on half-scale MSE bridge abutments subjected to shaking in the longitudinal and transverse directions. Experimental design of the scale model followed established similitude relationships for shaking table testing in a 1*g* gravitational field, including scaling for geometry, geosynthetic reinforcement stiffness, backfill soil modulus, bridge surcharge stress, and characteristics of the earthquake motions. The following conclusions were drawn from evaluation of the results:

1. Despite the heavy load associated with the MSE bridge abutment models, the shaking table performed well in displacement-control mode for earthquake motions and the steel connection beams and sliding platform successfully transmitted table motions to the base of the support wall. Although the acceleration time history of the shaking table has larger peak acceleration values than the target input (i.e., overshooting), the pseudo-spectral accelerations of the shaking table and target motion are in good agreement for all three earthquake motions, which indicates that the shaking table adequately reproduced the salient characteristics of the target input motions.
2. Results from the system identification tests indicated changes of fundamental frequencies for the bridge system during successive shaking events. For the baseline case, the MSE bridge abutment had a fundamental frequency of 11.9 Hz before shaking, decreased to 11.3 Hz after the Imperial Valley motion, and then decreased further to 10.9 Hz after the Maule motion. These decreases are attributed to shear modulus reduction of the backfill soil associated with shear strain development during shaking.
3. For the baseline case model subjected to shaking in the longitudinal direction, the incremental maximum dynamic facing displacements during shaking increased almost linearly with elevation. However, the dynamic facing displacements were largely recovered after shaking, especially for the upper section of the wall. The maximum incremental residual facing displacements for the longitudinal centerline section L1 are 0.06, 0.04, and 0.13 inches for the Imperial Valley, Maule, and Northridge motion, respectively.
4. The average incremental residual bridge seat settlements for the baseline case are 0.06 inches for the Imperial Valley and Maule motions, and 0.09 inches for the Northridge motion, which yield incremental vertical strains of 0.07% and 0.10% for the MSE bridge abutment. The magnitudes of residual bridge seat settlements are small and would not be expected to cause significant damages to typical bridge structures.
5. The acceleration amplification ratios, defined as the root-mean-square (RMS) acceleration at a certain location divided by the actual shaking table RMS acceleration, were observed to increase with elevation in the MSE bridge abutment. The acceleration amplification ratios increase slightly from the retained soil zone to reinforced soil zone to wall facing.

The accelerations for the bridge seat and bridge beam were also observed to be amplified above the acceleration of the shaking table, and the bridge beam generally was observed to have larger amplification ratios than the bridge seat. Results indicate that the acceleration amplification ratios are different for the MSE bridge abutment, bridge seat, and bridge beam.

6. Reinforcement strains for the longitudinal section were observed to increase throughout the height of the MSE bridge abutment during shaking. The location of the incremental maximum reinforcement strain was observed to be under the bridge seat in the upper reinforcement layers, but was near the facing block connections in the lower layers.
7. For shaking in the longitudinal direction, reinforcement spacing and stiffness were observed to have significant effects on the seismic performance of MSE bridge abutments. Facing displacements and bridge seat settlements increase significantly with increasing reinforcement spacing and decreasing reinforcement stiffness. The average incremental residual bridge seat settlement of 0.06 inches after the Imperial Valley motion for the baseline case (reinforcement spacing S_v = 6 inches and reinforcement stiffness $J_{5\%}$ = 26 kips/ft) is smaller than the values of 0.22 inches for increased reinforcement spacing (S_v = 12 inches and $J_{5\%}$ = 26 kips/ft) and 0.13 inches for reduced reinforcement stiffness (S_v = 6 inches and $J_{5\%}$ = 13 kips/ft).
8. Greater bridge surcharge stress was observed to have larger facing displacements and bridge seat settlements for static loading conditions. However, the greater bridge surcharge stress led to smaller values of lateral facing displacements and bridge seat settlements for seismic loading conditions, which is attributed to the increase in backfill soil stiffness with confining stress caused by the greater bridge surcharge stress.
9. For the conditions investigated, the acceleration amplification ratios for the lower MSE wall were observed to increase with increasing bridge surcharge stress, decreasing reinforcement spacing, and increasing reinforcement stiffness. The acceleration amplification ratio of bridge beam for reduced bridge surcharge stress is larger than the other cases, which is likely due to the smaller weight of bridge beam.
10. Reinforcement strains were found to increase significantly with increasing reinforcement spacing and decreasing reinforcement stiffness. The incremental residual reinforcement strains under the bridge seat in layer 13 for the longitudinal section L1 after the Imperial Valley motion are 0.21% for increased reinforcement spacing (S_v = 12 inches and $J_{5\%}$ = 26 kips/ft) and 0.14% for reduced reinforcement stiffness (S_v = 6 inches and $J_{5\%}$ = 13 kips/ft), which are much larger than the value of 0.04% for the baseline case (S_v = 6 inches and $J_{5\%}$ = 26 kips/ft).
11. For shaking in the transverse direction, the two side walls of the MSE bridge abutment moved in-phase during shaking, which is similar to soil behavior when subjected to simple shear conditions. After shaking, most of the dynamic facing displacements for the transverse sections were recovered.

12. The bridge seat settlements during shaking in the transverse direction are larger than those observed during shaking in the longitudinal direction. The incremental average residual settlement for the Maule motion is 0.19 inches for shaking in the transverse direction, which is three time larger than the value of 0.06 inches for shaking in the longitudinal direction. The larger settlements for the transverse shaking test are attributed to the lack of lateral confinement for the side walls and resulting simple shear deformation response of the abutment, whereas the reaction wall provided confinement at the back of the abutment for the longitudinal shaking test. Another likely contributing factor was the lack of soil confinement on both sides of the bridge seat in the transverse direction, whereas the back of the bridge seat was confined by backfill soil in the longitudinal direction. Some soil was lost from the corners of the MSE bridge abutment specimens, which may have caused a slight increase in reinforcement strains near the connections in the corners
13. For shaking in the transverse direction, reinforcement strains near the connections with the facing blocks for the transverse sections can increase significantly, which indicates that the analysis of reinforcement-block connection strengths for the transverse section is important for seismic design.
14. Shaking in the longitudinal direction resulted in facing displacements and reinforcement strains in the transverse direction. Similarly, shaking in the transverse direction was also found to result in lateral facing displacements and reinforcement strains in the longitudinal direction. This indicates that, in addition to the analysis of reinforcement in the direction of shaking, the analysis of reinforcement perpendicular to the direction of shaking is also important for the seismic design.
15. The width of the expansion joint was observed to vary during shaking due to sliding of the bridge beam with respect to the bridge seat (i.e., sliding on the bearing pads). Horizontal contact forces between the bridge seat and bridge beam were generated when the width of the expansion joint reduces to zero because the bridge beam moved out of phase with respect to the bridge seat during shaking. Joint closure occurred during the Northridge motion and resulted in horizontal contact forces. However, this may have partially occurred due to the different initial joint width between the bridge beam and bridge seat for this motion due to permanent changes in joint width during the preceding earthquake motions. The horizontal contact forces are relatively large after applying scaling factors, so they may need to be considered in the seismic design of MSE bridge abutments.

6.2 Recommendations

The following topics are recommended for future research:

1. Results of this study provide valuable experimental data that can be used for calibration of 3D numerical models of MSE bridge abutments under both static and dynamic loading. Validated numerical models can be used to investigate the effects of multi-directional shaking on the 3D dynamic response of MSE bridge abutments.
2. Further numerical analyses using a validated numerical model are needed to provide detailed design recommendations on the seismic design of MSE bridge abutments, including selection of design accelerations for the reinforced soil zone, retained soil zone, bridge seat, and bridge beam, maximum reinforcement tensile force line for seismic loading conditions, consideration of potential horizontal contact forces between the bridge seat and bridge beam.
3. The testing program performed in this study was limited by the size and payload capacity of the UCSD Powell Structural Laboratory shaking table. The width of the MSE bridge abutment model was smaller than a typical full-scale MSE bridge abutment in the field, which likely produced some differences in seismic response for the model. In particular, overlap of geogrid reinforcements in the transverse and longitudinal directions across the entire abutment model may have produced an overly stiff response for the model, where such overlap would be limited to the regions near the corners for a MSE bridge abutment in the field. Also, MSE bridge abutments in the field have a much larger retained soil mass behind the reinforced soil zone, which may reduce the constraints on the deformation response of the wall in the longitudinal direction which may potentially increase wall facing displacements, bridge seat settlements, and reinforcement strains. Additional shaking table tests on full-scale MSE bridge abutments are recommended to alleviate these effects.

References

Abu-Hejleh, N., Zornberg, J.G., Wang, T., and Watcharamonthein, J. (2002). "Monitored displacements of unique geosynthetic-reinforced soil bridge abutments." *Geosynthetics International*, 9(1), 71-95.

Adams, M. (1997). "Performance of a prestrained geosynthetic reinforced soil bridge pier." *Mechanically Stabilized Backfill*, Balkema, Rotterdam, Netherland, 35-53.

Adams, M., Nicks, J., Stabile, T., Wu, J., Schlatter, W., and Hartmann, J. (2011a). "Geosynthetic reinforced soil integrated bridge system interim implementation guide." *FHWA-HRT-11-026*, U.S. DOT, Washington, D.C.

Adams, M., Nicks, J., Stabile, T., Wu, J., Schlatter, W., and Hartmann, J. (2011b). "Geosynthetic reinforced soil integrated bridge system synthesis report." *FHWA-HRT-11-027*, U.S. DOT, Washington, D.C.

Adams, M.T., Ooi, P.S., and Nicks, J.E. (2014). "Mini-pier testing to estimate performance of full-scale geosynthetic reinforced soil bridge abutments." *Geotechnical Testing Journal*, 37(5), 884-894.

Adams, M.T., Schlatter, W., and Stabile, T. (2007). "Geosynthetic-reinforced soil integrated abutments at the Bowman Road Bridge in Defiance County, Ohio." *Geo-Denver 2007*, ASCE, Reston, VA, USA, 1-10.

Adams, M.T., Schlatter, W., and Stabile, T. (2008). "Geosynthetic-reinforced soil integrated system." *EuroGeo4*, Paper No. 271, Edinburgh, UK.

Bathurst, R.J. (2006). "Reinforced soil retaining wall testing, modeling and design." *12th Indian Geotechnical Conference*, Madras, India, 21-32.

Bathurst, R. J., Allen, T. M., and Walters, D. L. (2002). "Short-Term Strain and Deformation Behavior of Geosynthetic Walls at Working Stress Conditions." *Geosynthetics International*, Vol. 9, Nos. 5-6, 451-482.

Bathurst, R.J., Nernheim, A., Walters, D.L., Allen, T.M., Burgess, P., and Saunders, D.D. (2009). "Influence of reinforcement stiffness and compaction on the performance of four geosynthetic reinforced soil walls." *Geosynthetics International*, 16(1), 43-59.

Bathurst, R.J., Vlachopoulos, N., Walters, D.L., Burgess, P.G., and Allen, T.M. (2006). "The influence of facing stiffness on the performance of two geosynthetic reinforced soil retaining walls." *Canadian Geotechnical Journal*, 43(12), 1225-1237.

Bathurst, R.J., Walters, D., Vlachopoulos, N., Burgess, P., and Allen, T.M. (2000). "Full scale testing of geosynthetic reinforced walls." *Advances in Transportation and Geoenvironmental Systems using Geosynthetics*, *GeoDenver 2000*, Denver, Colorado, 201-217.

Berg, R.R., Christopher, B.R., and Samtani, N. (2009). "Design and construction of mechanically stabilized earth walls and reinforced soil slopes – Volume I." *FHWA-NHI-10-024/FHWA GEC 011-Vol I*, U.S. DOT, Washington, D.C.

Budge, A.S., Dasenbrock, D.D., Mattison, D.J., Bryant, G.K., Grosser, A.T., Adams, M., and, Nicks, J. (2014). Instrumentation and early performance of a large grade GRS-IBS wall. *Geo-Congress 2014*, ASCE, Reston, VA, USA, 4213-4227.

Budhu, M., and Halloum, M. (1994). "Seismic external stability of geotextile reinforced walls." *5th International Conference on Geotextiles, Geomembranes and Related Products*, Singapore, 529-532.

Caltrans. (2004). Section 5 - Retaining Walls, *Bridge Design Specifications*, August 2004.

Caltrans. (2017). Memo to Designers 5-1, March 2017.

Chida, S., Minami, K., and Adachi, K. (1982). "Test de stabilité de remblais en Terre Armée". (translated from Japanese)

Ehrlich, M., and Mirmoradi, S.H. (2013). "Evaluation of the effects of facing stiffness and toe resistance on the behavior of GRS walls." *Geotextiles and Geomembranes*, 40, 28-36.

Ehrlich, M., Mirmoradi, S.H., and Saramago, R.P. (2012). "Evaluation of the effect of compaction on the behavior of geosynthetic-reinforced soil walls." *Geotextiles and Geomembranes*, 34, 108-115.

El-Emam, M., and Bathurst, R.J. (2004). "Experimental design, instrumentation and interpretation of reinforced soil wall response using a shaking table." *International Journal of Physical Modelling in Geotechnics*, 4(4), 13-32.

El-Emam, M., and Bathurst, R.J. (2005). "Facing contribution to seismic response of reduced-scale reinforced soil walls." *Geosynthetics International*, 12(5), 215-238.

El-Emam, M., and Bathurst, R.J. (2007). "Influence of reinforcement parameters on the seismic response of reduced-scale reinforced soil retaining walls." *Geotextiles and Geomembranes*, 25(1), 33-49.

Fairless, G.J. (1989). "Seismic performance of reinforced earth walls." *Ph.D. Thesis*, University of Canterbury, Christchurch, New Zealand.

Fox, P.J., Andrew, A.C., Elgamal, A., Greco, P., Isaacs, D., Stone, M., and Wong, S. (2015). "Large soil confinement box for seismic performance testing of geo-structures." *Geotechnical Testing Journal*, 38(1), 72-84.

Fox, P.J., Rowland, M.G., Scheithe, J.R., Davis, K.L., Supple, M.R., and Crow, C.C. (1997). "Design and evaluation of a large direct shear machine for geosynthetic clay liners." *Geotechnical Testing Journal*, 20(3), 279-288.

Fox, P.J., Nye, C.J., Morrison, T.C., Hunter, J.G., and Olsta, J.T. (2006). "Large dynamic direct shear machine for geosynthetic clay liners." *Geotechnical Testing Journal*, 29(5), 392-400.

Gotteland, P., Gourc, J.P., and Villard, P. (1997). "Geosynthetic reinforced structures as bridge abutments: Full scale experimentation and comparison with modelisations." *Mechanically Stabilized Backfill*, Balkema, Rotterdam, Netherland, 25-34.

Guler, E., and Enunlu, A.K. (2009). "Investigation of dynamic behavior of geosynthetic reinforced soil retaining structures under earthquake loads." *Bulletin of Earthquake Engineering*, 7(3), 737-777.

Guler, E., and Selek, O (2014). “Reduced-scale shaking table tests on geosynthetic-reinforced soil walls with modular facing.” *Journal of Geotechnical and Geoenvironmental Engineering*, 10.1061/(ASCE)GT.1943-5606.0001102, 04014015.

Helwany, S.M.B., Wu, J.T.H., and Meinholz, P. (2012). Seismic design of geosynthetic-reinforced soil bridge abutments with modular block facing. *NCHRP Web-Only Document 187*, Transportation Research Board, Washington, D.C.

Iai, S. (1989) “Similitude for shaking table tests on soil-structure-fluid models in 1 g gravitational fields.” *Soils and Foundations*, 29(1), 105-118.

Iwamoto, M.K., Ooi, P.S., Adams, M.T., and Nicks, J.E. (2015). “Composite properties from instrumented load tests on mini-piers reinforced with geotextiles.” *Geotechnical Testing Journal*, 38(4), 397-408.

Ketchart, K., and Wu, J.T.H. (1997). “Performance of geosynthetic-reinforced soil bridge pier and abutment, Denver, Colorado, USA.” *Mechanically Stabilized Backfill*, Balkema, Rotterdam, Netherland, 101-116.

Khosravi, A., Ghayoomi, M., McCartney, J.S., and Ko, H.-Y. (2010). “Impact of effective stress on the dynamic shear modulus of unsaturated sands.” *GeoFlorida 2010: Advances in Analysis, Modeling & Design*, Orlando, FL, 410-419.

Koga, Y., Itoh, Y., Washida, S., and Shimazu, T. (1988). “Seismic resistance of reinforced embankment by model shaking tests.” *International Geotechnical Symposium on Theory and Practice of Earth Reinforcement*, *IS-Kyushu’88*, Fukuoka, Balkema, Rotterdam, 413-418.

Koga, Y, and Washida, S. (1992). “Earthquake resistant design method of geotextile reinforced embankments.” *International Geotechnical Symposium on Theory and Practice of Earth Reinforcement*, *IS-Kyushu’92*, Fukuoka, 255-259.

Koseki, J., Munaf, Y., Tatsuoka, F., Tateyama, M., Kojima, K., and Sato, T. (1998). “Shaking and tilt table tests of geosynthetic-reinforced soil and conventional-type retaining walls.” *Geosynthetics International*, 5(1-2), 73-96.

Kramer, S.L., *Geotechnical Earthquake Engineering*, Prentice Hall, Upper Saddle River, NJ, 1996, 653pp.

Krishna, A.M., and Latha, G.M. (2009). “Seismic behavior of rigid-faced reinforced soil retaining wall models: reinforcement effect.” *Geosynthetics International*, 16(5), 364-373.

Latha, G.M., and Krishna, A.M. (2008). “Seismic response of reinforced soil retaining wall models: Influence of backfill relative density.” *Geotextiles and Geomembranes*, 26, 335-349.

Latha, G.M., and Santhanakumar, P. (2015). “Seismic response of reduced-scale modular block and rigid faced reinforced walls through shaking table tests.” *Geotextiles and Geomembranes*, 43(4), 307-316.

Lee, K.Z.Z., and Wu, J.T.H. (2004). “A synthesis of case histories on GRS bridge-supporting structures with flexible facing.” *Geotextiles and Geomembranes*, 22(4), 181-204.

Ling, H.I., Leshchinsky, D., Mohri, Y., and Wang, J. (2012). "Earthquake response of reinforced segmental retaining walls backfilled with substantial percentage of fines." *Journal of Geotechnical and Geoenvironmental Engineering*, 138(8), 934-944.

Ling, H.I., Mohri, Y., Leshchinsky, D., Burke, C., Matsushima, K., and Liu, H. (2005). "Large scale shaking table tests on modular block reinforced soil retaining wall." *Journal of Geotechnical and Geoenvironmental Engineering*, 131(4), 465-476.

Liu, H., Wang, X., and Song, E. (2010). "Centrifuge testing of segmental geosynthetic-reinforced soil retaining walls subjected to modest seismic loading." *GeoFlorida 2010: Advanced in Analysis, Modeling & Design*, Florida, USA, 2992-2998.

Lu, N., Godt, J.W., and Wu, D.T. (2010). "A closed-form equation for effective stress in unsaturated soil." *Water Resources Research*, 46, W05515, 10.1029/2009WR008646.

Matsuo, O., Tsutsumi, T., Yokoyama, K., and Saito, Y. (1998). "Shaking table tests and analyses of geosynthetic-reinforced soil retaining walls." *Geosynthetics International*, 5(1-2), 97-126.

Mirmoradi, S.H., and Ehrlich, M. (2016). "Evaluation of the effect of toe resistance on GRS walls." *Transportation Geotechnics*, 8, 35-44.

Mirmoradi, S.H., Ehrlich, M., and Dieguez, C. (2016). "Evaluation of the combined effect of toe resistance and facing inclination on the behavior of GRS walls." *Geotextiles and Geomembranes*, 44(3), 287-294.

Murata, O., Tateyama, M., Tatsuoka, F. (1994). "Shaking table tests on a large geosynthetic-reinforced soil retaining walls model." *Recent Case Histories of Permanent Geosynthetic-reinforced Soil Walls*, *Seiken Symposium*, Tokyo, 259-264.

Nagel, R.B., and Elms, D.G. (1985). "Seismic behavior of reinforced earth walls." *Research Report No. 85-4*, University of Canterbury, Christchurch, New Zealand.

Nicks, J.E., Adams, M.T., Ooi, P.S.K., and Stabile, T. (2013). "Geosynthetic reinforced soil performance testing – axial load deformation relationships." *FHWA-HRT-13-066*, U.S. DOT, Washington, D.C.

Nicks, J.E., Esmaili, D., and Adams, M.T. (2016). "Deformations of geosynthetic reinforced soil under bridge service loads." *Geotextiles and Geomembranes*, 44(4), 641-653Saghebfar, M., Abu-Farsakh, M., Ardah, A., Chen, Q., 2017. Performance monitoring of Geosynthetic Reinforced Soil Integrated Bridge System (GRS-IBS) in Louisiana." *Geotextiles and Geomembranes*, Vol. 45, No. 2, 34-47.

Nova-Roessig, L., and Sitar, N. (2006). "Centrifuge model studies of the seismic response of reinforced soil slopes." *Journal of Geotechnical and Geoenvironmental Engineering*, 132(3), 388-400.

Panah, A. K., Yazdi, M., and Ghalandarzadeh, A. (2015). "Shaking table tests on soil retaining walls reinforced by polymeric strips." *Geotextiles and Geomembranes*, 43(2), 148-161.

Ramakrishnan, K, Budhu, M., and Britto, A. (1998). "Laboratory seismic tests on geotextile wrap-faced and geotextile-reinforced segmental retaining walls." *Geosynthetics International*, 5(1-2), 55-71.

Richardson, G.N., Feger, D., Fong, A., and Lee, K.L. (1977). “Seismic testing of reinforced earth walls.” *Journal of Geotechnical Engineering Division*, 103(1), 1–17.

Richardson, G.N., and Lee, K.L. (1975). “Seismic design of reinforced earth walls.” *Journal of Geotechnical Engineering Division*, 101(2), 167–188.

Saghebfar, M., Abu-Farsakh, M., Ardah, A., and Chen, Q. (2017). Performance monitoring of Geosynthetic Reinforced Soil Integrated Bridge System (GRS-IBS) in Louisiana.” *Geotextiles and Geomembranes*, 45(2), 34-47.

Sakaguchi, M. (1996). “A study of the seismic behavior of geosynthetic reinforced walls in Japan.” *Geosynthetics International*. 3(1), 13–40.

Sakaguchi, M., Muramatsu, M., and Nagura, K. (1992). “A discussion on reinforced embankment structures having high earthquake resistance.” *International Geotechnical Symposium on Theory and Practice of Earth Reinforcement*, *IS-Kyushu’92*, Fukuoka, 287-292.

Siddharthan, R.J., Ganeshwara, V., Kutter, B.L., El-Desouky, M., and Whitman, R.V. (2004). “Seismic deformation of bar mat mechanically stabilized earth walls. I: Centrifuge tests.” *Journal of Geotechnical and Geoenvironmental Engineering*, 130(1), 14-25.

Stein, W.J., and Neuman, T.R. (2007). Mitigation strategies for design exceptions. *FHWA-SA-07-011*, Federal Highway Administration, Washington, D.C., USA.

Sugimoto, M., Ogawa, S., and Moriyama, M. (1994). “Dynamic characteristics of reinforced embankments with steep slope by shaking model tests.” *Recent Case Histories of Permanent Geosynthetic-Reinforced Soil walls*, *Seiken Symposium*, Tokyo, 271-275.

Takemura, J., and Takahashi, A. (2003). “Centrifuge modeling of seismic performance of reinforced earth structure.” *Reinforced soil engineering: Advances in research and practice*, Marcel Dekker, New York, 417–442.

Telekes, G., Sugimoto, M., and Agawa, S., (1994). “Shaking table tests on reinforced embankment models.” *13th International Conference on Soil Mechanics and Foundation Engineering*, New Delhi, 649-644.

Trautner, C.A., Zheng, Y., McCartney, J.S., and Hutchinson, T C. (2017). “An approach for shake table performance evaluation during repair and retrofit actions.” *Earthquake Engineering and Structural Dynamics*, 10.1002/eqe.2942.

Vahedifard, F., Leshchinsky, B., Sehat, S., and Leshchinsky, D. (2014). “Impact of cohesion on seismic design of geosynthetic-reinforced earth structures.” *Journal of Geotechnical and Geoenvironmental Engineering*, 10.1061/(ASCE)GT.1943-5606.0001099, 04014016.

Vahedifard, F., Leshchinsky, B., Mortezaei, K., and Lu, N. (2015). “Active earth pressures for unsaturated retaining structures.” *Journal of Geotechnical and Geoenvironmental Engineering*, 10.1061/(ASCE)GT.1943-5606.0001356, 04015048.

van Genuchten, M.T. (1980). “A closed-form equation for predicting the hydraulic conductivity of unsaturated soils.” *Soil Science Society of America Journal*, 44(5), 892–898.

Warren, K.A., Schlatter, W., Adams, M., Stabile, T., and LeGrand, D. (2010). Preliminary results for a GRS Integrated Bridge System supporting a large single span bridge. *2010 Earth Retention Conference*, ASCE, Reston, VA, USA, 612-619.

Wolfe, W.E., Lee, K.L., Rea, D., and Yourman, A.M. (1978). "The effect of vertical motion on the seismic stability of reinforced earth walls." *Symposium on Earth Reinforcement*, ASCE, Reston, VA, 856-879.

Won, G.W., Hull, T., and De Ambrosis, L. (1996). "Performance of a geosynthetic segmental block wall structure to support bridge abutments." *Earth Reinforcement*, Vol. 1, Balkema, Rotterdam, Netherlands, 543–548.

Wu, J.T.H., Ketchart, K., and Adams, M. (2001). GRS bridge piers and abutments. *FHWA-RD-00-038*, U.S. DOT, Washington, DC.

Wu, J.T.H., Lee, K.Z.Z, Helwany, S.B., and Ketchart, K. (2006a). Design and construction guidelines for geosynthetic-reinforced soil bridge abutments with a flexible facing. *NCHRP Report 556*, Transportation Research Board, Washington, DC.

Wu, J.T.H., Lee, K.Z.Z, and Pham, T. (2006b). "Allowable bearing pressures of bridge sills on GRS abutments with flexible facing." *Journal of Geotechnical and Geoenvironmental Engineering*, 132(7), 830-841.

Yen, W.-H.P., Chen, G., Buckle, I., Allen, T., Alzamora, D., Ger, J., and Arias, J.G. (2011). Post-earthquake reconnaissance report on transportation infrastructure: Impact of the February 27, 2010, offshore Maule Earthquake in Chile, *FHWA-HRT-11-030*, U.S. DOT, Washington, D.C.

Appendix 1 – Shaking Table Test Data

The data of each of the six shaking table tests during the Imperial Valley, Maule, and Northridge motions are presented in this section. The general instrumentation plan are shown in Figure 3.25 for Tests 1 to 5 and in Figure 3.27 for Test 6. Some sensors did not work during the tests, thus those data are not available. Data presented mainly include displacements for wall facing, bridge seat, and bridge beam, accelerations for wall facing, backfill soil, bridge seat, and bridge beam, vertical and lateral stresses, reinforcement strains, and contact forces between the bridge seat and bridge beam.

A1.1 Test 1

A1.1.1 Imperial Valley Motion

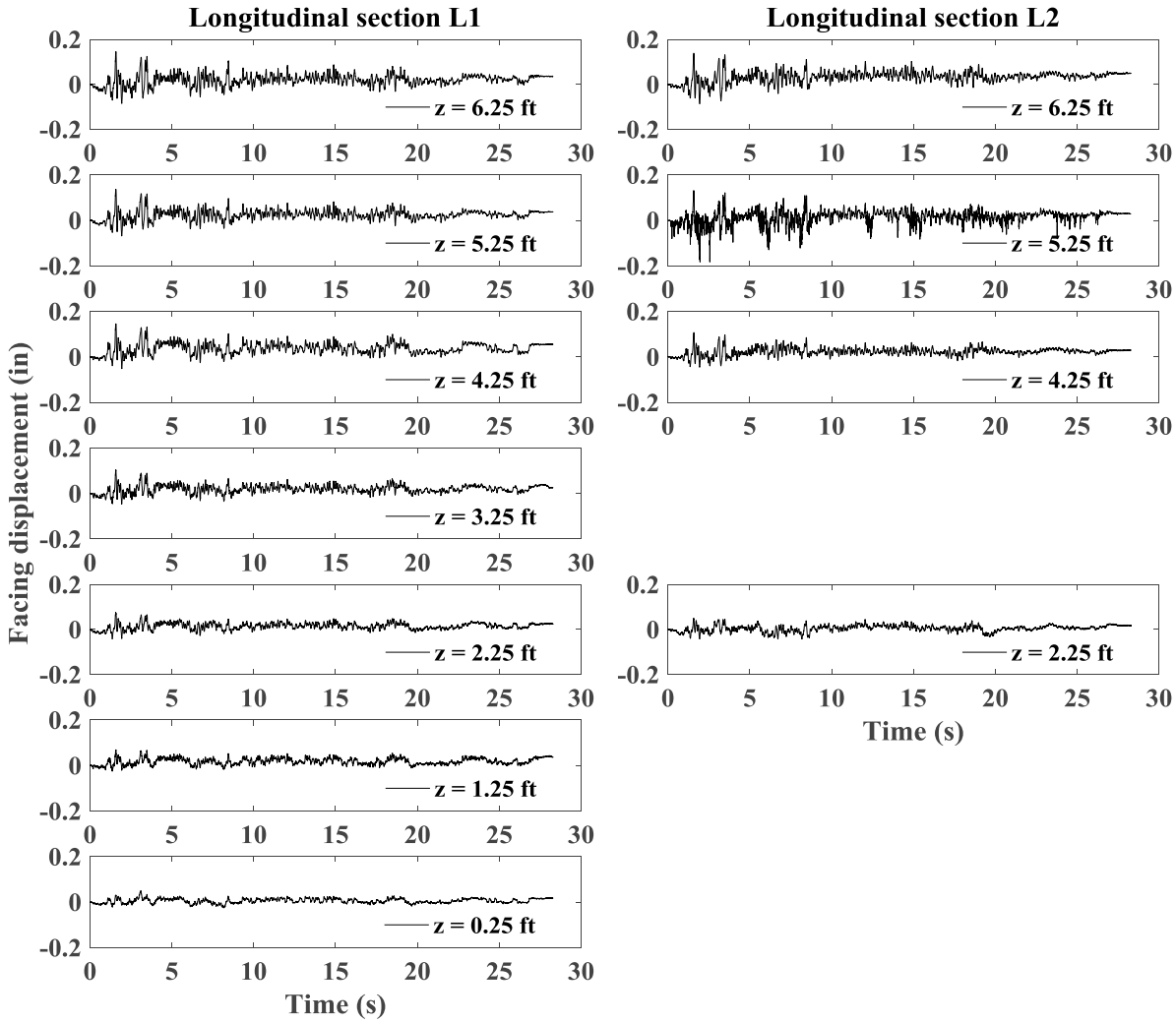

Figure A1.1 Time histories of incremental facing displacement for longitudinal sections L1 and L2.

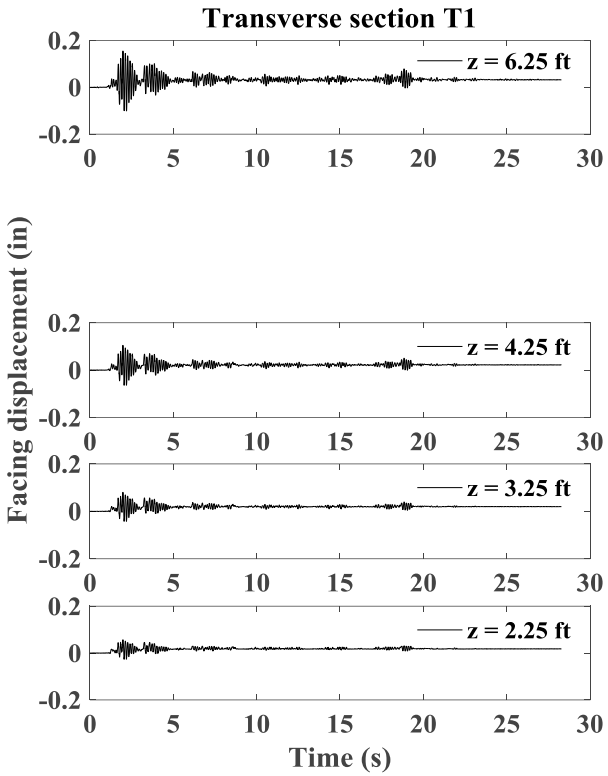

Figure A1.2 Time histories of incremental facing displacement for transverse section T1.

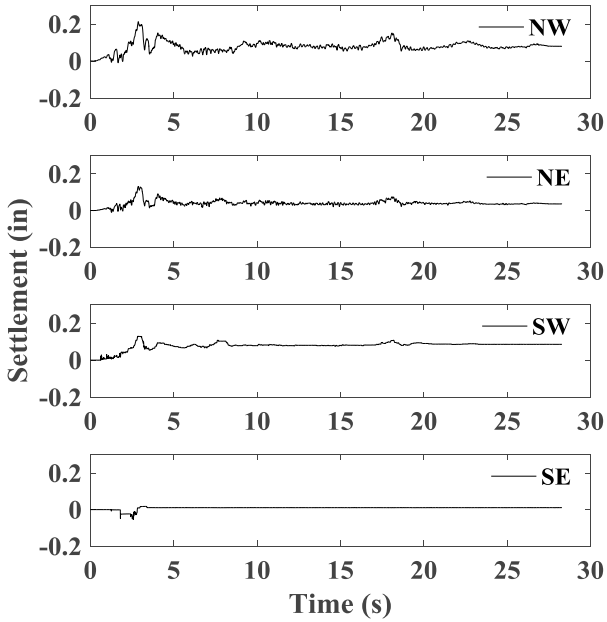

Figure A1.3 Time histories of incremental settlement for bridge seat.

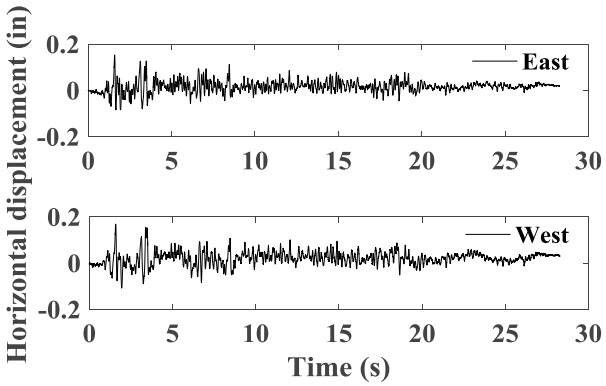

Figure A1.4 Time histories of incremental horizontal displacement for bridge seat.

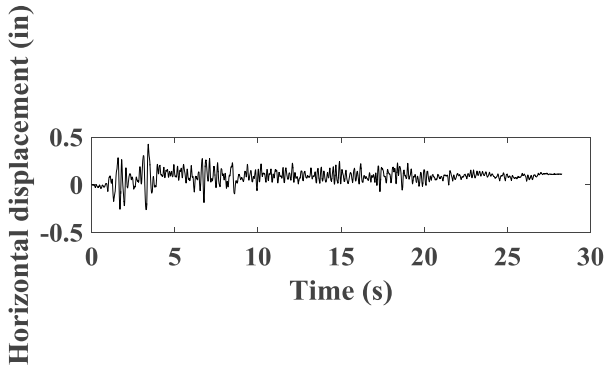

Figure A1.5 Time histories of incremental horizontal displacement for bridge beam.

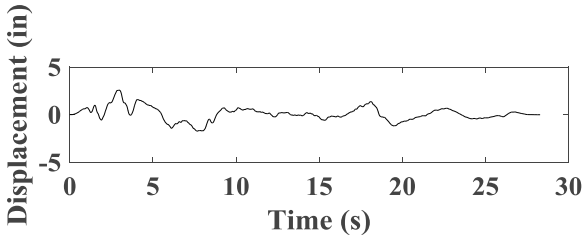

Figure A1.6 Time histories of horizontal displacement for shaking table.

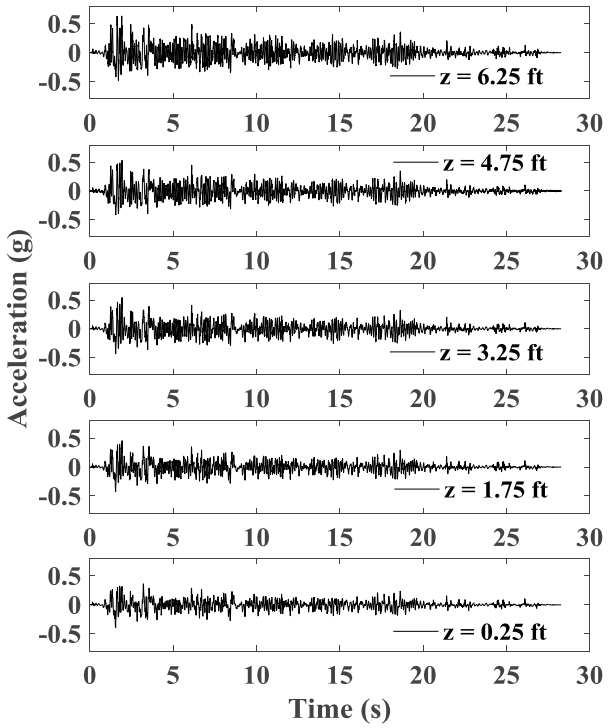

Figure A1.7 Time histories of acceleration for wall facing in longitudinal section L1.

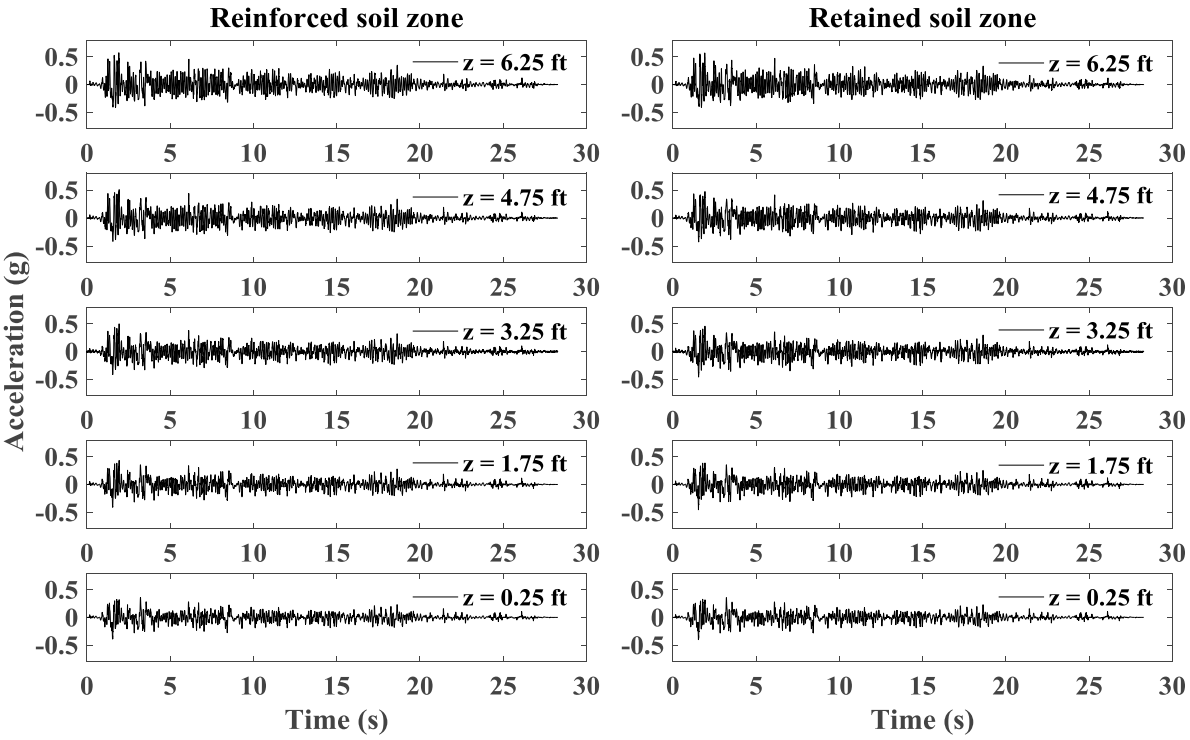

Figure A1.8 Time histories of acceleration for reinforced soil zone and retained soil zone in longitudinal section L1.

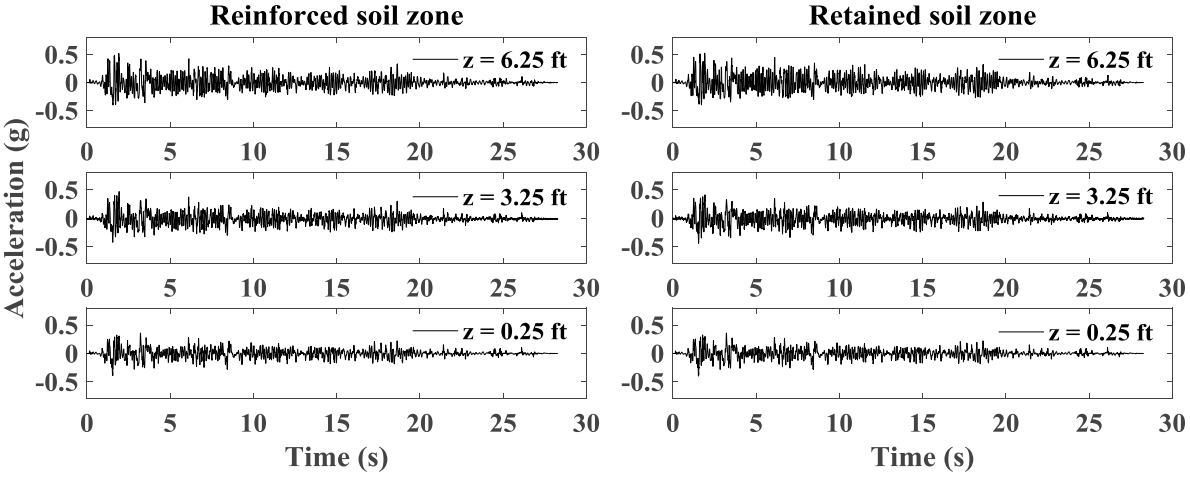

Figure A1.9 Time histories of acceleration for reinforced soil zone and retained soil zone in longitudinal section L2.

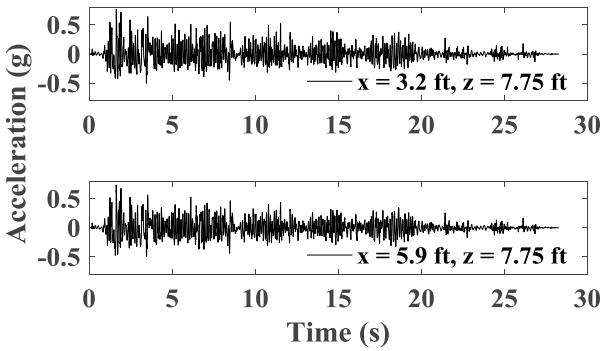

Figure A1.10 Time histories of acceleration for backfill soil in upper wall.

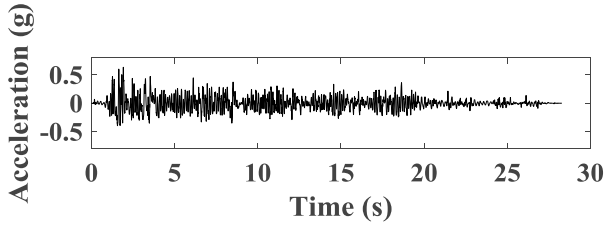

Figure A1.11 Time histories of acceleration for bridge seat.

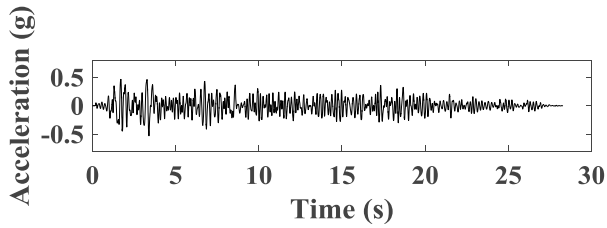

Figure A1.12 Time histories of acceleration for bridge beam.

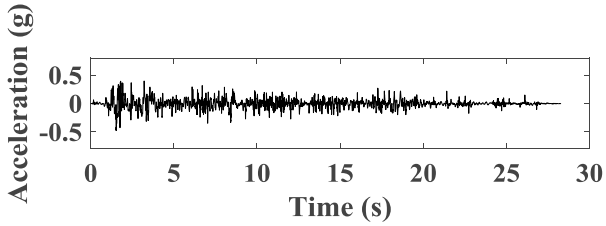

Figure A1.13 Time histories of acceleration for support wall.

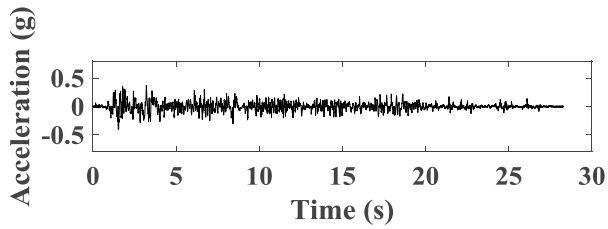

Figure A1.14 Time histories of acceleration for shaking table.

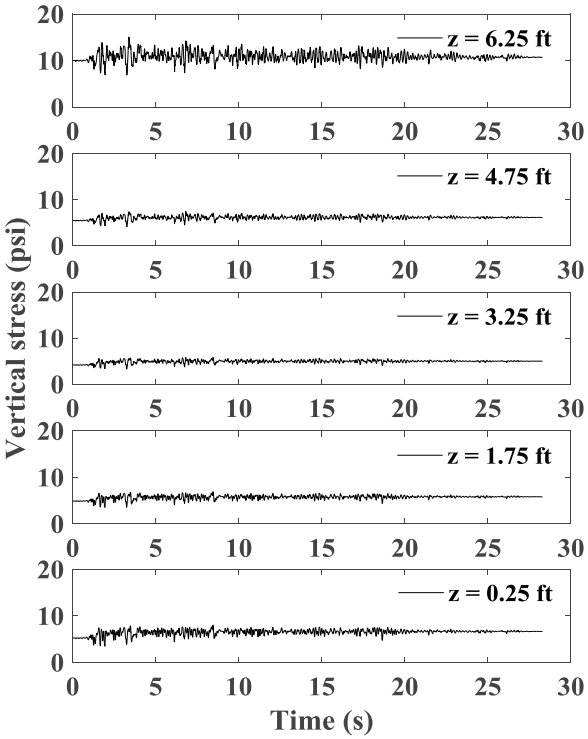

Figure A1.15 Time histories of vertical stress behind wall facing.

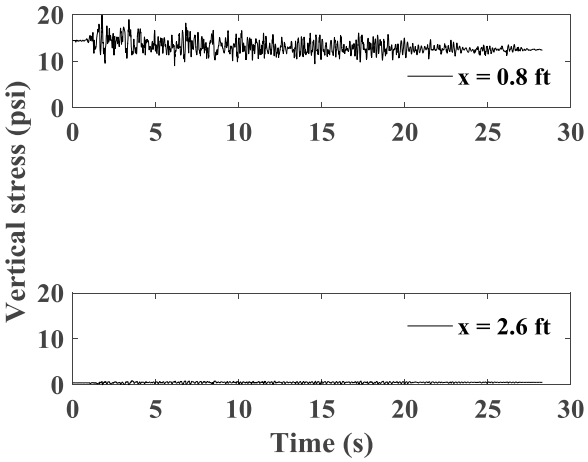

Figure A1.16 Time histories of vertical stress under bridge seat.

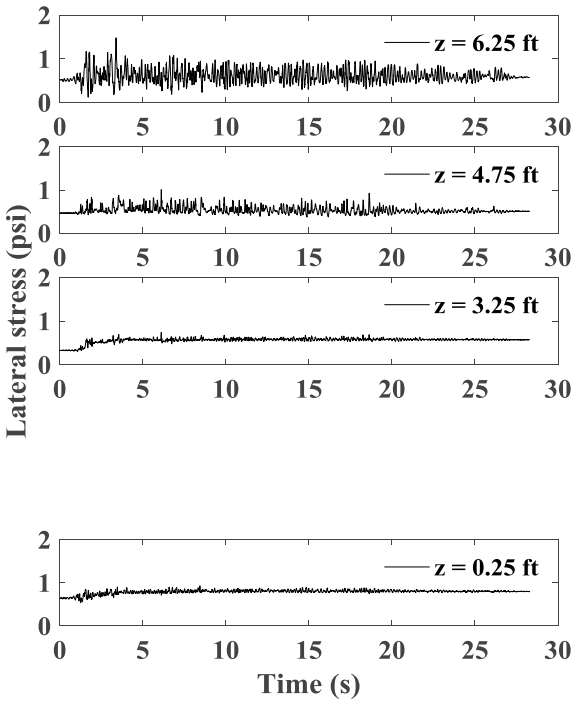

Figure A1.17 Time histories of lateral stress behind wall facing.

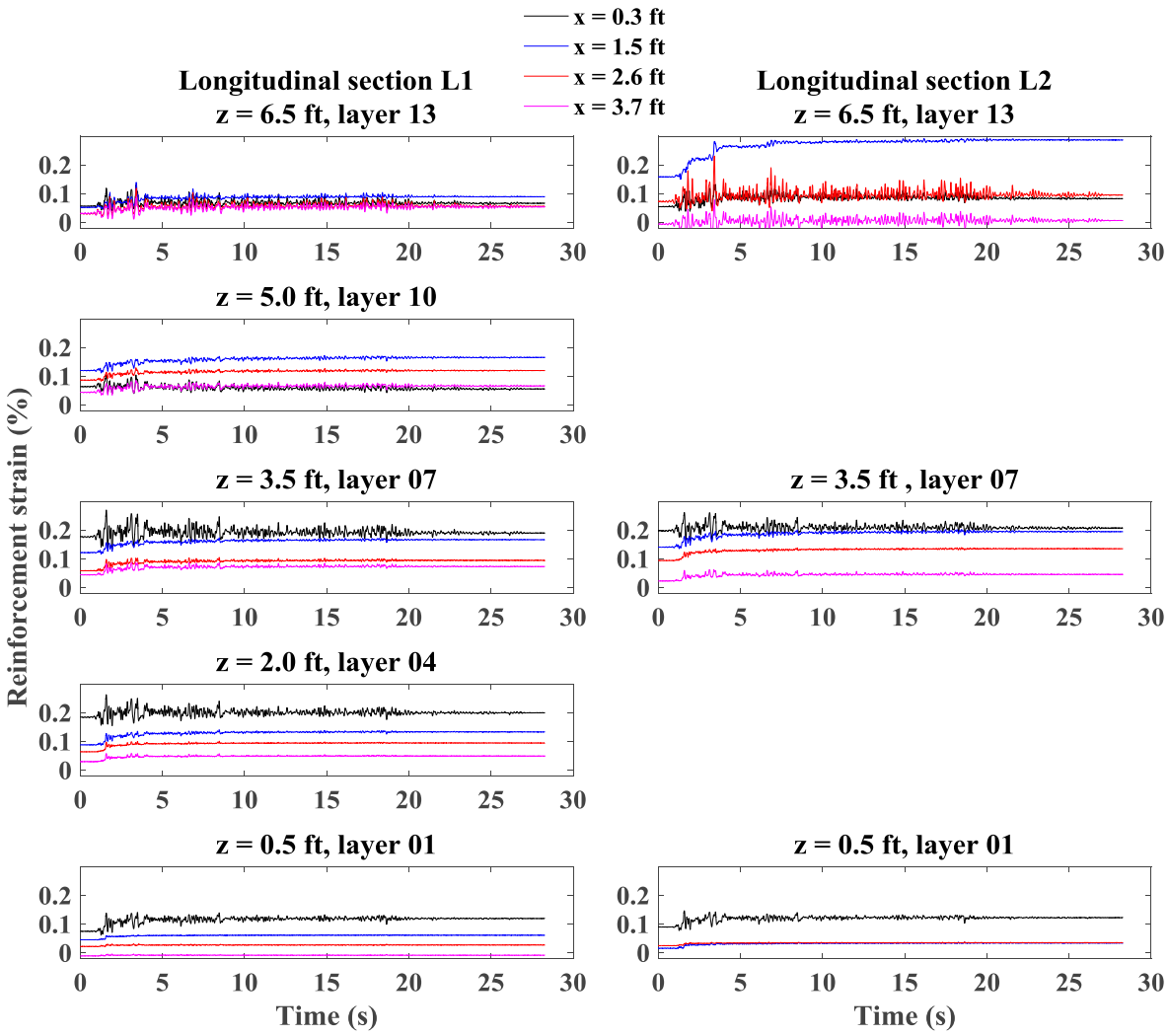

Figure A1.18 Time histories of reinforcement strain for longitudinal sections L1 and L2.

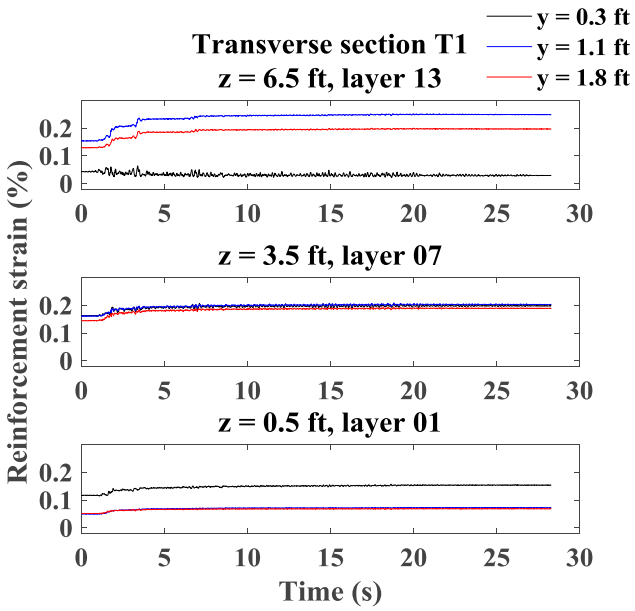

Figure A1.19 Time histories of reinforcement strain for transverse section T1.

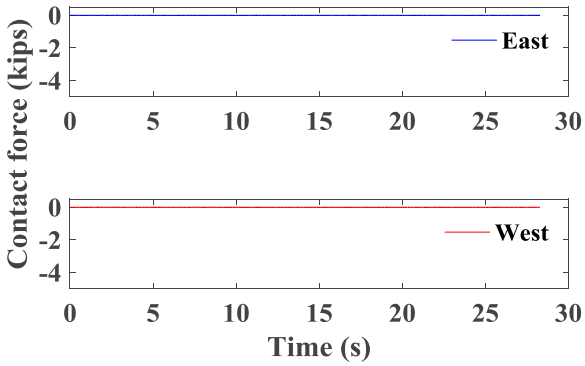

Figure A1.20 Time histories of contact force between bridge seat and bridge beam.

A1.1.2 Maule Motion

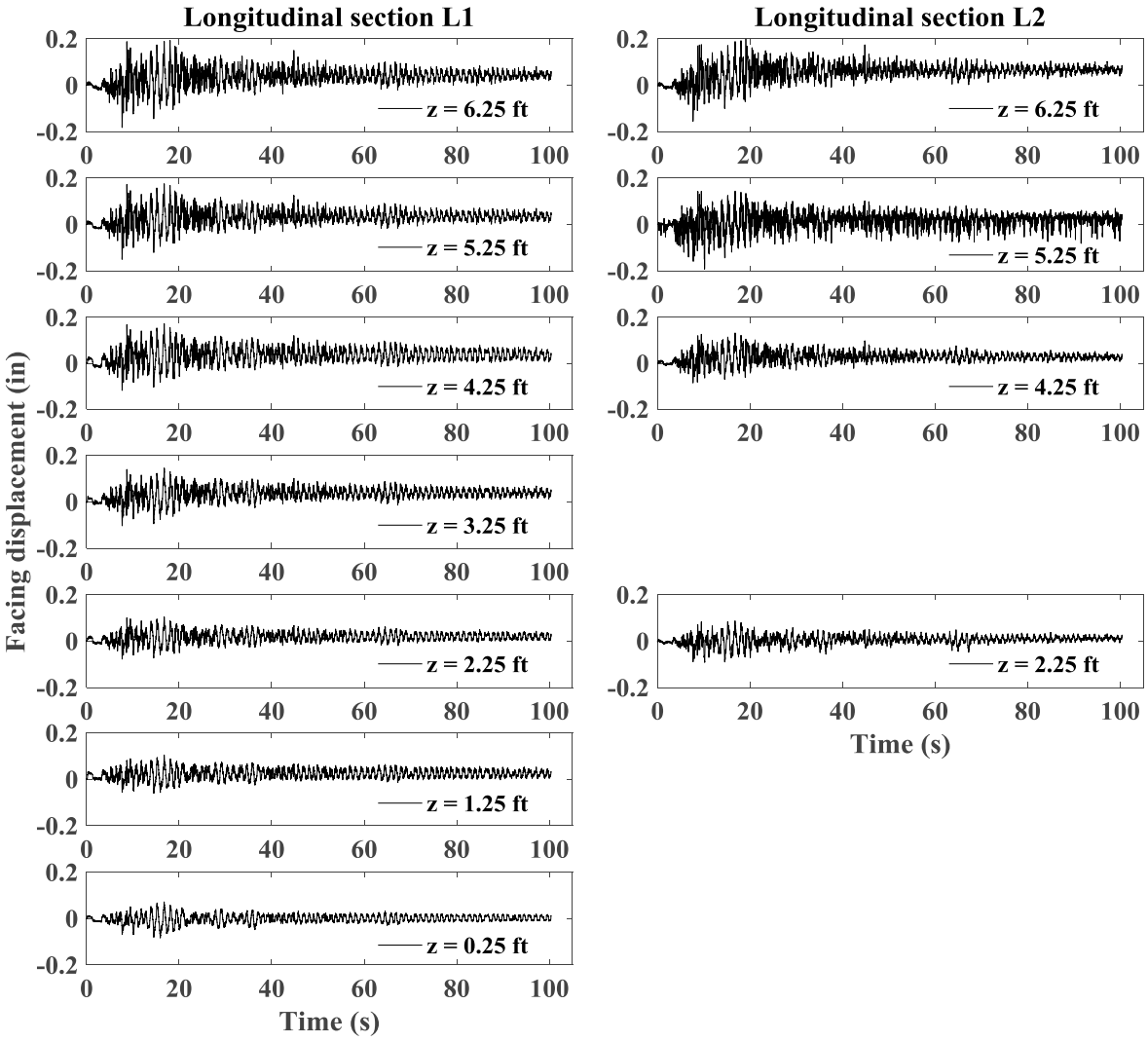

Figure A1.21 Time histories of incremental facing displacement for longitudinal sections L1 and L2.

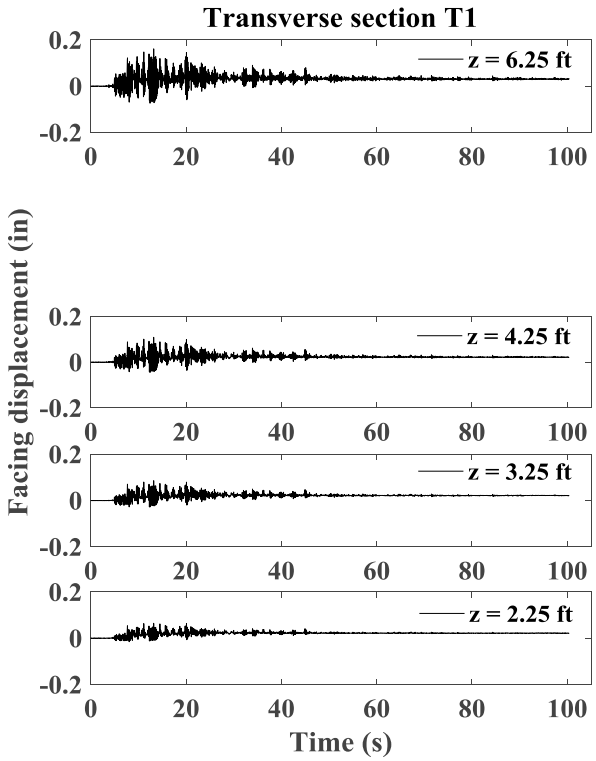

Figure A1.22 Time histories of incremental facing displacement for transverse section T1.

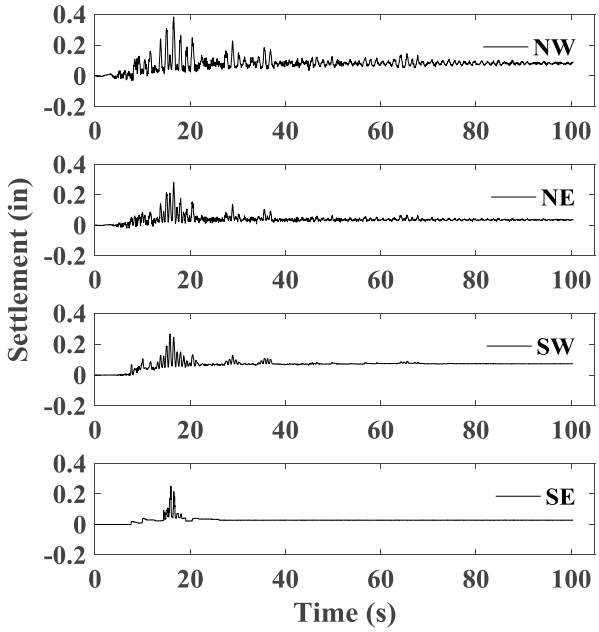

Figure A1.23 Time histories of incremental settlement for bridge seat.

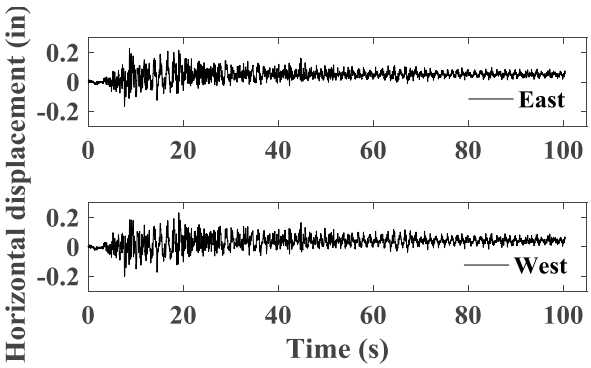

Figure A1.24 Time histories of incremental horizontal displacement for bridge seat.

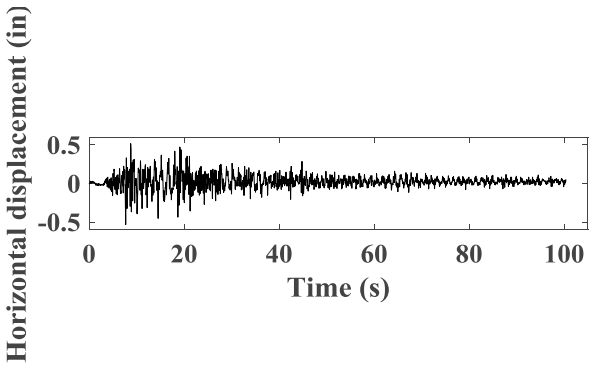

Figure A1.25 Time histories of incremental horizontal displacement for bridge beam.

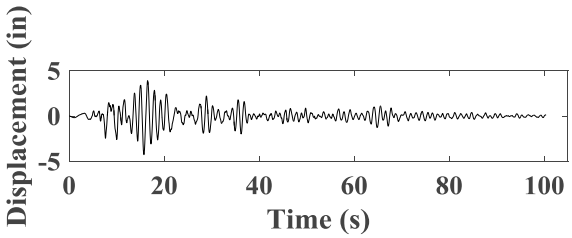

Figure A1.26 Time histories of horizontal displacement for shaking table.

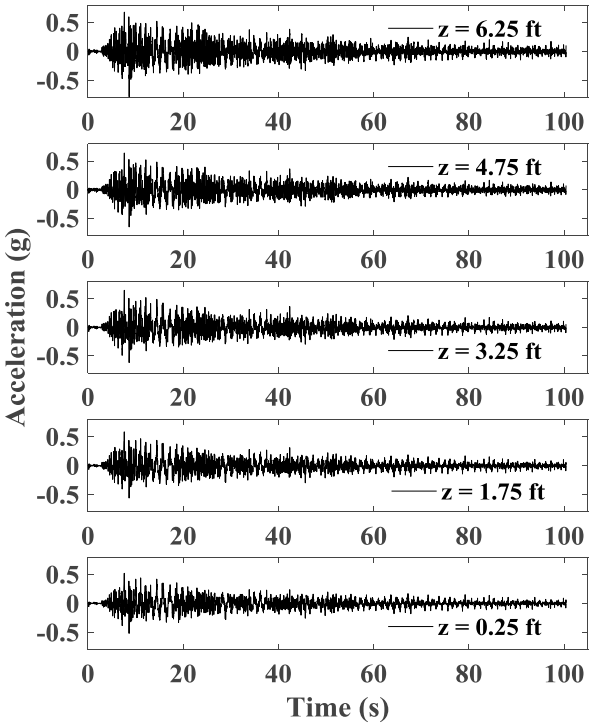

Figure A1.27 Time histories of acceleration for wall facing in longitudinal section L1.

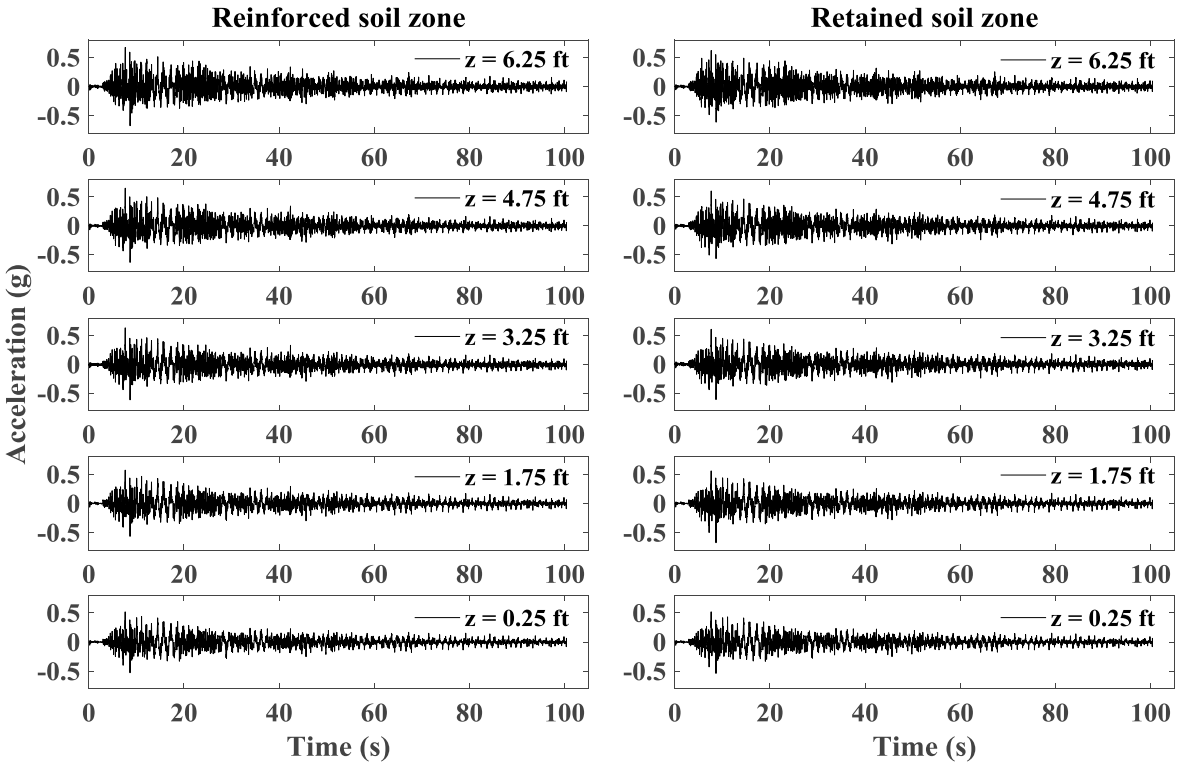

Figure A1.28 Time histories of acceleration for reinforced soil zone and retained soil zone in longitudinal section L1.

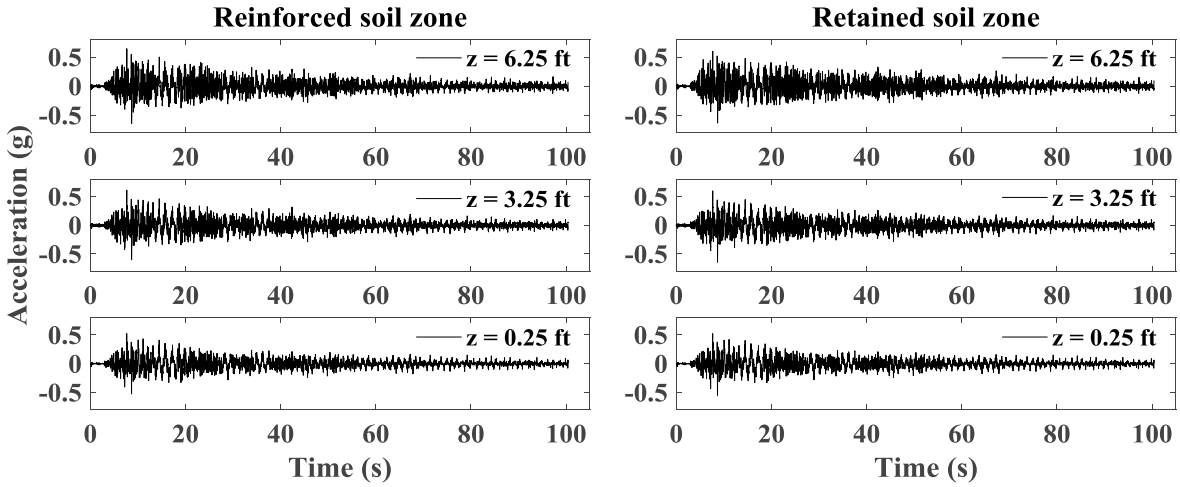

Figure A1.29 Time histories of acceleration for reinforced soil zone and retained soil zone in longitudinal section L2.

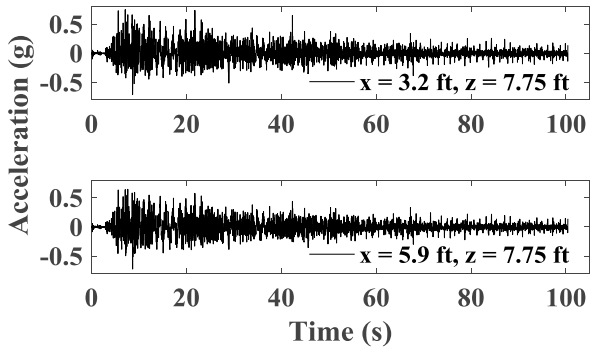

Figure A1.30 Time histories of acceleration for backfill soil in upper wall.

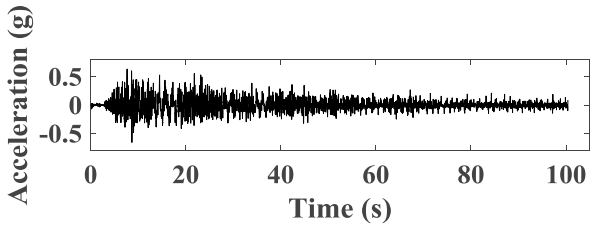

Figure A1.31 Time histories of acceleration for bridge seat.

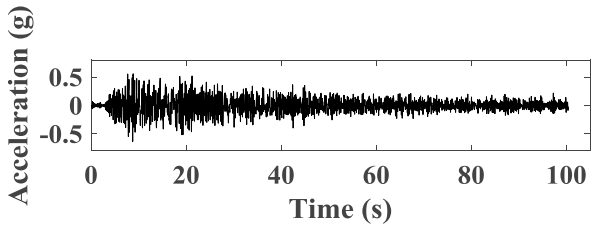

Figure A1.32 Time histories of acceleration for bridge beam.

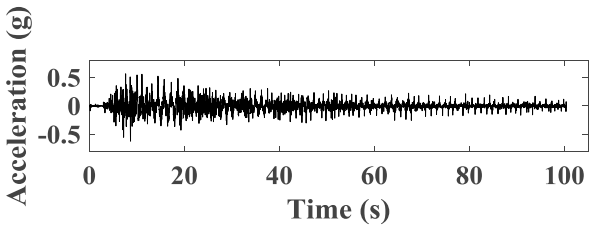

Figure A1.33 Time histories of acceleration for support wall.

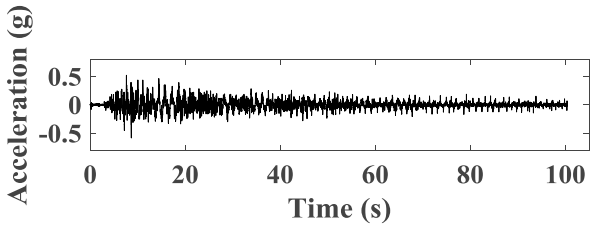

Figure A1.34 Time histories of acceleration for shaking table.

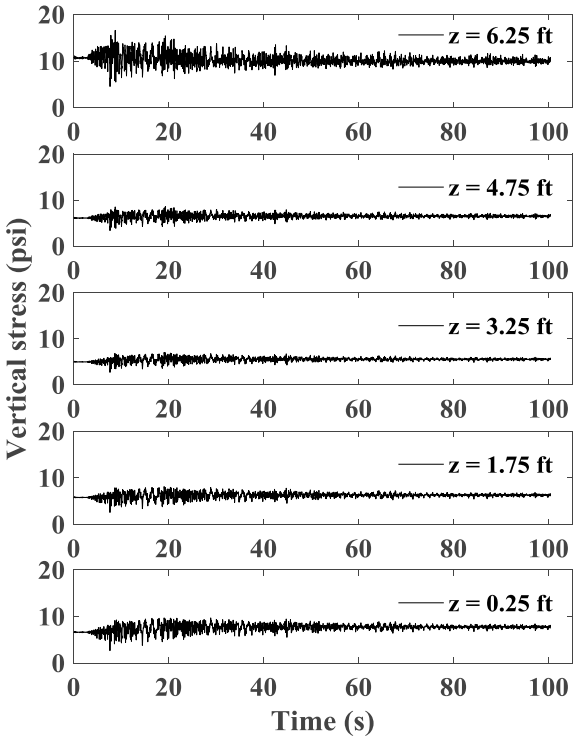

Figure A1.35 Time histories of vertical stress behind wall facing.

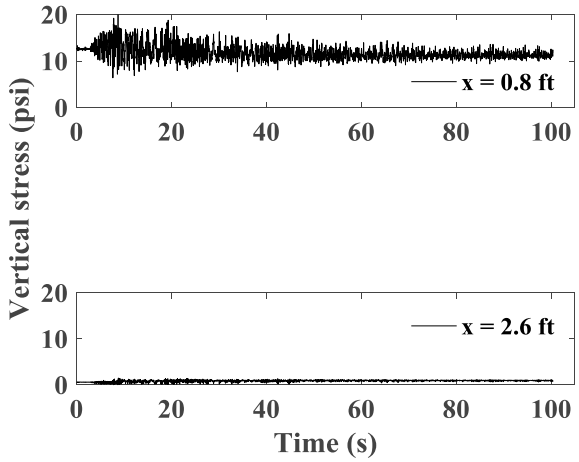

Figure A1.36 Time histories of vertical stress under bridge seat.

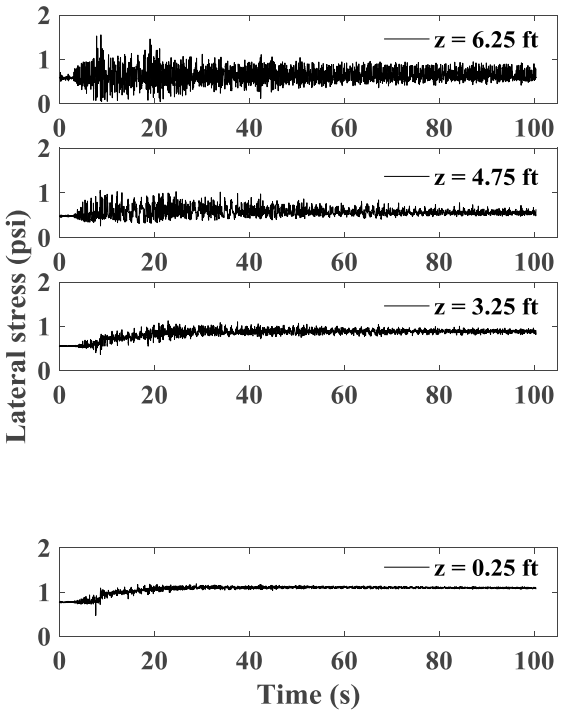

Figure A1.37 Time histories of lateral stress behind wall facing.

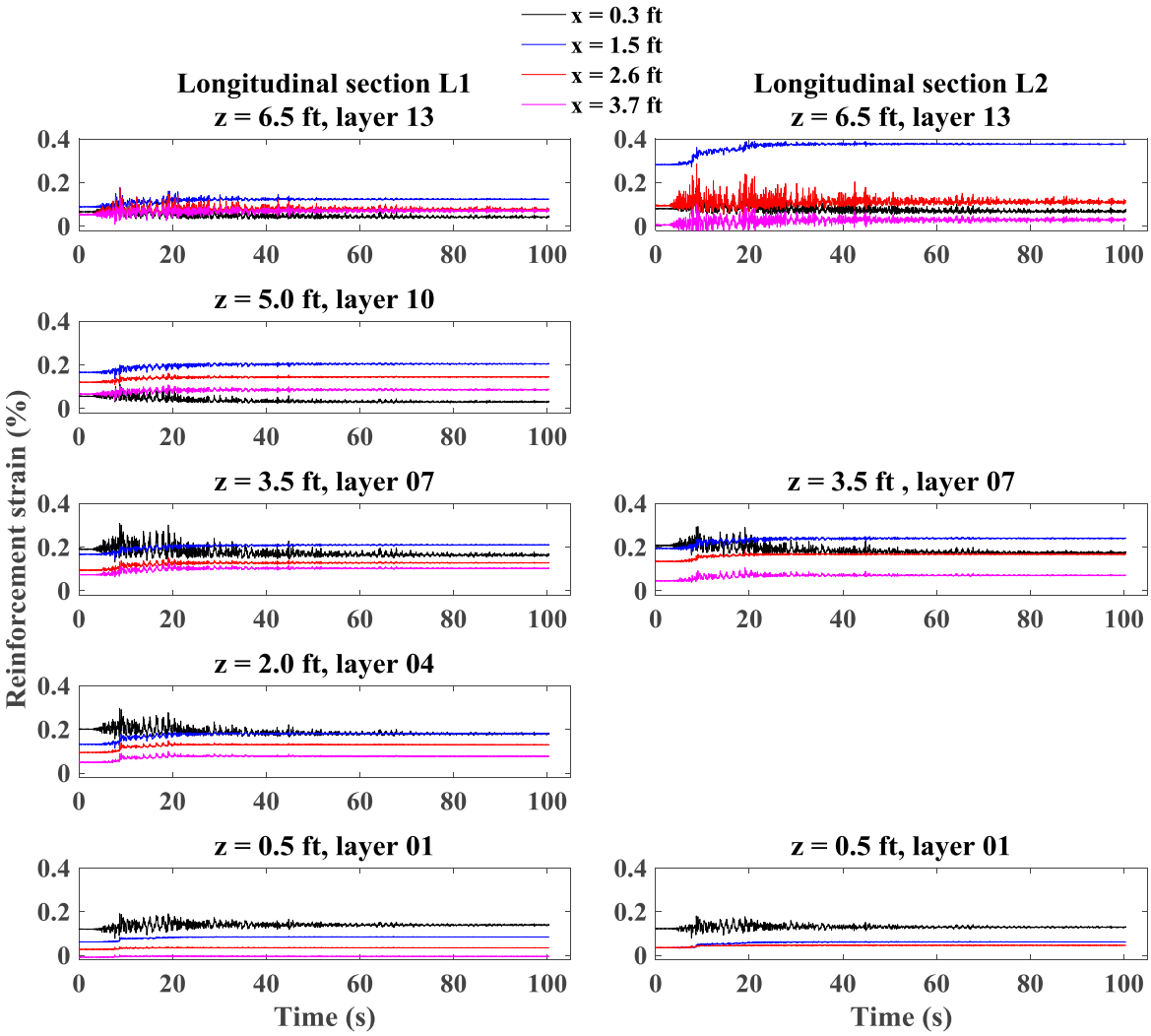

Figure A1.38 Time histories of reinforcement strain for longitudinal sections L1 and L2.

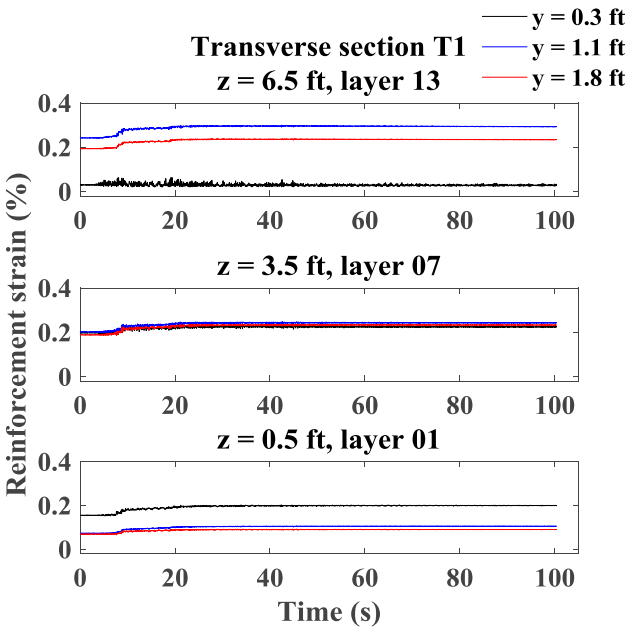

Figure A1.39 Time histories of reinforcement strain for transverse section T1.

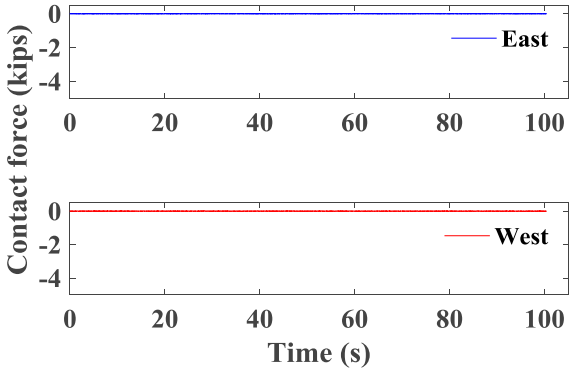

Figure A1.40 Time histories of contact force between bridge seat and bridge beam.

A1.1.3 Northridge Motion

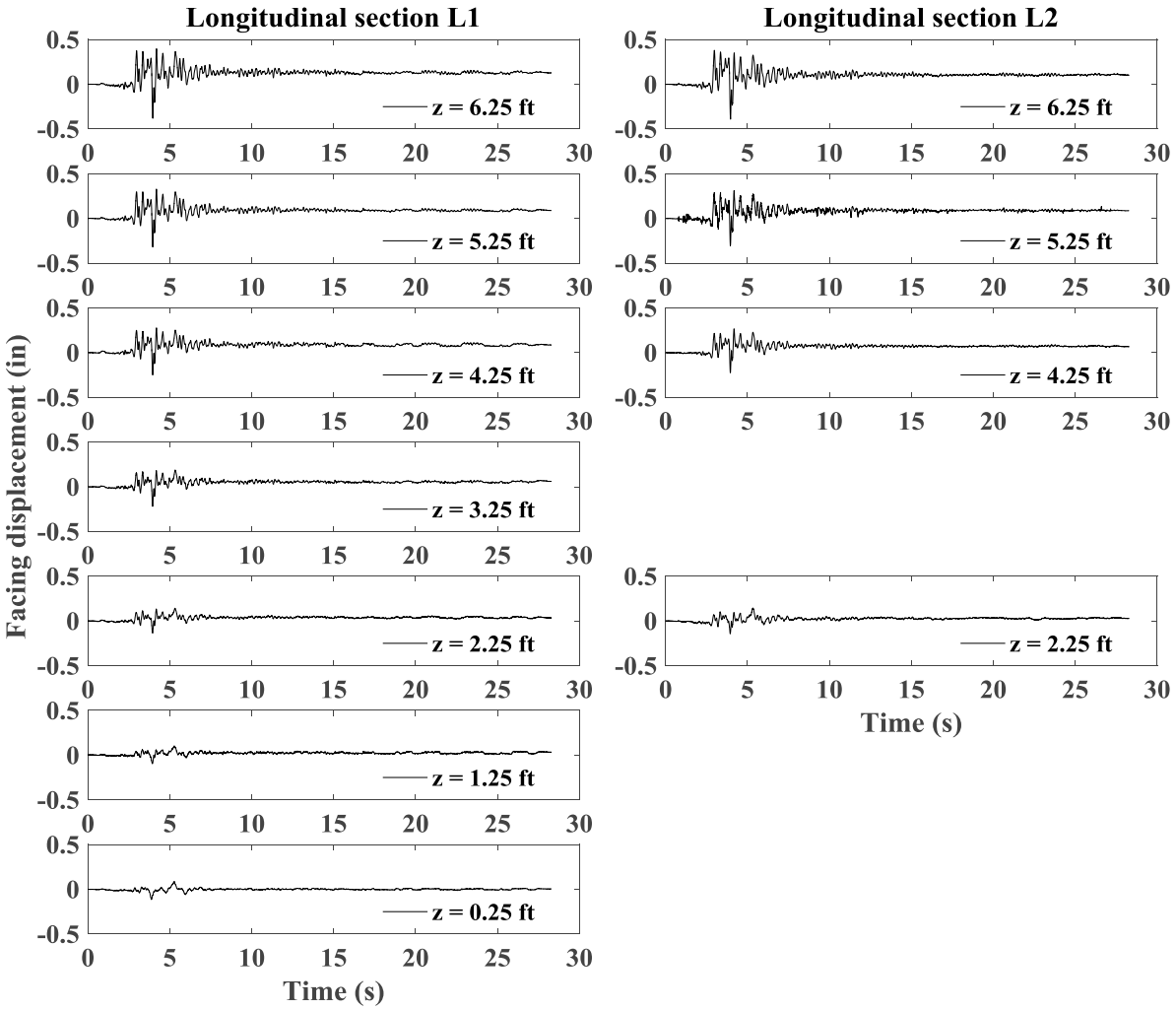

Figure A1.41 Time histories of incremental facing displacement for longitudinal sections L1 and L2.

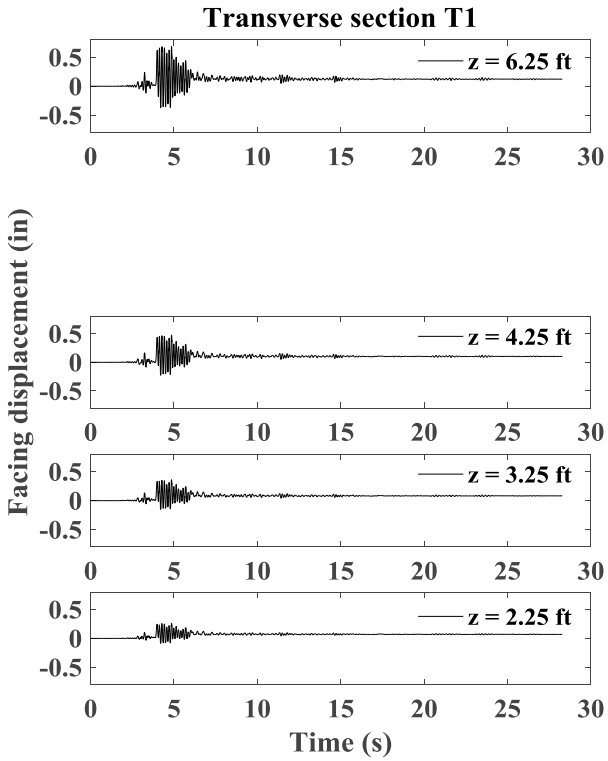

Figure A1.42 Time histories of incremental facing displacement for transverse section T1.

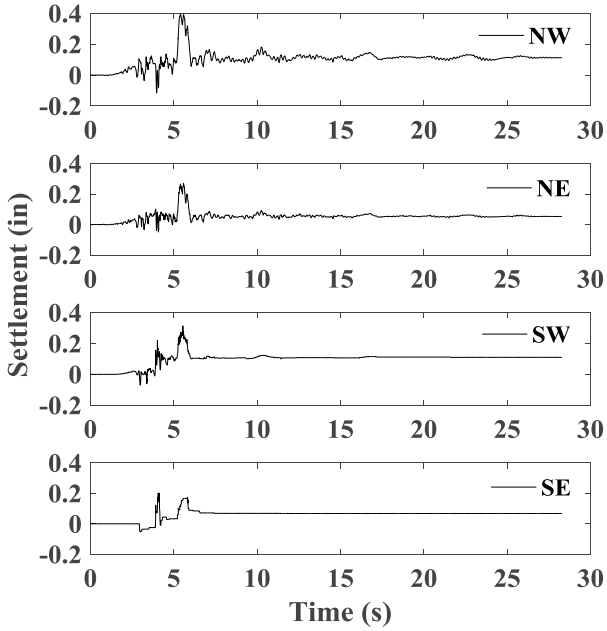

Figure A1.43 Time histories of incremental settlement for bridge seat.

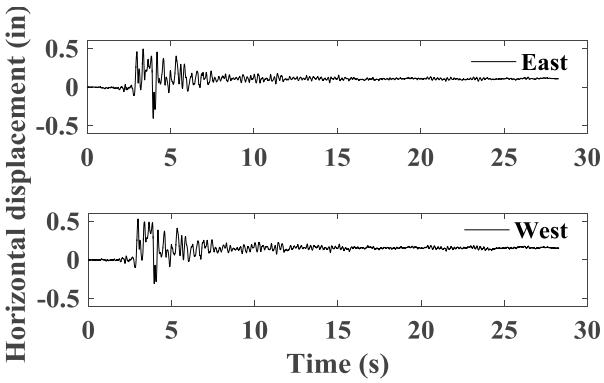

Figure A1.44 Time histories of incremental horizontal displacement for bridge seat.

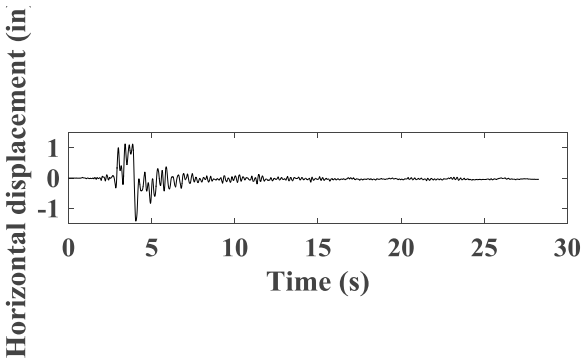

Figure A1.45 Time histories of incremental horizontal displacement for bridge beam.

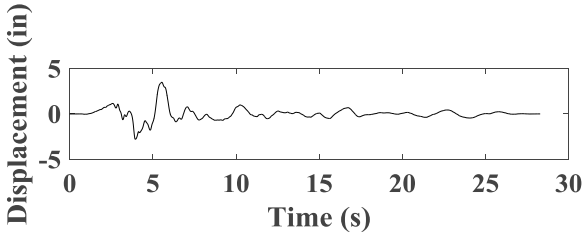

Figure A1.46 Time histories of horizontal displacement for shaking table.

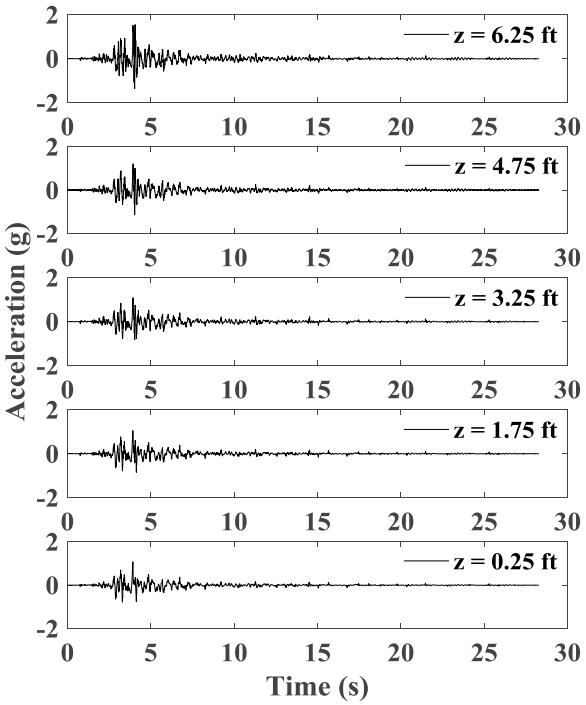

Figure A1.47 Time histories of acceleration for wall facing in longitudinal section L1.

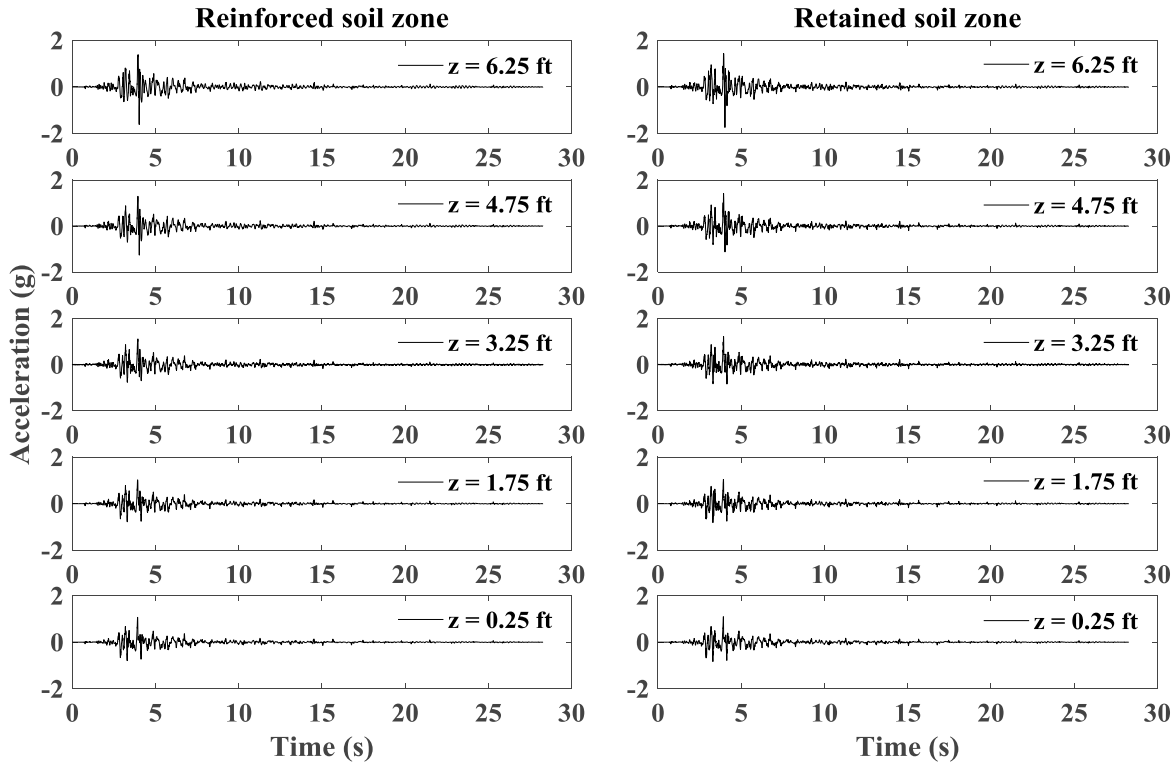

Figure A1.48 Time histories of acceleration for reinforced soil zone and retained soil zone in longitudinal section L1.

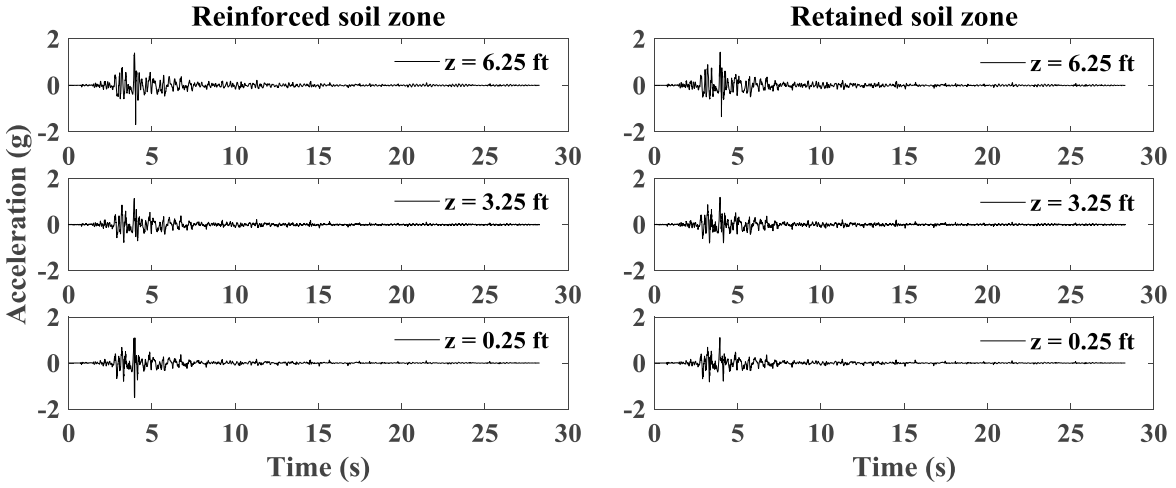

Figure A1.49 Time histories of acceleration for reinforced soil zone and retained soil zone in longitudinal section L2.

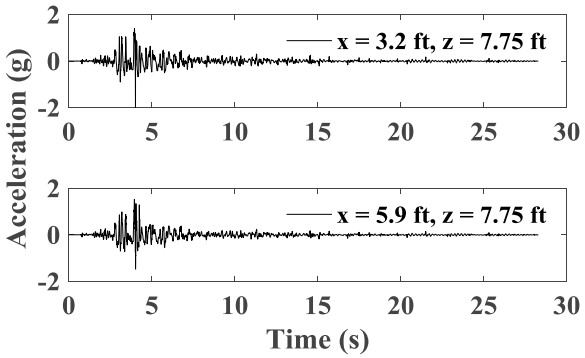

Figure A1.50 Time histories of acceleration for backfill soil in upper wall.

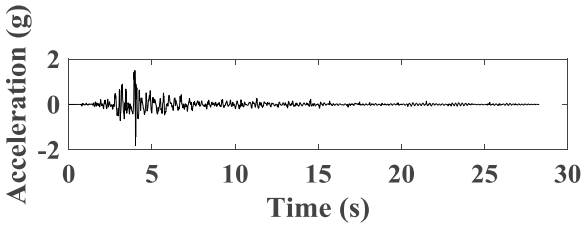

Figure A1.51 Time histories of acceleration for bridge seat.

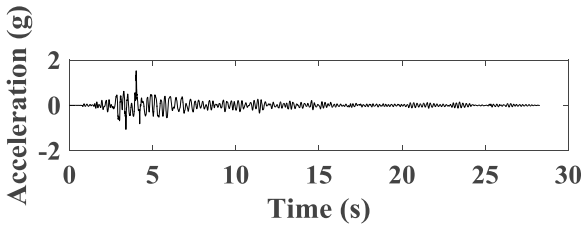

Figure A1.52 Time histories of acceleration for bridge beam.

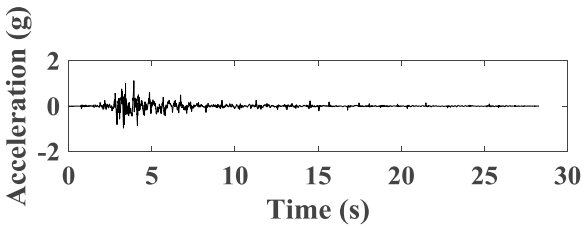

Figure A1.53 Time histories of acceleration for support wall.

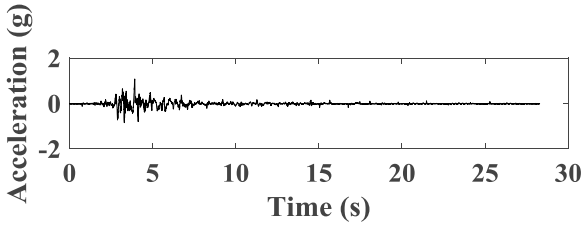

Figure A1.54 Time histories of acceleration for shaking table.

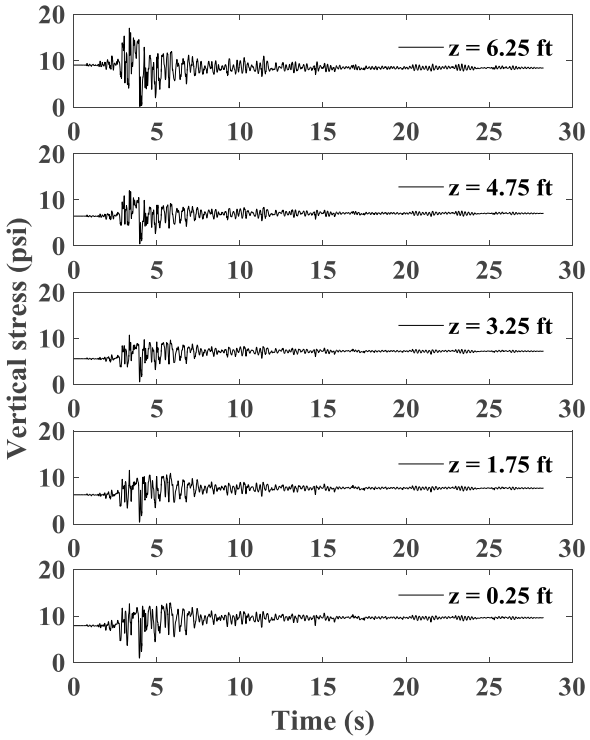

Figure A1.55 Time histories of vertical stress behind wall facing.

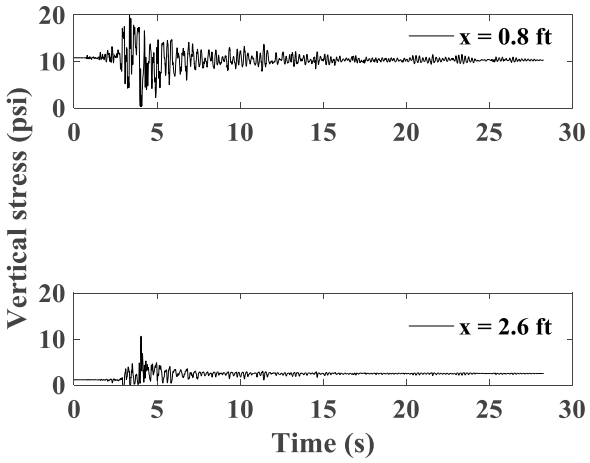

Figure A1.56 Time histories of vertical stress under bridge seat.

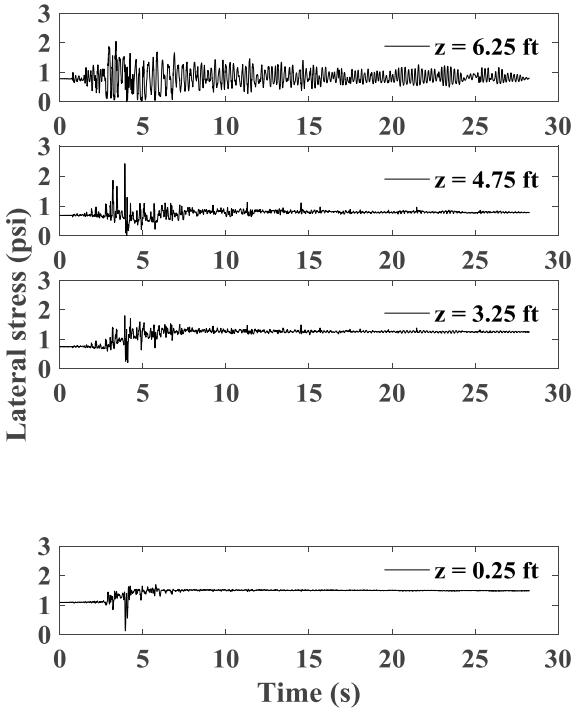

Figure A1.57 Time histories of lateral stress behind wall facing.

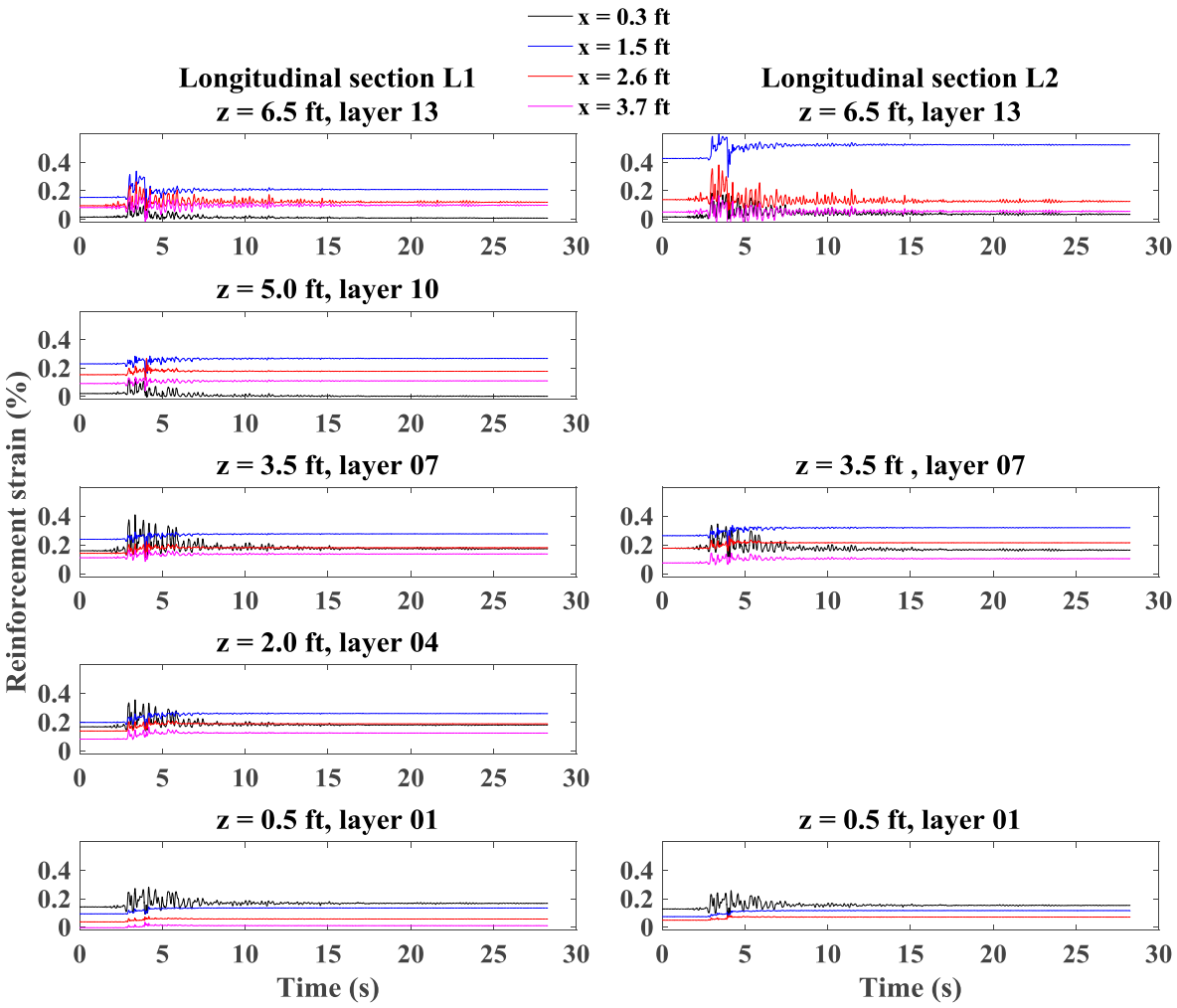

Figure A1.58 Time histories of reinforcement strain for longitudinal sections L1 and L2.

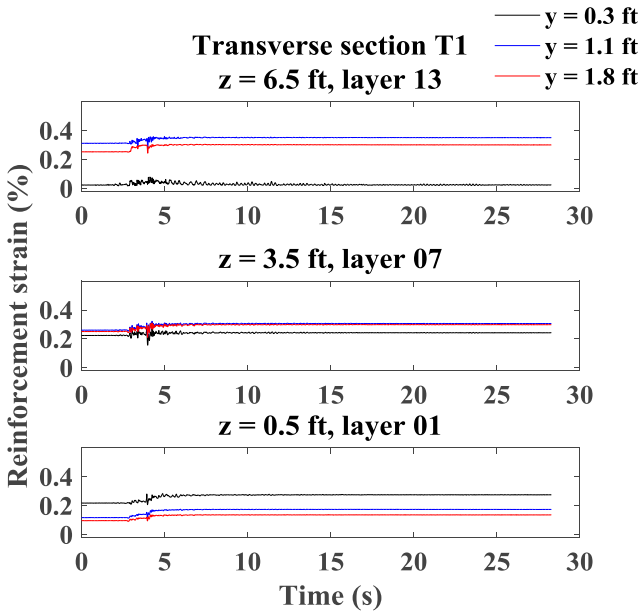

Figure A1.59 Time histories of reinforcement strain for transverse section T1.

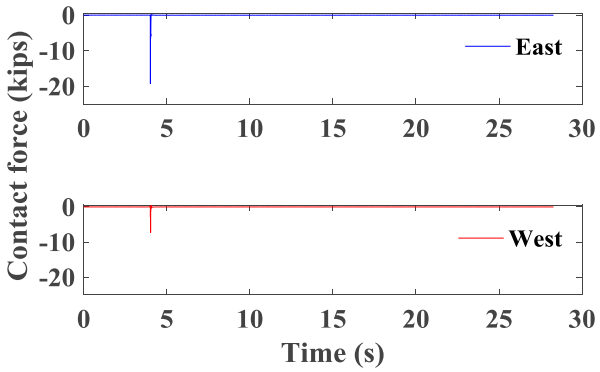

Figure A1.60 Time histories of contact force between bridge seat and bridge beam.

A1.2 Test 2

A1.2.1 Imperial Valley Motion

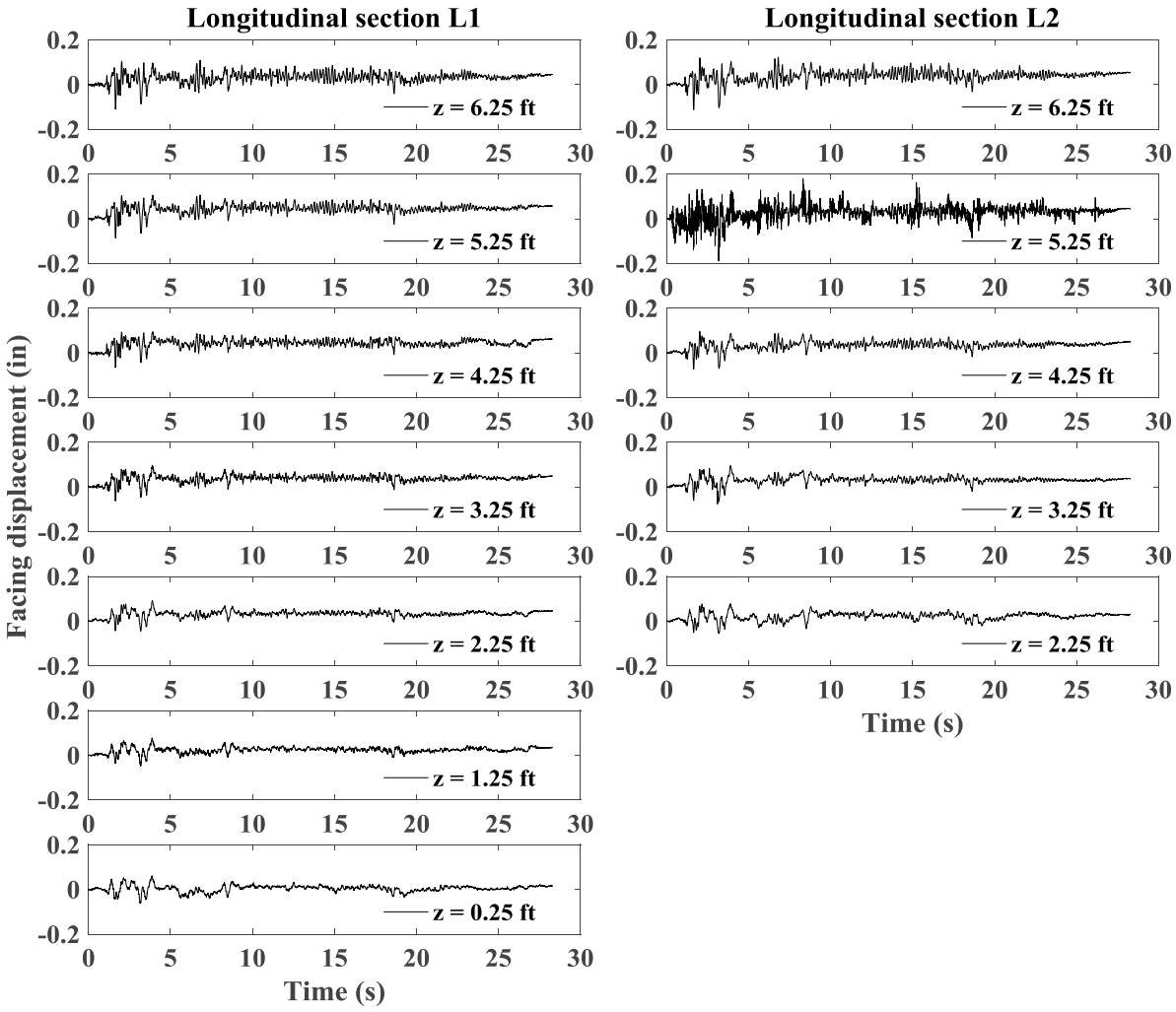

Figure A1.61 Time histories of incremental facing displacement for longitudinal sections L1 and L2.

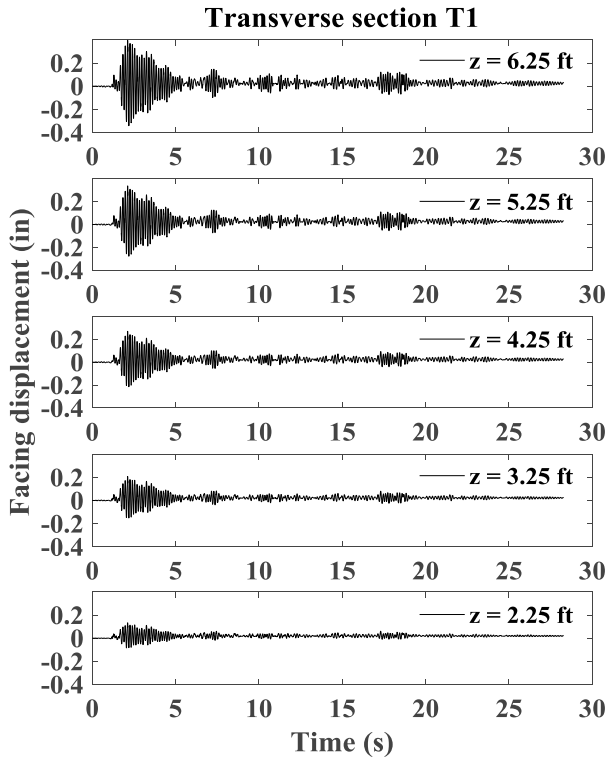

Figure A1.62 Time histories of incremental facing displacement for transverse section T1.

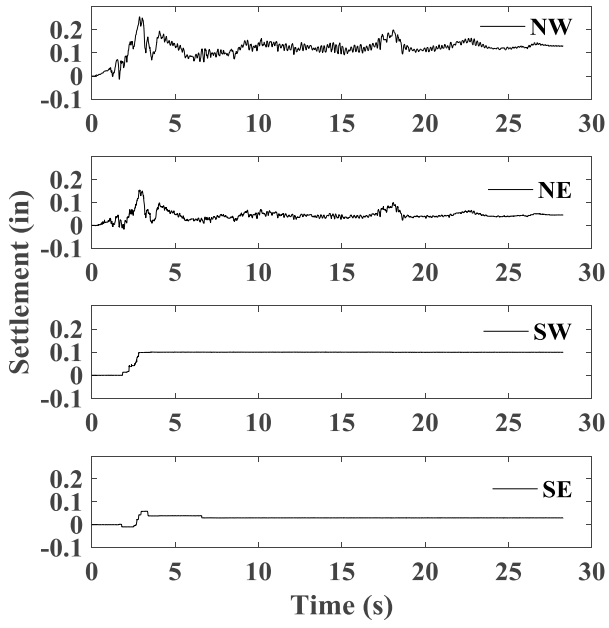

Figure A1.63 Time histories of incremental settlement for bridge seat.

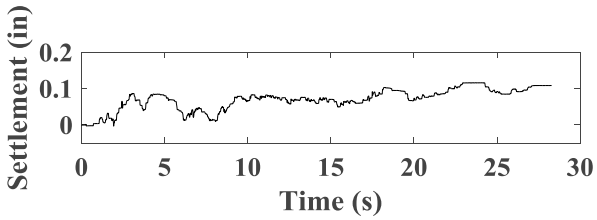

Figure A1.64 Time histories of incremental settlement for backfill soil in upper wall.

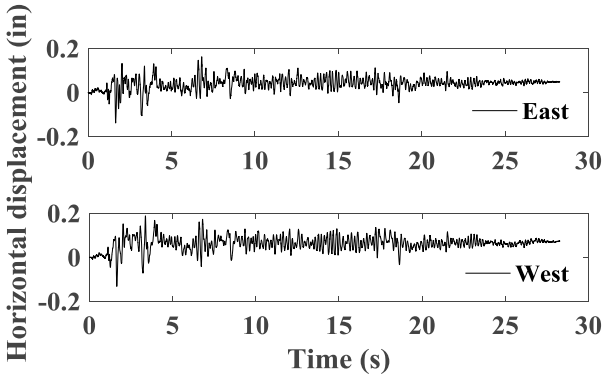

Figure A1.65 Time histories of incremental horizontal displacement for bridge seat.

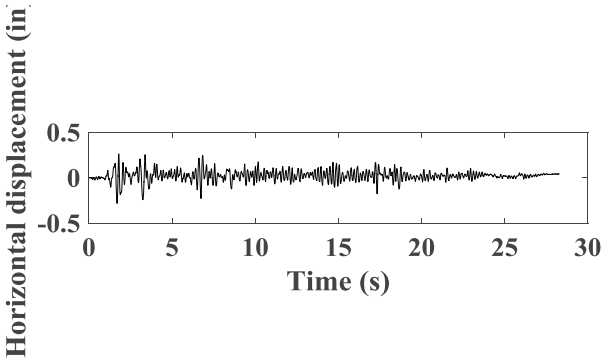

Figure A1.66 Time histories of incremental horizontal displacement for bridge beam.

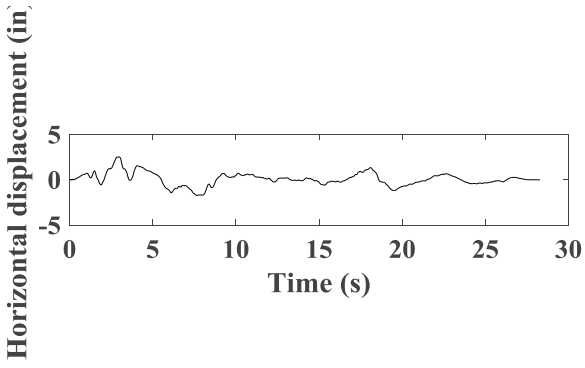

Figure A1.67 Time histories of horizontal displacement for support wall.

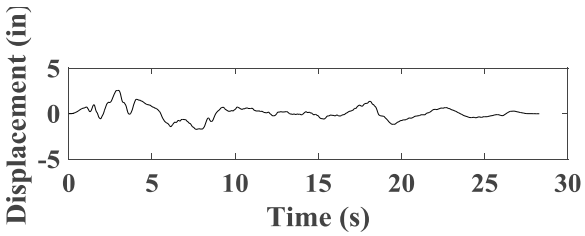

Figure A1.68 Time histories of horizontal displacement for shaking table.

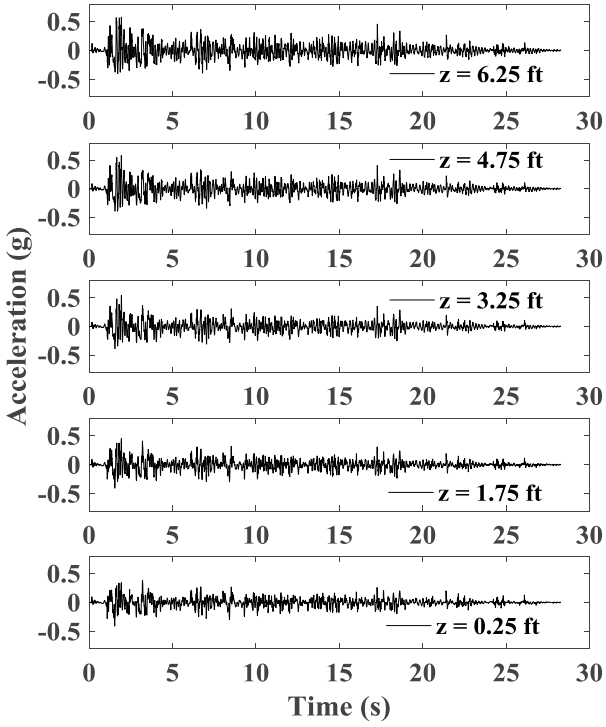

Figure A1.69 Time histories of acceleration for wall facing in longitudinal section L1.

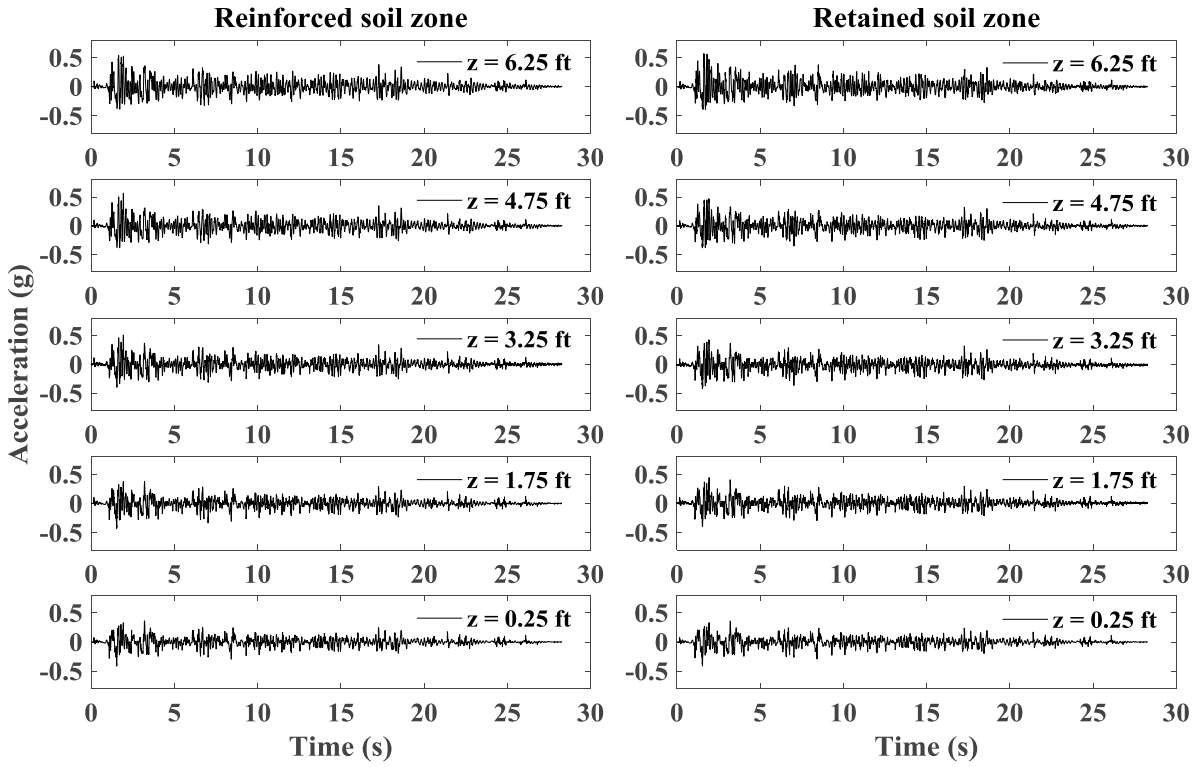

Figure A1.70 Time histories of acceleration for reinforced soil zone and retained soil zone in longitudinal section L1.

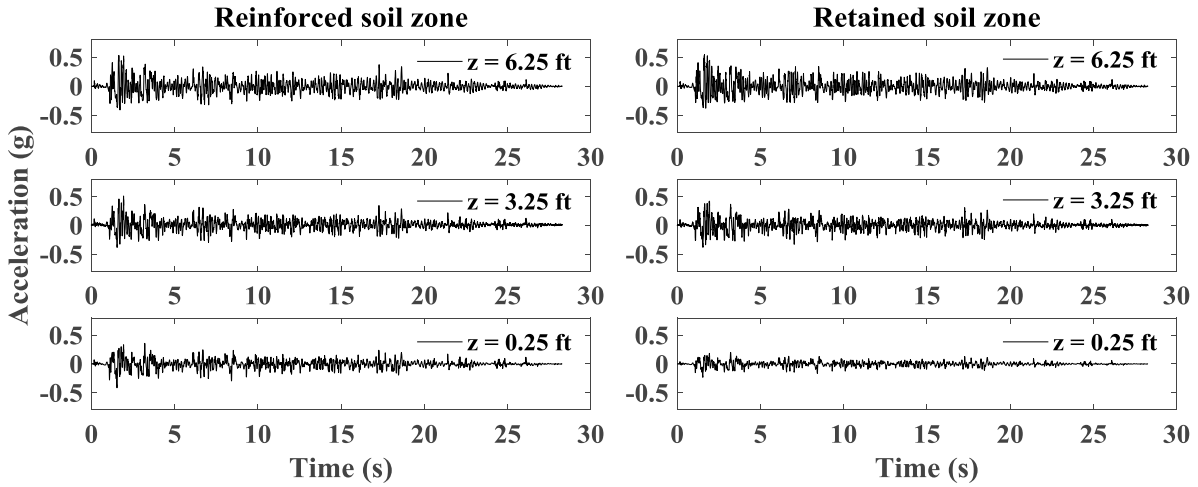

Figure A1.71 Time histories of acceleration for reinforced soil zone and retained soil zone in longitudinal section L2.

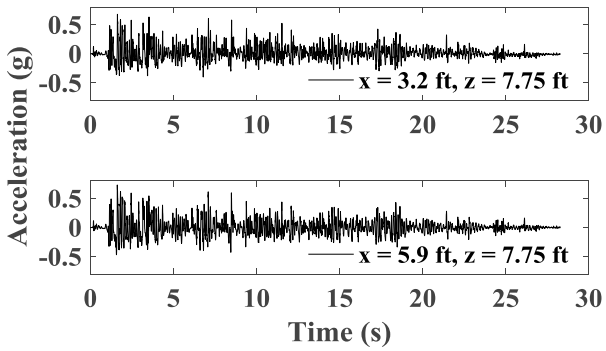

Figure A1.72 Time histories of acceleration for backfill soil in upper wall.

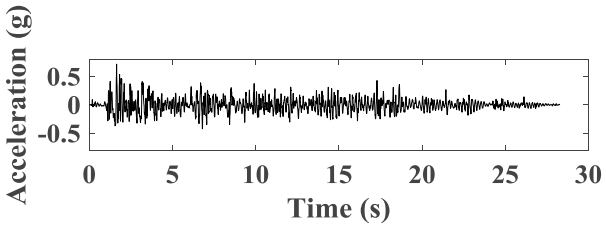

Figure A1.73 Time histories of acceleration for bridge seat.

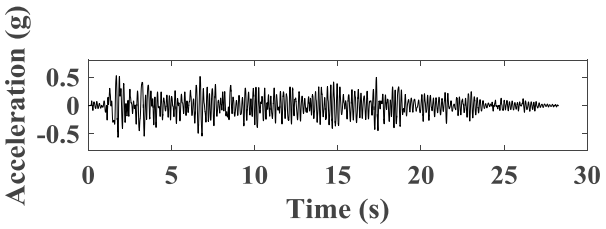

Figure A1.74 Time histories of acceleration for bridge beam.

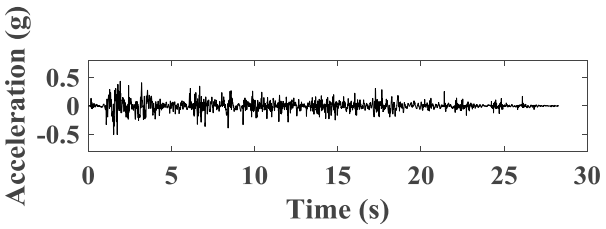

Figure A1.75 Time histories of acceleration for support wall.

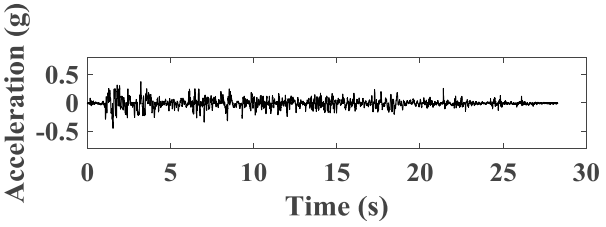

Figure A1.76 Time histories of acceleration for shaking table.

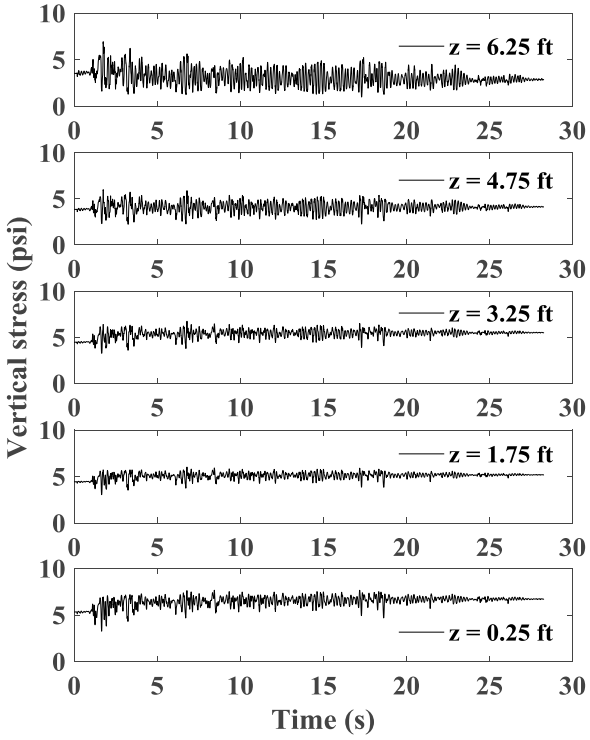

Figure A1.77 Time histories of vertical stress behind wall facing.

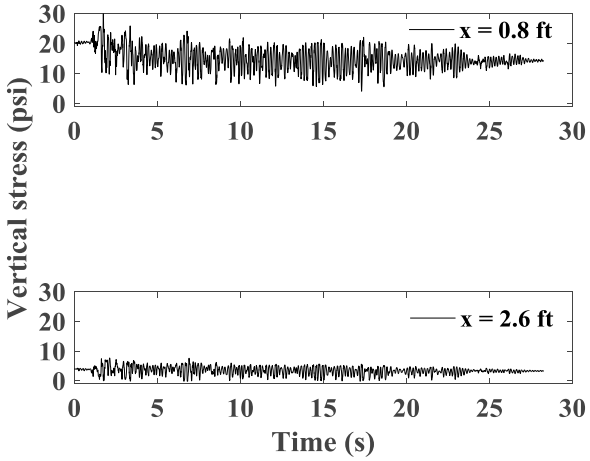

Figure A1.78 Time histories of vertical stress under bridge seat.

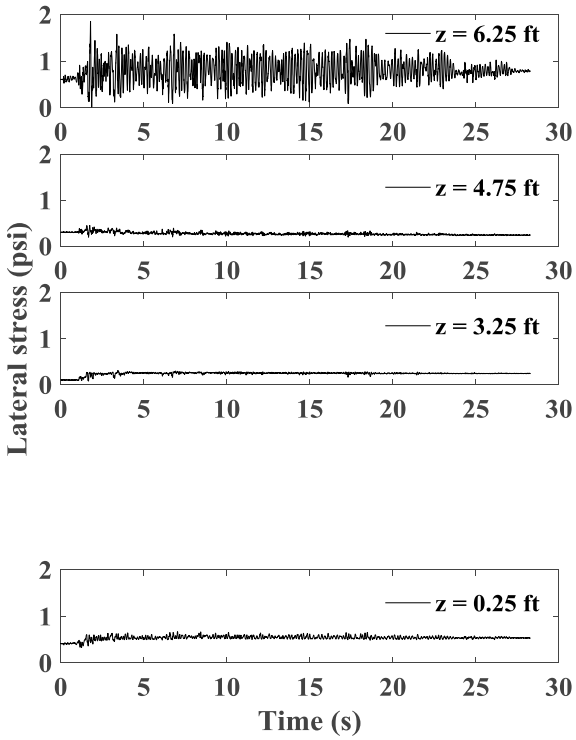

Figure A1.79 Time histories of lateral stress behind wall facing.

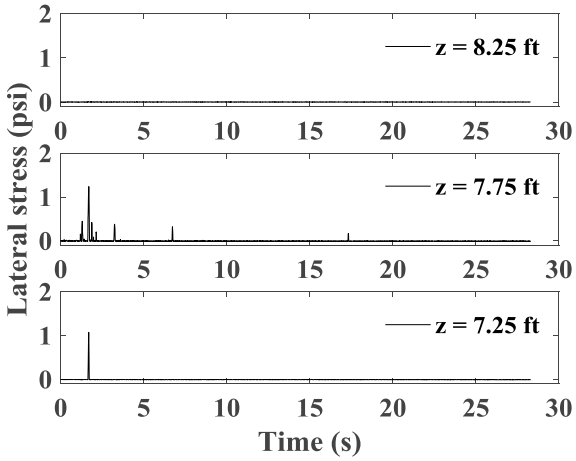

Figure A1.80 Time histories of lateral stress behind upper wall.

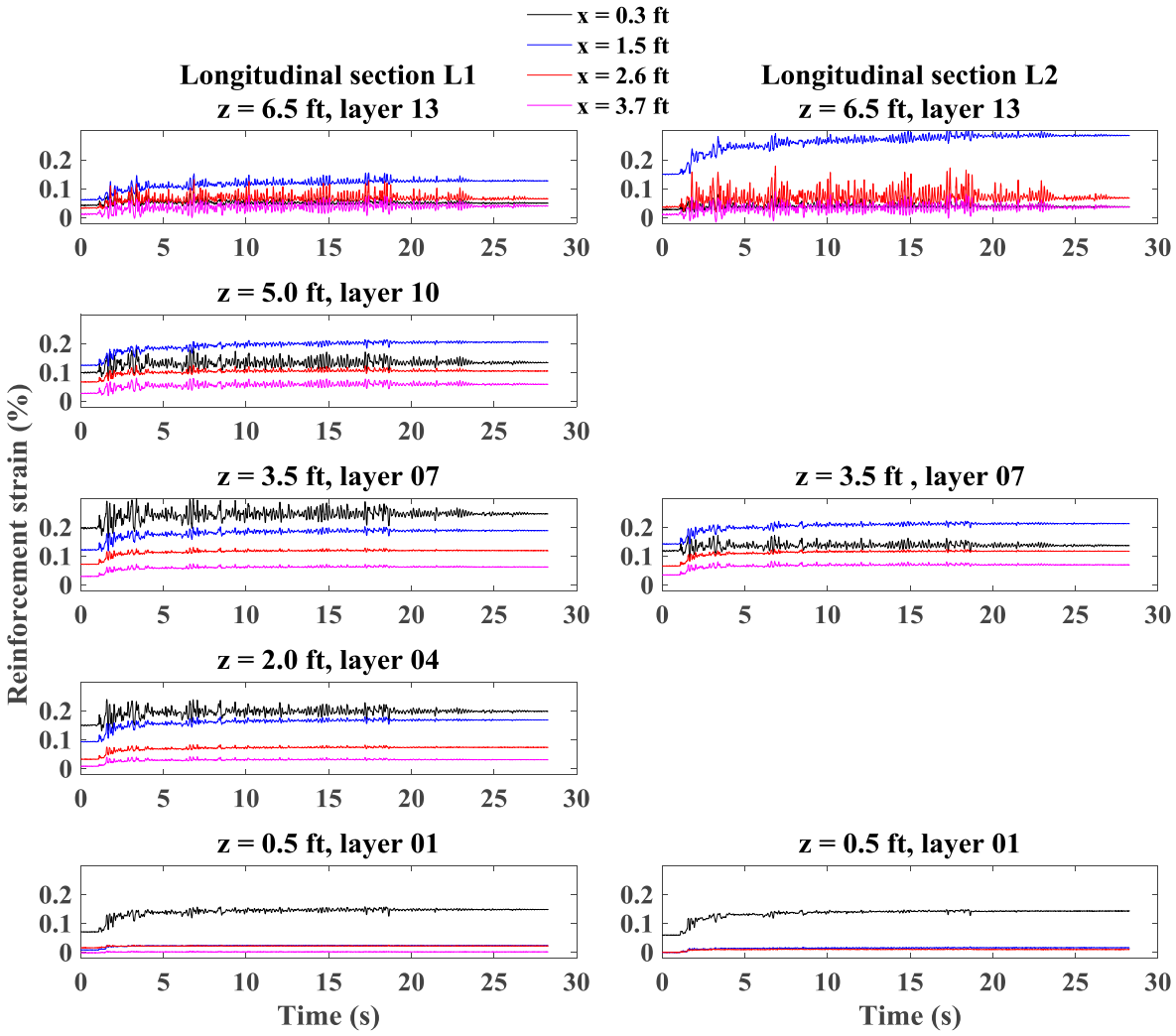

Figure A1.81 Time histories of reinforcement strain for longitudinal sections L1 and L2.

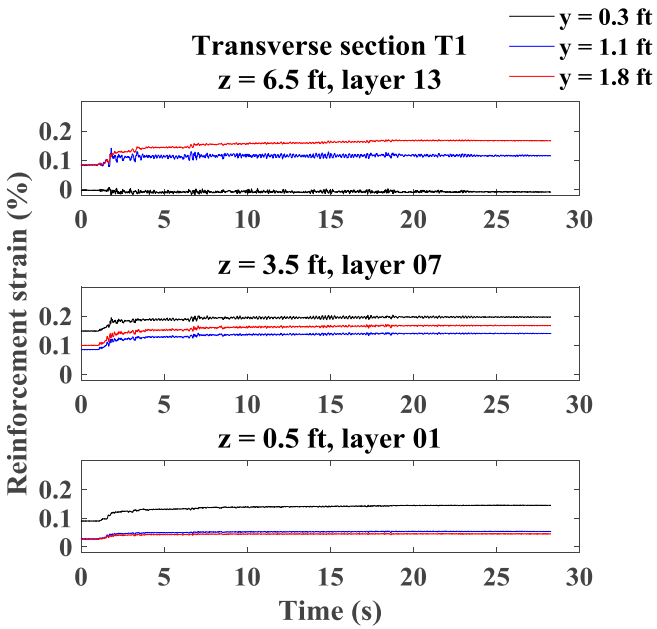

Figure A1.82 Time histories of reinforcement strain for transverse section T1.

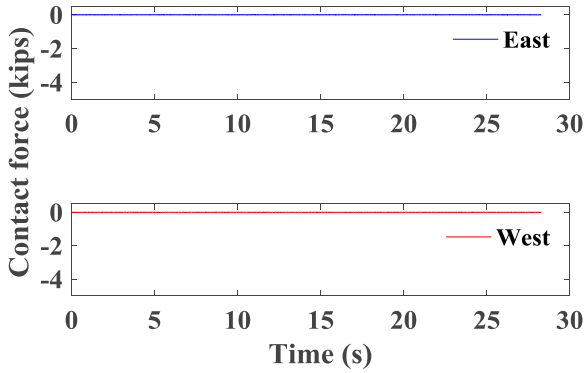

Figure A1.83 Time histories of contact force between bridge seat and bridge beam.

A1.2.2 Maule Motion

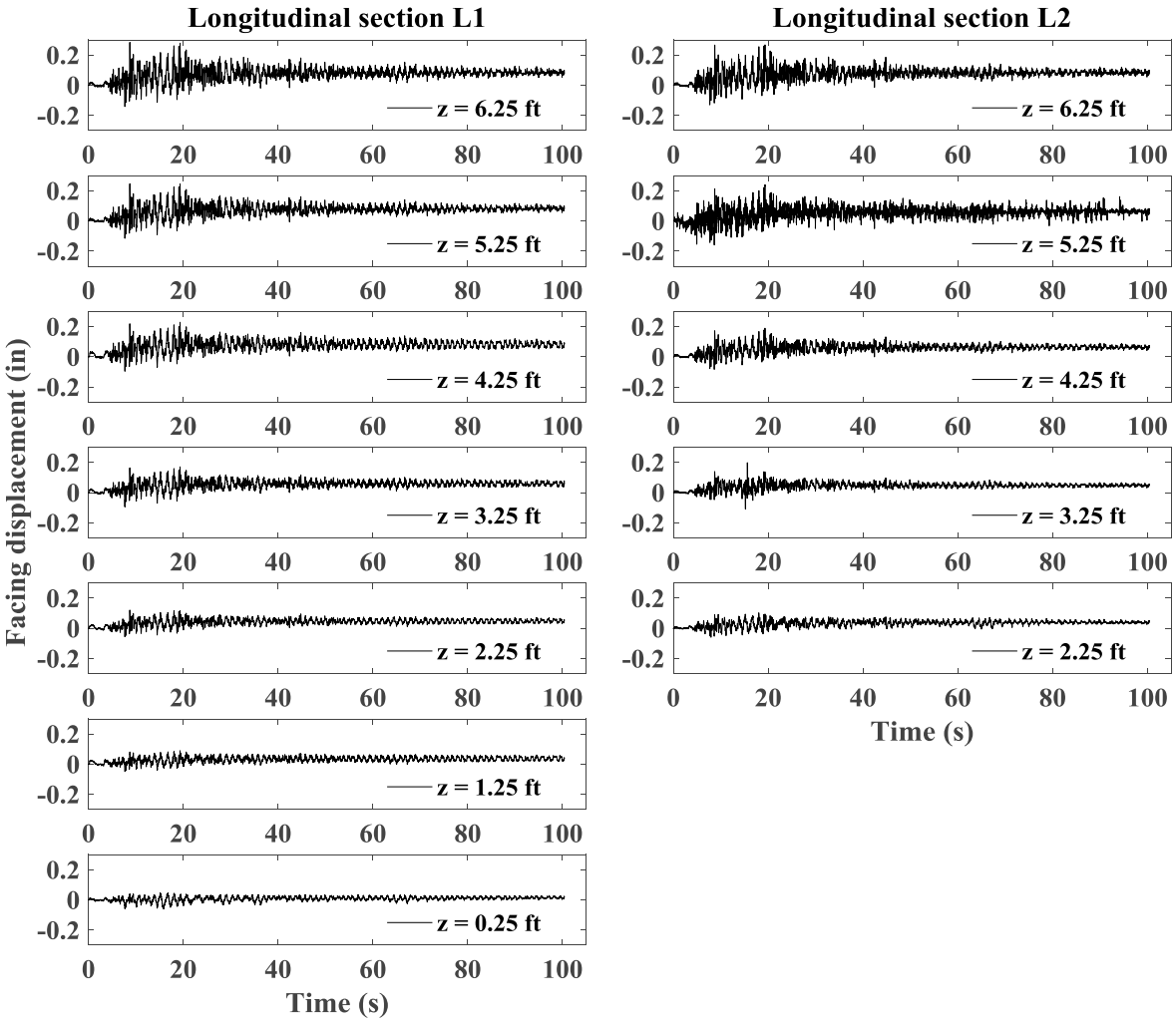

Figure A1.84 Time histories of incremental facing displacement for longitudinal sections L1 and L2.

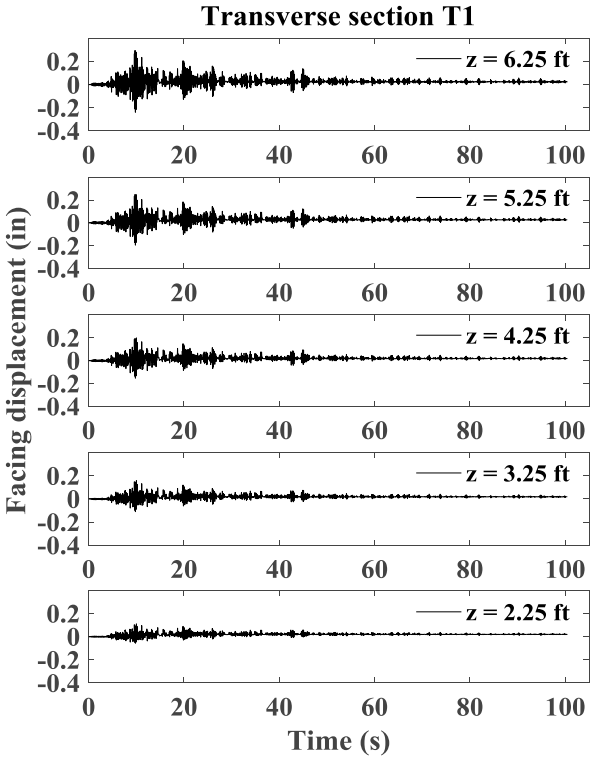

Figure A1.85 Time histories of incremental facing displacement for transverse section T1.

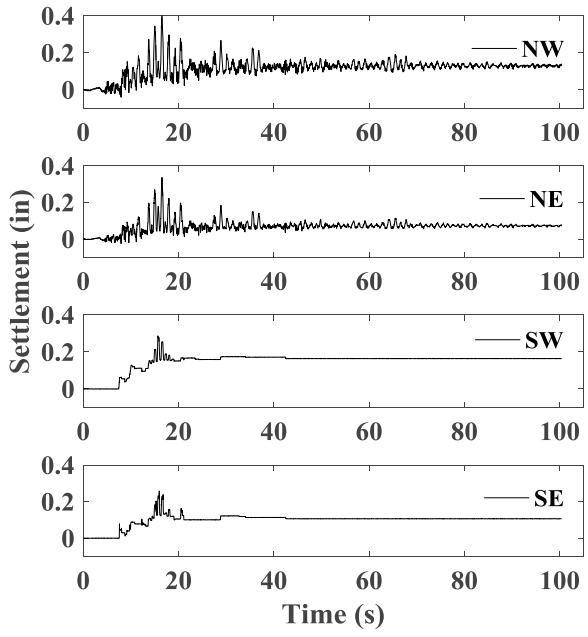

Figure A1.86 Time histories of incremental settlement for bridge seat.

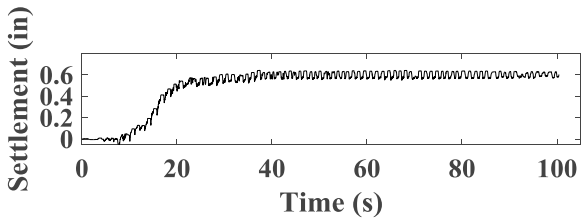

Figure A1.87 Time histories of incremental settlement for backfill soil in upper wall.

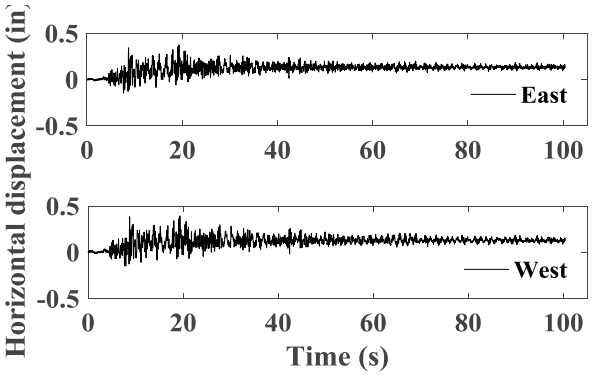

Figure A1.88 Time histories of incremental horizontal displacement for bridge seat.

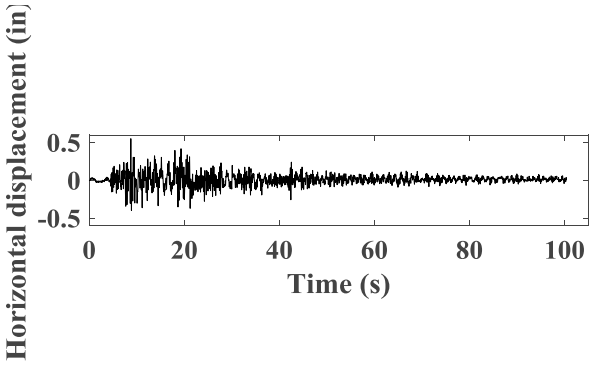

Figure A1.89 Time histories of incremental horizontal displacement for bridge beam.

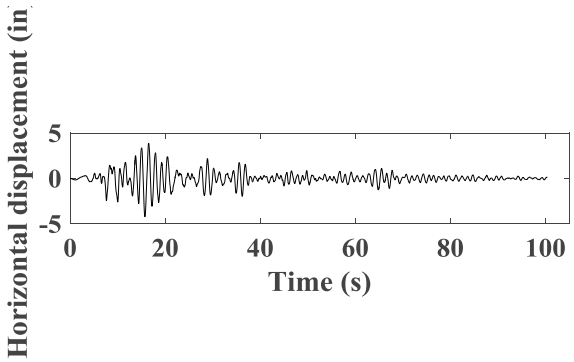

Figure A1.90 Time histories of horizontal displacement for support wall.

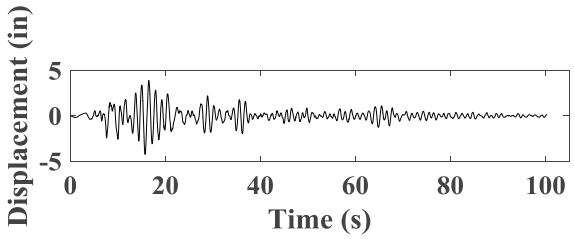

Figure A1.91 Time histories of horizontal displacement for shaking table.

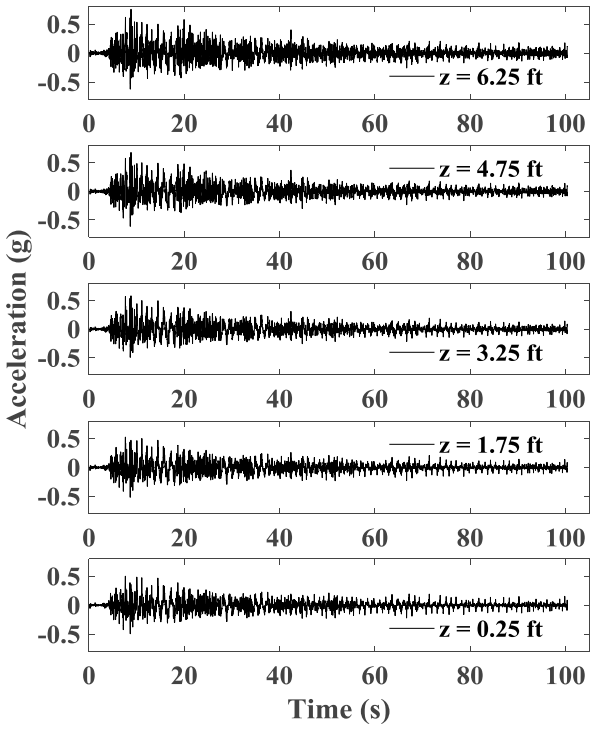

Figure A1.92 Time histories of acceleration for wall facing in longitudinal section L1.

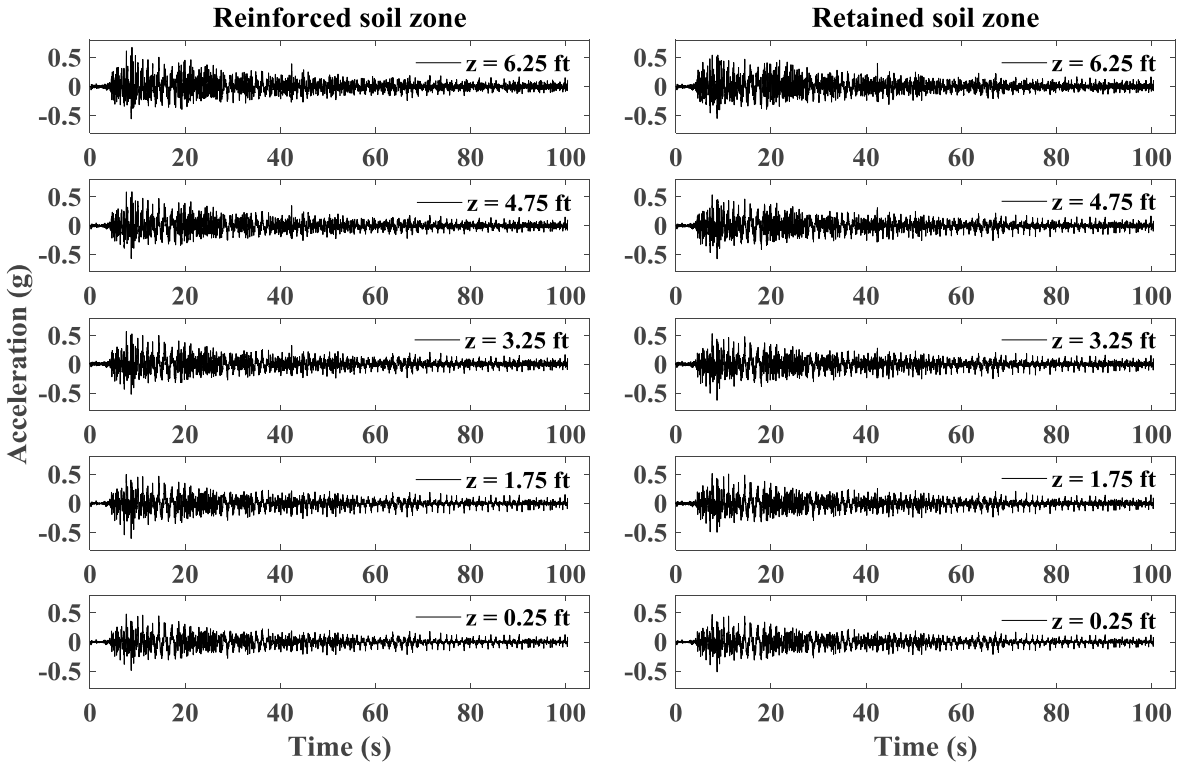

Figure A1.93 Time histories of acceleration for reinforced soil zone and retained soil zone in longitudinal section L1.

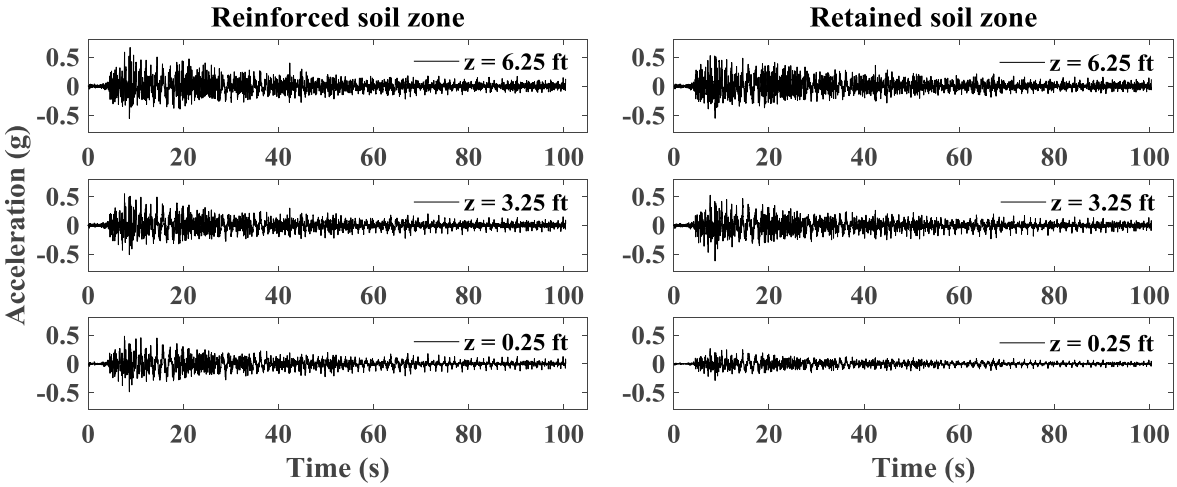

Figure A1.94 Time histories of acceleration for reinforced soil zone and retained soil zone in longitudinal section L2.

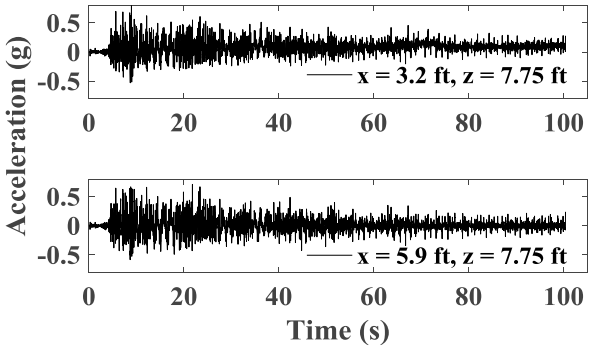

Figure A1.95 Time histories of acceleration for backfill soil in upper wall.

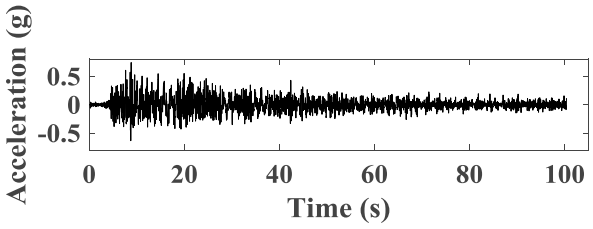

Figure A1.96 Time histories of acceleration for bridge seat.

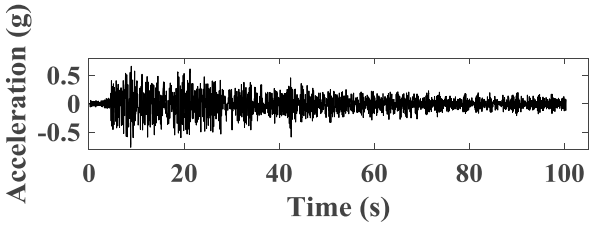

Figure A1.97 Time histories of acceleration for bridge beam.

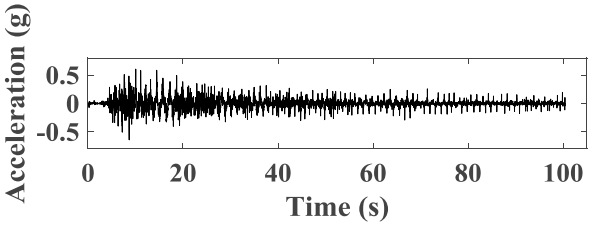

Figure A1.98 Time histories of acceleration for support wall.

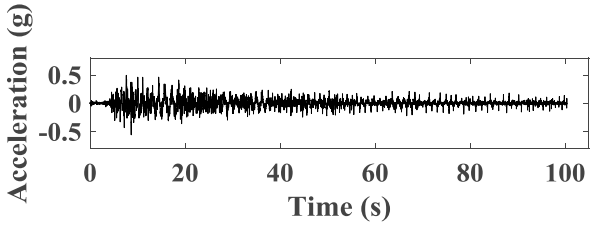

Figure A1.99 Time histories of acceleration for shaking table.

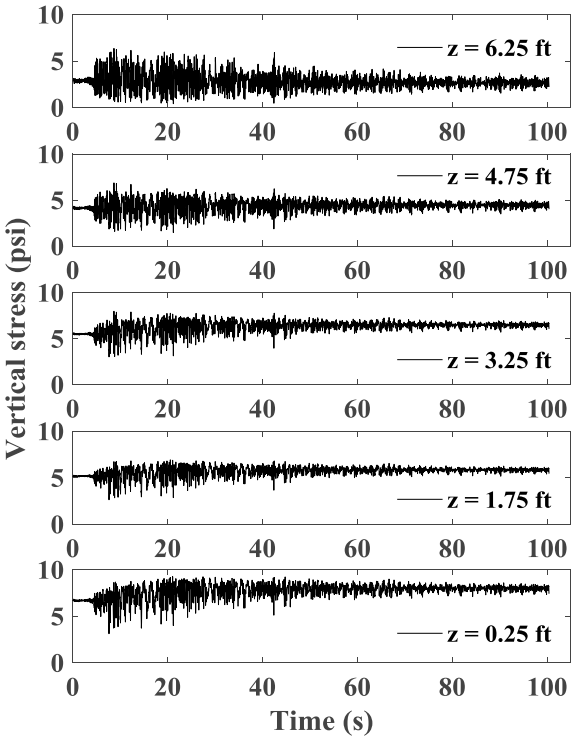

Figure A1.100 Time histories of vertical stress behind wall facing.

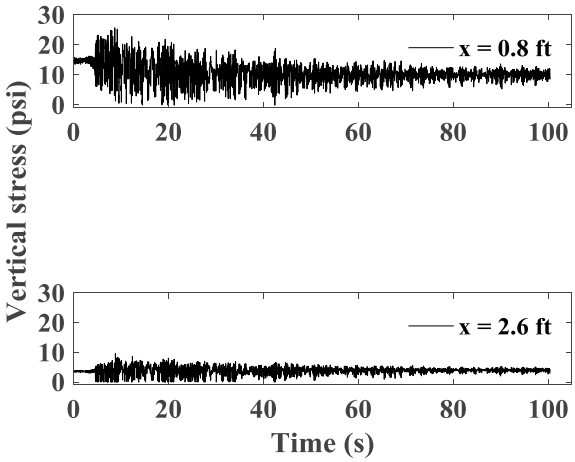

Figure A1.101 Time histories of vertical stress under bridge seat.

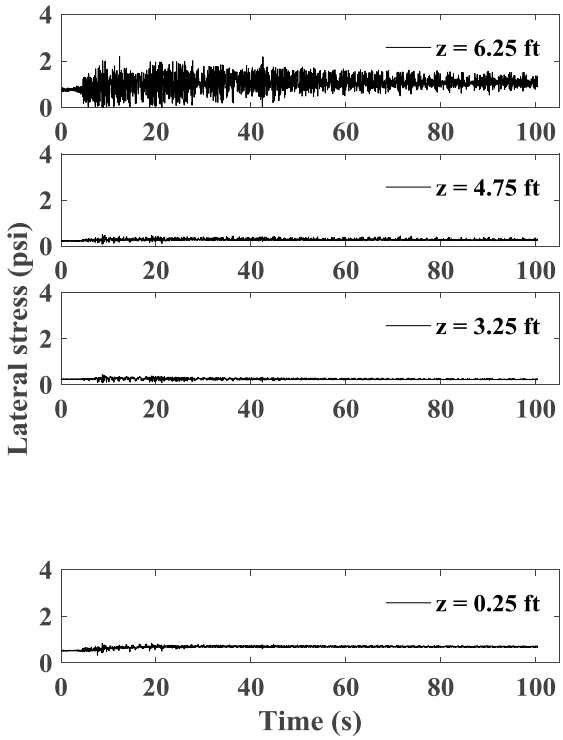

Figure A1.102 Time histories of lateral stress behind wall facing.

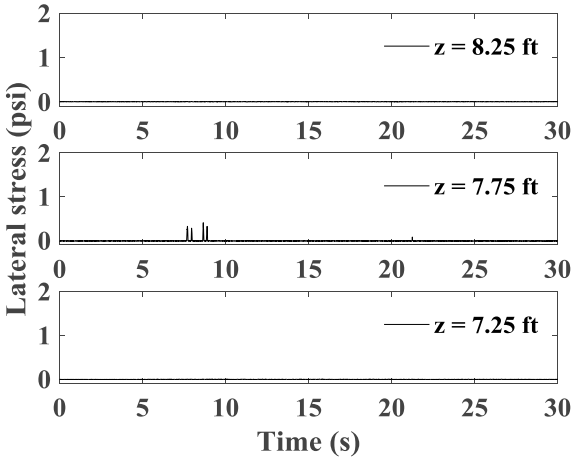

Figure A1.103 Time histories of lateral stress behind upper wall.

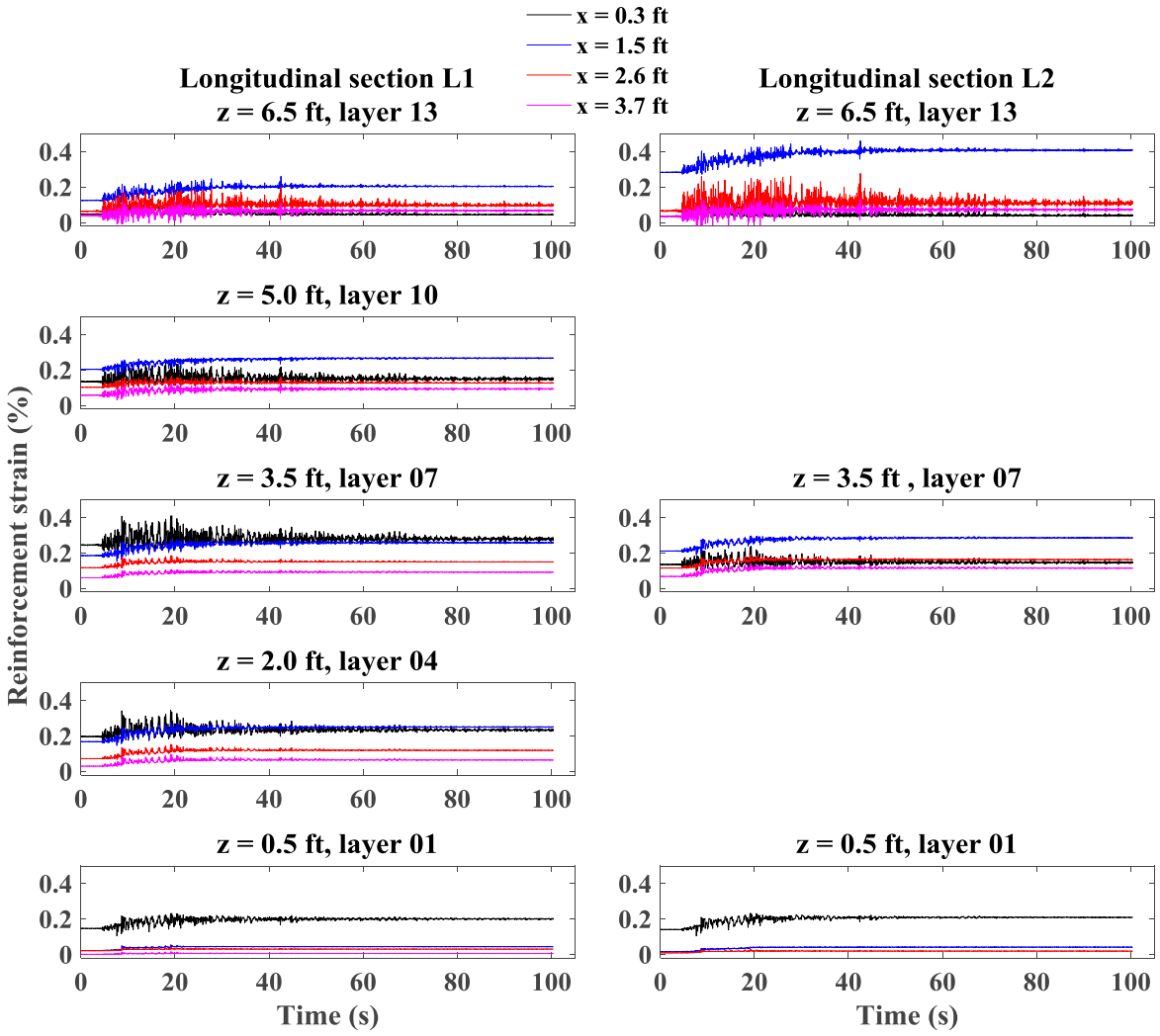

Figure A1.104 Time histories of reinforcement strain for longitudinal sections L1 and L2.

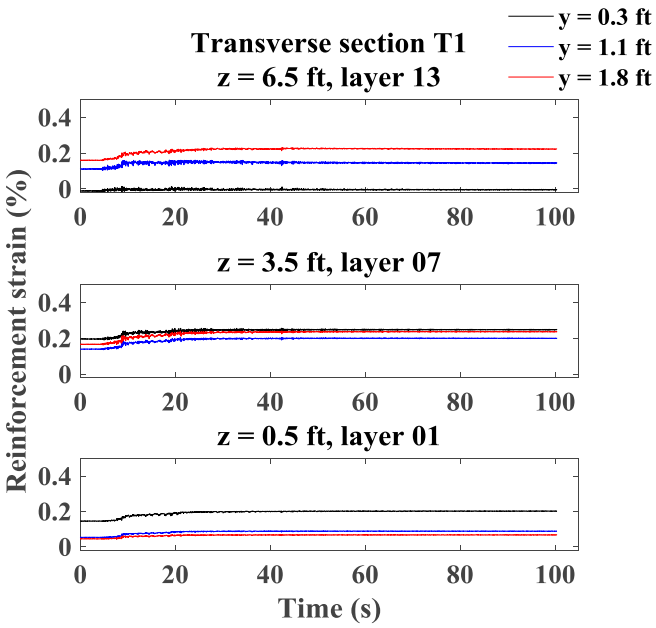

Figure A1.105 Time histories of reinforcement strain for transverse section T1.

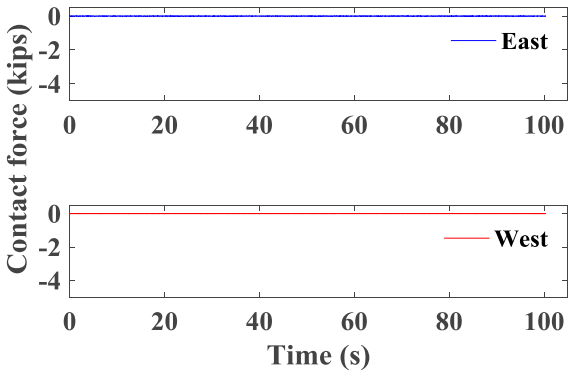

Figure A1.106 Time histories of contact force between bridge seat and bridge beam.

A1.2.3 Northridge Motion

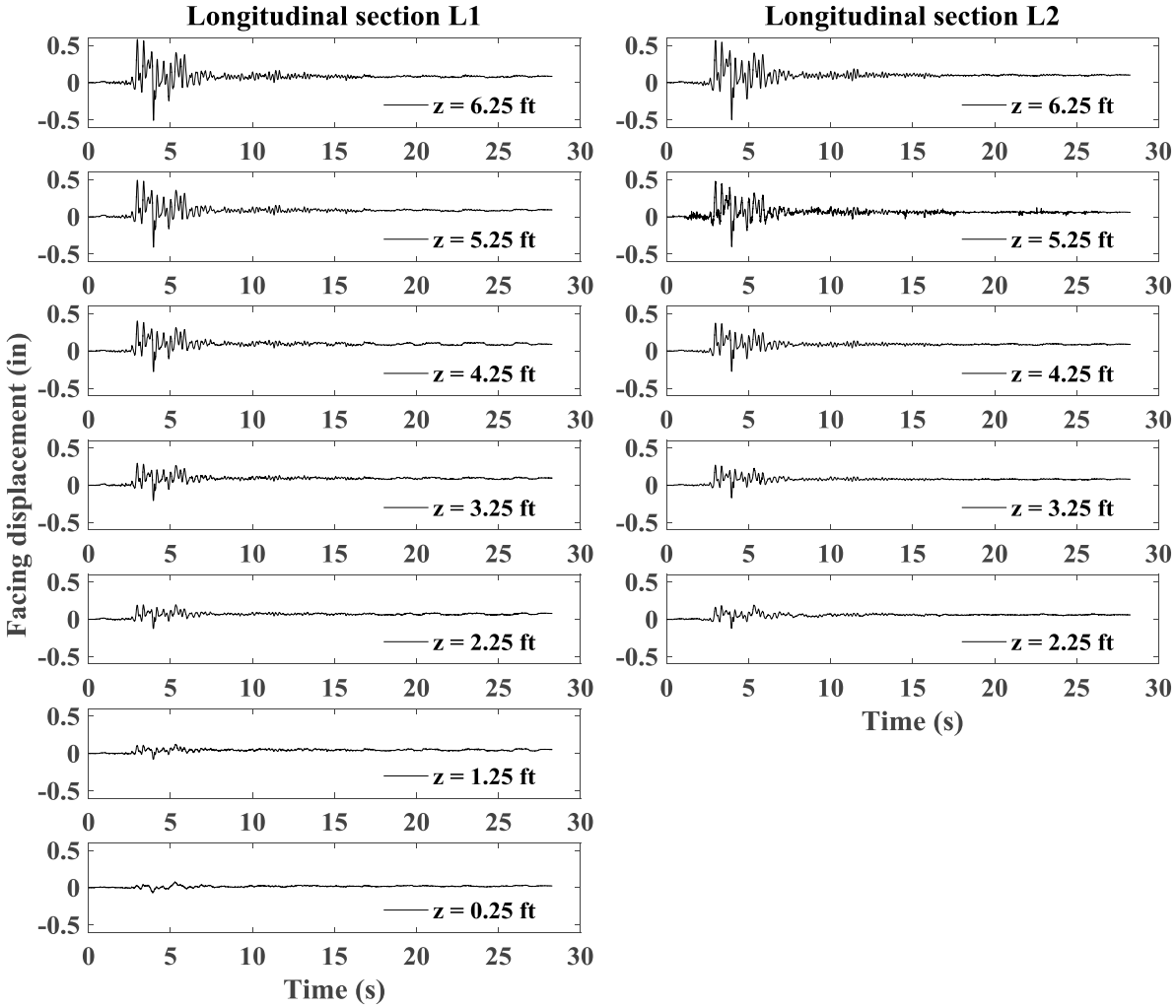

Figure A1.107 Time histories of incremental facing displacement for longitudinal sections L1 and L2.

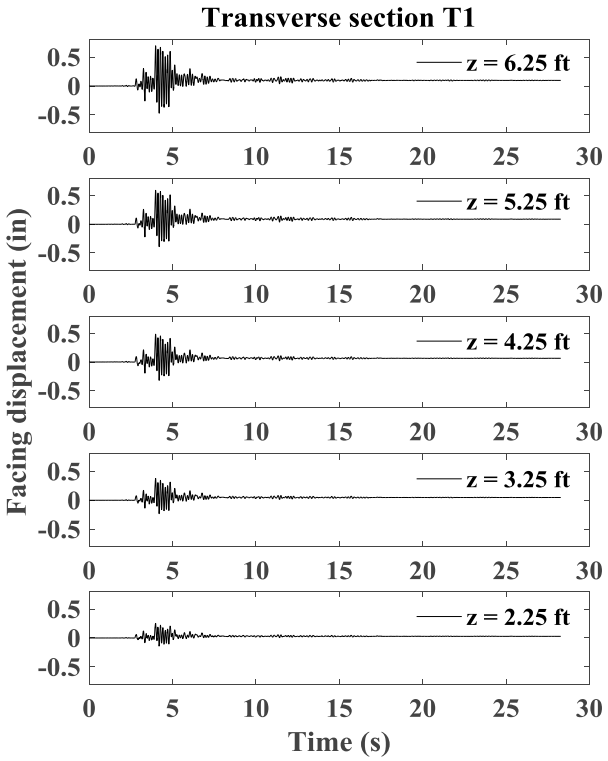

Figure A1.108 Time histories of incremental facing displacement for transverse section T1.

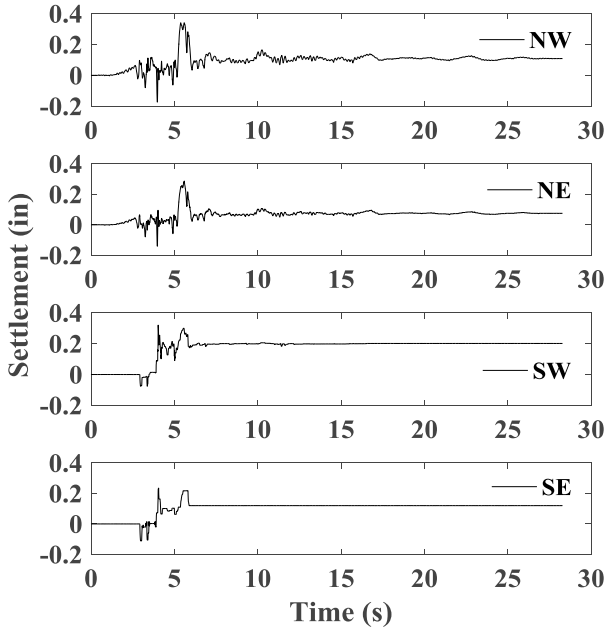

Figure A1.109 Time histories of incremental settlement for bridge seat.

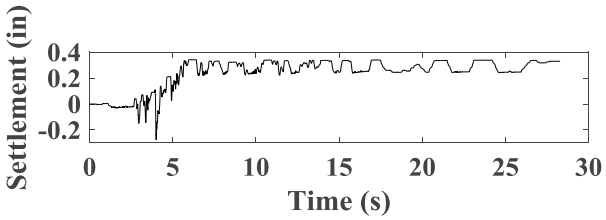

Figure A1.110 Time histories of incremental settlement for backfill soil in upper wall.

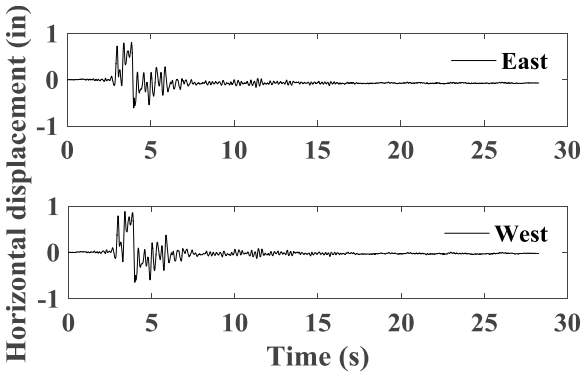

Figure A1.111 Time histories of incremental horizontal displacement for bridge seat.

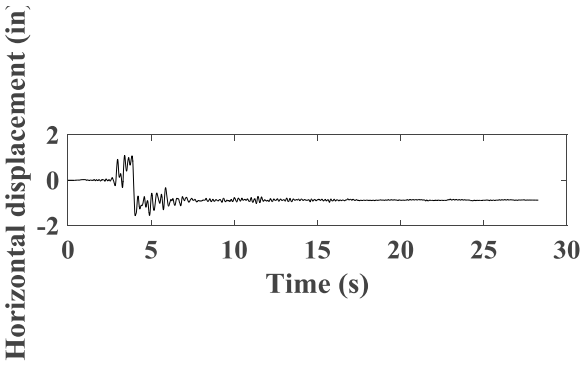

Figure A1.112 Time histories of incremental horizontal displacement for bridge beam.

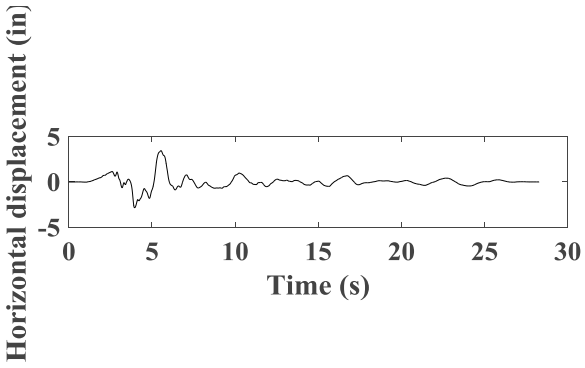

Figure A1.113 Time histories of horizontal displacement for support wall.

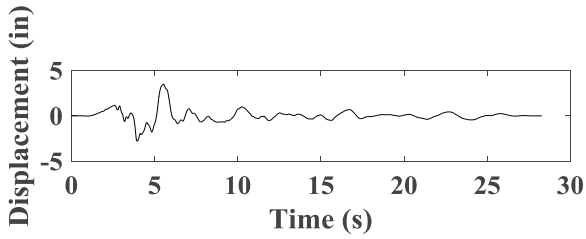

Figure A1.114 Time histories of horizontal displacement for shaking table.

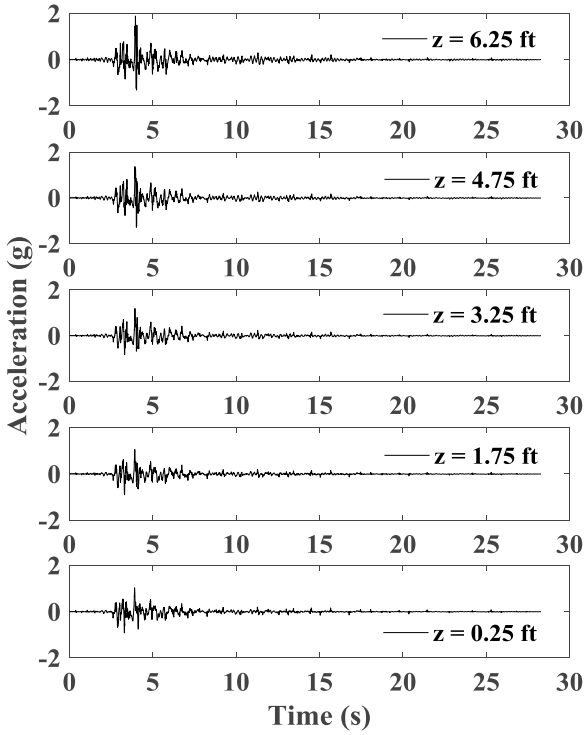

Figure A1.115 Time histories of acceleration for wall facing in longitudinal section L1.

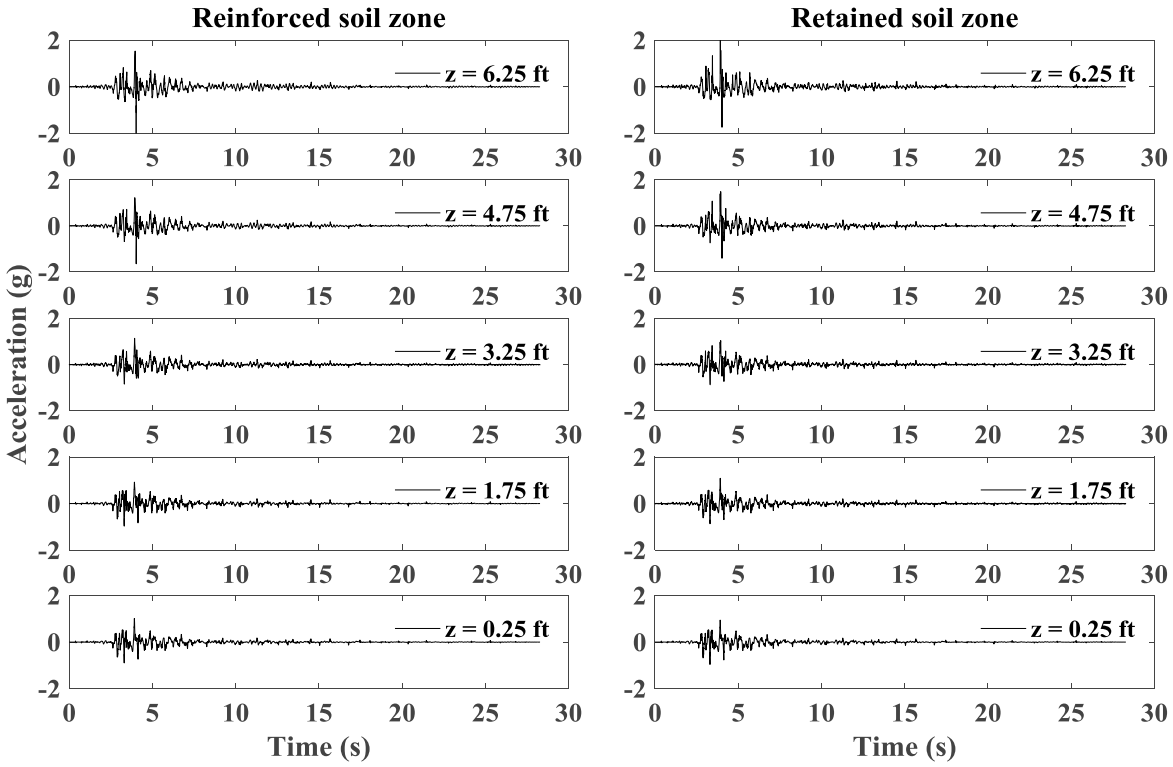

Figure A1.116 Time histories of acceleration for reinforced soil zone and retained soil zone in longitudinal section L1.

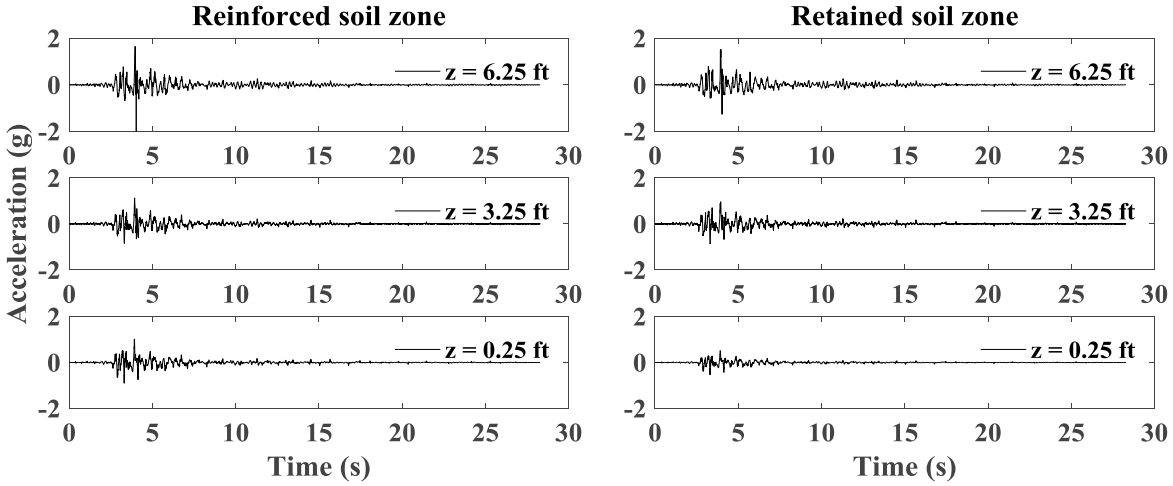

Figure A1.117 Time histories of acceleration for reinforced soil zone and retained soil zone in longitudinal section L2.

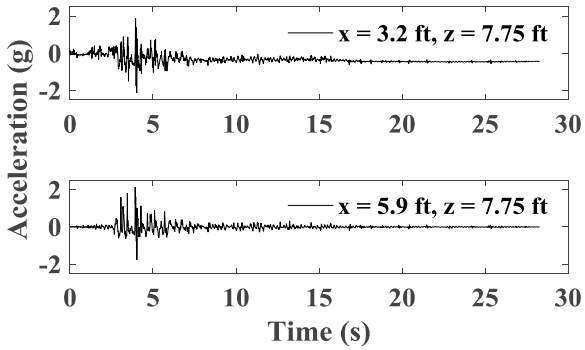

Figure A1.118 Time histories of acceleration for backfill soil in upper wall.

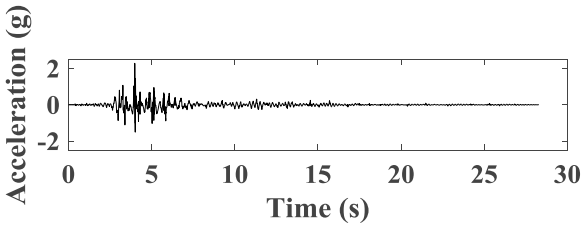

Figure A1.119 Time histories of acceleration for bridge seat.

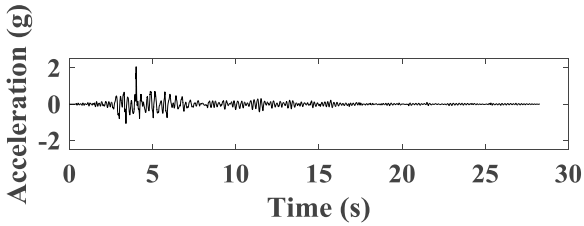

Figure A1.120 Time histories of acceleration for bridge beam.

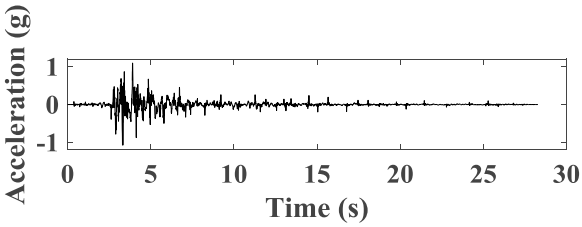

Figure A1.121 Time histories of acceleration for support wall.

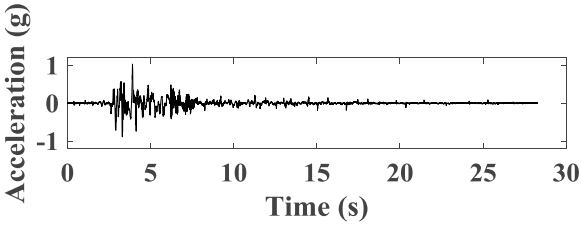

Figure A1.122 Time histories of acceleration for shaking table.

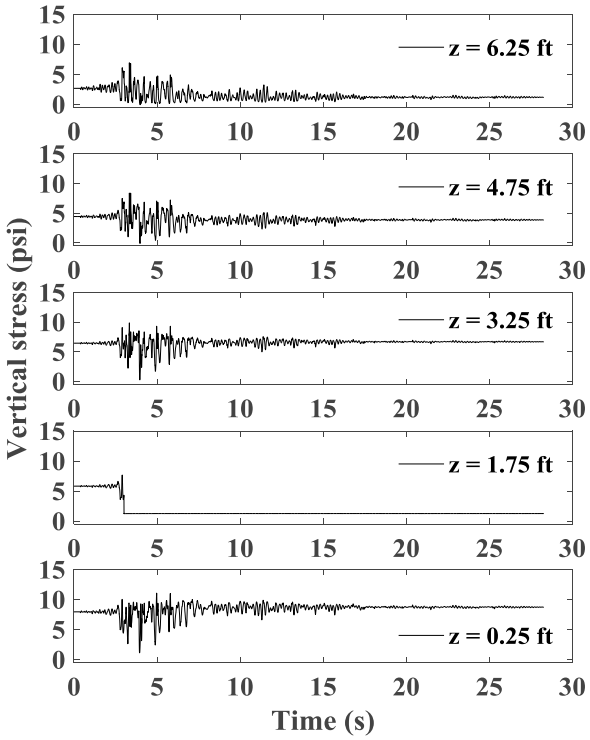

Figure A1.123 Time histories of vertical stress behind wall facing.

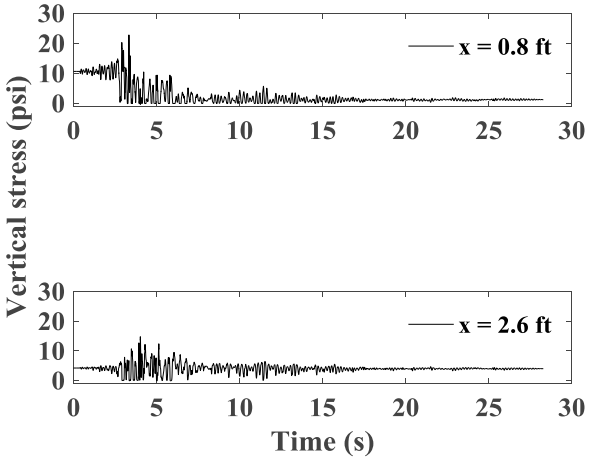

Figure A1.124 Time histories of vertical stress under bridge seat.

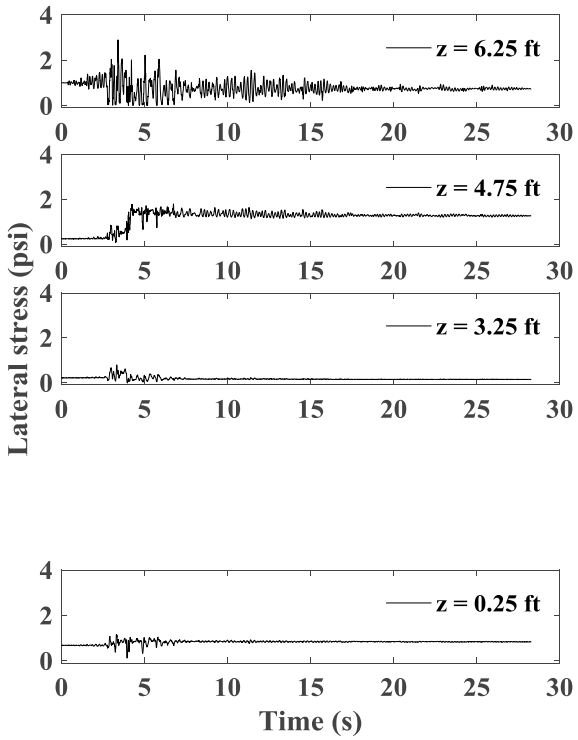

Figure A1.125 Time histories of lateral stress behind wall facing.

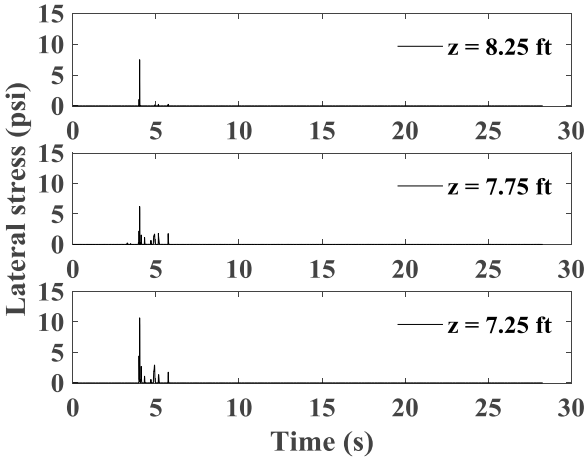

Figure A1.126 Time histories of lateral stress behind upper wall.

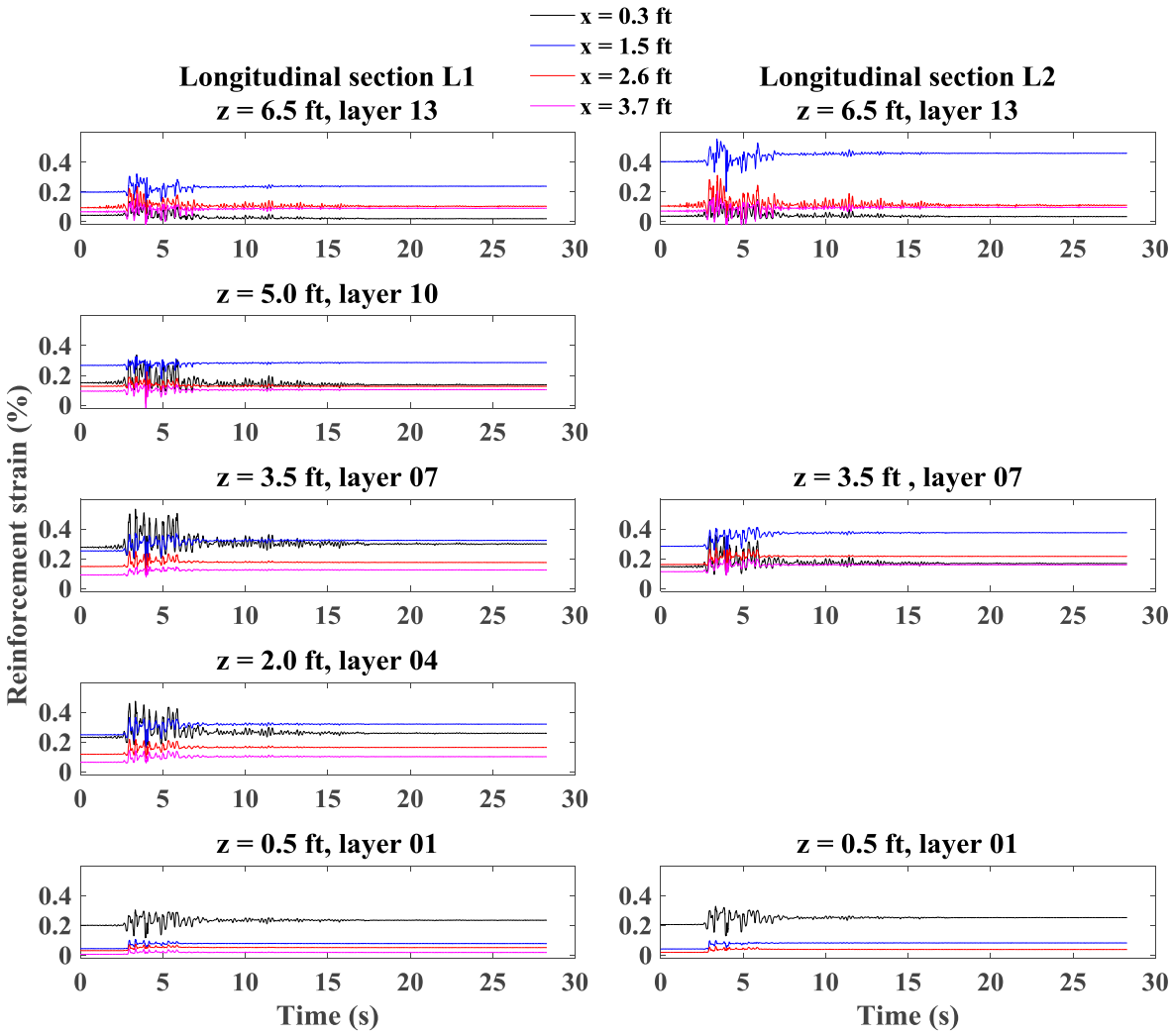

Figure A1.127 Time histories of reinforcement strain for longitudinal sections L1 and L2.

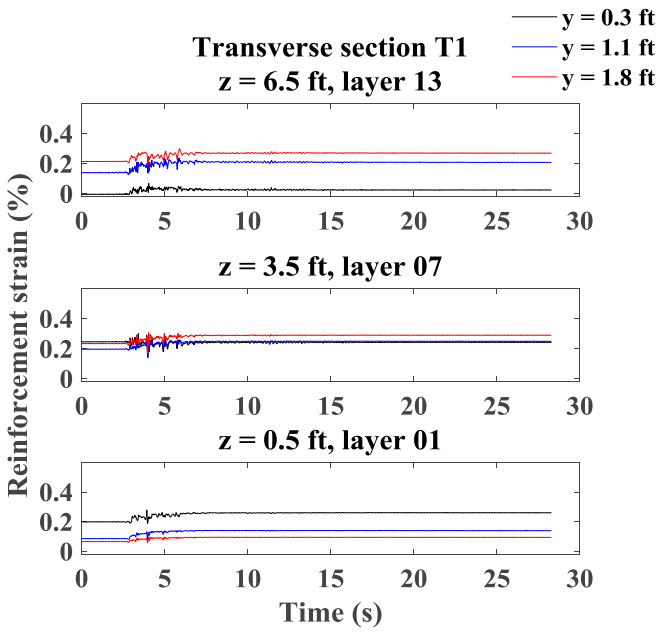

Figure A1.128 Time histories of reinforcement strain for transverse section T1.

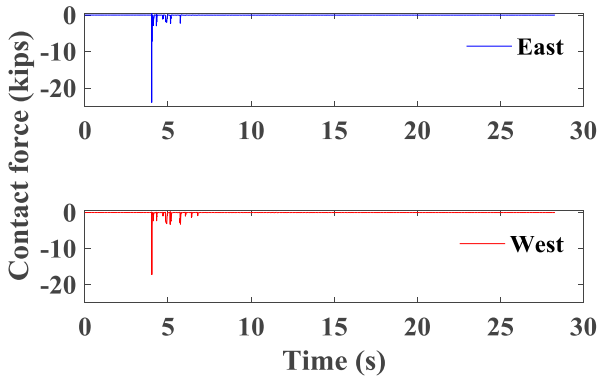

Figure A1.129 Time histories of contact force between bridge seat and bridge beam.

A1.3 Test 3

A1.3.1 Imperial Valley Motion

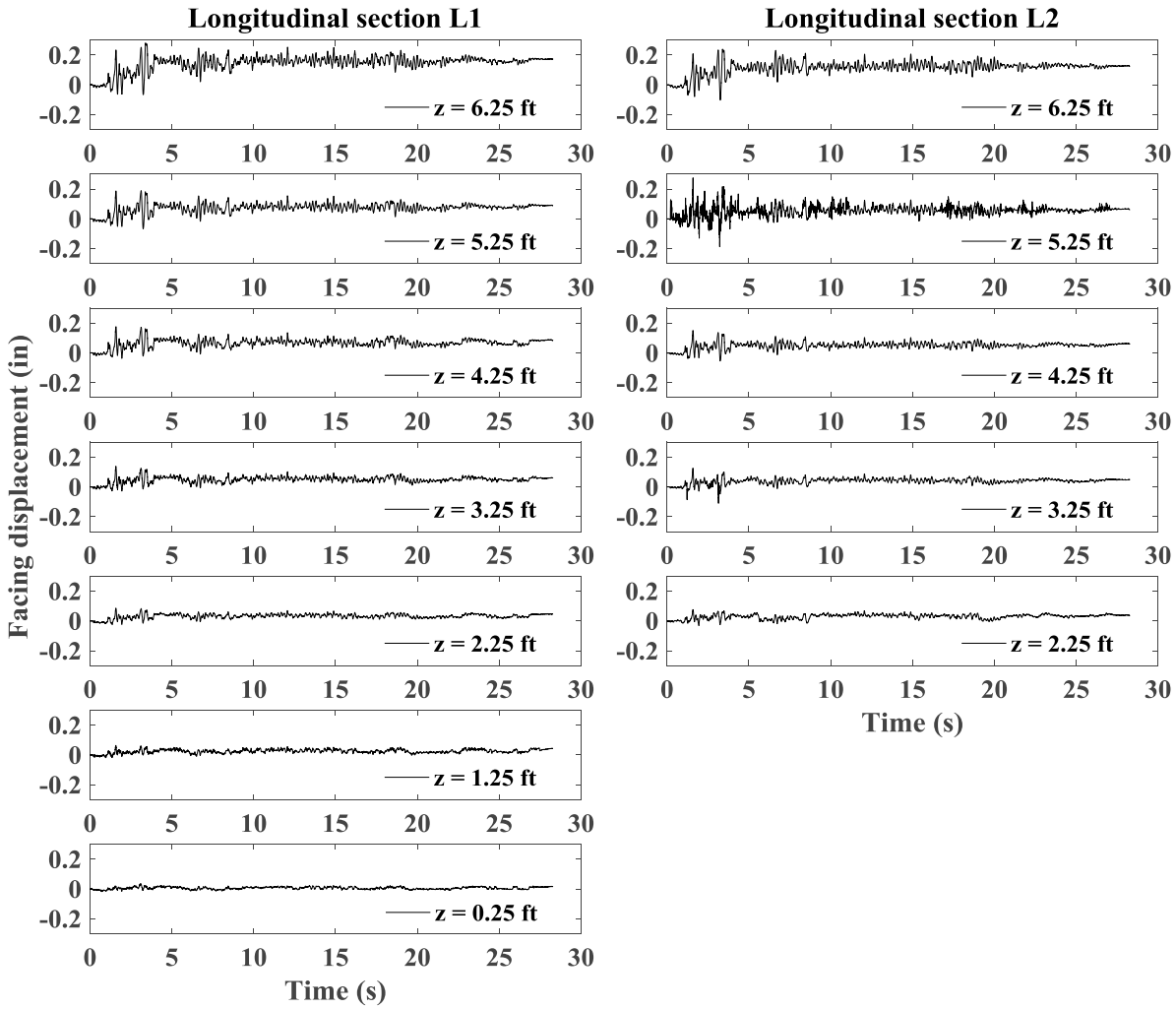

Figure A1.130 Time histories of incremental facing displacement for longitudinal sections L1 and L2.

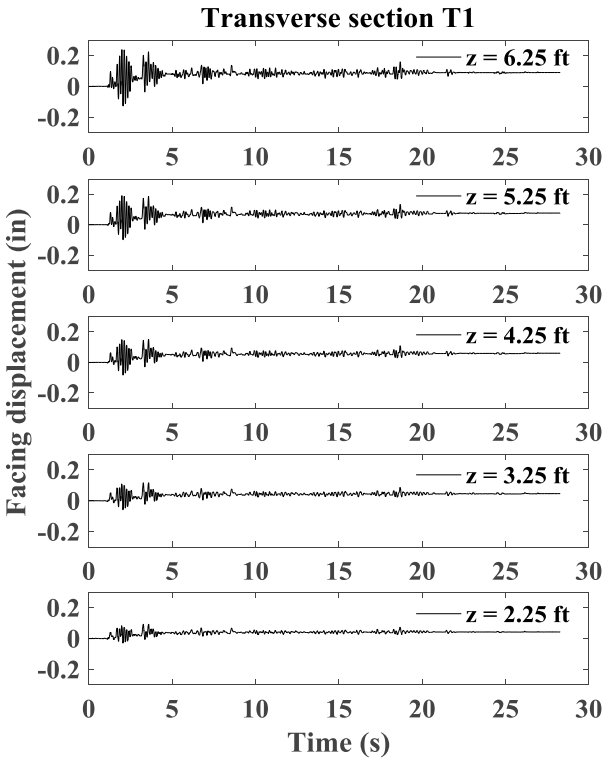

Figure A1.131 Time histories of incremental facing displacement for transverse section T1.

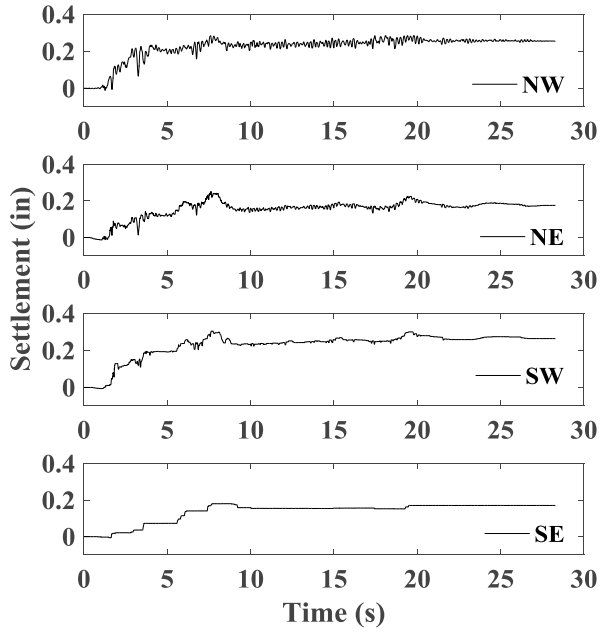

Figure A1.132 Time histories of incremental settlement for bridge seat.

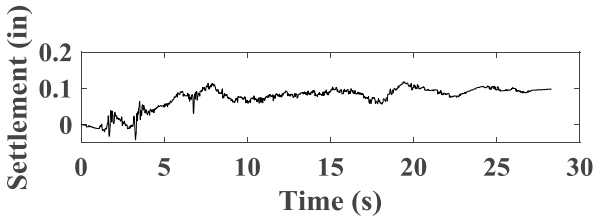

Figure A1.133 Time histories of incremental settlement for backfill soil in upper wall.

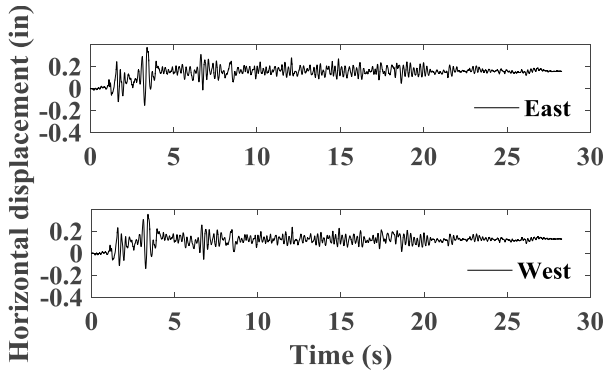

Figure A1.134 Time histories of incremental horizontal displacement for bridge seat.

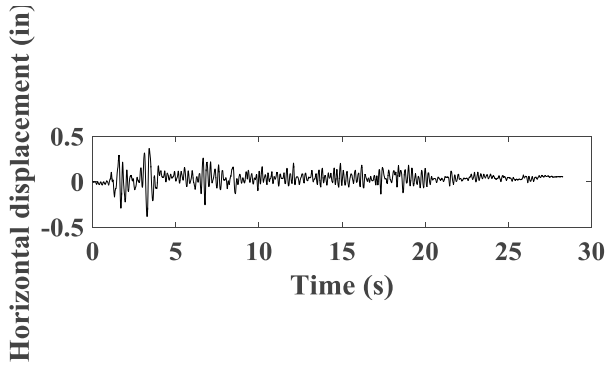

Figure A1.135 Time histories of incremental horizontal displacement for bridge beam.

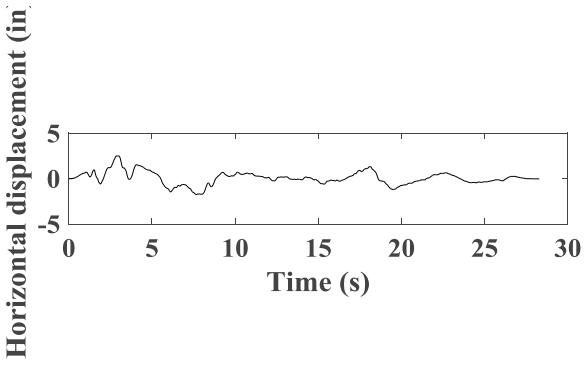

Figure A1.136 Time histories of horizontal displacement for support wall.

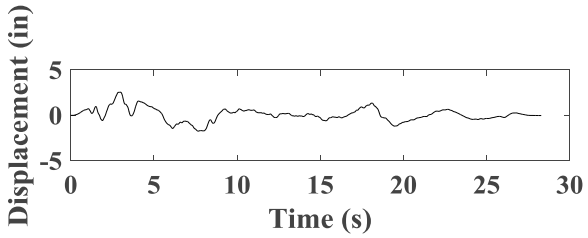

Figure A1.137 Time histories of horizontal displacement for shaking table.

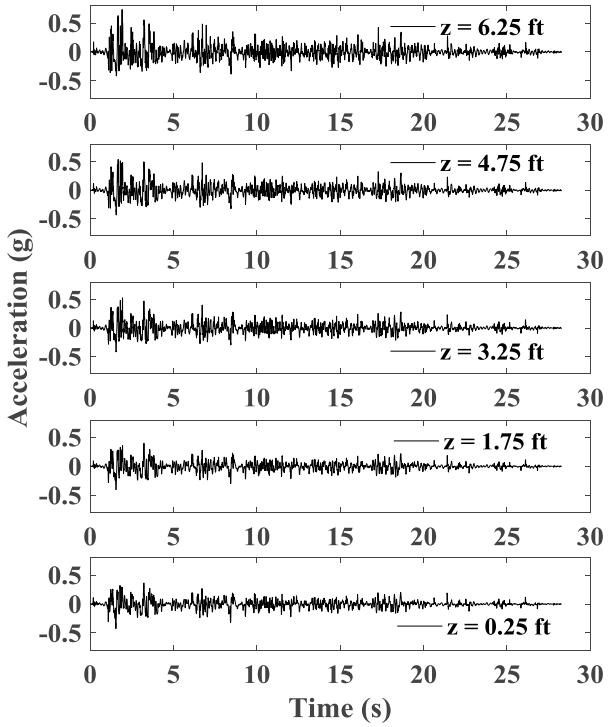

Figure A1.138 Time histories of acceleration for wall facing in longitudinal section L1.

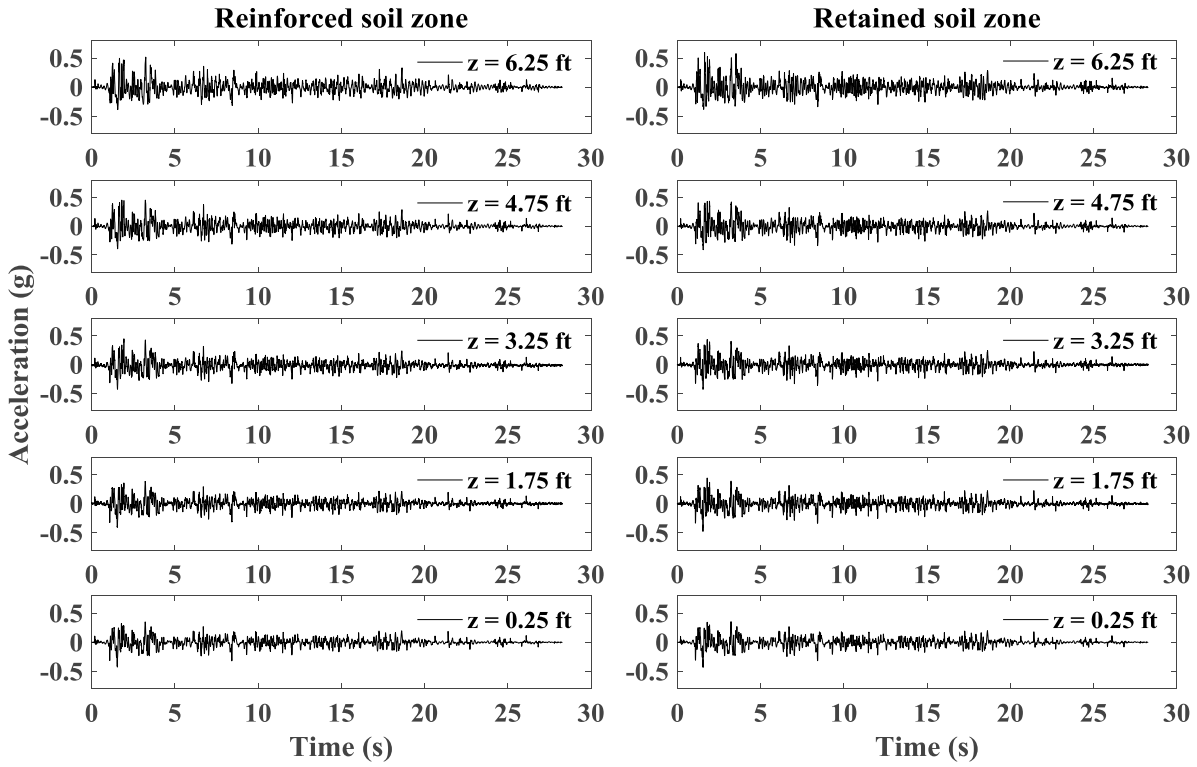

Figure A1.139 Time histories of acceleration for reinforced soil zone and retained soil zone in longitudinal section L1.

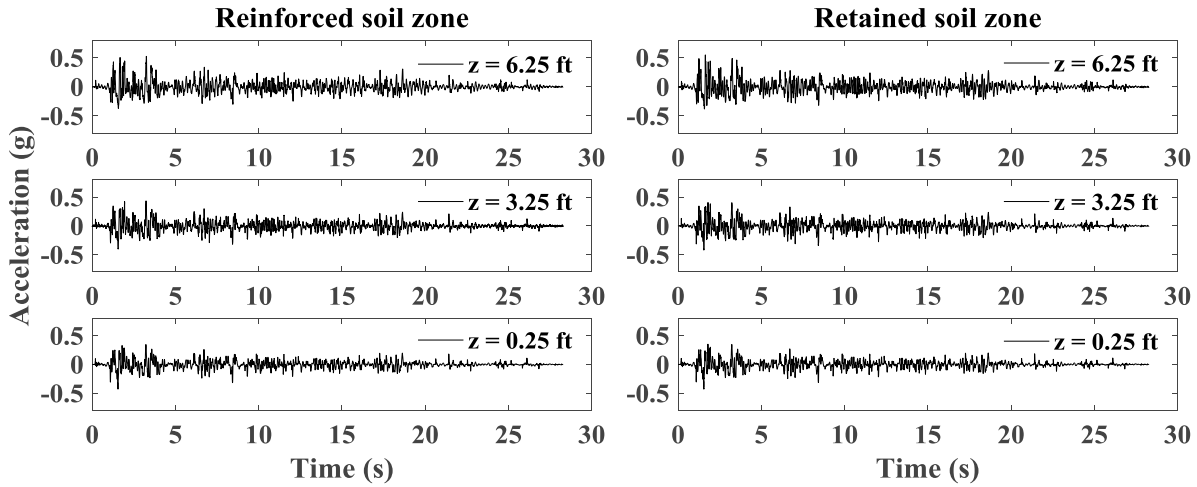

Figure A1.140 Time histories of acceleration for reinforced soil zone and retained soil zone in longitudinal section L2.

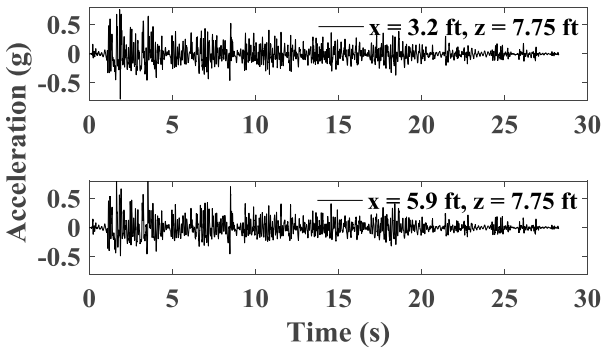

Figure A1.141 Time histories of acceleration for backfill soil in upper wall.

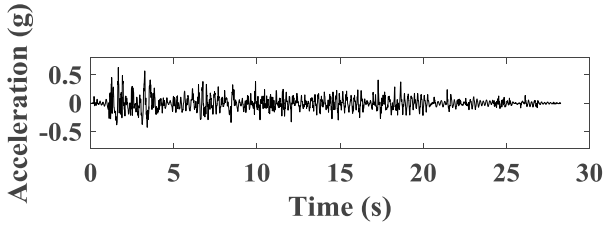

Figure A1.142 Time histories of acceleration for bridge seat.

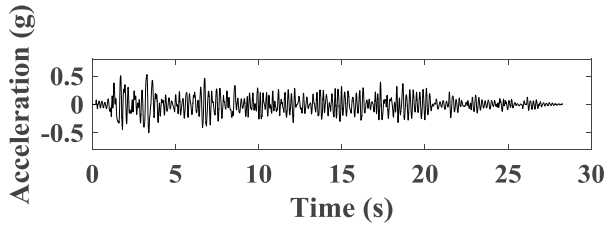

Figure A1.143 Time histories of acceleration for bridge beam.

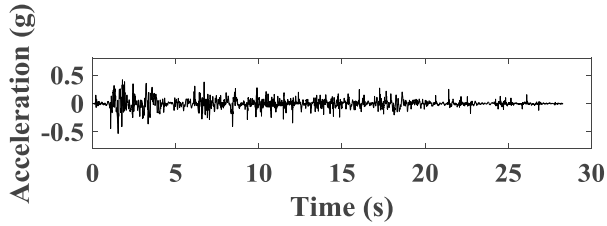

Figure A1.144 Time histories of acceleration for support wall.

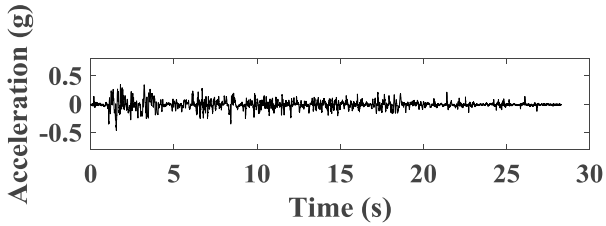

Figure A1.145 Time histories of acceleration for shaking table.

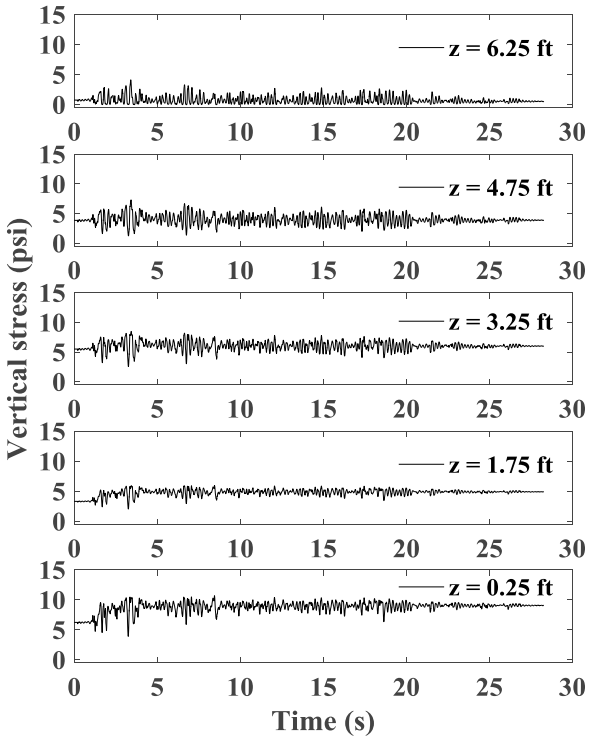

Figure A1.146 Time histories of vertical stress behind wall facing.

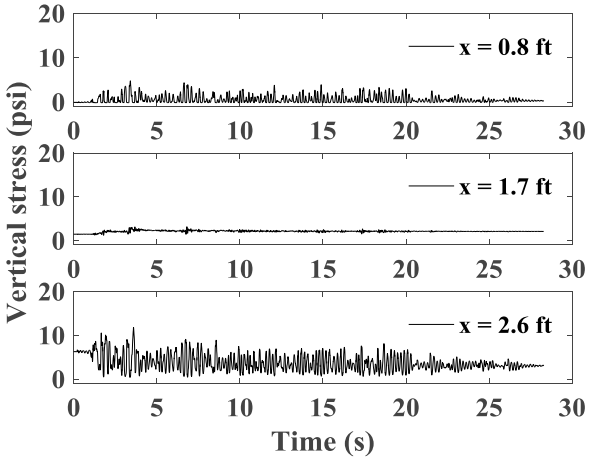

Figure A1.147 Time histories of vertical stress under bridge seat.

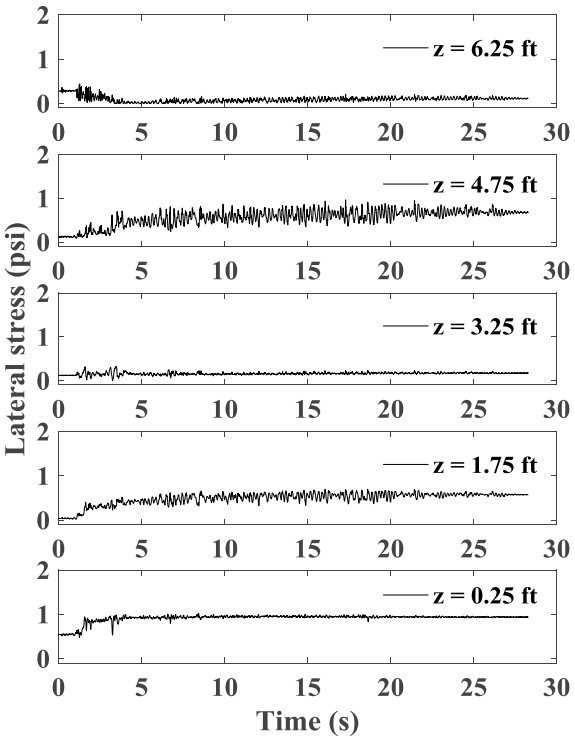

Figure A1.148 Time histories of lateral stress behind wall facing.

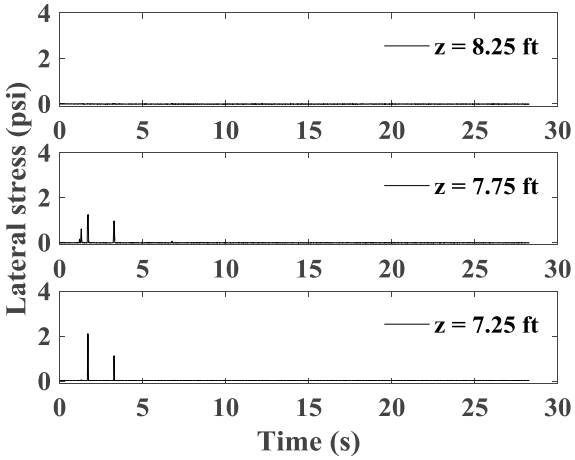

Figure A1.149 Time histories of lateral stress behind upper wall.

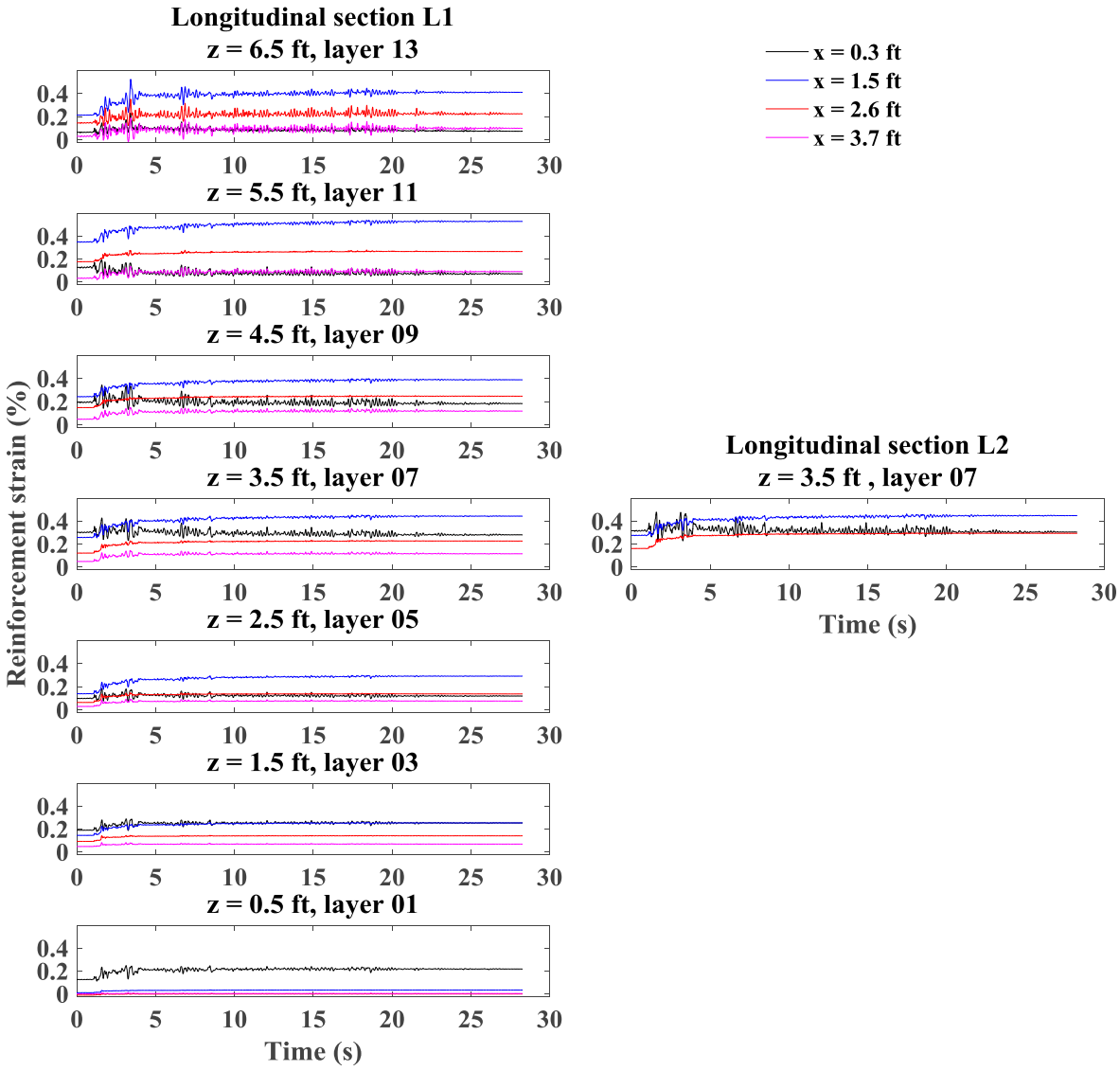

Figure A1.150 Time histories of reinforcement strain for longitudinal sections L1 and L2.

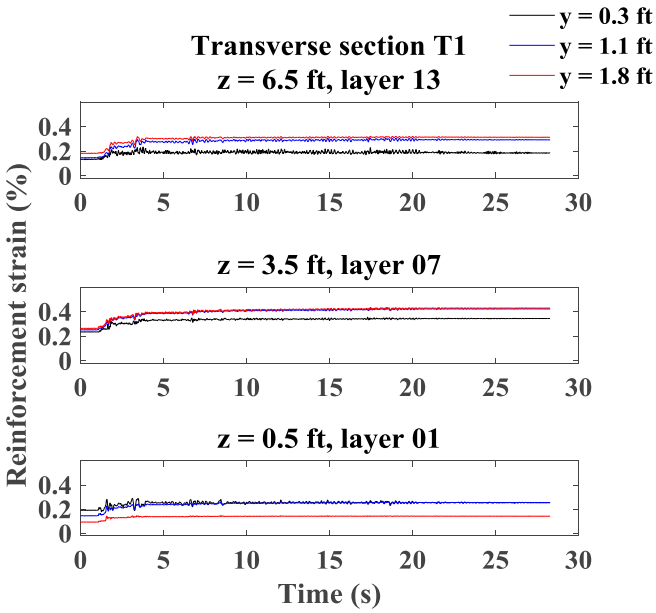

Figure A1.151 Time histories of reinforcement strain for transverse section T1.

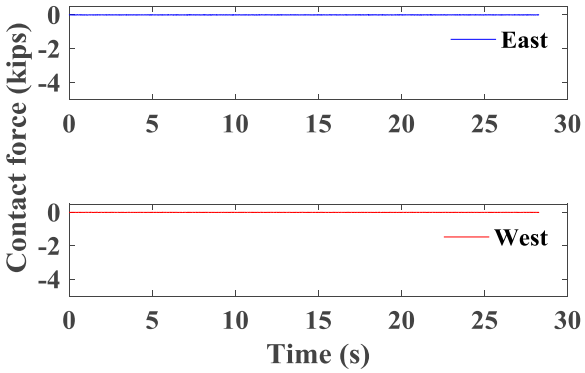

Figure A1.152 Time histories of contact force between bridge seat and bridge beam.

A1.3.2 Maule Motion

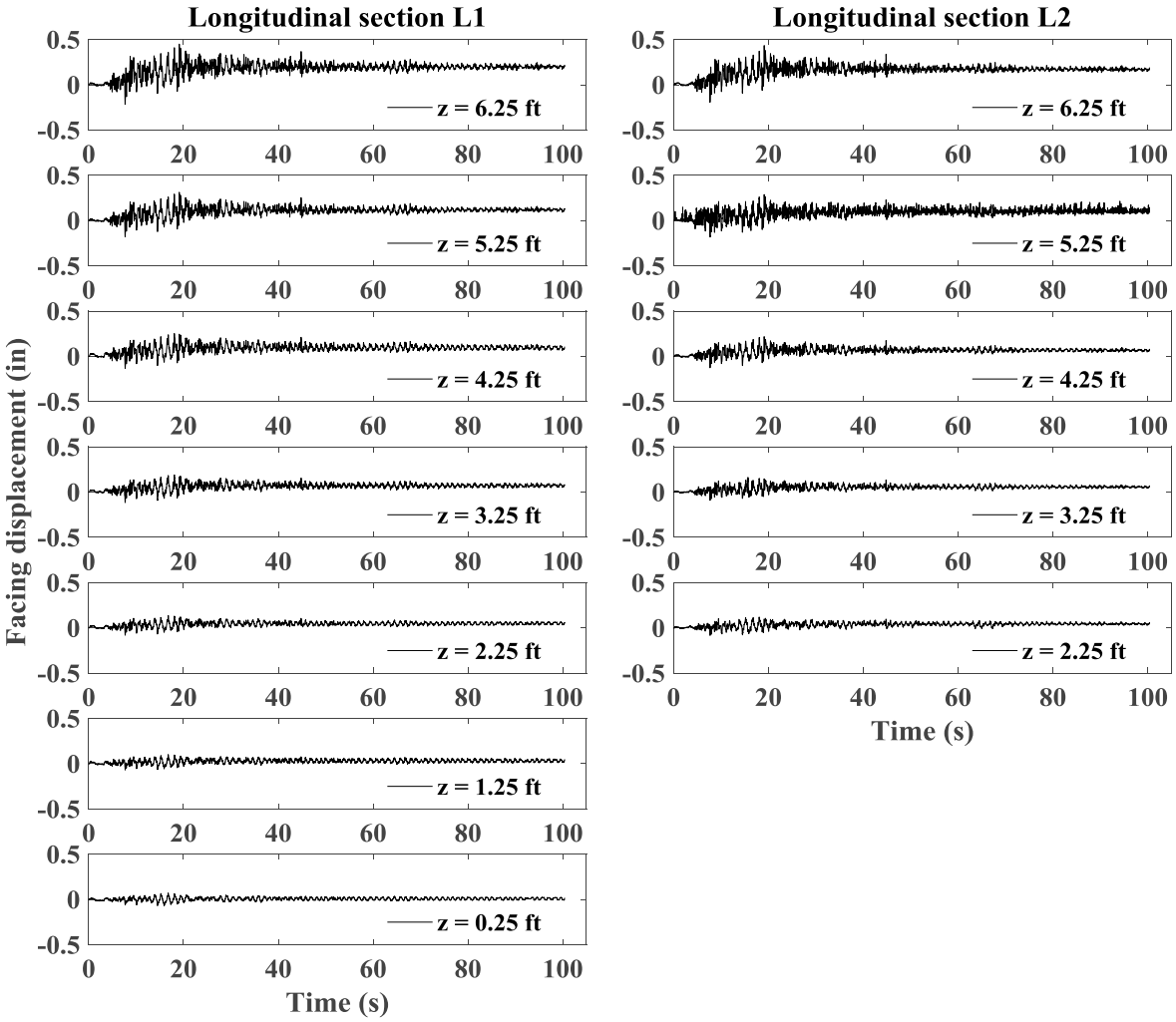

Figure A1.153 Time histories of incremental facing displacement for longitudinal sections L1 and L2.

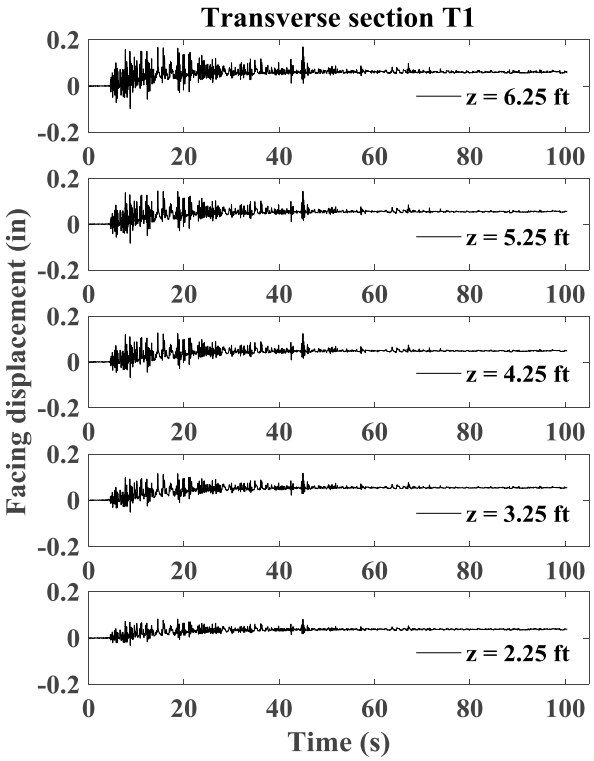

Figure A1.154 Time histories of incremental facing displacement for transverse section T1.

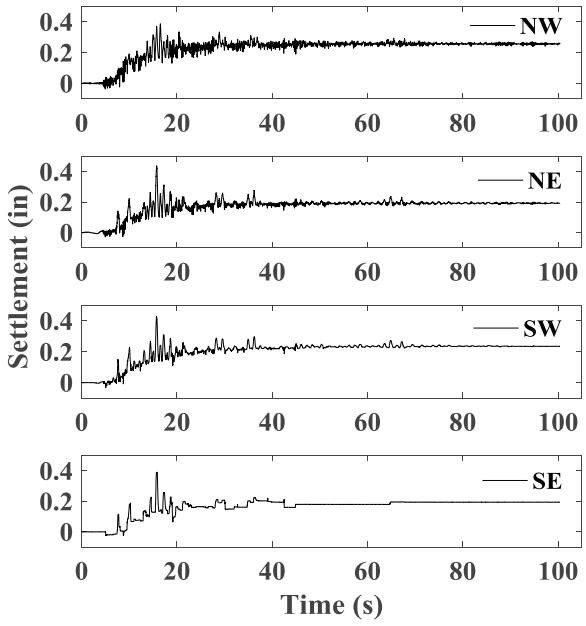

Figure A1.155 Time histories of incremental settlement for bridge seat.

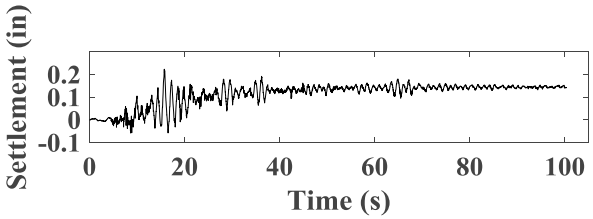

Figure A1.156 Time histories of incremental settlement for backfill soil in upper wall.

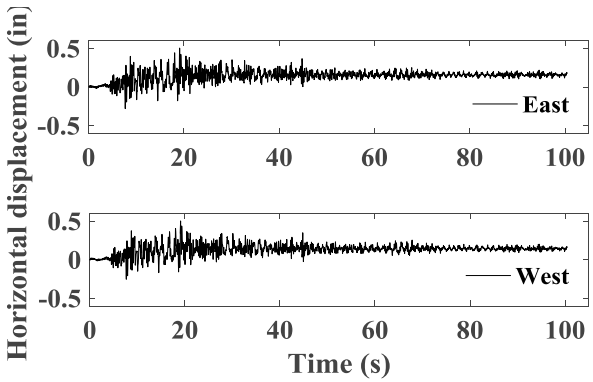

Figure A1.157 Time histories of incremental horizontal displacement for bridge seat.

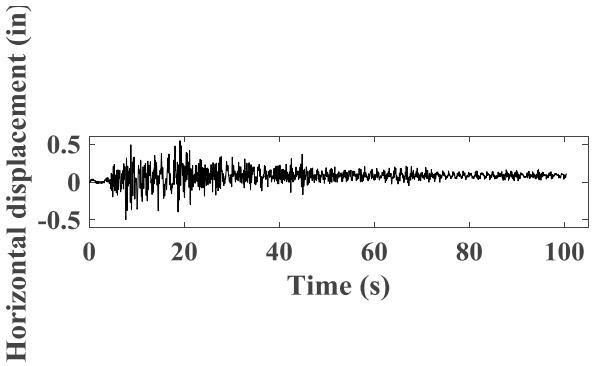

Figure A1.158 Time histories of incremental horizontal displacement for bridge beam.

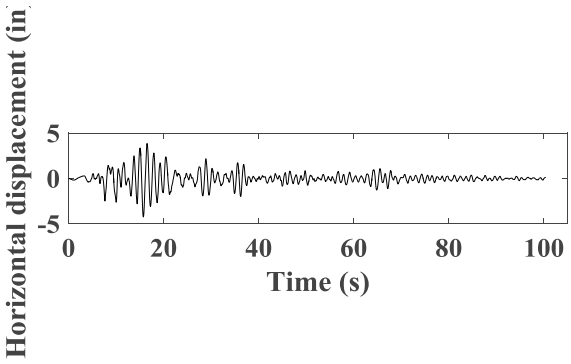

Figure A1.159 Time histories of horizontal displacement for support wall.

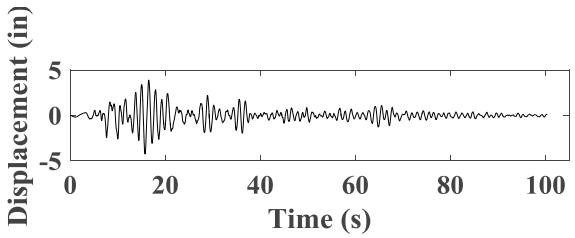

Figure A1.160 Time histories of horizontal displacement for shaking table.

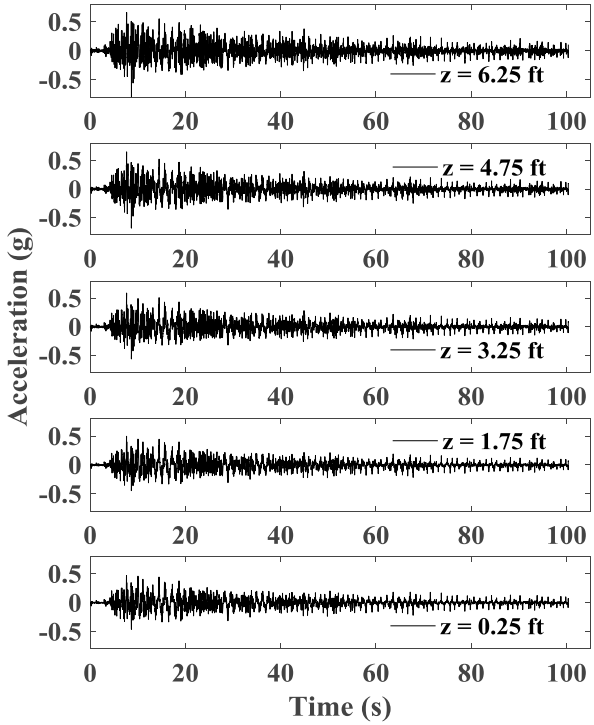

Figure A1.161 Time histories of acceleration for wall facing in longitudinal section L1.

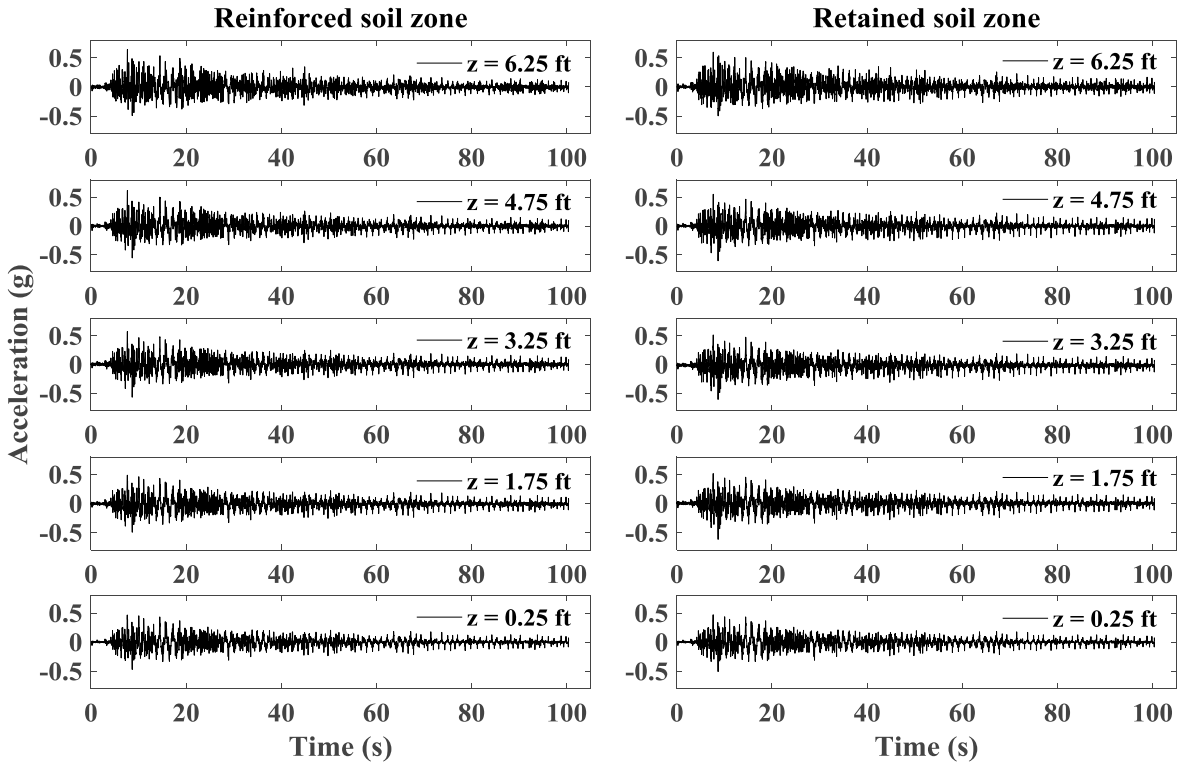

Figure A1.162 Time histories of acceleration for reinforced soil zone and retained soil zone in longitudinal section L1.

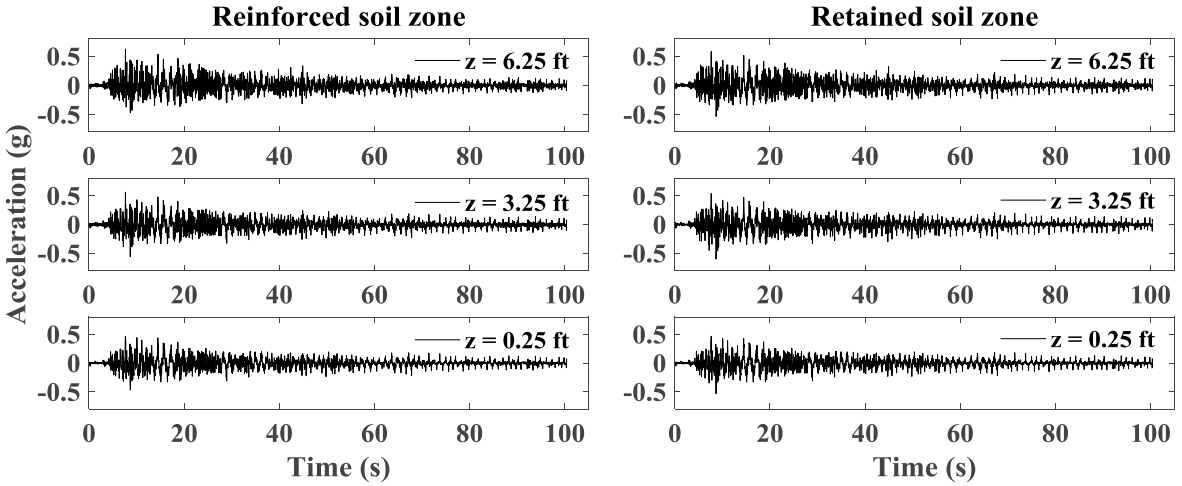

Figure A1.163 Time histories of acceleration for reinforced soil zone and retained soil zone in longitudinal section L2.

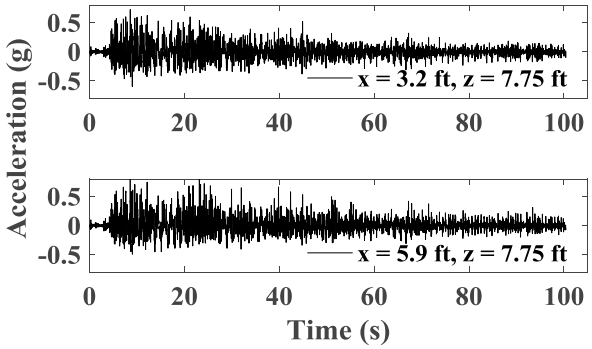

Figure A1.164 Time histories of acceleration for backfill soil in upper wall.

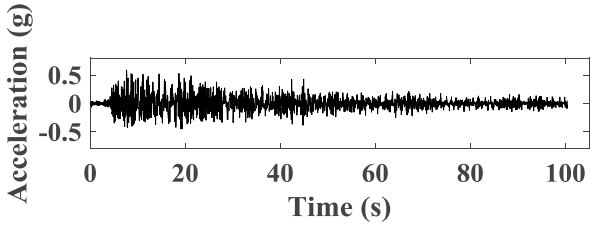

Figure A1.165 Time histories of acceleration for bridge seat.

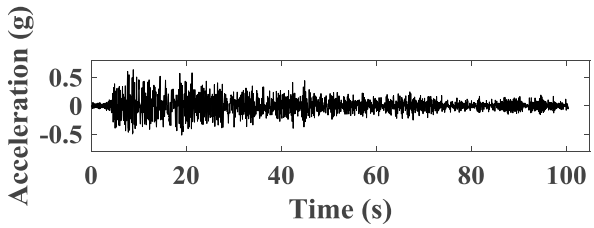

Figure A1.166 Time histories of acceleration for bridge beam.

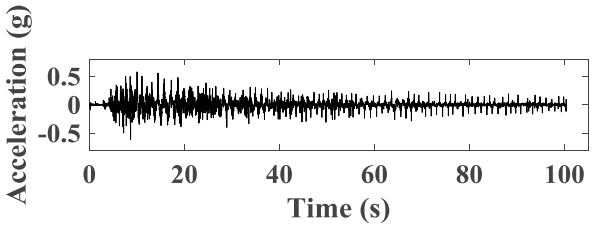

Figure A1.167 Time histories of acceleration for support wall.

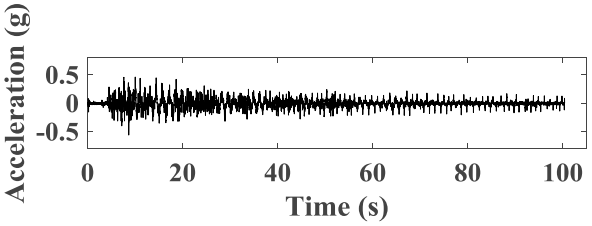

Figure A1.168 Time histories of acceleration for shaking table.

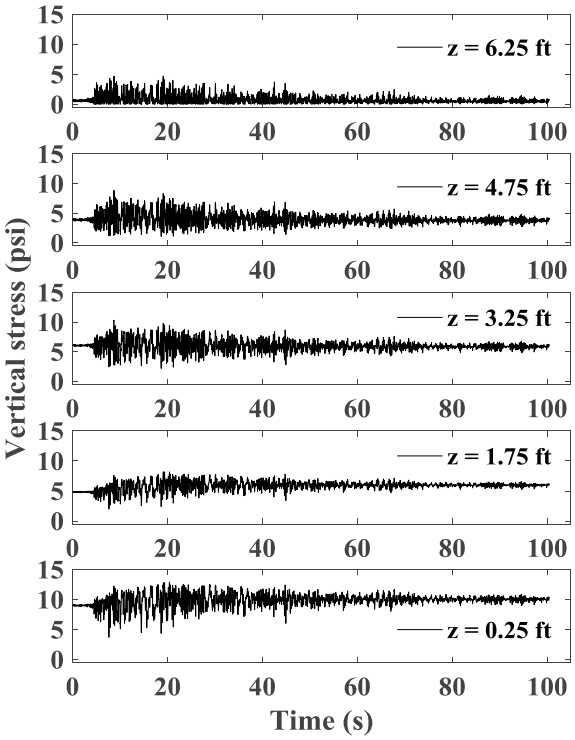

Figure A1.169 Time histories of vertical stress behind wall facing.

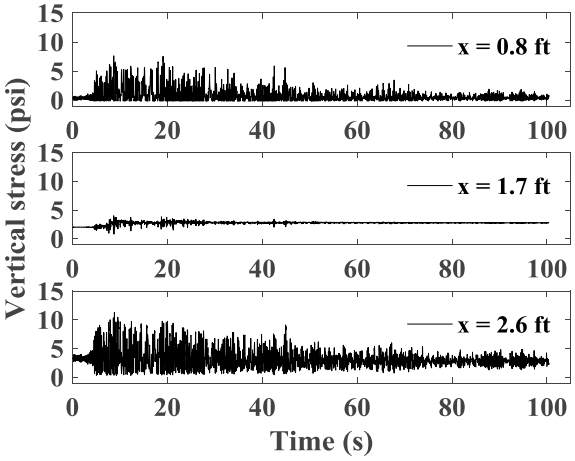

Figure A1.170 Time histories of vertical stress under bridge seat.

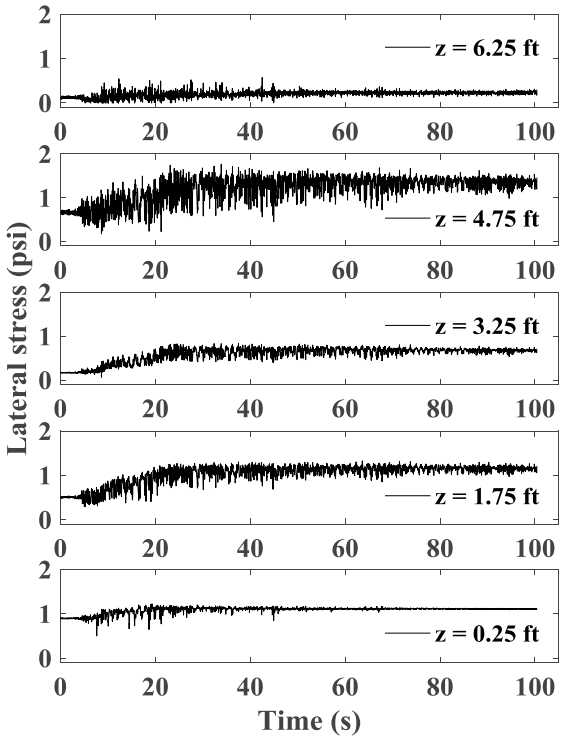

Figure A1.171 Time histories of lateral stress behind wall facing.

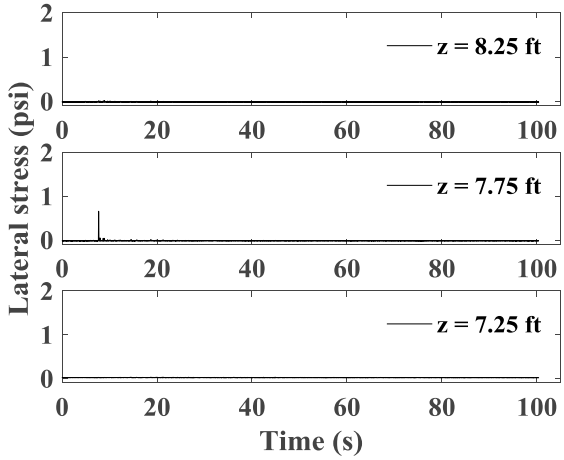

Figure A1.172 Time histories of lateral stress behind upper wall.

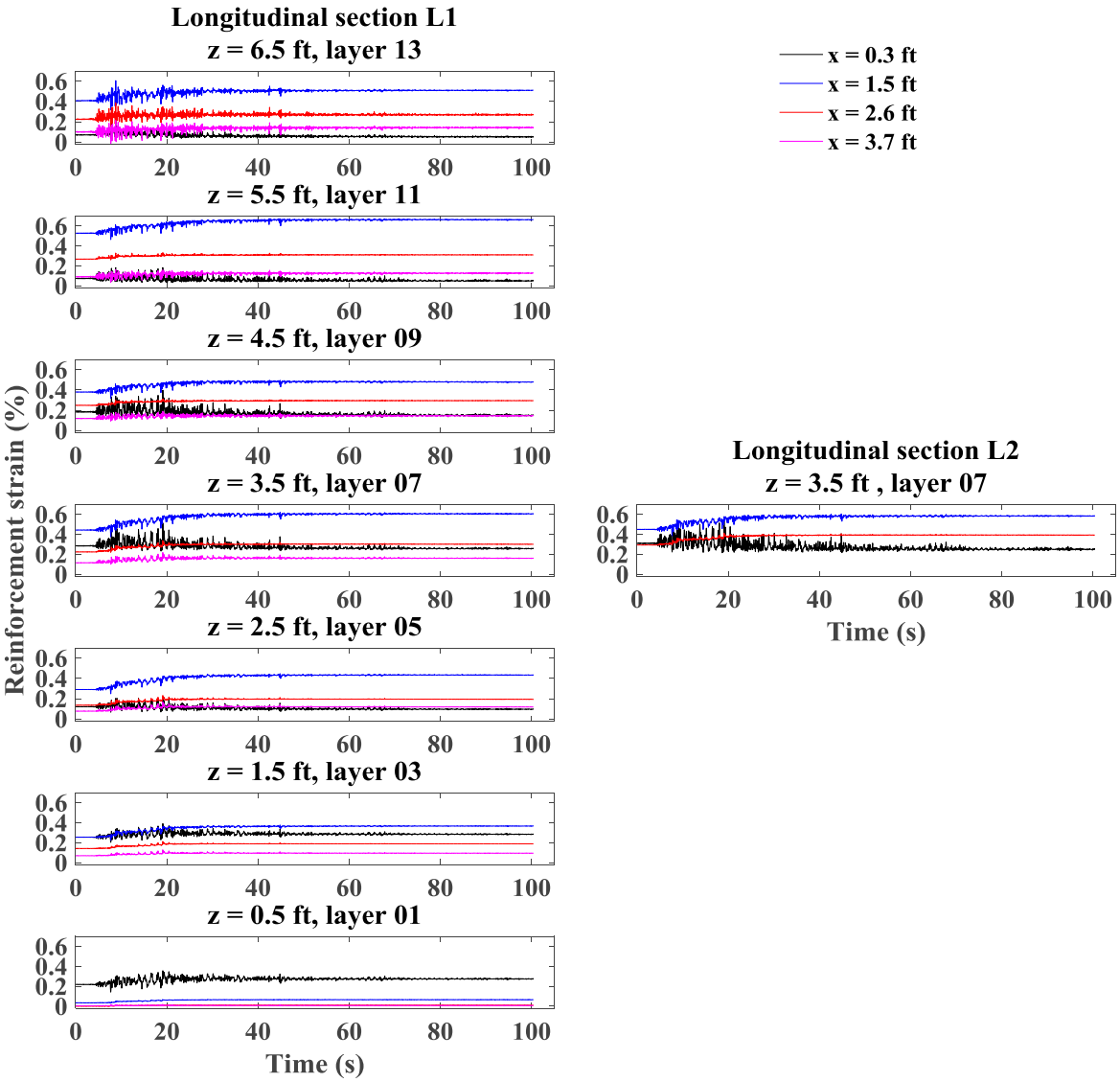

Figure A1.173 Time histories of reinforcement strain for longitudinal sections L1 and L2.

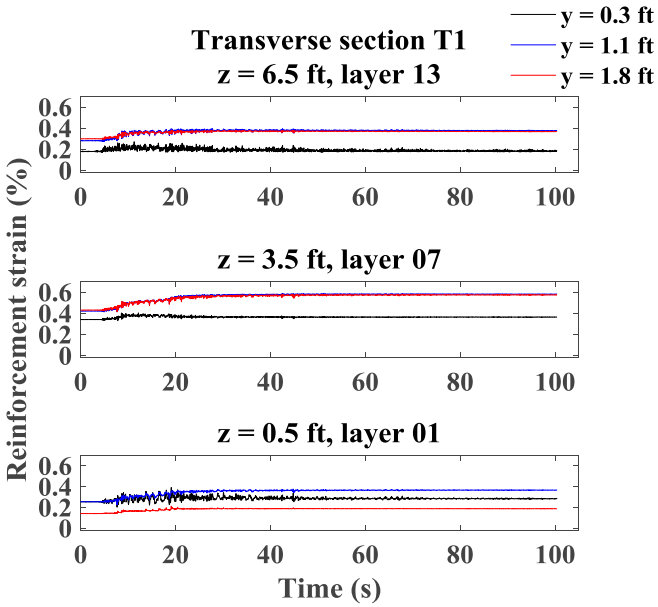

Figure A1.174 Time histories of reinforcement strain for transverse section T1.

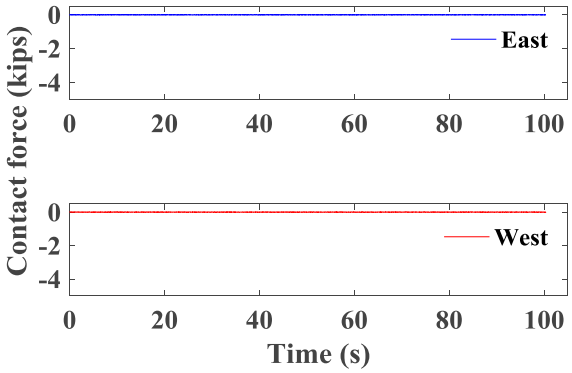

Figure A1.175 Time histories of contact force between bridge seat and bridge beam.

A1.3.3 Northridge Motion

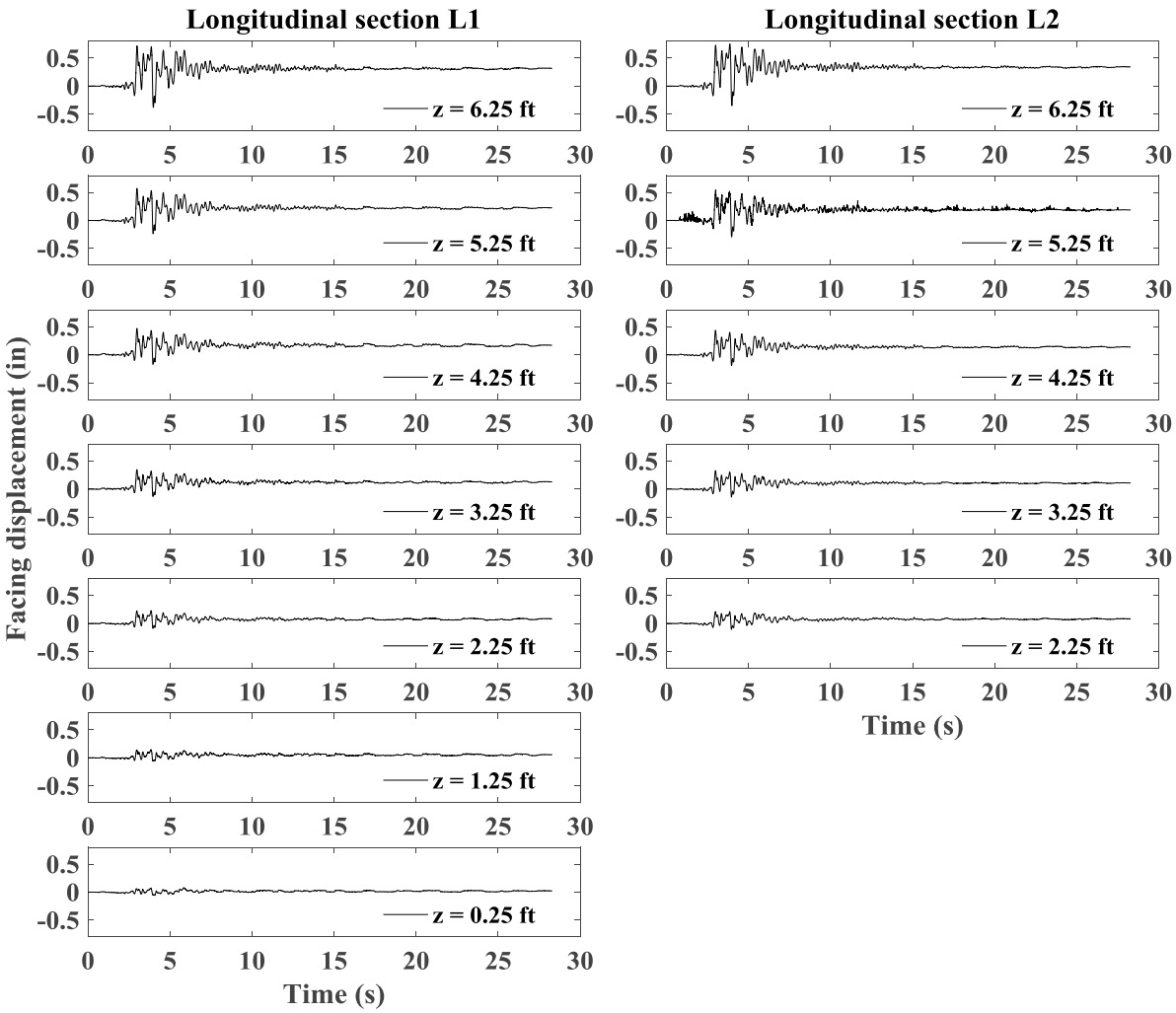

Figure A1.176 Time histories of incremental facing displacement for longitudinal sections L1 and L2.

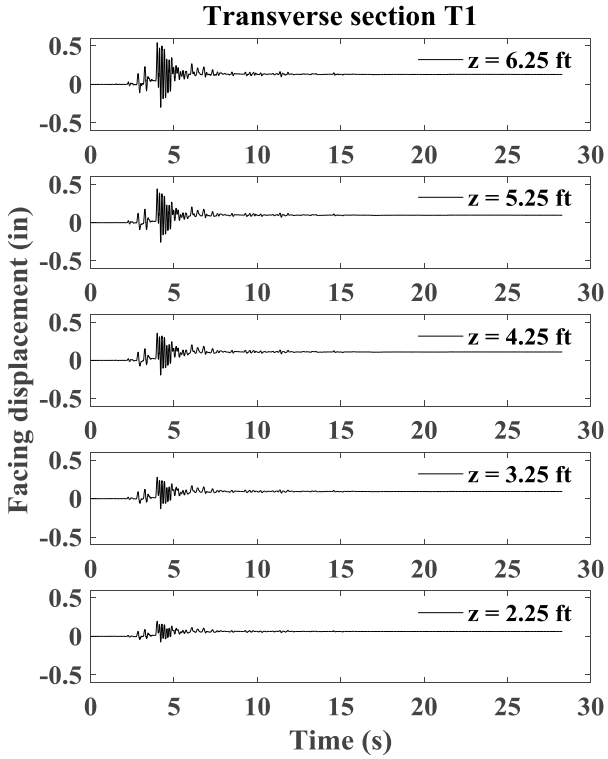

Figure A1.177 Time histories of incremental facing displacement for transverse section T1.

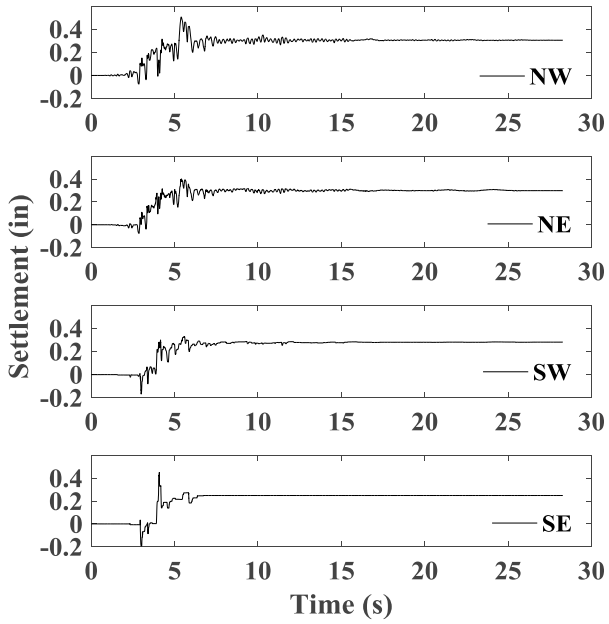

Figure A1.178 Time histories of incremental settlement for bridge seat.

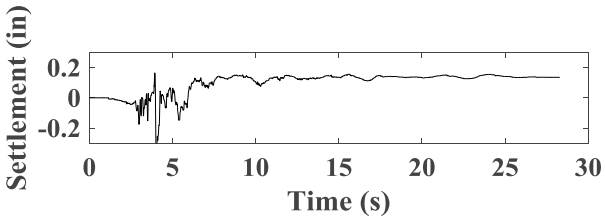

Figure A1.179 Time histories of incremental settlement for backfill soil in upper wall.

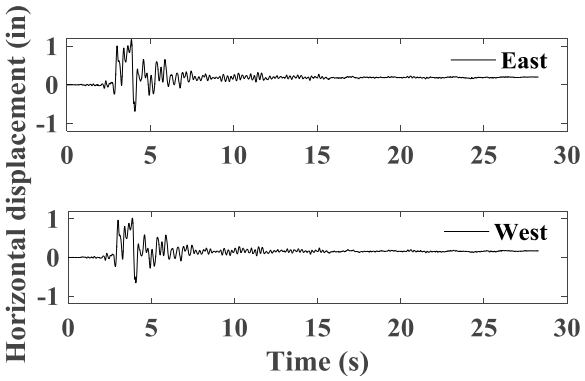

Figure A1.180 Time histories of incremental horizontal displacement for bridge seat.

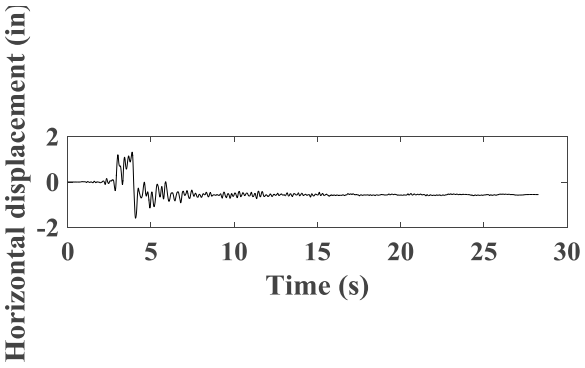

Figure A1.181 Time histories of incremental horizontal displacement for bridge beam.

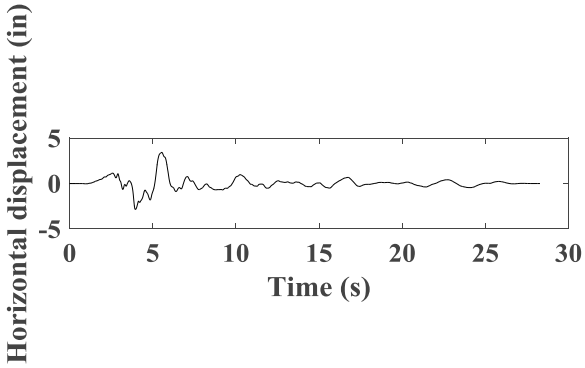

Figure A1.182 Time histories of horizontal displacement for support wall.

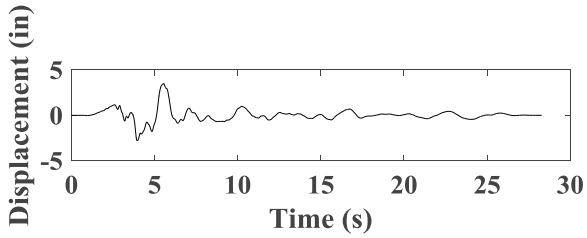

Figure A1.183 Time histories of horizontal displacement for shaking table.

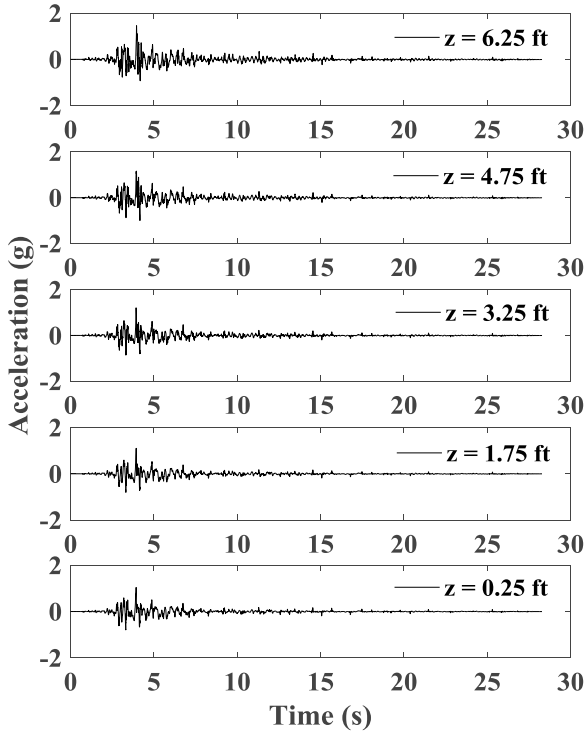

Figure A1.184 Time histories of acceleration for wall facing in longitudinal section L1.

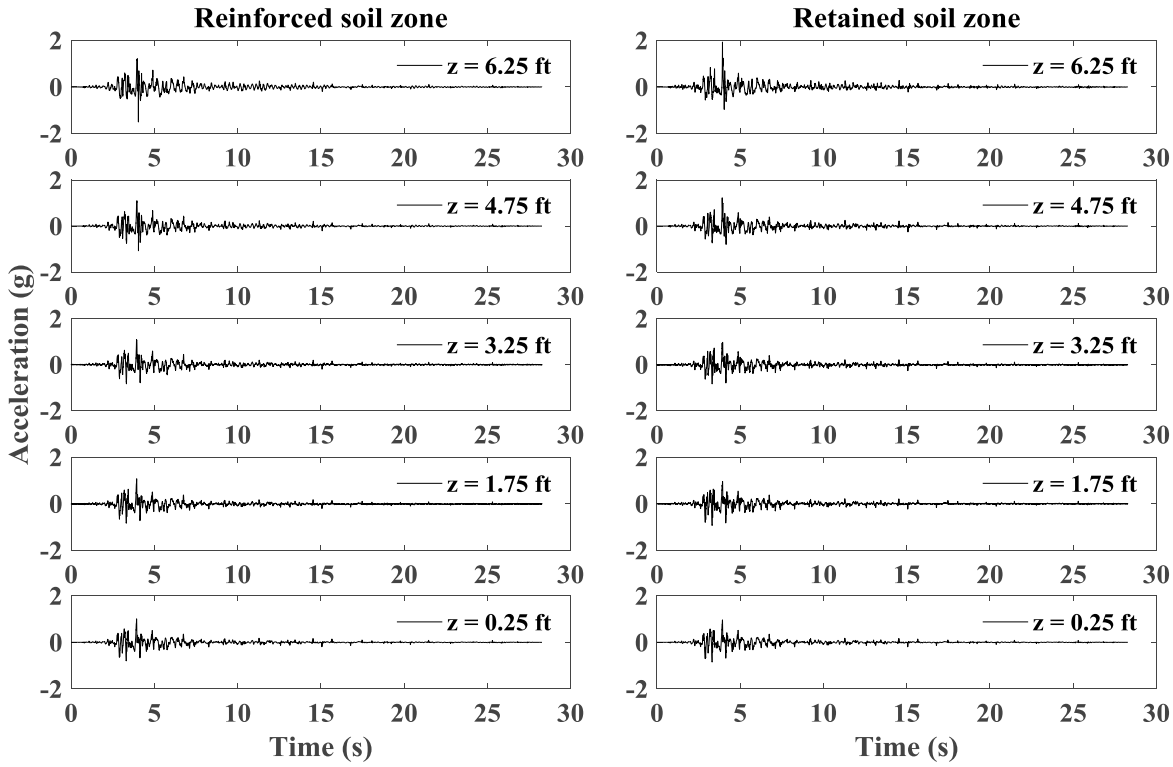

Figure A1.185 Time histories of acceleration for reinforced soil zone and retained soil zone in longitudinal section L1.

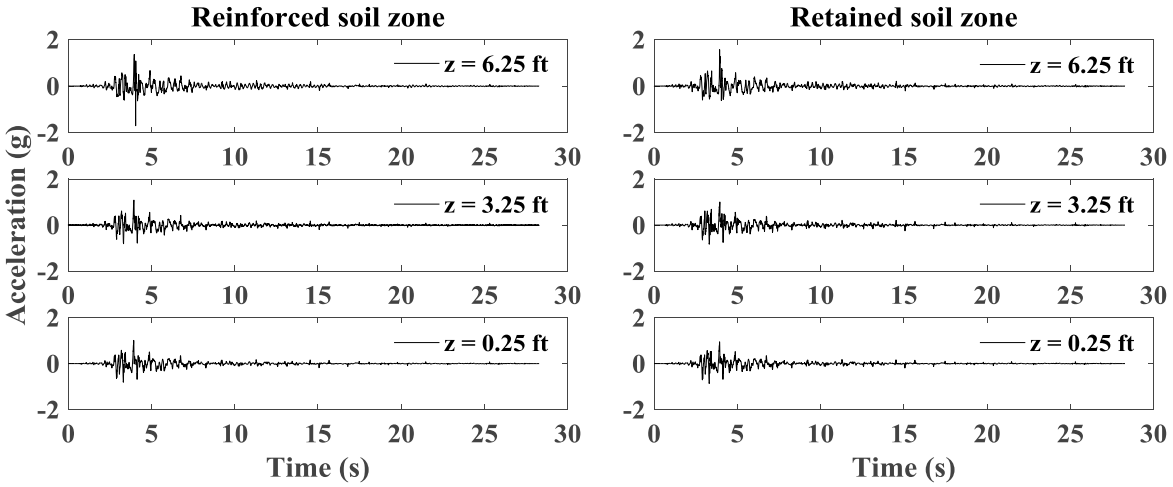

Figure A1.186 Time histories of acceleration for reinforced soil zone and retained soil zone in longitudinal section L2.

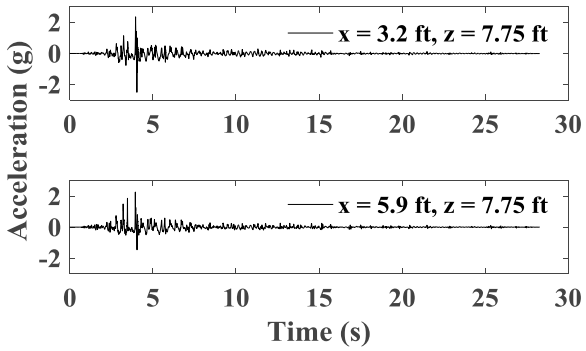

Figure A1.187 Time histories of acceleration for backfill soil in upper wall.

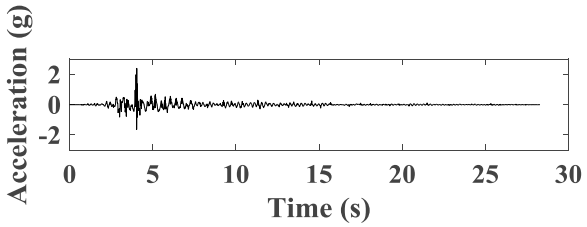

Figure A1.188 Time histories of acceleration for bridge seat.

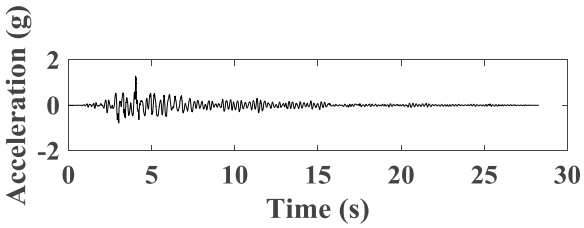

Figure A1.189 Time histories of acceleration for bridge beam.

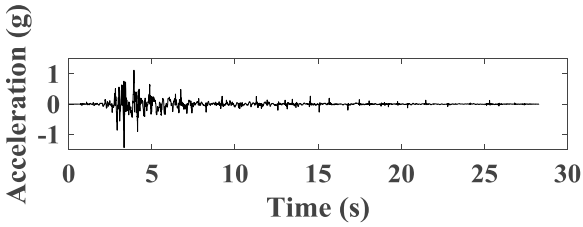

Figure A1.190 Time histories of acceleration for support wall.

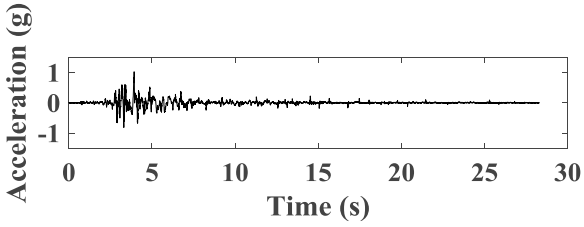

Figure A1.191 Time histories of acceleration for shaking table.

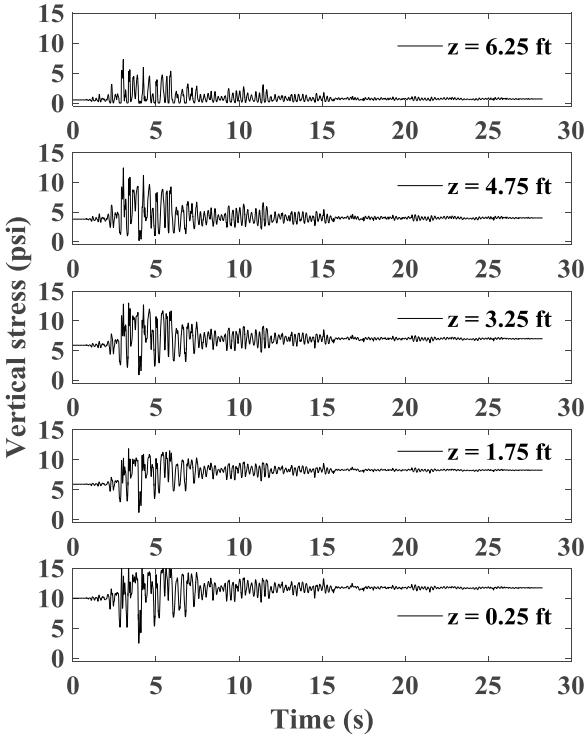

Figure A1.192 Time histories of vertical stress behind wall facing.

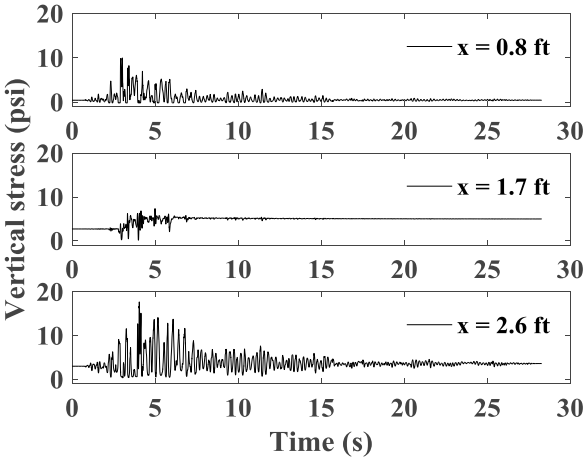

Figure A1.193 Time histories of vertical stress under bridge seat.

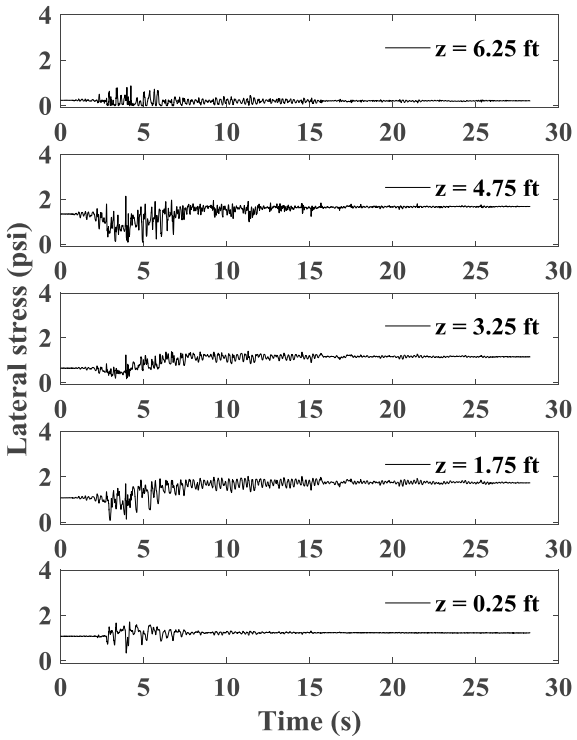

Figure A1.194 Time histories of lateral stress behind wall facing.

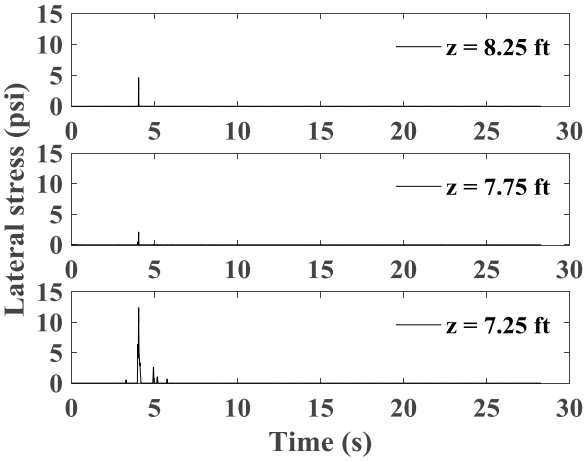

Figure A1.195 Time histories of lateral stress behind upper wall.

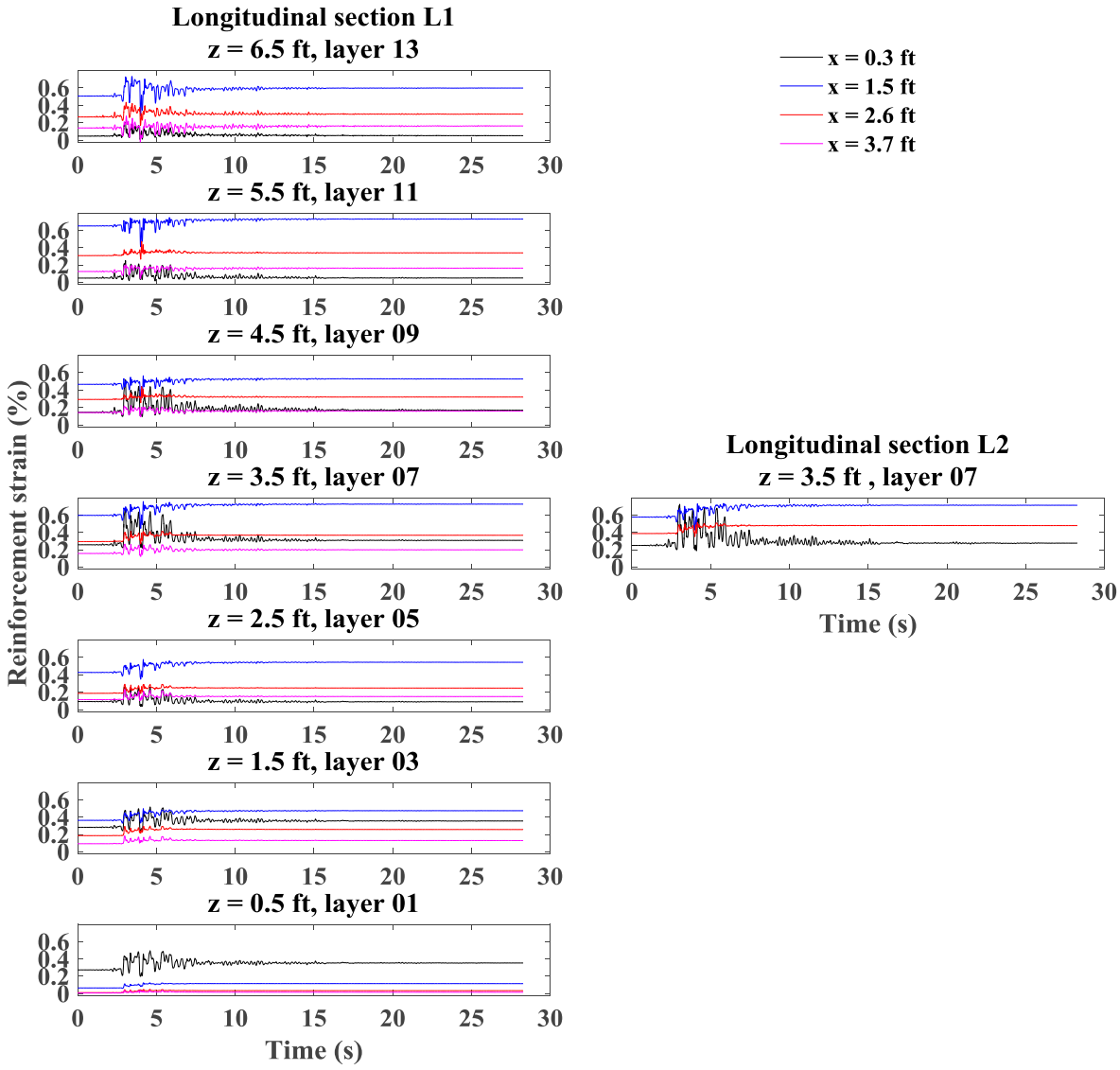

Figure A1.196 Time histories of reinforcement strain for longitudinal sections L1 and L2.

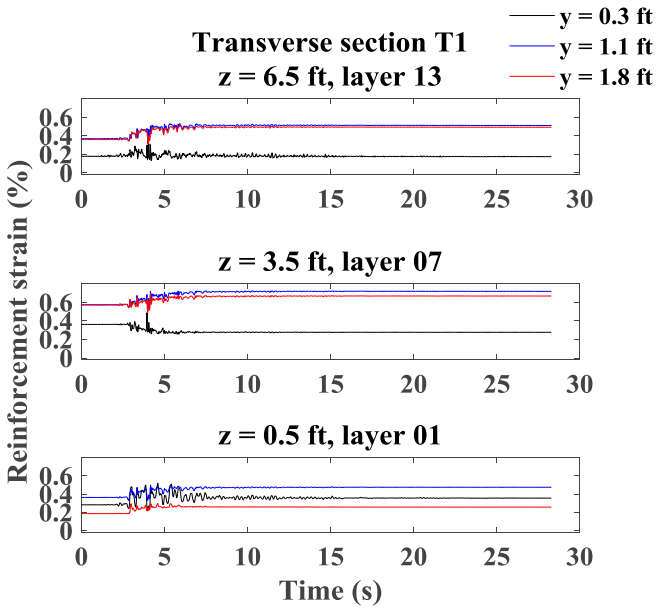

Figure A1.197 Time histories of reinforcement strain for transverse section T1.

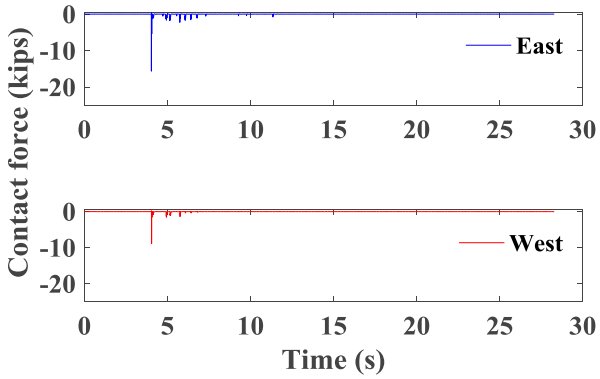

Figure A1.198 Time histories of contact force between bridge seat and bridge beam.

A1.4 Test 4

A1.4.1 Imperial Valley Motion

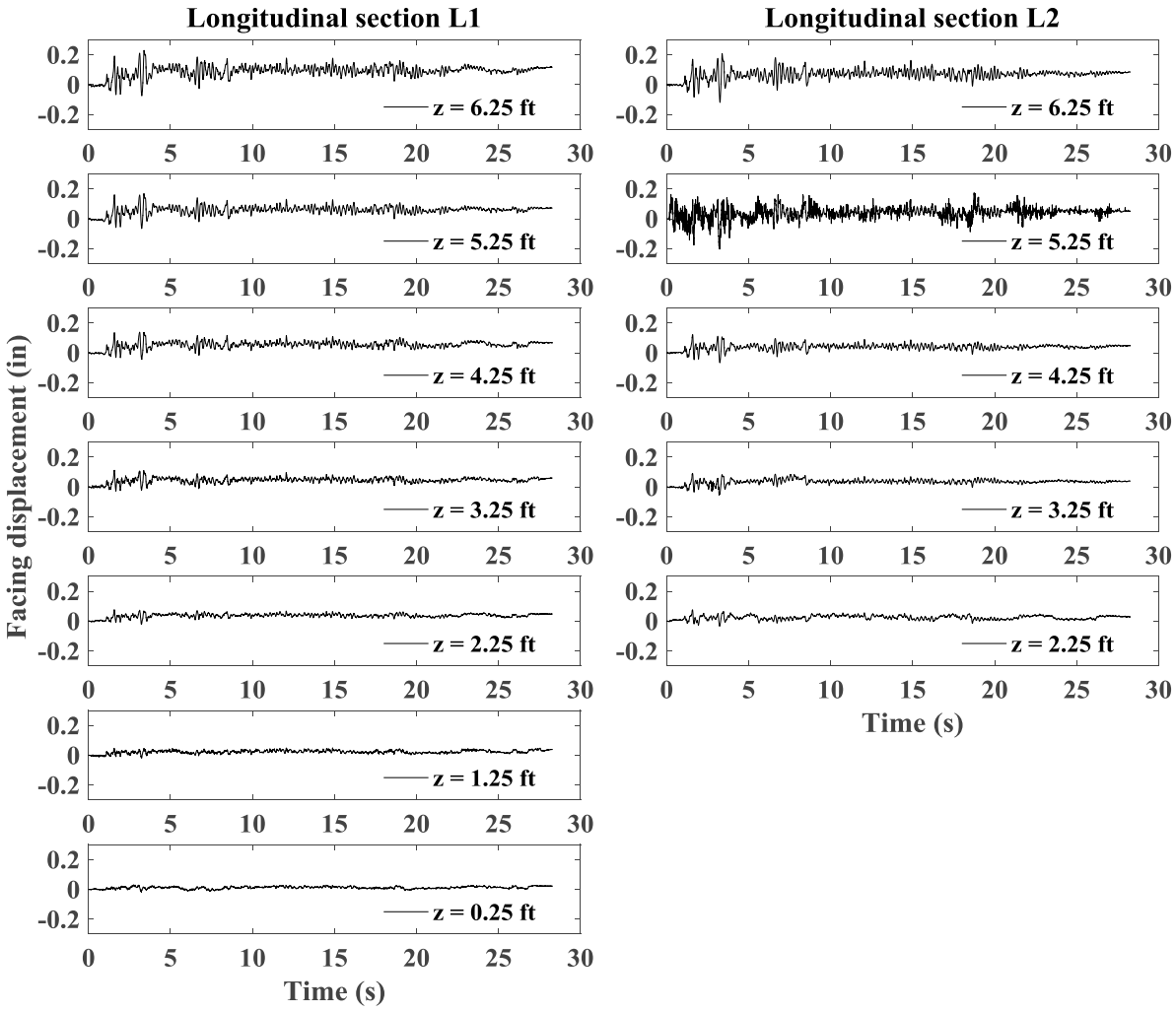

Figure A1.199 Time histories of incremental facing displacement for longitudinal sections L1 and L2.

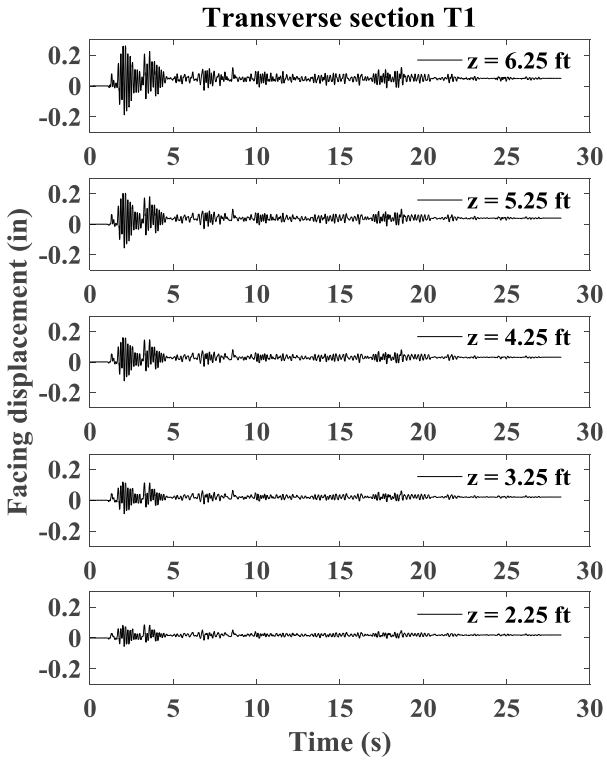

Figure A1.200 Time histories of incremental facing displacement for transverse section T1.

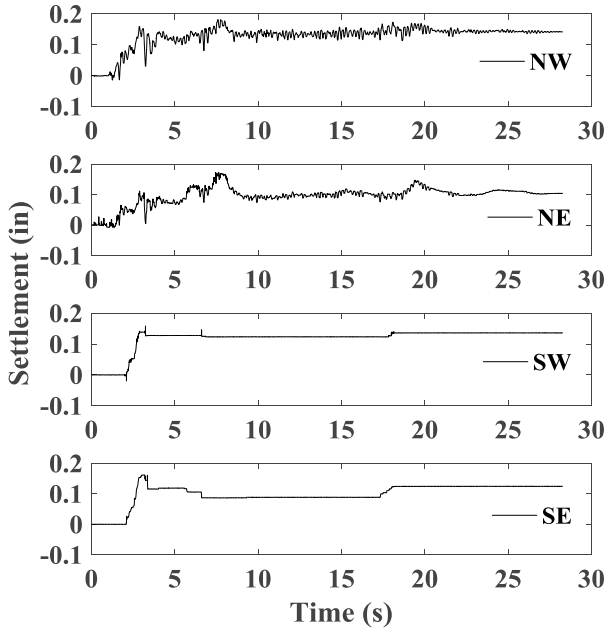

Figure A1.201 Time histories of incremental settlement for bridge seat.

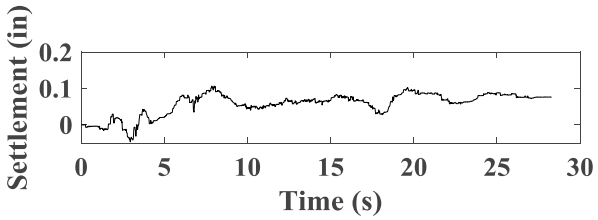

Figure A1.202 Time histories of incremental settlement for backfill soil in upper wall.

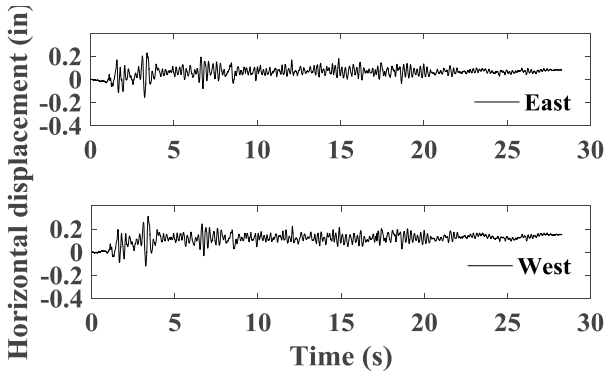

Figure A1.203 Time histories of incremental horizontal displacement for bridge seat.

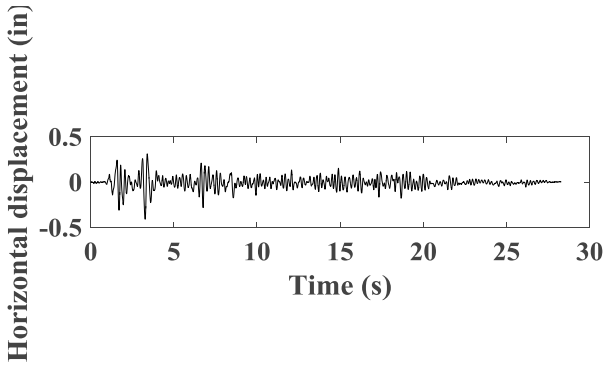

Figure A1.204 Time histories of incremental horizontal displacement for bridge beam.

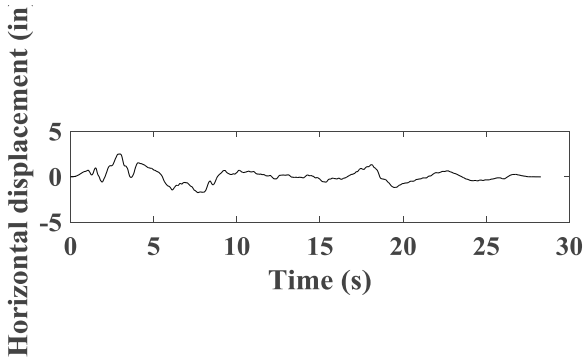

Figure A1.205 Time histories of horizontal displacement for support wall.

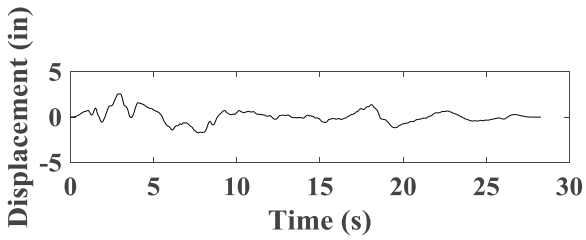

Figure A1.206 Time histories of horizontal displacement for shaking table.

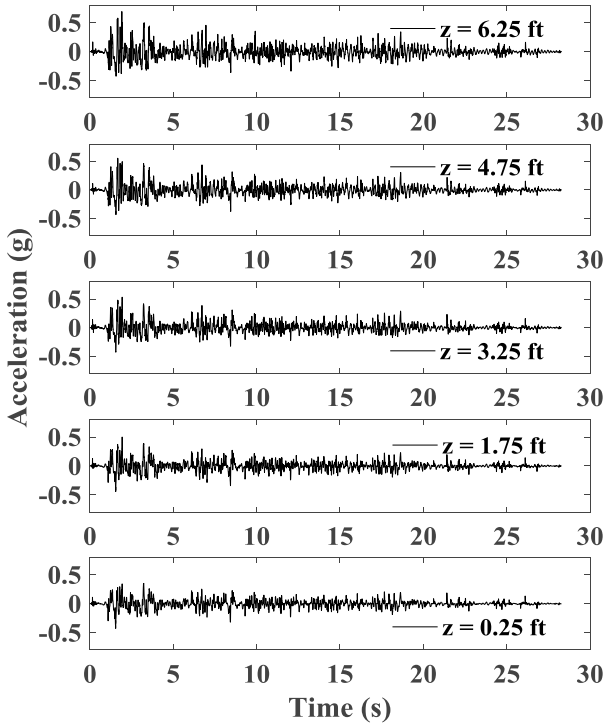

Figure A1.207 Time histories of acceleration for wall facing in longitudinal section L1.

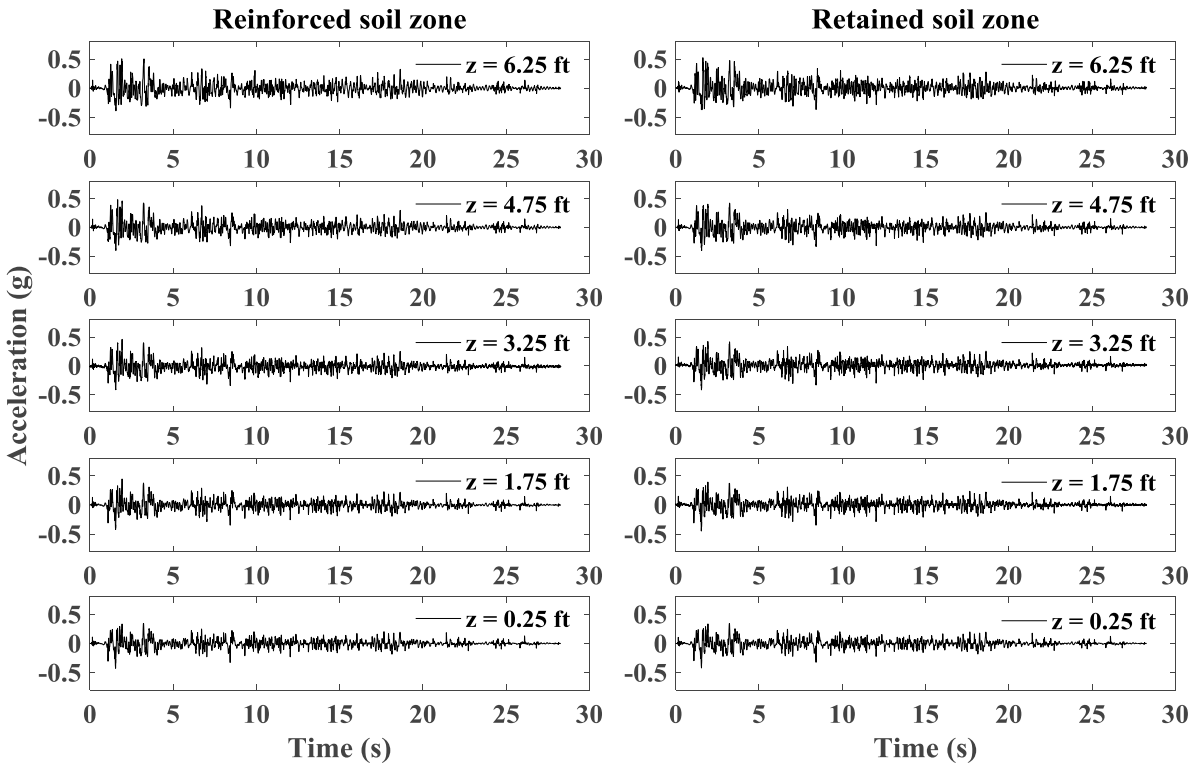

Figure A1.208 Time histories of acceleration for reinforced soil zone and retained soil zone in longitudinal section L1.

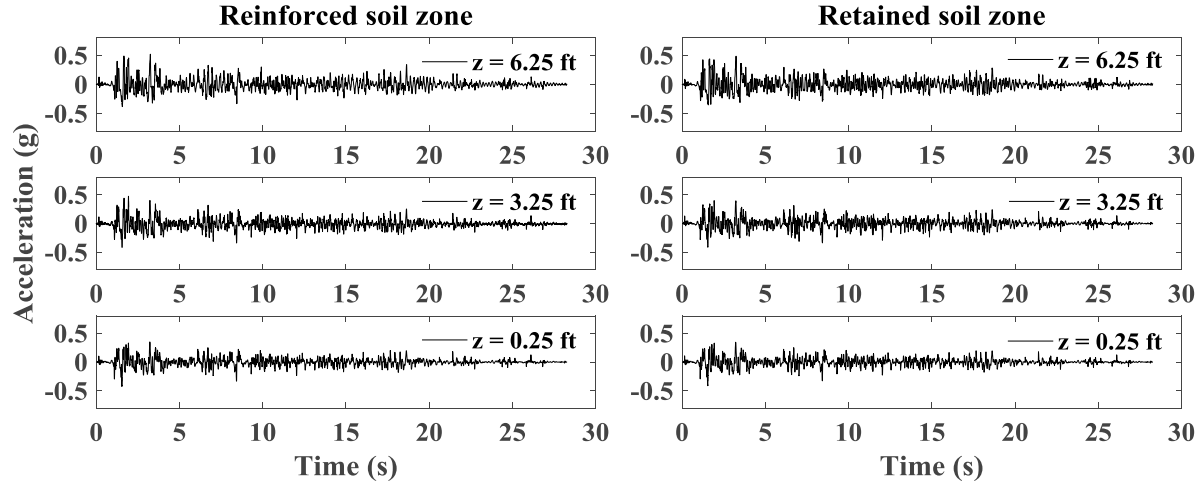

Figure A1.209 Time histories of acceleration for reinforced soil zone and retained soil zone in longitudinal section L2.

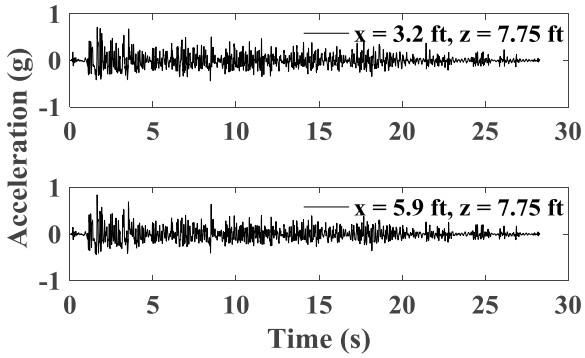

Figure A1.210 Time histories of acceleration for backfill soil in upper wall.

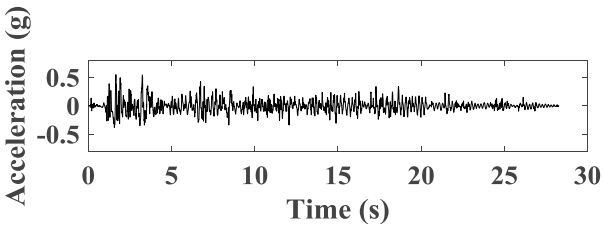

Figure A1.211 Time histories of acceleration for bridge seat.

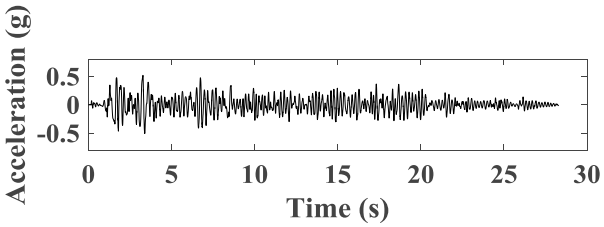

Figure A1.212 Time histories of acceleration for bridge beam.

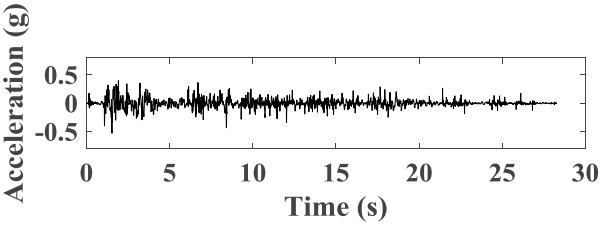

Figure A1.213 Time histories of acceleration for support wall.

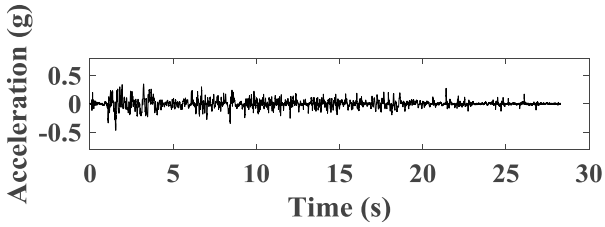

Figure A1.214 Time histories of acceleration for shaking table.

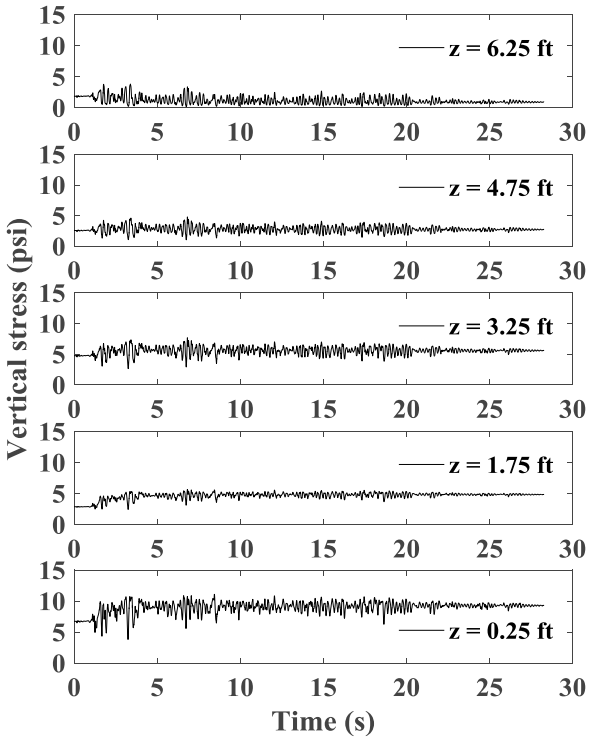

Figure A1.215 Time histories of vertical stress behind wall facing.

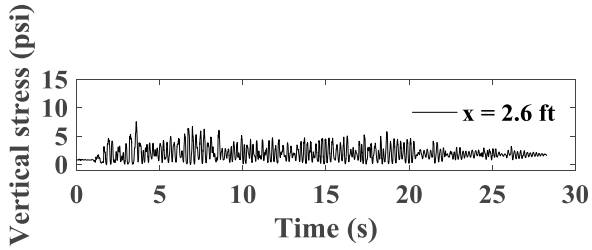

Figure A1.216 Time histories of vertical stress under bridge seat.

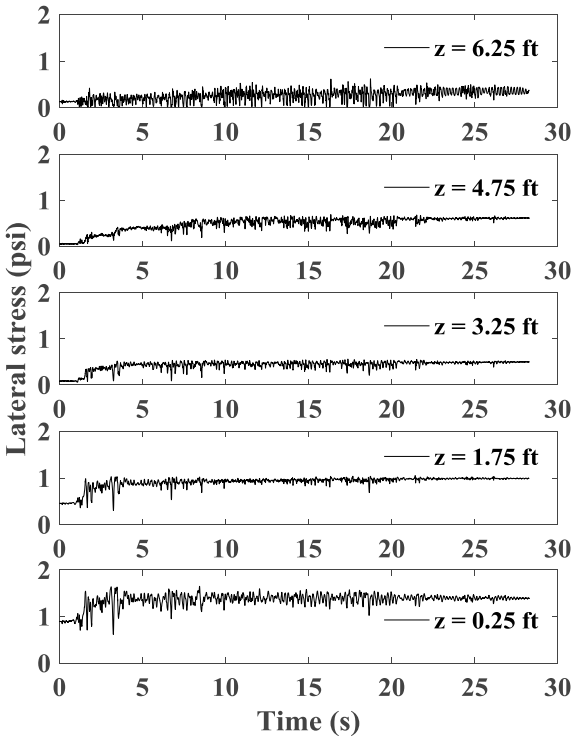

Figure A1.217 Time histories of lateral stress behind wall facing.

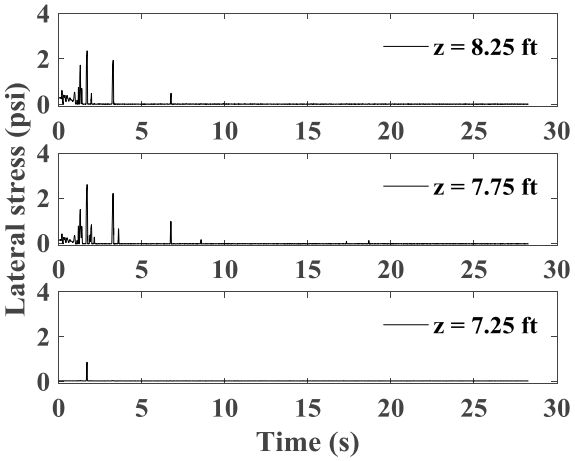

Figure A1.218 Time histories of lateral stress behind upper wall.

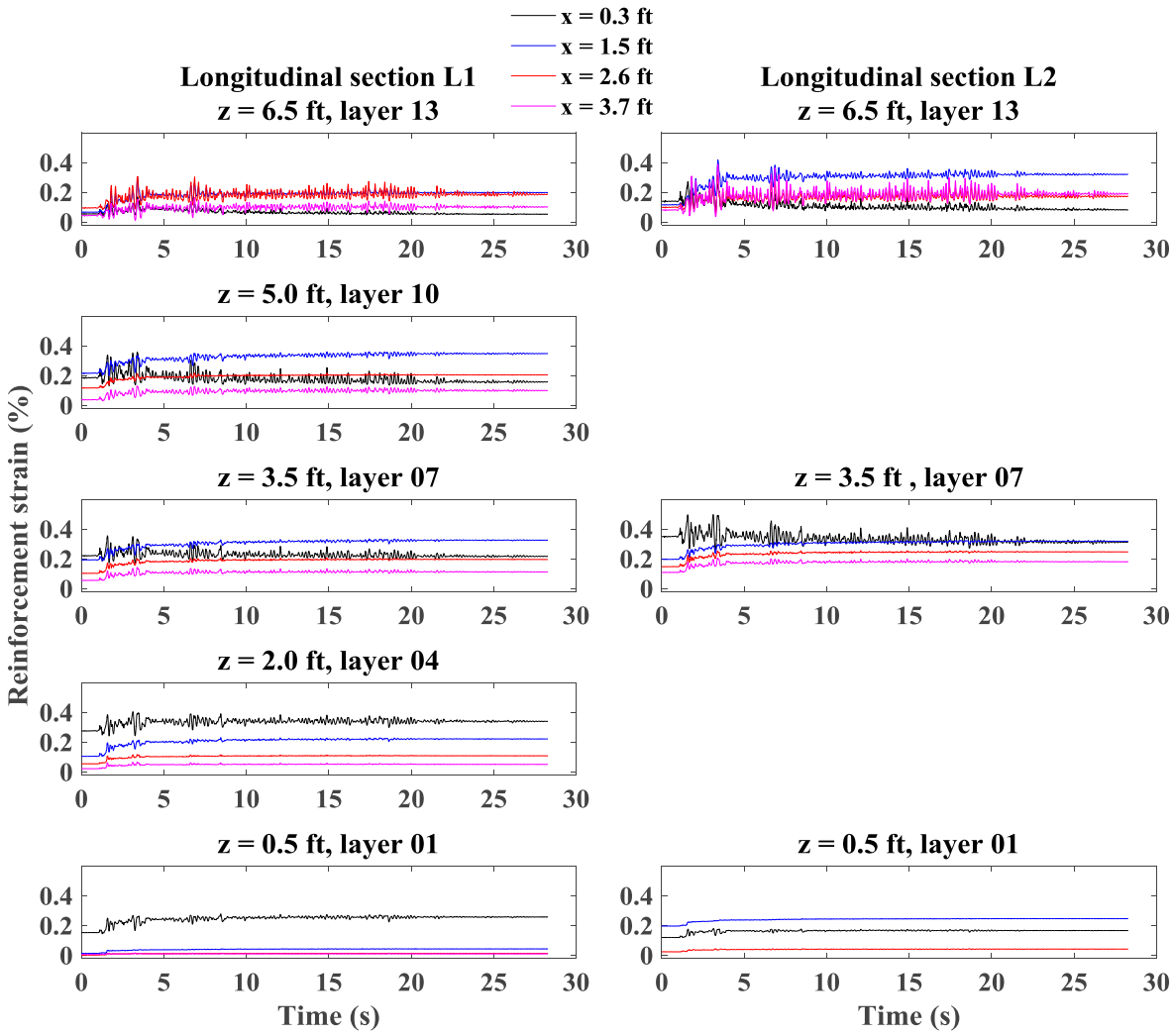

Figure A1.219 Time histories of reinforcement strain for longitudinal sections L1 and L2.

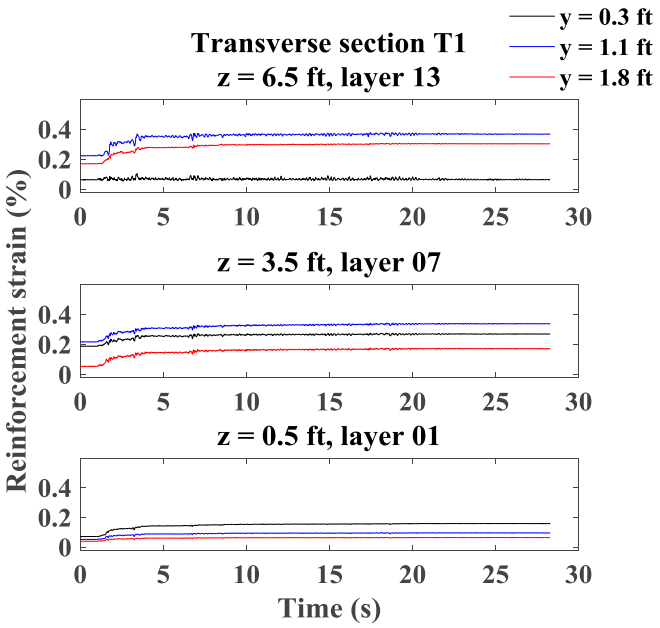

Figure A1.220 Time histories of reinforcement strain for transverse section T1.

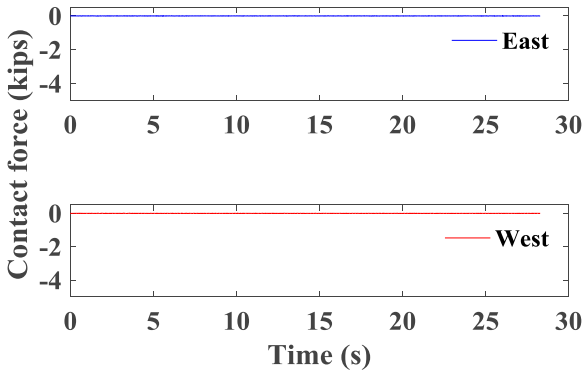

Figure A1.221 Time histories of contact force between bridge seat and bridge beam.

A1.4.2 Maule Motion

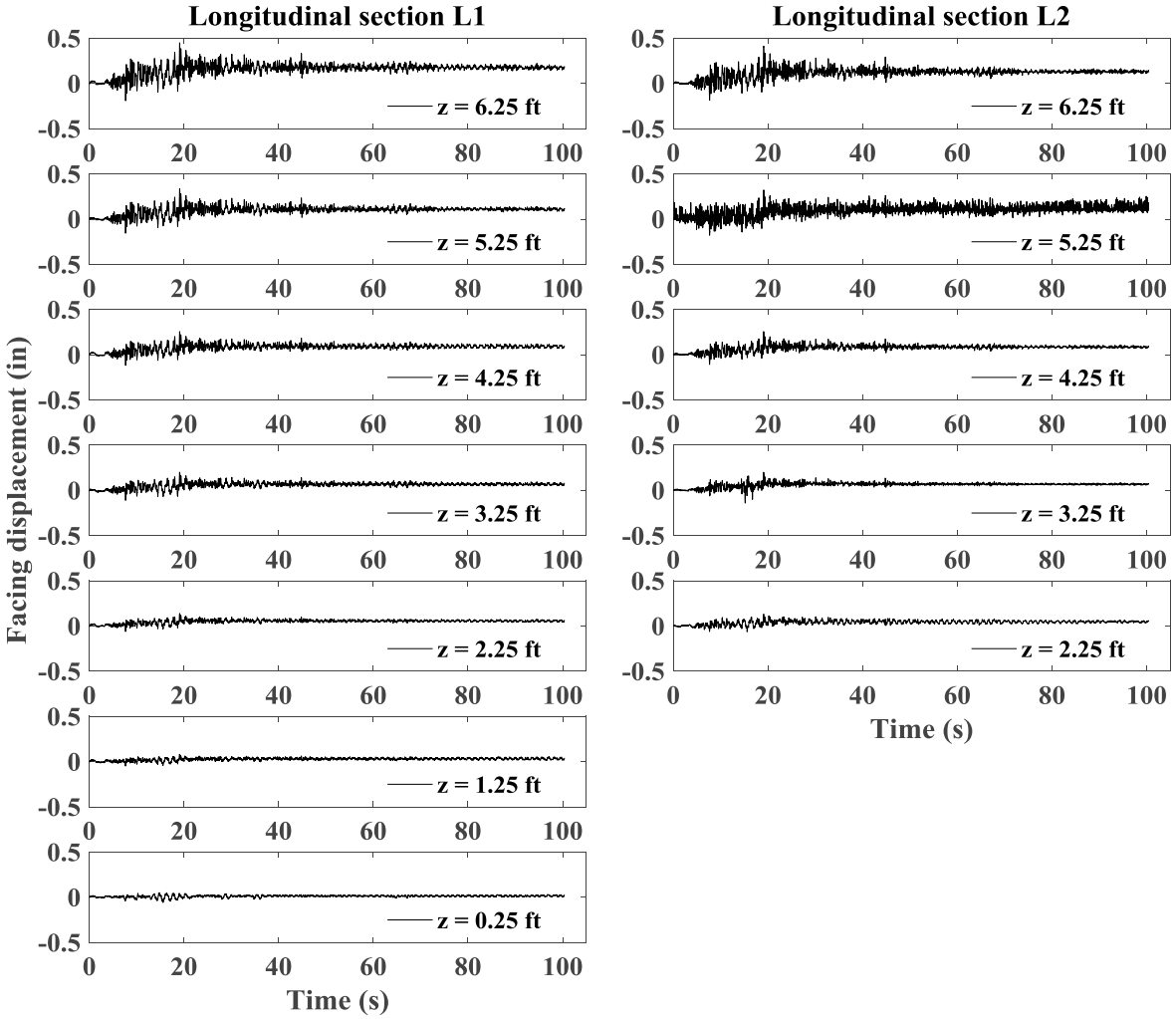

Figure A1.222 Time histories of incremental facing displacement for longitudinal sections L1 and L2.

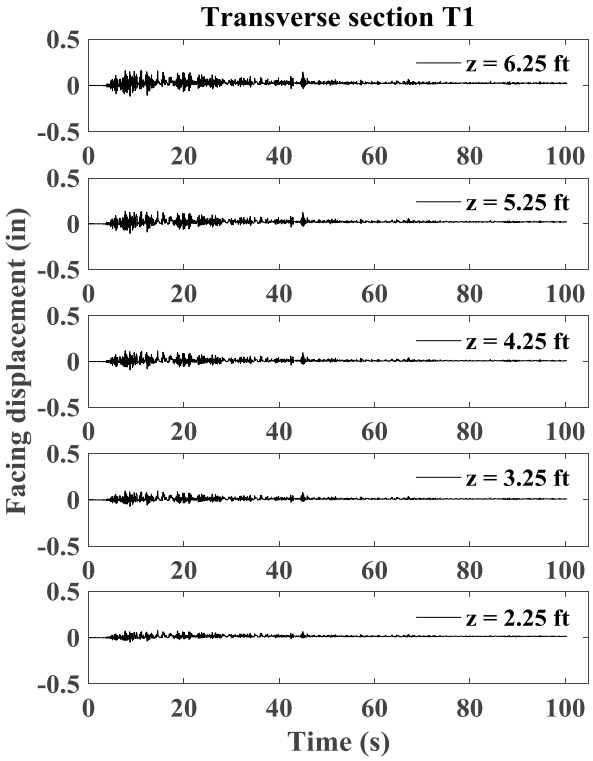

Figure A1.223 Time histories of incremental facing displacement for transverse section T1.

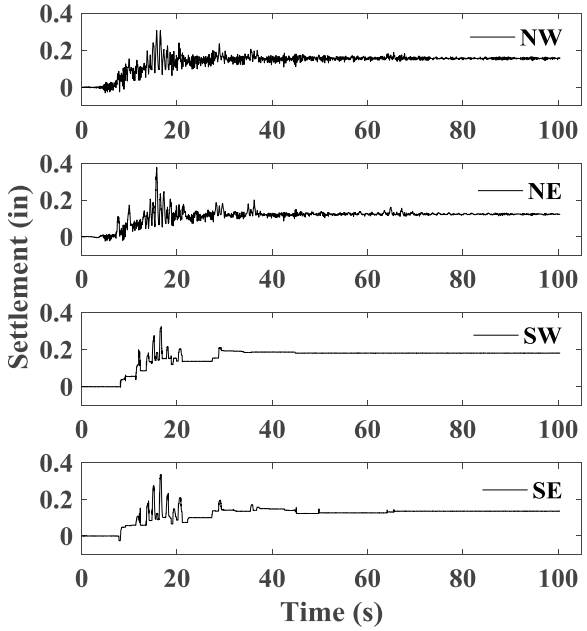

Figure A1.224 Time histories of incremental settlement for bridge seat.

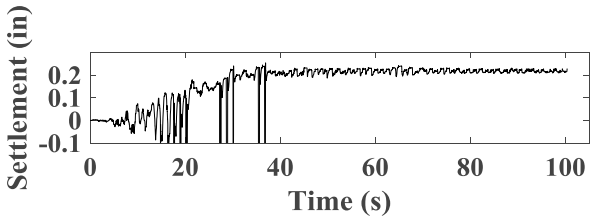

Figure A1.225 Time histories of incremental settlement for backfill soil in upper wall.

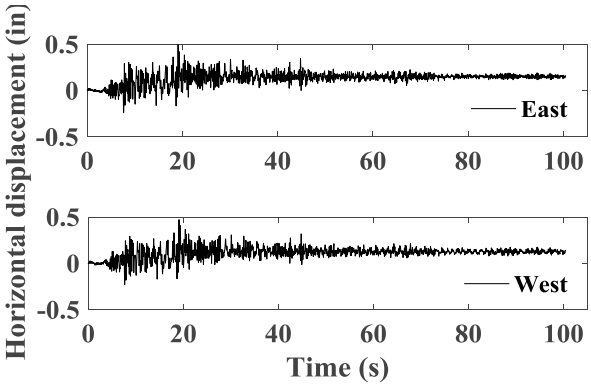

Figure A1.226 Time histories of incremental horizontal displacement for bridge seat.

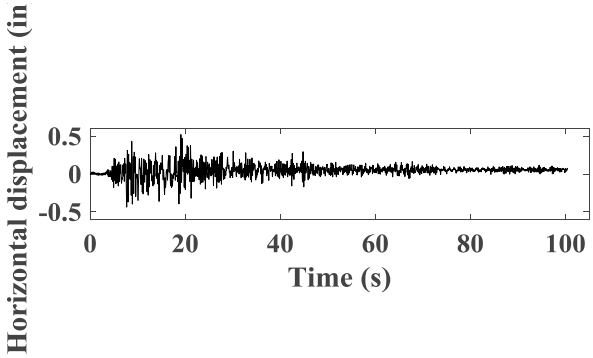

Figure A1.227 Time histories of incremental horizontal displacement for bridge beam.

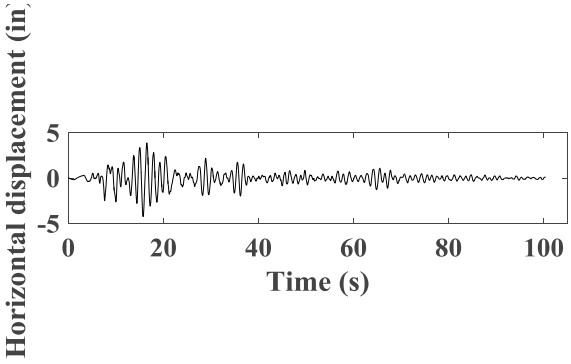

Figure A1.228 Time histories of horizontal displacement for support wall.

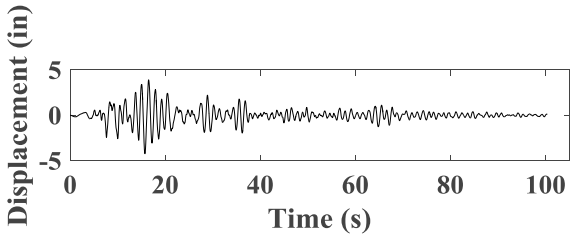

Figure A1.229 Time histories of horizontal displacement for shaking table.

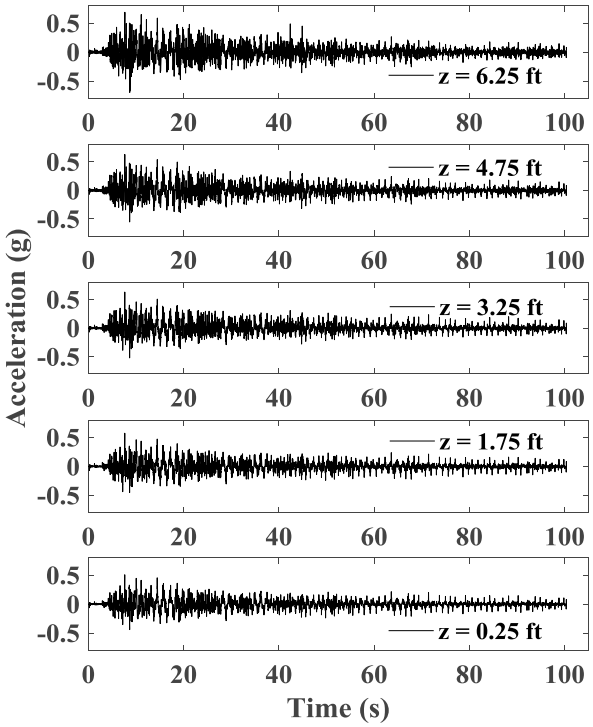

Figure A1.230 Time histories of acceleration for wall facing in longitudinal section L1.

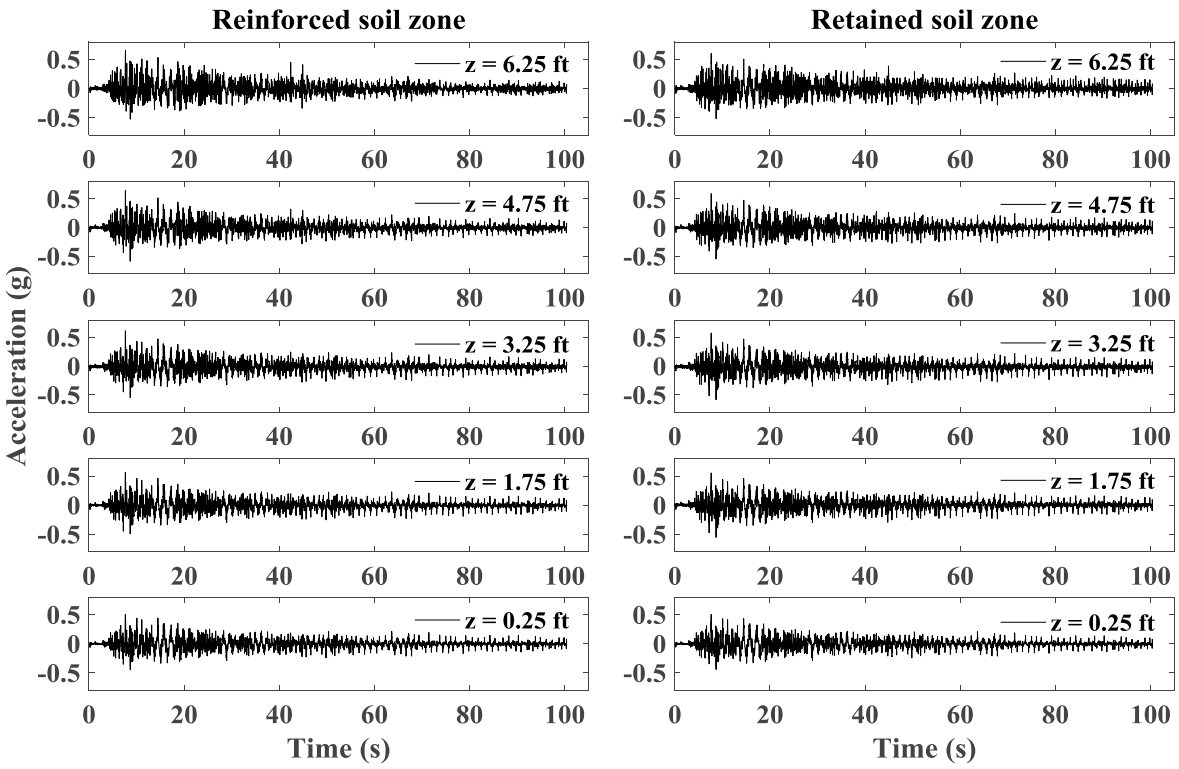

Figure A1.231 Time histories of acceleration for reinforced soil zone and retained soil zone in longitudinal section L1.

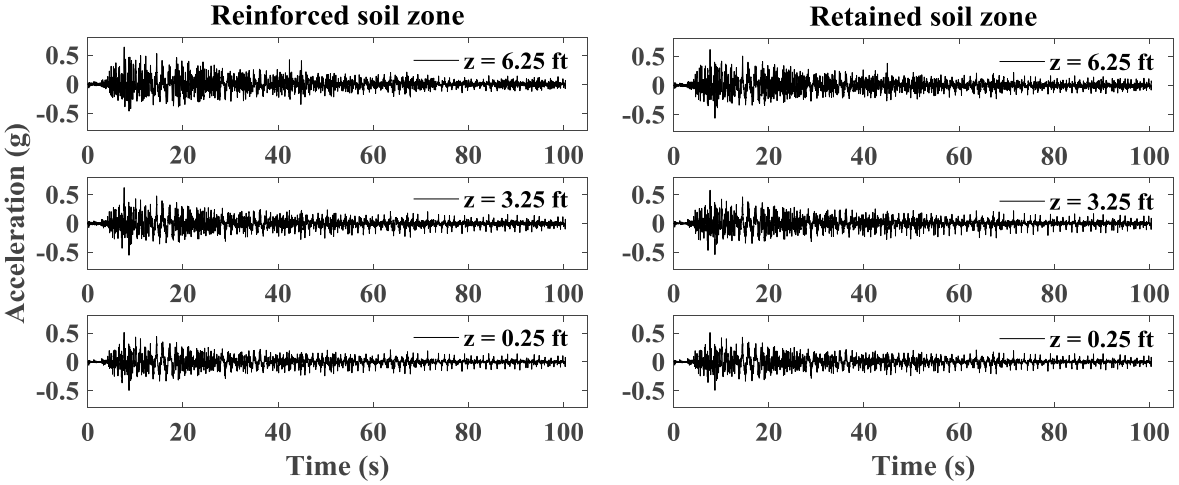

Figure A1.232 Time histories of acceleration for reinforced soil zone and retained soil zone in longitudinal section L2.

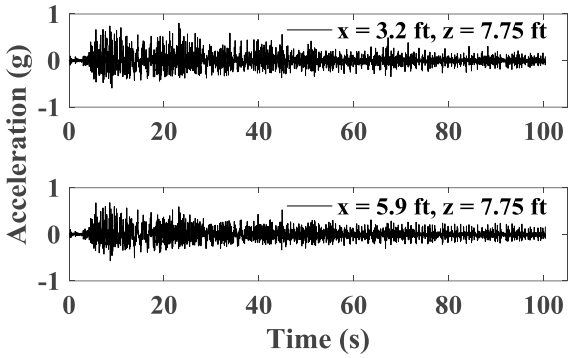

Figure A1.233 Time histories of acceleration for backfill soil in upper wall.

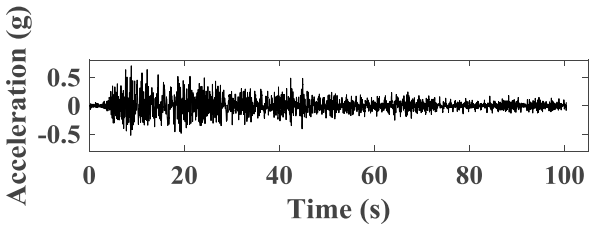

Figure A1.234 Time histories of acceleration for bridge seat.

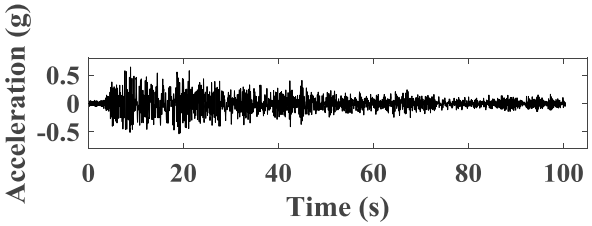

Figure A1.235 Time histories of acceleration for bridge beam.

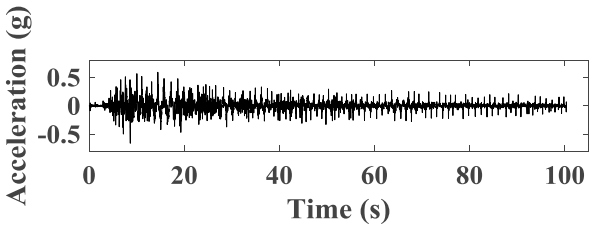

Figure A1.236 Time histories of acceleration for support wall.

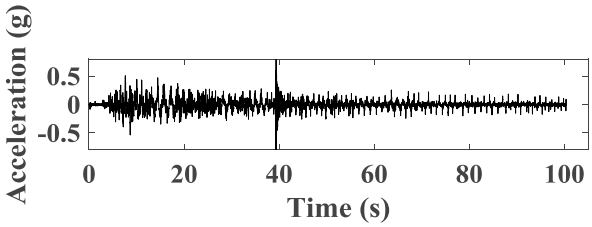

Figure A1.237 Time histories of acceleration for shaking table.

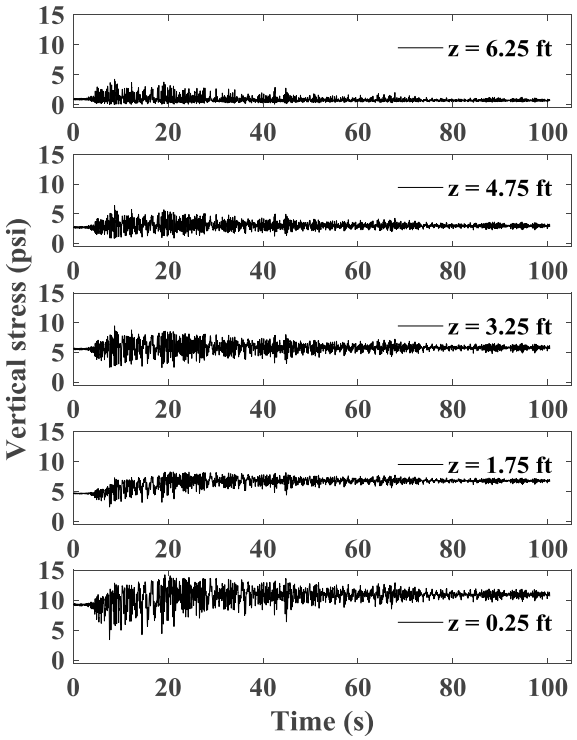

Figure A1.238 Time histories of vertical stress behind wall facing.

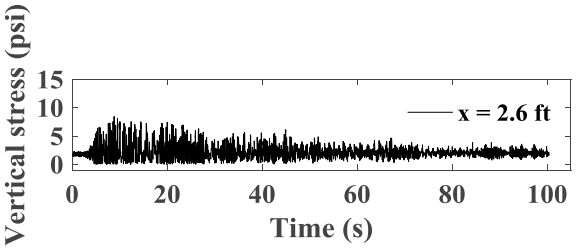

Figure A1.239 Time histories of vertical stress under bridge seat.

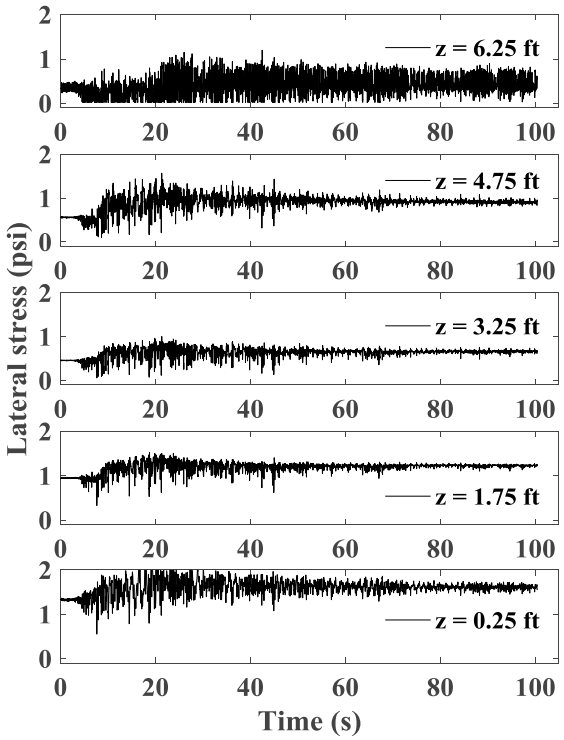

Figure A1.240 Time histories of lateral stress behind wall facing.

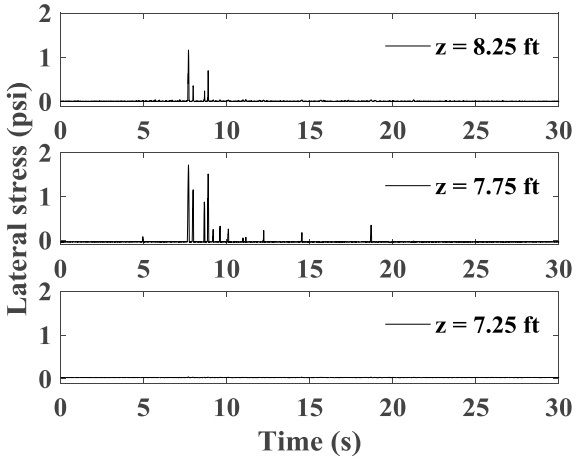

Figure A1.241 Time histories of lateral stress behind upper wall.

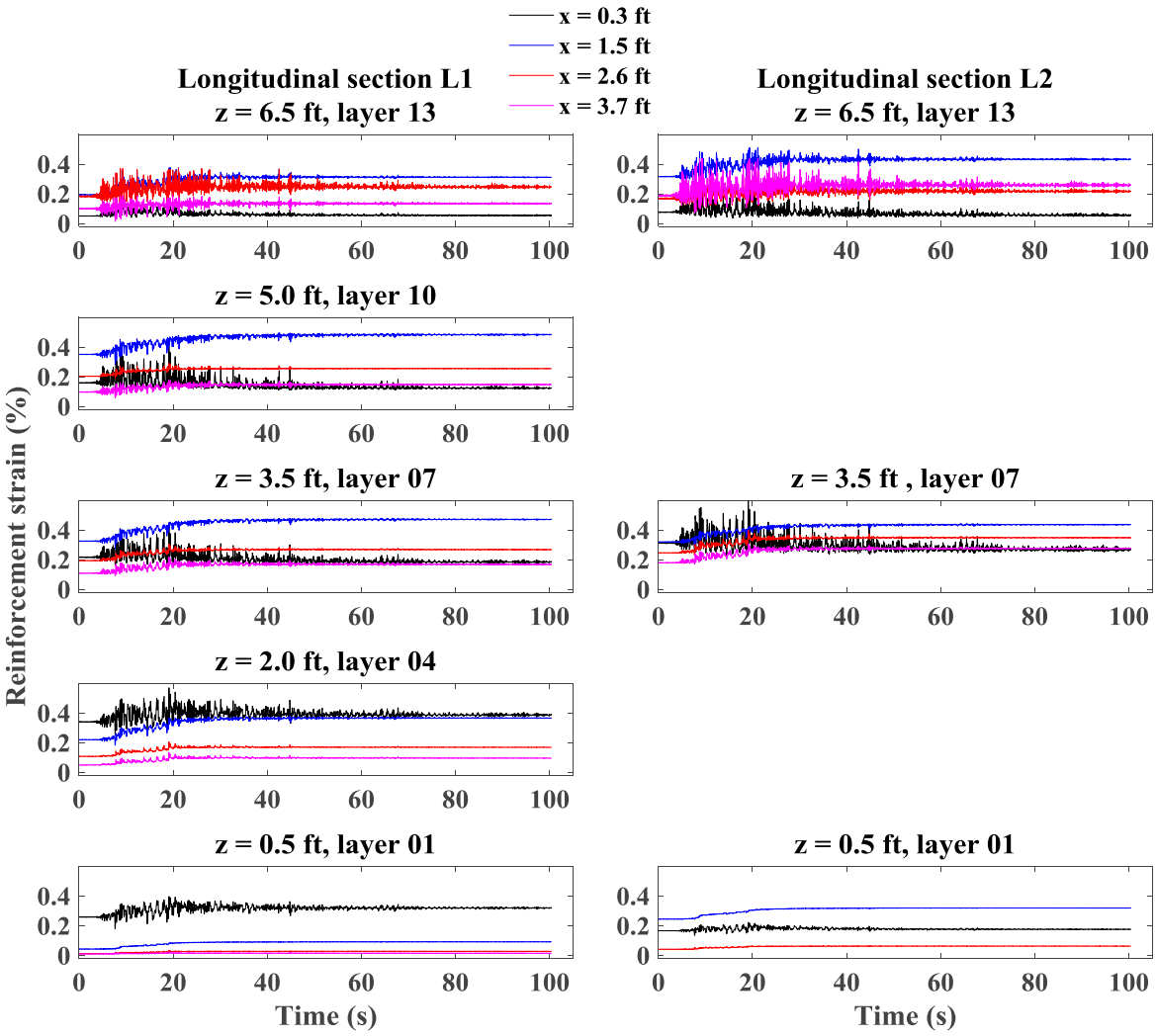

Figure A1.242 Time histories of reinforcement strain for longitudinal sections L1 and L2.

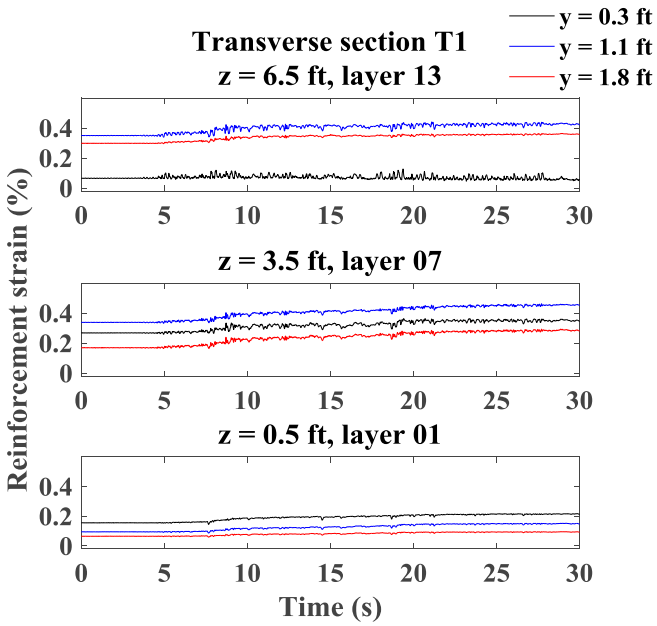

Figure A1.243 Time histories of reinforcement strain for transverse section T1.

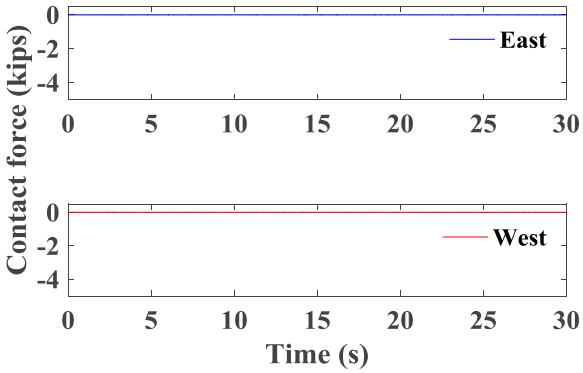

Figure A1.244 Time histories of contact force between bridge seat and bridge beam.

A1.4.3 Northridge Motion

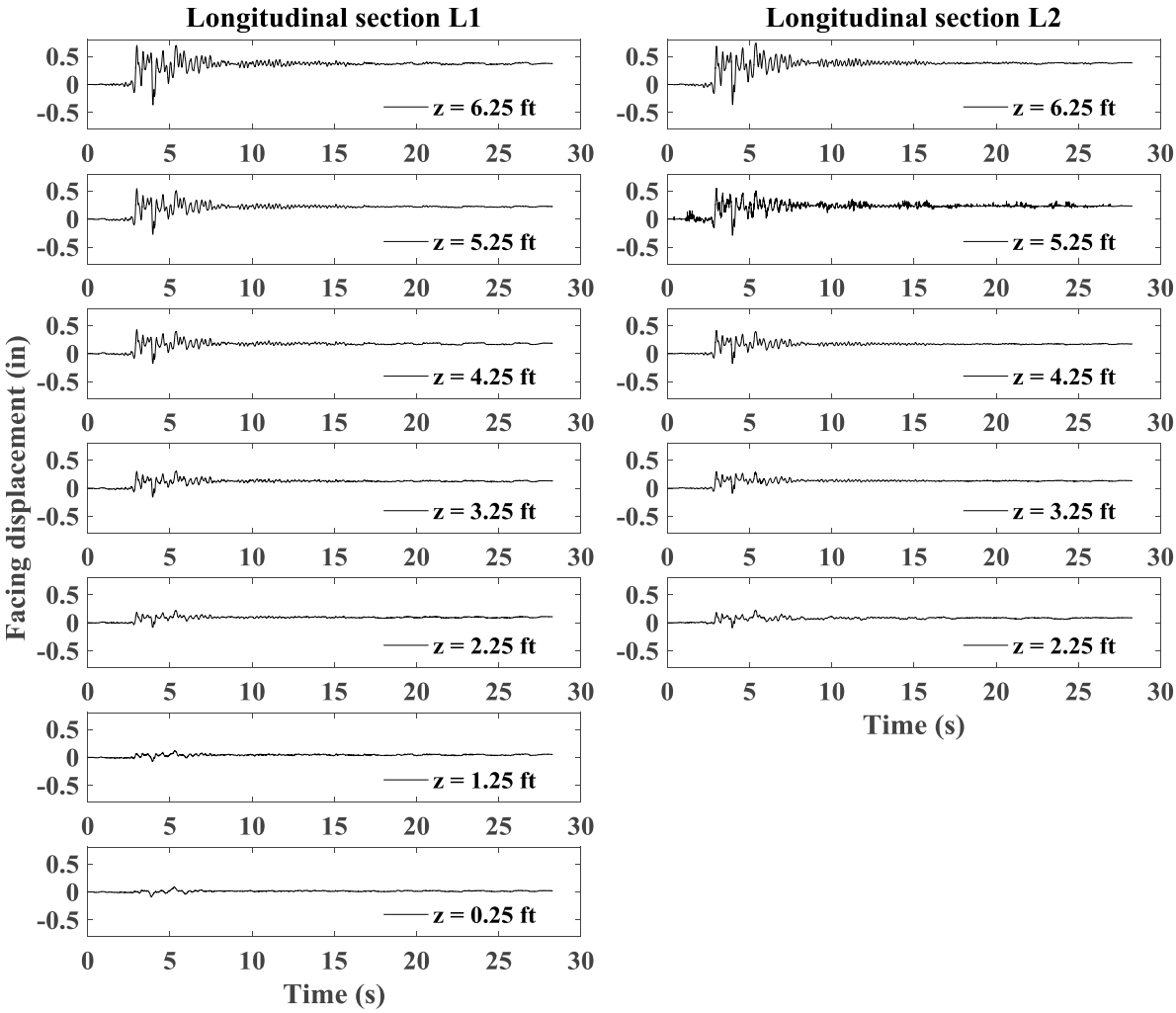

Figure A1.245 Time histories of incremental facing displacement for longitudinal sections L1 and L2.

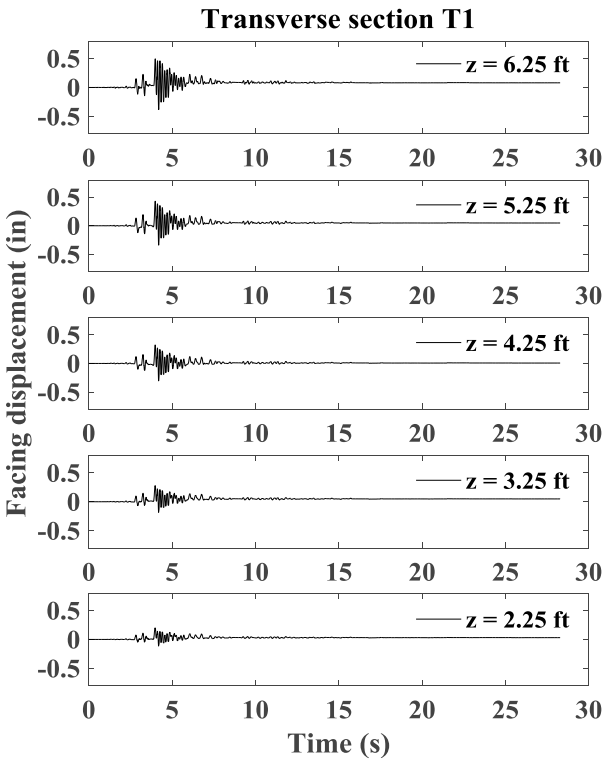

Figure A1.246 Time histories of incremental facing displacement for transverse section T1.

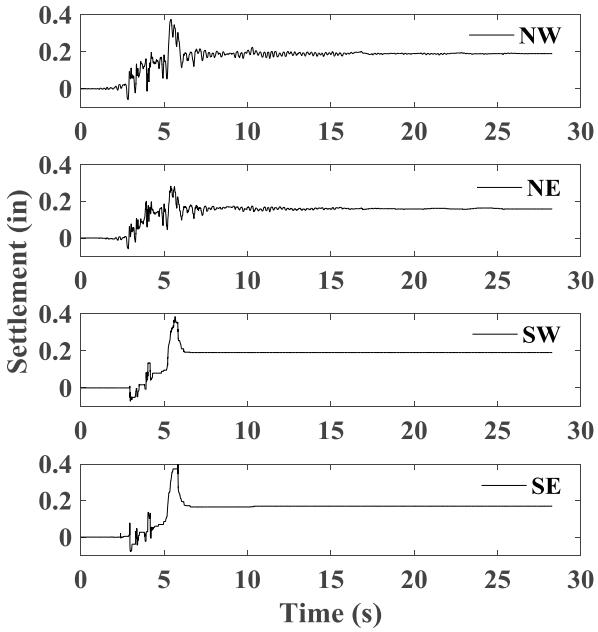

Figure A1.247 Time histories of incremental settlement for bridge seat.

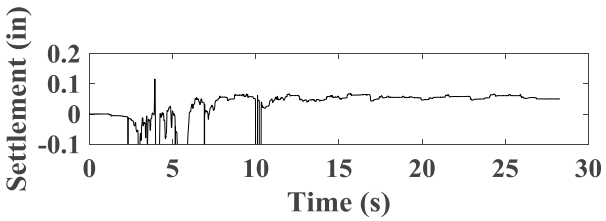

Figure A1.248 Time histories of incremental settlement for backfill soil in upper wall.

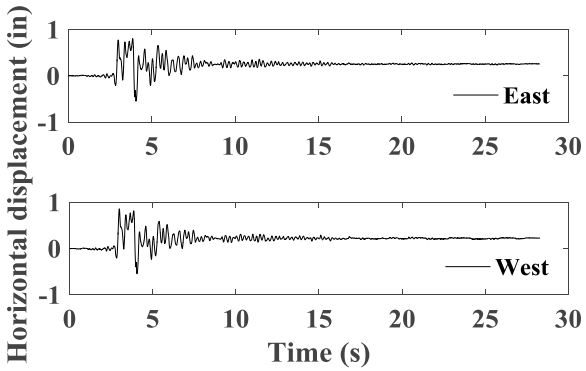

Figure A1.249 Time histories of incremental horizontal displacement for bridge seat.

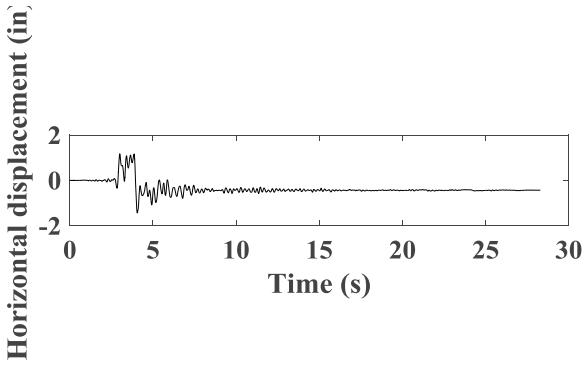

Figure A1.250 Time histories of incremental horizontal displacement for bridge beam.

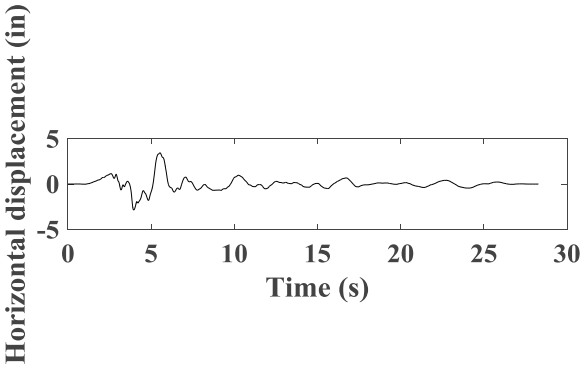

Figure A1.251 Time histories of horizontal displacement for support wall.

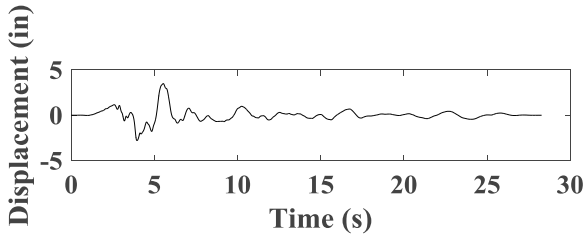

Figure A1.252 Time histories of horizontal displacement for shaking table.

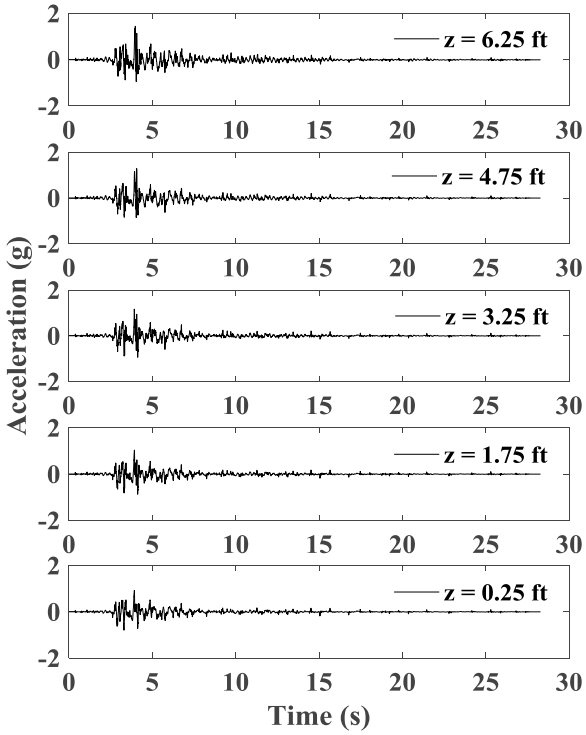

Figure A1.253 Time histories of acceleration for wall facing in longitudinal section L1.

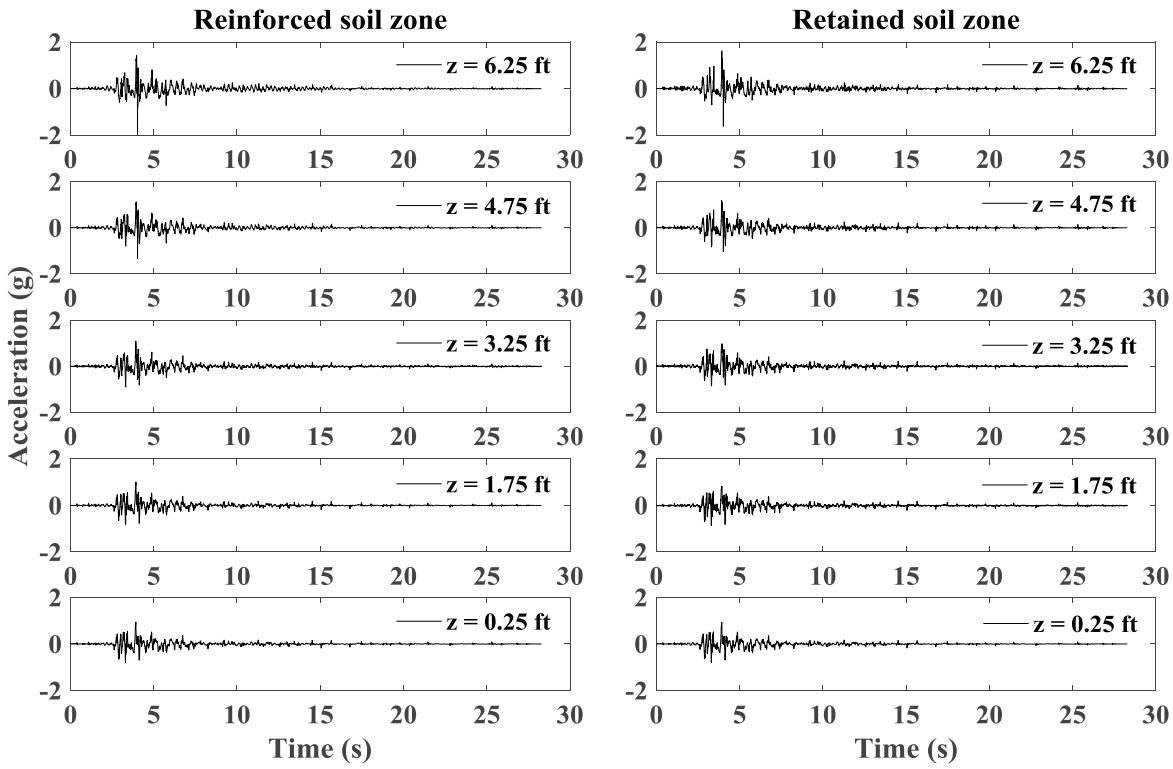

Figure A1.254 Time histories of acceleration for reinforced soil zone and retained soil zone in longitudinal section L1.

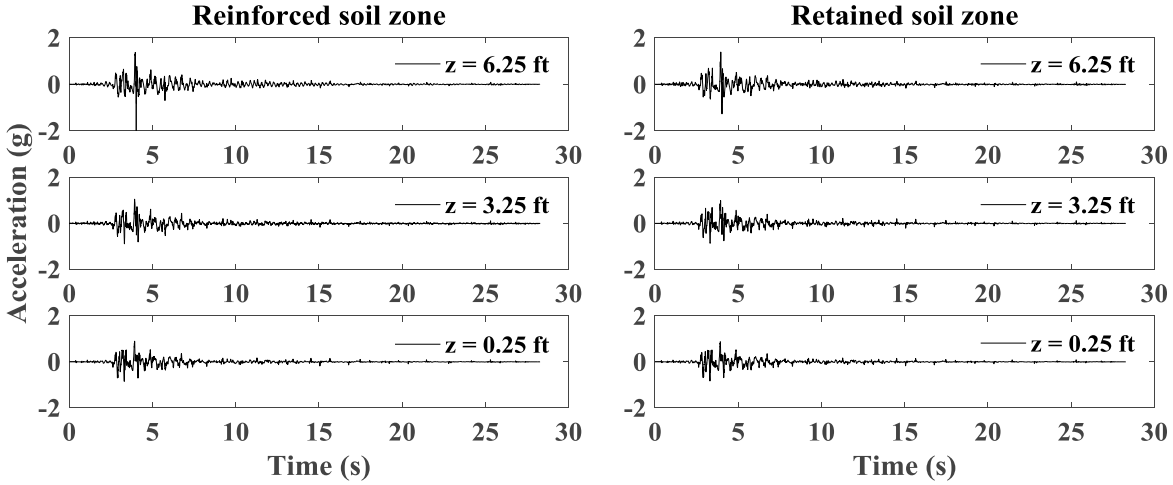

Figure A1.255 Time histories of acceleration for reinforced soil zone and retained soil zone in longitudinal section L2.

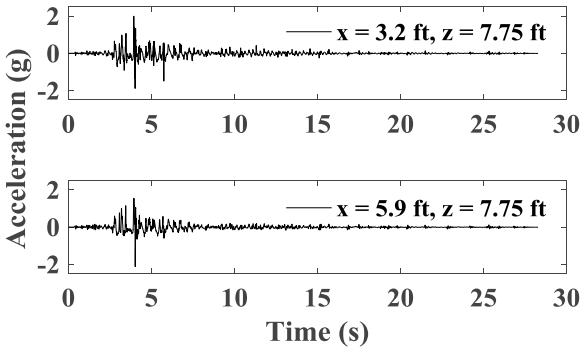

Figure A1.256 Time histories of acceleration for backfill soil in upper wall.

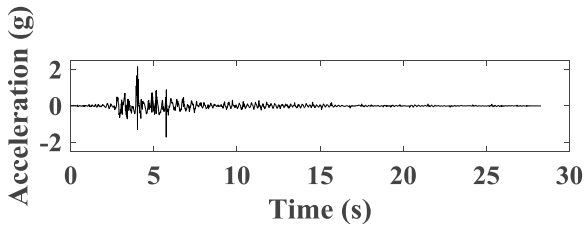

Figure A1.257 Time histories of acceleration for bridge seat.

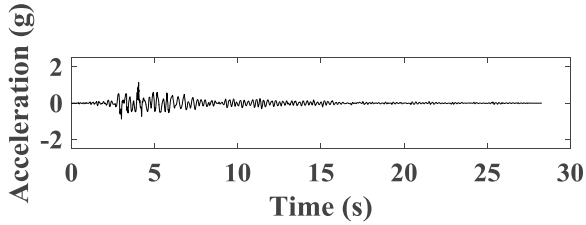

Figure A1.258 Time histories of acceleration for bridge beam.

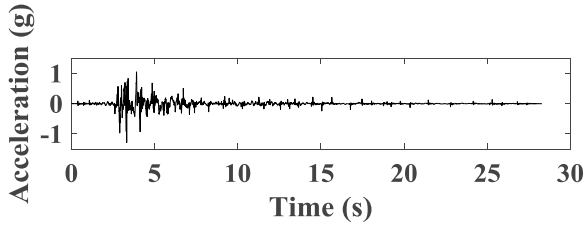

Figure A1.259 Time histories of acceleration for support wall.

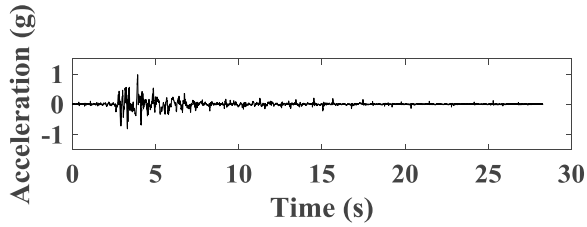

Figure A1.260 Time histories of acceleration for shaking table.

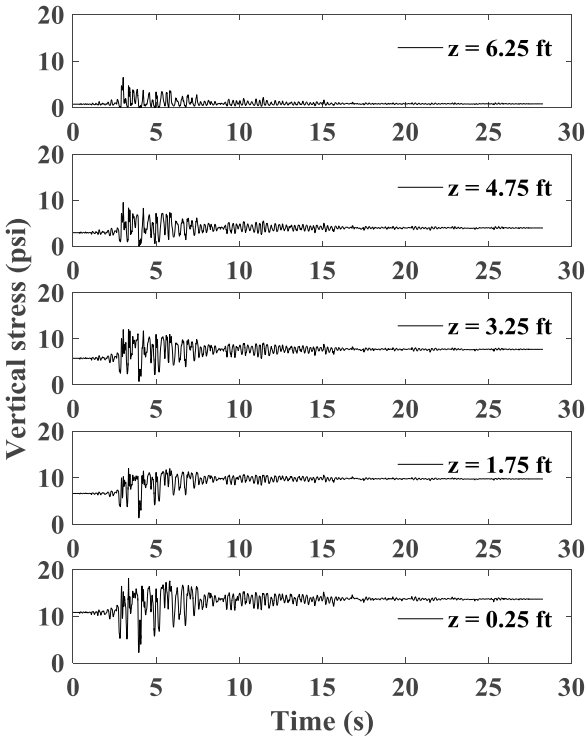

Figure A1.261 Time histories of vertical stress behind wall facing.

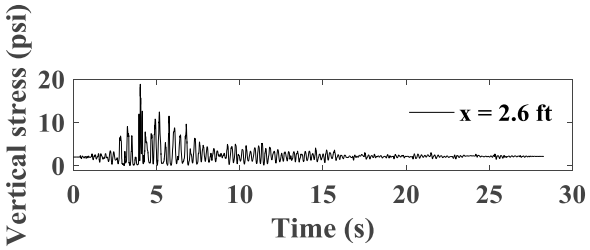

Figure A1.262 Time histories of vertical stress under bridge seat.

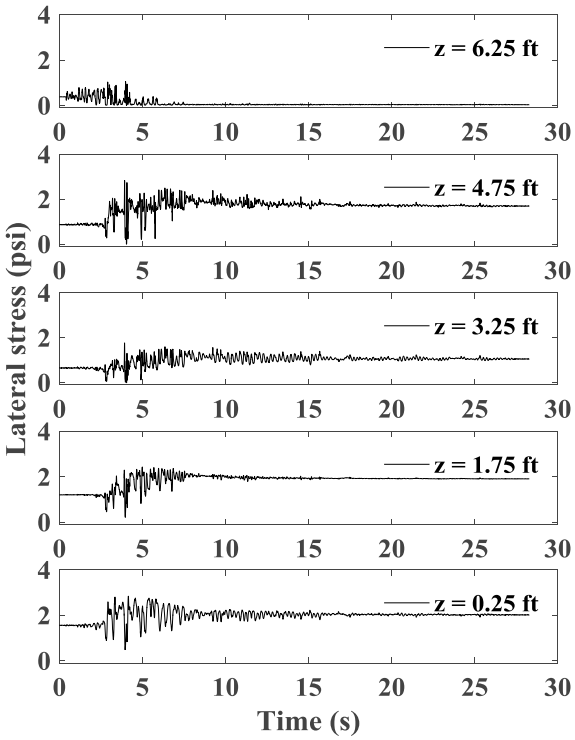

Figure A1.263 Time histories of lateral stress behind wall facing.

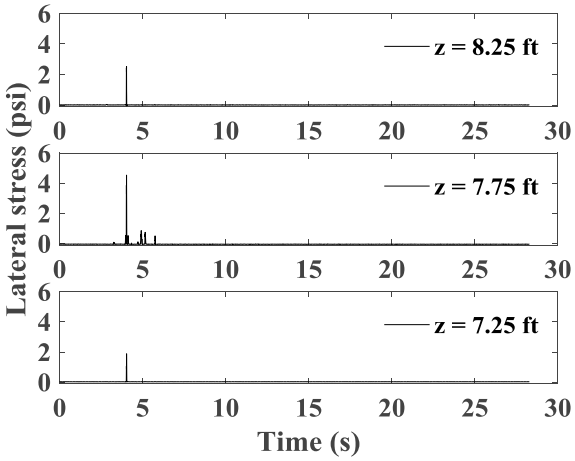

Figure A1.264 Time histories of lateral stress behind upper wall.

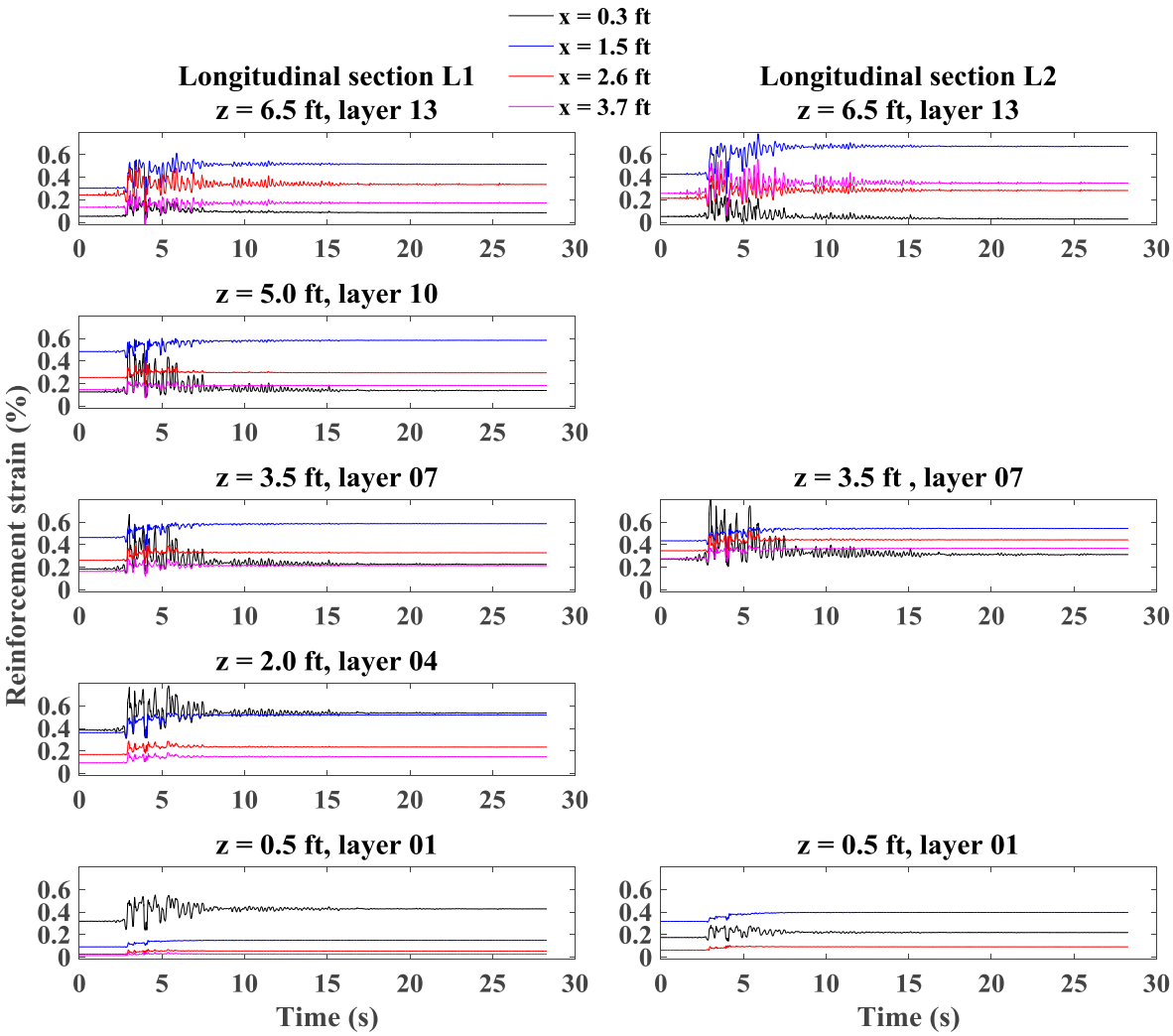

Figure A1.265 Time histories of reinforcement strain for longitudinal sections L1 and L2.

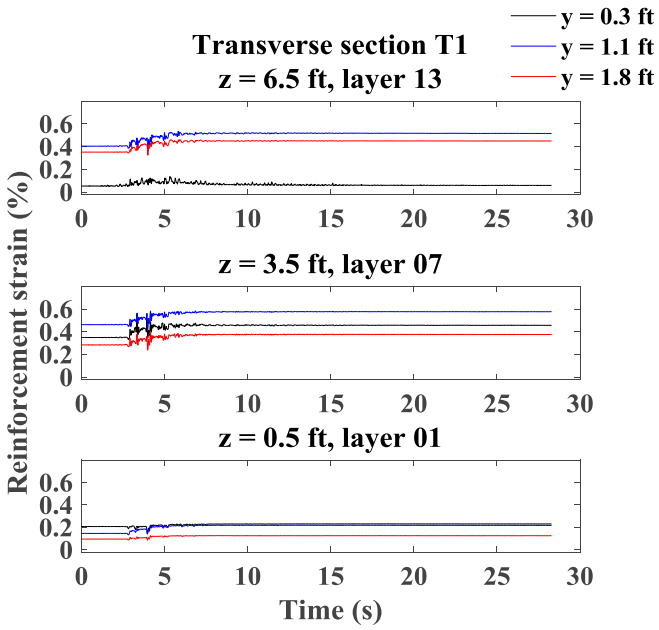

Figure A1.266 Time histories of reinforcement strain for transverse section T1.

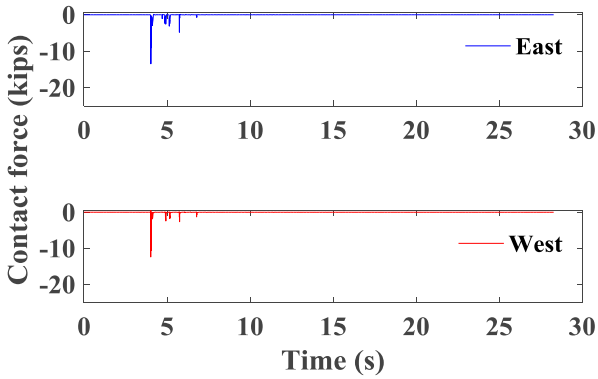

Figure A1.267 Time histories of contact force between bridge seat and bridge beam.

A1.5 Test 5

A1.5.1 Imperial Valley Motion

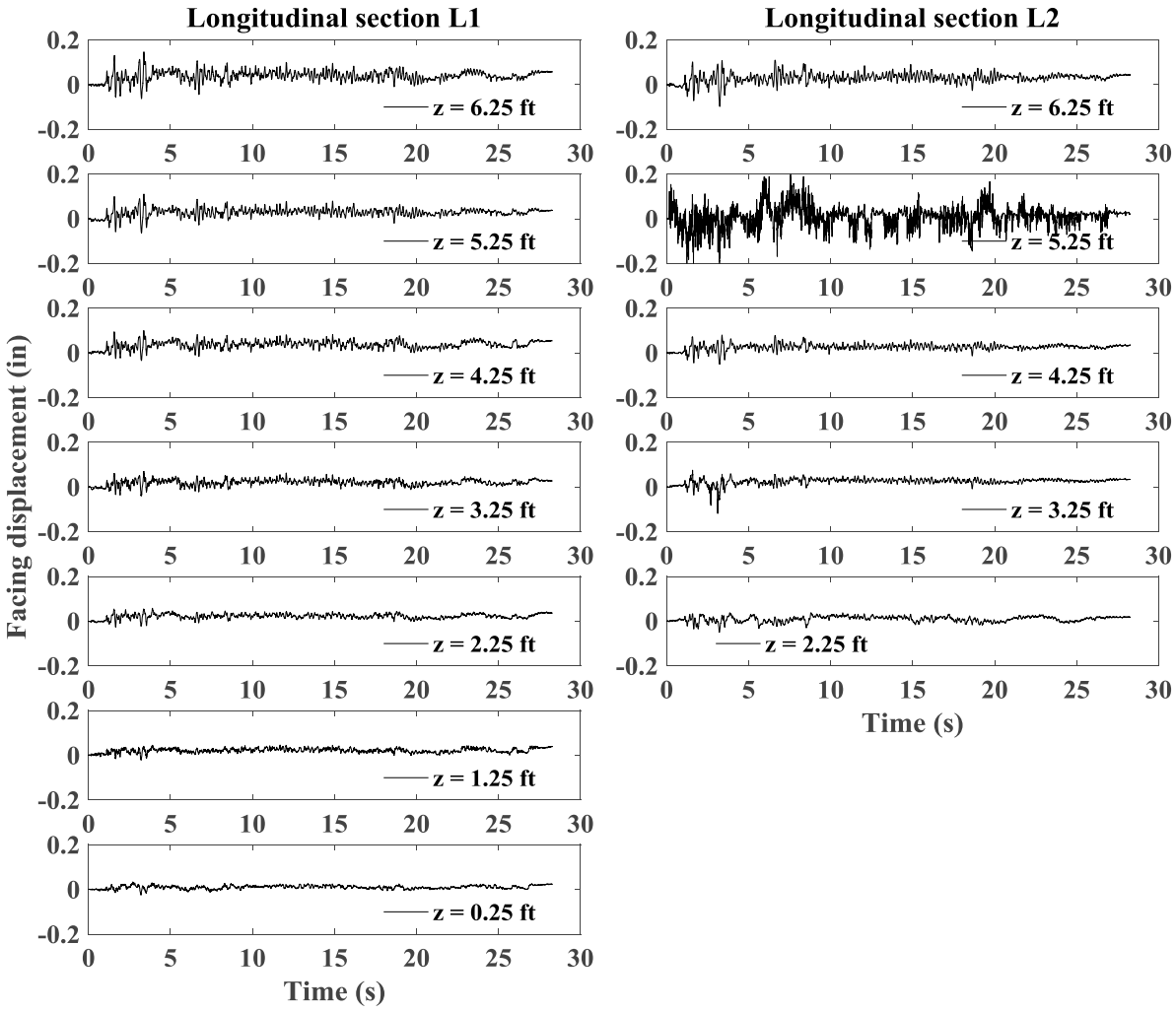

Figure A1.268 Time histories of incremental facing displacement for longitudinal sections L1 and L2.

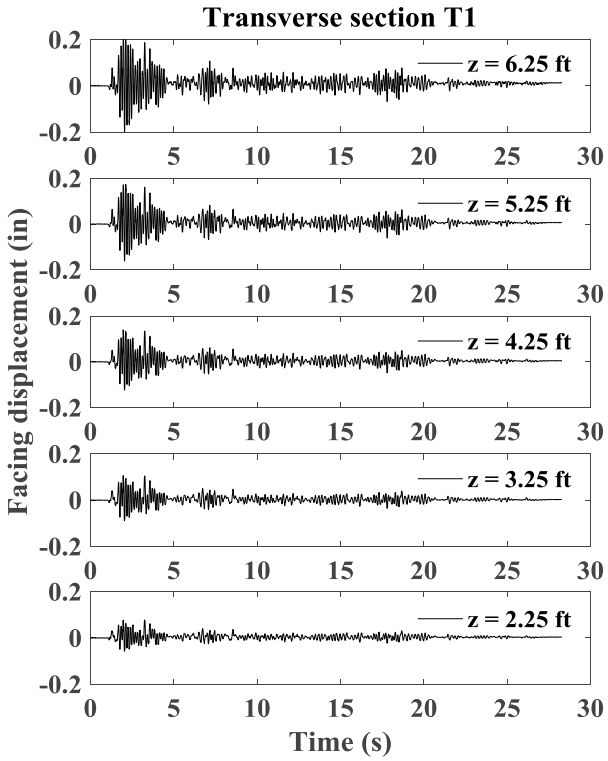

Figure A1.269 Time histories of incremental facing displacement for transverse section T1.

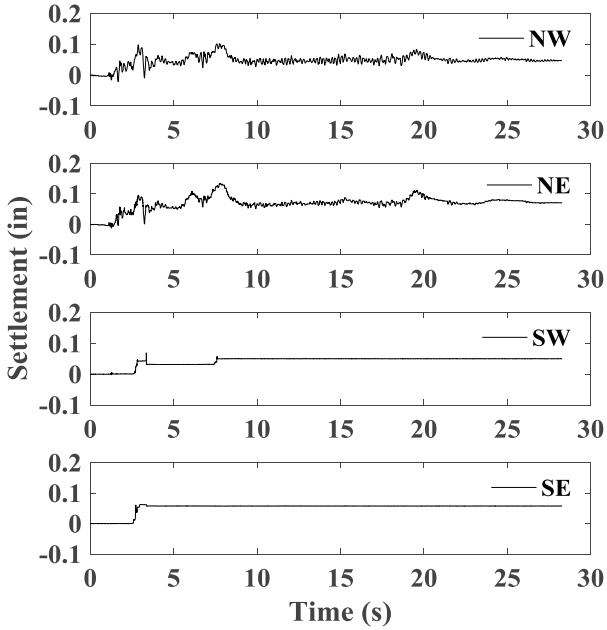

Figure A1.270 Time histories of incremental settlement for bridge seat.

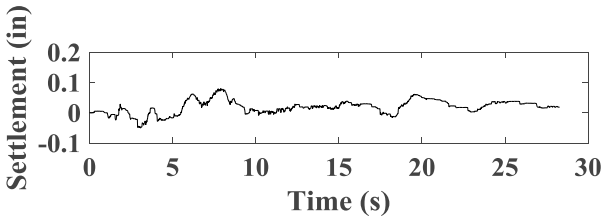

Figure A1.271 Time histories of incremental settlement for backfill soil in upper wall.

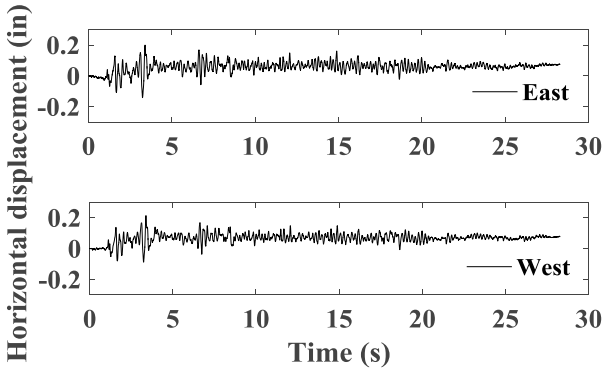

Figure A1.272 Time histories of incremental horizontal displacement for bridge seat.

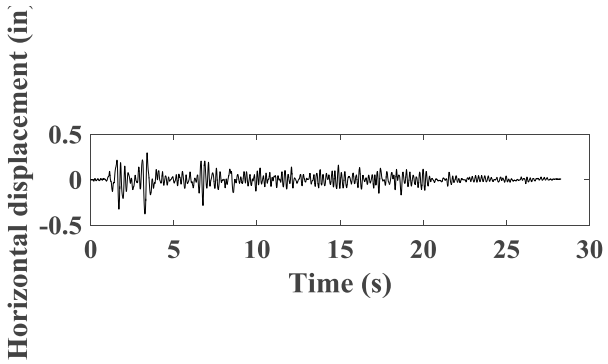

Figure A1.273 Time histories of incremental horizontal displacement for bridge beam.

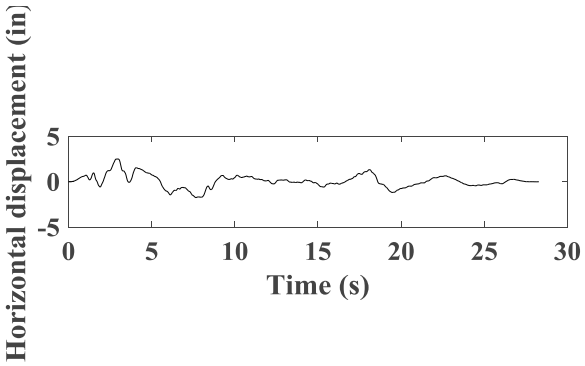

Figure A1.274 Time histories of horizontal displacement for support wall.

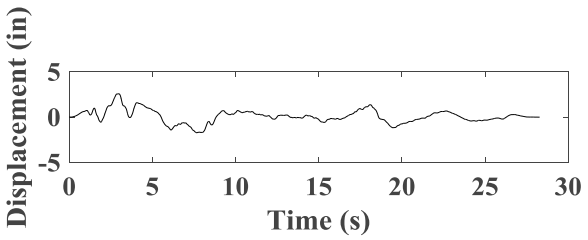

Figure A1.275 Time histories of horizontal displacement for shaking table.

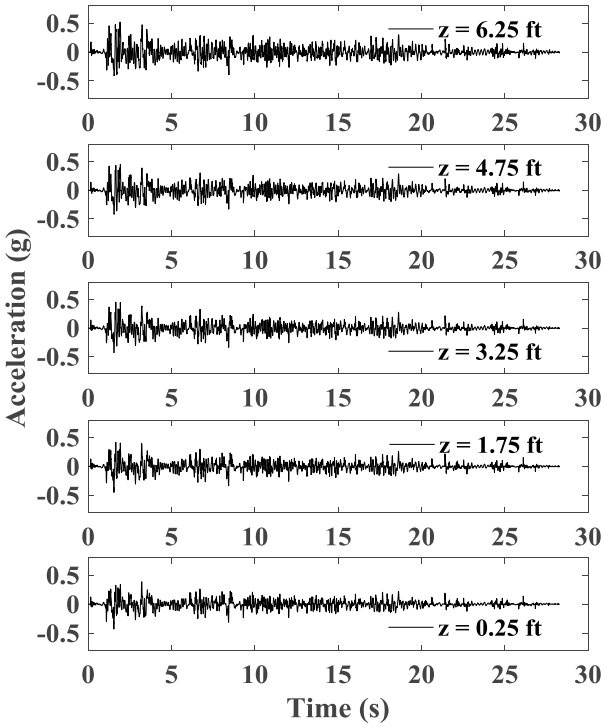

Figure A1.276 Time histories of acceleration for wall facing in longitudinal section L1.

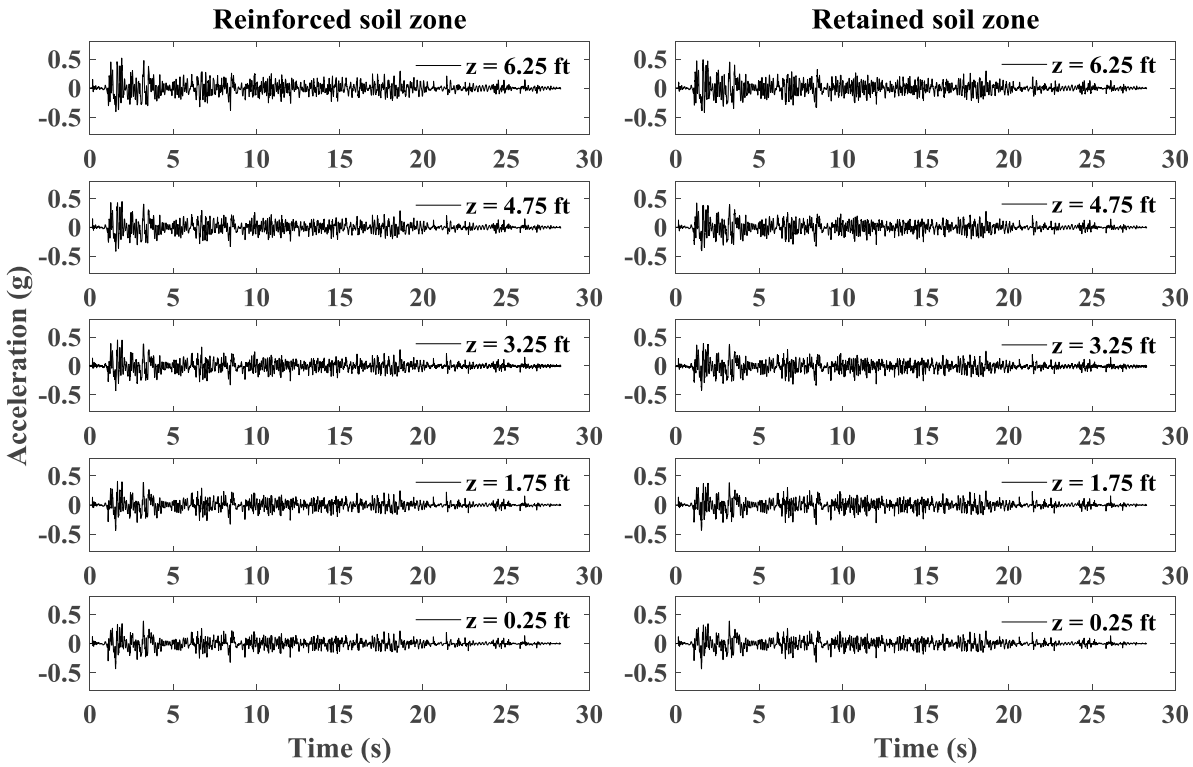

Figure A1.277 Time histories of acceleration for reinforced soil zone and retained soil zone in longitudinal section L1.

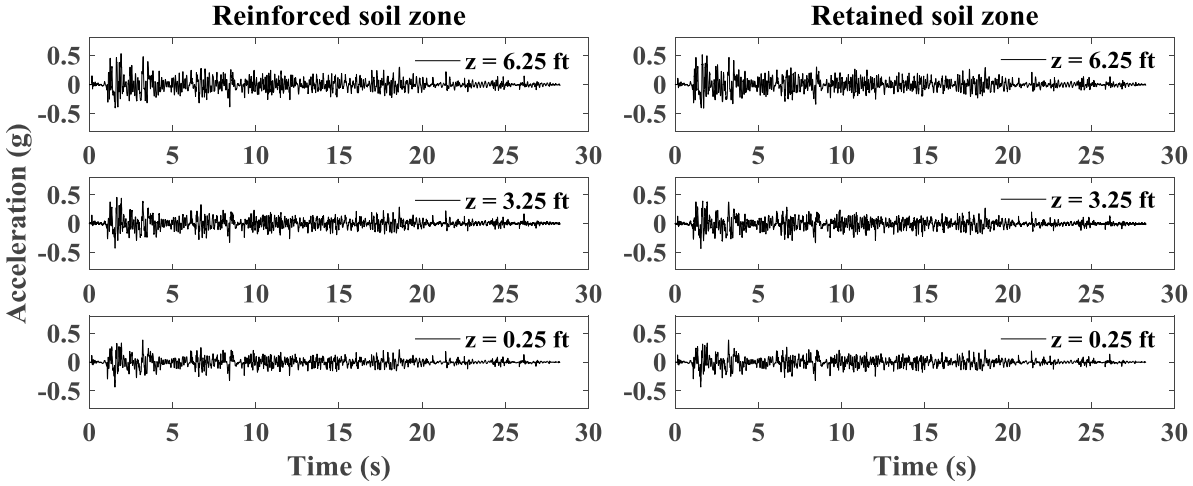

Figure A1.278 Time histories of acceleration for reinforced soil zone and retained soil zone in longitudinal section L2.

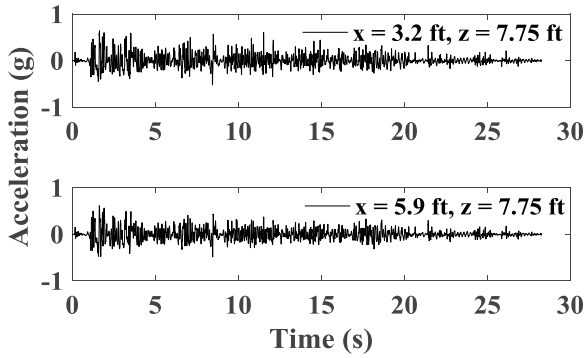

Figure A1.279 Time histories of acceleration for backfill soil in upper wall.

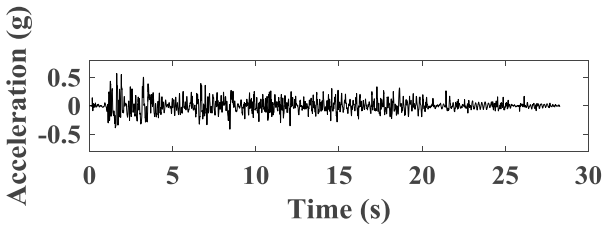

Figure A1.280 Time histories of acceleration for bridge seat.

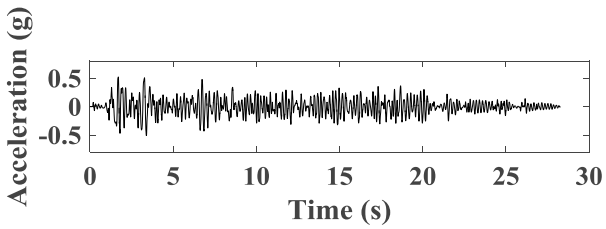

Figure A1.281 Time histories of acceleration for bridge beam.

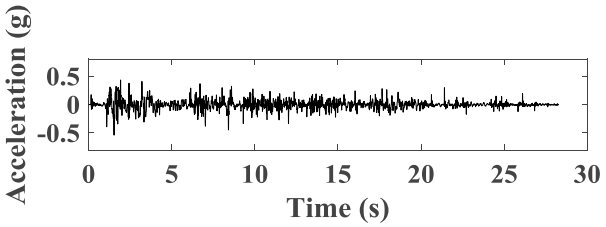

Figure A1.282 Time histories of acceleration for support wall.

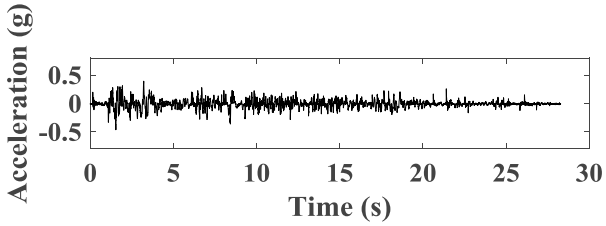

Figure A1.283 Time histories of acceleration for shaking table.

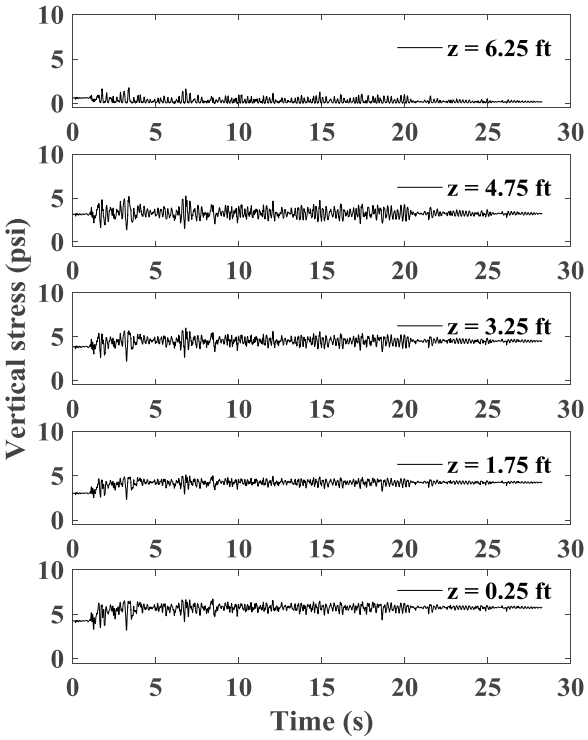

Figure A1.284 Time histories of vertical stress behind wall facing.

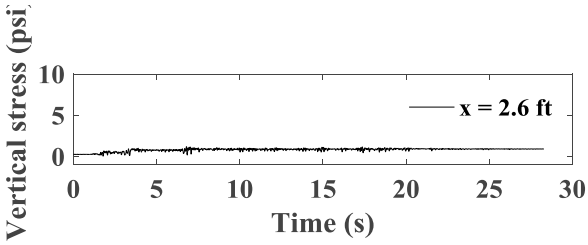

Figure A1.285 Time histories of vertical stress under bridge seat.

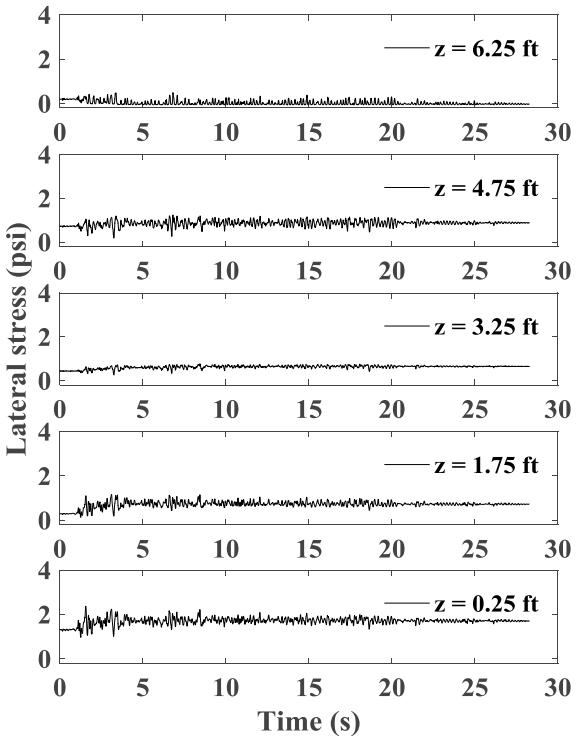

Figure A1.286 Time histories of lateral stress behind wall facing.

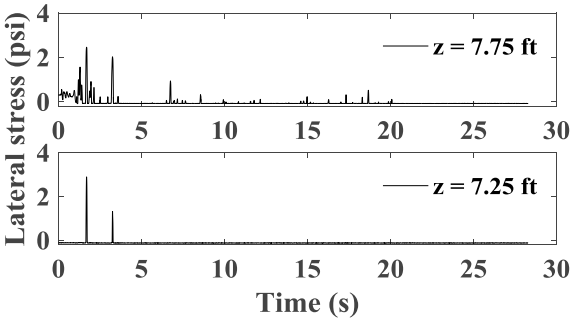

Figure A1.287 Time histories of lateral stress behind upper wall.

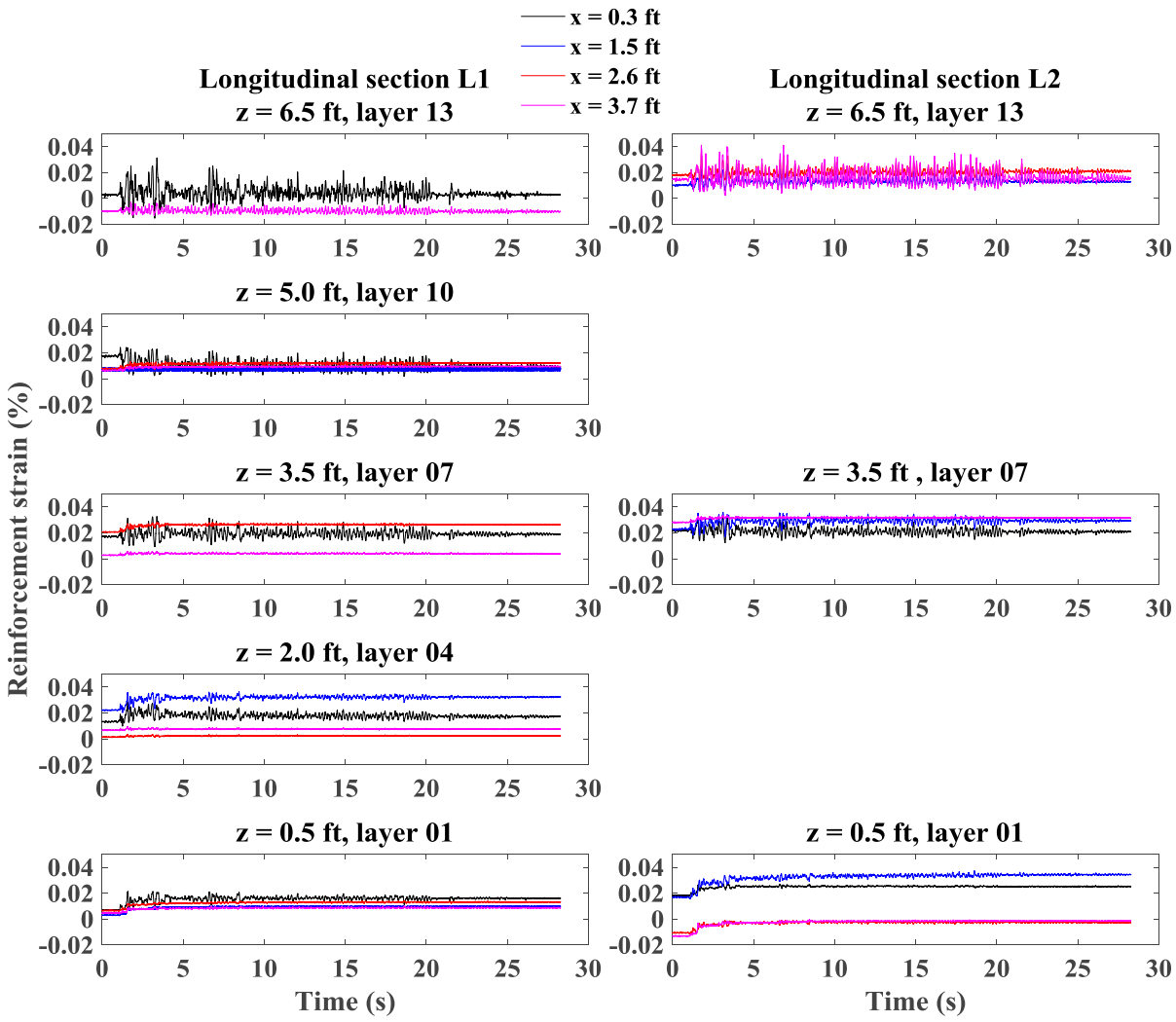

Figure A1.288 Time histories of reinforcement strain for longitudinal sections L1 and L2.

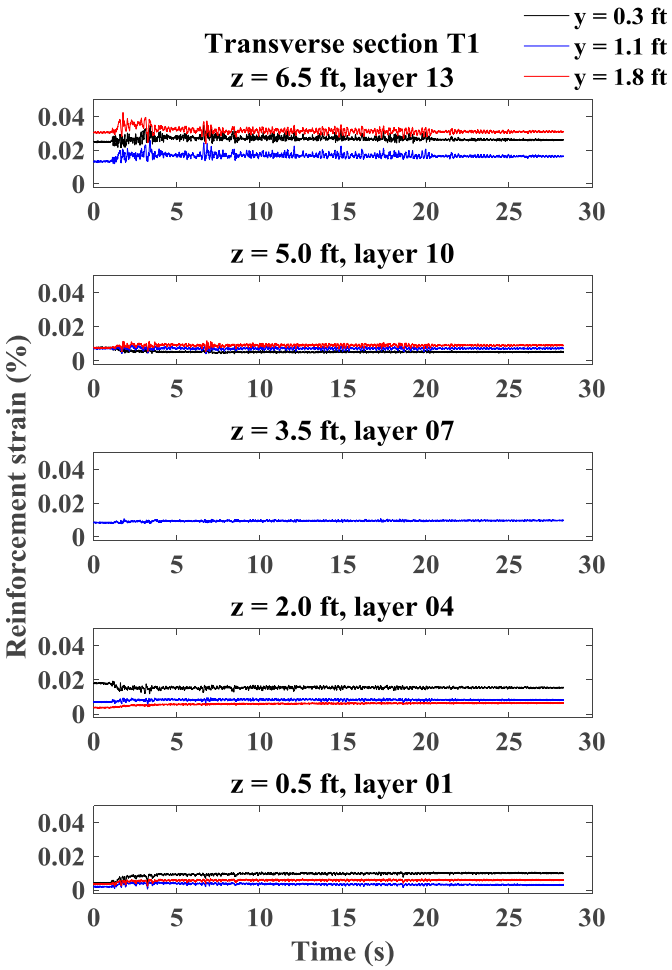

Figure A1.289 Time histories of reinforcement strain for transverse section T1.

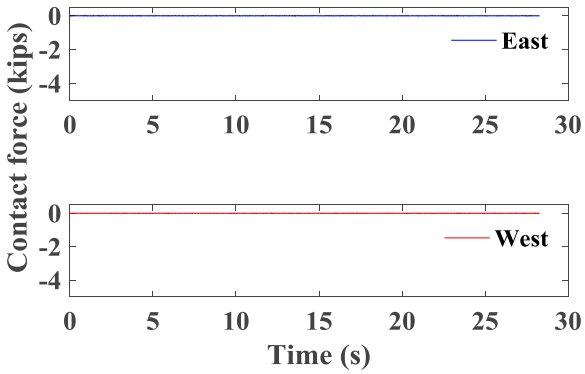

Figure A1.290 Time histories of contact force between bridge seat and bridge beam.

A1.5.2 Maule Motion

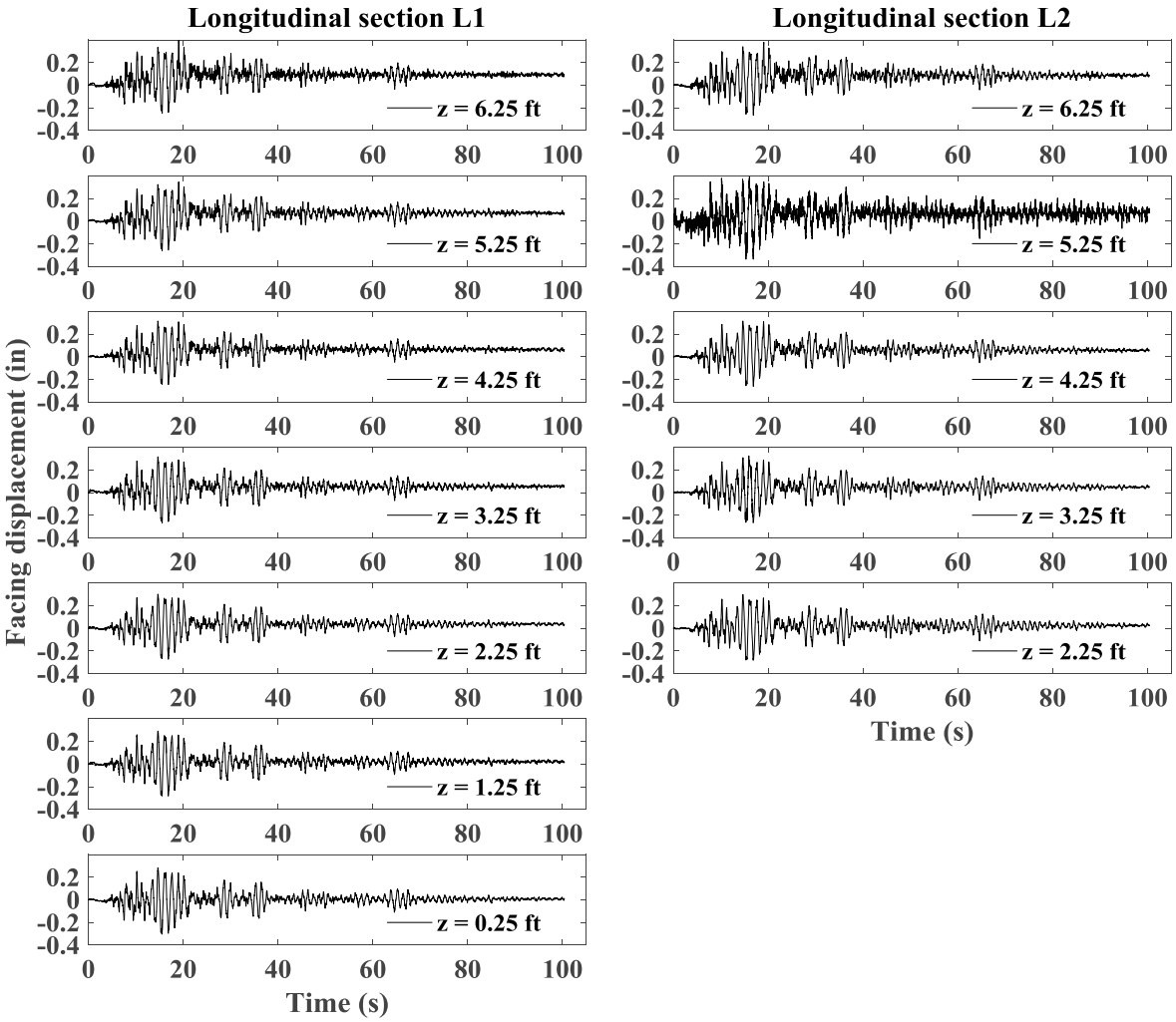

Figure A1.291 Time histories of incremental facing displacement for longitudinal sections L1 and L2.

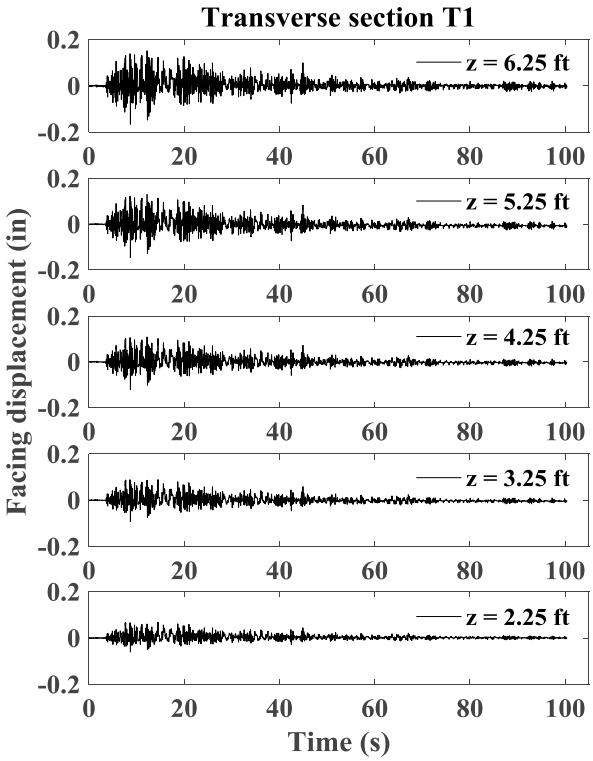

Figure A1.292 Time histories of incremental facing displacement for transverse section T1.

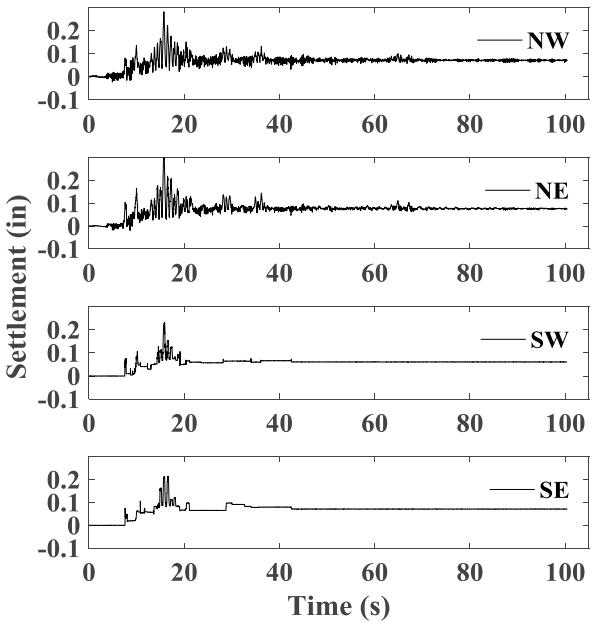

Figure A1.293 Time histories of incremental settlement for bridge seat.

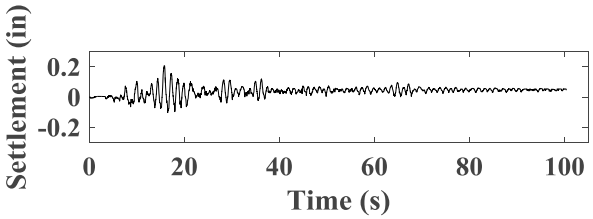

Figure A1.294 Time histories of incremental settlement for backfill soil in upper wall.

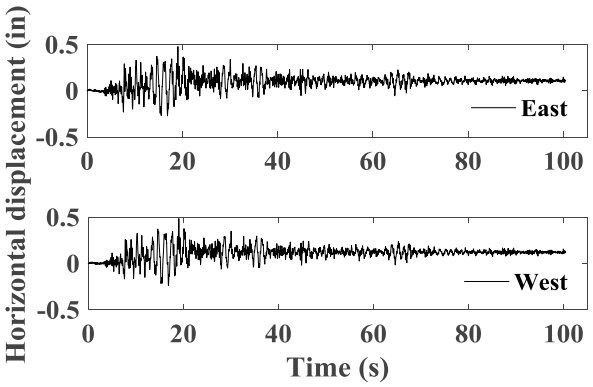

Figure A1.295 Time histories of incremental horizontal displacement for bridge seat.

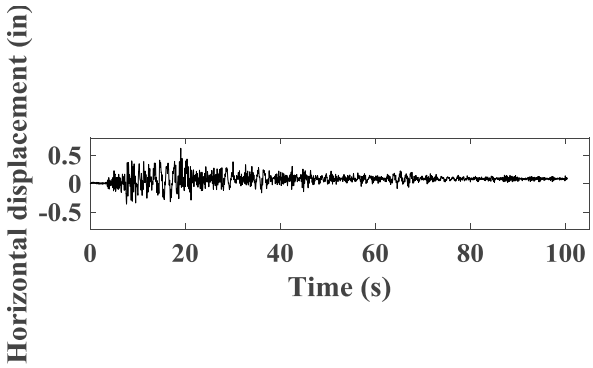

Figure A1.296 Time histories of incremental horizontal displacement for bridge beam.

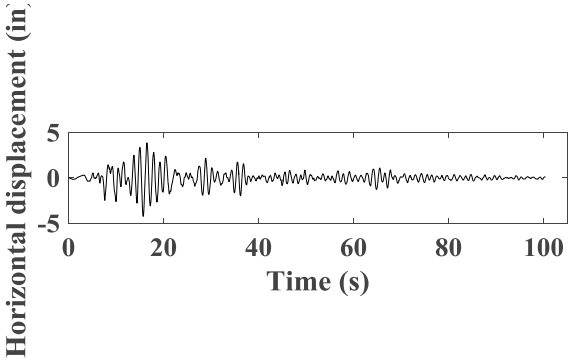

Figure A1.297 Time histories of horizontal displacement for support wall.

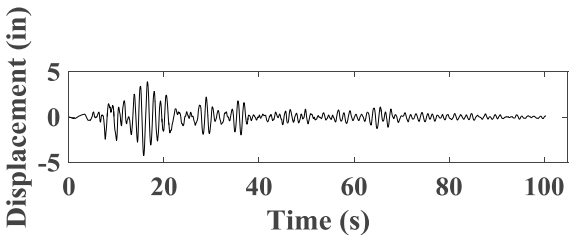

Figure A1.298 Time histories of horizontal displacement for shaking table.

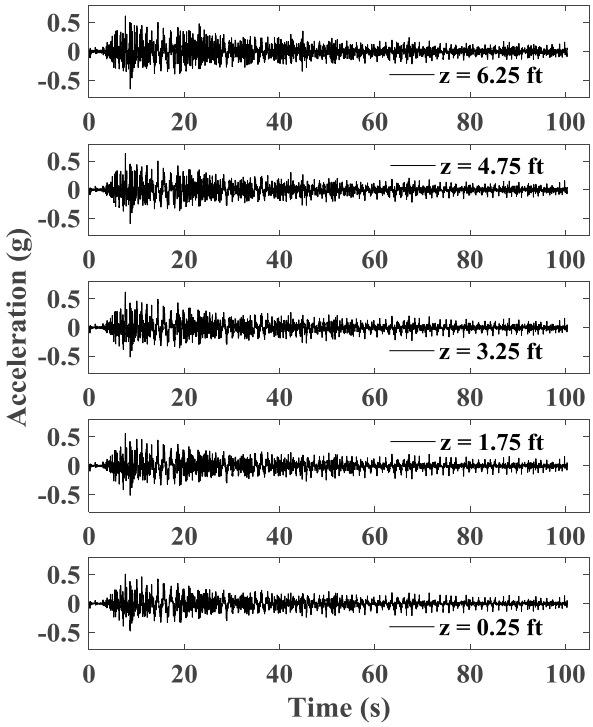

Figure A1.299 Time histories of acceleration for wall facing in longitudinal section L1.

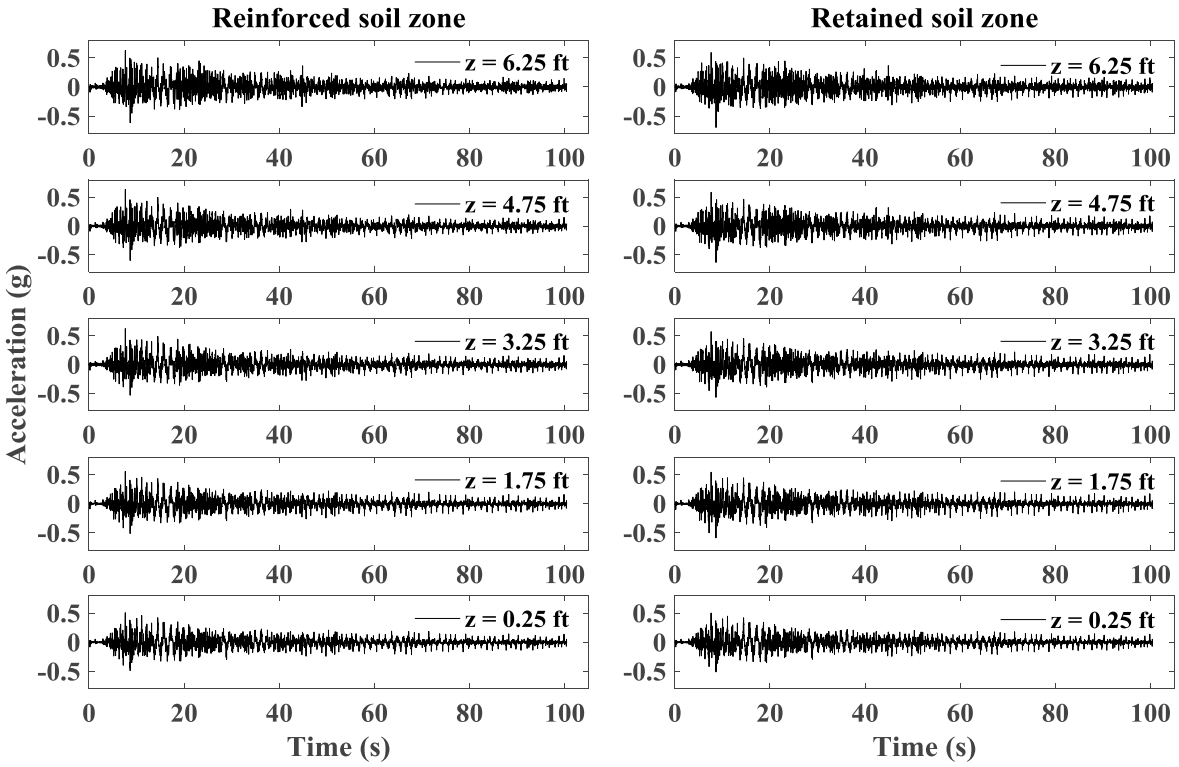

Figure A1.300 Time histories of acceleration for reinforced soil zone and retained soil zone in longitudinal section L1.

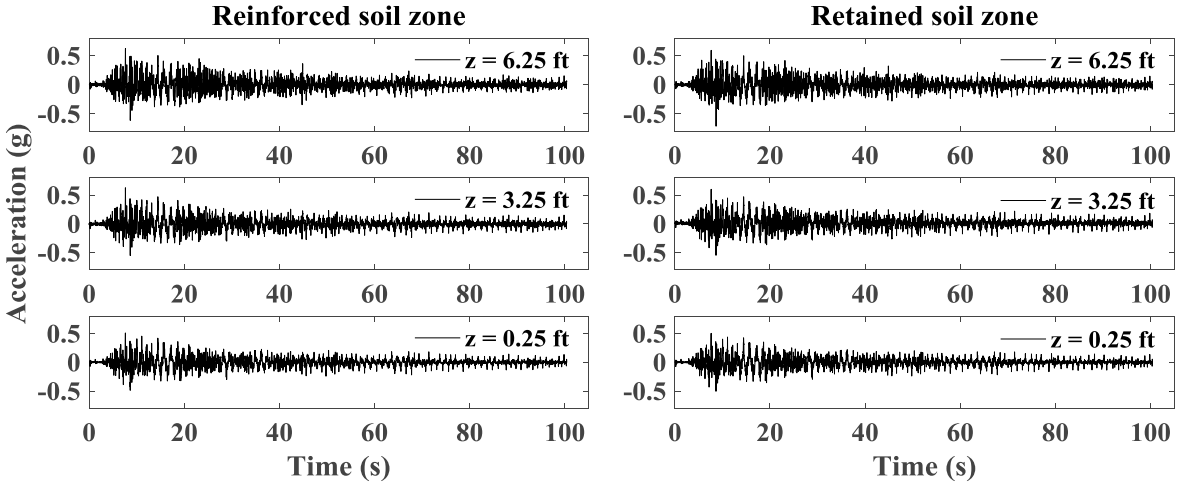

Figure A1.301 Time histories of acceleration for reinforced soil zone and retained soil zone in longitudinal section L2.

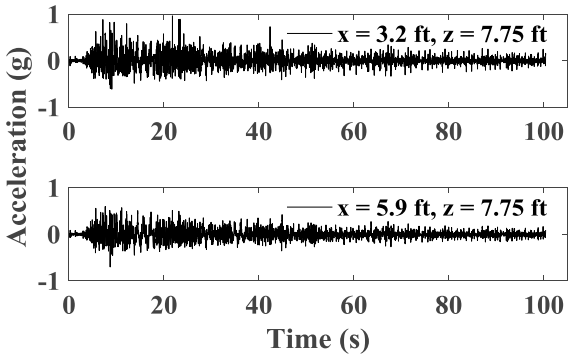

Figure A1.302 Time histories of acceleration for backfill soil in upper wall.

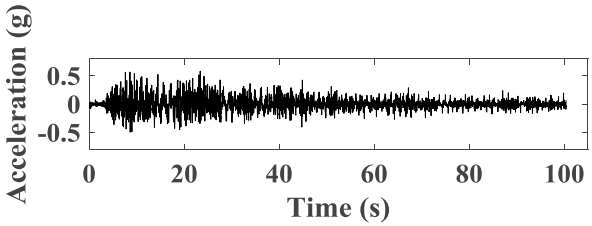

Figure A1.303 Time histories of acceleration for bridge seat.

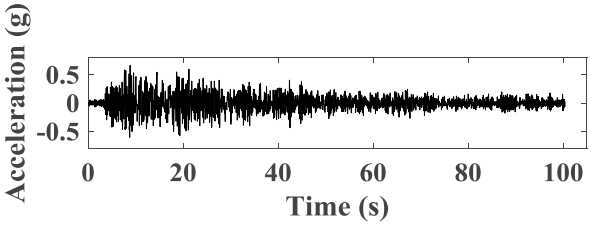

Figure A1.304 Time histories of acceleration for bridge beam.

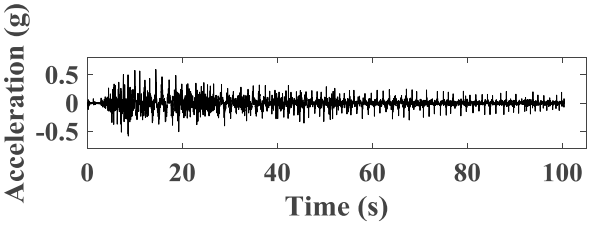

Figure A1.305 Time histories of acceleration for support wall.

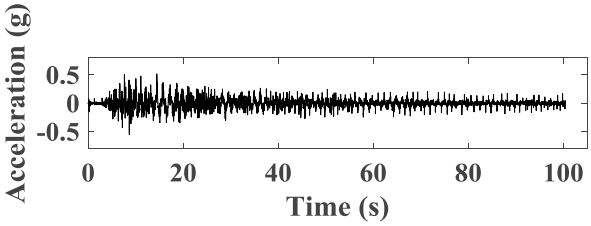

Figure A1.306 Time histories of acceleration for shaking table.

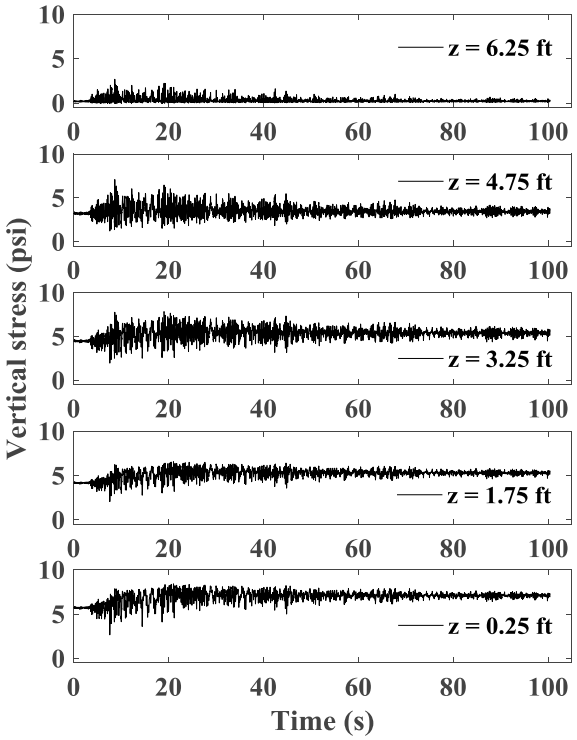

Figure A1.307 Time histories of vertical stress behind wall facing.

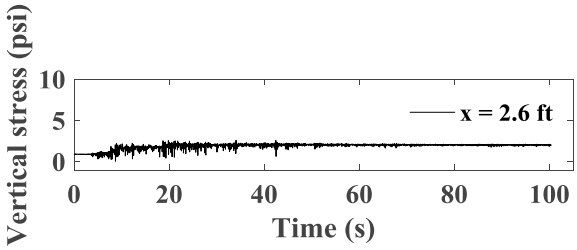

Figure A1.308 Time histories of vertical stress under bridge seat.

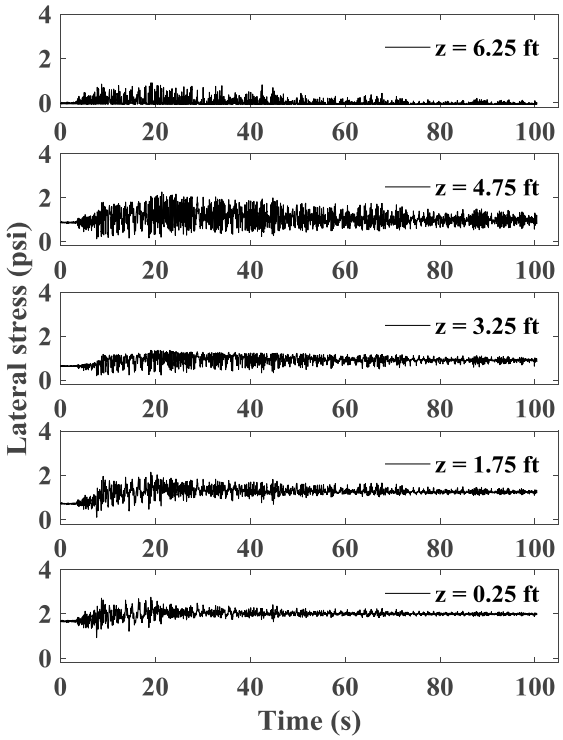

Figure A1.309 Time histories of lateral stress behind wall facing.

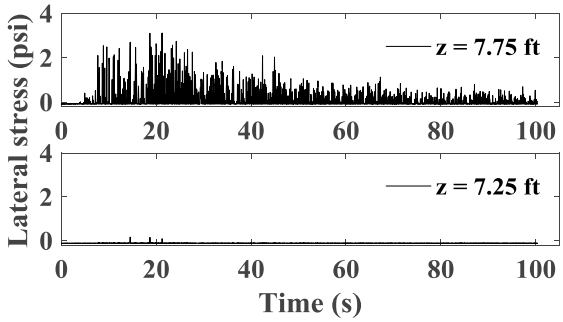

Figure A1.310 Time histories of lateral stress behind upper wall.

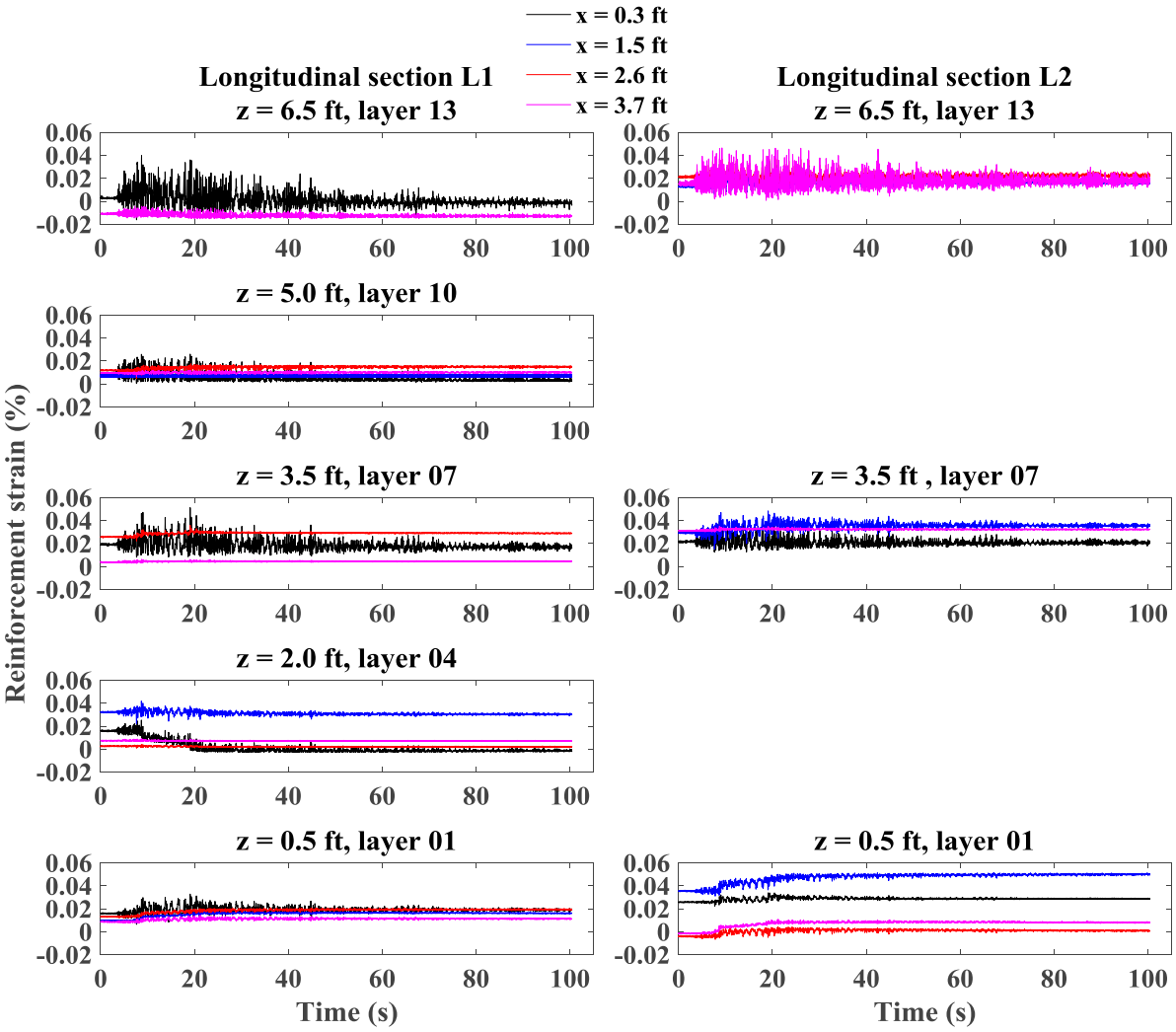

Figure A1.311 Time histories of reinforcement strain for longitudinal sections L1 and L2.

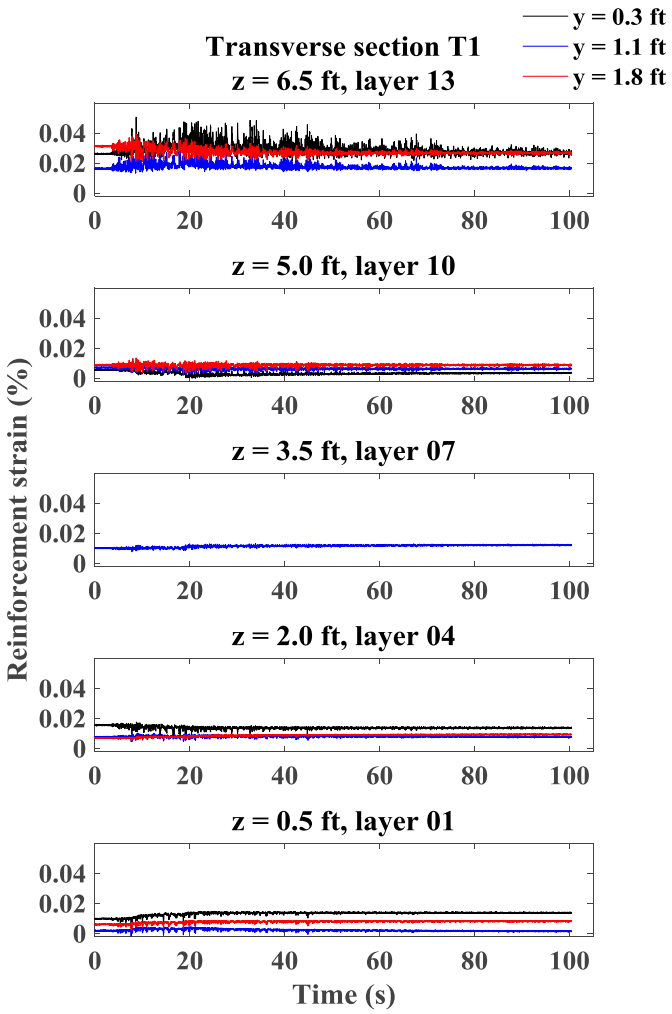

Figure A1.312 Time histories of reinforcement strain for transverse section T1.

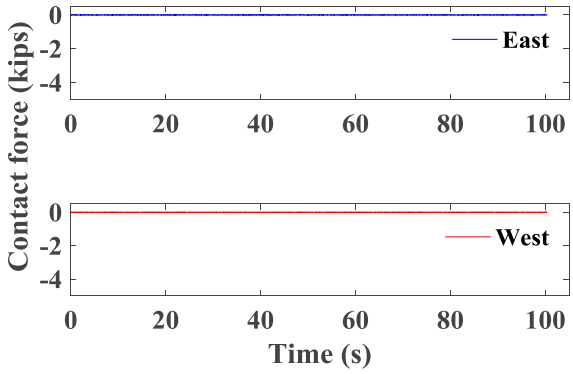

Figure A1.313 Time histories of contact force between bridge seat and bridge beam.

A1.5.3 Northridge Motion

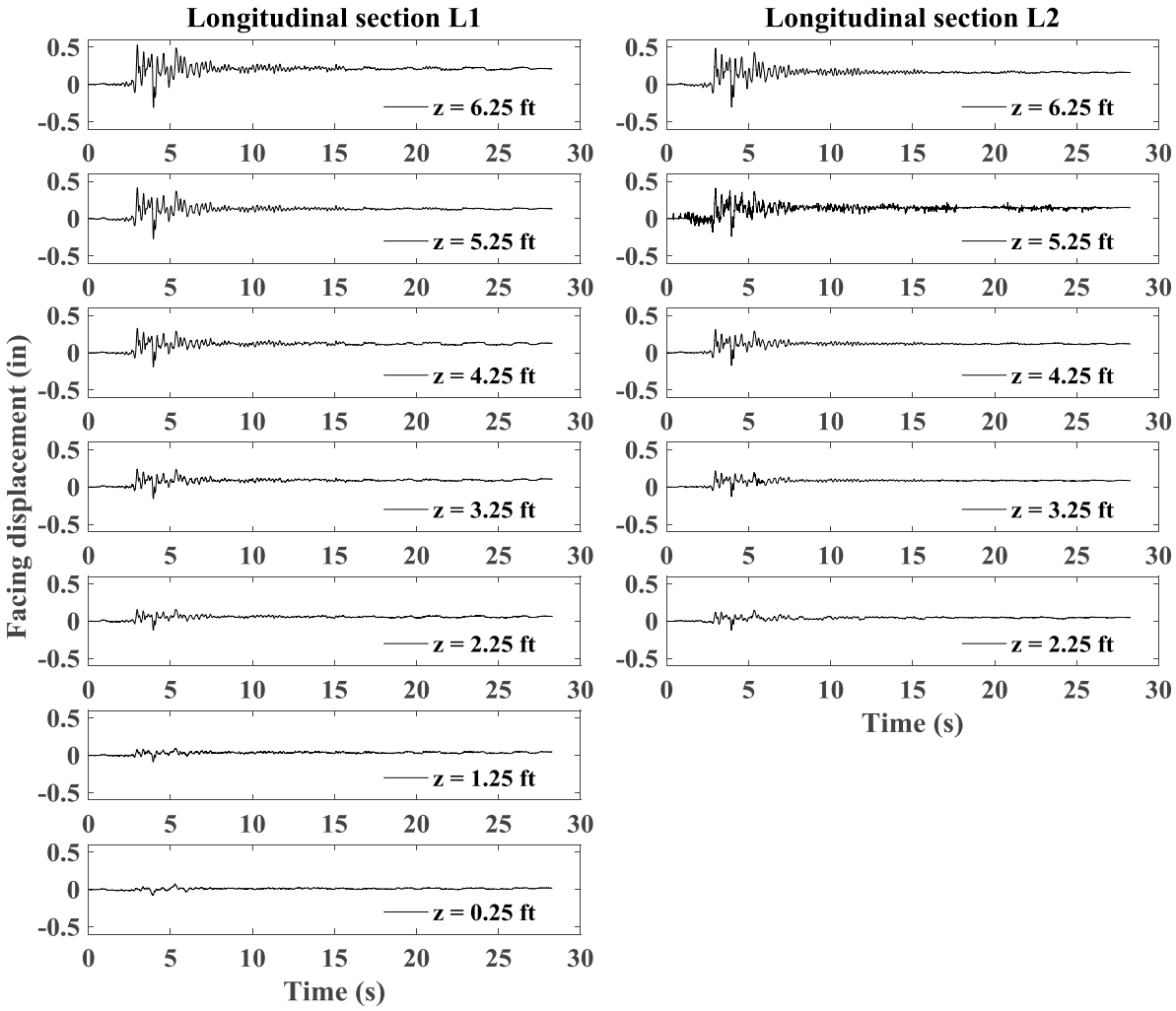

Figure A1.314 Time histories of incremental facing displacement for longitudinal sections L1 and L2.

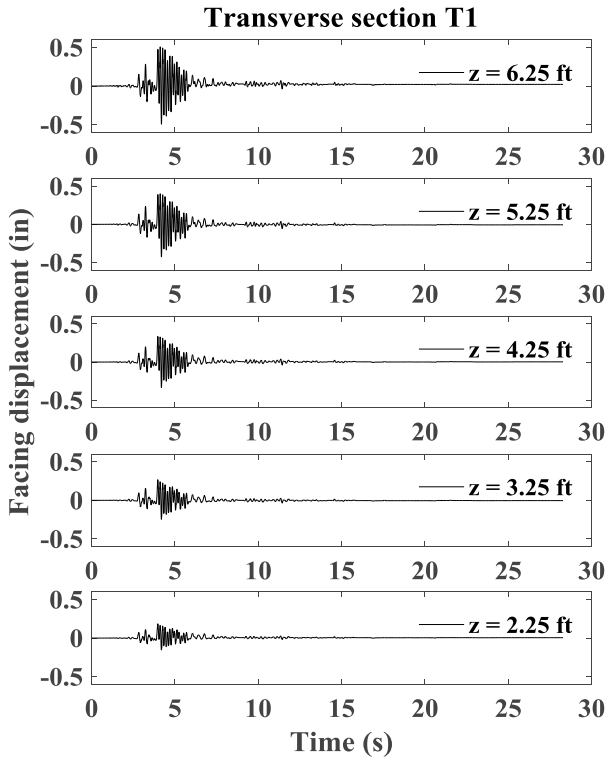

Figure A1.315 Time histories of incremental facing displacement for transverse section T1.

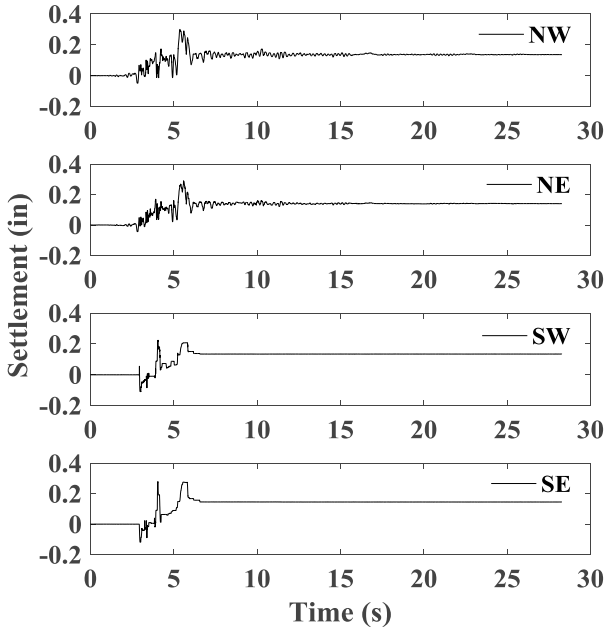

Figure A1.316 Time histories of incremental settlement for bridge seat.

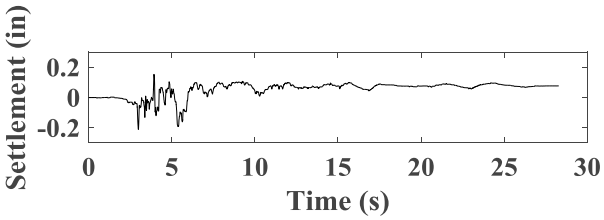

Figure A1.317 Time histories of incremental settlement for backfill soil in upper wall.

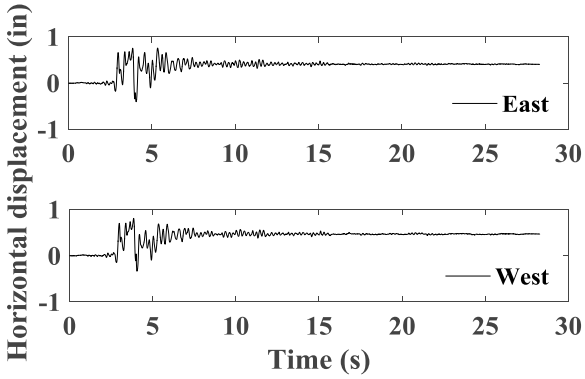

Figure A1.318 Time histories of incremental horizontal displacement for bridge seat.

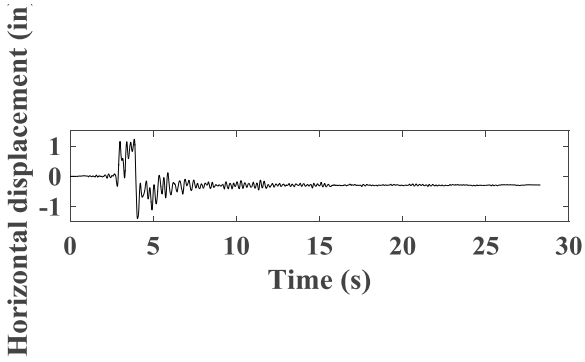

Figure A1.319 Time histories of incremental horizontal displacement for bridge beam.

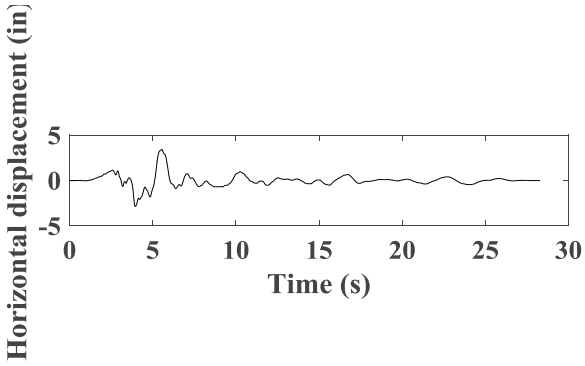

Figure A1.320 Time histories of horizontal displacement for support wall.

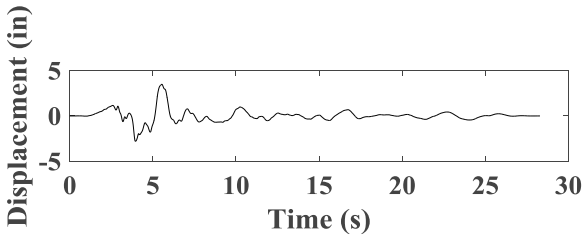

Figure A1.321 Time histories of horizontal displacement for shaking table.

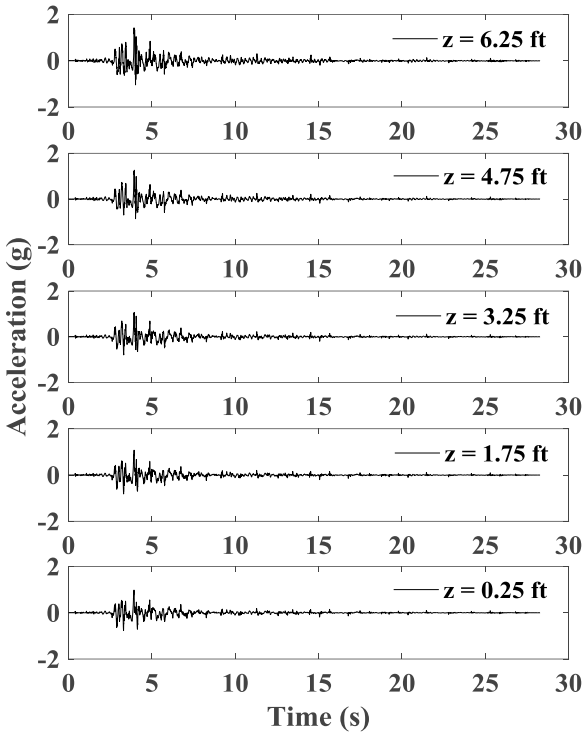

Figure A1.322 Time histories of acceleration for wall facing in longitudinal section L1.

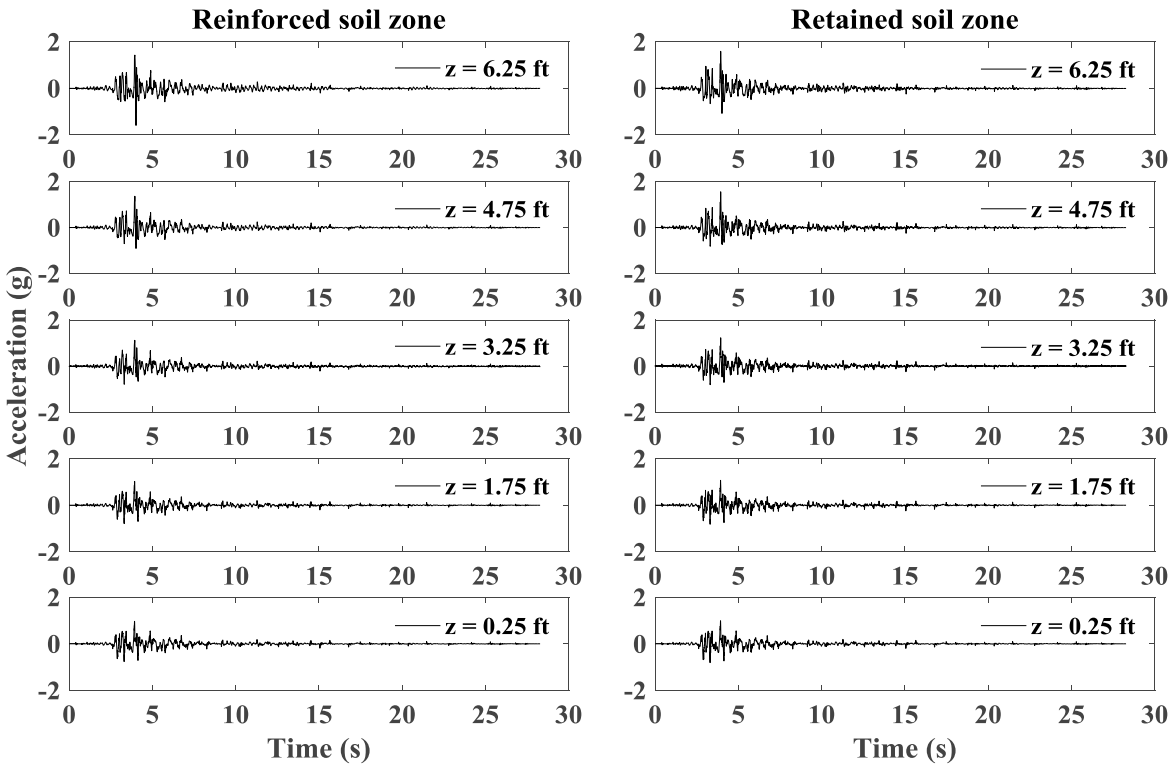

Figure A1.323 Time histories of acceleration for reinforced soil zone and retained soil zone in longitudinal section L1.

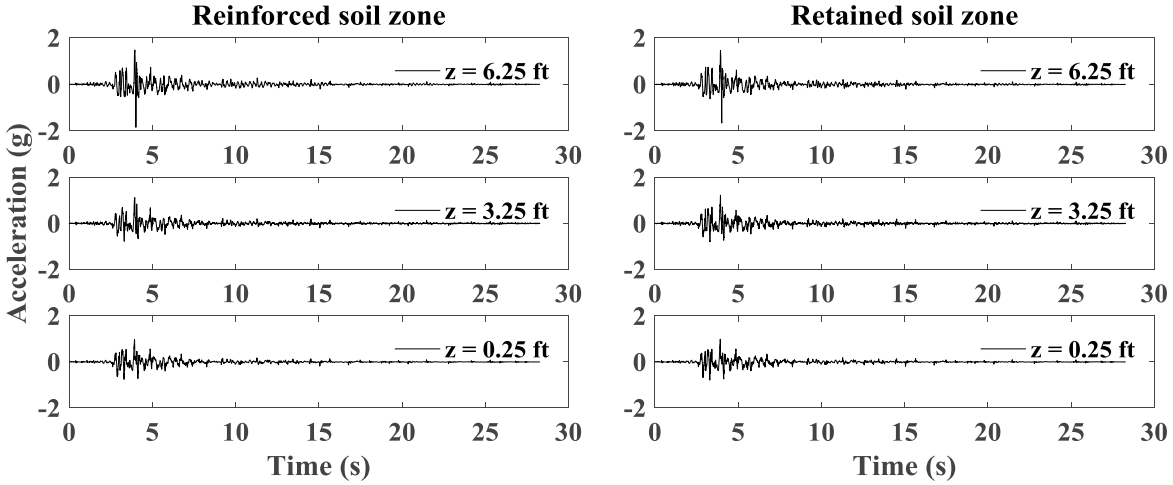

Figure A1.324 Time histories of acceleration for reinforced soil zone and retained soil zone in longitudinal section L2.

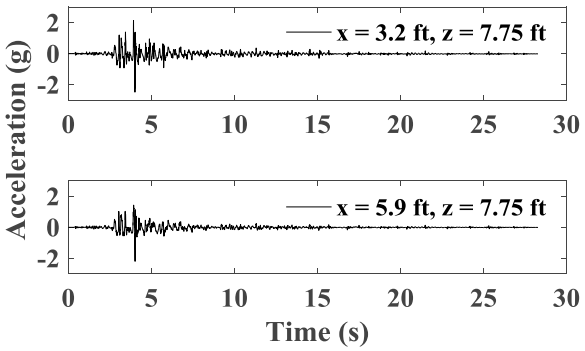

Figure A1.325 Time histories of acceleration for backfill soil in upper wall.

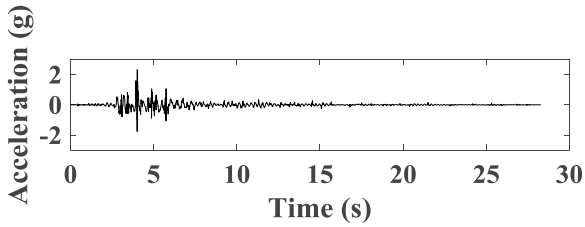

Figure A1.326 Time histories of acceleration for bridge seat.

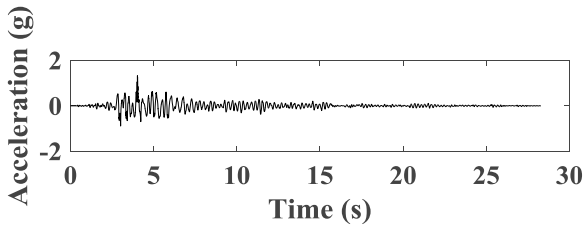

Figure A1.327 Time histories of acceleration for bridge beam.

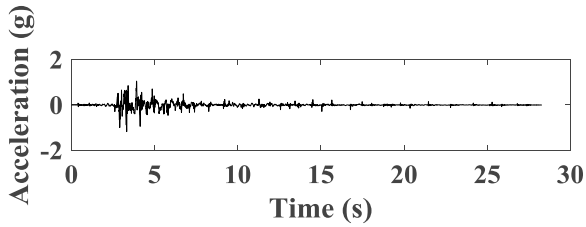

Figure A1.328 Time histories of acceleration for support wall.

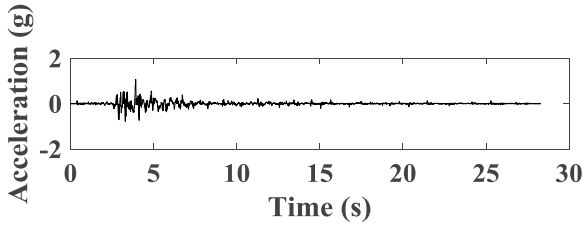

Figure A1.329 Time histories of acceleration for shaking table.

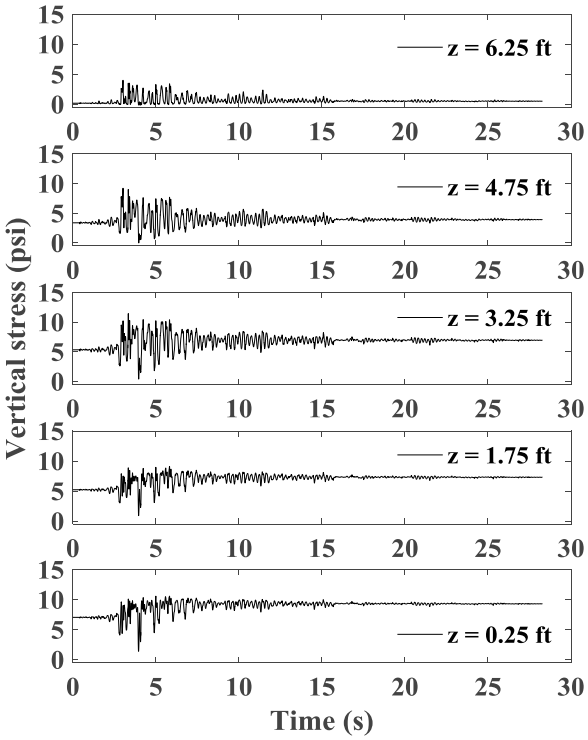

Figure A1.330 Time histories of vertical stress behind wall facing.

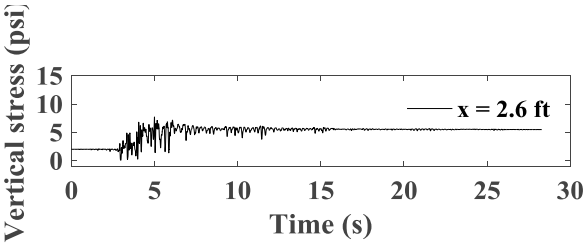

Figure A1.331 Time histories of vertical stress under bridge seat.

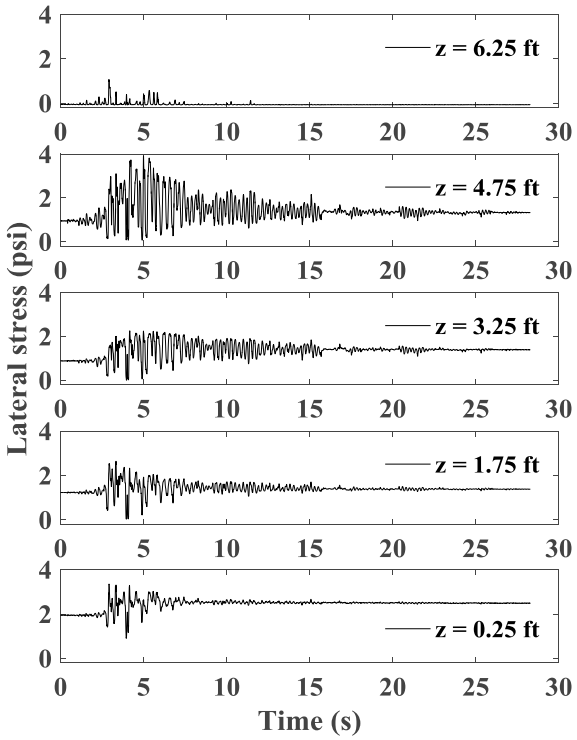

Figure A1.332 Time histories of lateral stress behind wall facing.

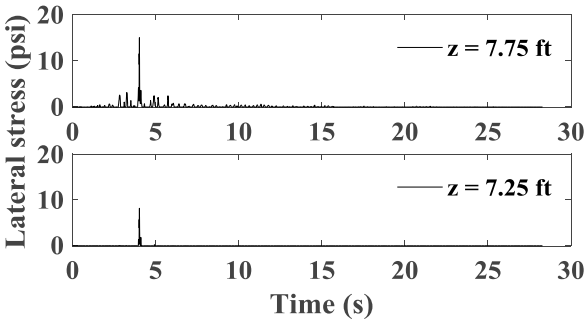

Figure A1.333 Time histories of lateral stress behind upper wall.

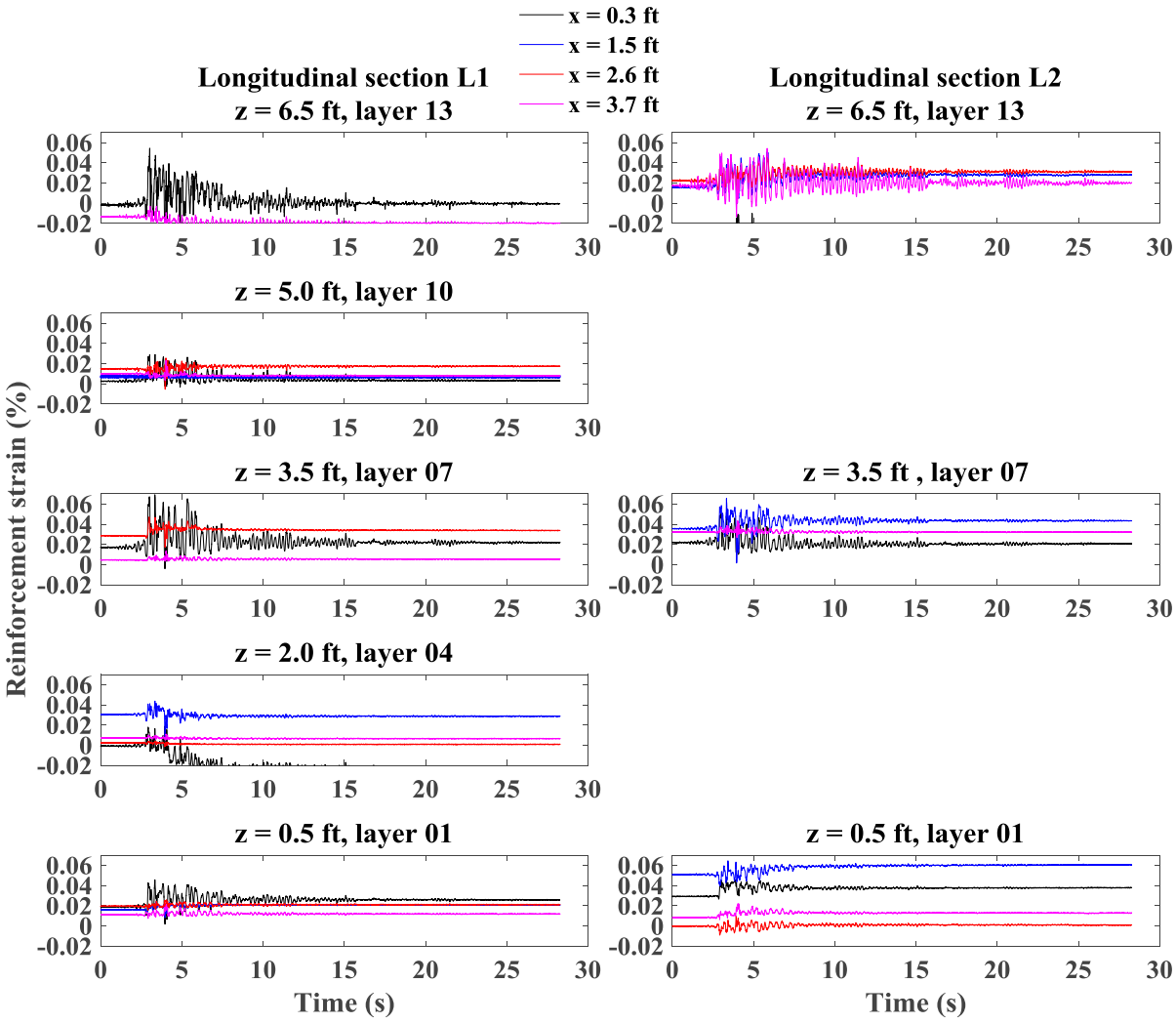

Figure A1.334 Time histories of reinforcement strain for longitudinal sections L1 and L2.

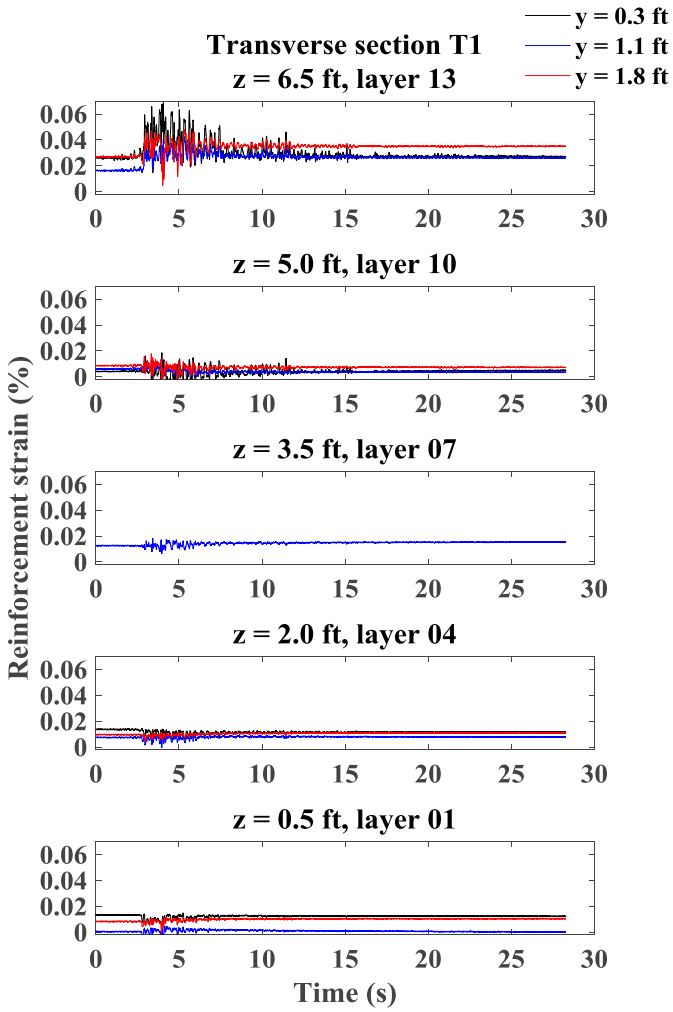

Figure A1.335 Time histories of reinforcement strain for transverse section T1.

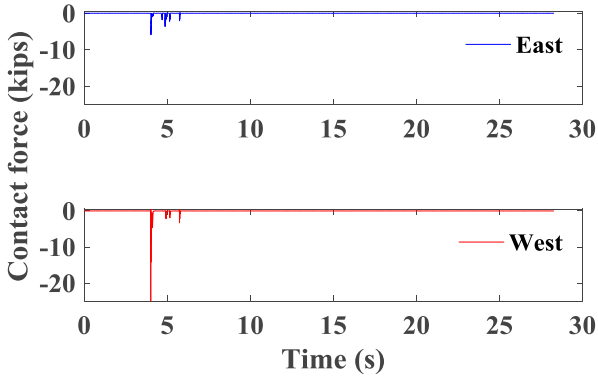

Figure A1.336 Time histories of contact force between bridge seat and bridge beam.

A1.6 Test 6

A1.6.1 Imperial Valley Motion

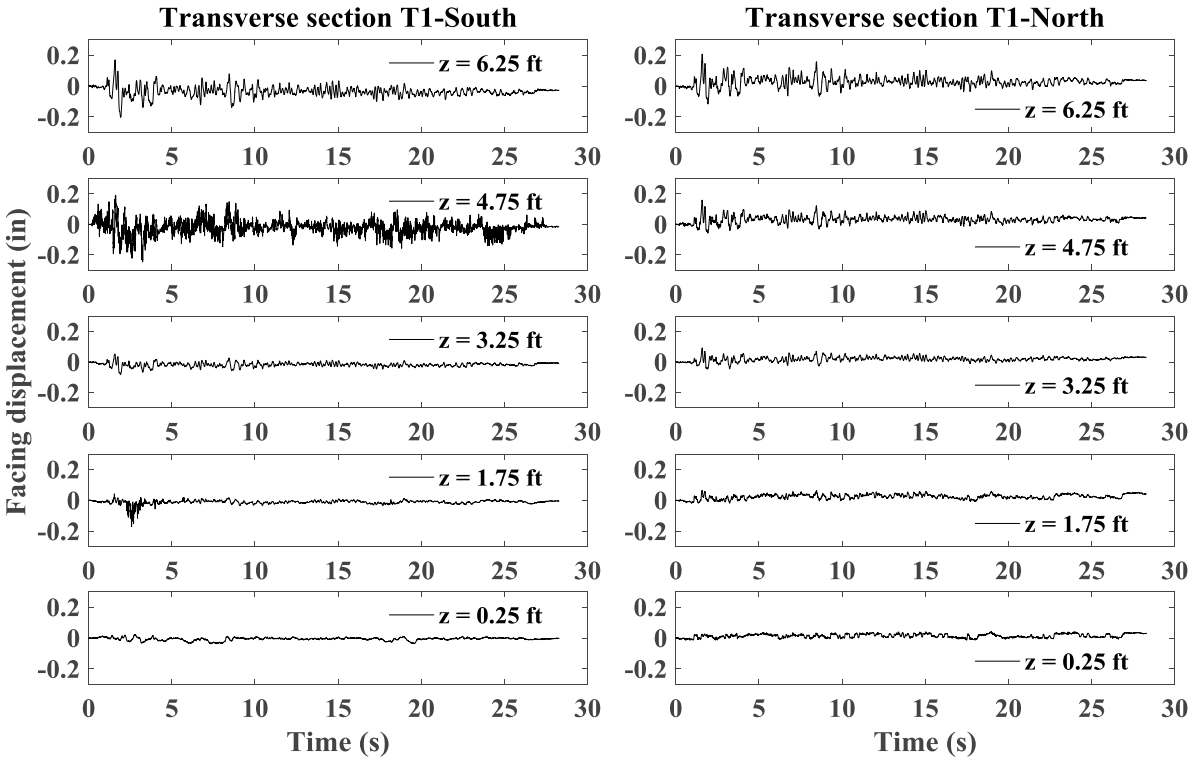

Figure A1.337 Time histories of incremental facing displacement for transverse sections T1-South and T1-North.

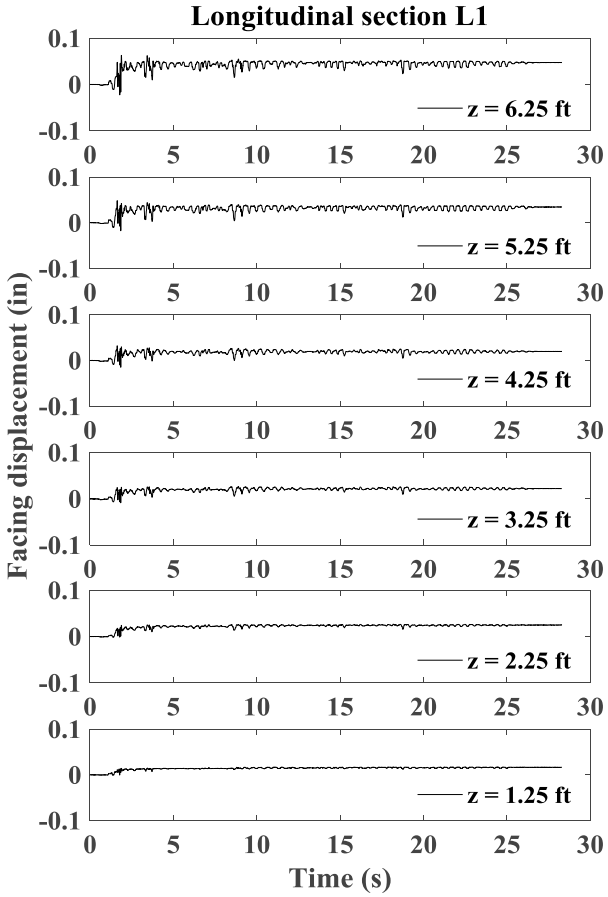

Figure A1.338 Time histories of incremental facing displacement for longitudinal section L1.

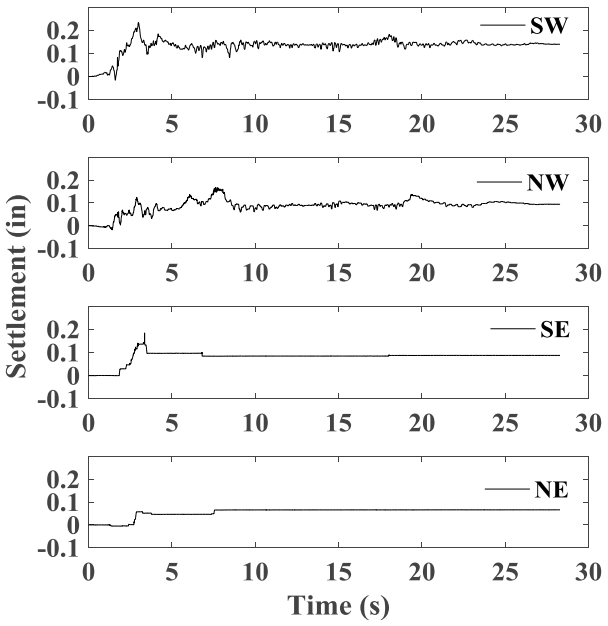

Figure A1.339 Time histories of incremental settlement for bridge seat.

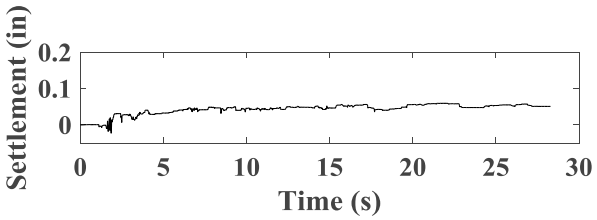

Figure A1.340 Time histories of incremental settlement for backfill soil in upper wall.

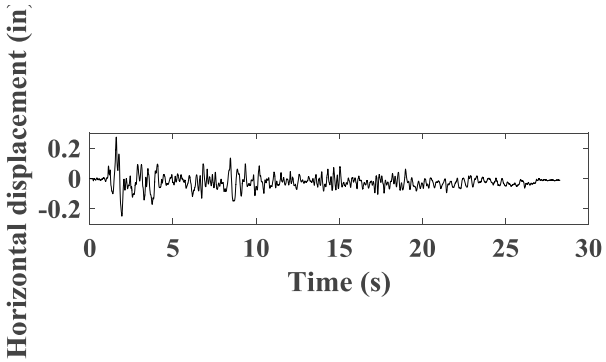

Figure A1.341 Time histories of incremental horizontal displacement for bridge seat.

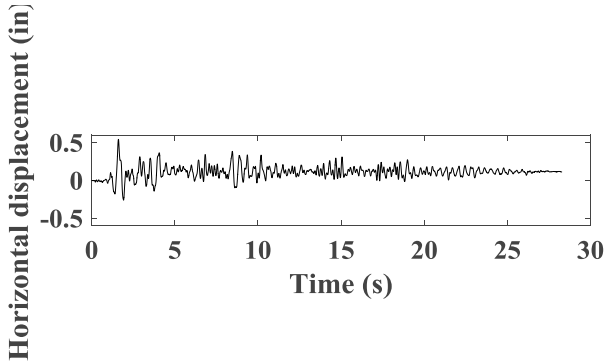

Figure A1.342 Time histories of incremental horizontal displacement for bridge beam.

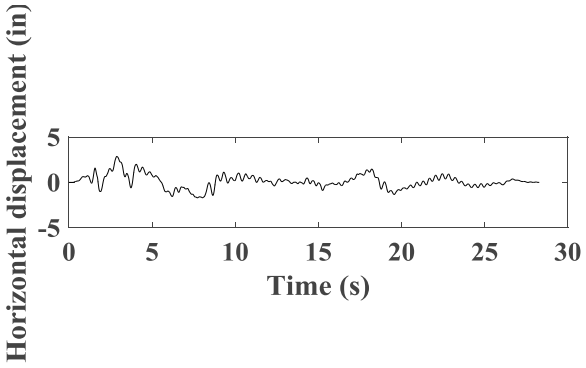

Figure A1.343 Time histories of horizontal displacement for support wall.

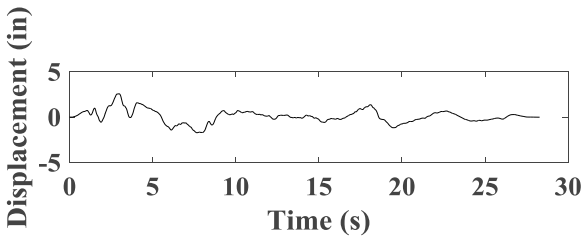

Figure A1.344 Time histories of horizontal displacement for shaking table.

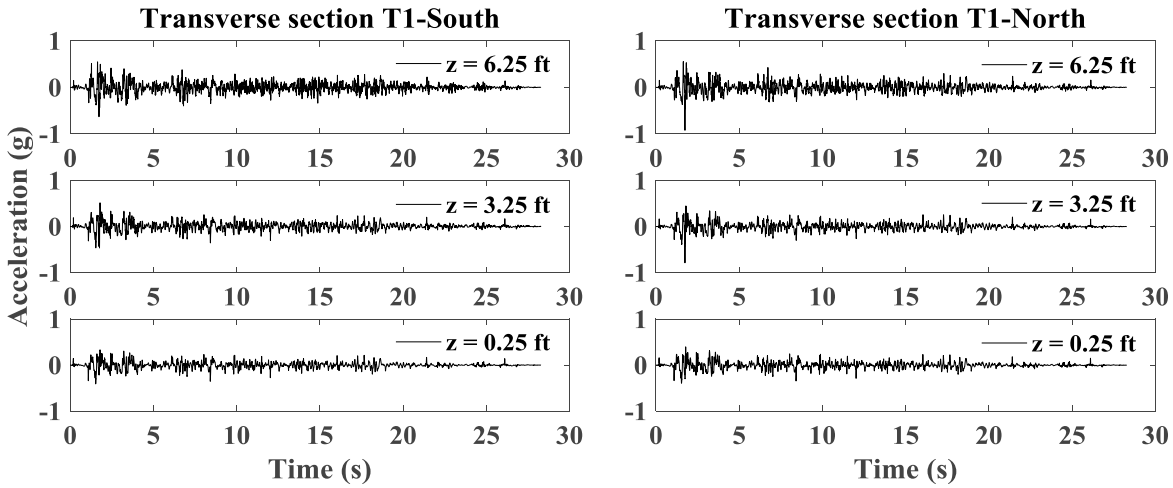

Figure A1.345 Time histories of acceleration for wall facing in transverse sections T1-South and T1-North.

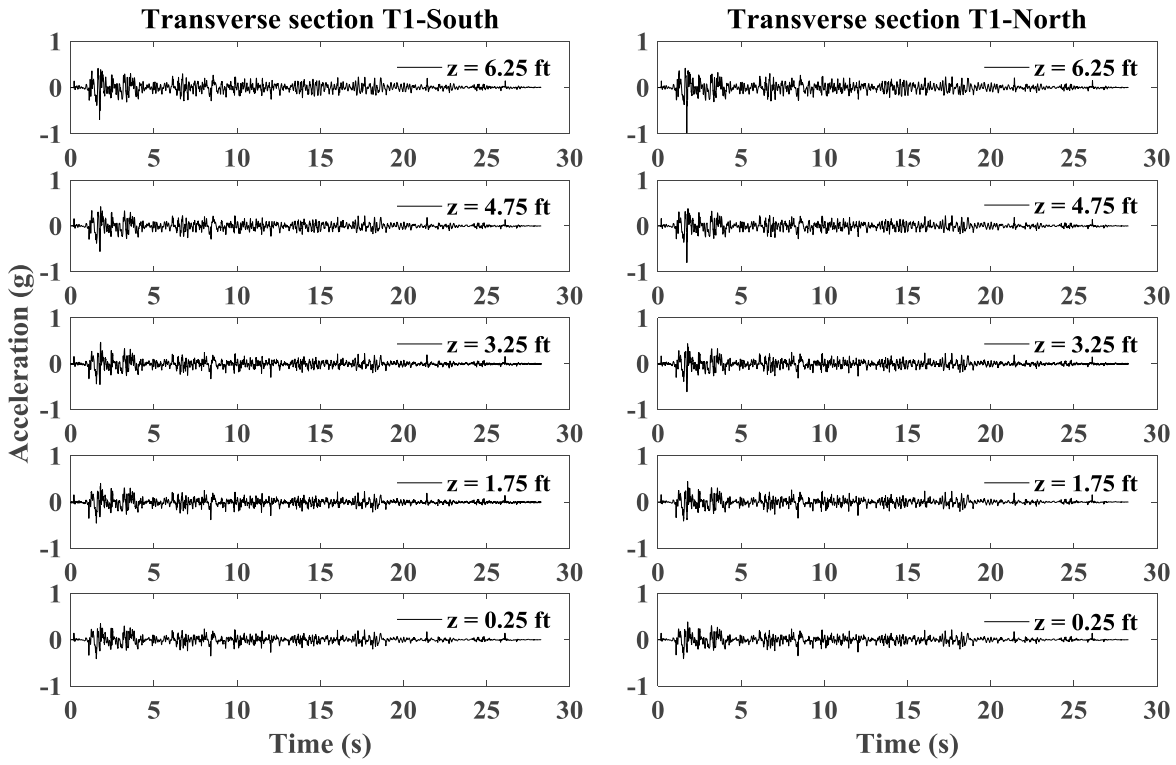

Figure A1.346 Time histories of acceleration for reinforced soil zone in transverse sections T1-South and T1-North.

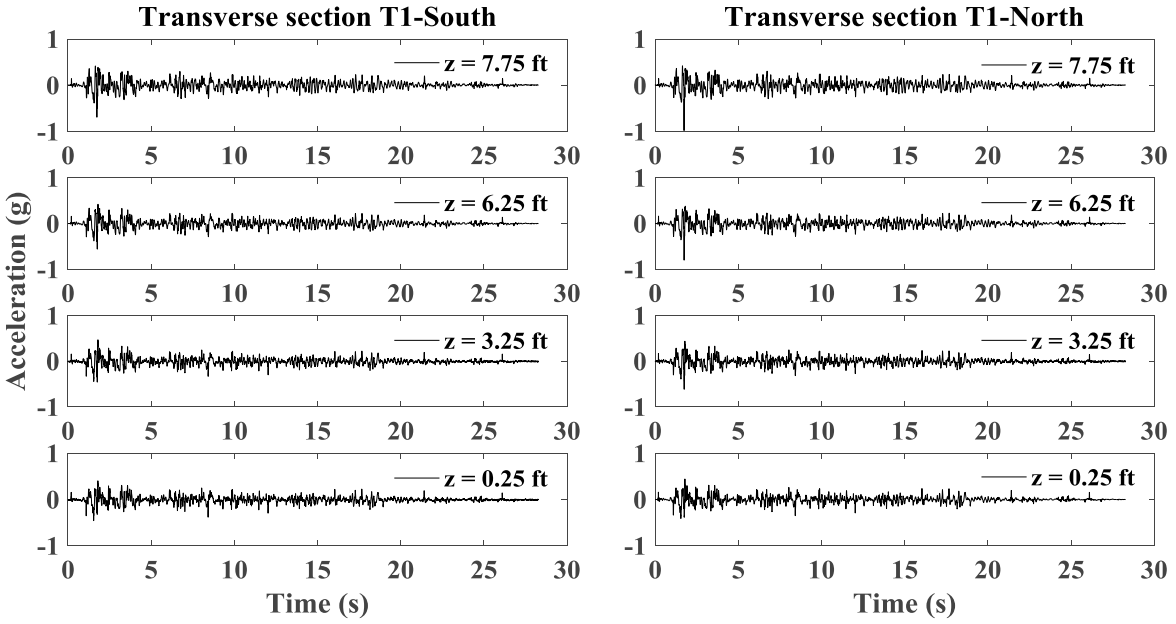

Figure A1.347 Time histories of acceleration for reinforced soil zone in transverse section T2-South and T2-North.

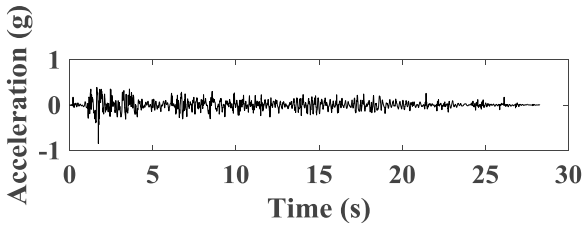

Figure A1.348 Time histories of acceleration for bridge seat.

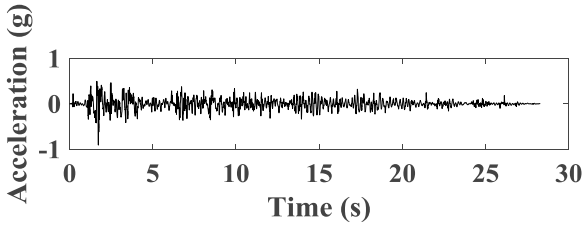

Figure A1.349 Time histories of acceleration for bridge beam.

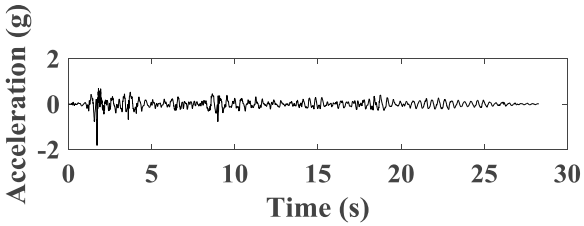

Figure A1.350 Time histories of acceleration for support wall.

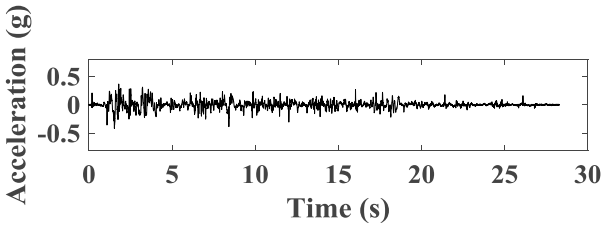

Figure A1.351 Time histories of acceleration for shaking table.

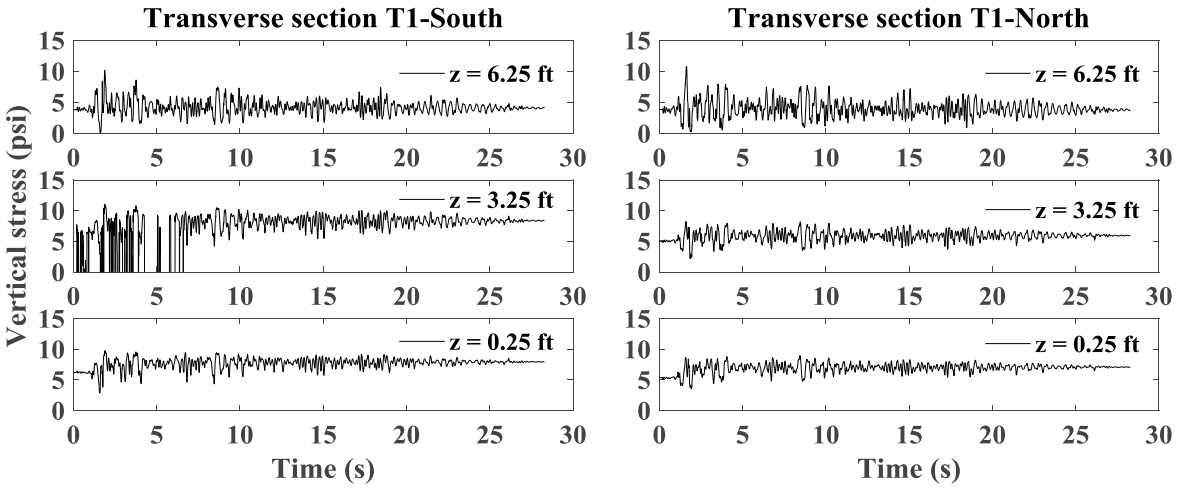

Figure A1.352 Time histories of vertical stress behind wall facing.

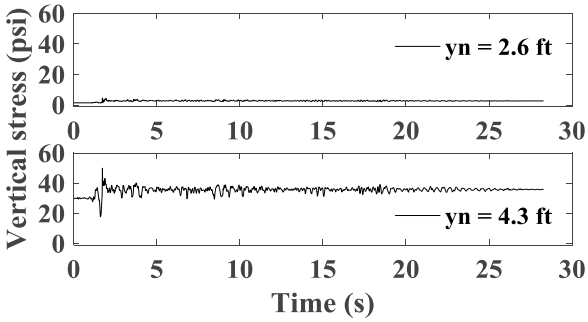

Figure A1.353 Time histories of vertical stress under bridge seat.

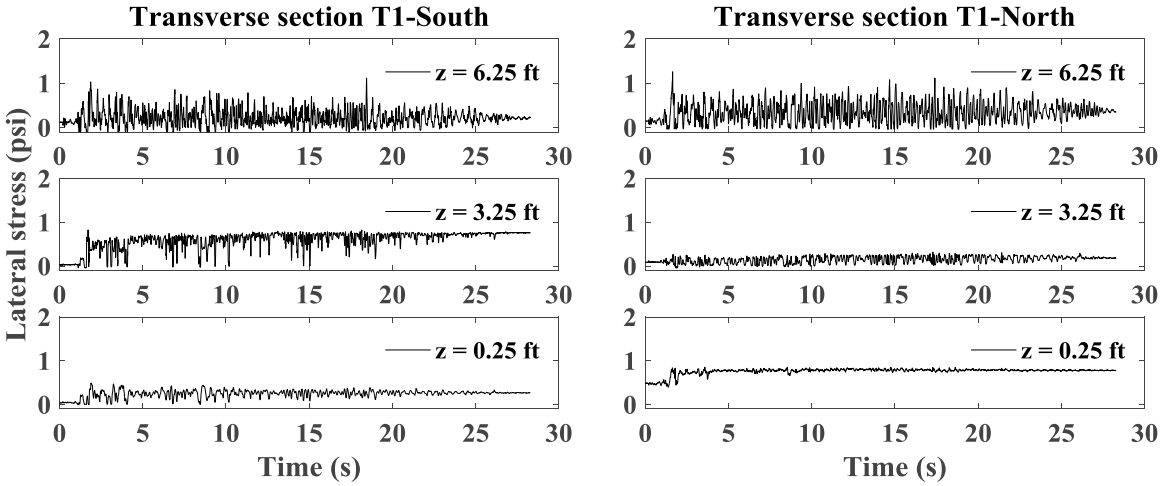

Figure A1.354 Time histories of lateral stress behind wall facing.

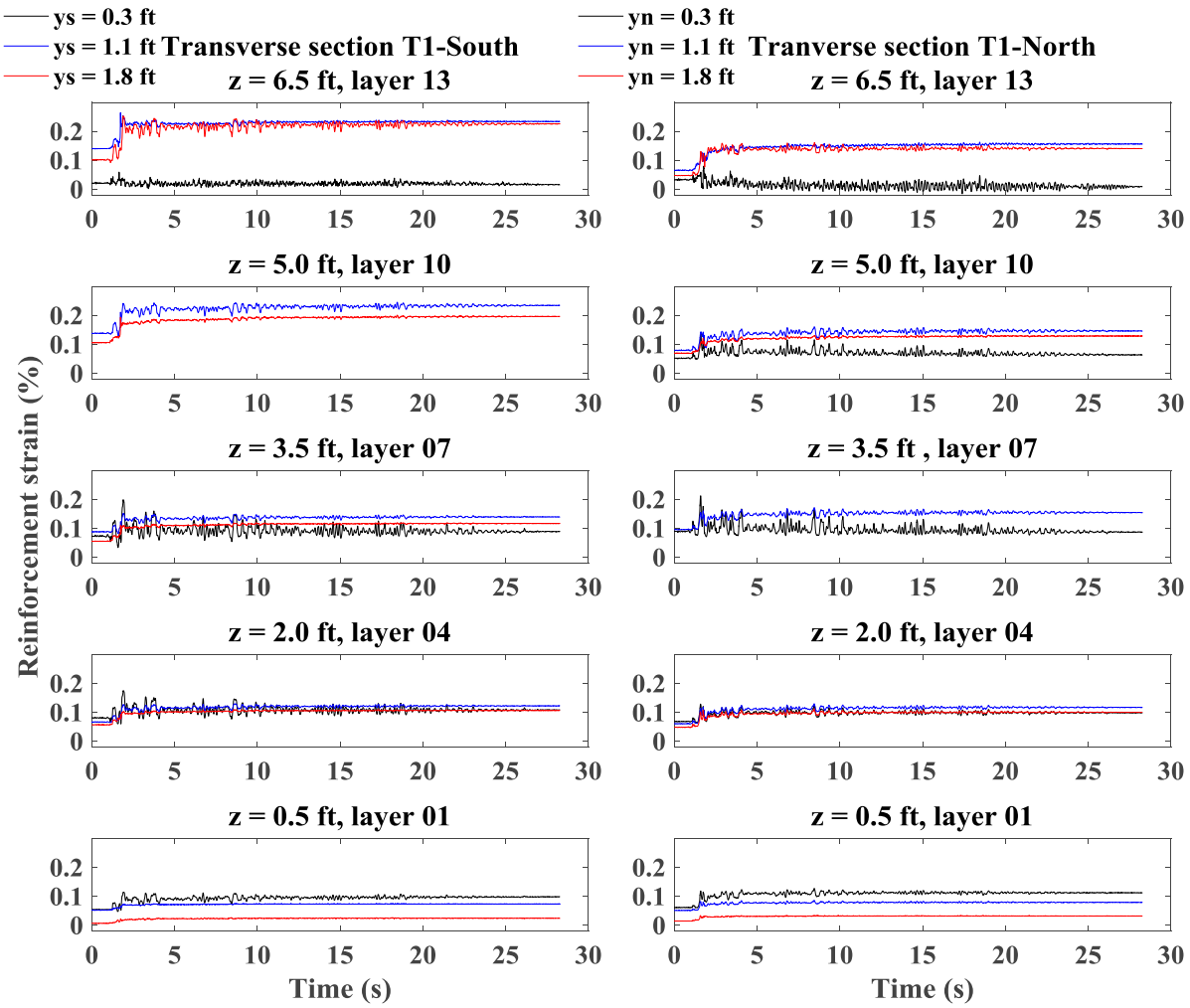

Figure A1.355 Time histories of reinforcement strain for transverse sections T1-South and T1-North.

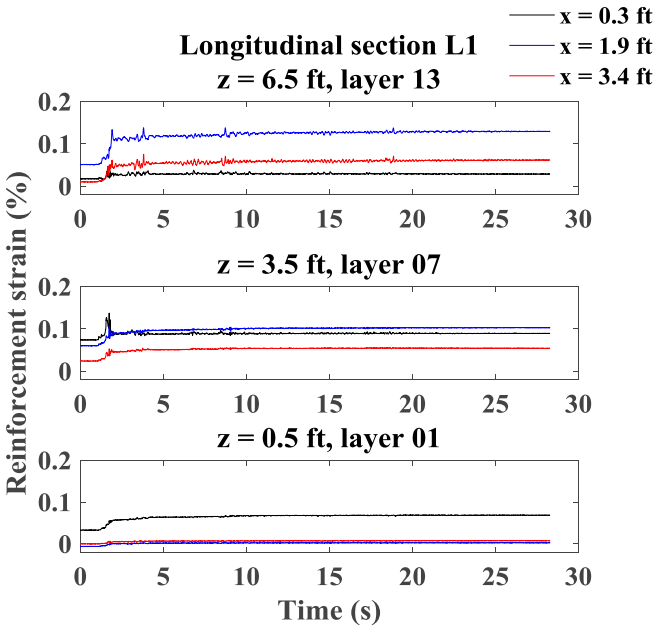

Figure A1.356 Time histories of reinforcement strain for longitudinal section L1.

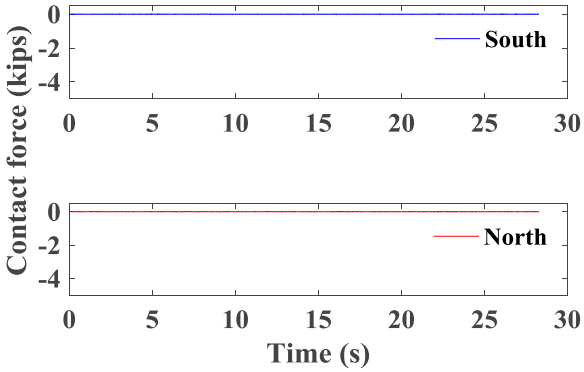

Figure A1.357 Time histories of contact force between bridge seat and bridge beam.

A1.6.2 Maule Motion

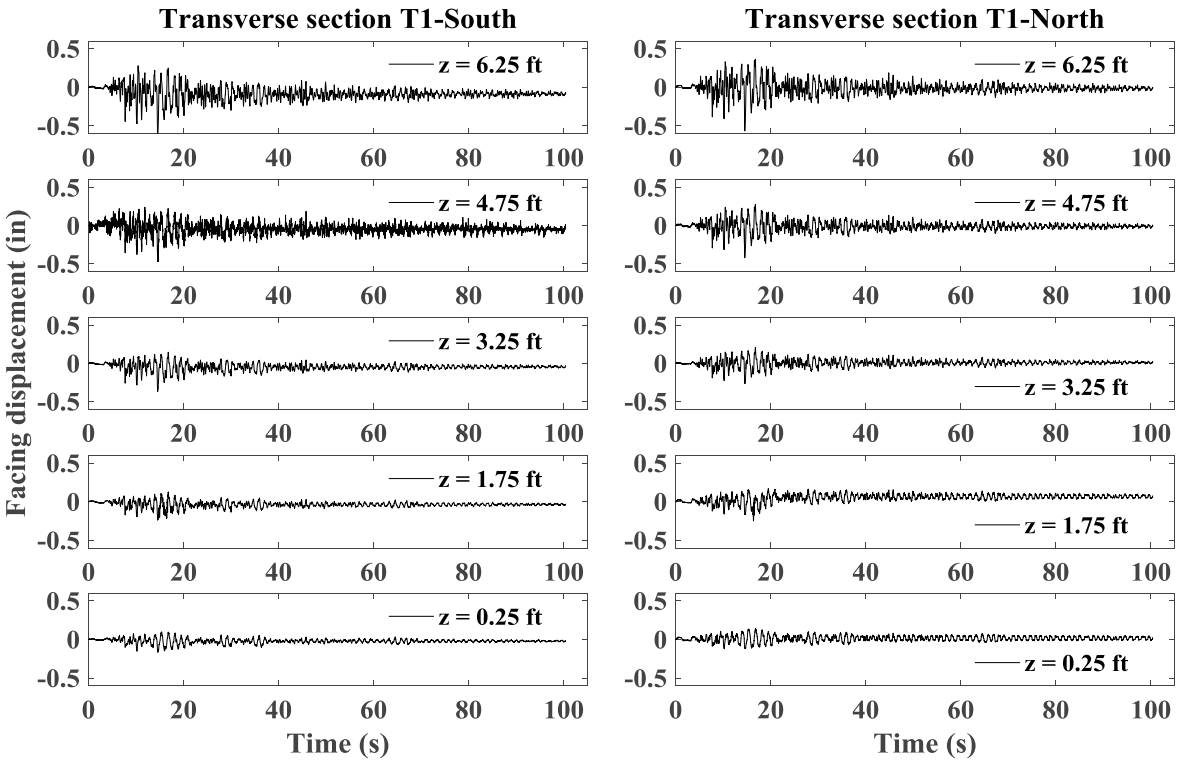

Figure A1.358 Time histories of incremental facing displacement for transverse sections T1-South and T1-North.

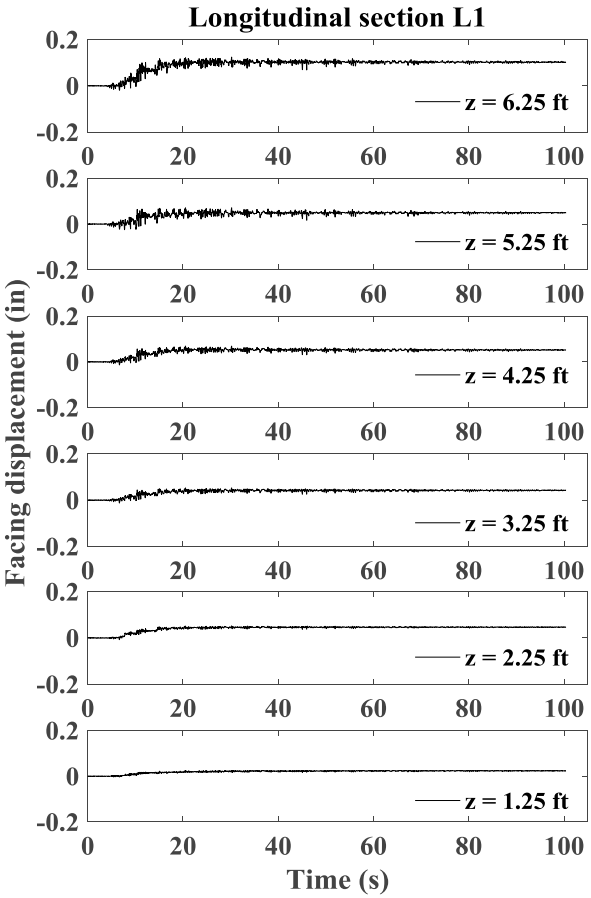

Figure A1.359 Time histories of incremental facing displacement for longitudinal section L1.

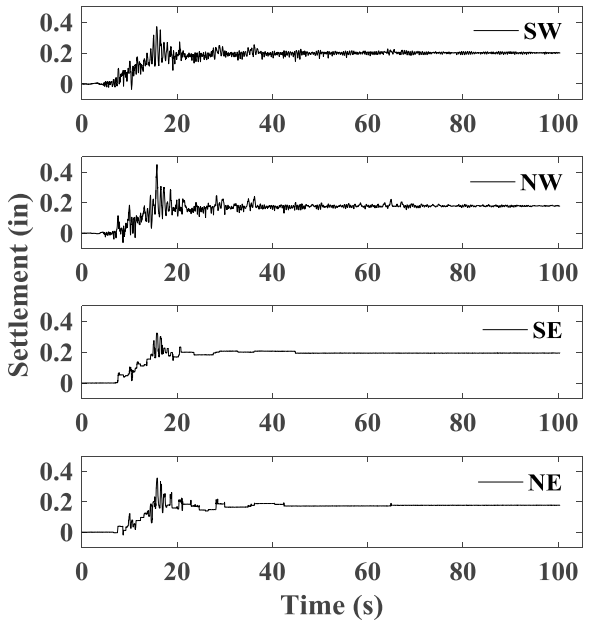

Figure A1.360 Time histories of incremental settlement for bridge seat.

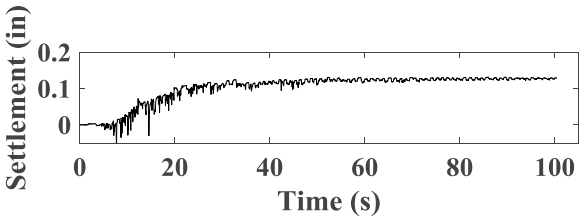

Figure A1.361 Time histories of incremental settlement for backfill soil in upper wall.

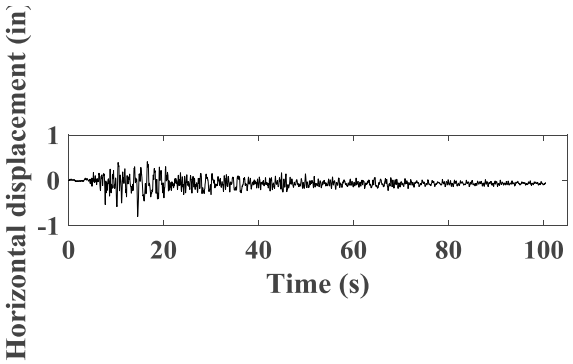

Figure A1.362 Time histories of incremental horizontal displacement for bridge seat.

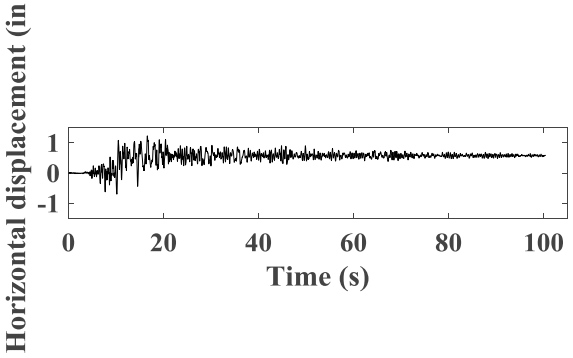

Figure A1.363 Time histories of incremental horizontal displacement for bridge beam.

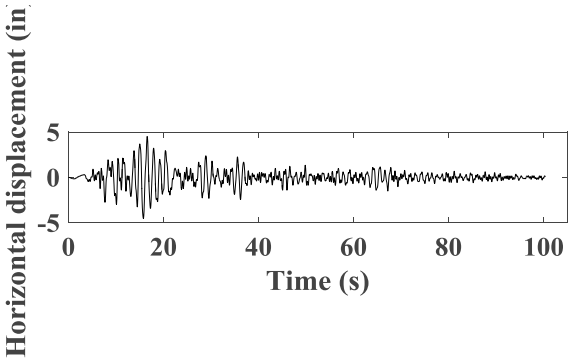

Figure A1.364 Time histories of horizontal displacement for support wall.

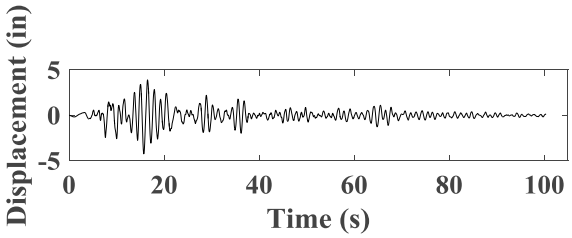

Figure A1.365 Time histories of horizontal displacement for shaking table.

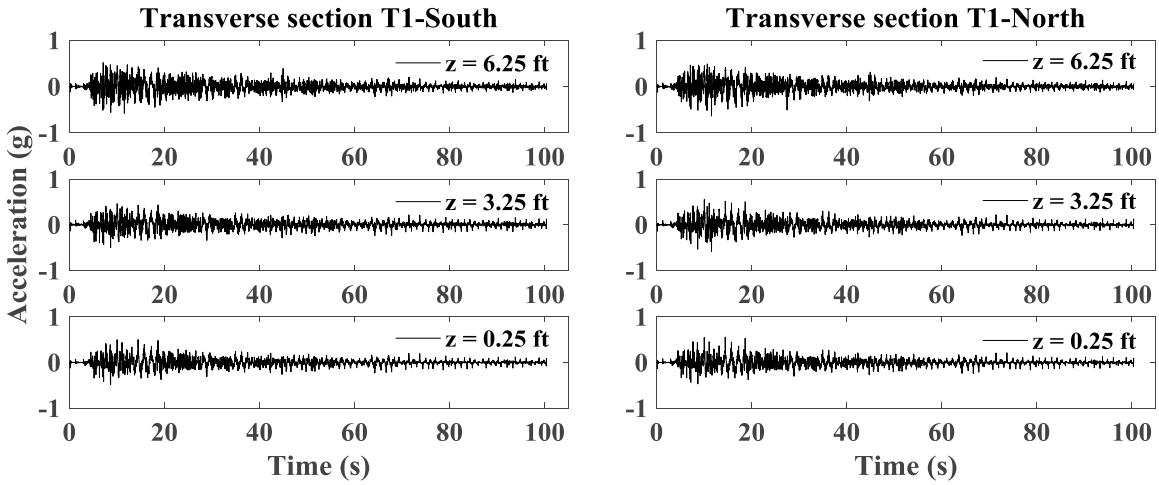

Figure A1.366 Time histories of acceleration for wall facing in transverse sections T1-South and T1-North.

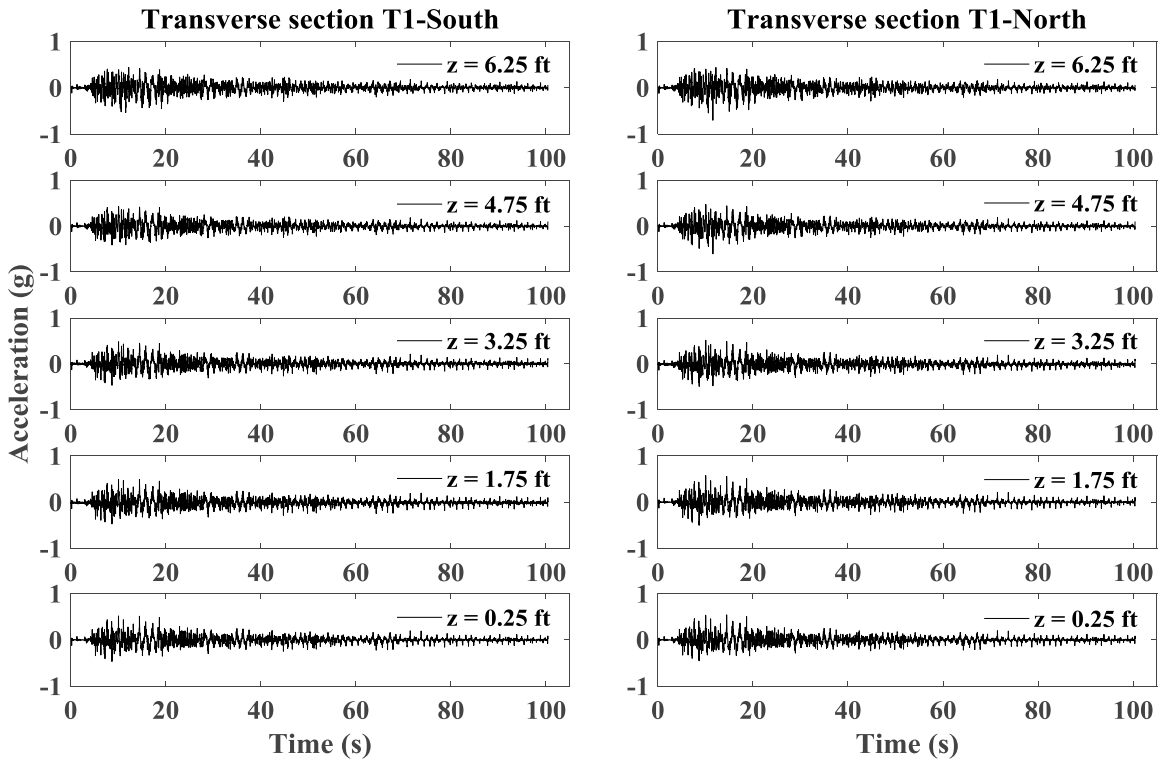

Figure A1.367 Time histories of acceleration for reinforced soil zone in transverse sections T1-South and T1-North.

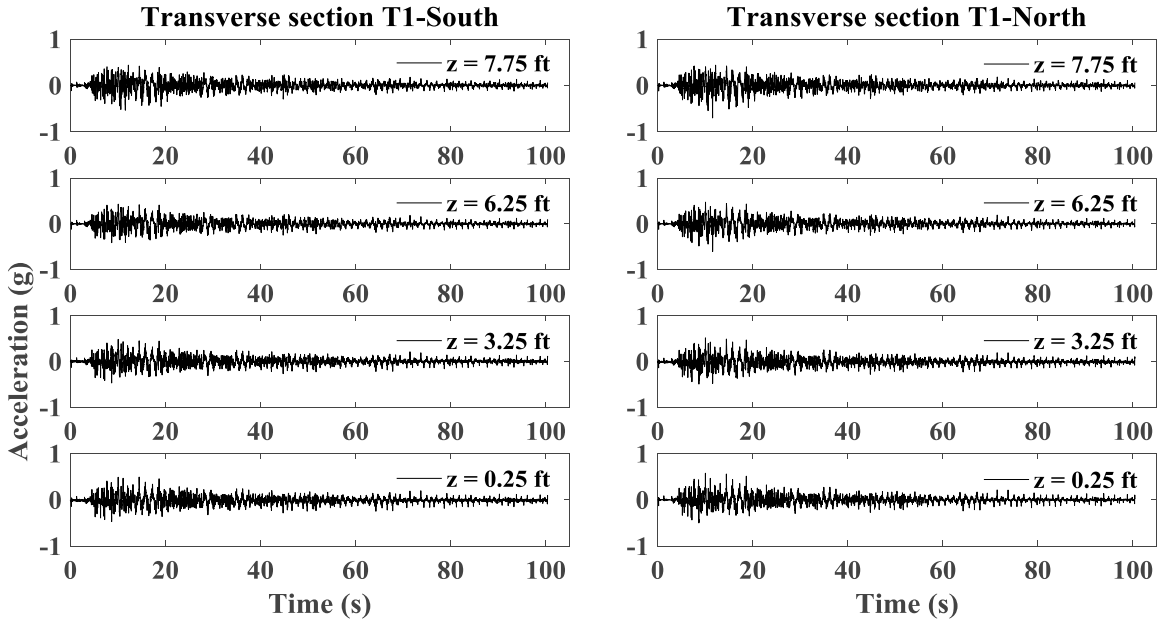

Figure A1.368 Time histories of acceleration for reinforced soil zone in transverse section T2-South and T2-North.

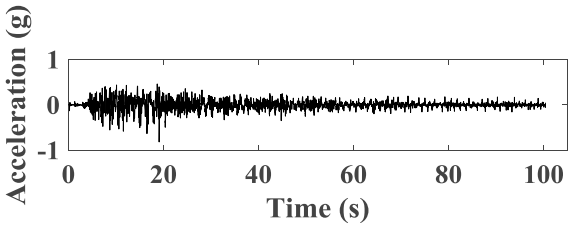

Figure A1.369 Time histories of acceleration for bridge seat.

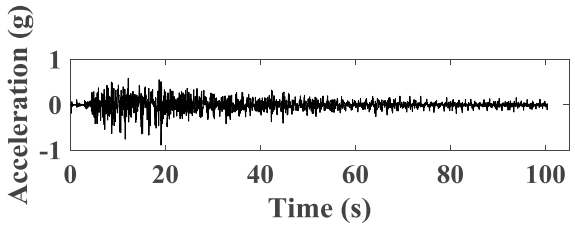

Figure A1.370 Time histories of acceleration for bridge beam.

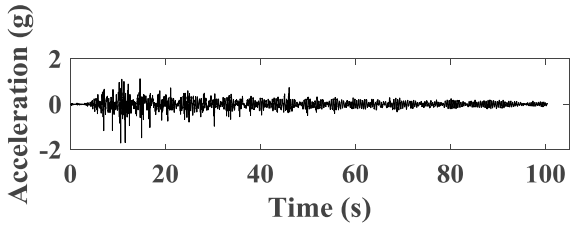

Figure A1.371 Time histories of acceleration for support wall.

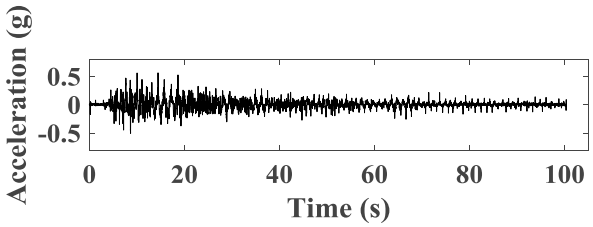

Figure A1.372 Time histories of acceleration for shaking table.

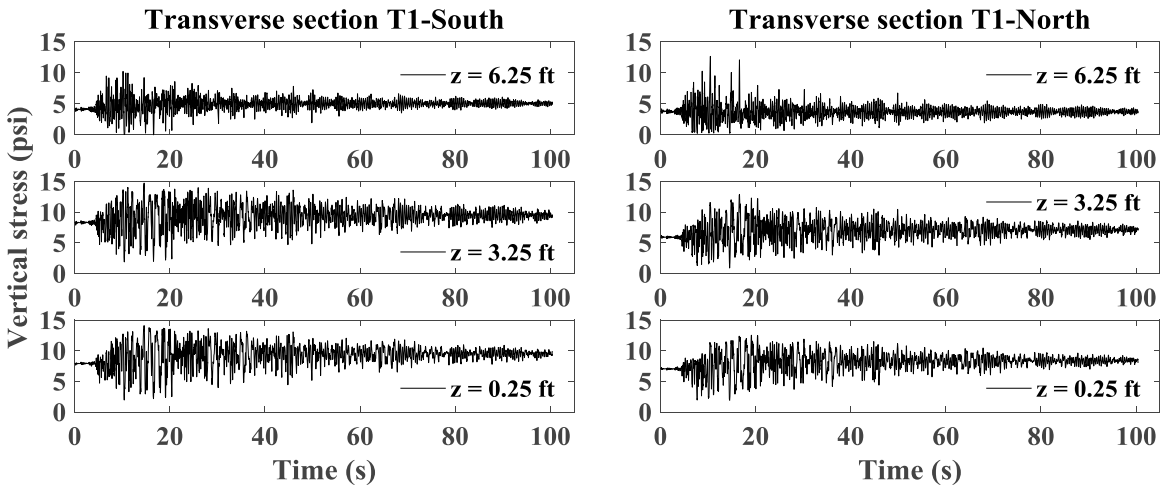

Figure A1.373 Time histories of vertical stress behind wall facing.

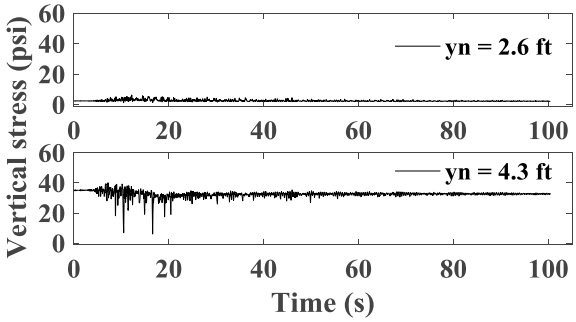

Figure A1.374 Time histories of vertical stress under bridge seat.

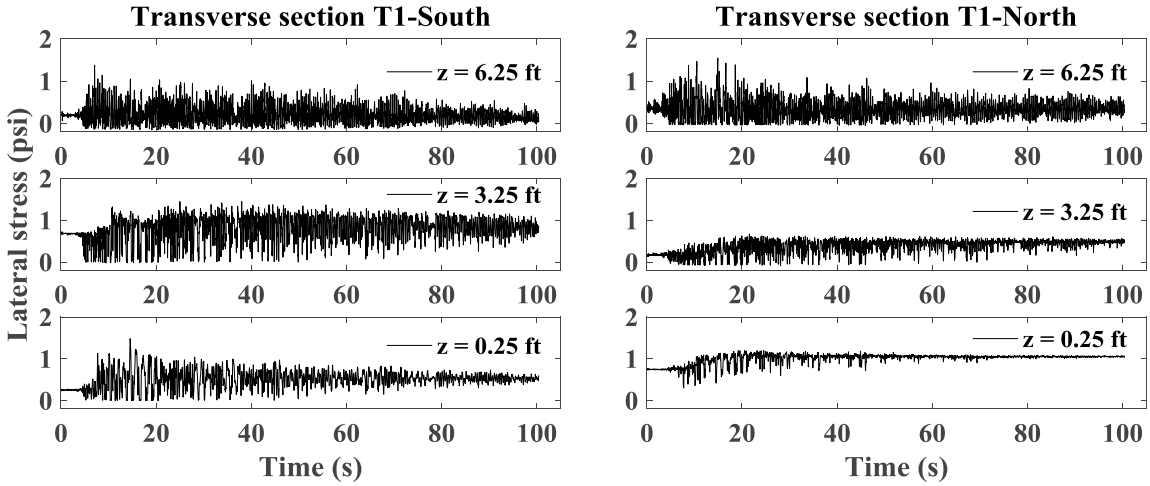

Figure A1.375 Time histories of lateral stress behind wall facing.

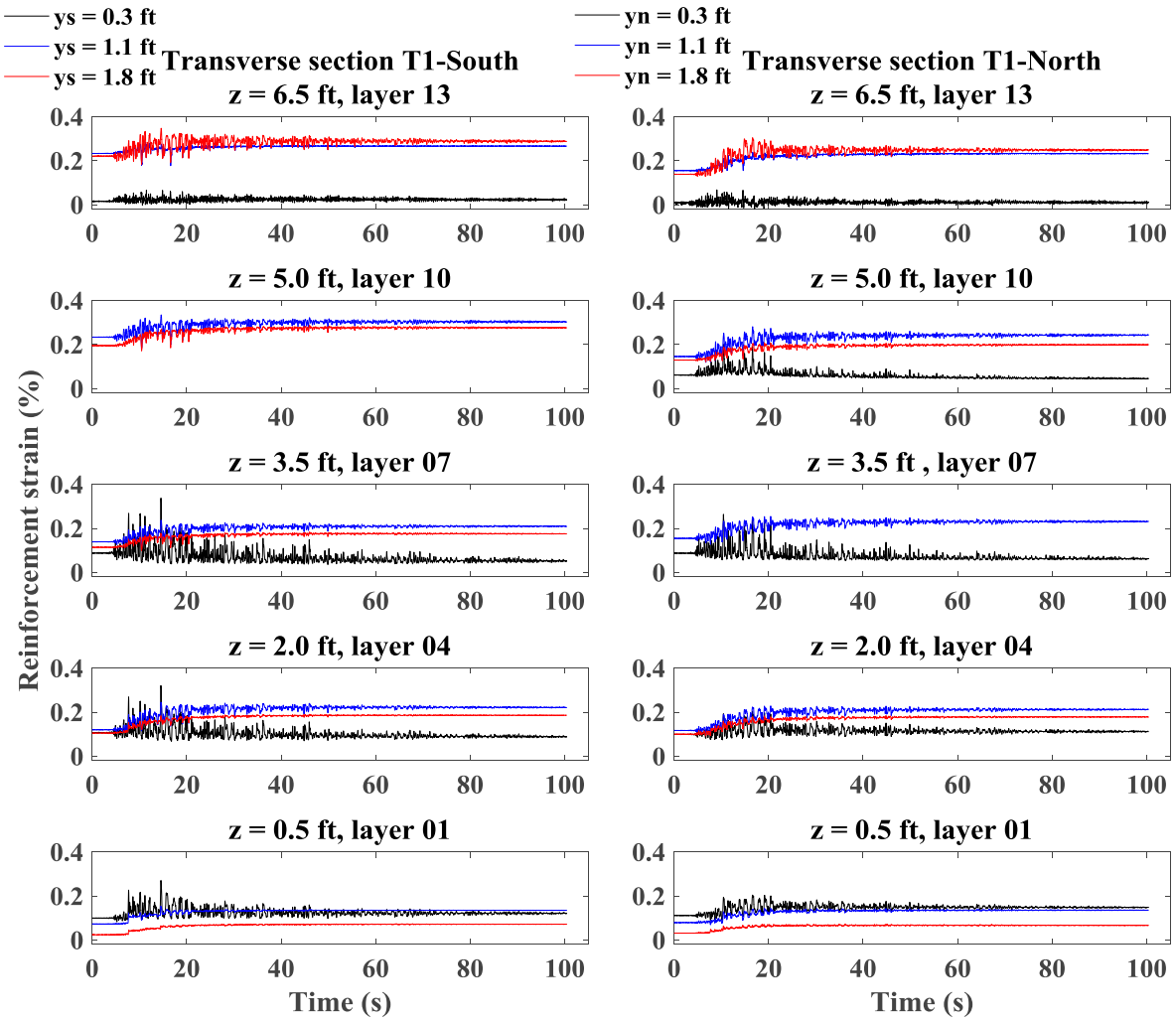

Figure A1.376 Time histories of reinforcement strain for transverse sections T1-South and T1-North.

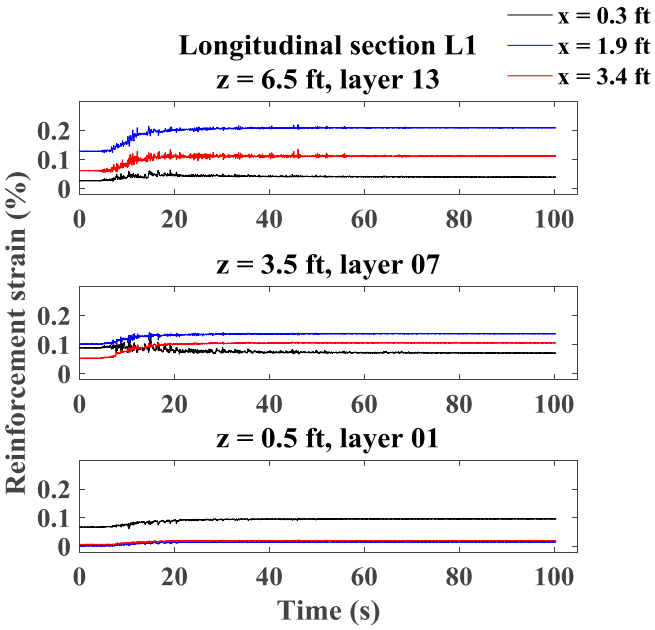

Figure A1.377 Time histories of reinforcement strain for longitudinal section L1.

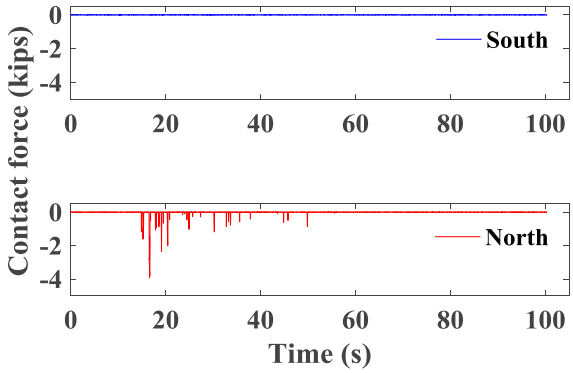

Figure A1.378 Time histories of contact force between bridge seat and bridge beam.

A1.6.3 Northridge Motion

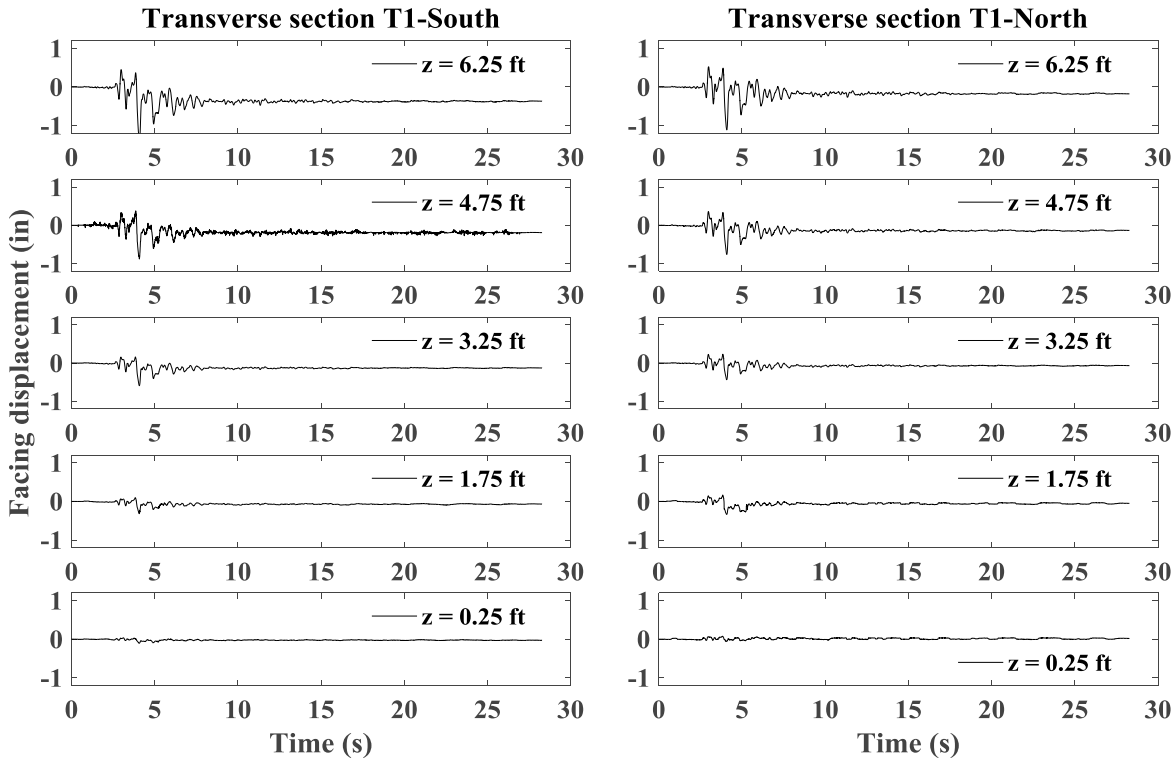

Figure A1.379 Time histories of incremental facing displacement for transverse sections T1-South and T1-North.

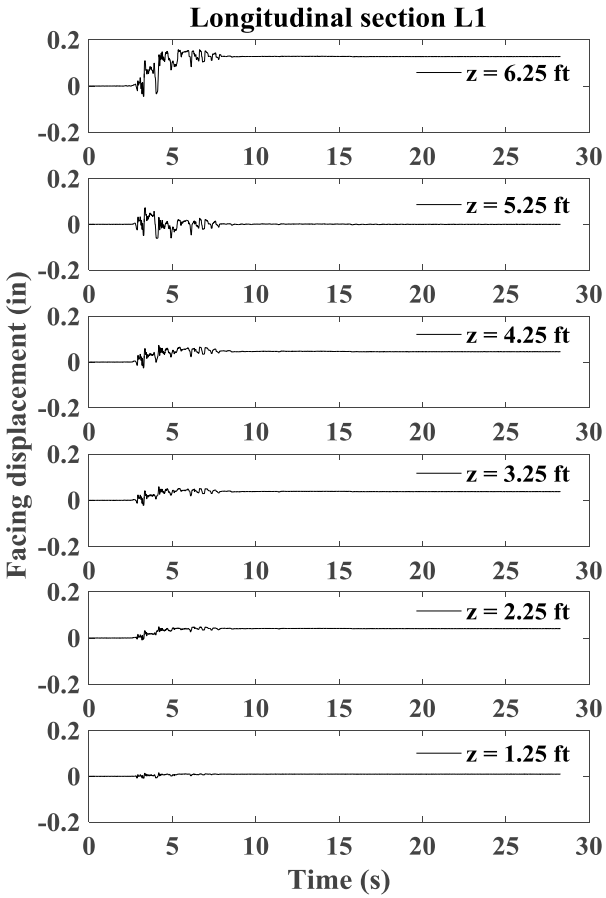

Figure A1.380 Time histories of incremental facing displacement for longitudinal section L1.

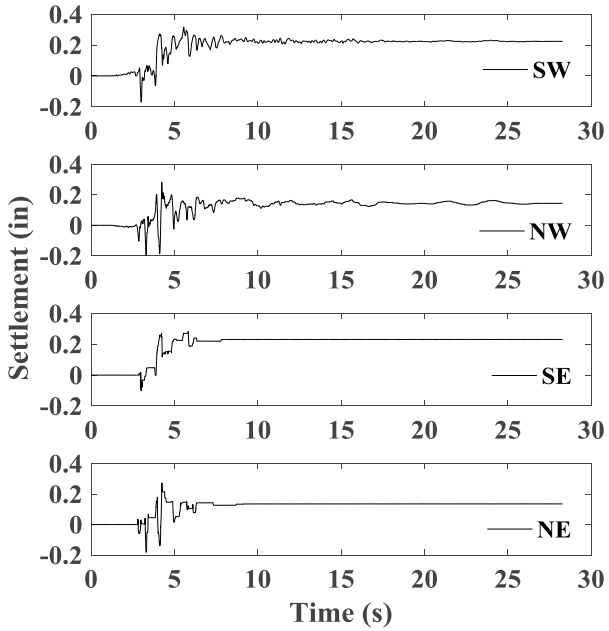

Figure A1.381 Time histories of incremental settlement for bridge seat.

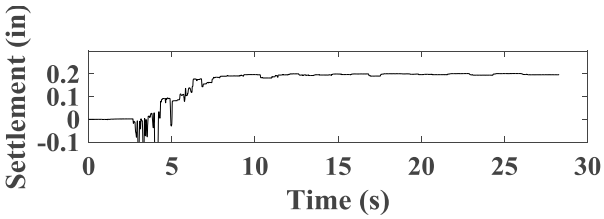

Figure A1.382 Time histories of incremental settlement for backfill soil in upper wall.

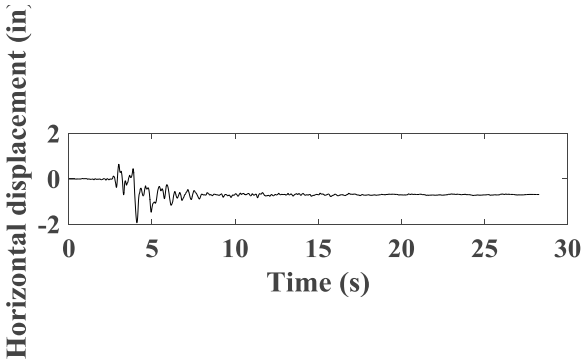

Figure A1.383 Time histories of incremental horizontal displacement for bridge seat.

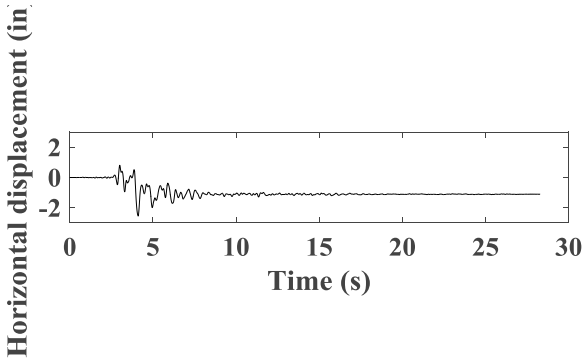

Figure A1.384 Time histories of incremental horizontal displacement for bridge beam.

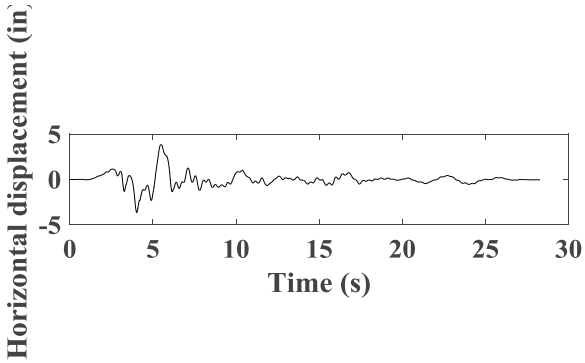

Figure A1.385 Time histories of horizontal displacement for support wall.

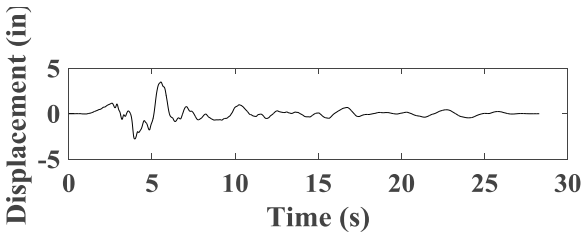

Figure A1.386 Time histories of horizontal displacement for shaking table.

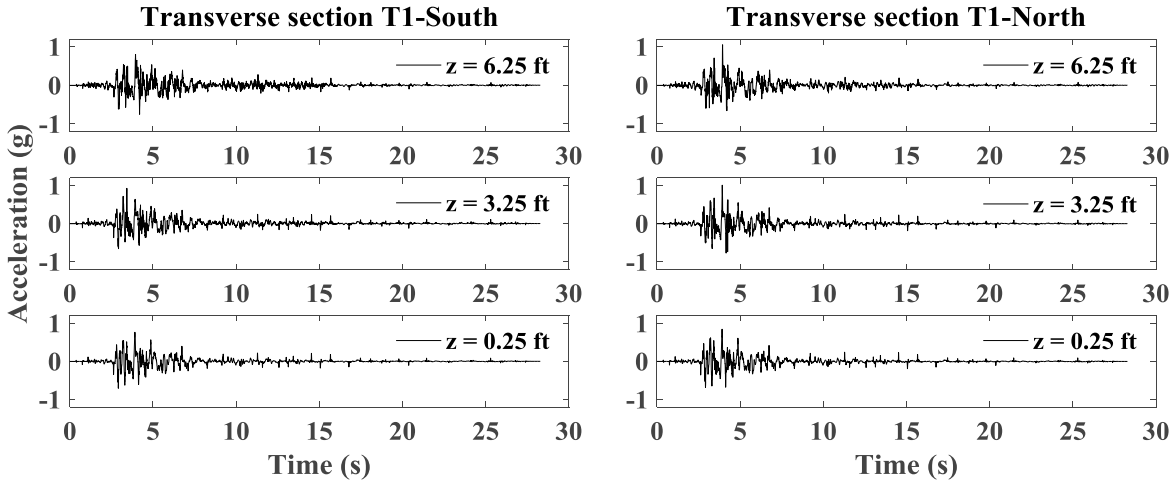

Figure A1.387 Time histories of acceleration for wall facing in transverse sections T1-South and T1-North.

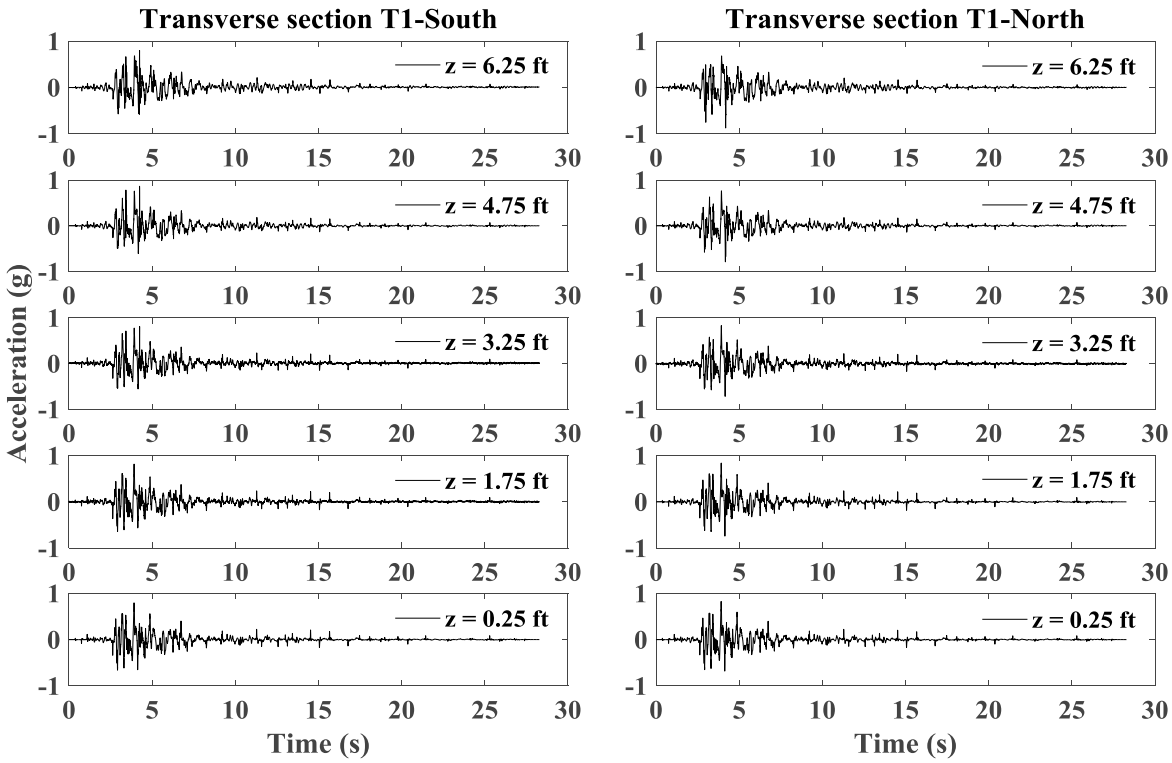

Figure A1.388 Time histories of acceleration for reinforced soil zone in transverse sections T1-South and T1-North.

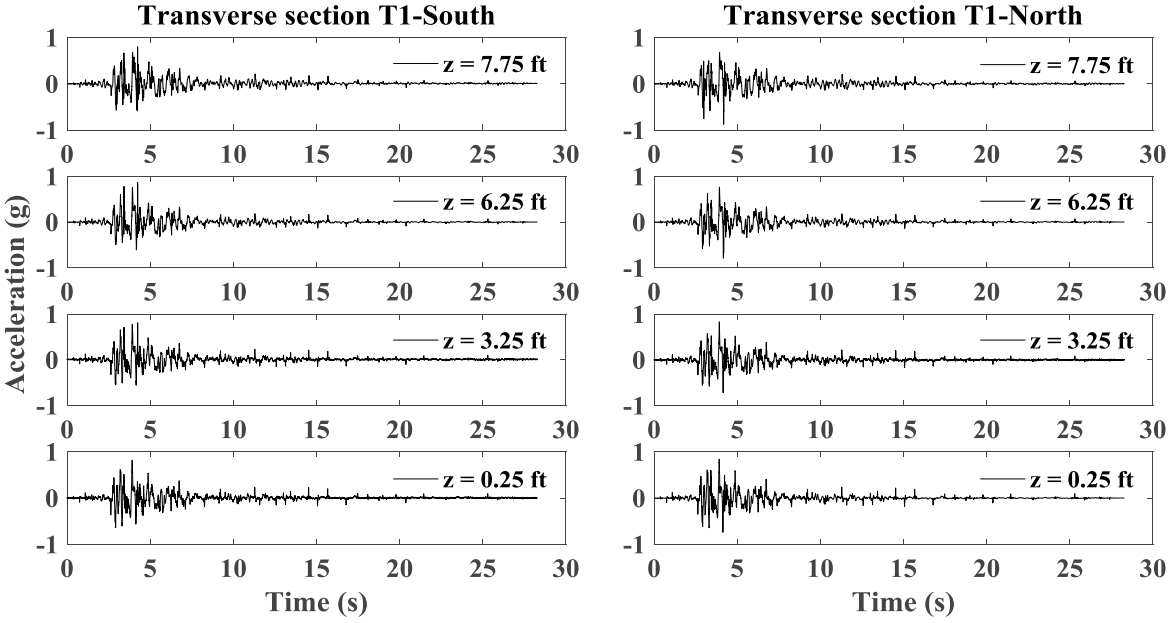

Figure A1.389 Time histories of acceleration for reinforced soil zone in transverse section T2-South and T2-North.

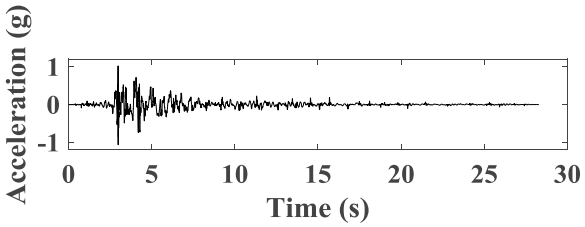

Figure A1.390 Time histories of acceleration for bridge seat.

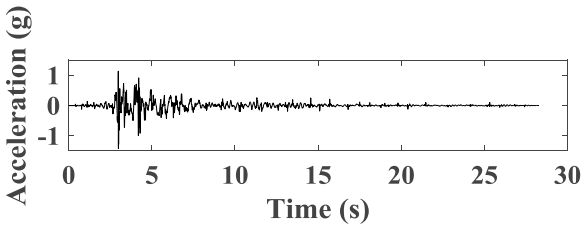

Figure A1.391 Time histories of acceleration for bridge beam.

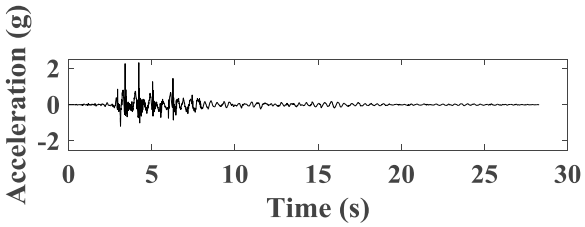

Figure A1.392 Time histories of acceleration for support wall.

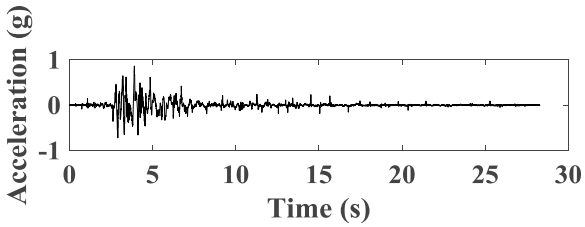

Figure A1.393 Time histories of acceleration for shaking table.

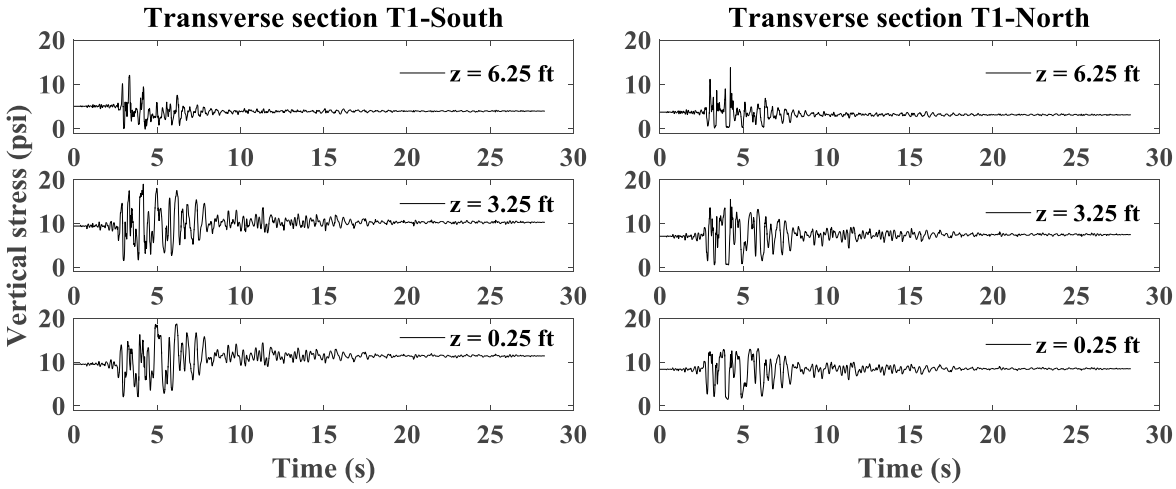

Figure A1.394 Time histories of vertical stress behind wall facing.

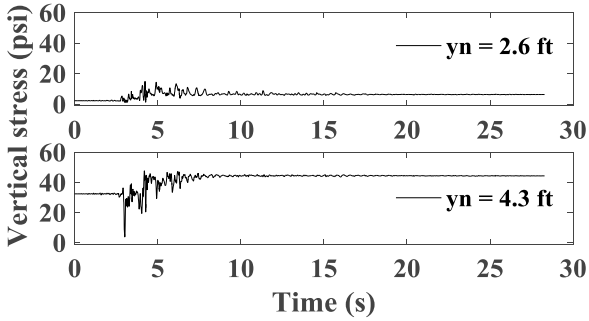

Figure A1.395 Time histories of vertical stress under bridge seat.

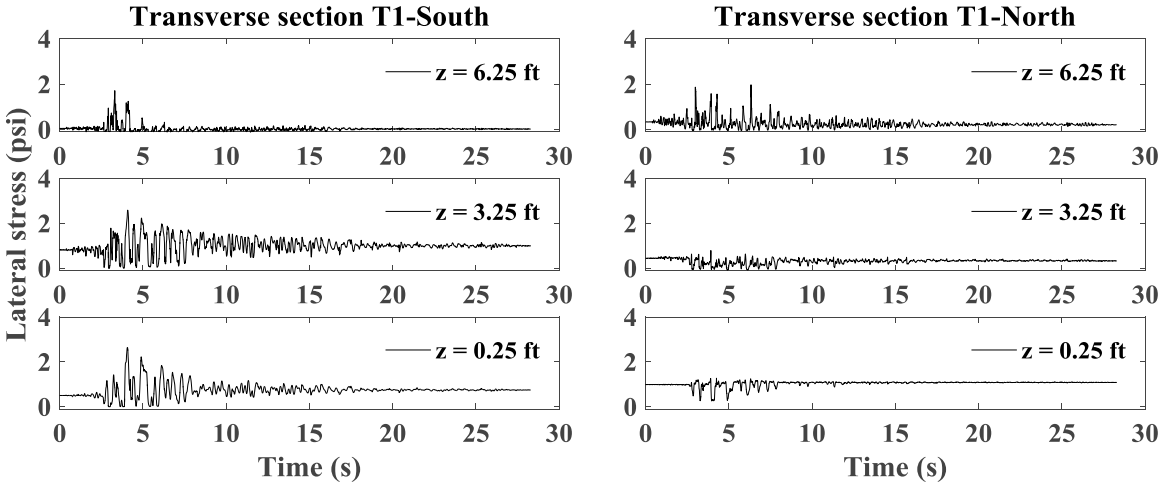

Figure A1.396 Time histories of lateral stress behind wall facing.

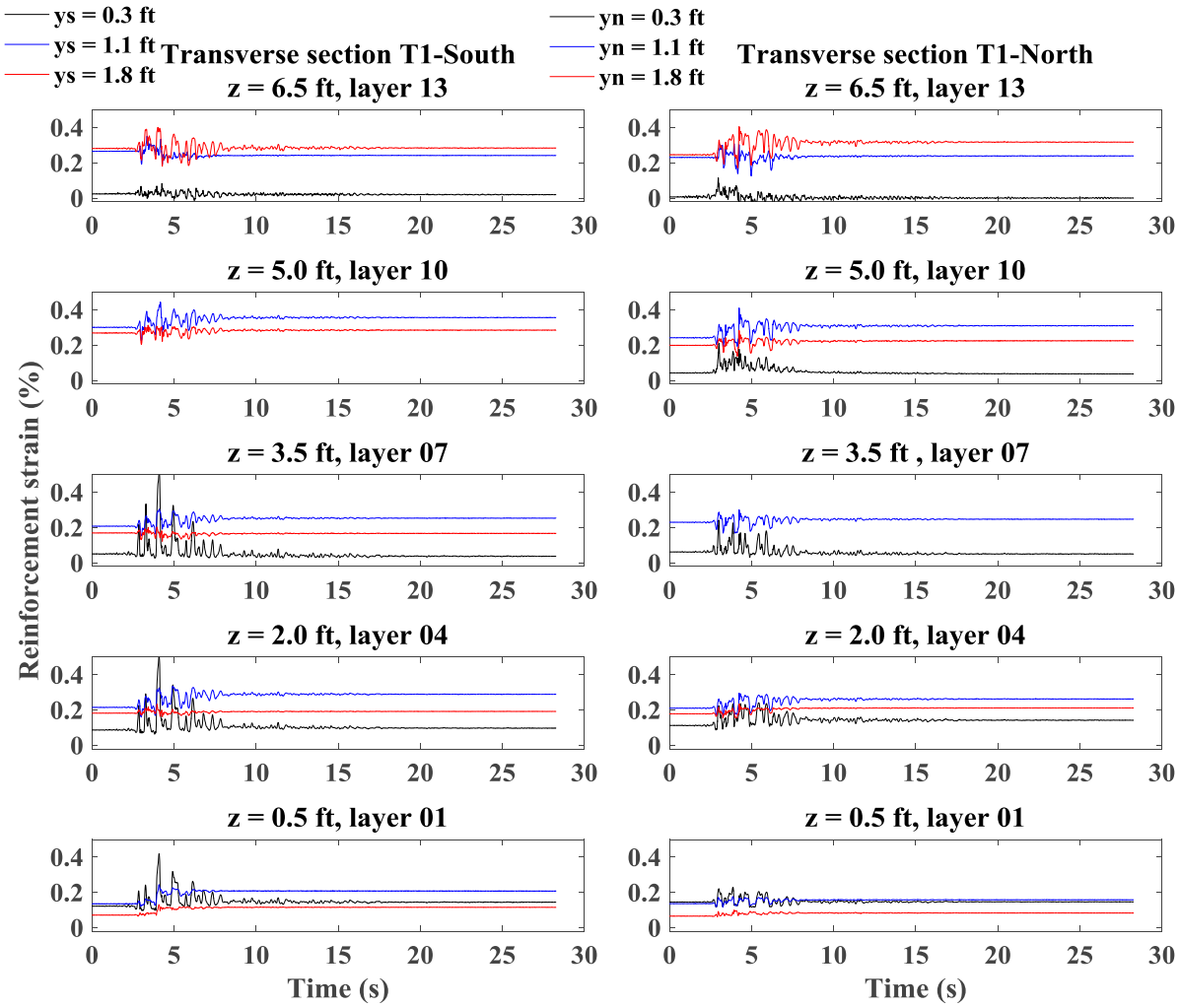

Figure A1.397 Time histories of reinforcement strain for transverse sections T1-South and T1-North.

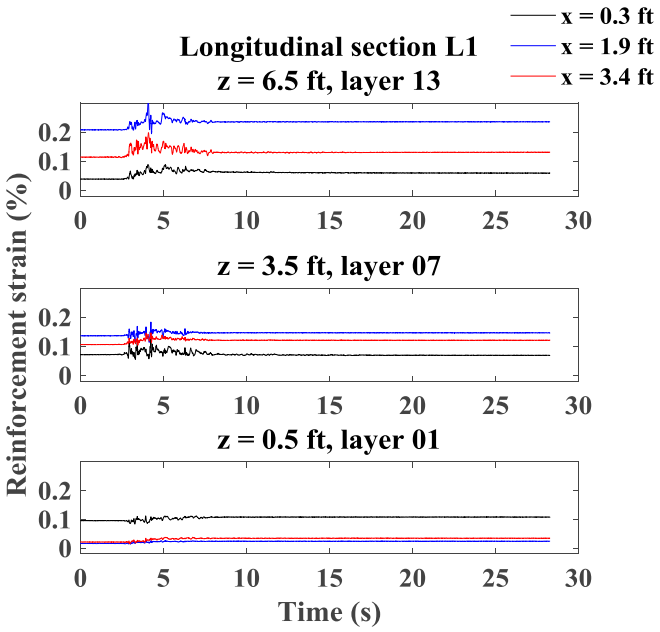

Figure A1.398 Time histories of reinforcement strain for longitudinal section L1.

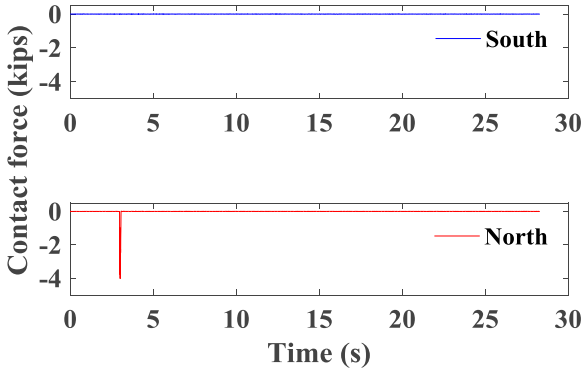

Figure A1.399 Time histories of contact force between bridge seat and bridge beam.

Appendix 2 – Photographs

A2.1 General Observations from Photographs

The next section of this appendix present photographs from different stages of the six different tests, including during construction, after construction, and after application of different earthquake motions. The construction photographs show the construction and instrumentation details for the MSE bridge abutment specimens. The post-construction photographs show the constructed specimens from different vantage points. The post-shaking photographs show the conditions of the MSE bridge abutment specimens after selected input motions. Some general observations of minor testing issues can be made from the visual observations of the MSE bridge abutment specimens:

- It was observed that some backfill soil escaped from the corners of the lower MSE wall and upper wall after the earthquake shaking events. However, this loss of backfill soil (which was collected on the shaking table) amounted only to a negligible fraction of the total backfill soil within the wall. It is not expected that this loss of material significantly affected the bridge seat settlement measurements associated with the reinforced backfill soil under the bridge seat observed during subsequent shaking events.
- During shaking, the facing blocks near the top corners of the lower MSE walls experienced relatively large movements, and the uppermost corner block fell off in some tests as it was not grouted in place.
- Tension cracks were observed to form in the backfill soil in the upper wall after several shaking events, and the width and depth increased as the shaking motion proceeded, and were present due to apparent cohesion in the unsaturated backfill soil. The locations of the tension cracks were either directly behind the bridge seat or at the transition point between the reinforced and retained soil zones where there was a break in the transverse reinforcements from the side walls.

These observations of minor testing issues are more obvious in Tests 3, 4, and 5 due to the lower global stiffness of the specimens for Tests 3 and 4, and due to the smaller contact area between the backfill material and steel mesh for Test 5. Assessment of the instrumentation results confirm that these minor testing issues did not have a significant effect on the performance of the MSE bridge abutment specimens, although they may be useful in discerning some trends in the data when comparing with forthcoming numerical simulations.

A2.2 Construction Photographs

Figure A2.1 Reaction wall.

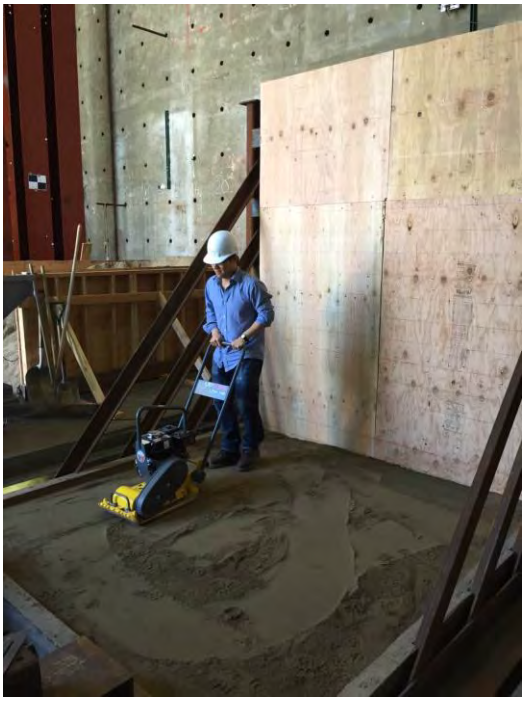

Figure A2.2 Compaction of the foundation soil layer.

Figure A2.3 Level of the first course of facing blocks (with 1 inch elevation offset).

Figure A2.4 Longitudinal reinforcement layer.

Figure A2.5 Transverse reinforcement layers.

Figure A2.6 Transverse reinforcement layers for Test 5.

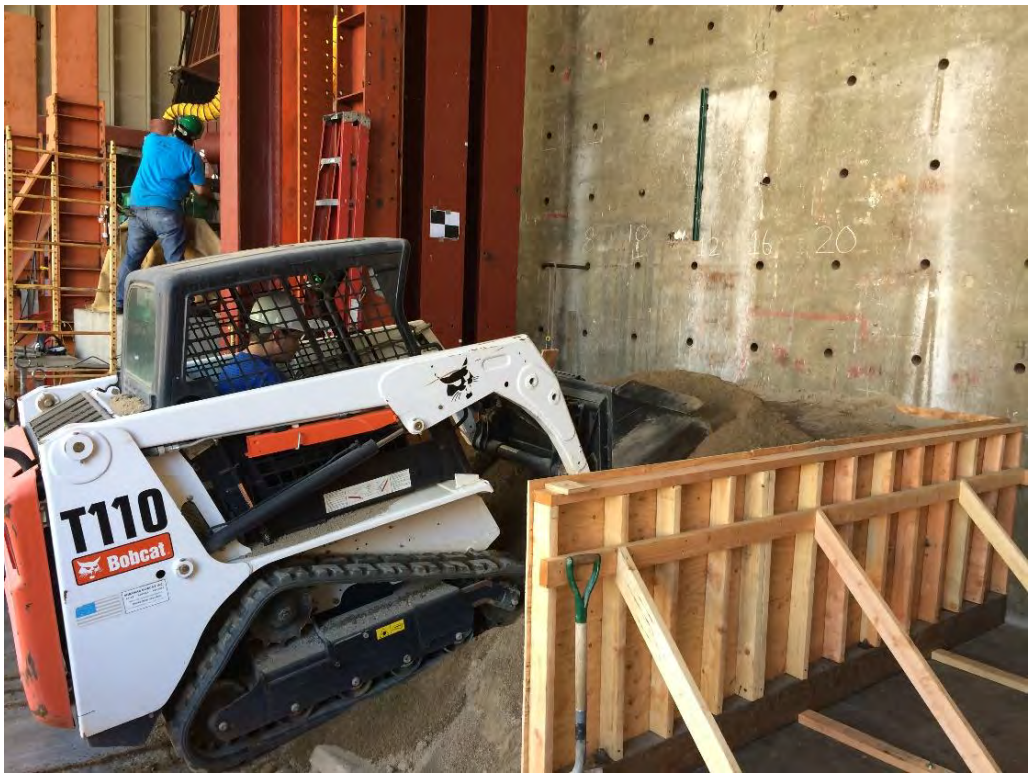

Figure A2.7 Bobcat to load sand.


Figure A2.8 Concrete hopper to dump sand.

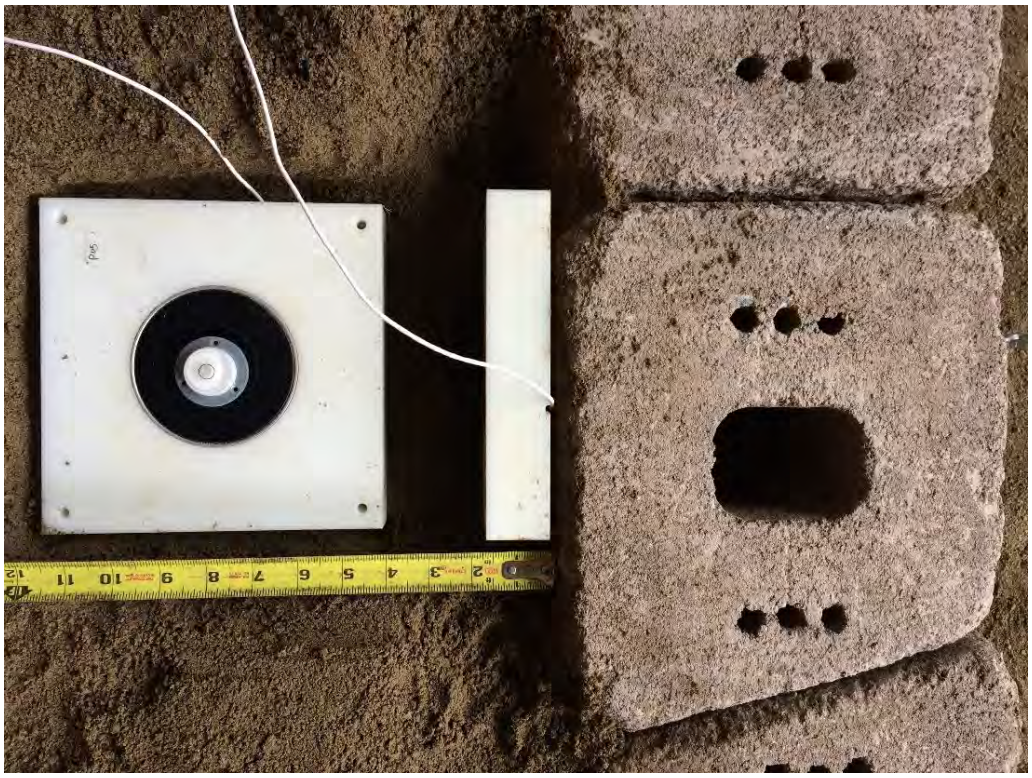

Figure A2.9 Total pressure cells placed behind wall facing.

Figure A2.10 String potentiometer connected during construction.

Figure A2.11 Sand cone test to measure compaction density.

Figure A2.12 Placement of plastic cover to prevent loss of moisture.

Figure A2.13 End of construction of the lower wall.

Figure A2.14 End of construction of the MSE abutment.

Figure A2.15 Ball bearings on the stainless steel plate.

Figure A2.16 Support wall on the sliding platform.

Figure A2.17 Placement of the bridge beam.

Figure A2.18 End of construction of the bridge system.

Figure A2.19 Accelerometers on the facing block and bridge seat.

Figure A2.20 Load cells embedded at the end of bridge beam.

A2.2 Post-Construction Photographs

Figure A2.21 Constructed specimen for Test 1.

Figure A2.22 Constructed specimen for Test 1.

Figure A2.23 Constructed specimen for Test 1.

Figure A2.24 Constructed specimen for Test 1.

Figure A2.25 Constructed specimen for Test 2.

Figure A2.26 Constructed specimen for Test 3.

Figure A2.27 Constructed specimen for Test 4.

Figure A2.28 Constructed specimen for Test 4.

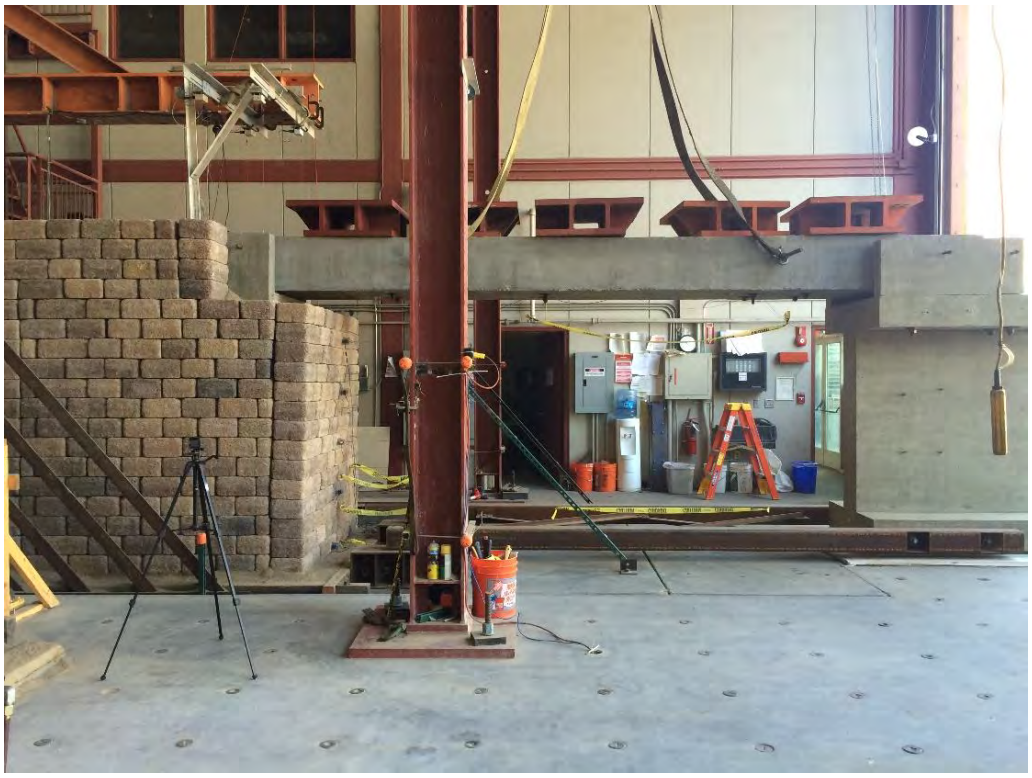

Figure A2.29 Constructed specimen for Test 5.

Figure A2.30 Constructed specimen for Test 6.

Figure A2.31 Constructed specimen for Test 6.

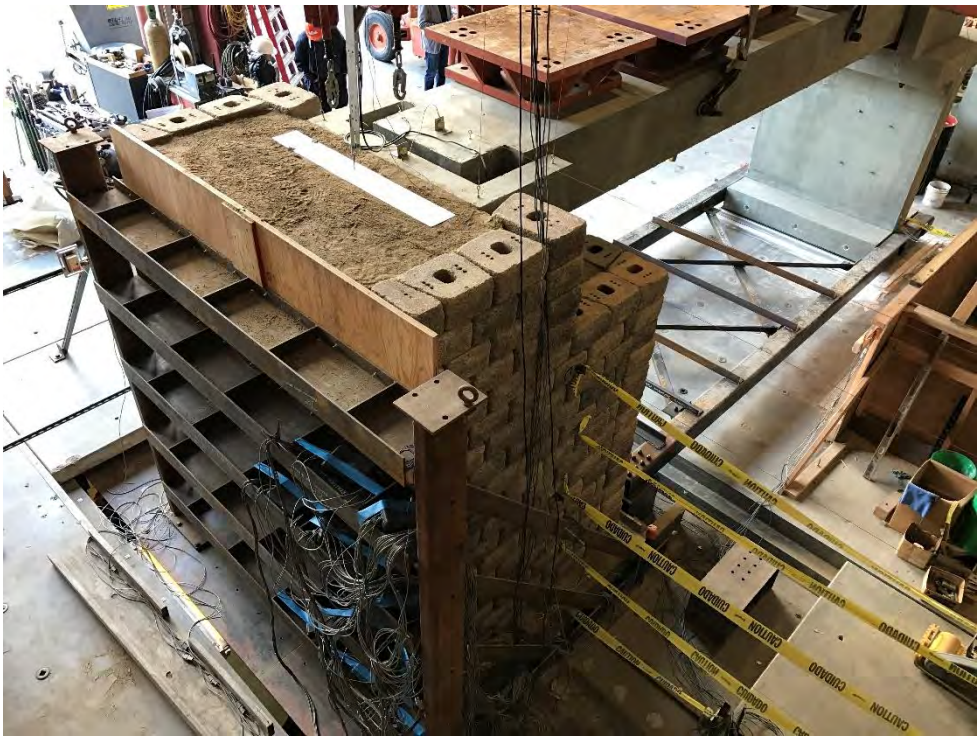

Figure A2.32 Constructed specimen for Test 6.

A2.3 Post-Shaking Photographs

Figure A2.33 Top view after the Maule motion for Test 1.

Figure A2.34 Corner of the abutment after all shaking motions for Test 1.

Figure A2.35 Upper wall backfill surface after all shaking motions for Test 1.

Figure A2.36 Minor crack after the Northridge motion for Test 2.

Figure A2.37 Crack after all shaking motions for Test 2.

Figure A2.38 Top view after the Maule motion for Test 3.

Figure A2.39 Top view after the Northridge motion for Test 3.

Figure A2.40 Top view after all shaking motions for Test 3.

Figure A2.41 Movements of the top corner blocks after all shaking motions for Test 3.

Figure A2.42 Top view after the Maule motion for Test 4.

Figure A2.43 Top view after the Northridge motion for Test 4.

Figure A2.44 Gaps between the top corner blocks after the Northridge motion for Test 4.

Figure A2.45 Top view after the sinusoidal motion for Test 4.

Figure A2.46 Top view after the Maule motion for Test 5.

Figure A2.47 Top view after the Northridge motion for Test 5.

Figure A2.48 Top view after all shaking motions for Test 5.

Figure A2.49 Upper wall backfill surface after the Maule motion for Test 6.

Figure A2.50 Minor crack after the Northridge motion for Test 6.